frontiers | Research Topics

Air pollution and climate change: Interactions and co-mitigation

Edited by
Shupeng Zhu, Haofei Yu, Michael MacKinnon, Yuzhong Zhang and Yuqiang Zhang

Published in
Frontiers in Environmental Science
Frontiers in Ecology and Evolution

ISSN 1664-8714
ISBN 978-2-83251-137-4
DOI 10.3389/978-2-83251-137-4

About Frontiers

Frontiers is more than just an open access publisher of scholarly articles: it is a pioneering approach to the world of academia, radically improving the way scholarly research is managed. The grand vision of Frontiers is a world where all people have an equal opportunity to seek, share and generate knowledge. Frontiers provides immediate and permanent online open access to all its publications, but this alone is not enough to realize our grand goals.

Frontiers journal series

The Frontiers journal series is a multi-tier and interdisciplinary set of open-access, online journals, promising a paradigm shift from the current review, selection and dissemination processes in academic publishing. All Frontiers journals are driven by researchers for researchers; therefore, they constitute a service to the scholarly community. At the same time, the *Frontiers journal series* operates on a revolutionary invention, the tiered publishing system, initially addressing specific communities of scholars, and gradually climbing up to broader public understanding, thus serving the interests of the lay society, too.

Dedication to quality

Each Frontiers article is a landmark of the highest quality, thanks to genuinely collaborative interactions between authors and review editors, who include some of the world's best academicians. Research must be certified by peers before entering a stream of knowledge that may eventually reach the public - and shape society; therefore, Frontiers only applies the most rigorous and unbiased reviews. Frontiers revolutionizes research publishing by freely delivering the most outstanding research, evaluated with no bias from both the academic and social point of view. By applying the most advanced information technologies, Frontiers is catapulting scholarly publishing into a new generation.

What are Frontiers Research Topics?

Frontiers Research Topics are very popular trademarks of the *Frontiers journals series*: they are collections of at least ten articles, all centered on a particular subject. With their unique mix of varied contributions from Original Research to Review Articles, Frontiers Research Topics unify the most influential researchers, the latest key findings and historical advances in a hot research area.

Find out more on how to host your own Frontiers Research Topic or contribute to one as an author by contacting the Frontiers editorial office: frontiersin.org/about/contact

Air pollution and climate change: Interactions and co-mitigation

Topic editors

Shupeng Zhu — University of California, Irvine, United States
Haofei Yu — University of Central Florida, United States
Michael MacKinnon — University of California, Irvine, United States
Yuzhong Zhang — Westlake University, China
Yuqiang Zhang — Shandong University, China

Citation

Zhu, S., Yu, H., MacKinnon, M., Zhang, Y., Zhang, Y., eds. (2023). *Air pollution and climate change: Interactions and co-mitigation*. Lausanne: Frontiers Media SA. doi: 10.3389/978-2-83251-137-4

Table of contents

frontiers | Frontiers in Environmental Science

TYPE Editorial
PUBLISHED 12 December 2022
DOI 10.3389/fenvs.2022.1105656

OPEN ACCESS

EDITED AND REVIEWED BY
Hong Liao,
Nanjing University of Information Science and Technology, China

*CORRESPONDENCE
Shupeng Zhu,
sz@apep.uci.edu

SPECIALTY SECTION
This article was submitted to Atmosphere and Climate, a section of the journal Frontiers in Environmental Science

RECEIVED 22 November 2022
ACCEPTED 29 November 2022
PUBLISHED 12 December 2022

CITATION
Zhu S, Yu H, Zhang Y, Zhang Y and Kinnon MM (2022), Editorial: Air pollution and climate change: Interactions and co-mitigation. *Front. Environ. Sci.* 10:1105656. doi: 10.3389/fenvs.2022.1105656

Editorial: Air pollution and climate change: Interactions and co-mitigation

Shupeng Zhu[1]*, Haofei Yu[2], Yuqiang Zhang[3], Yuzhong Zhang[4] and Michael Mac Kinnon[1]

[1]Advanced Power and Energy Program, University of California, Irvine, Irvine, CA, United States, [2]Department of Civil, Environmental and Construction Engineering, University of Central Florida, Orlando, FL, United States, [3]Environment Research Institute, Shandong University, Jinan, Shandong, China, [4]Key Laboratory of Coastal Environment and Resources of Zhejiang Province, School of Engineering, Westlake University, Hangzhou, China

KEYWORDS

air pollution, climate change, co-mitigation, PM2.5, ozone, GHG (green house gas) emission

Editorial on the Research Topic
Air pollution and climate change: Interactions and co-mitigation

Introduction

Air pollution and climate change are two important environmental factors that are tightly interconnected. Climate change can impact the physical, chemical, and biological processes associated with air pollution. On the other hand, emissions of air pollutants can also affect climate through their direct and indirect radiative forcing. However, significant uncertainties exist regarding their interactions, and additional insights are needed to better understand the mechanisms and outcomes associated with both. Moreover, greenhouse gases (GHGs) are often co-emitted with air pollutants; thus, synergistic or combined mitigation efforts could be designed to achieve optimized co-benefits. However, the current literature lacks an understanding of these co-benefits.

In this Research Topic, we aim to present a collection of original articles and reviews that address the interconnections between these two environmental factors. We also included original research that improves our understanding of air pollutant formation and removal, air pollution space-time patterns, and source attribution. This Research Topic collected a total of 17 papers, which can be largely divided into the following Four areas.

1) Feedback between climate change and air pollution, a total of four papers, including interactions between meteorology, emissions, pollutant formation, and emissions mitigation.

2) Interactions between air quality and other confronting factors, a total of five papers, including urbanization, emissions control, biogenic emissions, celestial phenomenon, and regional transport.
3) Air pollution characteristics and source attribution, a total of six papers, including space-time patterns, chemical composition, optical characteristics, and source classification.
4) Mechanisms behind pollutant formation and removal, a total of two papers, including new particle formation mechanisms and a new air purification technique.

Feedback between climate change and air pollution

Im et al. provided a detailed literature review on the interactions between climate change and air pollution in Europe. They concluded that ozone concentrations in Europe would likely increase by up to 9 ppb [−4 + 9.3], in the second half of the century, much higher than the first century (±1.5 ppb). The feedback between climate change and surface ozone are mainly dominated by increased temperatures and biogenic volatile organic emissions (VOC), while the feedback from surface particular matter is lesser and more uncertain. Similar to ozone, larger changes in particular matter concentrations are projected in the second half of the century. Zhu et al. provided an estimation of reactive ammonia uptake by secondary organic aerosol (SOA) under changing climate, and they found that including the NH3-SOA feedback could affect the meteorological conditions.

Moreover, the changing climate could also affect air quality predictions. Hu et al. provided a novel methodology for studying the impacts of climate change on meteorology and air stagnation through dynamic downscaling methods. By using dynamic downscaling, they can make realistic predictions of future climate in China with high resolution. They concluded that the occurrence of wintertime air stagnation would reduce slightly by the mid-century over China, with the largest reduction projected under the business-as-usual scenario. However, they also found that long-lasting air stagnation events are projected to increase in the future. These changes also show distinct spatial variations. Wang et al. provided us with novel findings about the previously neglected methane emissions from older fishing vessels in China. They adopted a real-world measurement technique and discussed the emission factors from these vessels. Their study calls for urgency on methane emission inventory in shipping.

Interactions between air quality and other confronting factors

Fine particulate matter ($PM_{2.5}$) and ground-level ozone (O_3) are two of the most important ambient air pollutants. Their concentrations are known to be impacted by many factors, particularly emissions of precursor gases such as NO_x (nitrogen oxides) and VOC, meteorology, and associated physical and chemical processes. An in-depth understanding of the different factors contributing to pollution is the key to design effective mitigation strategies.

In this article collection, Zhang et al. applied the MEGAN (model of emissions of gases and aerosols from nature) model and estimated BVOC (biogenic volatile organic compounds) emissions over the Sichuan Basin, China. The significant impacts of BVOC emissions on regional O_3 pollution were subsequently quantified through CMAQ simulations. Liang et al. analyzed the trend of O_3 pollution in Jinan China, between 2013 and 2020 and investigated the impact of synoptic weather patterns on O_3 pollution. Features such as low sea level pressure, high temperature, and strong UV radiation were found to be the most prevalent synoptic patterns that likely favor O_3 formation. He et al. applied the WRF-CMAQ model and analyzed the evolution of $PM_{2.5}$ pollution during stable synoptic conditions in Shanghai, China. The development of $PM_{2.5}$ pollution was divided into four stages. The contributions from factors such as meteorology, emissions, and regional transport were found to vary significantly among stages.

Wang et al. simulated how land use and land cover change as the results of urbanization affect the dynamics of urban air quality. In this study, urban expansion was found to significantly impact meteorology near the surface, which consequently altered physical and chemical processes associated with $PM_{2.5}$ and O_3 pollution. Interestingly, urbanization was found to generally decrease $PM_{2.5}$ pollution due to enhanced vertical mixing and weakened aerosol production, but increase O_3 pollution around 8 p.m. as the result of reduction in horizontal advection. Finally, Tian et al. examined the impact of solar eclipse event on O_3 pollution in Yunnan, China. Substantially decreased O_3 pollution (up to 40%) were observed during the solar eclipse, likely due to drastically reduced solar radiation, and different meteorological conditions during the event. O_3 in severely polluted cities was also found to be more sensitive to nitrogen dioxide (NO_2) and carbon monoxide (CO) during the eclipse.

These articles provided valuable insights into the different factors impacting ambient $PM_{2.5}$ and O_3 pollution. The diversity of topics also highlights the complexity of this problem.

Air pollution characteristics and source attribution

Air pollutant species could have distinct space-time patterns and chemical compositions due to their emission sources, driving meteorology, and surrounding topography. Understanding those characteristics is crucial in advancing our knowledge of pollution formation and source attribution, which in term helps the design

of pollution control and mitigation policies. Based on a state-of-the-art chemical transport model (WRF-CMAQ), Mao et al. simulated the long-term $PM_{2.5}$ and O_3 distribution in China at a 36 × 36 km scale between 2013 and 2019. In general, they found an increasing trend of O_3 and decreasing trend of $PM_{2.5}$, and a negative correlation is found between O_3 and $PM_{2.5}$ for most regions except for the Pearl River Delta and Yangtze River Delta. Another modeling work conducted by Yan et al., applied the advanced Source Apportionment Method (ISAM) to investigate the evolution mechanism and conduct source attribution of an extreme O_3 episode in the Sichuan Basin, southwestern China. The inadequate ventilation, in combination with stagnant conditions, is found to be the trigger of the episode, and the emissions from industrial and transportation sectors have the largest impacts on elevated O_3 concentrations. However, natural sources could also be a major player in pollution formation. As pointed out in the study of Liu et al., soil dust and fugitive dust are the top two sources of coarse particulate matter (PM_{10}) pollution in the Arid Region of Northwest China based on field measurement and backward trajectories calculated using the HYSPLIT model. Similar work is conducted by Zeb et al. for the Semiarid region in Pakistan. The average PM_{10} concentration in industrial locations (505.1 μg m^{-3}) is about twice that in urban and suburban locations. Their results showed that the pollution originated from local sources like cement industries, brick kiln industries, and others. Acuña Askar et al. Explored the detailed chemical composition and optical properties of $PM_{2.5}$ and water-soluble organic carbon (WSOC) of these particles in Northeastern Mexico. Where a close connection is found between WSOC compounds and brown carbon chromophores, and the terrestrial and microbial origin of WSOC. Finally, Lee et al.investigated the temporal variability of five air pollutants in megacities of South Korea between 2002 and 2020 based on monitoring data. Similar to the observation by Mao et al. for China, they also found O_3 to be the only pollutant with increasing trends in South Korea. The interconnections between human activities and seasonal and weekly patterns of major pollutants are also investigated, which provides valuable insights for air quality control.

Mechanisms behind pollutant formation and removal

Understanding chemical mechanisms behind pollutant formation and removal is not only important scientific knowledge but also provides critical insights into control and mitigation. Quantum chemistry calculations provide a useful tool to probe these mechanisms from the first principle. Liu et al. investigated new particle formation from the methanesulfonic acid–methylamine–ammonia system under acid-rich conditions using quantum chemistry calculations. Their calculations revealed stable cluster structures formed in this system. They found that methylamine and ammonia have a synergistic effect on new particle formation, and the role of ammonia increases with cluster sizes. Also using quantum chemistry calculations, Yang et al., applied the technique to study air pollutant adsorption on Pt-decorated N3-carbon-nanotubes, as a potential pollutant control technology. Their calculation showed that a suite of air pollutants could be removed by the adsorbent with adsorption energies ranging from -0.81~-4.28 eV, driven by the overlaps between the Pt 5d orbitals and the outmost p orbitals of the coordination atoms (C, N, O, and S atoms) in the gas molecules. These findings from quantum chemistry calculations provide microscopic insights into the pollution formation and removal processes that are valuable for developing policy and technology.

The 17 papers in this Research Topic use field observations, laboratory measurements, and numerical models and provide in-depth and detailed discussions on air pollution characteristics and source attribution, mechanisms between formation and removal, interactions with climate and other confronting factors, and obtained very interesting and meaningful results. We thank the authors and reviewers who contributed to this Research Topic. Together these papers provide valuable insight into the discussion of air pollution and climate interactions, and open up exciting avenues for future research.

Author contributions

All authors listed have made a substantial, direct, and intellectual contribution to the work and approved it for publication.

Conflict of interest

The authors declare that the research was conducted in the absence of any commercial or financial relationships that could be construed as a potential conflict of interest.

Publisher's note

frontiers in Environmental Science

ORIGINAL RESEARCH
published: 03 February 2022
doi: 10.3389/fenvs.2022.843582

Variation in Coarse Particulate Matter (PM_{10}) and Its Characterization at Multiple Locations in the Semiarid Region

Bahadar Zeb[1], Khan Alam[2], Allah Ditta[3,4]*, Sami Ullah[5,6], Hayssam M. Ali[7], Muhammad Ibrahim[8]* and Mohamed Z.M. Salem[9]*

[1]Department of Mathematics, Shaheed Benazir Bhutto University, Sheringal, Dir (Upper), Pakistan, [2]Department of Physics, University of Peshawar, Peshawar, Pakistan, [3]Department of Environmental Sciences, Shaheed Benazir Bhutto University, Sheringal, Pakistan, [4]School of Biological Sciences, The University of Western Australia, Perth, WA, Australia, [5]Department of Forestry, Shaheed Benazir Bhutto University, Sheringal, Pakistan, [6]GIS and Space Application in Geosciences (G-SAGL) Lab, National Center of GIS and Space Application (NCGSA), Institute of Space Technology, Islamabad, Pakistan, [7]Botany and Microbiology Department, College of Science, King Saud University, Riyadh, Saudi Arabia, [8]Department of Environmental Sciences and Engineering, Government College University, Faisalabad, Pakistan, [9]Forestry and Wood Technology Department, Faculty of Agriculture (EL-Shatby), Alexandria University, Alexandria, Egypt

OPEN ACCESS

Edited by:
Shupeng Zhu,
University of California, Irvine, United States

Reviewed by:
Kai Wu,
University of California, Davis, United States
Prashant Rajput,
Banaras Hindu University, India
Xiang Li,
Fudan University, China

***Correspondence:**
Bahadar Zeb
zebsbbu@gmail.com
Allah Ditta
allah.ditta@sbbu.edu.pk
Muhammad Ibrahim
ebrahem.m@gmail.com

Specialty section:
This article was submitted to Atmosphere and Climate, a section of the journal Frontiers in Environmental Science

Received: *26 December 2021*
Accepted: *13 January 2022*
Published: *03 February 2022*

Citation:
Zeb B, Alam K, Ditta A, Ullah S, Ali HM, Ibrahim M and Salem MZM (2022) Variation in Coarse Particulate Matter (PM_{10}) and Its Characterization at Multiple Locations in the Semiarid Region. Front. Environ. Sci. 10:843582. doi: 10.3389/fenvs.2022.843582

Introduction: The elemental composition and morphological study of particulate matter are very important to understand the nature of particles influencing the environment, climate, soil, and health.

Methods: The PM_{10} samples were collected during the winter season (2018) in Nowshera city, KPK, Pakistan, in three locations, namely, urban, industrial, and suburban. Scanning electron microscopy (SEM) and electron-dispersive X-ray (EDX) spectroscopy were used to examine the PM samples for morphological examination and elemental composition.

Results: The average mass concentrations of particulate matter (PM_{10}) at the urban, industrial, and suburban locations were 238.5, 505.1, and 255.0 μg m^{-3}, respectively. The average PM_{10} mass concentration was higher than the WHO and National Ambient Air Quality Standards (NAAQS). The results of EDX showed that samples contained variable amounts of thirteen elements, such as oxygen, carbon, silicon, magnesium, sodium, calcium, iron, aluminum, potassium, sulfur, titanium, gold, and chlorine. The probable sources of PM were biogenic like plant debris, pollen, and diatoms; geogenic like road dust and resuspended soil dust; and anthropogenic like carbonaceous particles and fly ash, as confirmed by SEM–EDX. The carbonaceous species, that is, OC and EC, had average values of 55.8 ± 13.1 and 4.6 ± 0.6, 5.2 ± 3.2, and 36.4 ± 10.4, 40.0 ± 2.6 and, 6.3 ± 0.2 in industrial, urban, and suburban locations, respectively. Similarly, OC/EC had average values of 12.0 ± 1.2, 8.0 ± 3.0, and 6.3 ± 0.2 in industrial, urban, and suburban locations, respectively. Highly significant correlations among water-soluble ions (K^+), OC, and EC were found in each location.

Conclusions: The examined PM_{10} mass concentration in Nowshera city was above the thresholds of National Ambient Air Quality Standards (NAAQS) set by the U.S. Environmental Protection Agency (EPA). In addition, the concentration of pollutants

was the highest at the industrial site compared to the other sites. The HYSPLIT model showed that the air mass originated from local sources like cement industries, brick kiln industries, and others.

Keywords: particulate matter, Nowshera, SEM–EDX, OC, EC, OC/EC ratio

INTRODUCTION

Ambient air pollution is one of the biggest threats all around the world. In various countries, governments are developing technologies to decrease pollutants in the air. A different pollutant source emits pollutants in the form of gases and particulates into the earth's atmosphere. Particulate matter (PM) is a suspended combination of solid particles and liquid droplets. Suspended PM contains dust and other particulates of size << 1–200 μm (Chandrasekaran et al., 1997). The most important physical properties of PM are its size and shape. Thus, the PM based on size is divided into two main groups or types. The aerodynamic diameter of the coarse particles spans from 2.5 to 10 μm. Mechanical disruption, that is, crushing, grinding, dust from roads, uncovered sand, industry, and construction fly ash from fossil fuel burning, as well as from non-combustible material, such as pollen grain and mold spores, causes them to form. The life span of coarse particles (PM_{10}) ranges from minutes to hours, and their transit distance varies from 1 to 10 km. The aerodynamic diameter of fine particles ($PM_{2.5}$) is less than 2.5 μm and comprises multiple sulfates, nitrates, and carbon compounds, as well as ammonium, hydrogen ions, and metals (Pb, Cu, Zn, Mn, and Fe). Fossil fuel combustion, biomass burning, smelting, and metal processing are the main producers of $PM_{2.5}$. Their life span ranges from days to weeks, and they may travel between 100 and 1,000 km (Pipal and Satsangi, 2015).

PM has a key role in changing the Earth's climate (Fowler et al., 2009). Particulate matter with an aerodynamic diameter of 2.5–10 μm ($PM_{10\text{-}2.5}$) can readily pass through and settle in a thoracic area of airways (Berube et al., 2007). On the other hand, PM with an aerodynamic diameter between 1 and 2.5 μm ($PM_{2.5\text{-}1}$) can enter deep into the distal lung, which eventually intensifies never-ending respiratory and cardiovascular diseases (Stevanovic et al., 2013). The number of particles and their surface area are also important because of the ultrafine proportion of coarse particles (Levin et al., 2016). There are very limited studies about the characterization of the size, chemical composition, and morphology of PM, which can provide substantial insights into their origin (Khan et al., 2010; Deshmukh et al., 2012; Kumar et al., 2013). The chemical composition of PM plays a significant function in its characterization and identification of various emission sources (Wu et al., 2013). For the determination of the chemical composition of PM, various techniques are used like XRF, ICP-MS, PIXE, INAA, and XPS. However, most of these techniques do not reveal chemical composition based on the shape and size of the object (Ram et al., 2012). For that reason, SEM-EDS is used to find sources based on morphological properties such as size, shape, equivalent spherical diameter, aspect ratio, circulatory, and perimeter (Kulkarni et al., 2011; Satsangi and Yadav, 2014; Mishra et al., 2015).

Because of the climatic implications, atmospheric carbonaceous particles have a key role (Frazer, 2002; Rajput et al., 2014). The types of carbonaceous PM including elemental carbon (EC) are generated from the combustion process and are called primary pollutants. Similarly, organic carbon (OC) can be emitted directly from anthropogenic and biogenic sources, that is, primary organic carbon, or it can be generated in the atmosphere by photochemical reactions, that is, secondary organic compounds *via* volatile organic carbon gas-to-particle conversion (Cao et al., 2003; Satsangi et al., 2012). Elemental carbon is strongly absorbed *via* solar radiation and has a significant role in climate change after CO_2 (Hansen et al., 2000; Rajput et al., 2013). Similarly, OC scatters solar radiation and causes negative radiative forcing (Li and Bai, 2009).

Most cities in the world are facing challenges associated with air pollution. Air pollution has become a severe problem in densely populated nations like Pakistan, owing to industrialization and the uncontrolled release of air-polluting agents (Liu and Diamond, 2005; Bradsher and Barboza, 2006; Kahn and Yardley, 2007; Kerchich et al., 2011). Air pollution is caused by particulate matter (PM_{10}, $PM_{2.5}$) and other organic agents emitted by congested road traffic systems, as well as other reasons (Chow et al., 1994; Eldred et al., 1997). Dust, particles, and aerosols all contribute to air pollution, which disrupts the dynamic atmospheric balance (Dhakal, 2003; Rajput et al., 2017). PM, one of the most frequent ambient air pollutants, is currently the subject of epidemiological and toxicological research.

Previous research revealed that environmental epidemiologists focused mostly on PM with an aerodynamic diameter of 10 μm (PM_{10}) (Goldberg et al., 2001; Janssen et al., 2002). According to a recent report by the World Health Organization (WHO) on ambient air pollution, annual mean PM_{10} concentrations increased by more than 5% in 720 cities throughout the world between 2008 and 2013 (Goel and Kumar, 2014). There are very limited studies on the characterization of PM in the Khyber Pakhtunkhwa Province of Pakistan (Alam et al., 2015; Zeb et al., 2018), and there is no study in Nowshera city. As per the National Disaster Management Plan 2012-22, Nowshera has been regarded as the most "at-risk district" in Khyber Pakhtunkhwa, Pakistan. Various types of hazards have been proposed for Nowshera, such as riverine floods, flash floods, earthquakes, land sliding, soil erosion, epidemics, drought, pest attacks, waterborne disease, hailstorms, as well as industrial fires, sectarian violence, terrorism, and refuges (District Disaster Management Unit, 2014). Therefore, it is the need of the hour to find the extent of different types of pollutants, especially air pollutants, including particulate matter. In the current study, we attempted to study the concentration of PM_{10}, its chemical composition, and morphological analysis collected from three locations in

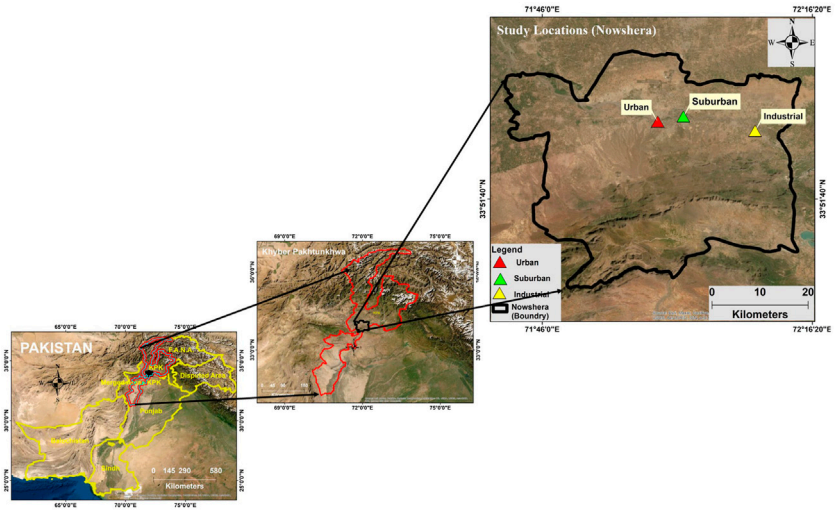

FIGURE 1 | Map of study locations of Nowshera.

Nowshera city. The morphology and chemical composition of samples were carried out through SEM and SEM–EDX, respectively. The current research will aid in the understanding of air quality, chemical composition, and sources of PM in Nowshera city. Furthermore, this study will help the researchers' study the other types of PM in Nowshera.

MATERIALS AND METHODS

Descriptions of the Study Site

Nowshera lies on a sandy plain surrounded by small hills. The city is an important hub connected by rails and roads to various locations of the country, like Malakand, Mardan, Peshawar, and Islamabad. The city is also surrounded by national highways (N-5) and motorways (M-1). Nowshera city is the fastest growing city with a population of 1.394 million and lies between 34.01°N latitude and 71.97°E longitude having an altitude of 128 m, which covers an area of 1748 km^3. The climate of Nowshera is a local steppe climate. The winters are chilly from November to February, and the summers are hot from June to August. The average annual temperature is 22.4°C, and the rainfall is 532 mm (Bibi et al., 2015). The study was carried out in three locations in Nowshera city, namely, 1) urban location, 2) industrial location, and 3) suburban location (**Figure 1**).

At the urban location, the sampling was performed at the top of a three-story building of Apostle Degree College located in the main city of Nowshera, near the main general bus stand and the main bazaar. In this area, there are many vehicle workshops and a huge traffic. Samplings were collected from the industrial location of Adamzai at the top of a two-story building surrounded by several factories, operating in the area, such as the Pakistan Tobacco Company, cotton, wool, newsprint, paper, marble, cement, and glass industries. The industrial location is also surrounded by mining areas. The sampling at a suburban location was performed in the city campus of Northern University at the top of a two-story building situated in Hakimabad. In Hakimabad, there are many housing colonies. This site is 5 km away from the urban location. Agricultural lands, woodlands, tea plantations, riverine, and marshy areas make up the majority of the region.

Particulate Matter Sampling and Its Analysis

Sample Collection

During March, April, and May 2018, a low-volume sampler (LVS) with one head was used to collect PM_{10} samples from 8 to 8 a.m. The LVS was run at a constant flow rate of 16 L/M for 24 h. PM_{10} was collected on quartz fiber filter substrates with a diameter of 47 mm and a pore size of 0.4 μm. The PM filters were removed using forceps, kept in a petri dish, conditioned, weighed, and stored in the refrigerator at 4°C for further investigation to prevent thermal deterioration and evaporation of volatile components. Using a microbalance, the gravimetric PM masses were computed by subtracting the blank filter's initial average mass from the sampled filter's final average mass. Before and after sampling, each filter substrate was weighted three times, and the mean value was computed.

Scanning Electron Microscopy With Energy Dispersive X-Ray

Scanning electron microscopy (SEM) is an electron beam–based high-resolution surface imaging technique. The samples were analyzed by SEM (JSM-5910, JEOL Japan) equipped with energy-dispersive X-ray spectroscopy (INCA-200, United Kingdom) at the Centralized Resource Laboratory in the Department of Physics, University of Peshawar, to determine their shape and elemental composition. The PM produced from various sources may be recognized using this crucial technique, which is based on the shape and chemical content. Sections of a filter (1 mm by 1 mm) were cut from the center with scissors and put on an

aluminum stub for analysis with double-sided tape. A very thin layer of gold (Au) was coated on the surface of each sample using a vacuum coating equipment called a gold sputter coater (SPI MODULE, United States) to improve conductivity and reduce electron charge. Six samples can be prepared at the same time using the sputter. Two photos of each sample were captured after they were placed in the corner of the SEM–EDX chamber. A microscope magnification of 550 was utilized to examine coarse particles, allowing detection areas of 60 × 150 m. The backscattered electron model was utilized to examine the particle shape and position. Every signal has an embedded detector that recognizes its related signal and rejects others, effectively blocking undesirable or background transmissions. The morphological parameters such as particle shape and physical diameter were manually measured by using all the images recorded for each field and particle (minimum, maximum, and mean). The findings were obtained from three randomly selected fields for each filter substrate, which offered representative results and minimized subjectivity. Individual EDX spectra of PM particles were obtained after scanning an electron beam to determine the elemental composition of the particles. The distinct peaks were recognized, and the peak intensities were converted to weight using the computer program's quantifying function (Pipal and Satsangi, 2015). The Au data from EDX could not be used for quantitative purposes since the samples were Au-coated. As a result, the Au contribution was manually removed from the EDX spectra evaluation. SEM–EDX has also been used by other researchers to analyze the morphology and chemical composition (Chabas and Lefevre, 2000; Ma et al., 2001; Liu et al., 2005; Li et al., 2011).

Calculation of Element Percent Weight

The weight of individual elements was determined by the EDX examination of each particle. Blank quartz fiber filters were also subjected to EDX analysis, with the spectra results manually removed from those of the real individual aerosol particles. The weight of different elements was determined from the EDX spectra of each particle. For PM_{10}, the average weight percent of each constituent was computed after determining the total number of particles in each constituent.

Carbonaceous Species Analysis and Quality Control

A portion of the sample, 1.5 cm^2, was cut and analyzed by using a thermal/optical carbon aerosol analyzer (Sunset Laboratory, Forest Grove, OR) using the NIOSH 5040 (National Institute of Occupational Safety and Health) protocol based on thermal optical transmittance for the measurement of the carbonaceous group in PM like OC, EC, CC, and TC (TOT). Satsangi et al. (2012) present a precise approach for the analysis of OC-EC. Sucrose solution (3.2 g L^{-1}) was used to standardize the instrument. A 10 L solution yields 32.0 1.8 g OC. Every day, the analyzer was calibrated for quality control using a blank punch of preheated quartz fiber filter and standard sucrose solutions. For blank filters, quartz filters were also sampled and evaluated in the same way. The overall blank concentrations for OC and EC were 0.5, 0.2, and 0.0, 0.02 g cm^{-2}, respectively, from the quartz filters. These were removed from the aerosol samples' observed OC and EC values. With 3 mM MSA (methane sulfonic acid) as eluent, water-soluble K^+ was measured using a Dionex ICS 1100 Ion Chromatograph on an SCS 1 Cation Column and SCG 1 Guard Column. K^+ has a detection limit of 0.06 ppm, a precision of 3.7%, and an accuracy of 1.5%. The blank filter was retrieved and examined for blank adjustments and then subtracted from the observed K^+ concentrations in the PM samples for quality control.

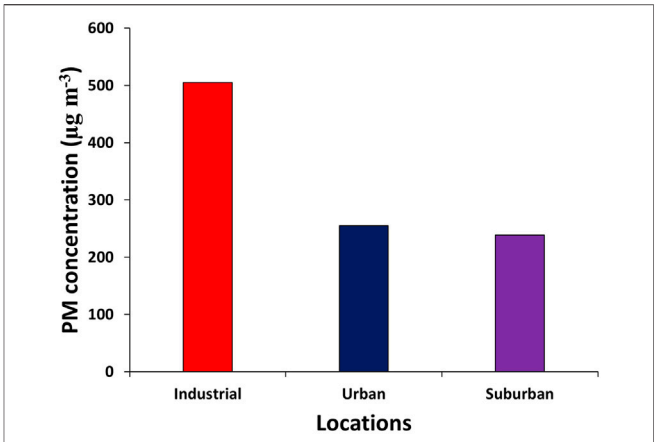

FIGURE 2 | Mean PM_{10} concentration at three locations of Nowshera during the winter season.

RESULTS AND DISCUSSION

Particulate Matter Mass Concentration

The 24 h average PM mass concentrations at the three locations, that is, urban, industrial, and suburban, are investigated, as shown in **Figure 2**. The PM_{10} mass concentration at the industrial, urban, and suburban locations ranged from 412.52 to 597.60 μg m^{-3}, 198.84–278.12 μg m^{-3} and 164.32–345.77 μg m^{-3}, with an average value of 505.06, 255.04, and 238.48 μg m^{-3}, respectively. The WHO permissible limit for 24 h PM_{10} mass concentrations is 50 μg m^{-3} and that of the National Ambient Air Quality Standards (NAAQS) is 150 μg m^{-3} (Davidson et al., 2005). In the three locations, that is, industrial, urban, and suburban locations, the measured values of PM mass concentration were 10.1, 5.1, and 4.8 times greater than the WHO standard and 3.4, 1.7, and 1.6 times higher than the NAAQS levels. There are heterogeneous sources of PM in the present study sites of Nowshera city. The urban location is surrounded by heavy transport and mechanical workshops; the industrial site is surrounded by Pakistan Tobacco Company, many small marble industries, vehicles, etc. At the suburban site, the emission sources were biomass burning and resuspended road dust. The high value of PM in these sites was due to the lack of vegetation cover area, bare earth, drought situation, unpaved roads, jammed traffic, and low-quality engines and fuels. The other reasons for high PM in the city were vehicular emissions, industrial emissions, re-suspension of road dust, emissions from brick kilns, and domestic combustion (Alam et al., 2011; Alam et al., 2015).

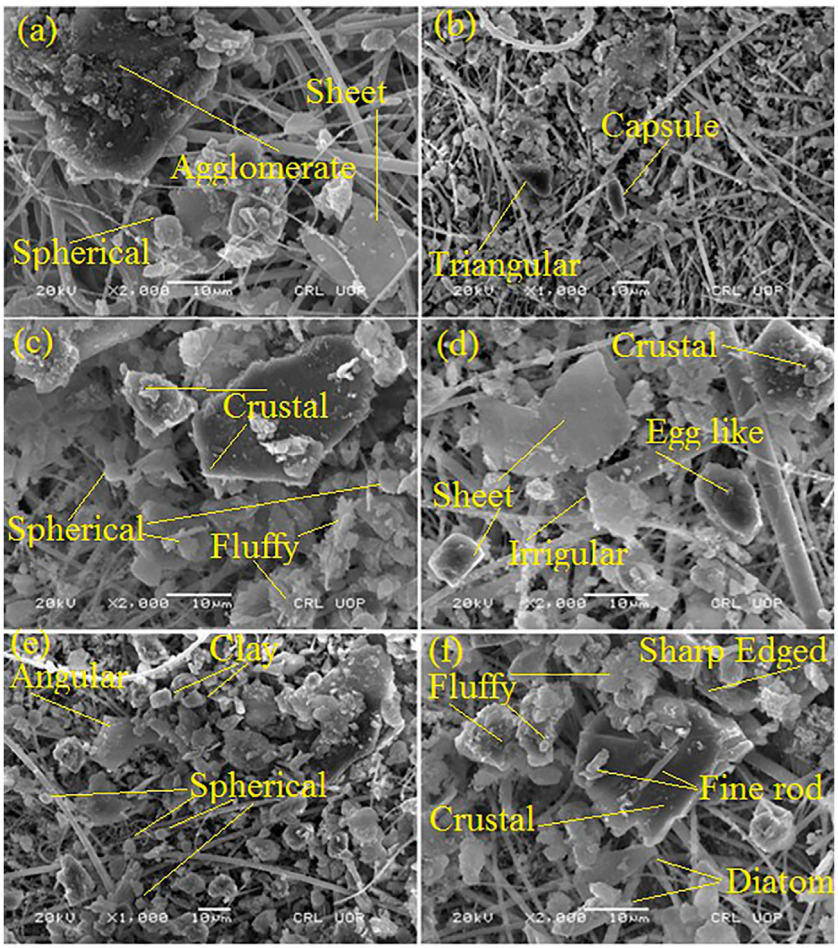

FIGURE 3 | SEM images of collected PM in three locations that is, industrial **(A,B)**, urban **(C,D)**, and suburban **(E,F)**.

Various researchers have found different concentrations of PM under different scenarios. For example, Zeb et al. (2018) reported a PM_{10} concentration of 638 μg m^{-3} during the autumn season in Peshawar city, which was high as compared to that of the present study. However, Mehmood et al. (2018) reported the PM_{10} mass concentration of 152.4, 97.22, 86.52, and 40.45 μg m^{-3} during autumn, winter, spring, and summer seasons, respectively, in Islamabad city which is a low concentration in comparison to the present study. Khodeir et al. (2012) and Yadav et al. (2014) also reported a low concentration of PM_{10}. A PM_{10} concentration value of 480 ± 83 μg m^{-3} was recorded in Peshawar city using the GRIMM instrument, which is similar to the present study (Alam et al., 2015). Nowshera had higher concentrations than other cities such as Lahore, Pakistan (406 g m^{-3}), Kolkata, India (197 g m^{-3}), Quetta, Pakistan (331 g m^{-3}), Karachi, Pakistan (302 g m^{-3}), Islamabad, Pakistan (280 g m^{-3}), Hangzhou, China (119 g m^{-3}), Punjab, India (116 g m^{-3}), Beijing-China (140 μg m^{-3}), Shanghai-China (100 μg m^{-3}), and Taipei-China (60 μg m^{-3}) (Karar and Gupta, 2007; Cao et al., 2009; Awasthi et al., 2011).

Morphological Characteristics of Coarse Particulate Matter in Three Locations

The scanning electron microscopic images of PM_{10} collected in three locations (industrial, urban, and suburban) in Nowshera city are shown in **Figures 3A–F**. SEM micrographs of PM at three locations show that particles were of various shapes and sizes, like triangular, oval, capsule, sharp-edged, spherical, fluffy, rod-like, angular, agglomerates, and diatom sheets. Other researchers also pointed out particles of various shapes (Prabhu et al., 2019). One of the key processes in the formation of irregular particles is the aggregation process (Rodríguez et al., 2009). The incomplete combustion of fossil fuels and biomass combustion are the primary causes of agglomeration particle emissions (Li et al., 2016). In the present study, carbonaceous chains and agglomerates were also observed, which are emitted from the combustion of fossil fuel in vehicles and industries (Mogo et al., 2005; Prabhu et al., 2019). Spherical particles were largely seen in micrographs, which were usually investigative of high-temperature processes or burning processes (Mogo et al., 2005). Particulate matter from sheet-like structures and

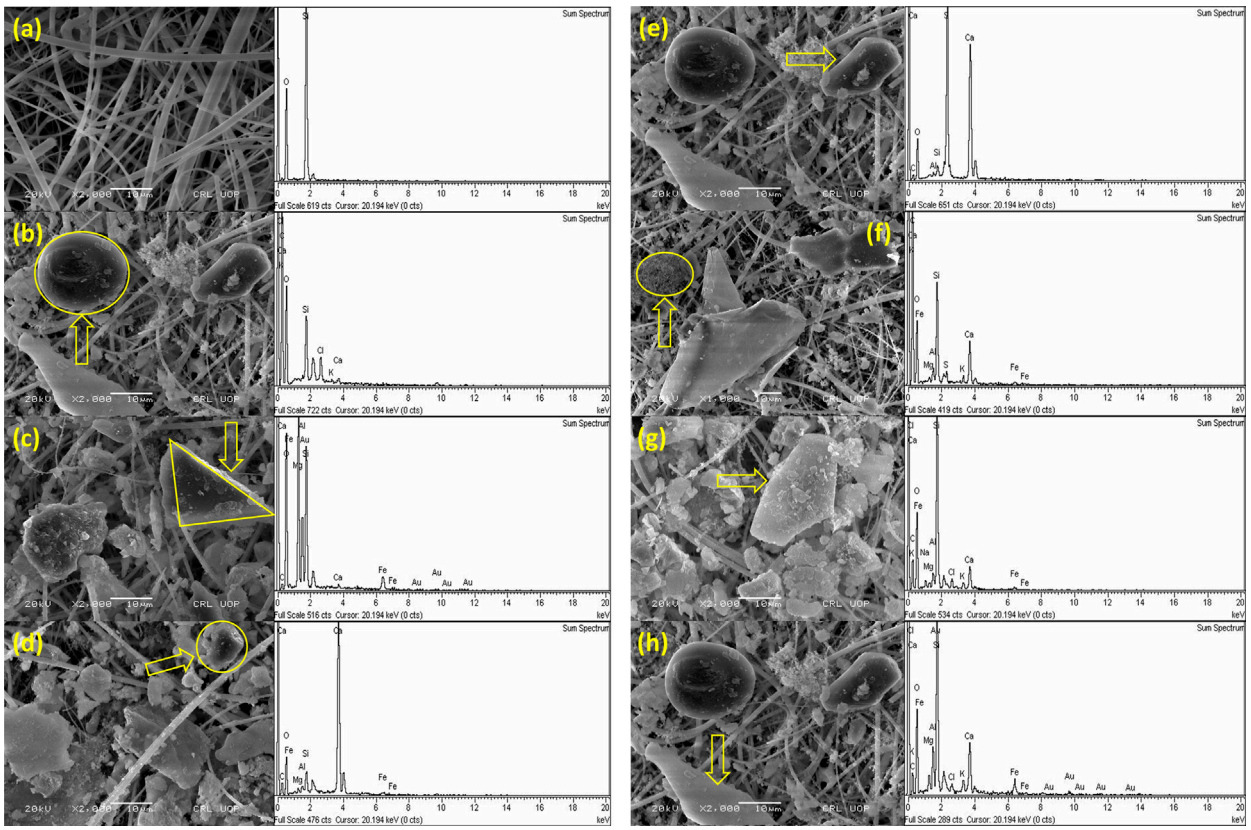

FIGURE 4 | SEM–EDX of particulates. **(A)** Blank filter, **(B)** carbonaceous particles, **(C)** aluminosilicate particles, **(D)** calcium-rich particles, **(E)** sulfate particles, **(F)** carbonaceous agglomerates, **(G)** iron-rich particles, and **(H)** biological particles.

spherical carbonaceous particles were also observed. The existence of sheet-like structures related to clay is produced from geogenic sources, which are later resuspended from the surface of the earth by the wind. **Figures 3E,F** depict sharp-edged particles generated by anthropogenic activities such as construction and vehicular moments on the road. The figure also indicated biogenic particles, such as diatoms. The biological particles can be transported from 100 to 1,000 km from one place to another (Sofiev et al., 2006), which can also work as cloud condensation nuclei (Steiner et al., 2015). Fine PMs of size less than 1.5 μm are generated from fly ash emitted from the combustion process, and fine dust particles are produced from vehicular movement and construction activities (Mogo et al., 2005). The combustion of coal and biomass is one of the key sources of spherical soot particles. There are a large number of brick kilns surrounding the studied locations. The particles of irregular morphology are produced from crustal and construction activities. Therefore, the identified PM was grouped into geogenic, biogenic, and anthropogenic sources based on morphology.

Energy Dispersive X-Ray Measurement

Aluminosilicates

High concentrations of Si and Al, as well as varied proportions of Mg, K, Fe, and Ca, distinguish aluminosilicates (Cuadros et al., 2015) and have diverse sources and compositions. Aluminosilicate particles of triangular shape are shown in **Figure 4C**. **Figure 4A** shows the presence of Si and O in the blank filter. Aluminosilicates, quartz, chlorides, calcium, and iron particles are found in irregular shapes (Pipal et al., 2011; Pachauri et al., 2013). The largest quantity of aerosol mass in the atmosphere is made up of these particles (Pipal and Satsangi, 2015). Soil dust, resuspended dust from roads and the earth's crust, and anthropogenic activities (constructions, combustion processes, agriculture fields, and moments of vehicles on roads) are the main sources of these particles (Satsangi and Yadav, 2014).

Aggregated Carbonaceous and Tarball Particle

Aggregate carbonaceous particles are shown in **Figure 4F**. Aggregated carbonaceous particles are generated from the combustion of fossil fuel and can be simply detected by their unique structure, varying from linear to complex forms (Tumolva et al., 2010). High-temperature process regions such as industries emit these types of particles (Gao and Ji, 2018). Near the study locations, the construction activities were the source of carbonaceous particles. **Figure 4B** shows tarball particles with spherical morphology. The special property of tarballs is recognized by their spherical and amorphous structures and generally is not aggregated with other particles (Cong et al., 2010). The typical source of tarballs is incomplete biomass and fossil fuel burning.

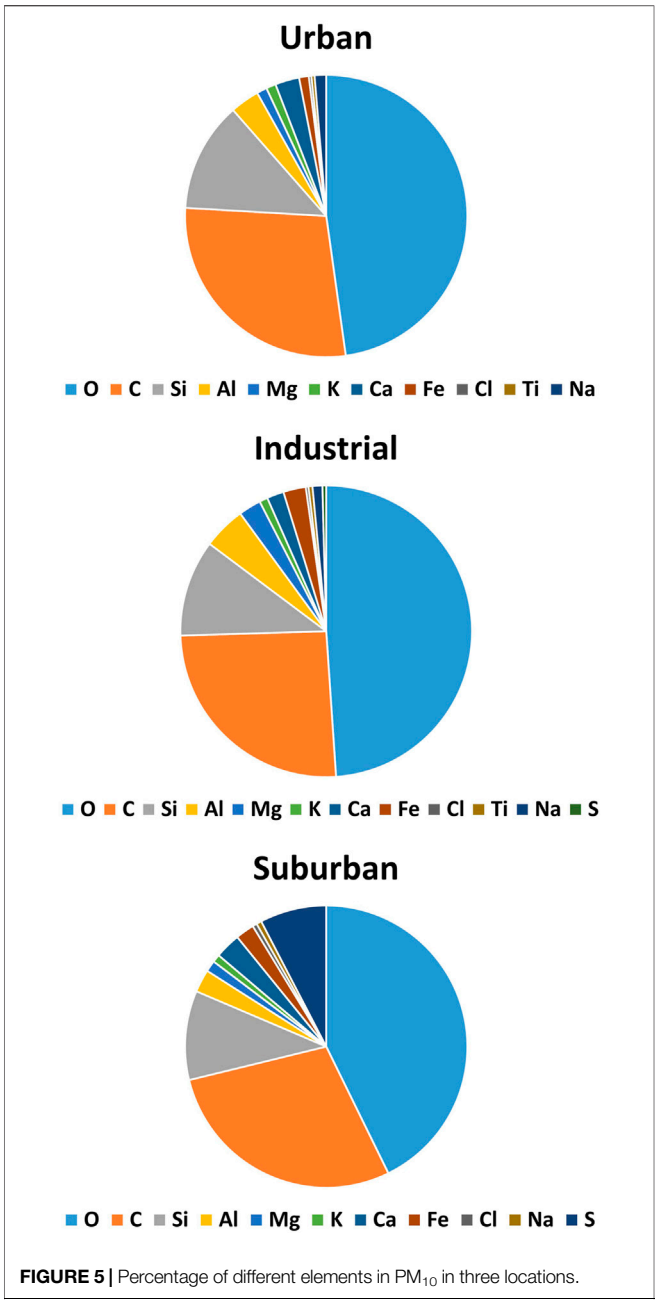

FIGURE 5 | Percentage of different elements in PM_{10} in three locations.

The existence of tarballs in the atmosphere has a key role in climate forcing and the regional haze because these affect the absorption and scattering of light efficiently (Hand et al., 2005). At Nowshera city, there was a mix of human activities including significant traffic congestion, which resulted in the emission of burnt or semi-burnt motor fuels, coal used in industries, generators used in suburban facilities, and tire abrasion (Satsangi and Yadav, 2014). Similar findings were reported in China by Cao et al. (2004).

Calcium-Rich Particles

The calcium (Ca) particles of irregular shape are shown in **Figure 4D**. These particles are rich in Ca and are found in various shapes and sizes. The sources of Ca-rich particles are natural, as well as anthropogenic, that is, marble industries produce marble dust during their processes (Reist, 1993).

Iron (Fe)-Rich Particles

As indicated in **Figure 4G**, Fe-rich particles were also found, emitted from a variety of sources. Fe particles are released into the atmosphere by both natural and manmade activities. With the combination of mineral dust elements such as C, Al, K, Si, Ca, Na, and Mg, Fe-rich particles are found abundantly in Fe, Ti, and O. Fe oxides with irregular shapes make up the majority of this type of particles.

Sulfate Particles

The existence of sulfur (S) particles confirms their source from the process of combustion. Generally, sulfate particles are generated from sulfur dioxide (SO_2) emitted through biomass and fossil fuel combustion (Pósfai et al., 1999). SO_2 is adsorbed on the surface of already existing particles and results in secondary minerals (Li and Shao, 2009). The high concentration of S is produced in the atmosphere through the combustion process of diesel inside heavy-duty vehicles and is very dangerous to human health. The sulfate particles having a rotundate rectangular shape of the size of the order of 8.4 μm are shown in **Figure 4E**.

Biological Particles

Biological particles were detected, as shown in **Figure 4H**, containing >80% (C + O) and a small amount (<10%) of Na, Si, and Al. These particles are generated due to the existence of pollen, algae, protozoa, bacteria, and fragments of leaves. The excrements and fragments are also the sources of biological particles. Since there are a large number of trees, plants, and vegetation areas around the sampling sites, these particles are found in various shapes and sizes.

Elemental Contribution to Particulate Matter in Three Locations

Figures 5, **6** show the variation in the atomic percentage of thirteen elements, that is, carbon (C), oxygen (O), silicon (Si),

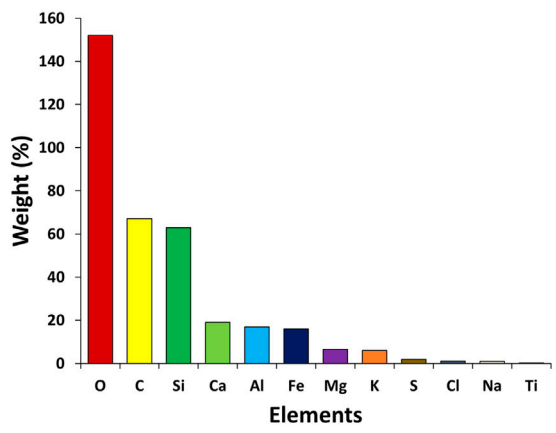

FIGURE 6 | Average elemental weight percent in the area in Nowshera city.

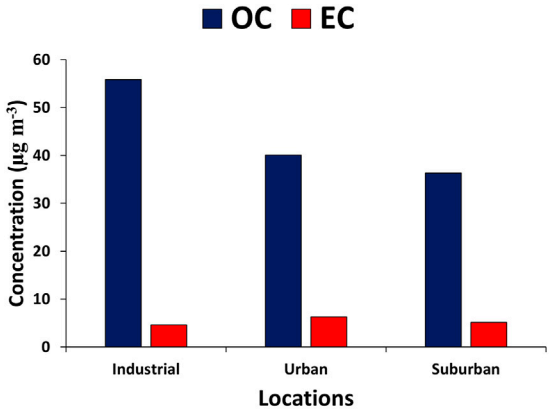

FIGURE 7 | Concentration of OC and EC in three locations of the study area.

magnesium (Mg), sodium (Na), calcium (Ca), iron (Fe), aluminum (Al), potassium (K), sulfur (S), titanium (Ti), gold (Au), and chlorine (Cl) calculated from EDX spectra at three sites. The elemental arrangements at 1) industrial, 2) urban, and 3) suburban locations are O > C > Si > Al > Mg > K > Ca > Fe > Cl > Ti > Na > S, O > C > Si > Al > Mg > K > Ca > Fe > Cl > Na > S, and O > C > Si > Al > Mg > K > Ca > Fe > Cl > Ti > Na, respectively. The elemental compositions of PM_{10} in three locations are very similar. The difference between the two elements, that is, S and Ti, is observed in the locations. Sulfur was found only at industrial and urban sites, and titanium was found at urban and industrial sites. A large number of industries, such as brick kilns, pharmaceutical, steel and iron, and electroplating industries, were around the sampling locations. Oxygen was found in high amounts in all sites, which might be due to oxides of metals emitted from the burning of fossil fuels, vehicular exhaust, and different industries. After O, C was found to be the major element during the study.

The high amount of C after O in all three sites is a straightforward indicator of the various emission sources like fossil fuel and biomass burning, vehicular and coal burning emissions, energy sources in the industries, generator sets used in suburban facilities, and abraded vehicle tires (Shahid et al., 2013). Si is one of the most abundant elements in soil-derived mineral particles, according to the research. As a result, it could be caused by the transfer of airborne soil particles or fly ash created during industrial combustion. These particles were common in heavily industrialized areas and frequently contained Si (Herman et al., 1997; Baron and Willeke, 2001; Houghton et al., 2001). The anthropogenic sources of Al and Fe are industrial emissions, and their natural sources are mineral dust. The presence of soil-based elements like Ca, K, and Mg shows their existence from natural sources such as crustal resuspension and mineral dust (Kulshrestha et al., 2003; Kulshrestha et al., 2009; Tiwari et al., 2015). Regular open-air solid waste burning, as well as diverse industrial operations, can contribute to the elevated levels of Al (Pant et al., 2016; Mehra et al., 2020; Bangar et al., 2021) as found in the present study. From soil dust, Na was recognized as a crustal element. The presence of K has been linked to vegetation and biomass burning, and Cl has been linked to industrial emissions because it is not found in ambient natural minerals but is commonly used in industrial processes (Hsu et al., 2016). Due to building and road renovations/construction, Ca and Al are produced, which cause mineral dust (Wang et al., 2013; Mustaffa et al., 2014; Rajput et al., 2018).

The Concentration of Carbonaceous Species in Coarse Particulate Matter, That Is, PM_{10}

Figure 7 depicts the mass concentrations of carbonaceous species such as OC and EC across the study period. In the industrial, urban, and suburban locations, OC ranged from 46.61 to 65.08, 29.01 to 43.69, and 38.19 to 41.91 μg m^{-3}, with an average value of 55.85 ± 13.06, 36.35 ± 10.38, and 40.05 ± 2.64 μg m^{-3}, respectively. Similarly, EC ranged from 4.18 to 5.06, 2.88 to 7.46, and 6.16 to 6.51 μg m^{-3}, with an average value of 4.62 ± 0.62, 5.17 ± 3.23, and 6.33 ± 0.24 μg m^{-3} in the industrial, urban, and suburban locations, respectively. There are numerous sources of EC, including traffic pollutants, gasoline, diesel cars, and biomass burning (Ghauri et al., 2007; Zhang et al., 2008). OC is released directly from the combustion of fossil fuels or biomass, or by a chemical reaction known as secondary organic carbon (Satsangi et al., 2012). The high value of EC during the winter season might be due to less dispersion, wood burning, fuel burning, and coal burning in the region. Various researchers have also noted similar results regarding OC and EC values in different cities. For example, Satsangi et al. (2012) recorded OC and EC values during winter (37.4 ± 23.4, 6.3 ± 4.7 μg m^{-3}), post-monsoon (33.0 ± 17.5, 3.4 ± 2.0 μg m^{-3}), summer (29.4 ± 20.0, 2.6 ± 1.4 μg m^{-3}), and monsoon (9.8 ± 9.6, 1.7 ± 1.3 μg m^{-3}) in Dayalbagh, India. Similarly, Alam et al. (2012) reported the OC (63 ± 42 μg m^{-3}) and EC (21 ± 15 μg m^{-3}) values in the urban environment of Lahore, and these values were close to those observed in the present study.

The OC/EC, K^+/OC, and K^+/EC and Origin of Carbonaceous Aerosols

To validate the presence of primary and secondary organic aerosols, the ratios of organic carbon to elemental carbon (OC/EC) are utilized (Chow et al., 1996). OC/EC ratios have been reported by many researchers for various sources of emissions, such as biomass burning (3.8–13.2) (Zhang et al., 2007), coal smoke (2.5–10.5) (Chen et al., 2006), vehicular exhaust (2.5–5.00) (Schauer et al., 2002), kitchen emissions (4.3–7.7) (See and Balasubramanium, 2008), and wood combustion (16.8–40.00) (Schauer et al., 2001). In the present study, the ratios (OC/EC) ranged from 11.13 to 12.86, 5.85 to 10.06, and 6.19 to 6.44, with average values of 12 ± 1.22, 7.95 ± 2.96, and 6.32 ± 0.17 in the industrial, urban, and suburban locations, respectively (**Table 1**). The larger values of the OC/EC ratio have a variety of reasons, including the combustion of wood and coal during the winter season, which results in large emissions of volatile organic precursors. During the winter season, stagnant meteorological circumstances produce a large amount of secondary organic aerosols (SOA). The high OC/EC values during the winter season are noted by different researchers

TABLE 1 | Ratio of OC/EC, K^+/OC, and K^+/EC in three locations of the study area.

	Industrial			Urban			Suburban		
	OC/EC	K^+/OC	K^+/EC	OC/EC	K^+/OC	K^+/EC	OC/EC	K^+/OC	K^+/EC
Min	11.13	0.05	0.55	5.85	0.04	0.31	6.19	0.03	0.22
Max	12.86	0.06	0.77	10.06	0.05	0.43	6.44	0.04	0.56
Mean	12.00	0.05	0.66	7.95	0.05	0.37	6.32	0.03	0.24
STD	1.22	0.007	0.15	2.96	0.007	0.38	0.17	0.004	0.022

TABLE 2 | Correlations between OC, EC, and water-soluble ions (K^+) in study locations.

	Industrial		Urban		Suburban	
	EC	K^+	EC	K^+	EC	K^+
OC	0.92	0.78	0.89	0.71	0.85	0.81
EC		0.75		0.73		0.87

in different sites in China, including Shanghai (Feng et al., 2009), Tianjin (Li and Bai, 2009), Taiyuan (Meng et al., 2007), and Beijing (Dan et al., 2004). According to Alam et al., 2012, OC/EC ranged from 1.5 to 7.6, with an average value of 3.92 in the urban environment of Lahore, and was attributed to both biogenic and secondary aerosol formations. **Table 1** shows the K^+/OC and K^+/EC ratios for the three locations examined. In comparison to fossil fuels, K^+/OC and K^+/EC ratios can be utilized to classify carbonaceous aerosol emission sources such as biomass burning. The K^+/EC ratio has been reported to be high (0.21–0.46) for biomass burning and low (0.025–0.09) for fossil fuel emissions (Ram and Sarin, 2010). In the present work, in industrial locations, K^+/OC and K^+/EC ranged from 0.05 to 0.06 and 0.55 to 0.77, with an average of 0.05 ± 0.007 and 0.66 ± 0.15, respectively. K^+/OC and K^+/OC varied from 0.04–0.05, 0.31–0.43, with an average value of 0.050.007 and 0.370.38, respectively, across urban locations. K^+/OC varied from 0.03 to 0.04, with an average value of 0.03, 0.004. K^+/EC ranged from 0.22 to 0.56, with an average value of 0.24 0.022 in suburban locations, respectively. The average K^+/EC (0.560.32) value was discovered to be suggestive of biomass burning. According to Ram and Sarin (2010), the K^+/EC ratio has varied between 0.30 and 0.69, 0.08 and 0.19, and 0.15 and 0.98 in Allahabad, Jaduguda, and Kanpur, respectively.

Correlation Between OC, EC, and Water-Soluble Ion (K^+)

The correlation between OC, EC, and water-soluble ions (K^+) is presented in **Table 2**. The origin of carbonaceous aerosols can be investigated by the correlation between OC and EC (Chow et al., 1996; Li and Bai, 2009). A very good correlation of OC to EC is found with a correlation coefficient of 0.92, 0.89, and 0.85 in industrial, urban, and suburban locations. OC has a good correlation with K^+ in industrial (0.78), urban (0.71) and suburban (0.81) locations. Similarly, EC shows a strong relationship with K^+ in three different settings: industrial (0.75), urban (0.73), and domestic (0.73) (0.87). The OC/EC ratios are commonly employed to interpret carbonaceous aerosol emission and transformation features. Our findings reveal that OC and EC are proportionate, implying that the main sources of OC and EC are the same, that is, motor vehicle exhaust, coal combustion, and biomass burning (Li and Bai, 2009). Similarly, K^+ produced during combustion is utilized as a marker of biomass burning (Deshmukh et al., 2010; Deshmukh et al., 2012). At the three locations, there is a strong association between water-soluble ion (K^+), OC, and EC, indicating that biomass burning is a significant source of carbonaceous aerosols (Pachauri et al., 2013). Earlier, Stone et al. (2010) found a strong correlation between OC, coal combustion, and other unidentified sources, which is in line with the findings of the present study.

Water-Soluble Ion Concentration

The number of water-soluble ions found in PM_{10} in three locations is listed in **Table 3**. In each location, the water-soluble ions followed the trend, that is, $Ca^{2+} > Na^+ > K^+ > Mg^{2+} > NH_4^+$. The values of the mass concentration of water-soluble ions in the industrial, urban and suburban locations were Ca^{2+} (30.05 ± 6.85, 18.31 ± 6.58, 17.87 ± 1.74 μg m^{-3}) >Na^+ (5.24 ± 0.17, 5.17 ± 0.40, 5.12 ± 0.09 μg m^{-3}) > K^+ (3.13 ± 1.13, 1.77 ± 0.77, 1.50 ± 0.84 μg m^{-3}) > Mg^{2+} (2.50 ± 0.47, 1.27 ± 0.47, 1.26 ± 0.12 μg m^{-3}). The values were high in the industrial region, followed by the urban and suburban regions. The concentration of NH_4^+ (1.25 ± 0.72 μg m^{-3}) was highest in urban areas, followed by suburban (0.77 ± 0.14) and industrial (0.71 ± 0.02 μg m^{-3}) locations. NH_4^+ was produced during the reactions of NH_3 with HNO_3, H_2SO_4, and their precursors. Generally, NH_3 is generated from anthropogenic sources, particularly from agricultural activities and fossil fuel burning (Meng et al., 2011). During winter season, NH_3 release from agricultural activities is decreased; therefore, NH_4^+ in winter is associated with traffic, coal combustion, and biomass burning activities against cold weather. The concentration of different soluble ions is similar to that of Shahid et al. (2019) who found the concentration of different ions as Na^+ (4.4 ± 0.4 μg m^{-3}), Ca^{2+} (42.6 ± 15.4 μg m^{-3}) K^+ (2.5 ± 0.5 μg m^{-3}), Mg^{2+} (0 0.8 ± 0.3 μg m^{-3}), and NH_4^+ (1.3 ± 0.7 μg m^{-3}).

Analysis of the Air Mass Backward Trajectory

The results discussed in the previous sections show that biomass burning, cement, vehicular emissions, biological and brick kiln emissions were recognized to play a significant role in affecting the air quality of Nowshera city. However, it is suggested to have

TABLE 3 | Mass concentration of water-soluble ions in PM_{10} in three locations.

Ion	Industrial			Urban			Suburban		
	Min	Max	AVG ± SD	Min	Max	AVG ± SD	Min	Max	AVG ± SD
Na^+	5.12	5.36	5.24 ± 0.17	4.89	5.46	5.17 ± 0.40	5.05	5.19	5.12 ± 0.09
NH_4^+	0.70	0.73	0.71 ± 0.02	0.74	1.77	1.25 ± 0.72	0.67	0.87	0.77 ± 0.14
K^+	2.33	2.93	3.13 ± 1.13	1.23	2.32	1.77 ± 0.77	1.44	1.56	1.50 ± 0.84
Mg^{2+}	2.16	2.83	2.50 ± 0.47	0.93	1.60	1.27 ± 0.47	1.17	1.34	1.26 ± 0.12
Ca^{2+}	25.20	34.89	30.05 ± 6.85	13.65	22.96	18.31 ± 6.58	16.57	19.02	17.87 ± 1.74

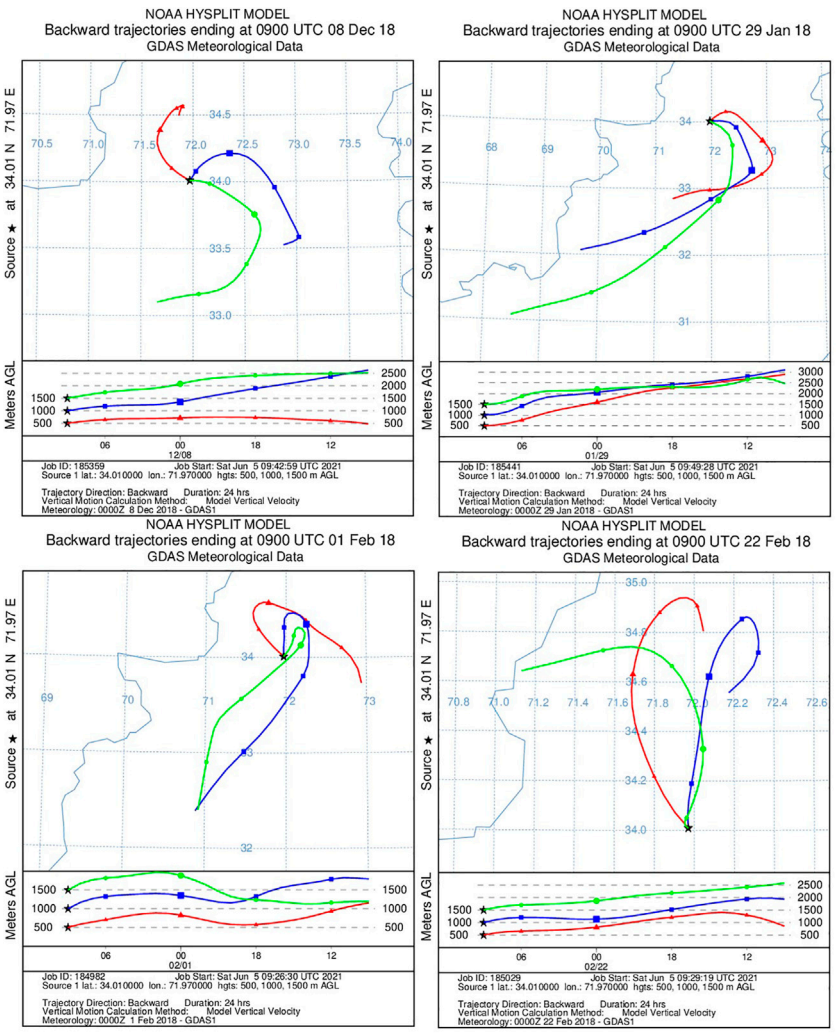

FIGURE 8 | Five-day air mass back trajectories during the winter season (December, January, and February), calculated for three heights (500, 1,000, and 1,500 m) above the ground level indicating short trajectories from localized sources.

in-depth knowledge of the pathways traversed by the air masses converging in Nowshera city. Thus, to find out the source region of the air masses, analyses using the Hybrid-Single-Particle-Lagrangian Integrated-Trajectory (HYSPLIT) model were performed. The National Oceanic and Atmospheric Administration (NOAA) Air Resource Laboratory (ARL) Hybrid Single-Particle Lagrangian Integrated Trajectory (HYSPLIT) model was used to obtain these air mass back trajectories using the Global Data Assimilation System model's final run data archive. In **Figure 8**, five-day back trajectory studies of the winter months were simulated at the local standard time (noon) at three heights (500, 1,000, and 1,500 m) above ground level at three heights (500, 1,000, and 1,500 m) above ground level. The obtained data suggest that anthropogenic emission sources dominate short trajectories coming from local areas near Nowshera city.

CONCLUSION

The current study has investigated the atmospheric pollution in Nowshera city for the first time. The examined PM mass concentration in Nowshera city was confirmed to be above the Environmental Protection Agency's (EPA) and National Ambient Air Quality Standards (NAAQS) thresholds. This study revealed that the concentration of pollution was highest at the industrial site than at the other sites. The morphological and elemental characterization of the atmosphere of Nowshera has been investigated through SEM and EDX, respectively. Individual particulate matter characterizations through SEM–EDX have provided helpful insights corresponding to the PM sources based on the shape and size of particulates. Particulates produced from anthropogenic and geogenic sources were usually spherical and irregular in shape, but particles emitted from biogenic sources had a specific shape, according to the morphological investigation of particulate matter. The SEM results revealed various morphological shapes and sizes of pollutants, that is, sheets like rod-like, irregular, angular, triangular, spherical, agglomerates, and soot particles. The EDX results showed that O (oxygen), C (carbon), and Si (silicon) were the major pollutants in the study area. We have observed the values of OC and EC in industrial (55.85 ± 13.06 and 4.62 ± 0.62), urban (5.17 ± 3.23 and 36.35 ± 10.38), and suburban (40.05 ± 2.64 and 6.33 ± 0.24) locations. Similarly, the average values of OC/EC were 12 ± 1.22, 7.95 ± 2.96, and 6.32 ± 0.17 in industrial, urban, and suburban locations, respectively. In industrial, urban, and suburban locations, the values of K^+/OC and K^+/EC are found to be (0.05 ± 0.007 and 0.66 ± 0.15), (0.05 ± 0.007 and 0.37 ± 0.38), and (0.03 ± 0.004 and 0.24 ± 0.022), respectively. In our study, we observed a good correlation of water-soluble ions (K^+), OC, and EC, which supports the idea that the sources of carbonaceous matter are biomass burning. In addition, Nowshera city has a large number of factories, that is, cement industries, brick kiln industries, and others that release a large number of emissions because of the poor technology used in the manufacturing processes. For that reason, it can be interesting to note that the air masses from various directions have a significant effect on the air quality in Nowshera city. The results of the HYSPLIT model show that the air mass originates from local sources.

DATA AVAILABILITY STATEMENT

The original contributions presented in the study are included in the article/supplementary material; further inquiries can be directed to the corresponding authors.

AUTHOR CONTRIBUTIONS

BZ contributed to conceptualization; BZ and SU helped with data curation; BZ, KA, AD, and SU assissted with formal analysis; HA, MI, and MS acquired funding; KA and SU framed the methodology; KA, HA, MI, and MS involved in project administration; KA, AD, and SU helped with software; AD, HA, MI, and MS validated the study; AD contributed to visualization; BZ and KA wrote the original draft; and BZ, AD, SU, HA, MI, and MS reviewed and edited the manuscript. All authors have read and agreed to the published version of the manuscript.

ACKNOWLEDGMENTS

The authors thank the Director of the Centralized Resource Laboratory University of Peshawar for help with SEM–EDX analysis. The authors thank the working team (http://ready.arl.noaa.gov) for the HYSPLIT trajectories. The authors acknowledge the financial support by Researchers Supporting Project number (RSP-2021/123) King Saud University, Riyadh, Saudi Arabia.

REFERENCES

Alam, K., Blaschke, T., Madl, P., Mukhtar, A., Hussain, M., Trautmann, T., et al. (2011). Aerosol Size Distribution and Mass Concentration Measurements in Various Cities of Pakistan. *J. Environ. Monit.* 13, 1944–1952. doi:10.1039/c1em10086f

Alam, K., Rahman, N., Khan, H. U., Haq, B. S., and Rahman, S. (2015). Particulate Matter and its Source Apportionment in Peshawar, Northern Pakistan. *Aerosol Air Qual. Res.* 15, 634–647. doi:10.4209/aaqr.2014.10.0250

Alam, K., Trautmann, T., Blaschke, T., and Majid, H. (2012). Aerosol Optical and Radiative Properties during Summer and Winter Seasons over Lahore and Karachi. *Atmos. Environ.* 50, 234–245. doi:10.1016/j.atmosenv.2011.12.027

Awasthi, A., Agarwal, R., Mittal, S. K., Singh, N., Singh, K., and Gupta, P. K. (2011). Study of Size and Mass Distribution of Particulate Matter Due to Crop Residue Burning with Seasonal Variation in Rural Area of Punjab, India. *J. Environ. Monit.* 13, 1073–1081. doi:10.1039/c1em10019j

Bangar, V., Mishra, A. K., Jangid, M., and Rajput, P. (2021). Elemental Characteristics and Source Apportionment of $PM_{2.5}$ during the post-monsoon Season in Delhi, India. *Front. Sustain. Cities* 3, 18. doi:10.3389/frsc.2021.648551

Baron, P. A., and Willeke, K. (2001). *Aerosol Measurement: Principles, Techniques, and Applications*. Second ed. New York: John Wiley & Sons, 15.

BéruBé, K., Balharry, D., Sexton, K., Koshy, L., and Jones, T. (2007). Combustion-derived Nanoparticles: Mechanisms of Pulmonary Toxicity. *Clin. Exp. Pharmacol. Physiol.* 34 (10), 1044–1050. doi:10.1111/j.1440-1681.2007.04733.x

Bibi, S., Alam, K., Bibi, H., Khan, H., and SafyaHaq, B. (2015). Variation in Aerosol Optical Depth and its Impact on Longwave Radioactive Properties in Northern Areas of Pakistan. *J. GeoSpace Sci.* 1, 28–43.

Bradsher, K., and Barboza, D. (2006). Pollution from Chinese Coal Casts a Global Shadow. *The New York Times*.

Cao, J.-J., Zhu, C.-S., Chow, J. C., Watson, J. G., Han, Y.-M., Wang, G.-h., et al. (2009). Black Carbon Relationships with Emissions and Meteorology in Xi'an, China. *Atmos. Res.* 94 (2), 194–202. doi:10.1016/j.atmosres.2009.05.009

Cao, J. J., Lee, S. C., Ho, K. F., Zou, S. C., Fung, K., Li, Y., et al. (2004). Spatial and Seasonal Variations of Atmospheric Organic Carbon and Elemental Carbon in Pearl River Delta Region, China. *Atmos. Environ.* 38, 4447–4456. doi:10.1016/j.atmosenv.2004.05.016

Cao, J., Lee, S. C., Ho, K. F., Zhang, X. Y., Zou, S. C., Fung, K., et al. (2003). Characteristics of Carbonaceous Aerosol in Pearl River Delta Region, China during 2001 Winter Period. *Atmos. Environ.* 37, 1451–1460. doi:10.1016/s1352-2310(02)01002-6

Chabas, A., and Lefèvre, R. A. (2000). Chemistry and Microscopy of Atmospheric Particulates at Delos (Cyclades-Greece). *Atmos. Environ.* 34 (2), 225–238. doi:10.1016/s1352-2310(99)00255-1

Chandrasekaran, G. E., Ravichandran, C., and Shetty, N. (1997). Ambient Air Quality at Selected Sites in Bangalore City. *Indian J. Environ. Protect.* 17 (3), 184–188.

Chen, J., Tan, M., Nemmar, A., Song, W., Dong, M., Zhang, G., et al. (2006). Quantification of Extrapulmonary Translocation of Intratracheal-Instilled Particles *In Vivo* in Rats: Effect of Lipopolysaccharide. *Toxicology* 222 (3), 195–201. doi:10.1016/j.tox.2006.02.016

Chow, J. C., Watson, J. G., Fujita, E. M., Lu, Z., Lawson, D. R., and Ashbaugh, L. L. (1994). Temporal and Spatial Variations of PM2.5 and PM10 Aerosol in the Southern California Air Quality Study. *Atmos. Environ.* 28 (12), 2061–2080. doi:10.1016/1352-2310(94)90474-x

Chow, J. C., Watson, J. G., Lu, Z., Lowenthal, D. H., Frazier, C. A., Solomon, P. A., et al. (1996). Descriptive Analysis of PM2.5 and PM10 at Regionally Representative Locations during SJVAQS/AUSPEX. *Atmos. Environ.* 30, 2079–2112. doi:10.1016/1352-2310(95)00402-5

Cong, Z., Kang, S., Dong, S., Liu, X., and Qin, D. (2010). Elemental and Individual Particle Analysis of Atmospheric Aerosols from High Himalayas. *Environ. Monit. Assess.* 160 (1), 323–335. doi:10.1007/s10661-008-0698-3

Cuadros, J., Diaz-Hernandez, J. L., Sanchez-Navas, A., and Garcia-Casco, A. (2015). Role of clay Minerals in the Formation of Atmospheric Aggregates of Saharan Dust. *Atmos. Environ.* 120, 160–172. doi:10.1016/j.atmosenv.2015.08.077

Dan, M., Zhuang, G., Li, X., Tao, H., and Zhuang, Y. (2004). The Characteristics of Carbonaceous Species and Their Sources in PM2.5 in Beijing. *Atmos. Environ.* 38, 3443–3452. doi:10.1016/j.atmosenv.2004.02.052

Davidson, C. I., Phalen, R. F., and Solomon, P. A. (2005). Airborne Particulate Matter and Human Health: a Review. *Aerosol Sci. Techn.* 39 (8), 737–749. doi:10.1080/02786820500191348

Deshmukh, D. K., Deb, M. K., Tsai, Y. I., and Mkoma, S. L. (2010). Atmospheric Ionic Species in PM2.5 and PM1 Aerosols in the Ambient Air of Eastern central India. *J. Atmos. Chem.* 66, 81–100. doi:10.1007/s10874-011-9194-1

Deshmukh, D. K., Tsai, Y. I., Deb, M. K., and Zarmpas, P. (2012). Characteristics and Sources of Water-Soluble Ionic Species Associated with PM10 Particles in the Ambient Air of central India. *Bull. Environ. Contam. Toxicol.* 89, 1091–1097. doi:10.1007/s00128-012-0806-5

Dhakal, S. (2003). Implications of Transportation Policies on Energy and Environment in Kathmandu Valley, Nepal. *Energy Policy* 31 (14), 1493–1507. doi:10.1016/s0301-4215(02)00205-7

District Disaster Management Unit (2014). *District Disaster Risk Management Plan Nowshera DDMU*. Peshawar: Provincial Disaster Management Authority. Retrieved from: https://www.pdma.gov.pk/sub/uploads/drm_road_map_2014-19%20(1).pdf.

Eldred, R. A., Cahill, T. A., and Flocchini, R. G. (1997). Composition of PM2.5 and PM10 Aerosols in the IMPROVE Network. *J. Air Waste Manag. Assoc.* 47 (2), 194–203. doi:10.1080/10473289.1997.10464422

Feng, Y., Chen, Y., Guo, H., Zhi, G., Xiong, S., Li, J., et al. (2009). Characteristics of Organic and Elemental Carbon in PM2.5 Samples in Shanghai, China. *Atmos. Res.* 92, 434–442. doi:10.1016/j.atmosres.2009.01.003

Fowler, D., Pilegaard, K., Sutton, M. A., Ambus, P., Raivonen, M., Duyzer, J., et al. (2009). Atmospheric Composition Change: Ecosystems-Atmosphere Interactions. *Atmos. Environ.* 43 (33), 5193–5267. doi:10.1016/j.atmosenv.2009.07.068

Frazer, L. (2002). Seeing through Soot. *Environ. Health Perspect.* 110, A471–A473. doi:10.1289/ehp.110-a470

Gao, Y., and Ji, H. (2018). Microscopic Morphology and Seasonal Variation of Health Effect Arising from Heavy Metals in PM2.5 and PM10: One-Year Measurement in a Densely Populated Area of Urban Beijing. *Atmos. Res.* 212, 213–226. doi:10.1016/j.atmosres.2018.04.027

Ghauri, B., Lodhi, A., and Mansha, M. (2007). Development of Baseline (Air Quality) Data in Pakistan. *Environ. Monit. Assess.* 127, 237–252. doi:10.1007/s10661-006-9276-8

Goel, A., and Kumar, P. (2014). A Review of Fundamental Drivers Governing the Emissions, Dispersion and Exposure to Vehicle-Emitted Nanoparticles at Signalised Traffic Intersections. *Atmos. Environ.* 97, 316–331. doi:10.1016/j.atmosenv.2014.08.037

Goldberg, M. S., Burnett, R. T., Bailar, J. C., III, Brook, J., Bonvalot, Y., Tamblyn, R., et al. (2001). The Association between Daily Mortality and Ambient Air Particle Pollution in Montreal, Quebec. *Environ. Res.* 86 (1), 12–25. doi:10.1006/enrs.2001.4242

Hand, J. L., Malm, W. C., Laskin, A., Day, D., Lee, T., Wang, C., et al. (2005). Optical, Physical, and Chemical Properties of Tar Balls Observed during the Yosemite Aerosol Characterization Study. *J. Geophys. Res. Atmos.* 110, 1–14. doi:10.1029/2004jd005728

Hansen, J., Sato, M., Ruedy, R., Lacis, A., and Oinas, V. (2000). Global Warming in the Twenty-First Century: An Alternative Scenario. *Proc. Natl. Acad. Sci.* 97, 9875–9880. doi:10.1073/pnas.170278997

Herman, J. R., Bhartia, P. K., Torres, O., Hsu, C., Seftor, C., and Celarier, E. (1997). Global Distribution of UV-Absorbing Aerosols from Nimbus 7/TOMS Data. *J. Geophys. Res.* 102, 16911–16922. doi:10.1029/96jd03680

Houghton, J. T., Ding, Y., Griggs, D. J., Noguer, M., van der Linden, P. J., Dai, X., et al. (2001). *Climate Change*. Cambridge, United Kingdom and New York, NY, USA: Cambridge University Press, pp881.

Hsu, C.-Y., Chiang, H.-C., Lin, S.-L., Chen, M.-J., Lin, T.-Y., and Chen, Y.-C. (2016). Elemental Characterization and Source Apportionment of PM 10 and PM 2.5 in the Western Coastal Area of central Taiwan. *Sci. Total Environ.* 541, 1139–1150. doi:10.1016/j.scitotenv.2015.09.122

Janssen, N. A. H., Schwartz, J., Zanobetti, A., and Suh, H. H. (2002). Air Conditioning and Source-specific Particles as Modifiers of the Effect of PM(10) on Hospital Admissions for Heart and Lung Disease. *Environ. Health Perspect.* 110 (1), 43–49. doi:10.1289/ehp.0211043

Kahn, J., and Yardley, J. (2007). As China Roars, Pollution Reaches Deadly Extremes. *New York Times* 26 (8), A1.

Karar, K., and Gupta, A. K. (2007). Source Apportionment of PM10 at Residential and Industrial Sites of an Urban Region of Kolkata, India. *Atmos. Res.* 84, 30–41. doi:10.1016/j.atmosres.2006.05.001

Kerchich, Y., Kerbachi, R., and Khatraoui, H. (2011). Ambient Air Levels of Aromatic Organic Compounds in the Urban Area of Algiers, Algeria. *Asian J. Chem.* 23 (1), 323.

Khan, M. F., Shirasuna, Y., Hirano, K., and Masunaga, S. (2010). Characterization of PM2.5, PM2.5-10 and PM>10 in Ambient Air, Yokohama, Japan. *Atmos. Res.* 96 (1), 159–172. doi:10.1016/j.atmosres.2009.12.009

Khodeir, M., Shamy, M., Alghamdi, M., Zhong, M., Sun, H., Costa, M., et al. (2012). Source Apportionment and Elemental Composition of PM2.5 and PM10 in Jeddah City, Saudi Arabia. *Atmos. Pollut. Res.* 3, 331–340. doi:10.5094/apr.2012.037

Kulkarni, P., Baron, P. A., and Willeke, K. (2011). *Aerosol Measurement: Principles, Techniques, and Applications*. 3rd ed. Hoboken: Wiley.

Kulshrestha, U. C., Kulshrestha, M. J., Sekar, R., Sastry, G. S. R., and Vairamani, M. (2003). Chemical Characteristics of Rainwater at an Urban Site of South-central India. *Atmos. EnvironmentEnviron* 37, 3019–3026. doi:10.1016/s1352-2310(03)00266-8

Kulshrestha, U. C., Reddy, L. A. K., Satyanarayana, J., and Kulshrestha, M. J. (2009). Real-time Wet Scavenging of Major Chemical Constituents of Aerosols and

Role of Rain Intensity in Indian Region. *Atmos. Environ.* 43, 5123–5127. doi:10.1016/j.atmosenv.2009.07.025

Kumar, S., Verma, M. K., and Srivastava, A. K. (2013). Ultrafine Particles in Urban Ambient Air and Their Health Perspectivesfine Particles in Urban Ambient Air and Their Health Perspectives. *Rev. Environ. Health* 28, 117–128. doi:10.1515/reveh-2013-0008

Levin, M., Witschger, O., Bau, S., Jankowska, E., Koponen, I. K., Koivisto, A. J., et al. (2016). Can We Trust Real Time Measurements of Lung Deposited Surface Area Concentrations in Dust from Powder Nanomaterials? *Aerosol Air Qual. Res.* 16, 1105–1117. doi:10.4209/aaqr.2015.06.0413

Li, W., and Bai, Z. (2009). Characteristics of Organic and Elemental Carbon in Atmospheric Fine Particles in Tianjin, China. *Particuology* 7, 432–437. doi:10.1016/j.partic.2009.06.010

Li, W. J., and Shao, L. Y. (2009). Observation of Nitrate Coatings on Atmospheric mineral Dust Particles. *Atmos. Chem. Phys.* 9, 1863–1871. doi:10.5194/acp-9-1863-2009

Li, W., Shao, L., Shen, R., Yang, S., Wang, Z., and Tang, U. (2011). Internally Mixed Sea Salt, Soot, and Sulfates at Macao, a Coastal City in South China. *J. Air Waste Manag. Assoc.* 61 (11), 1166–1173. doi:10.1080/10473289.2011.603996

Li, W., Shao, L., Zhang, D., Ro, C.-U., Hu, M., Bi, X., et al. (2016). A Review of Single Aerosol Particle Studies in the Atmosphere of East Asia: Morphology, Mixing State, Source, and Heterogeneous Reactions. *J. Clean. Prod.* 112, 1330–1349. doi:10.1016/j.jclepro.2015.04.050

Liu, J., and Diamond, J. (2005). China's Environment in a Globalizing World. *Nature* 435 (7046), 1179–1186. doi:10.1038/4351179a

Liu, X., Zhu, J., Van Espen, P., Adams, F., Xiao, R., Dong, S., et al. (2005). Single Particle Characterization of spring and Summer Aerosols in Beijing: Formation of Composite Sulfate of Calcium and Potassium. *Atmos. Environ.* 39 (36), 6909–6918. doi:10.1016/j.atmosenv.2005.08.007

Ma, C.-J., Kasahara, M., Höller, R., and Kamiya, T. (2001). Characteristics of Single Particles Sampled in Japan during the Asian Dust-Storm Period. *Atmos. Environ.* 35 (15), 2707–2714. doi:10.1016/s1352-2310(00)00410-6

Mehmood, T., Tianle, Z., Ahmad, I., Li, X., Shen, F., Akram, W., et al. (2018). "Variations of PM2. 5, PM10 Mass Concentration and Health Assessment in Islamabad, Pakistan," in IOP Conference Series: Earth and Environmental Science, Shanghai, China, January 19–21, 2018, 012031.

Mehra, M., Zirzow, F., Ram, K., and Norra, S. (2020). Geochemistry of PM2.5 Aerosols at an Urban Site, Varanasi, in the Eastern Indo-Gangetic Plain during Pre-monsoon Season. *Atmos. Res.* 234, 104734. doi:10.1016/j.atmosres.2019.104734

Meng, Z. Y., Jiang, X. M., Yan, P., Lin, W. L., Zhang, H. D., and Wang, Y. (2007). Characteristics and Sources of PM2.5 and Carbonaceous Species during Winter in Taiyuan, China. *Atmos. Environ.* 41, 6901–6908. doi:10.1016/j.atmosenv.2007.07.049

Meng, Z. Y., Lin, W. L., Jiang, X. M., Yan, P., Wang, Y., Zhang, Y. M., et al. (2011). Characteristics of Atmospheric Ammonia over Beijing, China. *Atmos. Chem. Phys.* 11, 6139–6151. doi:10.5194/acp-11-6139-2011

Mishra, S. K., Agnihotri, R., Yadav, P. K., Singh, S., Prasad, M. V. S. N., Praveen, P. S., et al. (2015). Morphology of Atmospheric Particles over Semi-arid Region (Jaipur, Rajasthan) of India: Implications for Optical Properties. *Aerosol Air Qual. Res.* 15, 974–984. doi:10.4209/aaqr.2014.10.0244

Mogo, S., Cachorro, V. E., and de Frutos, A. M. (2005). Morphological, Chemical and Optical Absorbing Characterization of Aerosols in the Urban Atmosphere of Valladolid. *Atmos. Chem. Phys.* 5 (10), 2739–2748. doi:10.5194/acp-5-2739-2005

Mustaffa, N. I. H., Latif, M. T., Ali, M. M., and Khan, M. F. (2014). Source Apportionment of Surfactants in marine Aerosols at Different Locations along the Malacca Straits. *Environ. Sci. Pollut. Res.* 21, 6590–6602. doi:10.1007/s11356-014-2562-z

Pachauri, T., Singla, V., Satsangi, A., Lakhani, A., and Kumari, K. M. (2013). SEM-EDX Characterization of Individual Coarse Particles in Agra, India. *Aerosol Air Qual. Res.* 13, 523–536. doi:10.4209/aaqr.2012.04.0095

Pant, P., Baker, S. J., Goel, R., Guttikunda, S., Goel, A., Shukla, A., et al. (2016). Analysis of Size-Segregated winter Season Aerosol Data from New Delhi, India. *Atmos. Pollut. Res.* 7, 100–109. doi:10.1016/j.apr.2015.08.001

Pipal, A. S., and Gursumeeran Satsangi, P. (2015). Study of Carbonaceous Species, Morphology and Sources of fine (PM2.5) and Coarse (PM10) Particles along with Their Climatic Nature in India. *Atmos. Res.* 154, 103–115. doi:10.1016/j.atmosres.2014.11.007

Pipal, A. S., Kulshrestha, A., and Taneja, A. (2011). Characterization and Morphological Analysis of Airborne PM2.5 and PM10 in Agra Located in north central India. *Atmos. EnvironmentEnviron* 45, 3621–3630. doi:10.1016/j.atmosenv.2011.03.062

Pósfai, M., Anderson, J. R., Buseck, P. R., Sievering, H., and Buseck, P. R. (1999). Soot and Sulfate Particles in the Remote Marine Troposphere. *J. Geophys. Res.* 104, 21685–21693.

Prabhu, V., Shridhar, V., and Choudhary, A. (2019). Investigation of the Source, Morphology, and Trace Elements Associated with Atmospheric PM10 and Human Health Risks Due to Inhalation of Carcinogenic Elements at Dehradun, an Indo-Himalayan City. *SN Appl. Sci.* 1 (5), 429. doi:10.1007/s42452-019-0460-1

Rajput, P., Anjum, M. H., and Gupta, T. (2017). One Year Record of Bioaerosols and Particles Concentration in Indo-Gangetic Plain: Implications of Biomass Burning Emissions to High-Level of Endotoxin Exposure. *Environ. Pollut.* 224, 98–106. doi:10.1016/j.envpol.2017.01.045

Rajput, P., Sarin, M., and Kundu, S. S. (2013). Atmospheric Particulate Matter (PM2.5), EC, OC, WSOC and PAHs from NE-Himalaya: Abundances and Chemical Characteristics. *Atmos. Pollut. Res.* 4 (2), 214–221. doi:10.5094/apr.2013.022

Rajput, P., Sarin, M., Sharma, D., and Singh, D. (2014). Characteristics and Emission Budget of Carbonaceous Species from post-harvest Agricultural-Waste Burning in Source Region of the Indo-Gangetic Plain. *Tellus B: Chem. Phys. Meteorology* 66 (1), 21026. doi:10.3402/tellusb.v66.21026

Rajput, P., Singh, D. K., Singh, A. K., and Gupta, T. (2018). Chemical Composition and Source-Apportionment of Sub-micron Particles during Wintertime over Northern India: New Insights on Influence of Fog-Processing. *Environ. Pollut.* 233, 81–91. doi:10.1016/j.envpol.2017.10.036

Ram, K., and Sarin, M. M. (2010). Spatio-temporal Variability in Atmospheric Abundances of EC, OC and WSOC over Northern India. *J. Aerosol Sci.* 41, 88–98. doi:10.1016/j.jaerosci.2009.11.004

Ram, S. S., Majumdar, S., Chaudhuri, P., Chanda, S., Santra, S. C., Maiti, P. K., et al. (2012). SEMEDS: An Important Tool for Air Pollution Bio-Monitoring. *Micron* 43, 490–493. doi:10.1016/j.micron.2011.07.007

Reist, P. C. (1993). *Aerosol Science and Technology*. Second ed. North Carolina, USA: R.R. Donnelley & Sons Company, 5.

Rodríguez, I., Galí, S., and Marcos, C. (2009). Atmospheric Inorganic Aerosol of a Non-industrial City in the center of an Industrial Region of the North of Spain, and its Possible Influence on the Climate on a Regional Scale. *Environ. Geol.* 56 (8), 1551–1561. doi:10.1007/s00254-008-1253-9

Satsangi, A., Pachauri, T., Singla, V., Lakhani, A., and Kumari, K. M. (2012). Organic and Elemental Carbon Aerosols at a Suburban Site. *Atmos. Res.* 113, 13–21. doi:10.1016/j.atmosres.2012.04.012

Satsangi, P. G., and Yadav, S. (2014). Characterization of PM2.5 by X-ray Diffraction and Scanning Electron Microscopy-Energy Dispersive Spectrometer: its Relation with Different Pollution Sourcesffraction and Scanning Electron Microscopy–Energy Dispersive Spectrometer: its Relation with Different Pollution Sources. *Int. J. Environ. Sci. Technol.* 11, 217–232. doi:10.1007/s13762-012-0173-0

Schauer, J. J., Kleeman, M. J., Cass, G. R., and Simoneit, B. R. T. (2001). Measurement of Emissions from Air Pollution Sources. 3. C1–C29 Organic Compounds from Fireplace Combustion of Wood. *Environ. Sci. Technol.* 35, 1716–1728. doi:10.1021/es001331e

Schauer, J. J., Kleeman, M. J., Cass, G. R., and Simoneit, B. R. T. (2002). Measurement of Emissions from Air Pollution Sources. 5. C1–C32 Organic Compounds from Gasoline-Powered Motor Vehicles. *Environ. Sci. Technol.* 36, 1169–1180. doi:10.1021/es0108077

See, S. W., and Balasubramanium, R. (2008). Chemical Characteristics of Fine Particles Emitted from Different Gas Cooking Methods. *Atmos. Environ.* 42, 8852–8862. doi:10.1016/j.atmosenv.2008.09.011

Shahid, I., Kistler, M., Shahid, M. Z., and Puxbaum, H. (2019). Aerosol Chemical Characterization and Contribution of Biomass Burning to Particulate Matter at a Residential Site in Islamabad, Pakistan. *Aerosol Air Qual. Res.* 19 (1), 148–162. doi:10.4209/aaqr.2017.12.0573

Shahid, M. A. K., Awan, M. S., Hussain, K., and Sabir, R. (2013). Scanning and Transmission Electron Microscopical and Dynamical Characterization of Soot Coated Solid Aerosols. *Peak J. Phys. Environ. Sci. Res.* 1 (1), 1–11.

Sofiev, M., Siljamo, P., Ranta, H., and Rantio-Lehtimäki, A. (2006). Towards Numerical Forecasting of Long-Range Air Transport of Birch Pollen: Theoretical Considerations and a Feasibility Study. *Int. J. Biometeorol.* 50 (6), 392–402. doi:10.1007/s00484-006-0027-x

Steiner, A. L., Brooks, S. D., Deng, C., Thornton, D. C. O., Pendleton, M. W., and Bryant, V. (2015). Pollen as Atmospheric Cloud Condensation Nuclei. *Geophys. Res. Lett.* 42 (9), 3596–3602. doi:10.1002/2015gl064060

Stevanovic, S., Miljevic, B., Surawski, N. C., Fairfull-Smith, K. E., Bottle, S. E., Brown, R., et al. (2013). Influence of Oxygenated Organic Aerosols (OOAs) on the Oxidative Potential of Diesel and Biodiesel Particulate Matterfluence of Oxygenated Organic Aerosols (OOAs) on the Oxidative Potential of Diesel and Biodiesel Particulate Matter. *Environ. Sci. Technol.* 47 (14), 7655–7662. doi:10.1021/es4007433

Stone, E., Schauer, J., Quraishi, T. A., and Mahmood, A. (2010). Chemical Characterization and Source Apportionment of fine and Coarse Particulate Matter in Lahore, Pakistan. *Atmos. Environ.* 44 (8), 1062–1070. doi:10.1016/j.atmosenv.2009.12.015

Tiwari, S., Pipal, A. S., Hopke, P. K., Bisht, D. S., Srivastava, A. K., Tiwari, S., et al. (2015). Study of the Carbonaceous Aerosol and Morphological Analysis of fine Particles along with Their Mixing State in Delhi, India: a Case Study. *Environ. Sci. Pollut. Res.* 22 (14), 10744–10757. doi:10.1007/s11356-015-4272-6

Tumolva, L., Park, J.-Y., Kim, J.-s., Miller, A. L., Chow, J. C., Watson, J. G., et al. (2010). Morphological and Elemental Classification of Freshly Emitted Soot Particles and Atmospheric Ultrafine Particles Using the TEM/EDSfication of Freshly Emitted Soot Particles and Atmospheric Ultrafine Particles Using the TEM/EDS. *Aerosol Sci. Techn.* 44, 202–215. doi:10.1080/02786820903518907

Wang, J., Hu, Z., Chen, Y., Chen, Z., and Xu, S. (2013). Contamination Characteristics and Possible Sources of PM10 and PM2.5 in Different Functional Areas of Shanghai, China. *Atmos. Environ.* 68, 221–229. doi:10.1016/j.atmosenv.2012.10.070

Wu, S., Deng, F., Wang, X., Wei, H., Shima, M., Huang, J., et al. (2013). Association of Lung Function in a Panel of Young Healthy Adults with Various Chemical Components of Ambient fine Particulate Air Pollution in Beijing, Chinafine Particulate Air Pollution in Beijing, China. *Atmos. Environ.* 77, 873–884. doi:10.1016/j.atmosenv.2013.06.018

Yadav, R., Sahu, L. K., Jaaffrey, S. N. A., and Beig, G. (2014). Temporal Variation of Particulate Matter (PM) and Potential Sources at an Urban Site of Udaipur in Western India. *Aerosol Air Qual. Res.* 14, 1613–1629. doi:10.4209/aaqr.2013.10.0310

Zeb, B., Khan Alam, K., Armin Sorooshian, A., Blaschke, T., Ahmad, I., and Shahid, I. (2018). On the Morphology and Composition of Particulate Matter in an Urban Environment. *Aerosol Air Qual. Res.* 18 (6), 1431–1447. doi:10.4209/aaqr.2017.09.0340

Zhang, Y.-x., Shao, M., Zhang, Y.-h., Zeng, L.-m., He, L.-y., Zhu, B., et al. (2007). Source Profiles of Particulate Organic Matters Emitted from Cereal Straw Burnings. *J. Environ. Sci.* 19, 167–175. doi:10.1016/s1001-0742(07)60027-8

Zhang, Y., Quraishi, T., and Schauer, J. J. (2008). Daily Variations in Sources of Carbonaceous Aerosol in Lahore, Pakistan during a High Pollution Spring Episode. *Aerosol Air Qual. Res.* 8, 130–146. doi:10.4209/aaqr.2007.09.0042

Conflict of Interest: The authors declare that the research was conducted in the absence of any commercial or financial relationships that could be construed as a potential conflict of interest.

Publisher's Note: All claims expressed in this article are solely those of the authors and do not necessarily represent those of their affiliated organizations, or those of the publisher, the editors, and the reviewers. Any product that may be evaluated in this article, or claim that may be made by its manufacturer, is not guaranteed or endorsed by the publisher.

frontiers in Environmental Science

ORIGINAL RESEARCH
published: 28 March 2022
doi: 10.3389/fenvs.2022.858685

Contributions of Regional Transport Versus Local Emissions and Their Retention Effects During $PM_{2.5}$ Pollution Under Various Stable Weather in Shanghai

Baoshan He[1,2], Guangyuan Yu[1], Xin Zhang[3], Zhiyin He[1], Qian Wang[4], Qizhen Liu[4], Jingbo Mao[1] and Yan Zhang[1,2,5]*

[1]Shanghai Key Laboratory of Atmospheric Particle Pollution and Prevention, National Observations and Research Station for Wetland Ecosystems of the Yangtze Estuary, Department of Environmental Science and Engineering, Fudan University, Shanghai, China, [2]IRDR ICoE on Risk Interconnectivity and Governance on Weather/Climate Extremes Impact and Public Health, Institute of Atmospheric Science, Fudan University, Shanghai, China, [3]Shanghai Central Meteorological Observatory, Shanghai, China, [4]Shanghai Environmental Monitoring Center, Shanghai, China, [5]Shanghai Institute of Eco-Chongming (SIEC), Shanghai, China

OPEN ACCESS

Edited by:
Shupeng Zhu,
University of California, United States

Reviewed by:
Kai Wu,
University of California, United States
Jianlin Hu,
Nanjing University of Information Science and Technology, China

***Correspondence:**
Yan Zhang
yan_zhang@fudan.edu.cn

Specialty section:
This article was submitted to Atmosphere and Climate, a section of the journal Frontiers in Environmental Science

Received: 20 January 2022
Accepted: 22 February 2022
Published: 28 March 2022

Citation:
He B, Yu G, Zhang X, He Z, Wang Q, Liu Q, Mao J and Zhang Y (2022) Contributions of Regional Transport Versus Local Emissions and Their Retention Effects During $PM_{2.5}$ Pollution Under Various Stable Weather in Shanghai. Front. Environ. Sci. 10:858685. doi: 10.3389/fenvs.2022.858685

Understanding the formation and development processes of air pollution events is key to improving urban air quality. In this study, the air pollution episodes in stable synoptic conditions were selected to analyze the multi-phase evolution processes of heavy air pollution in Shanghai, a coastal city. The observation data and the WRF-CMAQ model were used to diagnose and simulate the pollution characteristics of the heavy pollution episodes. The results showed that the transport and dilution characteristics of $PM_{2.5}$ were different during autumn and winter in Shanghai as a receptor of pollution transport. The development of $PM_{2.5}$ pollution events were divided into four stages: accumulation stage, stagnation stage, enhancement stage, and dilution stage. The accumulation stage was before stable weather, and provided the foundations for $PM_{2.5}$ pollution. The stagnation stage was nighttime during stable weather, in which the low wind speed and temperature inversion weakened regional transport and the dilution of $PM_{2.5}$, which was defined as "retention effect". The "retention effect" played a dominant role during the stagnation stage, accounting for 71.2% and 41.2% of total $PM_{2.5}$ in winter and autumn case, respectively. The enhancement stage followed the stagnation stage, in which the newly regional transport was occurred due to stronger wind speed, accounting for 86.3% and 46.2% in winter and autumn episodes, respectively. The dilution stage was after the whole stable weather, when meteorological conditions were beneficial for $PM_{2.5}$ dilution. Local emissions were dominant (63.0%) for $PM_{2.5}$ pollution in the autumn case but regional transport was dominant (81.3%) in the winter case. Therefore, preventing the heavy particulate pollution caused by the diverse stable weather calls for the suitable emission control in a regional scale. Our study also shows that the simulation accuracy during stable weather needs to be improved in future studies.

Keywords: stable weather, PM2.5, WRF-CMAQ, shanghai, regional transport, retention effect

HIGHLIGHTS

1. The multi-stage analysis of air pollution events during stable weather helps to better understand the formation of air pollution.
2. The regional transport of air pollutants in pre-stagnation stage was proved to be fundamental to air pollution episodes by the retention effects.
3. Probing the external and local contributions to air pollution during stable weather provides rationales to make air pollution control strategies.

INTRODUCTION

In recent years, air pollution under stable weather conditions have been paid more and more attention (Shu, et al., 2017; Xiang, et al., 2019) for its adverse health and economic impacts (Zhang, et al., 2020a). The meteorological conditions in local and regional scale play an essential role in the day-to-day variation and the long-term trend of air quality. Many studies have shown that stable weather prevents the development of vertical air movement and the dilution of pollutants in the vertical direction (Zhu and Lu, 2008; Chen, et al., 2016) from causing heavy air pollution. Generally, during stable weather, the wind speed is low, and the dynamic and thermal characteristics of the lower atmosphere are stable. In China, stable weather often occurs in autumn and winter when the temperature is low. The contribution of stable weather to air pollution has been a wide concern (Daneshpajooh and Azoji, 2020; Peng, et al., 2021a). Since 2013, the annual average concentration of $PM_{2.5}$ in China has decreased year by year (Hou, et al., 2019), but heavy pollution cases in the Yangtze River Delta (YRD) region are still frequent (Chen, et al., 2019), and these pollution events were strongly affected by weather conditions (Zhang, et al., 2019). For the YRD region, stable weather is one of the most important reasons for heavy pollution of $PM_{2.5}$. For example, Yu, et al. (2021) studied a case of heavy pollution in Zhejiang Province in the southern YRD in 2013, which was caused by the combined effect of large-scale circulation (e.g., the weakening of the East Asian Trough) and local weather conditions [e.g., low wind speed and planetary boundary layer height (PBLH)]. In addition, under special weather conditions, the aerosol–boundary layer interaction can amplify the haze regional transport, and the transport distance can reach more than 1,000 km (Huang, et al., 2020). Meteorological conditions and pollutant emission reduction are equally important for air pollution prevention, and an important evidence was that heavy pollution events could not be avoided even under the condition that the pollutant emissions were greatly reduced during the COVID-19 lockdown (Wang, et al., 2020a).

Urban air pollution during stable weather in China has been widely studied in recent years. Beijing was often polluted due to stable weather, and the stable weather index calculated by Zhang, et al. (2017) was closely related to $PM_{2.5}$, which can quantify the contribution of local emissions and meteorological conditions to $PM_{2.5}$ pollution. In Shanghai, $PM_{2.5}$ and O_3 showed that regional transport from north China was an important factor for the stable weather in the region (Li, et al., 2019; Zhang, et al., 2020b). However, due to substantial and complex local emission sources (industry, agriculture, traffic, etc.), the contribution of local pollution cannot be ignored (Yu, et al., 2021). Autumn and winter were the seasons of frequent stable weather in Guanzhong area, which made it difficult for pollutants to be diluted, forming a heavy haze by local emission (Hu, et al., 2020). A study in Ningbo found that the dominant components of $PM_{2.5}$ during stable weather under different meteorological conditions were different, which provides a new idea for stable weather pollution control in different regions (Zhang, et al., 2020c).

The model simulation based on observation data could help analyze the processes of urban air pollution during stable weather. The principal component analysis in T-mode (PCT) was often used in weather classification. A study based on PCT in Chengdu showed the characteristics of two typical heavy pollution synoptic types, quantitatively calculating the potential contribution of the $PM_{2.5}$ concentration during stable weather (Zhang, et al., 2020d). The Weather Research and Forecast model (WRF) has been proved to capture mesoscale meteorological characteristics (Zhang, et al., 2012; Businger, et al., 2015; Li and Chen, 2017). A study based on the WRF-chem model in Shanghai showed that anthropogenic emission regional transport and meteorological condition during stable weather contributed 32.2% and 17.2% to $PM_{2.5}$, respectively (Chang, et al., 2016). A similar study in Beijing found that meteorological factors accounted for approximately 51% of $PM_{2.5}$ during stable weather in winter (Xu, et al., 2020a). The Community Multiscale Air Quality (CMAQ) driven by the WRF (WRF-CMAQ) has been widely used in the assessment of atmospheric pollutants such as O_3 and $PM_{2.5}$ (Fann and FulcherK Baker, 2013; Baker JKelly, 2014; Zawacki, et al., 2018), and it is advantageous to calculate the contribution of local emissions or regional transport. A study in Chengdu based on the WRF-CMAQ showed that automobile emission (29%), dust (26%), and domestic pollution (24%) were the main sources of the total $PM_{2.5}$ during stable weather (Xu and Xue, 2020b). There are other models to study meteorology and air quality, such as the Computational Fluid Dynamics (CFD) (Tominaga and Stathopoulos, 2013; Yin, et al., 2019), the WRF-CHIMERE (Dumka, et al., 2021), the Artificial Neural Network (ANN) (Feng, et al., 2015). Although there were a lot of studies on the impact of stable weather on air pollution (Cheng, et al., 2015; Chen, et al., 2018; Dong and Li, 2018), few elaborated the multi-phase evolution processes of air pollution during stable weather in detail (Cai, et al., 2020).

Shanghai, located in front of the YRD, is frequently affected by regional and cross-regional transport (Chen, et al., 2020). As a megacity with a resident population of 24.87 million (by 2021), local emissions are also important, leading to the complexity in the formation mechanism of air pollution. Stable conditions such as the low PBLH and the air flow from the polluted area are important factors for the formation of air pollution in the area. Based on the long-term observation data and the WRF-CMAQ model, this study aimed to analyze the detailed processes of the heavy air pollution events during stable weather taking megacity Shanghai as an example, including the estimate of the

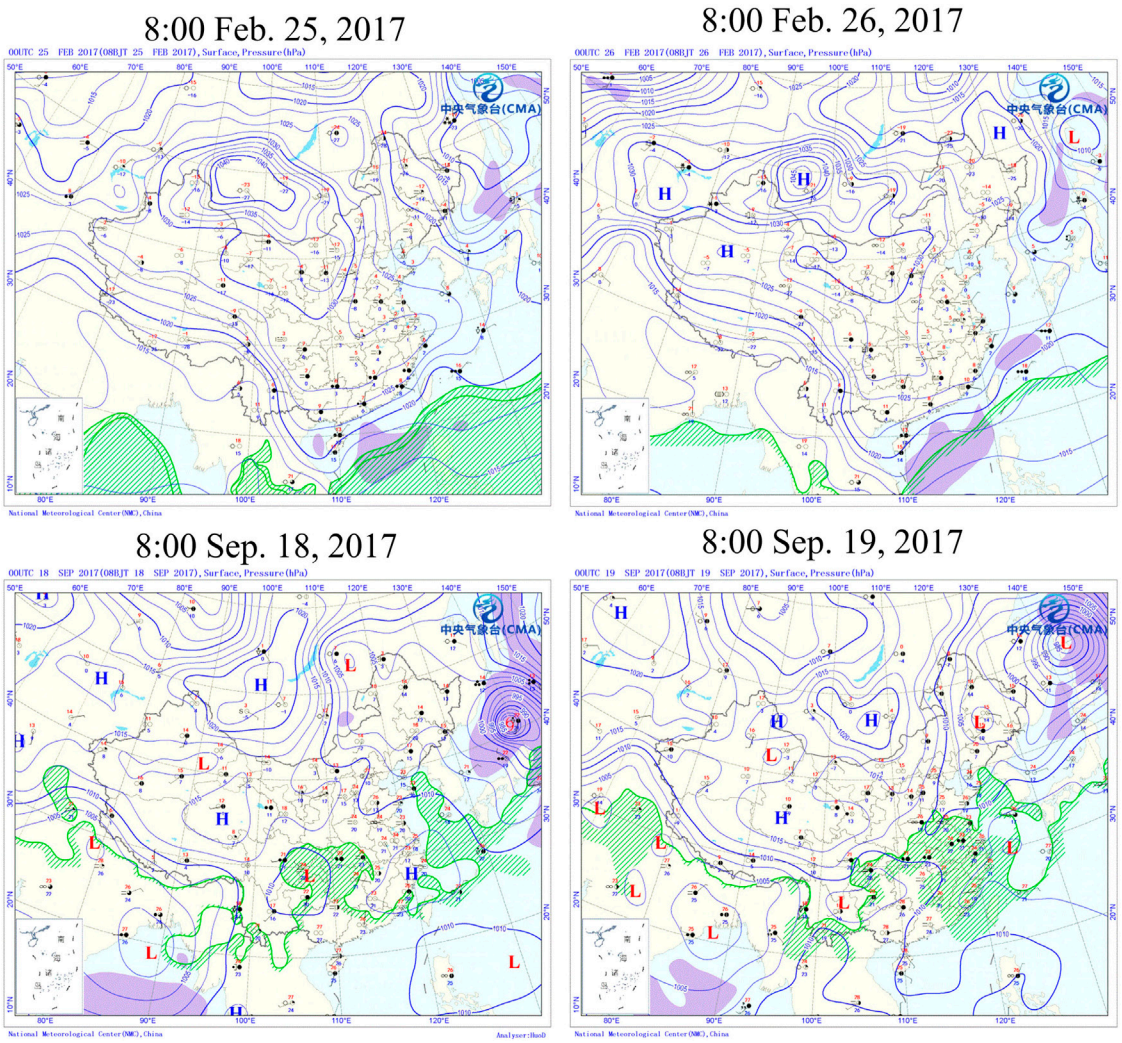

FIGURE 1 | CMAQ model nested simulation domains (domain 1: 81 km × 81 km, domain 2: 9 km × 9 km, domain 3: 1 km × 1 km) and distribution map of Shanghai meteorological stations (triangles) and air quality stations (pentagrams).

TABLE 1 | Descriptions of stable weather cases.

Case number	Date (2017)	$PM_{2.5}$ ($\mu g \cdot m^{-3}$)	O_3 ($\mu g \cdot m^{-3}$)	Surface wind speed ($m \cdot s^{-1}$)	500 hPa wind speed ($m \cdot s^{-1}$)	Precipitation (mm)
Winter Case	February 25	81.17	78.04	1.08	20.06	0
	February 26	116.48	84.94	1.09	24.95	0
Autumn Case	September 18	56.74	112.48	1.26	19.03	0
	September 19	70.34	128.87	1.37	18.52	0.2

contribution of regional transport and local emissions to air pollution. Two stable weather cases in February and September of 2017 were selected. Specifically, we divided the pollution events into four stages, which helps us understand the evolution process and the source contribution for $PM_{2.5}$, and provide a reference for accurate pollution control.

MODEL AND METHODOLOGY

Model Configuration

In this study, we used the WRF-CMAQ (www.cmascenter.org/cmaq) to simulate the meteorology and air quality. In general, the grid ratio between inner and outer domains in the WRF model is

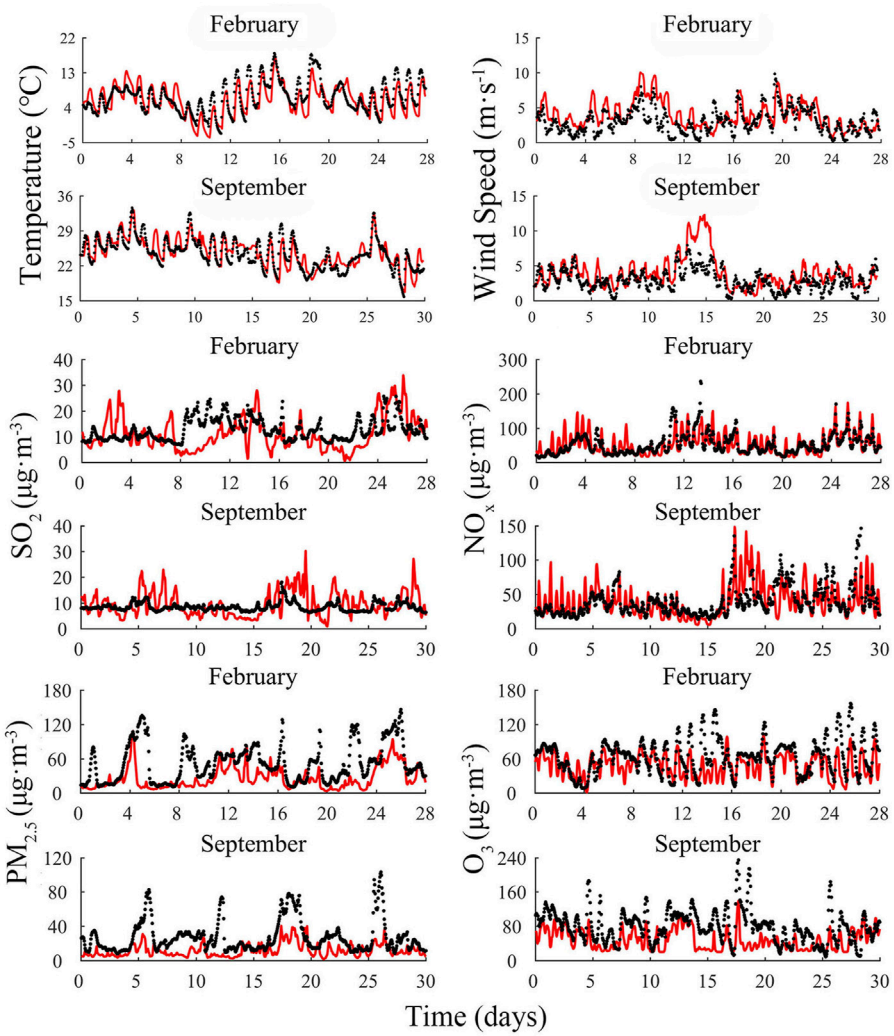

FIGURE 2 | Meteorological parameters (temperature and wind speed) and air pollutants (SO_2, NO_x, $PM_{2.5}$, and O_3) comparison of observed (black) and simulated (red) in February and September in 2017.

always 3 or 4 to avoid the numerical cumulative error in the downscaling process (Cheng, et al., 2019; Yan, et al., 2020). The WRF model was in a nested operation, and the resolutions of the three horizontal regions are 81 km, 27 km, 9 km, 3 km, and 1 km, respectively. With the accuracy guaranteed by simulation, the CMAQ_v5.0.2 model was in a nested operation, and the resolution of the three horizontal regions are 81 km, 9 km, and 1 km, respectively, which can reduce a lot of tedious work. This study area focused on the third domain, which covered the whole Shanghai area and a part of the YRD downstream area (**Figure 1**). The coverage ranged from (31.9729°N, 120.6536°E) to (30.4067°N, 122.5857°E), and the horizontal grid unit is 1 km × 1 km (155 × 143 grid points). Time-varying chemical lateral boundary conditions were derived from the 108-km-resolution hemispheric WRF-CMAQ (Mathur, et al., 2017) simulation for the 1990–2010 period (Xing, et al., 2015). The meteorological field used to couple the CMAQ model was provided by the WRF_v3.9 (Skamarock, et al., 2008). The global atmospheric reanalysis data provided by the National Center for Environmental Prediction (NCEP) were used for the initial and boundary data of the model, whose spatial resolution was 1° × 1° and temporal resolution was 6 h. The input data of topographic materials and underlying surface can be divided into three parts: the initial data of the WRF model were used in areas outside Jiangsu, Zhejiang, and Shanghai, which were the underlying surface data provided by United States Geological Survey (USGS); the land use type data of 2000 Landsat TM image interpretation were used in Jiangsu, Zhejiang, and Shanghai; and the land use type data of 2015 were used in China. The meteorological chemical interface program (mcip4.3) generated the CMAQ compatible meteorological fields (Wong, et al., 2012). In the vertical direction, the meteorological field was resolved into 29 layers, from the surface to about 18 km above the sea level. In this study, the air quality field output is 15 layers, and the height extended from the surface to about 5 km above the

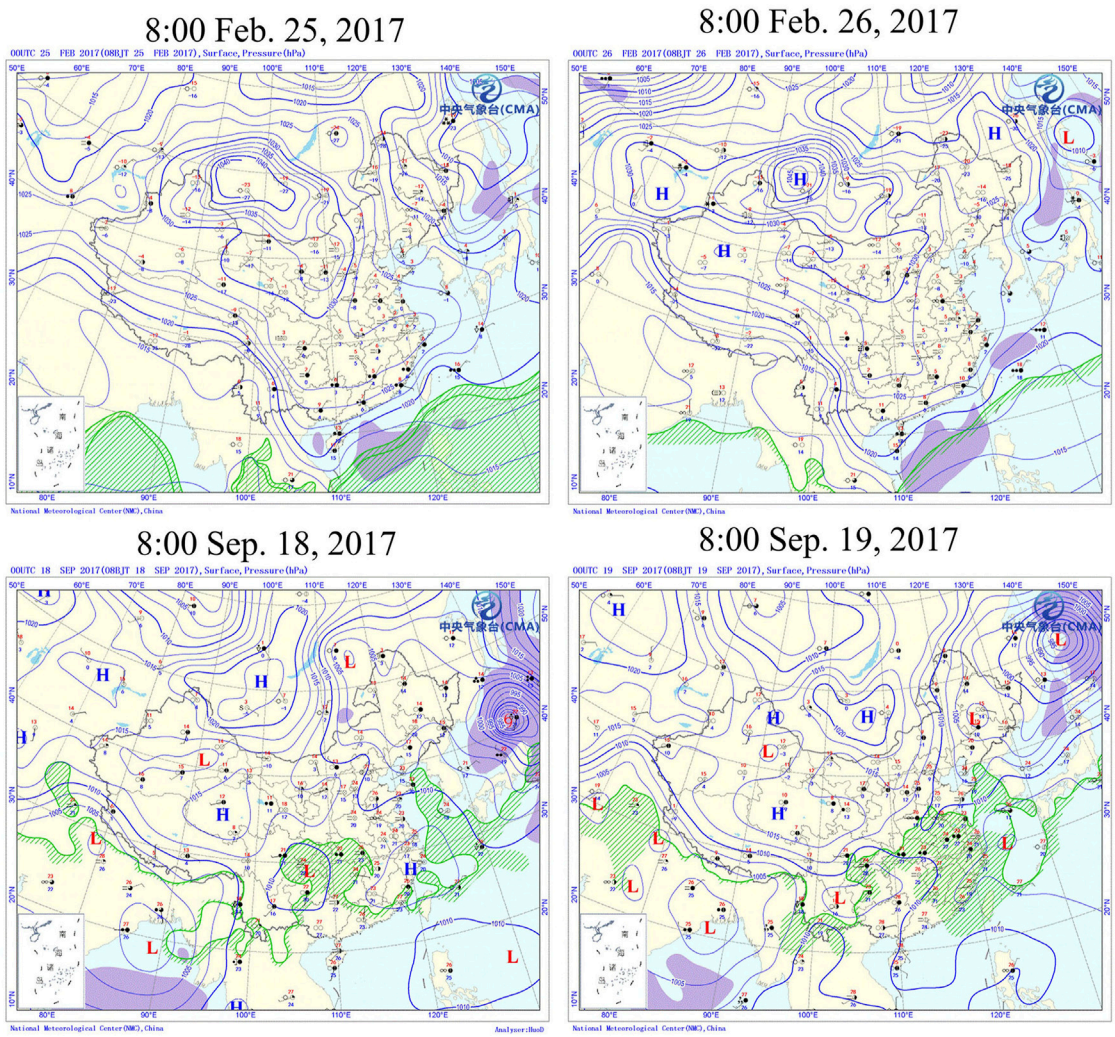

FIGURE 3 | Ground map of typical time in February and September cases (http://www.cma.gov.cn/).

sea level. The simulation period was February and September of 2017, and all meteorological fields and air quality simulation had a 2-day spin-up period before starting the simulation for the sake of reducing the impact of the initial field. The chemical mechanism used in this study was CB05 (Yarwood, et al., 2005) and AERO6 (Carlton, et al., 2010) issued by the United States Environmental Protection Agency. The specific parameterization schemes for the main physicochemical processes involved in WRF and CMAQ are shown in **Supplementary Table S3**.

Emission Inventories

The Multi-resolution Emission Inventory for China (MEIC) (Squires, et al., 2020; Chen, et al., 2021a) was used for domain 1 and domain 2. The emission data from a previous study (An, et al., 2021) and some survey data from Shanghai Environmental Monitoring Center were combined for domain 3. The total emissions of SO_2, NO_x, CO, VOCs, PM_{10}, $PM_{2.5}$, and NH_3 in the Shanghai region in 2017 were 32.8, 381.8, 980.2, 209.0, 377.0, 160.8, and 52.2 Gg, respectively. VOCs and CO emissions were mainly from boilers, which accounted for 42.4% of VOCs and 74.1% of CO. The VOCs of biogenic emissions were 5,905.9 Mg generated by MEGAN (Wang, et al., 2021), whose oxidation could significantly contribute to SOA in PM at night. Mobile sources dominated NO_x emissions, contributing 52.0% of the total. SO_2 emissions were mainly from ship sources, making up 55.7% of the total. Road and construction dust sources accounted for 63.8 and 46.4% of PM_{10} and $PM_{2.5}$ emissions, respectively.

The Simulation Schemes to Estimate the Retention Effect and the Contributions of Regional Transport, and Local Emissions

The particles in the atmosphere in a certain area can decrease through dry and wet deposition, or can be removed out of the area through atmospheric movement. The "retention effect" of $PM_{2.5}$ in this study referred to $PM_{2.5}$ in the atmosphere of a certain region, which can hardly move due to the almost stagnation of

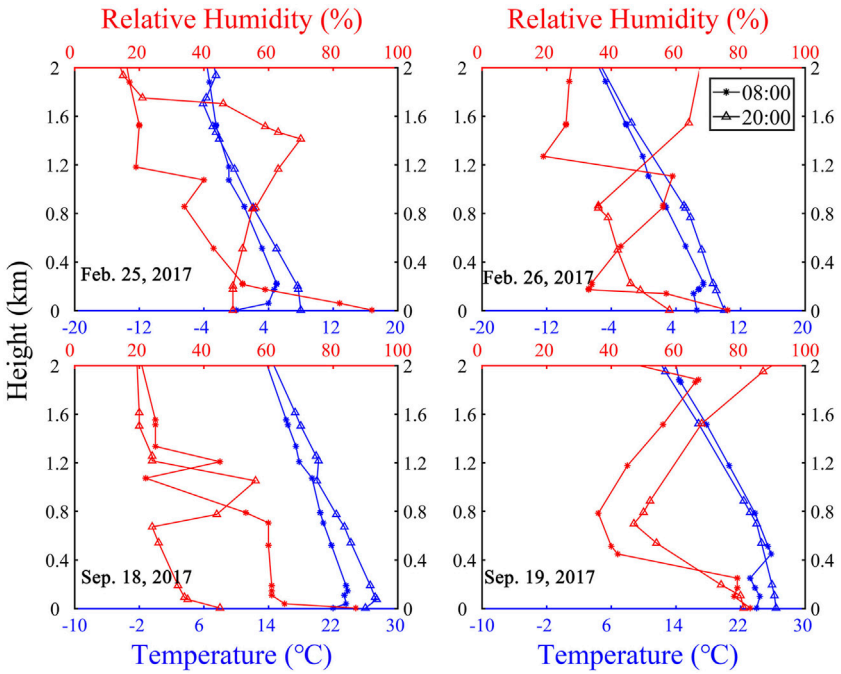

FIGURE 4 | Vertical temperature and relative humidity at Baoshan station.

atmospheric horizontal and vertical motion during stable weather.

In this study, all $PM_{2.5}$ already in Shanghai before the stable period (period I) was defined as the retention part of $PM_{2.5}$, and newly emerged $PM_{2.5}$ from local emissions and regional transport during stable weather (period II) was defined as new $PM_{2.5}$. Thus, $PM_{2.5}$ can be divided into four types: $PM_{2.5}$ related to regional transport in period I [RT (retention)] and in period II [RT (new)], and $PM_{2.5}$ related to local emissions in period I [LE (retention)] and in period II [LE (new)].

The switch method of emission inventory was used to obtain the respective contribution proportion and persistence time of local emissions and regional transport (Feng, et al., 2019). The absolute contribution of the pollution source can be obtained by the difference of two simulation schemes that can avoid systematic error and improve the reliability of the results (Stefanik, et al., 2020).

We designed 6 following simulation schemes shown in **Supplementary Table S1** to obtain the contributions of LE (new), LE (retention), RT (new), and RT (retention), respectively.

LE (new) = scheme 1 - scheme 3 (1). E (retention) = scheme 1 - scheme 2 (2) RT (new) = scheme 4 - scheme 6 (3). RT (retention) = scheme 4 - scheme 5 (4)

The Observation Data and the Air Pollution Cases During Stable Weather

The meteorological and air quality observation data in this study were provided by the Shanghai Meteorological Bureau and Shanghai Environmental Monitoring Center, both of which were in an hourly resolution. The meteorological data included 11 national monitoring stations in Shanghai, and the air quality observation data included 10 national monitoring stations and 45 municipal monitoring stations in Shanghai. The geographical distribution information of the meteorological and the air quality observation stations is shown in **Figure 1**. All observation stations are uniformly distributed in urban and suburban Shanghai. The vertical meteorological sounding data in this study were downloaded from the website of Wyoming University (http://weather.uwyo.edu/wyoming/). The components data of $PM_{2.5}$ were from Pudong Environmental Monitoring Centre in the central urban area of Shanghai, and the mass concentration of $PM_{2.5}$ was measured by an online particulate monitor (FH 62C14 series, Thermo Fisher Scientific Inc.). The study by Zhang, et al.(2020b) has a more detailed description of the measurement methods and instruments.

To determine the cases for analysis, we firstly chose the dates with the air quality index (IAQI) of $PM_{2.5}$ greater than 100 (Feng, et al., 2013), and then the ground pressure fields every 6 h of each date were analyzed. The cases with sparse isobars, low surface wind speed, and temperature inversion were selected as stable weather candidates. The parameters of the obtained cases were further verified including daily average wind speed near the ground (10 m) < 3.2 m/s, daily average wind speed in the middle troposphere (500 hPa) < 13 m/s, and daily accumulated precipitation <1 mm (Horton, et al., 2014; Zhang, et al., 2016). After quantitative screening, two cases closest to the constraint conditions were selected from different seasons in 2017 as typical cases (**Table 1**).

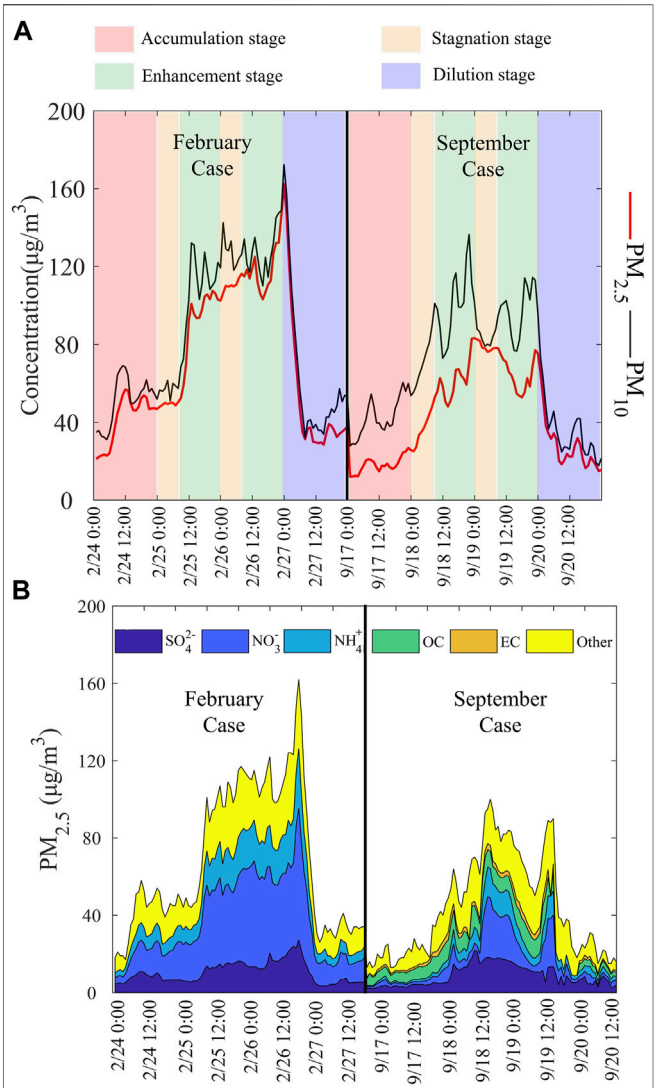

FIGURE 5 | Concentration of particulate matter in Shanghai **(A)** and the components of $PM_{2.5}$ in Pudong Monitoring Station **(B)** during two stable cases in 2017.

Two individual cases were representative of typical stable weather. The February case represented typical winter weather situation. Most parts of China (except for the northeast) were under the control of the cold high pressure, with a previous cold front already pressing south to the coastal areas of southern China and a supplementary cold front in Mongolia. During this period, Shanghai was located in the mean pressure field of the continental cold high pressure. In contrast, September is the seasonal transition month when cold and warm air confront each other. There was a cold high pressure in Mongolia, while Shanghai was located near the subtropical high pressure.

Model Validations

The simulated meteorological variables (temperature and wind speed) and the concentrations of air pollutants including SO_2, NO_x, $PM_{2.5}$, and O_3 in 2017 were validated by the observation data in Shanghai. As shown in **Figure 2**, the simulation results of the vertical meteorological conditions (temperature and relative humidity) correlated well with the sounding data (R^2 ranged from 0.51 to 0.97) (**Supplementary Figure S1**). The statistics of validations are listed in **Supplementary Table S2** in the supporting information including the root mean square error (RMSE), the mean fractional bias (MFB), and the mean fractional error (MFE) (Yu, et al., 2019). The scattering plot is shown in **Supplementary Figure S2**. Most of the indicators were within the ideal range (**Supplementary Table S2**). The simulated values of temperature and NO_x were closer to the observed data, which agreed with the results of Liu and Wang (2020a) and Liu and Wang (2020b). However the simulated average wind speed was about 35% higher, which was a problem that most WRF simulations of megacities meteorological field have encountered (Prieto-Herraez, et al., 2021) and were related to urban land use types and parameterization schemes. The simulated values of $PM_{2.5}$ were generally lower than the observed values, but the temporal variation was in good agreement (**Figure 2**). For SO_2, the average simulated values were close to the observation value, and the error was about 4%. The inventories had realistic statistics on the total emission of SO_2, but the variation trend was not well captured. The ozone was underestimated by about 36%, which was likely due to the lower simulated radiation intensity and temperature.

RESULTS AND DISCUSSION

The Meteorological Conditions of Stable Weather

The sea-level pressure fields, surface wind observation data, and vertical sounding data were used to describe the typical meteorological conditions during the selected two cases of stable weather.

We studied the regional synoptic pattern in the YRD to obtain the meteorological characteristics in Shanghai. In autumn and winter, the lower troposphere in the YRD is mostly controlled by the uniform pressure field or located at the top of the high pressure (Cheng, et al., 2020; Han and Ma, 2020; Peng, et al., 2021b). These weather conditions are conducive to the accumulation of $PM_{2.5}$, which is similar to this study. At the 500 hPa level of the troposphere, the general circulation in China was zonal flow, the meridional wind was weak, and the upper air wind speed was small (**Supplementary Figure S3**). When the two pollution cases occurred, the isobaric distribution of tropospheric 850 hPa showed that the YRD was controlled by a uniform pressure field or a high pressure (**Supplementary Figure S4**). The surface isobars in YRD were sparse and the wind speed was weak (**Figure 3**). After the air mass flowed southeastward, a wide range of weak high-pressure centers were formed near the YRD. The above weather situation of different altitude together hindered the vertical and horizontal atmosphere movement, which was a typical meteorological condition in a large scale for long duration, leading to severe $PM_{2.5}$ pollution. From February 27–28 and September 20–21, the trough moved eastward and brought marine flow, which contributed to pollution dilution.

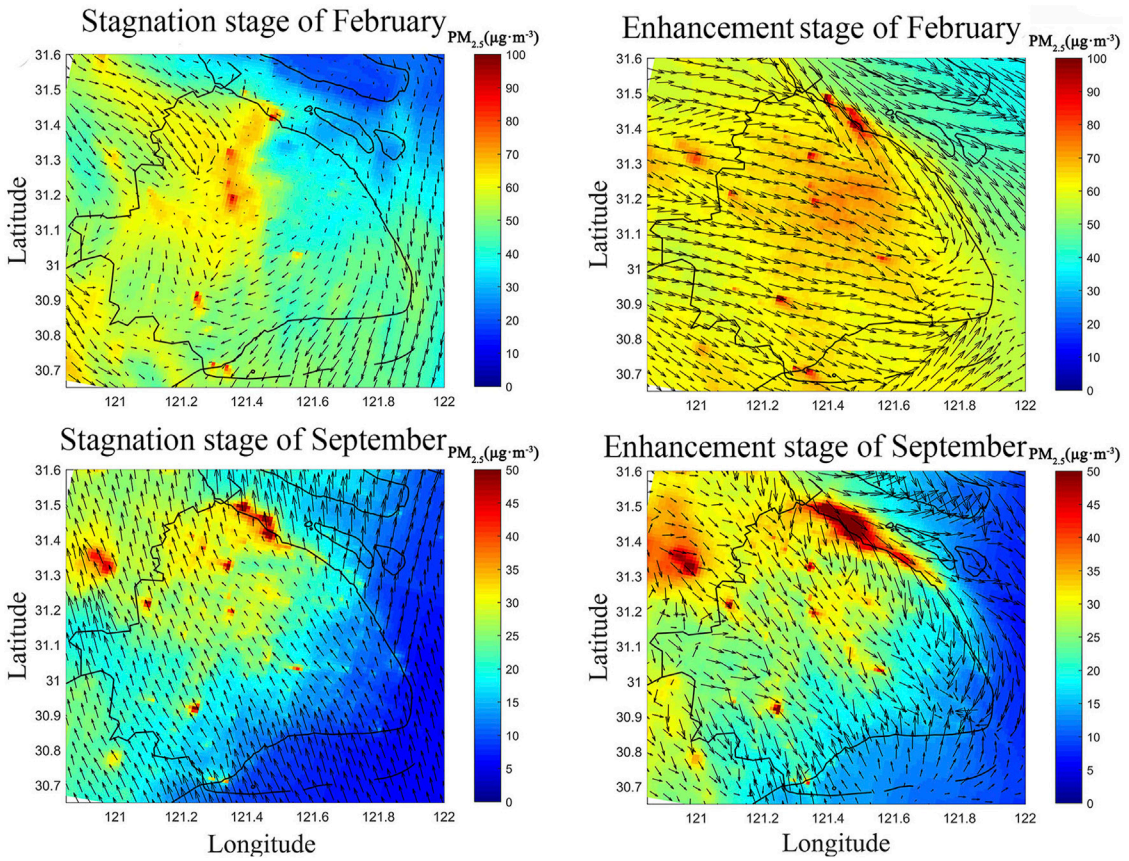

FIGURE 6 | Wind field of Shanghai during stable weather in February and September.

As shown in **Supplementary Figure S5**, for the winter and autumn cases, the wind speed in the YRD cities near Shanghai (a–f) was generally low during the period of stable weather, and the average wind speed in Shanghai (g–j) was even lower. During the nighttime in the period of stable weather, the average wind speed was 0–1 m/s, leading to the fact that air pollutants stagnated in the atmosphere and could not be transported further, while during the daytime in the period of stable weather, the average wind speed was 2–3 m/s, which provided the flowability of more polluted air mass transported into Shanghai. After stable weather, the southerly wind with the average speed back to the initial level was conducive to the dilution of pollutants.

Differently, within 1–2 days before stable weather, the YRD was controlled by the front of a high-pressure system in the February case, and by the typhoon periphery in the September case, although the wind direction in the YRD cities was generally north wind for both cases. However, the wind speed in the winter case reached around 5 m/s, while that in the autumn case was larger (7 m/s). During stable weather, on the ground and at the height of 850 hPa level, the wind speed was 1.6 m/s and 8.0 m/s in the winter case, and 2.7 m/s and 5.3 m/s in the autumn case, respectively. The wind speed at 850 hPa was lower in the autumn case, while the wind direction at 850 hPa in eastern China was not consistent, forming a barrier around the YRD, which was adverse to regional transport.

Figure 4 shows that temperature inversion was observed every day at local time 8:00 in two cases, even at local time 20:00 on September 18. The temperature inversion generally occurred at about 200 m above the ground except September 19 (about 500 m), which was not conducive to the vertical dilution and the transport of pollutants. It was worth noting that the slope between relative humidity and height at local time 08:00 was steeper than 20:00 within the inversion layer due to the evaporation of the ground surface, which was one evidence of vertical stable atmosphere in the boundary layer at night.

The Evolution Stages of the Air Pollution Episodes

During the two cases in stable weather, $PM_{2.5}$ broke the national air quality standard. As shown in **Figure 5A**, the peak $PM_{2.5}$ concentration in Shanghai reached 162.3 μg/m^3 and 83.2 μg/m^3 in the case of February and September, respectively. The $PM_{2.5}$ concentration remained at a relatively high level during the nighttime, but changed substantially during the daytime of stable weather. As shown in **Figure 5B**, the components of $PM_{2.5}$ showed similar characteristics. During the two stable episodes, the sulfate concentration varied most slightly, but the nitrate concentration varied most dramatically during the two

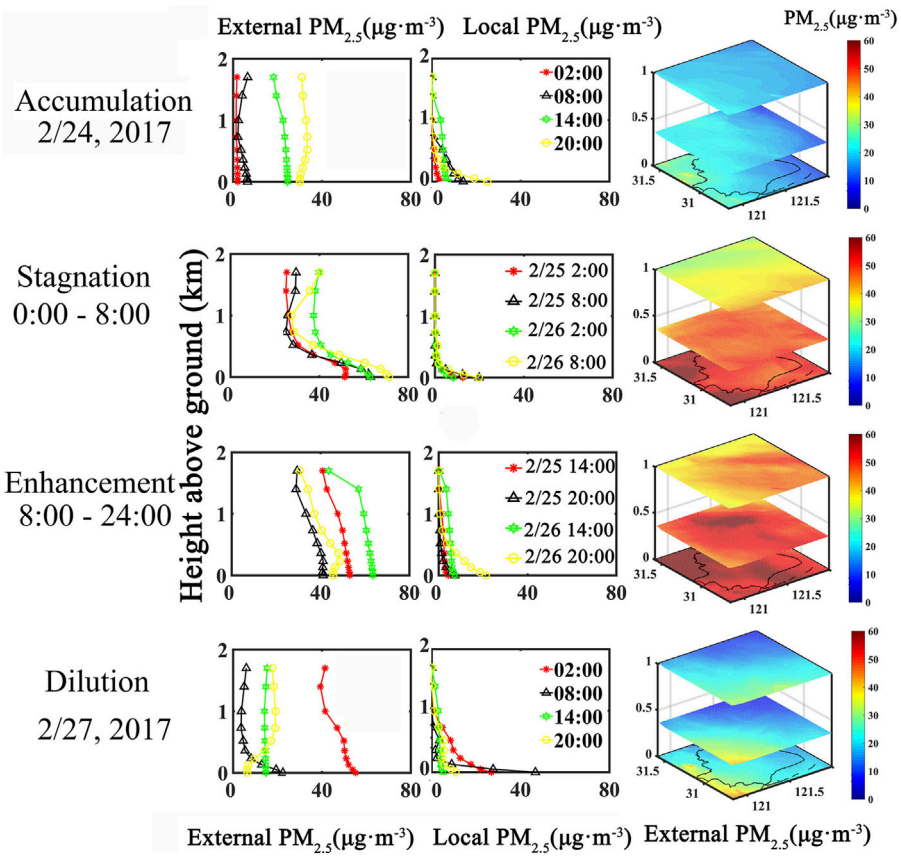

FIGURE 7 | Simulated local and external PM2.5 vertical profiles and vertical spatial distribution in four different stages in February 24–27, 2017.

stable periods. The rise of nitrate concentration was the main reason for the peak $PM_{2.5}$ concentration. The average values of the nitrate concentration during the two episodes reached 40.1 μg/m^3 and 12.2 μg/m^3, accounting for 41% and 19% of the total $PM_{2.5}$, respectively. In addition, the average concentrations of sulfate and ammonium were 14.0 μg/m^3 and 17.3 μg/m^3, accounting for 14% and 18% of the total $PM_{2.5}$ for the February case, and 12.8 μg/m^3 and 7.7 μg/m^3, accounting for 19% and 12% for the September case, respectively.

Figure 6 shows the wind and $PM_{2.5}$ concentration field in the Shanghai region, partially explaining the variation pattern of $PM_{2.5}$ characteristics during day and night. The $PM_{2.5}$ concentration was higher in the north and west than the south and east of Shanghai. When the wind speed was less than 1 m/s during the stagnation stage, the transport of $PM_{2.5}$ was hindered. When the wind speed was 2–3 m/s, the regional $PM_{2.5}$ from the north and west position was transported into Shanghai, and the contrary wind direction along the seashore was disadvantageous to the dilution of $PM_{2.5}$.

Based on the foregoing analysis, the $PM_{2.5}$ pollution episodes can be divided into the following four stages: the accumulation stage, the stagnation stage, the enhancement stage, and the dilution stage. In detail, the accumulation stage was the period before stable weather when the concentration of $PM_{2.5}$ was at a relatively low level. However, the higher wind speed at this stage was conducive to the regional transport of pollutants. The stagnation stage was in the wee hours (0:00–8:00) of stable weather, when the temperature inversion (**Figure 4**) and the small wind speed (**Figure 6**) occurred, which resulted in the $PM_{2.5}$ concentration having a flat trend. The enhancement stage was the remaining hours (8:00–24:00) during stable weather, when the temperature inversion disappeared, the PBLH increased, and the solar radiation led to the enhancement of vertical and horizontal convection. The wind speed was larger than that during the stagnation stage, which provided favorable conditions for regional transport. $PM_{2.5}$ during the enhancement stage experienced a substantial rise from 14:00 to 23:00 in the winter case and 16:00 to 23:00 in the autumn case. During the dilution stage, the stable meteorological conditions disappeared, and the $PM_{2.5}$ concentration declined rapidly within 2–3 h.

As shown in **Figure 5**, the components of $PM_{2.5}$ showed different characteristics under different stages. During the accumulation stage, there were small differences in concentration among $PM_{2.5}$ components, and the nitrate concentrations were in a relatively low percentage (30% for

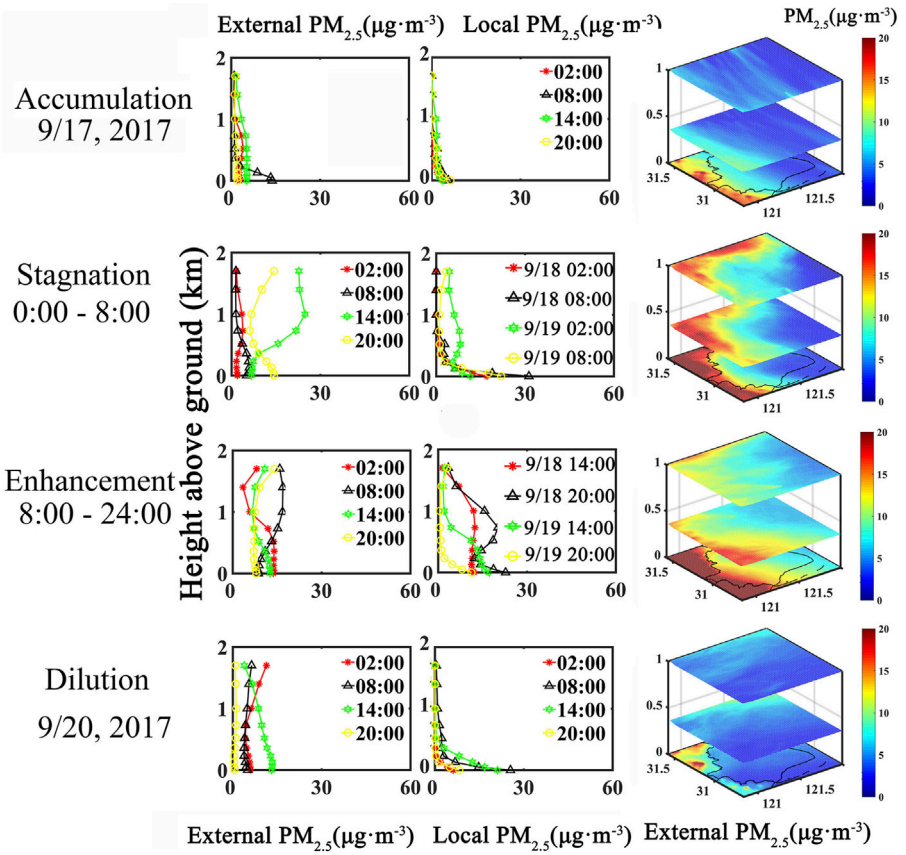

FIGURE 8 | Simulated local and external PM2.5 vertical profiles and vertical spatial distribution in four different stages in September 17–20, 2017.

the February case and 9% for the September case). During the stagnation stage, the characteristics of $PM_{2.5}$ components were constant and similar to the previous moment. Thus, for the February case, the characteristics of $PM_{2.5}$ components during the stagnation stage in February 25 were similar to the accumulation stage, but the characteristics of $PM_{2.5}$ components during the stagnation stage in February 26 were similar to the enhancement stage. During the enhancement stage, nitrate dominated in $PM_{2.5}$ and the concentrations were 44.7 μg/m^3 and 13.7 μg/m^3, which accounted for 41% and 19% of total $PM_{2.5}$ for the February and September case, respectively. After the stable period, the proportions of $PM_{2.5}$ components were similar to the accumulation stage (it may indicate that local emissions sources were relatively stable), and the percentages of nitrate were 33% and 13% for the February and September case, respectively.

It should be noted that the period during 0:00–8:00 was recognized as the stagnation stage rather than 20:00 to 8:00, because temperature inversion was not obvious at 20:00 (**Figure 4**), which did not meet the definition of stagnation stage. According to **Figure 5**, **Figure 9**, and previous research (Jing, et al., 2011; Liu, et al., 2019; Chen, et al., 2021b), the time from 8:00 to 24:00 was designated the enhancement stage, which guaranteed the accuracy of the definition of the stagnation stage.

The Diverse Contributions of Regional Transport and Local Emission and the Retention Effects During Stable Weather

The Contributions of Regional Transport and Local Emission

The contributions of regional transport and local sources to the pollution episodes was estimated based on the method in Section 2.3. The vertical profile of local and external sources of $PM_{2.5}$ concentrations is presented in **Figure 7**, and the analysis was conducted by stages.

The accumulation stage was February 24 and September 17. As shown in **Supplementary Figure S6** and **Supplementary Figure S7** for the winter case, the absolute concentration of $PM_{2.5}$ related to external sources on February 24 gradually increased over time in the atmosphere at different altitudes. For the autumn case, the wind direction and the wind speed were similar to those in the winter case, but there was typhoon in the East China Sea during September 14 to 17, whose cleaning effect blocked the accumulation of $PM_{2.5}$ (Chang, et al., 2011; Liu, et al., 2018). At the surface level, the local and external sources accounted for 41.7% and 58.3% of $PM_{2.5}$ in the winter case, respectively, while they accounted for 42.4% and 57.6% of $PM_{2.5}$ in the autumn case, respectively.

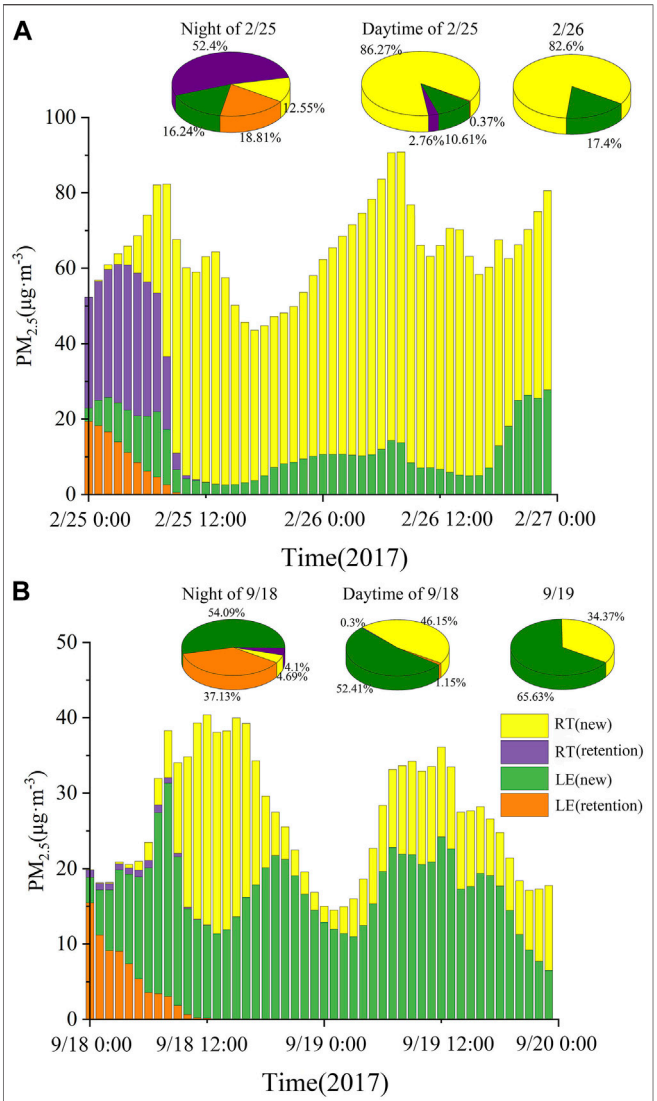

FIGURE 9 | The simulated $PM_{2.5}$ and pie chart of retention $PM_{2.5}$ and new $PM_{2.5}$ in Shanghai in February **(A)** and September **(B)** 2017 (RT: Regional Transport, LE: Local Emission.

The stagnation stage included 0:00–8:00 of February 25–26 and September 18–19. As shown in **Figure 7**, for the winter case, the $PM_{2.5}$ concentration from local emissions and regional transport both gradually decreased from the surface to about 2 km altitude. For the autumn case in **Figure 8**, only the $PM_{2.5}$ concentration from local emissions showed a similar trend to that for the winter case. In the winter case, the local (external) $PM_{2.5}$ concentration was 14.1 μg/m^3 (53.4 μg/m^3), accounting for 20.9% (79.1%) of the total $PM_{2.5}$. In the autumn case, the local (external) $PM_{2.5}$ concentration was 15.6 μg/m^3 (5.1 μg/m^3), contributing 75.4% (24.6%) to the total $PM_{2.5}$. The proportion of $PM_{2.5}$ concentration related to regional transport in the winter case was higher than that in the autumn case. On the one hand, the wind speed was lower in the winter case, resulting in a worse atmospheric diffusion condition. On the other hand, the typhoon in the autumn case blocked the accumulation of $PM_{2.5}$ during the stage to weaken the air pollution level in this episode.

The enhancement stage covered 8:00–24:00 of February 25–26 and September 18–19. As shown in **Figures 7**, **8**, the $PM_{2.5}$ concentrations from local emissions and regional transport both changed little with height, which was different from the stagnation stage. This result showed that the vertical convection was well mixed during the enhancement stage. In the winter case, the local $PM_{2.5}$ concentration was 9.2 μg/m^3 and accounted for 14.6% of the total $PM_{2.5}$, while the external $PM_{2.5}$ concentration was 53.6 μg/m^3 and accounted for 85.4% of the total $PM_{2.5}$. In contrast, in the autumn case, the local $PM_{2.5}$ concentration was 18.7 μg/m^3 and accounted for 60.6% of the total $PM_{2.5}$, while the external $PM_{2.5}$ concentration was 12.2 μg/m^3 and accounted for 39.4% of the total $PM_{2.5}$. The minor proportion (39.4%) of external $PM_{2.5}$ during the enhancement stage came from the weaker northwest wind speed (~<3 m/s) in the troposphere of 850 hPa (**Supplementary Figure S3**).

The reasons for the lower peak value of the $PM_{2.5}$ concentration in the autumn case were the larger wind speed on the ground, the typhoon before stable weather, and the messy wind direction in the troposphere of 850 hPa, which provided better dilution conditions, blocking up of $PM_{2.5}$ accumulation, and less regional transport, respectively.

The dilution stage was February 27 and September 20. After stable weather, the external $PM_{2.5}$ concentration at the surface level was lower than that in the upper air, while the local $PM_{2.5}$ concentration showed a reversed pattern. When the pollution episodes ended, the vertical distribution of the contribution of local and external sources switched to a normal result. In the winter case, the local and external $PM_{2.5}$ concentrations were 18.4 μg/m^3 and 26.3 μg/m^3, accounting for 41.2% and 58.8% of the total $PM_{2.5}$, respectively, while they were 10.2 μg/m^3 and 3.5 μg/m^3, accounting for 74.5% and 25.5% in the autumn case, respectively.

The Retention Effects of Regional Transport and Local Emissions

The "retention effect" was caused by the trapped air pollutants under stable weather conditions. As shown in **Figure 9A**, during the stagnation stage of February 25, the retention part dominated the $PM_{2.5}$ pollution by more than 70%, in which the external $PM_{2.5}$ was the main source of the total $PM_{2.5}$ (52.4%), whereas the local $PM_{2.5}$ only accounted for 18.8%, while during the enhancement stage of February 25, the vast majority of total $PM_{2.5}$ was attributed to the RT (new) with a contribution of 86.3%, but to a much lesser extent, the LE (new) only accounted for 10.6%. The higher wind speed and the northwesterly wind during the enhancement stage facilitated the transport of $PM_{2.5}$ from the inland YRD to Shanghai, resulting in the predominance of newly transported $PM_{2.5}$. At the same time, the wind direction at the seaside was disordered, forming a cyclone, and hence a rather weak outflow of highly polluted air mass over Shanghai.

However, as shown in **Figure 9B**, during the stagnation stage of September 18, the local emissions part dominated the $PM_{2.5}$ pollution by more than 90%, in which the retention

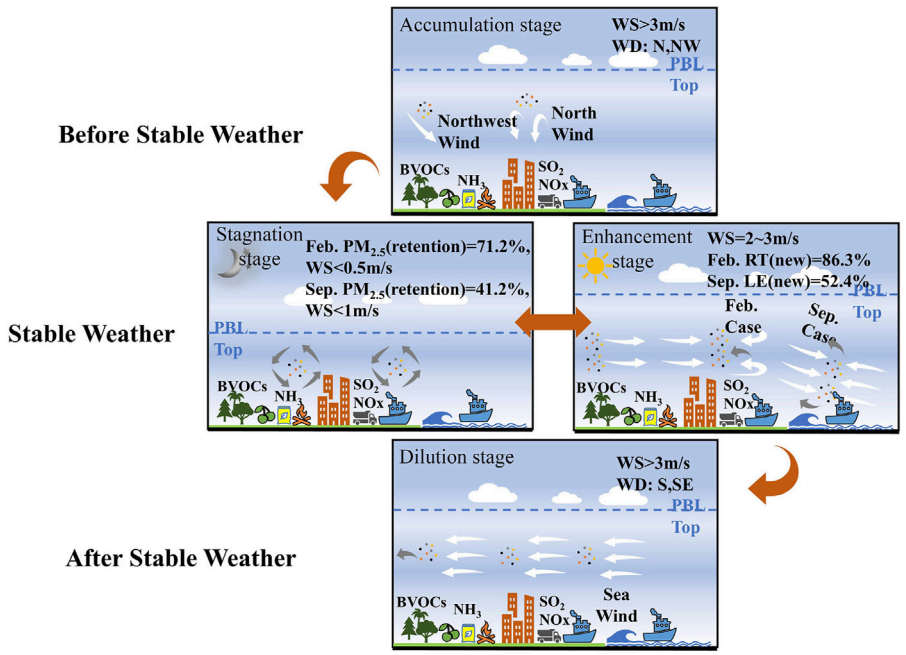

FIGURE 10 | The diagrammatic sketch of $PM_{2.5}$ pollution process in stable weather.

$PM_{2.5}$ was the main source of the total $PM_{2.5}$ (54.1%), whereas the new $PM_{2.5}$ only accounted for 37.1%. The minor proportion (8.2%) of RT compared to the winter case was caused by the blocking-up during the accumulation stage due to the typhoon. During the enhancement stage of September 18, the total $PM_{2.5}$ was mainly attributed to the LE (new) with a contribution of 52.4%, but to a lesser extent, the RT (new) only accounted for 46.2%. Compared with the winter case during the enhancement stage, the wind speed was weaker at the 850 hPa level, which resulted in the RT (new) accounting for a smaller portion of $PM_{2.5}$.

To sum up, the $PM_{2.5}$ concentration was dominated by regional transport of the winter case, while local emission was the main cause of the autumn case.

DISCUSSION

The general process of the two selected $PM_{2.5}$ pollution episodes in Shanghai, a coastal city, can be summarized in **Figure 10**, and the whole pollution process can be divided into four stages. The accumulation stage is the period before stable weather to provide the background of $PM_{2.5}$ for the following stable stage. If the accumulation stage is blocked, the pollution level will be effectively reduced during the stable period. The stagnation stage is the nighttime during stable weather, when temperature inversion and a fairly small wind speed occur, making the retention $PM_{2.5}$ highly stable, and the new air pollutants cannot be transported inside at the same time. The enhancement stage following the stagnation stage was key to deciding the air pollution level, but diverse with different stable weather types. The dilution stage comes after the stable stage, during which the $PM_{2.5}$ concentration will decline rapidly. For the prevention and control of heavy particulate pollution, the integration of local and regional emissions in the YRD considering the diversity of stable weather was of great importance (Wang, et al., 2020b).

It is noted that the simulation accuracy during stable weather is still challenging. As provided in Section 2.5, the monthly simulation accuracy evaluation was acceptable on the whole, but with a larger underestimation during the stable period (**Figure 2**). Thus, there must be some uncertainties raised in the retention effect results by the large underprediction in the high $PM_{2.5}$ in this study. We evaluated the simulation accuracy of the main components of $PM_{2.5}$ in **Supplementary Figure S8** to explain the underestimation in some degree. As shown in **Supplementary Figure S8**, according to the comparison of component observation data during two episodes, SO_4^{2-} was close to the observation data, but there was a large underestimation in NO_3^- and some other components of $PM_{2.5}$. The simulation of NH_4^+ was better in the September episode than that in the January episode. In September, the underestimation in nitrate, organic carbon, and elemental carbon concentrations was 5.4 μg/m^3, 5.0 μg/m^3, and 2.1 μg/m^3, accounting for 22%, 20%, and 9% of the $PM_{2.5}$ underestimation, respectively. However, in the January episode, the underestimation of NO_3^- and NH_4^+ reached 14.8 μg/m^3 and 9.1 μg/m^3, respectively, accounting for the

major part of underestimated $PM_{2.5}$. It indicated that the discrepancy between the simulated and observed components varied with the weather conditions. The underestimated key components of $PM_{2.5}$ in numerical simulations of stable weather need further attention in the future.

CONCLUSION

In this study, two air pollution cases in autumn and winter of 2017 were selected to probe the evolution process of heavy air pollution during stable weather, focusing on the contributions of regional transport and local emissions to $PM_{2.5}$ pollution. According to the concentration of $PM_{2.5}$ and meteorological conditions, we defined the development of pollution episodes into four stages: accumulation stage, stagnation stage, enhancement stage, and dilution stage.

The accumulation stage before stable weather provided the background of heavy $PM_{2.5}$ pollution, whose northwest wind was instrumental in regional transport. The "retention effects" led retention $PM_{2.5}$ to a dominant position during the stagnation stage, which accounted for 71.2% and 41.2% of total $PM_{2.5}$ in the winter and autumn case, respectively. The enhancement stage was conducive to regional transport, but not to the dilution of $PM_{2.5}$, which made RT (new) important during the enhancement stage. During the enhancement stage, newly transported $PM_{2.5}$ from regional transport accounted for 86.3% and 46.2% for the winter and autumn cases, respectively. The dilution stage was after stable weather when south or east clearer sea wind was instrumental in $PM_{2.5}$ dilution, and hence the $PM_{2.5}$ concentration reduced rapidly.

The $PM_{2.5}$ pollution in Shanghai was mainly from local emission in the autumn case but from regional transport in the winter case, accounting for 63.0% and 81.3%, respectively. The blocked accumulation stage by a typhoon and the weaker wind speed in the troposphere could reduce the pollution level during stable weather. Our results suggest that promoting air pollution control in the regional scale is very significant in the prevention and control of heavy particulate pollution caused by stable weather. Further studying the impact of meteorological factors under stable weather versus anthropogenic emissions as well as the precision of simulation is necessary in the near future.

DATA AVAILABILITY STATEMENT

The original contributions presented in the study are included in the article/**Supplementary Material**, Further inquiries can be directed to the corresponding author.

AUTHOR CONTRIBUTIONS

BH and YZ designed all simulation schemes, and BH wrote the first draft of the manuscript. BH, YZ, GY, and JM reviewed and modified the manuscript. XZ and ZH provided the standard of stable weather and selected the cases of stable weather. QW and QL provided the emission inventory of Shanghai. YZ was in charge of project administration. All authors contributed to manuscript revision, and read and approved the submitted version.

FUNDING

This work was supported by the Major Program of Shanghai Committee of Science and Technology, China (19DZ1205009), the National Natural Science Foundation of China (42077195), and the Program of Pudong Committee of Science and Technology, Shanghai (PKC2020-C004).

SUPPLEMENTARY MATERIAL

The Supplementary Material for this article can be found online at: https://www.frontiersin.org/articles/10.3389/fenvs.2022.858685/full#supplementary-material

REFERENCES

An, J. Y., Huang, Y. W., Huang, C., Wang, X., Yan, R. S., Wang, Q., et al. (2021). Emission Inventory of Air Pollutants and Chemical Speciation for Specific Anthropogenic Sources Based on Local Measurements in the Yangtze River Delta Region, China. *Atmos. Chem. Phys.* 21 (3), 2003–2025. doi:10.5194/acp-21-2003-2021

BakerJKelly, K. R. T. (2014). Single Source Impacts Estimated with Photochemical Model Source Sensitivity and Apportionment Approaches. *Atmos. Environ.* 96, 266–274. doi:10.1016/j.atmosenv.2014.07.042

Businger, S., Huff, R., Pattantyus, A., Horton, K., Sutton, A. J. T. Elias., et al. (2015). Observing and Forecasting Vog Dispersion from Kilauea Volcano, Hawaii. *Bull. Am. Meteorol. Soc.* 96 (10), 1667–1686. doi:10.1175/bams-d-14-00150.1

Cai, Z-y., Yang, X., Han, S-q., and YaoJ-l Liu, Q. (2020). Transport Characteristics of Air Pollution in Tianjin Based on Weather Background. *Huanjing Kexue* 41 (11), 4855–4863. doi:10.13227/j.hjkx.202004252

Carlton, A. G., Bhave, P. V., Napelenok, S. L., Edney, E. D., Sarwar, G., Pinder, R. W., et al. (2010). Model Representation of Secondary Organic Aerosol in CMAQv4.7. *Environ. Sci. Tech.* 44 (22), 8553–8560. doi:10.1021/es100636q

Chang, L. T. C., Tsai, J. H., Lin, J. M., Huang, Y. S., and Chiang, H. L. (2011). Particulate Matter and Gaseous Pollutants during a Tropical Storm and Air Pollution Episode in Southern Taiwan. *Atmos. Res.* 99 (1), 67–79. doi:10.1016/j.atmosres.2010.09.002

Chen, C. Q., Huang, L., Shi, J. H., Zhou, Y., Wang, J., Yao, X. H., et al. (2021a). Atmospheric Outflow of Anthropogenic Iron and its Deposition to China Adjacent Seas. *Sci. Total Environ.*, 750. doi:10.1016/j.scitotenv.2020.141302

Chen, H. M., Zhuang, B. L., Liu, J. N., Wang, T. J., Li, S., Xie, M., et al. (2019). Characteristics of Ozone and Particles in the Near-Surface Atmosphere in the Urban Area of the Yangtze River Delta, China. *Atmos. Chem. Phys.* 19 (7), 4153–4175. doi:10.5194/acp-19-4153-2019

Chen, L., Ma, J., and Xu, F. G. J. (2016). Analysis of a Typical Air Pollution Event in Shanghai. *Meteorol. Monthly* 42 (2), 203–212.

Chen, L., Zhou, G., Mao, Z., and Qu, Y. (2020). Variation Characteristics and Meteorological Impact Factors of Three Short-Time Severe Air Pollutions in Shanghai in 2017. *Meteorol. Monthly* 46 (5), 675–686.

Chen, T., Feng, X., Li, C., Wang, W., Song, W., and Wang, S. (2021b). Study on the Weather Conditions and Inversion Characteristics of Nine Sessions of Atmospheric Heavy Pollution in Chengdu in the winter from 2013 to 2018. *J. Lanzhou Univ. Nat. Sci.* 57 (1), 82.

Chen, Y. N., Zhu, Z. W., Luo, L., and Zhang, J. W. (2018). Severe Haze in Hangzhou in winter 2013/14 and Associated Meteorological Anomalies. *Dyn. Atmospheres Oceans* 81, 73–83. doi:10.1016/j.dynatmoce.2018.01.002

Cheng, J., Su, J. P., Cui, T., Li, X., Dong, X., Sun, F., et al. (2019). Dominant Role of Emission Reduction in PM2.5 Air Quality Improvement in Beijing during 2013-2017: a Model-Based Decomposition Analysis. *Atmos. Chem. Phys.* 19 (9), 6125–6146. doi:10.5194/acp-19-6125-2019

Cheng, N-l., Li, Y-t., Zhang, D-w., Nie, T., Qiu, Q-h., and Xu, W-s. (2015). Formation Mechanism of a Serious Pollution Event in January 2013 in Beijing. *Huanjing Kexue* 36 (4), 1154–1163.

Cheng, Y., Hou, X., Zhu, B., and Lu, W. (2020). The Meteorological Causes of a Heavy Pollution Process in BTH and YRD Area with Stable Weather Condition. *Acta Scientiae Circumstantiae* 40 (5), 1575–1586.

Daneshpajooh, N., and Azoji, M. A. (2020). PM Dispersion during Stable winter Episodes in Tehran and Effect of Governmental Emission Regulations. *Atmos. Pollut. Res.* 11 (8), 1316–1328. doi:10.1016/j.apr.2020.05.008

Dong, Z., Kong, H., and Li, H. (2018). Numerical Simulation and Transport Analysis of Three Heavy Air Pollution Processes in Henan Province in winter. *Acta Scientiae Circumstantiae* 38 (3), 1071–1079.

Dumka, U. C., Kaskaoutis, D. G., Verma, S., Ningombam, S. S., Kumar, S., and Ghosh, S. (2021). Silver Linings in the Dark Clouds of COVID-19: Improvement of Air Quality over India and Delhi Metropolitan Area from Measurements and WRF-CHIMERE Model Simulations. *Atmos. Pollut. Res.* 12 (2), 225–242. doi:10.1016/j.apr.2020.11.005

Fann, N., and FulcherK Baker, C. M. (2013). The Recent and Future Health Burden of Air Pollution Apportioned across US Sectors. *Environ. Sci. Tech.* 47 (8), 3580–3589. doi:10.1021/es304831q

Feng, J. L., Zhang, Y., Li, S. S., Mao, J. B., Patton, A. P., Zhou, Y. Y., et al. (2019). The Influence of Spatiality on Shipping Emissions, Air Quality and Potential Human Exposure in the Yangtze River Delta/Shanghai, China. *Atmos. Chem. Phys.* 19 (9), 6167–6183. doi:10.5194/acp-19-6167-2019

Feng, Q., Wu, S. J., Du, Y., Xue, H. P., Xiao, F., Ban, X., et al. (2013). Improving Neural Network Prediction Accuracy for PM10 Individual Air Quality Index Pollution Levels. *Environ. Eng. Sci.* 30 (12), 725–732. doi:10.1089/ees.2013.0164

Feng, X., Li, Q., Zhu, Y. J., Hou, J. X., JinJ, L. Y., and Wang, J. (2015). Artificial Neural Networks Forecasting of PM2.5 Pollution Using Air Mass Trajectory Based Geographic Model and Wavelet Transformation. *Atmos. Environ.* 107, 118–128. doi:10.1016/j.atmosenv.2015.02.030

Han, B., and Ma, X. (2020). Analysis of the Severe Haze Events in the Yangtze River Delta during the winter of 2014-2018 and the Impact of the Weather Situation on Severe Haze. *Acta Scientiae Circumstantiae* 40 (7), 2333–2345.

Horton, D. E., Skinner, C. B., Singh, D., and Diffenbaugh, N. S. (2014). Occurrence and Persistence of Future Atmospheric Stagnation Events. *Nat. Clim. Change* 4 (8), 698–703. doi:10.1038/nclimate2272

Hou, X. W., Zhu, B., and Lu, K. R. K. W. (2019). Inter-annual Variability in fine Particulate Matter Pollution over China during 2013-2018: Role of Meteorology. *Atmos. Environ.* 214. doi:10.1016/j.atmosenv.2019.116842

Hu, L., Cheng, L., Lin, Y., Hu, S., and He, X. (2020). A Conceptual Model of Regional Pollution and Meteorological Conditions in Guanzhong Region. *Arid Zone Res.* 37 (6), 1496–1503. doi:10.1039/c9py01701a

Huang, X., Ding, A. J., Wang, Z. L., Ding, K., Gao, J., Chai, F. H., et al. (2020). Amplified Transboundary Transport of Haze by Aerosol-Boundary Layer Interaction in China. *Nat. Geosci.* 13 (6), 428. doi:10.1038/s41561-020-0583-4

Jing, Y., Jiangyan, W. U., Xia, L. I., Chenghai, P., and Zhongwei, W. (2011). Analysis on Atmospheric Boundary Layer Structure and its Effect on Air Pollution over Urumqi City in Winter. *Arid Zone Res.* 28 (4), 717–723.

Li, L., An, J. Y., Huang, L., Yan, R. S., and Yarwood, C. H. (2019). Ozone Source Apportionment over the Yangtze River Delta Region, China: Investigation of Regional Transport, Sectoral Contributions and Seasonal Differences. *Atmos. Environ.* 202, 269–280. doi:10.1016/j.atmosenv.2019.01.028

Li, Y. L., and Chen, L. Y. (2017). Numerical Simulations of Two Trapped Mountain Lee Waves Downstream of Oahu. *J. Appl. Meteorology Climatology* 56 (5), 1305–1324. doi:10.1175/jamc-d-15-0341.1

Liu, N., Zhou, S., Liu, C. S., and Guo, J. P. (2019). Synoptic Circulation Pattern and Boundary Layer Structure Associated with PM2.5 during Wintertime Haze Pollution Episodes in Shanghai. *Atmos. Res.* 228, 186–195. doi:10.1016/j.atmosres.2019.06.001

Liu, W. J., Han, Y. X., Yin, Y., Duan, J. P., Gong, J. F., Liu, Z. H., et al. (2018). An Aerosol Air Pollution Episode Affected by Binary Typhoons in East and central China. *Atmos. Pollut. Res.* 9 (4), 634–642. doi:10.1016/j.apr.2018.01.005

Liu, Y. M., and Wang, T. (2020a). Worsening Urban Ozone Pollution in China from 2013 to 2017-Part 1: The Complex and Varying Roles of Meteorology. *Atmos. Chem. Phys.* 20 (11), 6305–6321. doi:10.5194/acp-20-6305-2020

Liu, Y. M., and Wang, T. (2020b). Worsening Urban Ozone Pollution in China from 2013 to 2017-Part 2: The Effects of Emission Changes and Implications for Multi-Pollutant Control. *Atmos. Chem. Phys.* 20 (11), 6323–6337. doi:10.5194/acp-20-6323-2020

Shu, L., Xie, M., Gao, D., Wang, T., Fang, D., and Liu, Q. (2017). Regional Severe Particle Pollution and its Association with Synoptic Weather Patterns in the Yangtze River Delta Region, China. *Atmos. Chem. Phys* 17 (21), 12871–12891. doi:10.5194/acp-17-12871-2017

Chang, L. Y., Xu, J. M., Zhou, G. Q., Wu, J. B., and Xie, Y. (2016). A Numerical Study of Typical Heavy Air Pollution Episode of PM2.5 in Shanghai. *Huanjing Kexue* 37 (3), 825–833.

Mathur, R., Xing, J., Gilliam, R., Sarwar, G., Hogrefe, C., Pleim, J., et al. (2017). Extending the Community Multiscale Air Quality (CMAQ) Modeling System to Hemispheric Scales: Overview of Process Considerations and Initial Applications. *Atmos. Chem. Phys.* 17 (20), 12449–12474. doi:10.5194/acp-17-12449-2017

Peng, W., LiKang, Y. N., Zhu, B., and Yu, X. (2021b). Characteristics and Comparative of Typical Haze Weather during Autumn and winter in the Yangtze River Delta. *China Environ. Sci.* 41 (7), 3043–3054.

Peng, Y., Wang, H., Zhang, X. Y., Zhao, T. L., Jiang, T., Che, H. Z., et al. (2021a). Impacts of PBL Schemes on PM2.5 Simulation and Their Responses to Aerosolradiation Feedback in GRAPES_CUACE Model during Severe Haze Episodes in Jing-Jin-Ji, China. *Atmos. Res.* 248. doi:10.1016/j.atmosres.2020.105268

Prieto-Herraez, D., Frias-Paredes, L., Cascon, J. M., Laguela-Lopez, S., Gaston-Romeo, M., Asensio-Sevilla, M. I., et al. (2021). Local Wind Speed Forecasting Based on WRF-HDWind Coupling. *Atmos. Res.* 248. doi:10.1016/j.atmosres.2020.105219

Squires, F. A., Nemitz, E., Langford, B., Wild, O., Drysdale, W. S., Acton, W. J. F., et al. (2020). Measurements of Traffic-Dominated Pollutant Emissions in a Chinese Megacity. *Atmos. Chem. Phys.* 20 (14), 8737–8761. doi:10.5194/acp-20-8737-2020

Stefanik, D., Matejovicova, J., Krajcovicova, J., Sediva, T., Nemcek, V., and Beno, J. (2020). Comparison of Two Methods of Calculating NO2 and PM10 Transboundary Pollution by CMAQ Chemical Transport Model and the Assessment of the Non-linearity Effect. *Atmos. Pollut. Res.* 11 (6), 12–23. doi:10.1016/j.apr.2020.02.012

Tominaga, Y., and Stathopoulos, T. (2013). CFD Simulation of Near-Field Pollutant Dispersion in the Urban Environment: A Review of Current Modeling Techniques. *Atmos. Environ.* 79, 716–730. doi:10.1016/j.atmosenv.2013.07.028

Skamarock, W. C., Klemp, J. B., Dudhia, J., Gill, D. O., Barker, D. M., Duda, M. G., et al. (2008). *A Description of the Advanced Research WRF Version 3. NCAR Technical Notes*. Note NCAR/TN-475+STR, 113. doi:10.5065/d68s4mvh

Wang, P. F., Chen, K. Y., Zhu, S. Q., and Zhang, P. W. H. L. (2020a). Severe Air Pollution Events Not Avoided by Reduced Anthropogenic Activities during COVID-19 Outbreak. *Resour. Conservation Recycling* 158. doi:10.1016/j.resconrec.2020.104814

Wang, Y. J., Liu, Z. Y., Huang, L., Lu, G. B., Gong, Y. G., Yaluk, E., et al. (2020b). Development and Evaluation of a Scheme System of Joint Prevention and Control of PM2.5 Pollution in the Yangtze River Delta Region, China. *J. Clean. Prod.* 275. doi:10.1016/j.jclepro.2020.122756

Wang, Y. J., Tan, X. J., Huang, L., Wang, Q., Li, H. L., Zhang, H. Y., et al. (2021). The Impact of Biogenic Emissions on Ozone Formation in the Yangtze River Delta Region Based on MEGANv3.1. *Air Qual. Atmosphere Health* 14 (5), 763–774. doi:10.1007/s11869-021-00977-0

Wong, D. C., Pleim, J., Mathur, R., Binkowski, F., Otte, T., Gilliam, R., et al. (2012). WRF-CMAQ Two-Way Coupled System with Aerosol Feedback: Software Development and Preliminary Results. *Geoscientific Model. Dev.* 5 (2), 299–312. doi:10.5194/gmd-5-299-2012

Xiang, Y., Zhang, T. S., Liu, J. G., Lv, L. H., and Chen, Y. S. D. Z. Y. (2019). Atmosphere Boundary Layer Height and its Effect on Air Pollutants in Beijing during winter Heavy Pollution. *Atmos. Res.* 215, 305–316. doi:10.1016/j.atmosres.2018.09.014

Xing, J., Mathur, R., Pleim, J., Hogrefe, C., Gan, C. M., Wong, D. C., et al. (2015). Observations and Modeling of Air Quality Trends over 1990-2010 across the Northern Hemisphere: China, the United States and Europe. *Atmos. Chem. Phys.* 15 (5), 2723–2747. doi:10.5194/acp-15-2723-2015

Xu, X. J., Jiang, Z. J., Li, J., Chu, Y. Q., Tan, W. S., and Li, C. C. (2020a). Impacts of Meteorology and Emission Control on the Abnormally Low Particulate Matter Concentration Observed during the winter of 2017. *Atmos. Environ.* 225. doi:10.1016/j.atmosenv.2020.117377

Xu, Y-l., Yi, A-h., and Xue, W-b. (2020b). Modeling Studies of Source Contributions to PM2.5 in Chengdu, China. *Huanjing Kexue* 41 (1), 50–56. doi:10.13227/j.hjkx.201905041

Yan, D. D., Liu, T. Y., Dong, W. J., Liao, X. H., Luo, S. Q., Wu, K., et al. (2020). Integrating Remote Sensing Data with WRF Model for Improved 2-m Temperature and Humidity Simulations in China. *Dyn. Atmospheres Oceans* 89. doi:10.1016/j.dynatmoce.2019.101127

Yarwood, G., Rao, S., Yocke, M., and Whitten, G. (2005). *Updates to the Carbon Bond Chemical Mechanism: CB05. Technical Report*. Final Report to US EPA. RT-0400675.

Yin, S., Nie, W., Liu, Q., and Hua, Y. (2019). Transient CFD Modelling of Space-Time Evolution of Dust Pollutants and Air-Curtain Generator Position during Tunneling. *J. Clean. Prod.* 239. doi:10.1016/j.jclepro.2019.117924

Yu, X., Venecek, M., Kumar, A., Hu, J. L., Tanrikulu, S., Soon, S. T., et al. (2019). Regional Sources of Airborne Ultrafine Particle Number and Mass Concentrations in California. *Atmos. Chem. Phys.* 19 (23), 14677–14702. doi:10.5194/acp-19-14677-2019

Yu, Y., Xu, H. H., Jiang, Y. J., Chen, F., Cui, X. D., He, J., et al. (2021). A Modeling Study of PM2.5 Transboundary Transport during a winter Severe Haze Episode in Southern Yangtze River Delta, China. *Atmos. Res.* 248. doi:10.1016/j.atmosres.2020.105159

Zawacki, M., Baker, K. R., Phillips, S., and Wolfe, K. D. P. (2018). Mobile Source Contributions to Ambient Ozone and Particulate Matter in 2025. *Atmos. Environ.* 188, 129–141. doi:10.1016/j.atmosenv.2018.04.057

Zhang, C. G., Zou, Z., Chang, Y. H., Zhang, Y., Wang, X. F., and Yang, X. (2020b). Source Assessment of Atmospheric fine Particulate Matter in a Chinese Megacity: Insights from Long-Term, High-Time Resolution Chemical Composition Measurements from Shanghai Flagship Monitoring Supersite. *Chemosphere* 251. doi:10.1016/j.chemosphere.2020.126598

Zhang, C. X., Wang, Y. Q., Lauer, A., and Hamilton, K. (2012). Configuration and Evaluation of the WRF Model for the Study of Hawaiian Regional Climate. *Monthly Weather Rev.* 140 (10), 3259–3277. doi:10.1175/mwr-d-11-00260.1

Zhang, H., Lu, M., Zhang, B., An, L., and Rao, X. (2016). Analysis of the Stagnant Meteorological Situation and the Transmission Condition of Continuous Heavy Pollution Course from February 20 to 26,2014 in Beijing-Tianjin-Hebei. *Acta Scientiae Circumstantiae* 36 (12), 4340–4351.

Zhang, H., Zhang, B., and An, M. L. (2017). Development and Application of Stable Weather Index of Beijing in Environmental Meteorology. *Meteorol. Monthly* 43 (8), 998–1004.

Zhang, X. Y., Xu, X. D., Ding, Y. H., Liu, Y. J., Zhang, H. D., Wang, Y. Q., et al. (2019). The Impact of Meteorological Changes from 2013 to 2017 on PM2.5 Mass Reduction in Key Regions in China. *Sci. China-Earth Sci.* 62 (12), 1885–1902. doi:10.1007/s11430-019-9343-3

Zhang, Y. R., Hong, Z. Y., Chen, J. S., Xu, L. L., Hong, Y. W., Li, M. R., et al. (2020c). Impact of Control Measures and Typhoon Weather on Characteristics and Formation of PM2.5 during the 2016 G20 summit in China. *Atmos. Environ.* 224. doi:10.1016/j.atmosenv.2020.117312

Zhang, Y., Wang, S., Ni, C., Zhang, X., Jia, X., and Feng, X. (2020d). Study on an Objective Synoptic Typing Method for Air Pollution Weather in Chengdu during Winter. *Environ. Sci. Tech.* 43 (5), 139–144.

Zhang, Y., Yang, P. L., Gao, Y., and Bell, R. L. L. M. L. (2020a). Health and Economic Impacts of Air Pollution Induced by Weather Extremes over the continental US. *Environ. Int.* 143. doi:10.1016/j.envint.2020.105921

Zhu, M., and Lu, T. W. Z. (2008). Analysis on Weather Conditions during Sustained Heavy Air Pollution Episode. *Scientia Meteorologlca Sinica* 28 (6), 673–677.

Conflict of Interest: The authors declare that the research was conducted in the absence of any commercial or financial relationships that could be construed as a potential conflict of interest.

frontiers in Environmental Science

ORIGINAL RESEARCH
published: 29 March 2022
doi: 10.3389/fenvs.2022.867908

Modeling Reactive Ammonia Uptake by Secondary Organic Aerosol in a Changing Climate: A WRF-CMAQ Evaluation

Shupeng Zhu[1]*, *Kai Wu*[1], *Sergey A. Nizkorodov*[2] and *Donald Dabdub*[3]*

[1]Advanced Power and Energy Program, University of California, Irvine, Irvine, CA, United States, [2]Department of Chemistry, University of California, Irvine, Irvine, CA, United States, [3]Computational Environmental Sciences Laboratory, Department of Mechanical and Aerospace Engineering, University of California, Irvine, Irvine, CA, United States

In addition to the well-constrained inorganic acid-base chemistry of ammonia resulting in fine particulate matter ($PM_{2.5}$) formation, ammonia also reacts with certain organic compounds in secondary organic aerosol (SOA) to produce less basic nitrogen-containing organic compounds. In this study, the potential meteorology and air quality impacts of the heterogeneous uptake of NH_3 by SOA are investigated using the WRF-CMAQ two-way coupled model, which calculates the two-way radiative forcing feedback caused by aerosol between meteorology and chemistry in a single simulation. Simulations with and without the NH_3-SOA uptake are performed over the contiguous US for July 2014 and July 2050 under the RCP 8.5 IPCC scenario to study the potential impact of climate change. A comparison with multiple observation network data shows that the NH_3-SOA uptake improves the model performance for $PM_{2.5}$ prediction (bias reduced from –22% to –17%), especially the underestimation of organic carbon over the Southeastern US (bias reduced from –17% to –7%). Secondly, the addition of the NH_3-SOA chemistry significantly impacts the concentration of NH_3 and NH_4^+, thus affecting the modeled particle acidity. Including the NH_3-SOA uptake also impacts the meteorological conditions through the WRF-CMAQ two-way feedback. Moreover, the impact on meteorological conditions results in different windspeed or dispersion conditions, thus affecting air quality predictions. Finally, simulations including the NH_3-SOA uptake under the warmer climate conditions of 2050 show a smaller impact on air quality predictions than it does under current climate conditions. This study confirms the importance and necessity of including NH_3-SOA chemistry in air quality predictions.

Keywords: ammonia, secondary organic aerosol (SOA), particulate matter, ammonium nitrate (AN), climate change, coupled meteorological and air quality modeling

OPEN ACCESS

Edited by:
Yang Gao,
Ocean University of China, China

Reviewed by:
Yang Yang,
Nanjing University of Information Science and Technology, China
Dan Chen,
China Meteorological Administration, China

***Correspondence:**
Shupeng Zhu
sz@apep.uci.edu
Donald Dabdub
ddabub@uci.edu

Specialty section:
This article was submitted to Atmosphere and Climate, a section of the journal Frontiers in Environmental Science

Received: *01 February 2022*
Accepted: *11 March 2022*
Published: *29 March 2022*

Citation:
Zhu S, Wu K, Nizkorodov SA and Dabdub D (2022) Modeling Reactive Ammonia Uptake by Secondary Organic Aerosol in a Changing Climate: A WRF-CMAQ Evaluation. Front. Environ. Sci. 10:867908. doi: 10.3389/fenvs.2022.867908

1 INTRODUCTION

As an important atmospheric trace gas, ammonia (NH_3) is found in various sources of natural and anthropogenic emissions (Bouwman et al., 1997). Globally, roughly half of the NH_3 emissions originates from agricultural activities, for example, satellite observations show ammonia hot spots in major agricultural areas (Clarisse et al., 2009). As a highly water-soluble molecule, the majority of atmospheric ammonia is lost by deposition on wet particles and aquatic surfaces (Dentener et al.,

2006) as part of the global nitrogen cycle. Ammonia has long been considered an important precursor to the inorganic component of fine particulate matter ($PM_{2.5}$, particles with sizes below 2.5 μm that penetrate easily the respiratory tract). Ammonia is converted into inorganic ammonium salts with low volatility by neutralizing inorganic acids commonly found in polluted air, such as sulfuric acid and nitric acid. Such salts accumulate as solids in $PM_{2.5}$ (Seinfeld and Pandis 2016). Ammonium nitrate and ammonium sulfate constitute an important fraction of the total $PM_{2.5}$ in many geographical areas (Behera and Sharma 2010).

In addition to the well-constrained inorganic acid-base chemistry of ammonia leading to $PM_{2.5}$ formation, there is experimental evidence that ammonia reacts with certain organic compounds in secondary organic aerosol (SOA) leading to the formation of nitrogen-containing organic compounds (NOC) (Bones et al., 2010). SOA produced by photooxidation of biogenic and anthropogenic volatile organic compounds (VOCs) represents a large fraction of $PM_{2.5}$. Although considerable uncertainty still exists over chemical reactions between NH_3 and SOA, the general mechanism involves the reaction of ammonia with carbonyls within the organic particles to produce relatively unstable imines and amines, which may be stabilized by intramolecular cyclization into heteroaromatic NOC based on imidazole, pyrrole, indole, etc., (Montoya-Aguilera et al., 2018). These reactions change the chemical composition of organic particles and their physical properties, such as color, viscosity, and condensed-phase diffusivity (Laskin, Laskin, and Nizkorodov 2015; Li et al., 2015; Bell et al., 2017; Liu et al., 2018).

Until recently, interactions between NH_3 and SOA (SOA-NH_3 uptake) were not considered in air quality models. In our previous work to incorporate such interactions into air quality models, a significant decrease was found in predicted NH_3 and inorganic $PM_{2.5}$ concentration in a regional study (Horne et al., 2018) on the South Coast Air Basin of California (SoCAB) using the UCI-CIT model (Nguyen and Dabdub 2002). Furthermore, we found a significant SOA concentration increase in the southeast of the US during the summertime in a national-scale study (Zhu et al., 2018) resulting from enhanced acid-catalyzed reactions (Pye et al., 2013) when the SOA-NH_3 uptake was incorporated into the Community Multiscale Air Quality (CMAQ v5.2) model (Byun and Schere 2006). In general, the ammonia loss to the SOA uptake is smaller than the traditional inorganic acidic uptake pathway. However, there are situations in which the SOA-NH_3 uptake becomes competitive and has a modest impact on organic aerosol and $PM_{2.5}$ concentrations.

An air quality model can either be an offline model where the meteorology is specified from a foreign source or an online model where the meteorology is adjusted based on the chemical constituents within the model. Our previous SOA-NH_3 uptake sensitivity studies (Horne et al., 2018; Zhu et al., 2018) were based on offline air quality models, which means no feedback was considered between pollutant concentration and meteorological conditions (Grell and Baklanov 2011). However, field experiments and satellite observation have shown that chemistry-atmosphere feedbacks play an essential role in the Earth system (Kaufman and Fraser 1997; Rosenfeld et al., 2007, 2008; Pausata et al., 2015). On the one hand, meteorological conditions dictate both the formation and transport of air pollutants. On the other hand, chemical species can also influence the meteorological parameters by changing the atmospheric radiation budget and through cloud formation. In this study, a more comprehensive air quality impact study of the effects of SOA-NH_3 uptake is conducted by including the chemistry-atmosphere feedbacks using the two-way coupled Weather Research and Forecasting—Community Multi-scale Air Quality (WRF-CMAQ) model (Wong et al., 2012). Developed by the US Environmental Protection Agency (EPA), the CMAQ model is an offline model historically and is widely used for air quality simulations worldwide (X. H. Liu et al., 2010; Canty et al., 2015; Sharma et al., 2016; Matthias 2008; de Almeida Albuquerque et al., 2018). In recent years, it was further developed and coupled with the Weather Research and Forecasting (WRF) model to simulate the two-way radiative forcing feedbacks caused by the aerosol direct effect between chemistry and meteorology (Wong et al., 2012). This new WRF-CMAQ coupled model has been evaluated in several applications and used to investigate aerosol direct effects on meteorology (Wang et al., 2014; Gan et al., 2015; Hogrefe et al., 2015; Xing et al., 2016; Hong et al., 2017).

Many studies (Brasseur et al., 2006; Fiore et al., 2012; Lin, Penner, and Zhou 2016; Campbell et al., 2018; Zhu et al., 2019) have demonstrated that climate change could impact significantly the physical and chemical processes that govern the formation of atmospheric pollutants, including ammonia and SOA. Furthermore, both emissions of ammonia (Skjøth and Geels 2013) and VOC precursors (Constable et al., 1999) are expected to increase in the future due to the rising temperature as a result of climate change. Combining these two factors is likely to lead to significant changes in the mass concentration and chemical composition of SOA. As a preliminary study, the potential impact of the physical and chemical processes alone due to the implementation of the SOA-NH_3 uptake mechanism is investigated under the changing climate using the WRF-CMAQ model. The Representative Concentration Pathway (RCP) 8.5 (business-as-usual) dataset for the year 2050 (Bruyère et al., 2013; Monaghan et al., 2014) is used here to provide a midterm outlook and the worst scenario estimation. Our results show that the inclusion of the NH_3-SOA uptake under the warmer climate conditions of 2050 produces a smaller impact on air quality predictions than under current climate conditions. But overall, this study highlights the importance and necessity of including NH_3-SOA chemistry in air quality predictions.

2 METHODOLOGY

2.1 Model Description

This study uses the two-way coupled WRF-CMAQ (WRF v3.8 and CMAQ v5.2) as the base platform to integrate the SOA-NH_3 uptake process to conduct regional meteorology and air quality simulations. WRF is the meteorology driver of the model, while

CMAQ handles the air quality dynamics. A detailed description of the two-way coupled WRF-CMAQ model is presented in Wong et al. (2012). The publicly available version used in this study supports the Rapid and accurate Radiative Transfer Model for General Circulation Models (RRTMG) radiation scheme (Clough et al., 2005) for shortwave aerosol direct effects. It uses a core-shell model to perform the aerosol optics calculation. The aerosol indirect effects that result from interactions between aerosols and cloud formation are not considered in this version.

For WRF configuration, the Asymmetric Convective model version 2 (ACM2) (Pleim 2007) is used as the planetary boundary layer scheme with the Pleim-Xiu land surface model (Xiu and Pleim 2001). The Morrison double-moment scheme (Morrison, Thompson, and Tatarskii 2009) is used for the microphysics option of WRF, and version 2 of Kain-Fritsch convective parametrization (Kain 2004) is used for cumulus physics. Both longwave and shortwave radiations are solved by the RRTMG scheme (Iacono et al., 2008). For the current scenarios, WRF input is derived from the National Centers for Environmental Prediction (NCEP) North American Mesoscale Forecast System (NAM) 12 km analysis data (NCEP 2015). For the future (year 2050) climate scenarios, the RCP 8.5 National Center for Atmospheric Research (NCAR) Community Earth System Model (CESM) global bias-corrected CMIP5 dataset (Monaghan et al., 2014) is used to provide a midterm outlook and the worst scenario estimation, where CAM-Chem (Lamarque et al., 2012) is used for chemistry-climate modeling and MOZART as the chemical mechanism (Emmons et al., 2010).

The CMAQ model is configured using the Carbon Bond 2006 (CB06) chemical mechanism for gas-phase chemistry (Yarwood et al., 2010), including 127 species as detailed on the model's website (Adams 2017). The aerosol dynamics are solved by the sixth-generation CMAQ aerosol module (AERO6) (Appel et al., 2013), which includes 21 inorganic species and 34 organic species (28 SOA and 6 primary organic species) as detailed on the CMASWIKI website (Pye 2016). The modeling domain is the same as Zhu et al. (2018), which covers the contiguous US (CONUS) with a 12 km × 12 km horizontal-grid resolution and a 29-layers logarithmic vertical structure. The initial and boundary conditions are downscaled from the Model for Ozone and Related Chemical Tracers (MOZART v4.0) (Emmons et al., 2010). Emissions are generated based on the 2014 National Emissions Inventory (NEI) version 2 (US EPA 2018) and spatially/temporally resolved using the Sparse Matrix Operator Kernel Emission (SMOKE, version 4.5) processor (US EPA 2017). Biogenic emissions are calculated using the Biogenic Emission Inventory System (BEIS) (Schwede et al., 2005). As a preliminary study and only accounting for the change in climate alone, the same emissions are used for both 2014 and 2050 cases.

The SOA-NH_3 uptake mechanism is incorporated into the AERO6 module using the same method as our previous study (Zhu et al., 2018). In AERO6, all particles are considered spherical and internally mixed, which means a homogeneous distribution of all chemical substances within the particle. However, as the uptake coefficient used in this study is measured from pure SOA particles, how the uptake coefficient could be changed with SOA mass ratios within the particle is unknown. In the absence of better information, we assume that the uptake coefficient is proportional to the SOA mass fraction within the particle. In general, the uptake of NH_3 by SOA is calculated based on the representative wet surface area concentration of SOA (S_{SOA}) and the reactive uptake coefficient γ. The calculation of S_{SOA} is based on the SOA mass ratios within the particle. Details of the calculation are presented in our previous work (Zhu et al., 2018). In general, the amount of NH_3 uptake by SOA is reduced from the bulk NH_3 concentration at each timestep before the all-other chemical mass-transfer calculation, and the mass of organic aerosol is kept constant during the process. The effective first-order rate constant for of the NH_3 uptake by SOA is calculated as follows:

$$k = \gamma \times \frac{v_{NH3} \times S_{SOA}}{4}$$

where v_{NH3} is the average speed of NH_3 molecules (609 ms^{-1} at 298 K). This first-order rate constant is then multiplied by the gas-phase NH_3 concentration to determine the loss rate of NH_3 in each grid cell at each time step. As explained in Zhu et al. (2018) in this method, the direct change of SOA mass due to the NH_3 uptake is neglected to simplify the calculation. This assumption is supported by the experimental observation that SOA particles exposed to ammonia in a smog chamber did not change their size distribution but showed clear evidence of incorporation of organic nitrogen into the particles in online and offline mass spectra, as described in Horne et al. (2018). As the existing laboratory data are still insufficient to determine the exact uptake coefficient for individual SOA species, a range of uptake coefficient γ is selected for sensitivity studies in our previous work (Zhu et al., 2018) between $\gamma = 10^{-5}$ to $\gamma = 10^{-3}$ based on the values reported (Y. J. Li et al., 2015). To avoid redundant sensitivity analysis, we only select the highest uptake coefficient $\gamma = 10^{-3}$ in this study to provide the largest possible impact estimation of the SOA-NH_3 uptake process.

TABLE 1 | Simulation case definition.

Conditions	2014	2050
No SOA-NH_3 uptake	Base_14	Base_50
With SOA-NH_3 uptake	UpTk_14	UpTk_50

In total, four simulations with two-way feedback are performed in this study, two for 2014 and two for 2050. For each year, there is one case considering the SOA-NH_3 uptake and one case without the uptake. **Table 1** summarizes the naming and definition of these six simulation cases. July is selected as the simulation period, with the first week discarded as a spin-up. Our previous study (Zhu et al., 2018) showed that SOA-NH_3 uptake produced an additional impact on acid-catalyzed SOA formation during the summer (Pye et al., 2013), suggesting that July is a good choice for this simulation.

TABLE 2 | Model performance statistics for $PM_{2.5}$, NH_4^+, and Organic Carbon (OC) under different scenarios. $PM_{2.5}$ and OC observation (Obs.) data are from three networks (IMPROVE, CSN and AQS); NH_4^+ observation data are from four networks (IMPROVE, CSN, CASTNET, and AQS). (Average—Avg.; Simulation—Sim.; Normalized Mean Bias—NMB; Normalized Mean Error—NME).

Case	Avg. Obs. (μg/m^3)	Avg. Sim. (μg/m^3)	NMB (%)	NME (%)	Correlation (%)
—	**$PM_{2.5}$ (1,391 sites)**				
Base_14	9.35	7.28	−22.14	22.44	60.69
UpTk_14	9.35	7.75	−17.08	21.06	51.41
—	**NH_4^+ (578 sites)**				
Base_14	0.54	0.34	−37.01	44.43	47.74
UpTk_14	0.54	0.39	−27.39	36.86	56.91
—	**OC (484 sites)**				
Base_14	1.57	1.29	−17.51	24.88	44.08
UpTk_14	1.57	1.46	−6.96	24.83	49.09

2.2 Observational Data and Model Validation

Model validation and performance analysis are quantified using the Atmospheric Model Evaluation Tool (AMET) (Appel et al., 2011) developed by the US EPA. AMET organizes, provides consistency, and speeds up the evaluation process for operational meteorological and air quality model simulations. It can match the model output for particular locations to the corresponding observed values from one or more monitor networks. For meteorological model evaluation, observations are obtained from NCEP Meteorological Assimilation Data Ingest System (MADIS) (NCEP 2019) and Baseline Surface Radiation Network (BSRN) (AWI 2019). For air quality model evaluation, measurement network data provided by AMET includes AErosol RObotic NETwork (AERONET) (NASA 2019), Ammonia Monitoring Network (AMoN) (NADP 2019), Air Quality System (AQS) (US EPA 2019a), Clean Air Status and Trends Network (CASTNET) (US EPA 2019c), Chemical Speciation Network (CSN) (US EPA 2019b), Interagency Monitoring of Protected Visual Environments (IMPROVE) (USGS 2019a), National Atmospheric Deposition Program (NADP), National Air Pollution Surveillance (NAPS) (Canada 2019), South-Eastern Aerosol Research and Characterization (SEARCH) (USGS 2019b), Tropospheric Ozone Assessment Report (TOAR) (Schultz et al., 2017). The model performance is evaluated and compared for the two 2014 cases in **section 3.1**.

3 RESULTS AND DISCUSSION

In this section, the impact on model performance by including the NH_3-SOA chemistry is first presented. Then, the chemical and meteorological impacts of the new chemistry are further investigated for the two 2014 cases. Finally, the sensitivity variation resulting from climate change is discussed by comparing the 2014 and 2050 cases.

3.1 Impact on Model Performance

The model performance of the 2014 simulations with and without ammonia uptake is evaluated for $PM_{2.5}$, NH_4^+, and Organic Carbon (OC) against multiple observation networks detailed in **section 2.2** (**Table 2**). The $PM_{2.5}$ model performance of both Base_14 and UpTk_14 satisfies the recommended performance criteria proposed by Emery et al. (2017), with normalized mean bias (NMB) < ± 30%, normalized mean error (NME) <40% and correlation >40%. The $PM_{2.5}$ is underestimated by 22.14% in the base case, while the NH_3-SOA uptake process reduced such underestimation bias to 17.08% across the U.S. The overall model error is also reduced, as most model improvements occur over the southeastern US, as presented in **Figure 1A**. The model performance for NH_4^+ is also largely improved after including the NH_3-SOA uptake process, with model bias reduced from −37.01% to −27.39%, model error reduced from 44.43 to 36.86% and correlation increased from 47.74 to 56.91%. With the NH_3-SOA uptake process included in the model, the underestimation of OC is also significantly improved, and the model bias is reduced from −17.51% to −6.96%. With more than 60% of the observation sites show decreased model error, **Figure 1B** shows the OC prediction is largely improved over the Southern and Eastern US, especially for the northeastern metropolitan regions like New York and Washington D.C. As underestimating OC is a common problem for air quality models (J. Li et al., 2017) such an improvement on OC prediction is promising. It confirms the importance of including the NH_3-SOA chemistry in air quality models. However, the NH_3-SOA uptake process only has little to no impact on the meteorological side of model performance [**Supplementary Figure S1** in the Supporting Information (SI)], such as the temperature and relative humidity (RH), only slight improvement is found for the stational pressure estimation. Although the overall averaged impact is minimum, impacts on some specific locations could still be visible and could influence air pollutant distribution through feedback. Those feedback impacts are driven by the changes in the short-wave radiation balance due to the changes in aerosol concentrations (Clough et al., 2005). In the following section, the impact on meteorological parameters will be more carefully examined.

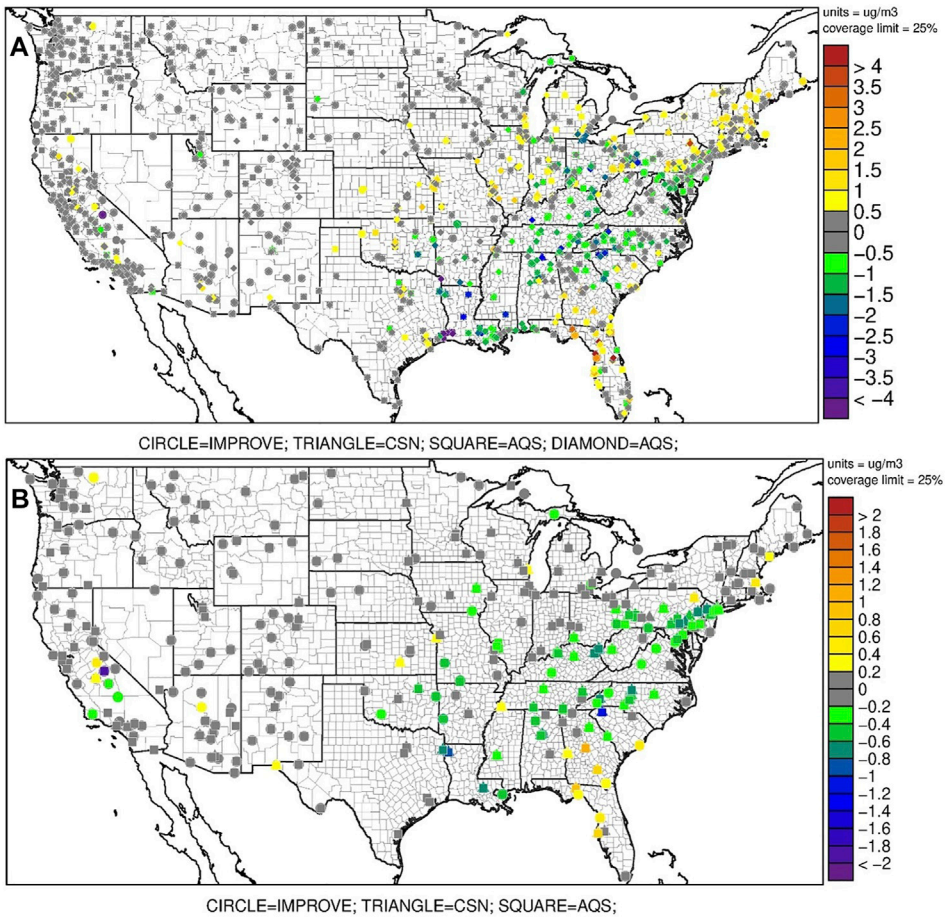

FIGURE 1 | Changes in model errors between Base_14 and UpTk_14 for **(A)** $PM_{2.5}$ and **(B)** OC at each observation site. Negative values indicate reduced model errors in UpTk_14 compares to Base-14. For **(A)**, the SQUARE (AQS sites) only records daily mean value, the DIAMOND (AQS sites) records hourly data.

3.2 Impact on Modeled NH3 and PM2.5

By comparing simulations UpTk_14 and Base_14, more details can be revealed on the impact on NH_3 and $PM_{2.5}$. **Figure 2A** shows the time-averaged NH_3 concentration over the simulation domain for Base_14. Hot spots can be identified in regions with high agricultural NH_3 emissions (e.g., California, North Carolina, Iowa, and Idaho, **Supplementary Figure S2** in the SI) or regions with intense wildfire activities (e.g., Washington, Oregon, and Texas, **Supplementary Figure S3** in the SI). **Figure 2B** shows the NH_3 concentration difference between UpTk_14 and Base_14. The inclusion of the NH_3-SOA uptake process results in an overall decrease in NH_3 concentration throughout the domain, with the most significant decrease of almost 30% in California. The enhanced NH_3 reduction for California is most likely due to the unique spatial overlap between domains of high NH_3 and SOA concentrations (**Supplementary Figure S4** in the SI). Among the states with top NH_3 emissions, Iowa is the only one increasing NH_3 concentration after including the NH_3-SOA uptake. A more detailed investigation shows this is most likely due to the meteorological feedback resulting from the changing air quality conditions. **Figure 2D** shows the changes of 10-m wind speed for Iowa after the addition of NH_3-SOA uptake. The overall reduction in wind speed indicates a loss in dispersion capability, especially over the northwest part of the state, where most of the NH_3 emissions are located (**Figure 2C**). As a result, more NH_3 is accumulated over those regions, resulting in the unusual increase of NH_3 concentrations (**Figure 2E**). This phenomenon also implies that the most effective meteorological factor that could impact the atmospheric chemical concentrations from the chemistry-atmosphere feedbacks would be the change in atmospheric dispersion capability.

The inclusion of NH_3-SOA uptake also resulted in significant changes on modeled $PM_{2.5}$. **Figure 3A** shows the changes of $PM_{2.5}$ and its components (e.g., NH_4^+ and SOA) for the entire CONUS and four states with the highest NH_3 emissions. In general, $PM_{2.5}$ and SOA increased after the inclusion of NH_3-SOA uptake, while NH_4^+ decreased. Among them, North Carolina shows the most significant decrease in NH_4^+ concentration and the largest increase in SOA. However, western states like California and Idaho exhibit both NH_4^+ and SOA decreases after implementing the NH_3-SOA uptake. **Figure 4A** shows the mean $PM_{2.5}$ concentration for Base_14. The high concentration along the southeast boundary of the domain is

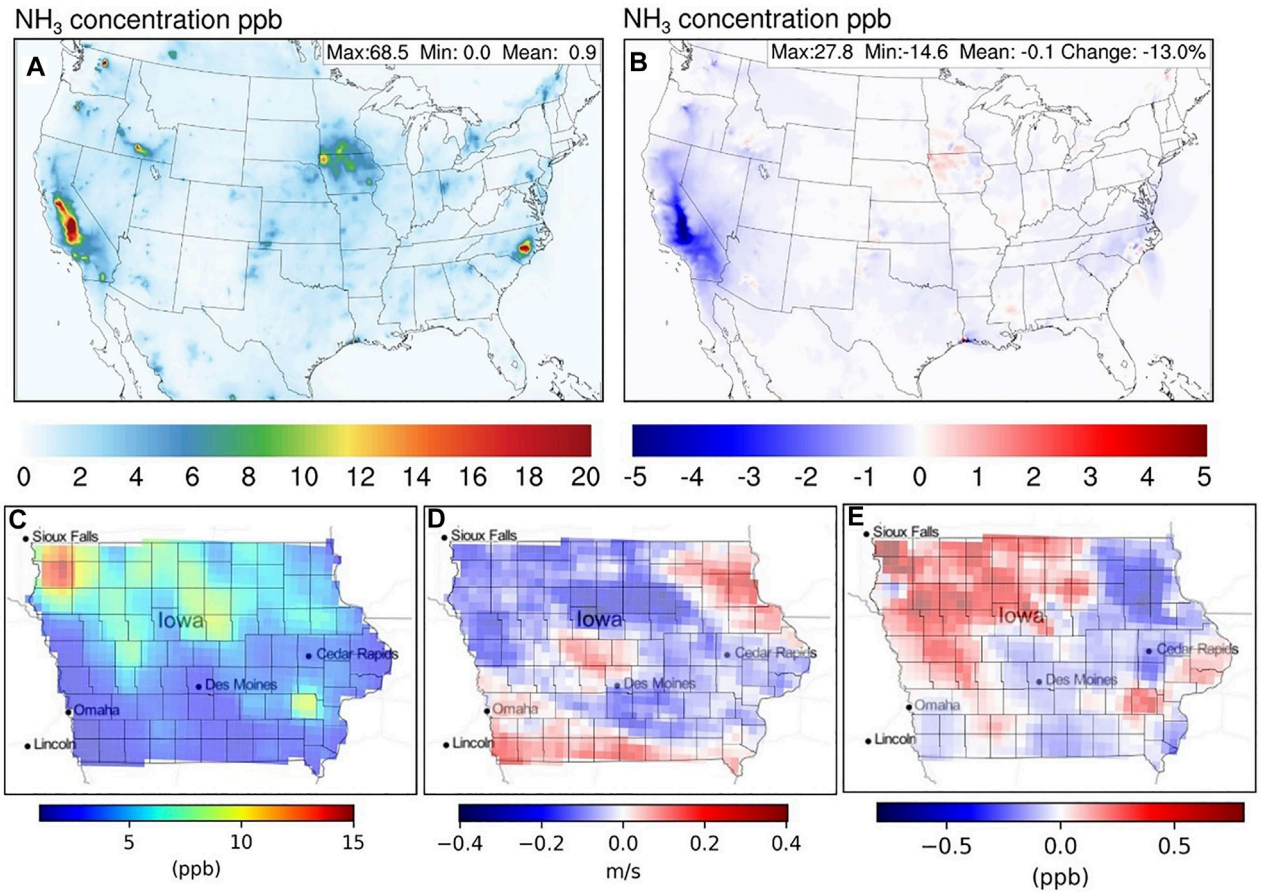

FIGURE 2 | Spatial distribution of time-averaged NH_3 concentration for Base_14 **(A)** CONUS and **(C)** State of Iowa. Spatial distribution of differences between UpTk_14 and Base_14 uptake case: **(B)** NH_3 concentration for CONUS, **(D)** 10-m wind speed for Iowa and **(E)** NH_3 concentration for Iowa.

caused by foreign $PM_{2.5}$ that originated from the western Sahara Desert in Africa.

At the same time, some hot spots with high $PM_{2.5}$ concentrations are caused by wildfires, like those in Washington, Oregon, and Texas. The result of the $PM_{2.5}$ distribution shows a clear pattern with the majority of the pollution happening over the eastern part of the CONUS, except for California. **Figure 4D** presents the change in $PM_{2.5}$ concentration after introducing the NH_3-SOA uptake. The overall impact on $PM_{2.5}$ is smaller than the impact on NH_3. The 4% increase of domain-wide $PM_{2.5}$ concentrations is still significant, with peak changes as large as 160 $\mu g/m^3$. Most of the increases occur over the eastern part of the CONUS, overlapped mainly with the region with high $PM_{2.5}$ concentration, except California. Such a distribution pattern is consistent with previous studies (Horne et al., 2018; Zhu et al., 2018). More detailed investigation shows that almost half of the $PM_{2.5}$ changes result from the increase of SOA concentrations (**Figure 4E**). The most impacted region states close to the lower Mississippi River (e.g., Louisiana, Alabama, Mississippi, and Georgia), which also have elevated SOA background concentrations (**Figure 4B**). The drive behind the increase of SOA concentration is a change in particle acidity as more NH_3 is consumed by the NH_3-SOA uptake process (**Figure 4C**). The acid-catalyzed SOA formation pathway of isoprene epoxydiols is enhanced by increasing particle acidity (Pye et al., 2013), which is also observed in our previous works (Zhu et al., 2018; Wu et al., 2021).

Interestingly, the situation is different in Florida, where a decrease in $PM_{2.5}$ and SOA concentration is predicted. Like the anomaly of increasing NH_3 in Iowa, this particular case also results from the meteorological feedback effects. **Figure 4F** shows the changes of 10-m wind speed after adding the NH_3-SOA uptake process, where a substantial increase in atmospheric dispersion is observed over Florida. Such an increase in wind speed clears out $PM_{2.5}$ and decreases its overall concentration. The exact magnitude correlations between the change in wind and air pollutant concentrations are likely to be affected by multiple factors (e.g., boundary lay high, topographic, etc.) and would be an interesting subject for future investigations.

3.3 Impact due to Climate Change

Changes in background meteorological conditions under RCP 8.5 climate scenarios largely altered the atmospheric chemistry conditions in the model. From the SI, **Supplementary Figure S5**

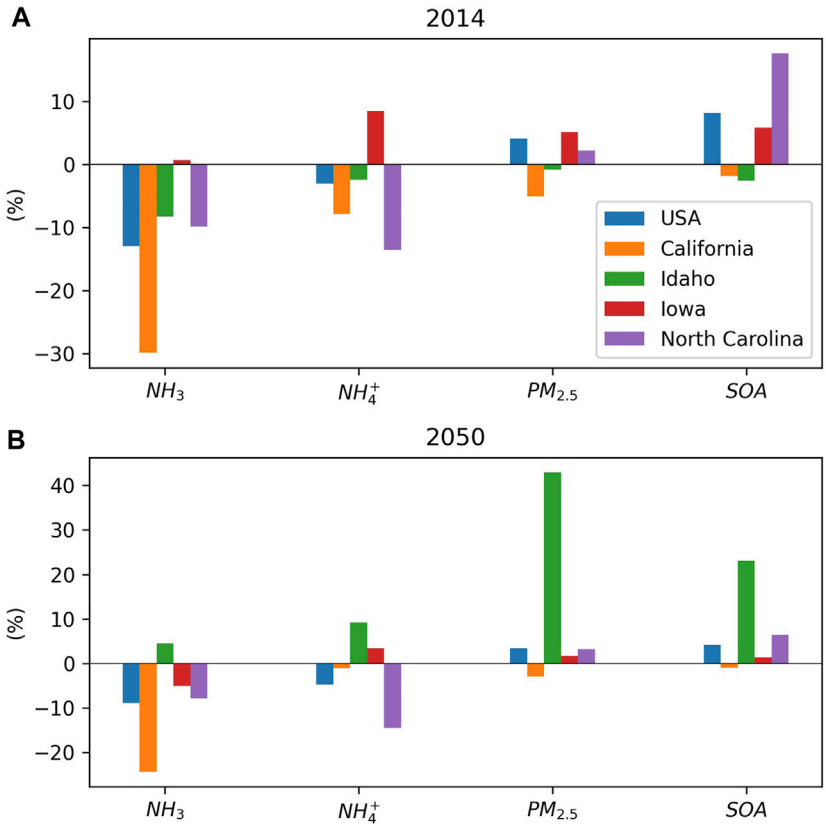

FIGURE 3 | Normalized averaged concentration changes due to the NH_3- SOA uptake for the United States and four states with top anthropogenic NH_3 emissions for the **(A)** 2014 case and **(B)** 2050 case.

shows the meteorological and air quality changes between Base_50 and Base_14. First, there is a general increase in the surface temperature and a decrease in 10-m wind speed over the continent. The particle acidity also experiences dramatic changes. Furthermore, there is some substantial increase in pH values over the southeastern of the US, largely overlapping with the high SOA region in **Figure 4B**. For air pollutants, the overall NH_3 concentration is decreased by 2.1%, with significant decreases in Washington, Oregon, and Texas. Decreases in those states have a direct connection with wildfire emissions. The plume rise or vertical distribution of wildfire emissions are calculated inline with the CMAQ model based on a Briggs plume rise formulation (Briggs 1982), which means the change in meteorological conditions (e.g., temperature, wind speed, and mixing height) could broadly impact the distribution of related emissions. In addition, the change in dispersion directions alters the distribution of NH_3 concentrations in California and North Carolina. Also, some significant increase in $PM_{2.5}$ concentration are observed in the southeast corner of the simulation domain, most likely due to the spread of the west Sahara original sandstorm from the boundary conditions under the new meteorology. Interestingly, SOA concentration decreases significantly over the southeastern CONUS, leading to a 15% decrease domain wide.

Figure 3B shows the impacts on air pollutants after including the NH_3-SOA uptake in the 2050 climate scenario. Compared to the impacts for the 2014 case (**Figure 3A**), the domain-wide NH_3 reduction is 30% smaller under the future climate scenario. One reason is that the lower background NH_3 concentration produced less NH_3 available for uptake. Another more important reason is the meteorological feedback due to the NH_3-SOA uptake changed the wildfire emission, and the gains in wildfire emissions counterbalanced the reduction caused by the NH_3-SOA uptake (**Figure 5A**). The significant increase in pollutants concentrations in Idaho is also caused by wildfire emissions (**Figures 5A–D**). For Iowa, the NH_3 anomaly is largely reduced as the overall wind speed increased by 1.7% (**Figure 5F**). Due to the decrease in background SOA concentration, the impact of SOA (**Figure 5C**) and particle acidity (**Figure 5E**) over the southeastern CONUS due to NH_3-SOA uptake is largely reduced compares to the 2014 case (**Figure 4**). Even with the additional gain from altered wildfire emissions, the increase of SOA is only about half of the 2014 case, and the decrease in pH is only 47%. Even for California, the impact caused by the NH_3-SOA uptake is also largely reduced. Only North Carolina shows similar impacts to the 2014 cases. Although, climate change could also impact the upstream emissions that have not been considered in this study.

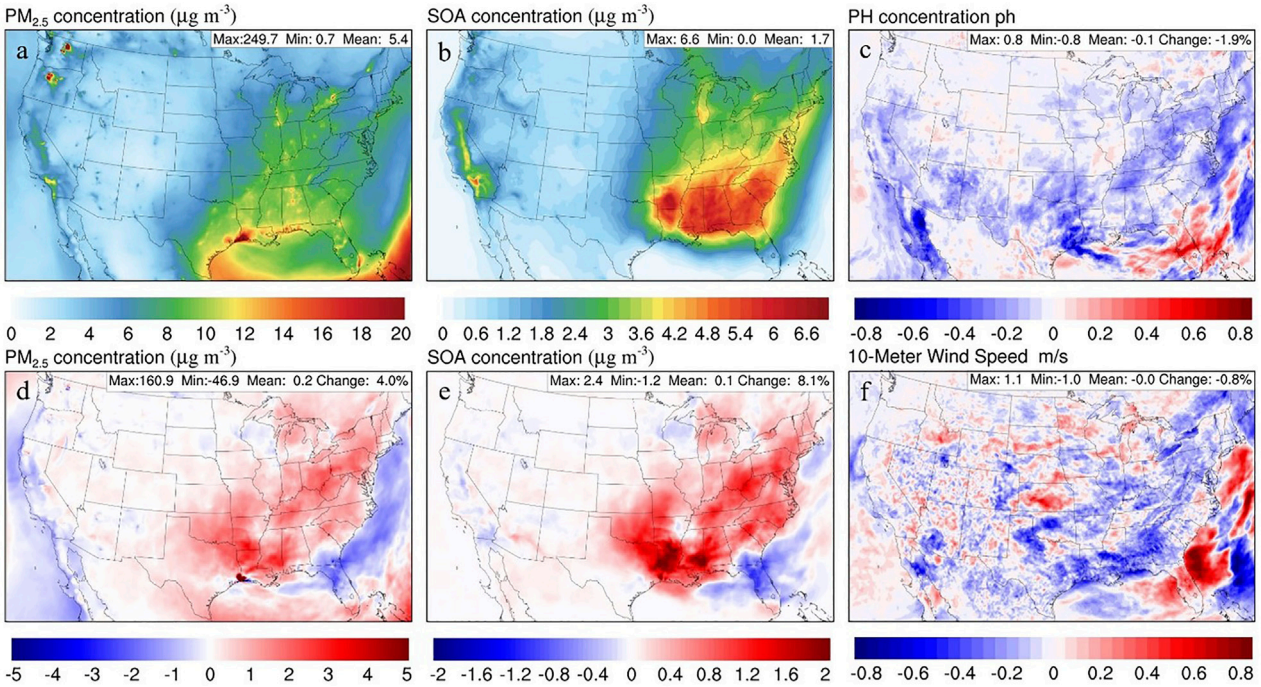

FIGURE 4 | Spatial distribution of time-averaged concentration for Base_14 **(A)** $PM_{2.5}$ and **(B)** SOA. Spatial distribution of differences between UpTk_14 and Base_14 uptake case: **(D)** $PM_{2.5}$, **(E)** SOA, **(C)** pH, and **(F)** 10-metter wind speed.

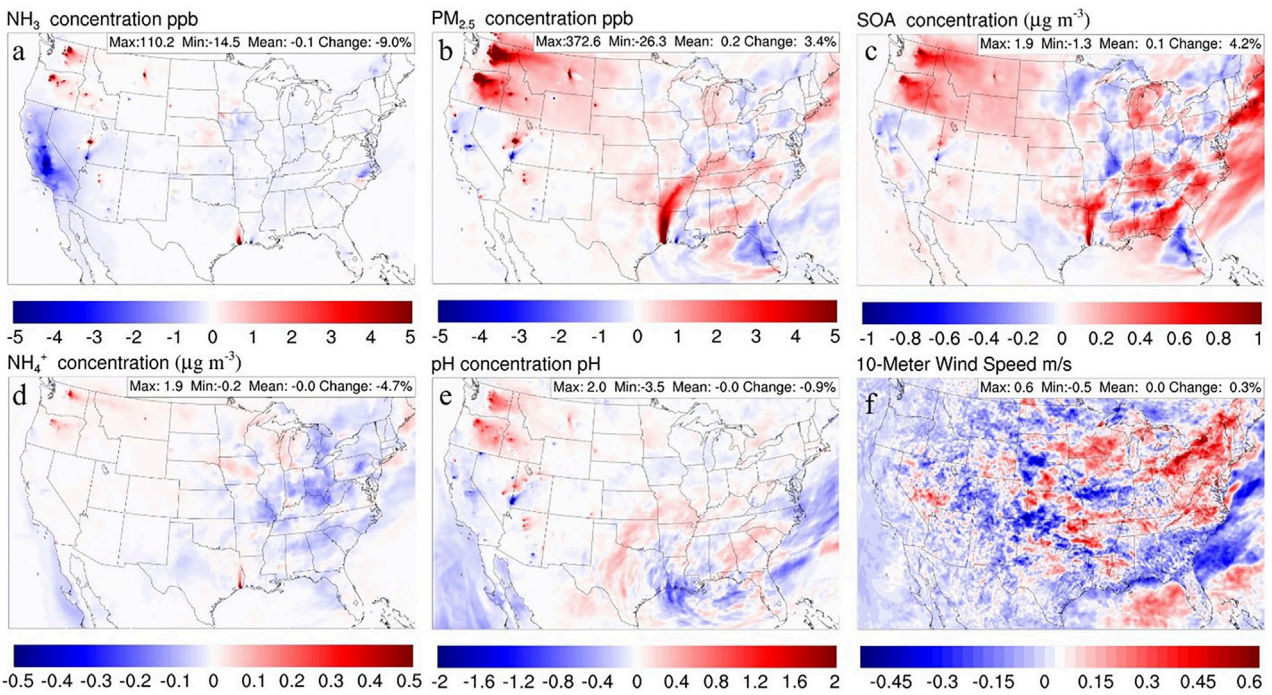

FIGURE 5 | Spatial distribution of differences between UpTk_50 and Base_50 uptake case: **(A)** NH_3, **(B)** $PM_{2.5}$, **(C)** SOA, **(D)** NH_4^+, **(E)** pH, and **(F)** 10-metter wind speed.

These preliminary results imply that under a warmer climate, the impact of the NH_3-SOA uptake might be reduced compared to current climate conditions. Also, the impact on smoke plume rise characters could be a significant factor during the meteorology and air quality two-way feedback, as observed in this study.

4 CONCLUSION

In this study, the potential meteorology and air quality impacts of the chemical uptake of NH_3 by SOA, resulting in nitrogen-containing organics, are investigated with the WRF-CMAQ two-way coupled model. Simulations over the continental US are performed for July 2014 and July 2050 under the RCP 8.5 IPCC scenario to study the potential joint impact due to climate change. First, results show that the NH_3-SOA uptake process could reduce the model underestimation of $PM_{2.5}$ (23% bias reduction), especially the underestimation of SOA over the southeastern CONUS (61% error reduction). Such an improvement in model performance indicates the importance of including NH_3-SOA chemistry in the air quality model and its potential benefits. Secondly, a significant reduction in the concentration of NH_3 was observed with the NH_3-SOA uptake turned on, which also increased the model predicted particle acidity. In general, the inclusion of the NH_3-SOA uptake would lead to lower ammonium concentrations but higher SOA concentrations, with some exceptions. Western U.S. states usually have decreased $PM_{2.5}$ concentrations with the uptake included, whereas Eastern U.S. states usually exhibit increased $PM_{2.5}$ concentrations. Most of the impact on pollution concentrations caused by the air quality and meteorology two-way feedback results from changes in wind speed and resulting dispersion conditions. As illustrated by the 2050 scenario, the impact on wildfire plume calculation due to the atmospheric chemistry and meteorology interaction through the two-way feedback could also significantly impact the resulting pollution distribution. Finally, as a preliminary study, we observe that under a warmer climate, including the NH_3-SOA uptake produces a lower impact on air quality predictions than it does in the current climate.

Results show that the inclusion of the two-way feedback process has significant impacts on model behaviors when the new mechanism is implemented. It is noted that results from this study only consider the shortwave feedback. There are other feedback processes between the air pollutant and meteorology, including longwave feedbacks, the oceanic response and other indirect effects (Seinfeld and Pandis 2016) that are not included in this study and could be explored in future research. Indirect effects like changes in cloud formation and cloud albedo due to changes in aerosol concentration could enhance the meteorological feedback and further affect aerosol predations (Menon et al., 2002). It is likely the indirect effects could enhance the feedback impact over the southeast of the U.S. The oceanic response due to changes in aerosol estimation could also affect large-scale circulations (Cai et al., 2006), which should be considered for long-term simulations but most likely to be insignificant in our short-term study. Moreover, it is also noted that the NH_3 uptake coefficient used in this study is on the higher end of current laboratory measurement ($\gamma = 10^{-3}$). Namely, the actual impact due to the NH_3 uptake process could be even smaller. Our previous study shows the impact on NH_3concentration is likely to be 7–12 times lower at the lower end of the uptake coefficient ($\gamma = 10^{-5}$), and the impact on $PM_{2.5}$ could be about 48–88 times lower (Zhu et al., 2018; Wu et al., 2021). Developing a more accurate and comprehensive SOA-NH_3 parameterization with improved observation data should be of significant priority for future work. Finally, results of this study highlight the potential impacts that can be caused due to climate change in model development.

DATA AVAILABILITY STATEMENT

The raw data supporting the conclusion of this article will be made available by the authors, without undue reservation.

AUTHOR CONTRIBUTIONS

SZ designed and conducted WRF-CMAQ simulations and SZ wrote the manuscript. SZ, KW, SN and DD reviewed and modified the manuscript. KW contributes analysis on meteorological results. SN provides the chemical mechanism of ammonia uptake by SOA. DD administered the project. All authors contributed to manuscript revision and read and approved the submitted version.

ACKNOWLEDGMENTS

This publication was developed under Assistance Agreement No. EPA 83588101 was awarded by the US Environmental Protection Agency to the Regents of the University of California. It has not been formally reviewed by the EPA. The views expressed in this document are solely those of the authors and do not necessarily reflect those of the agency. The EPA does not endorse any products or commercial services mentioned in this publication.

SUPPLEMENTARY MATERIAL

The Supplementary Material for this article can be found online at: https://www.frontiersin.org/articles/10.3389/fenvs.2022.867908/full#supplementary-material

REFERENCES

Adams, L. (2017). Mechanism for Cb6r3_ae6_aq Uses the Following Species. Available at: https://github.com/USEPA/CMAQ/blob/5.2/DOCS/User_Manual/Appendix_A/cb6r3_ae6_aq/CB6_species_table. (Accessed September 2, 2020).

Appel, K. W., Gilliam, R. C., Davis, N., Zubrow, A., and Howard, S. C. (2011). Overview of the Atmospheric Model Evaluation Tool (AMET) v1.1 for Evaluating Meteorological and Air Quality Models. *Environ. Model. Softw.* 26 (4), 434–443. doi:10.1016/j.envsoft.2010.09.007

Appel, K. W., Pouliot, G. A., Simon, H., Sarwar, G., Pye, H. O. T., Napelenok, S. L., et al. (2013). Evaluation of Dust and Trace Metal Estimates from the

Community Multiscale Air Quality (CMAQ) Model Version 5.0. *Geosci. Model. Dev.* 6 (4), 883–899. doi:10.5194/gmd-6-883-2013

AWI (2019). Baseline Surface Radiation Network: Baseline Surface Radiation Network. Available at: https://bsrn.awi.de/. (Accessed September 2, 2020).

Behera, S. N., and Sharma., M. (2010). Investigating the Potential Role of Ammonia in Ion Chemistry of Fine Particulate Matter Formation for an Urban Environment. *Sci. Total Environ.* 408 (17), 3569–3575. doi:10.1016/j.scitotenv.2010.04.017

Bell, D. M., Imre, D., T. Martin, S., and Zelenyuk, A. (2017). The Properties and Behavior of α-pinene Secondary Organic Aerosol Particles Exposed to Ammonia under Dry Conditions. *Phys. Chem. Chem. Phys.* 19 (9), 6497–6507. doi:10.1039/c6cp08839b

Bones, D. L., Henricksen, D. K., Man, S. A., Gonsior, M., Bateman, A. P., Nguyen, T. B., et al. (2010). Appearance of strong Absorbers and Fluorophores in Limonene-O3secondary Organic Aerosol Due to NH4+-mediated Chemical Aging over Long Time Scales. *J. Geophys. Res.* 115 (D5), D05203. doi:10.1029/2009JD012864

Bouwman, A. F., Lee, D. S., Asman, W. A. H., Dentener, F. J., Van Der Hoek, K. W., and Olivier, J. G. J. (1997). A Global High-Resolution Emission Inventory for Ammonia. *Glob. Biogeochem. Cycles* 11 (4), 561–587. doi:10.1029/97GB02266

Brasseur, G. P., Schultz, M., Granier, C., Saunois, M., Diehl, T., Botzet, M., et al. (2006). Impact of Climate Change on the Future Chemical Composition of the Global Troposphere. *J. Clim.* 19 (16), 3932–3951. doi:10.1175/JCLI3832.1

Briggs, G. A. (1982). "Plume Rise Predictions," in *Lectures on Air Pollution and Environmental Impact Analyses* (Boston, MA: American Meteorological Society), 59–111, 59–111. doi:10.1007/978-1-935704-23-2_3

Bruyère, C. L., DoneDoneHolland, J. M. Greg. J., Holland, G. J., and Fredrick, S. (2013). Bias Corrections of Global Models for Regional Climate Simulations of High-Impact Weather. *Clim. Dyn.* 43 (7–8), 1847–1856. doi:10.1007/s00382-013-2011-6

Byun, D., and Schere, K. L. (2006). Review of the Governing Equations, Computational Algorithms, and Other Components of the Models-3 Community Multiscale Air Quality (CMAQ) Modeling System. *Appl. Mech. Rev.* 59, 51. doi:10.1115/1.2128636

Cai, W., Bi, D., Church, J., Cowan, T., Dix, M., and Rotstayn, L. (2006). Pan-Oceanic Response to Increasing Anthropogenic Aerosols: Impacts on the Southern Hemisphere Oceanic Circulation. *Geophys. Res. Lett.* 33 (21), 1–5. doi:10.1029/2006GL027513

Campbell, P., Zhang, Y., Yan, F., Lu, Z., and Streets, D. (2018). Impacts of Transportation Sector Emissions on Future U.S. Air Quality in a Changing Climate. Part II: Air Quality Projections and the Interplay between Emissions and Climate Change. *Environ. Pollut.* 238 (July), 918–930. doi:10.1016/j.envpol.2018.03.016

Canada (2019). National Air Pollution Surveillance (NAPS) Program - Open Government Portal. Available at: https://open.canada.ca/data/en/dataset/1b36a356-defd-4813-acea-47bc3abd859b. (Accessed September 2, 2020).

Canty, T. P., Hembeck, L., Vinciguerra, T. P., Anderson, D. C., Goldberg, D. L., Carpenter, S. F., et al. (2015). Ozone and NOx Chemistry in the Eastern US: Evaluation of CMAQ/CB05 with Satellite (OMI) Data. *Atmos. Chem. Phys. Discuss.* 15 (4), 4427–4461. doi:10.5194/acpd-15-4427-2015

Clarisse, L., Clerbaux, C., Dentener, F., Hurtmans, D., and Coheur, P.-F. (2009). Global Ammonia Distribution Derived from Infrared Satellite Observations. *Nat. Geosci* 2, 479–483. doi:10.1038/ngeo551

Clough, S. A., Shephard, M. W., Mlawer, E. J., Delamere, J. S., Iacono, M. J., Cady-Pereira, K., et al. (2005). Atmospheric Radiative Transfer Modeling: A Summary of the AER Codes. *J. Quantitative Spectrosc. Radiative Transfer* 91 (2), 233–244. doi:10.1016/j.jqsrt.2004.05.058

Constable, J. V. H., Guenther, A. B., Schimel, D. S., and Monson, R. K. (1999). Modelling Changes in VOC Emission in Response to Climate Change in the Continental United States. *Glob. Change Biol.* 5 (7), 791–806. doi:10.1046/j.1365-2486.1999.00273.x

de Almeida Albuquerque, T. T., de Fátima Andrade, M., Ynou, R. Y., Moreira, D. M., Andreão, W. L., dos Santos, F. S., et al. (2018). WRF-SMOKE-CMAQ Modeling System for Air Quality Evaluation in São Paulo Megacity with a 2008 Experimental Campaign Data. *Environ. Sci. Pollut. Res.* 25 (36), 36555–36569. doi:10.1007/s11356-018-3583-9

Dentener, F., Drevet, J., Lamarque, J. F., Bey, I., Eickhout, B., Fiore, A. M., et al. (2006). Nitrogen and Sulfur Deposition on Regional and Global Scales: A Multimodel Evaluation. *Glob. Biogeochem. Cycles* 20 (4), a–n. doi:10.1029/2005GB002672

Emery, C., Liu, Z., Russell, A. G., Odman, M. T., Yarwood, G., and Kumar, N. (2017). Recommendations on Statistics and Benchmarks to Assess Photochemical Model Performance. *J. Air Waste Manage. Assoc.* 67 (5), 582–598. doi:10.1080/10962247.2016.1265027

Emmons, L. K., Walters, S., Hess, P. G., Lamarque, J.-F., Pfister, G. G., Fillmore, D., et al. (2010). Description and Evaluation of the Model for Ozone and Related Chemical Tracers, Version 4 (MOZART-4). *Geosci. Model. Dev.* 3 (1), 43–67. doi:10.5194/gmd-3-43-2010

Fiore, A. M., Naik, V., Spracklen, D. V., Steiner, A., Unger, N., Prather, M., et al. (2012). Global Air Quality and Climate. *Chem. Soc. Rev.* 41 (19), 6663. doi:10.1039/c2cs35095e

Gan, C. M., Binkowski, F., Pleim, J., Xing, J., Wong, D., Mathur, R., et al. (2015). Assessment of the Aerosol Optics Component of the Coupled WRF-CMAQ Model Using CARES Field Campaign Data and a Single Column Model. *Atmos. Environ.* 115 (August), 670–682. doi:10.1016/j.atmosenv.2014.11.028

Grell, G., and Baklanov, A. (2011). Integrated Modeling for Forecasting Weather and Air Quality: A Call for Fully Coupled Approaches. *Atmos. Environ.* 45 (38), 6845–6851. doi:10.1016/j.atmosenv.2011.01.017

Hogrefe, C., Pouliot, G., Wong, D., Torian, A., Roselle, S., Pleim, J., et al. (2015). Annual Application and Evaluation of the Online Coupled WRF-CMAQ System over North America under AQMEII Phase 2. *Atmos. Environ.* 115 (August), 683–694. doi:10.1016/j.atmosenv.2014.12.034

Hong, C., Zhang, Q., Zhang, Y., Tang, Y., Tong, D., and He, K. (2017). Multi-Year Downscaling Application of Two-Way Coupled WRF v3.4 and CMAQ v5.0.2 over East Asia for Regional Climate and Air Quality Modeling: Model Evaluation and Aerosol Direct Effects. *Geosci. Model. Dev.* 10 (6), 2447–2470. doi:10.5194/gmd-10-2447-2017

Horne, J. R., Zhu, S., Montoya-Aguilera, J., Hinks, M. L., Wingen, L. M., Nizkorodov, S. A., et al. (2018). Reactive Uptake of Ammonia by Secondary Organic Aerosols: Implications for Air Quality. *Atmos. Environ.* 189, 1–8. doi:10.1016/j.atmosenv.2018.06.021

Iacono, M. J., Delamere, J. S., Mlawer, E. J., Shephard, M. W., Clough, S. A., and Collins, W. D. (2008). Radiative Forcing by Long-Lived Greenhouse Gases: Calculations with the AER Radiative Transfer Models. *J. Geophys. Res.* 113 (13). doi:10.1029/2008JD009944

Kain, J. S. (2004). The Kain-Fritsch Convective Parameterization: An Update, *J. Appl. Meteorol.* 43, 1702–2181. doi:10.1175/1520-0450(2004)043<0170

Kaufman, Y. J., and Fraser., R. S. (1997). The Effect of Smoke Particles on Clouds and Climate Forcing. *Science* 277 (5332), 1636–1639. doi:10.1126/science.277.5332.1636

Lamarque, J.-F., Emmons, L. K., Hess, P. G., Kinnison, D. E., Tilmes, S., Vitt, F., et al. (2012). CAM-chem: Description and Evaluation of Interactive Atmospheric Chemistry in the Community Earth System Model. *Geosci. Model. Dev.* 5 (2), 369–411. doi:10.5194/gmd-5-369-2012

Laskin, A., Laskin, J., and Nizkorodov, S. A. (2015). Chemistry of Atmospheric Brown Carbon. *Chem. Rev.*, 115, 4335–4382. doi:10.1021/cr5006167

Li, J., Zhang, M., Wu, F., Sun, Y., and Tang, G. (2017). Assessment of the Impacts of Aromatic VOC Emissions and Yields of SOA on SOA Concentrations with the Air Quality Model RAMS-CMAQ. *Atmos. Environ.* 158, 105–115. doi:10.1016/j.atmosenv.2017.03.035

Li, Y. J., Liu, P., Gong, Z., Wang, Y., Bateman, A. P., Bergoend, C., et al. (2015). Chemical Reactivity and Liquid/Nonliquid States of Secondary Organic Material. *Environ. Sci. Technol.* 49 (22), 13264–13274. doi:10.1021/acs.est.5b03392

Lin, G., PennerPenner, J. E., and Zhou, C. (2016). How Will SOA Change in the Future? *Geophys. Res. Lett.* 43 (4), 1718–1726. doi:10.1002/2015GL067137

Liu, P., Li, Y. J., Wang, Y., Bateman, A. P., Zhang, Y., Gong, Z., et al. (2018). Highly Viscous States Affect the Browning of Atmospheric Organic Particulate Matter. *ACS Cent. Sci.* 4 (2), 207–215. doi:10.1021/acscentsci.7b00452

Liu, X.-H., Zhang, Y., Cheng, S.-H., Xing, J., Zhang, Q., Streets, D. G., et al. (2010). Understanding of Regional Air Pollution over China Using CMAQ, Part I Performance Evaluation and Seasonal Variation. *Atmos. Environ.* 44 (20), 2415–2426. doi:10.1016/j.atmosenv.2010.03.035

Matthias, V. (2008). The Aerosol Distribution in Europe Derived with the Community Multiscale Air Quality (CMAQ) Model: Comparison to Near

Surface *In Situ* and Sunphotometer Measurements. *Atmos. Chem. Phys.* 8 (17), 5077–5097. doi:10.5194/acp-8-5077-2008

Menon, S., AnthonyDel Genio, D., Koch, D., and George, T. (2002). GCM Simulations of the Aerosol Indirect Effect: Sensitivity to Cloud Parameterization and Aerosol Burden. *J. Atmos. Sci.* 59 (3 PT 2), 6922–7713. doi:10.1175/1520-0469(2002)059<0692:gsotai>2.0.co;2

Monaghan, A. J., Steinhoff, D. F., Bruyere, C. L., and Yates, D. (2014). *NCAR CESM Global Bias-Corrected CMIP5 Output to Support WRF/MPAS Research*. Available at: https://rda.ucar.edu/datasets/ds316.1/ (Accessed September 2, 2020). doi:10.5065/D6DJ5CN4

Montoya-Aguilera, J., Hinks, M. L., Aiona, P. K., Wingen, L. M., Horne, J. R., Zhu, S., et al. (2018). Reactive Uptake of Ammonia by Biogenic and Anthropogenic Organic Aerosols. *ACS Symp. Ser.* 1299, 127–147. doi:10.1021/bk-2018-1299.ch007

Morrison, H., Thompson, G., and Tatarskii, V. (2009). Impact of Cloud Microphysics on the Development of Trailing Stratiform Precipitation in a Simulated Squall Line: Comparison of One- and Two-Moment Schemes. *Monthly Weather Rev.* 137 (3), 991–1007. doi:10.1175/2008MWR2556.1

Nadp (2019). Atmospheric Ammonia Network. Available at: http://nadp.slh.wisc.edu/amon/ (Accessed September 2, 2020).

NASA (2019). Aerosol Robotic Network (AERONET) Homepage. Available at: https://aeronet.gsfc.nasa.gov/ (Accessed September 2, 2020).

Ncep (2019). NCEP Meteorological Assimilation Data Ingest System (MADIS). Available at: https://madis.ncep.noaa.gov/ (Accessed September 2, 2020).

Ncep (2015). *NCEP North American Mesoscale (NAM) 12 Km Analysis*. Boulder, Colo: Research Data Archive at the National Center for Atmospheric Research, Computational and Information Systems LaboratoryUpdated Daily. doi:10.5065/G4RC-1N91

Nguyen, K., and Dabdub, D. (2002). NO X and VOC Control and its Effects on the Formation of Aerosols. *Aerosol Sci. Tech.* 36 (5), 560–572. doi:10.1080/02786820252883801

Pausata, F. S. R., Gaetani, M., Messori, G., Kloster, S., and Dentener, F. J. (2015). The Role of Aerosol in Altering North Atlantic Atmospheric Circulation in Winter and its Impact on Air Quality. *Atmos. Chem. Phys.* 15 (4), 1725–1743. doi:10.5194/acp-15-1725-2015

Pleim, J. E. (2007). A Combined Local and Nonlocal Closure Model for the Atmospheric Boundary Layer. Part I: Model Description and Testing. *J. Appl. Meteorology Climatology* 46 (9), 1383–1395. doi:10.1175/JAM2539.1

Pye, H. O. T. (2016). CMAQv5.1 SOA Update - CMASWIKI. Available at: https://www.airqualitymodeling.org/index.php/CMAQv5.1_SOA_Update (Accessed May 15, 2020).

Pye, H. O. T., Pinder, R. W., Piletic, I. R. Ying. Xie., Xie, Y., Capps, S. L., Lin, Y.-H., et al. (2013). Epoxide Pathways Improve Model Predictions of Isoprene Markers and Reveal Key Role of Acidity in Aerosol Formation. *Environ. Sci. Technol.* 47 (19), 11056–11064. doi:10.1021/es402106h

Rosenfeld, D., Dai, J., Yu, X., Yao, Z., Xu, X., Yang, X., et al. (2007). Inverse Relations between Amounts of Air Pollution and Orographic Precipitation. *Science* 315 (5817), 1396–1398. doi:10.1126/science.1137949

Rosenfeld, D., Woodley, W. L., Axisa, D., Freud, E., Hudson, J. G., and Givati, A. (2008). Aircraft Measurements of the Impacts of Pollution Aerosols on Clouds and Precipitation over the Sierra Nevada. *J. Geophys. Res.* 113 (D15), D15203. doi:10.1029/2007JD009544

Schultz, M. G., Sabine, S., Lyapina, O., Cooper, O. R., Galbally, I., Petropavlovskikh, I., et al. (2017). Tropospheric Ozone Assessment Report, Links to Global Surface Ozone Datasets. (Elementa: Science of the Anthropocene), 5 (58), 1–26. doi:10.1525/elementa.244

Schwede, D. B., Schwede, D., George, P., and Pierce, T. (2005). Changes to the Biogenic Emissions Inventory System Version 3 (BEIS3)." in 4th Annual CMAS-3 Users' Conference, 26. Chapel hill, NC, 28.

Seinfeld, J. H., and Pandis, S. N. (2016). *Atmospheric Chemistry and Physics: From Air Pollution to Climate Change*. New York: John Wiley & Sons,. https://books.google.com/books?hl=en&lr=&id=n_RmCgAAQBAJ&oi=fnd&pg=PR5&dq=Atmospheric+chemistry+and+physics+Ltd+from+air+pollution+to+climate+change&ots=gRO7FJnjfQ&sig=RcpA08Z72j9hxQ6IbbAdtJxJKPA.

Sharma, S., Chatani, S., Mahtta, R., Goel, A., and Kumar, A. (2016). Sensitivity Analysis of Ground Level Ozone in India Using WRF-CMAQ Models. *Atmos. Environ.* 131 (April), 29–40. doi:10.1016/j.atmosenv.2016.01.036

Skjøth, C. A., and Geels, C. (2013). The Effect of Climate and Climate Change on Ammonia Emissions in Europe. *Atmos. Chem. Phys.* 13 (1), 117–128. doi:10.5194/acp-13-117-2013

US EPA (2018). 2014 National Emissions Inventory, Version 2 Technical Support Document. Available at: https://www.epa.gov/sites/production/files/2018-07/documents/nei2014v2_tsd_05jul2018.pdf (Accessed July 1, 2020).

US EPA (2019a). *Air Quality System (AQS)*. Available at: https://www.epa.gov/aqs/obtaining-aqs-data (Accessed July 1, 2020).

US EPA (2019b). *Chemical Speciation Network*. CSN) - General Information. Available at: https://www.epa.gov/amtic/chemical-speciation-network-csn (Accessed September 2, 2020).

US EPA (2019c). *Clean Air Status and Trends Network (CASTNET)*. Available at: https://www.epa.gov/castnet (Accessed July 1, 2020).

US EPA (2017). SMOKE v4.5 User's Manual. Available at: https://www.cmascenter.org/smoke/documentation/4.5/manual_smokev45.pdf (Accessed September 2, 2020).

USGS (2019a). Interagency Monitoring of Protected Visual Environments. Available at: https://my.usgs.gov/gcmp/program/show/941778 (Accessed September 2, 2020).

USGS (2019b). SouthEastern Aerosol Research and Characterization Network. Available at: https://my.usgs.gov/gcmp/program/show/943855 (Accessed September 2, 2020).

Wang, J., Wang, S., Jiang, J., Ding, A., Zheng, M., Zhao, B., et al. (2014). Impact of Aerosol-Meteorology Interactions on fine Particle Pollution during China's Severe Haze Episode in January 2013. *Environ. Res. Lett.* 9 (9), 094002. doi:10.1088/1748-9326/9/9/094002

Wong, D. C., Pleim, J., Mathur, R., Binkowski, F., Otte, T., Gilliam, R., et al. (2012). WRF-CMAQ Two-Way Coupled System with Aerosol Feedback: Software Development and Preliminary Results. *Geosci. Model. Dev.* 5 (2), 299–312. doi:10.5194/gmd-5-299-2012

Wu, K., Zhu, S., Liu, Y., Wang, H., Yang, X., Liu, L., et al. (2021). Modeling Ammonia and its Uptake by Secondary Organic Aerosol over China. *Geophys. Res. Atmos.* 126 (7), 1–20. doi:10.1029/2020JD034109

Xing, J., Wang, J., Mathur, R., Pleim, J., Wang, S., Hogrefe, C., et al. (2016). Unexpected Benefits of Reducing Aerosol Cooling Effects. *Environ. Sci. Technol.* 50 (14), 7527–7534. doi:10.1021/acs.est.6b00767

Xiu, A., and Pleim, J. E. (2001). Development of a Land Surface Model. Part I: Application in a Mesoscale Meteorological Model. *J. Appl. Meteorol.* 40, 192–209. doi:10.1175/1520-0450(2001)040<0192:doalsm>2.0.co;2

Yarwood, G., Whitten, G. Z., Jung, J., Heo, G., and Allen, D. (2010). *Development, Evaluation and Testing of Version 6 of the Carbon Bond Chemical Mechanism (CB6)*. Austin, TX: Final Report Prepared for Texas Commission on Environmental Quality.

Zhu, S., Horne, J. R., Mac Kinnon, M., Samuelsen, G. S., and Dabdub, D. (2019). Comprehensively Assessing the Drivers of Future Air Quality in California. *Environ. Int.* 125 (April), 386–398. doi:10.1016/j.envint.2019.02.007

Zhu, S., Horne, J. R., Montoya-Aguilera, J., Hinks, M. L., Nizkorodov, S. A., and Dabdub, D. (2018). Modeling Reactive Ammonia Uptake by Secondary Organic Aerosol in CMAQ: Application to the Continental US. *Atmos. Chem. Phys.* 18 (5), 3641–3657. doi:10.5194/acp-18-3641-2018

Conflict of Interest: The authors declare that the research was conducted in the absence of any commercial or financial relationships that could be construed as a potential conflict of interest.

Publisher's Note: All claims expressed in this article are solely those of the authors and do not necessarily represent those of their affiliated organizations, or those of the publisher, the editors and the reviewers. Any product that may be evaluated in this article, or claim that may be made by its manufacturer, is not guaranteed or endorsed by the publisher.

frontiers | Frontiers in Ecology and Evolution

ORIGINAL RESEARCH
published: 13 April 2022
doi: 10.3389/fevo.2022.875585

Microscopic Insights Into the Formation of Methanesulfonic Acid–Methylamine–Ammonia Particles Under Acid-Rich Conditions

Min Liu[1], Nanna Myllys[2], Yaning Han[1], Zhongteng Wang[1], Liang Chen[1], Wei Liu[1] and Jing Xu[1]**

[1] Department of Optical Engineering, College of Optical, Mechanical and Electrical Engineering, Zhejiang A&F University, Hangzhou, China, [2] Department of Chemistry, University of Jyväskylä, Jyväskylä, Finland

Understanding the microscopic mechanisms of new particle formation under acid-rich conditions is of significance in atmospheric science. Using quantum chemistry calculations, we investigated the microscopic formation mechanism of methanesulfonic acid (MSA)–methylamine (MA)–ammonia (NH_3) clusters. We focused on the binary $(MSA)_{2n}$-$(MA)_n$ and ternary $(MSA)_{3n}$-$(MA)_n$-$(NH_3)_n$, (n = 1–4) systems which contain more acid than base molecules. We found that the lowest-energy isomers in each system possess considerable thermodynamic and dynamic stabilities. In studied cluster structures, all bases are protonated, and they form stable ion pairs with MSA, which contribute to the charge transfer and the stability of clusters. MA and NH_3 have a synergistic effect on NPF under acid-rich conditions, and the role of NH_3 becomes more remarkable as cluster size increases. The excess of MSA molecules does not only enhance the stability of clusters, but provides potential sites for further growth.

Keywords: methanesulfonic acid–methylamine–ammonia particles, new particle formation, acid-rich condition, acid:base ratio, proton transfer

OPEN ACCESS

Edited by:
Shupeng Zhu,
University of California, Irvine, United States

Reviewed by:
Jingyuan Liu,
Harbin Institute of Technology, China
Yihong Ding,
Wenzhou University, China

****Correspondence:***
Jing Xu
jingxu@zafu.edu.cn
Wei Liu
weiliu@zafu.edu.cn

Specialty section:
This article was submitted to Interdisciplinary Climate Studies, a section of the journal Frontiers in Ecology and Evolution

Received: *14 February 2022*
Accepted: *21 March 2022*
Published: *13 April 2022*

Citation:
Liu M, Myllys N, Han Y, Wang Z, Chen L, Liu W and Xu J (2022) Microscopic Insights Into the Formation of Methanesulfonic Acid–Methylamine–Ammonia Particles Under Acid-Rich Conditions. Front. Ecol. Evol. 10:875585. doi: 10.3389/fevo.2022.875585

INTRODUCTION

Atmospheric aerosol particles are tiny liquid and/or solid particles suspended in the air, and exist in a wide range of chemical composition and size distribution (Putaud et al., 2010). Aerosol particles can directly influence global climate by scattering and absorbing solar radiation, or indirectly by acting as cloud condensation nuclei (CCN) and ice nuclei (IN) (Merikanto et al., 2009; Myhre et al., 2013; von Schneidemesser et al., 2015; Dunne et al., 2016). They can affect atmospheric chemical processes as a heterogeneous reaction interface to change the trace component of greenhouse gases (Makkonen et al., 2012), as well as impact visibility and human health (Yu et al., 2008). Therefore, the formation of atmospheric aerosols has been attracting topic over decades around the globe (Charlson et al., 1992; Steinfeld, 1998; Kulmala, 2003; Kittelson et al., 2004; Saxon and Diaz-Sanchez, 2005; Pope and Dockery, 2006; Lelieveld et al., 2015). New particle formation (NPF), a gas-to-particle conversion process (Zhang et al., 2012; Riccobono et al., 2014), is considered to be a dominant source of atmospheric aerosol particles (Spracklen et al., 2006; Zhang et al., 2012) and has been extensively studied both experimentally and theoretically (Berndt et al., 2013; Knopf et al., 2018). Atmospheric NPF process begins as a result of collisions and favorable interactions

(such as hydrogen bonding or proton transfer reactions) between gaseous vapors (Lehtinen and Kulmala, 2003; Wang et al., 2010; Zhang, 2010; Zhang et al., 2012; Kulmala et al., 2013). These newly formed stable clusters usually possess complex structures (Kulmala et al., 2014; Elm et al., 2020), multiple interactions (Sebastianelli et al., 2018), different component ratios (Chen et al., 2018; Perraud et al., 2020a), and undetectable sizes (Stolzenburg and McMurry, 1991; McMurry, 2000), which make challenging to understand the molecular-level NPF mechanisms. Therefore, we tackle these challenges here by exploring the structures, properties, chemical compositions, and stabilities of these small clusters from a microscopic perspective.

Sulfuric acid (H_2SO_4, SA) is known to be the most important driver of NPF in the atmosphere (Sipila et al., 2010; Kirkby et al., 2011; Kulmala et al., 2013), and its contribution to NPF is the most studied (Weber et al., 1995; Chan and Mozurkewich, 2001; Kuang et al., 2008; Sipila et al., 2010; Kirkby et al., 2011; Bzdek et al., 2012; Zollner et al., 2012; Almeida et al., 2013; Schobesberger et al., 2015; Elm, 2017). However, successive studies have found that pure sulfuric acid or sulfuric acid–water systems are not sufficient to explain the formation and growth of atmospheric nanoparticles (Weber et al., 1995, 1996; Kirkby et al., 2011). Subsequently, numerous experimental and theoretical studies have shown that base compounds, such as ammonia (NH_3) or amines, can significantly enhance sulfuric acid-driven particle formation (Kurten et al., 2008; Ge et al., 2011; Hanson et al., 2011; Kupiainen et al., 2012; Yu and Lee, 2012; Almeida et al., 2013; Jen et al., 2014; Olenius et al., 2017). Thereby, current studies focus on the acid–base particles with binary, ternary, or even quaternary components.

Similar to SA, methanesulfonic acid [$CH_3S(O)(O)OH$, MSA], another major oxidation product of dimethyl sulfide (DMS) (Glasow and Crutzen, 2004; Barnes et al., 2006), has been confirmed to be an important contributor to the NPF process in the presence of base compounds (Dawson et al., 2012, 2014; Ezell et al., 2014; Nishino et al., 2014; Chen et al., 2016; Chen and Finlayson-Pitts, 2017; Zhao et al., 2019; Perraud et al., 2020b). Finlayson-Pitts group systemically reported extensive experimental and theoretical studies based on MSA particles. They found that small alkylamines (methylamine, dimethylamine, and trimethylamine) have stronger nucleation capacity than NH_3 in MSA-driven NPF (Chen et al., 2016; Chen and Finlayson-Pitts, 2017; Perraud et al., 2020b). However, NH_3 can promote the formation of MSA–amines particles, and has a synergistic effect on particle formation and growth processes (Perraud et al., 2020b).

The cluster formation pathway, particle formation rate, and the microstructure of the critical nucleus are dependent on the molecular properties of acid and base compounds as well as environmental conditions (Chee et al., 2019, 2021). Therefore, obtaining a comprehensive understanding of atmospheric NPF process is extremely difficult task. For instance, some experimental studies have shown that acid and base molecules do not always nucleate in a simple 1:1 acid:base stoichiometric fashion (Kim et al., 2016; Lawler et al., 2016; Chen et al., 2018; Finlayson-Pitts et al., 2020; Perraud et al., 2020a). They found that although the acid has much lower concentrations than bases in the gas phase, the formed particles in small sizes are acidic, i.e., the measured acid:base ratio is larger than 1:1. Quantum chemistry is an effective method to obtain the microscopic information of nucleated clusters with different acid:base ratios. However, current theoretical studies of these small clusters mainly focus on the clusters with a same number of acid and base molecules. Hence, it is necessary to theoretically study the microstructure and reveal formation mechanism of acid–base particles under acid-rich conditions.

Here we focus on microscopic description of nanoparticles formed by the reaction of MSA with MA and NH_3 under acid-rich conditions, where the acid:base ratios correspond the detected experimental values reported by Finlayson-Pitts group (Perraud et al., 2020a). The binary $(MSA)_{2n}$-$(MA)_n$, (n = 1–4) and ternary $(MSA)_{3n}$-$(MA)_n$-$(NH_3)_n$, (n = 1–4) systems were investigated using computational tools. We have calculated the structures, energies, thermodynamic and dynamic stabilities, and related properties of these clusters at the level of B3LYP-D3/6-311+G(2d,2p)//B3LYP-D3/6-31G(d). The role of base synergy in acid-rich particles is also discussed.

MATERIALS AND METHODS

ABCluster software (Zhang and Dolg, 2015, 2016) with the artificial bee colony algorithm (Karaboga, 2005) was employed to search local minima on the potential energy surface of the studied clusters. In the process of cluster search, molecular monomers are usually used as the basic unit to construct the initial structure. In the current study of acid-base particles, stable clusters are usually ion pairs formed by proton transfer. To more efficiently obtain reliable low-energy isomers, beside single molecules, the possible acid-base ion pairs are also considered for screening initial structures. Hence, we totally employed three classes of building block as basic units (see **Scheme 1**). The first class consists of single molecules and the other two classes introduce two kinds of proton transferred clusters with 1:1 and 2:1 acid:base ratios as building blocks. In our cluster search strategy, 1,000 structures were randomly generated by ABCluster program based on each building block combinations, and total of 24,000 initial structures were generated for eight systems. Due to large number of calculations, it is necessary to adopt economic calculation strategy to avoid the exhaustive and unnecessary calculations. We followed the **Scheme 2** as: Firstly, 3,000 structures generated by ABCluster for each system were optimized using the PM7 semi-empirical method (Stewart, 2007; Hostaš et al., 2013). We selected the minimum structures within $\Delta E < 100$ kcal/mol of the lowest-energy isomer, which were further optimized at the level of B3LYP/3-21G. After that we reselected the structures within $\Delta E < 60$ kcal/mol of the lowest-energy cluster for the final optimization and vibrational frequency calculations using B3LYP functional with Grimme's dispersion correction and 6-31G(d) basis set. Finally, for conformers within $\Delta E < 20$ kcal/mol of the lowest energy structure, the single-point energy calculations were carried out to obtain more reliable energies at the level of B3LYP-D3/6-311+G(2d,2p), and the obtained isomers with lowest Gibbs free energy were confirmed as the global minima. Previous

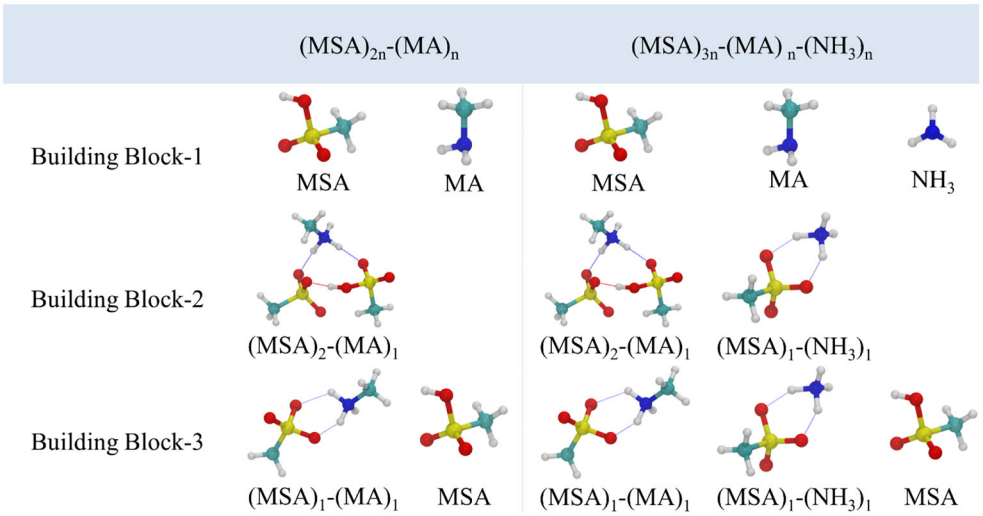

SCHEME 1 | Three classes of "Building Block."

studies have shown that B3LYP-D3 can reasonably predict the structure, energy and property of small clusters (Xantheas, 1995; Miller et al., 2007; Dawson et al., 2012; Chen et al., 2015, 2016; Perraud et al., 2020b). To verify the reliability of B3LYP-D3/6-311+G(2d,2p), we chose 2MSA-1MA as our test system and benchmarked the results against MP2/6-311+G(2d,2p). The test results showed that the lowest-energy isomers predicted by the two methods are consistent (see **Supplementary Table 1**, ESI†). Therefore, considering computational cost performance and complexity, B3LYP-D3/6-311+G(2d,2p) is sufficient to qualitatively predict the lowest energy isomers in this study. Normal-mode vibrational frequency analyses had confirmed that all the stable minima had positive vibrational frequencies. Natural bond orbital (NBO) analysis (Foster and Weinhold, 1980; Reed and Weinhold, 1983) was used to obtain partial charges (δ). All density functional theory (DFT) geometry optimizations and vibrational frequency calculations were performed using the Gaussian 16 program (Frisch et al., 2016).

To evaluate the dynamic stabilities of the obtained clusters, molecular dynamics simulations with semi-empirical quantum chemical potentials (PM6) (Takayanagi et al., 2008; Tosso et al., 2013; Wang et al., 2019) were carried out using the CP2K package (VandeVondele et al., 2005), on the gas-phase NVT canonical ensemble with Nose-Hover thermostats (Nosé, 1984; Hoover, 1985). In order to evaluate the reliability of PM6 for our clusters, we optimized all the lowest-energy structures at PM6 level. Test results showed that the geometries obtained at PM6 level are very close to those obtained by density functional theory. For each simulation, five trajectories were done, and each trajectory was propagated for 100 ps. The time step used here was 1 fs and the simulation temperature was at T = 300 K.

In order to explore the intermolecular interactions of acid–base clusters, we performed non-covalent interaction (NCI) analysis, which is used to describe the relationship between electron density $\rho(r)$ and reduced density gradient (RDG)

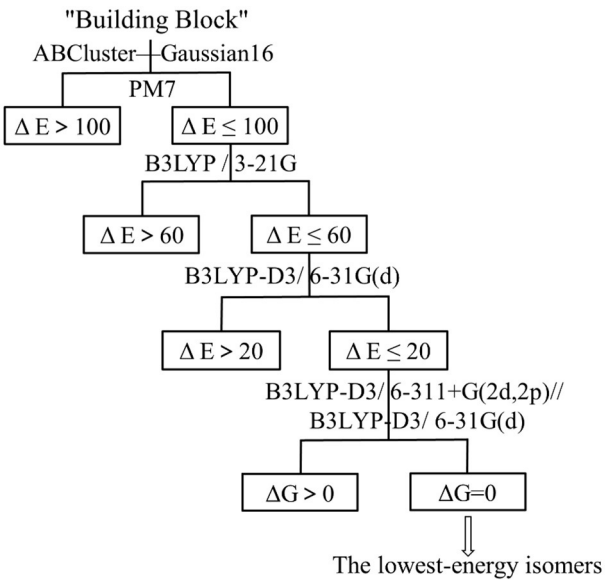

SCHEME 2 | The energetic calculation strategy for searching the lowest-energy isomers.

(Johnson et al., 2010). RDG(s) is calculated by Equation (1) in order to prove the deviation from the homogeneous distribution of electrons.

$$s = \frac{1}{2\left(3\pi^2\right)^{\frac{1}{3}}} \frac{|\nabla\rho|}{\rho^{\frac{4}{3}}} \quad (1)$$

where ρ is the electron density based on B3LYP-D3/6-311+G(2d,2p)//B3LYP-D3 /6-31G(d), ∇ is the gradient operator, and $|\nabla\rho|$ is the electronic density gradient mode.

The function sign(λ_2)ρ is obtained by multiplying the electron density $\rho(r)$ by the sign of the second Hessian eigenvalue (λ_2). The RDG-sign(λ_2)ρ scatter plots and the bonding iso-surface plots were made by Multiwfn (Johnson et al., 2010; Tian and Chen, 2012) and VMD (Humphrey et al., 1996; Illinois, 2014) programs, respectively. In addition, proton transfer was evaluated by a proton-transfer parameter (ρ_{PT}), which is based on the extension and contraction of bonds between atoms (Kurnig and Scheiner, 1987). The specific expression of ρ_{PT} in this work is given in Equation (2):

$$\rho_{PT} = \left(r_{OH} - r^0_{OH}\right) - \left(r_{H\cdots N} - r^0_{H\cdots N}\right) \quad (2)$$

where r^0_{OH} and $r^0_{H\cdots N}$ are the O-H and N-H bond distances in free MSA monomer and fully protonated MA and NH_3 ($CH_3NH_3^+$ and NH_4^+ion), respectively. Radiuses r_{OH} and $r_{H\cdots N}$ are those of hydrogen bond in the studied clusters.

RESULTS

In this work, binary $(MSA)_{2n}$-$(MA)_n$, (n = 1–4) and ternary $(MSA)_{3n}$-$(MA)_n$-$(NH_3)_n$, (n = 1–4) clusters were used as a representative set to investigate MSA-MA-NH_3 particles under acid-rich conditions. The acid:base ratios used here were based on the experimentally detected values of small size MSA-MA-NH_3 particles (<9 nm) by Perraud et al. (2020a) Hence, we used an acid:base ratio of 2:1 for binary MSA-MA particles, and 3:2 for ternary MSA-MA-NH_3 particles. Additionally, MA:NH_3 ratio is 1:1 in ternary system. Here we will discuss the molecular structures, intermolecular interactions and dynamic stabilities of the two- and three-component clusters.

Structure Analysis

Binary $(MSA)_{2n}$-$(MA)_n$ System

The obtained global free energy structures of the $(MSA)_{2n}$-$(MA)_n$, (n = 1–4) system at the level of B3LYP-D3/6-311+G(2d,2p)//B3LYP-D3/6-31G(d) are shown in **Figure 1**, and other high-energy isomers are shown in **Supplementary Figures 1–4**. For clarity, geometrical parameters for hydrogen bonds are omitted. All cluster structures in **Figure 1** possess the cage-like skeletons composed of hydrogen bonds (HBs), and the number of HBs (3, 8, 11, 13) increases with the increase of n. Generally, two types of HBs were found in binary clusters. The first type is N-H···O bond (shown by the blue dash line) formed between the hydrogen atom in MA and the oxygen atom in MSA, with bond lengths ranging from 1.64 to 1.99 Å. Three hydrogen atoms in MA consist of two hydrogen atoms from the original amino group and a proton transferred from MSA. In these structures, each MA molecule obtains a proton from MSA molecule forming the ion pair $[CH_3SO_3]^-[H_3NCH_3]^+$, which is consistent with previous studies of MSA–MA clusters (Xu et al., 2017; Perraud et al., 2020b). This is also supported by the partial charge (δ) obtained using natural bond orbital (NBO) analysis. All the MA moieties

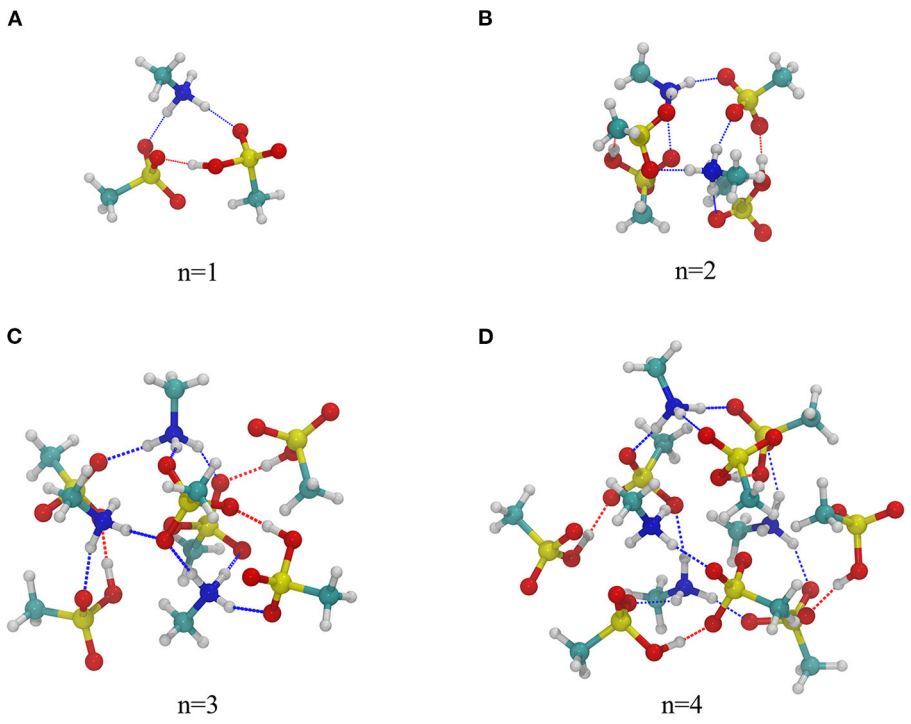

FIGURE 1 | The most stable structures of binary $(MSA)_{2n}$-$(MA)_n$, (n = 1–4) clusters at the level of B3LYP-D3/6-311+G(2d,2p)//B3LYP-D3/6-31G(d). Yellow, red, blue, cyan, and white spheres represent sulfur, oxygen, nitrogen, carbon, and hydrogen atoms, respectively. Dotted lines in blue and red represent N-H···O and O-H···O hydrogen bonds, respectively.

have positive charges (δ = 0.86–0.89) and the deprotonated MSA moieties have negative charges (δ = −0.84 to −0.81), indicating that MA acts as the hydrogen-bond acceptor and MSA is the donor. These closed ion pairs are always located in the center of the skeleton and they increase the structure stability. The second type is the O-H···O bond (shown by the red dash line) formed between anionic and neutral MSA monomers. The length of this HB ranges from 1.37 to 1.65 Å. Those MSA molecules that do not participate in proton transfer are distributed outside of the structure, and the corresponding partial charges are δ = −0.10 to −0.04. Clearly, when MSA exhibits a strong intermolecular interaction with MA, the formed ion pairs play an important role on charge transfer, and have the major contribution to the stability of a cluster. For surrounding MSA molecules, although their contributions to charge transfer are very small, they link to ion pairs *via* HBs increasing the structure stability and provide more potential hydrogen binding sites for further particle growth.

Ternary $(MSA)_{3n}$-$(MA)_n$-$(NH_3)_n$ System

Figure 2 shows the most stable structures for ternary $(MSA)_{3n}$-$(MA)_n$-$(NH_3)_n$ (n = 1–4) clusters, and other obtained structures with high energy are shown in **Supplementary Figures 5–8**. Like the binary structures, these global minimum free energy conformers also have cage skeletons, in which ion pairs formed by proton transfer between acid and base are located in the center of the skeleton and neutral MSA molecules surround the cage structure. As **Figure 2** demonstrates, both MA and NH_3 can accept a proton from MSA forming ion pairs $[CH_3SO_3]^-[H_3NCH_3]^+$ and $[CH_3SO_3]^-[H_4N]^+$, respectively. Therefore, in addition to the two kinds of HBs in binary system, there is another N-H···O hydrogen bond formed between NH_3 and MSA. The bond lengths of N-H···O hydrogen bond in ternary structures range from 1.64 to 1.99 Å and O-H···O hydrogen bonds are from 1.45 to 1.68 Å. Furthermore, NBO results show that the partial charge value (δ) of MA and NH_3 are very close (δ = 0.84–0.90). The corresponding values of MSA with and without proton transfer are δ = −0.88 to −0.79 and δ = −0.08 to −0.03, respectively. These results show that there is no significant difference in the action of the two bases with MSA under acid-rich conditions, although the basicity (both in aqueous and gas phase) of NH_3 is less than that of MA. In addition, with increasing n, the protonated NH_3 gradually replaces MA to be the inner of the cluster structure, which may be because NH_3 can form more hydrogen bonds to stabilize the structure, and the methyl group in MA has the steric hindrance effect. Similar structural effects have been found for sulfuric acid–dimethylamine–ammonia clusters (Myllys et al., 2019). In conclusion, in the presence of NH_3 and MA, more proton transfers and more HBs can be formed than in the presence of a single base. This base synergy enhances the stability of clusters and provides more sites to connect to other molecules. This is further discussed combining with stability analysis in the following section Stability Analysis.

Intermolecular Interactions

Intermolecular interactions in the acid–base clusters were studied using NCI index and proton transfer parameter (ρPT),

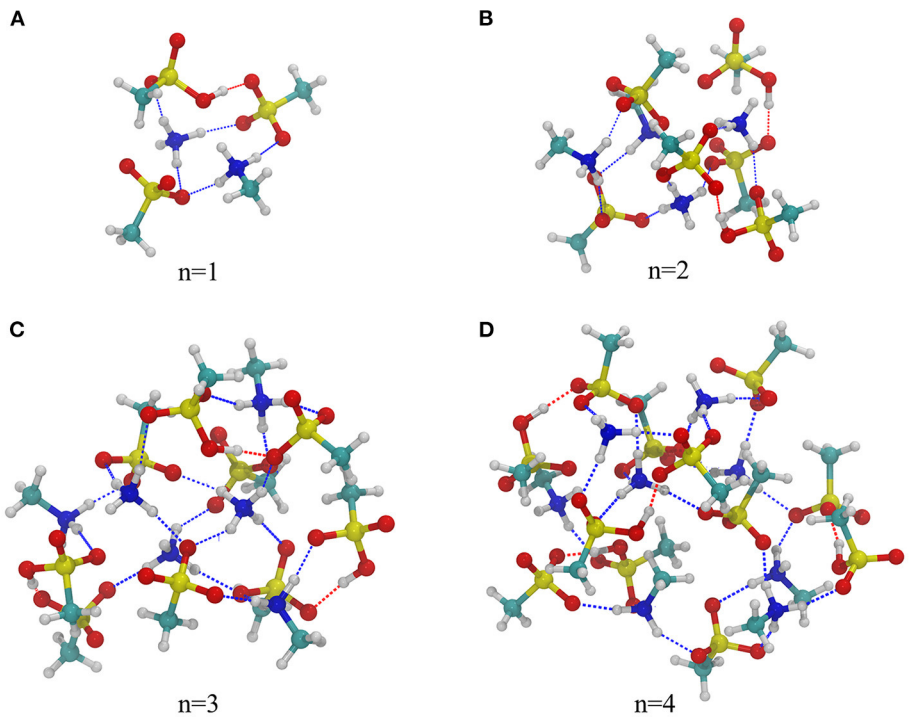

FIGURE 2 | The most stable structures of ternary $(MSA)_{3n}$-$(MA)_n$-$(NH_3)_n$, (n = 1–4) clusters at the level of B3LYP-D3/6-311+G(2d,2p)//B3LYP-D3/6-31G(d).

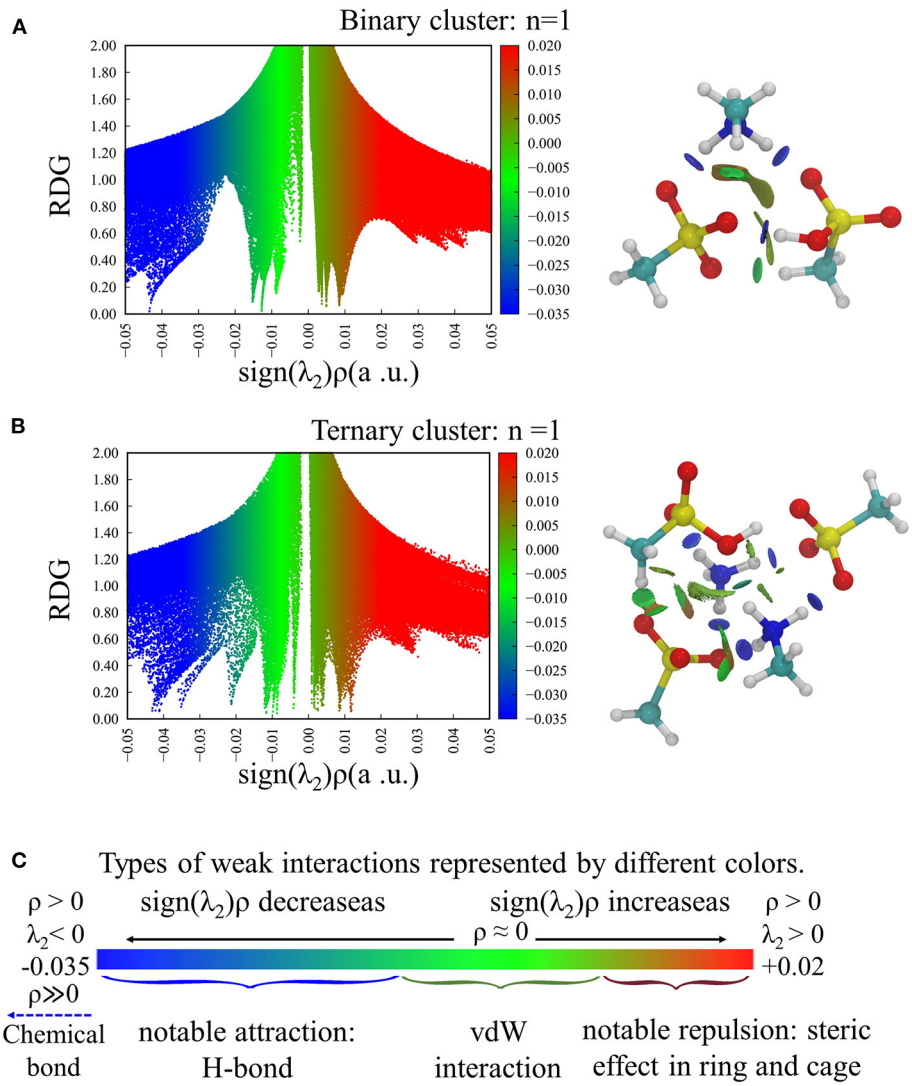

FIGURE 3 | The plots of RDG vs. sign(λ_2)ρ function (left) and the visualized bonding isosurfaces (right) for **(A)** $(MSA)_{2n}$-$(MA)_n$ (n =1), **(B)** $(MSA)_{3n}$-$(MA)_n$-$(NH_3)_n$ (n =1). **(C)** The values of $\rho(r)$ and λ_2 represented by different colors and the corresponding interaction types.

TABLE 1 | Proton-transfer parameter (ρ_{PT}, in Å) and the total number of proton transfers for the smallest binary and ternary clusters (n = 1).

Clusters	r_{OH}(Å)	$r_{H\cdots N}$(Å)	ρ_{PT}(Å)	Proton acceptor	Number
$(MSA)_2$ -$(MA)_1$	1.636	1.066	0.660	MA	1
$(MSA)_3$-$(MA)_1$-$(NH_3)_1$	1.744	1.047	0.768	MA	2
	1.714	1.050	0.737	NH_3	

r_{OH} and $r_{H\cdots N}$(Å) are the bond distances between O and H atoms and H and N atoms, respectively. The proton acceptors are also listed.

respectively. The former can judge the strength of interaction by the value of sign(λ_2)ρ, and the latter can evaluate the degree of ionization of proton transfer using the distance between atoms. Both of them have been successfully used to reveal the interaction in previous reports of acid–base particles (Kurnig and Scheiner, 1987; Hunt et al., 2003; Ling et al., 2018; Zhao et al., 2020). **Figures 3A,B** show the scatter plot of RDG(s) vs. sign(λ_2)ρ for the smallest binary and ternary clusters (n = 1) and the corresponding bonding isosurfaces, as well as the corresponding interaction types shown in different colors (**Figure 3C**). For other clusters, the plots are shown in **Supplementary Figures 9, 10**. We found that the most stable cluster in each system has the negative sign(λ_2)ρ values indicating the presence of HBs, meanwhile, van der Waals force [sign(λ_2)$\rho \sim 0$] and steric hindrance [sign(λ_2)$\rho > 0$] can be found in each cluster. These results are also supported by the visual bonding isosurfaces, and all the HBs can completely correspond to the structures in **Figures 1**, **2** through the disc-like isosurface. As n increases, the values corresponding to the spike in cyan area [with small negative sign(λ_2)ρ values] gradually

become larger. This is because the increased number of molecules increases the steric hindrance and weakens the strength of hydrogen bonds, which is consistent with the long bond length of HB in large system. In short, weak interactions have the major contribution in these clusters, and the abundant MSA molecules can saturate the interaction sites of the clusters.

Proton transfer parameters of the smallest systems (n = 1) are listed in **Table 1**, and other systems can be seen in **Supplementary Table 2**. Based on the equation of ρ_{PT}, if the proton transfer fully occurs, the H-O bond on the proton donor is stretched, the second term is zero and ρPT should be positive. This means that there is a real ion pair in the cluster, and the more positive the parameter value, the stronger the proton transfer degree and ionic properties of the cluster. For all the systems we studied, the ρ_{PT} values are always positive, indicating the presence of proton transfer, and the number of proton transfer is equal to the total number of base molecules involved.

Stability Analysis

To study cluster stabilities, thermodynamic analysis and molecular dynamic simulations were performed. The lowest-energy structures were determined using zero-point energy corrected energies (0 K) and Gibbs free energies (298.15 K). For those isomers within 20 kcal/mol of the lowest-energy isomer, the relative energies with zero-point energy correction (ΔE + ZPE) and Gibbs free energies (ΔG) are listed in the **Supplementary Tables 3–10**. The thermodynamic stabilities were evaluated using three possible dissociation reactions, and ΔG of dissociation path was calculated by Equation (3). The calculated ΔG values for studied clusters were plot in **Figure 4**, and the exact data is listed in **Supplementary Tables 11, 12**. As seen in **Figure 4**, the ΔG values of all reaction paths are positive, indicating the studied dissociation reactions are thermodynamically unfavorable. Moreover, with the increase of n, ΔG values increase for both binary and ternary systems, which is because more HBs exist in large systems. Furthermore, the dissociation energies for ternary clusters are much larger than the corresponding binary cluster. This is partly due for the fact that studied ternary systems contain total of 5n molecules whereas corresponding binary systems contain 3n molecules, meaning that with same n ternary system is larger and have more intermolecular interactions. Additionally, a reasonable assumption would be that three-component pathway can lead to higher particle formation potential than the two-component pathways for two main reasons: (1) stronger intermolecular forces and (2) synergistic effects. (1) This is consistent with the structural discussion above that NH_3 and MSA can form ion pairs and more HBs, thus increasing the stability of cluster. (2) In these acid-rich clusters, both MA and NH_3 have an important influence on the stability of clusters and play a synergistic role on NPF, which is consistent with previous studies (Perraud et al., 2020b).

$$\Delta G = \sum G\left(product\right) - \sum G\left(reactant\right) = \sum \nu_B G\left(basic\ unit,\ B\right) - G\left(global\ minima\right) \quad (3)$$

The dynamic stabilities of the studied clusters were verified by molecular dynamic simulations for 100 ps at 300 K. **Supplementary Figure 11** shows the energy change of each cluster during the whole simulation process, and the final structures at 100 ps are shown in **Supplementary Figure 12**. Throughout the simulation, the energy change is not significant and components do not evaporate from the cluster at room temperature. All the states of proton transfer remain unchanged, and the ion pairs still form cage-like skeletons with slightly different structural parameters. Therefore, we can conclude the studied binary and ternary clusters to be dynamically stable at room temperature.

Combining above structure, intermolecular interaction and stability analysis, it can be found that these acid-rich clusters possess high thermodynamic and dynamic stabilities. Hydrogen bonds and ion pairs formed by proton transfer reactions from acid to base play an important role in the formation of stable structures, and the synergistic effect between NH_3 and MA can

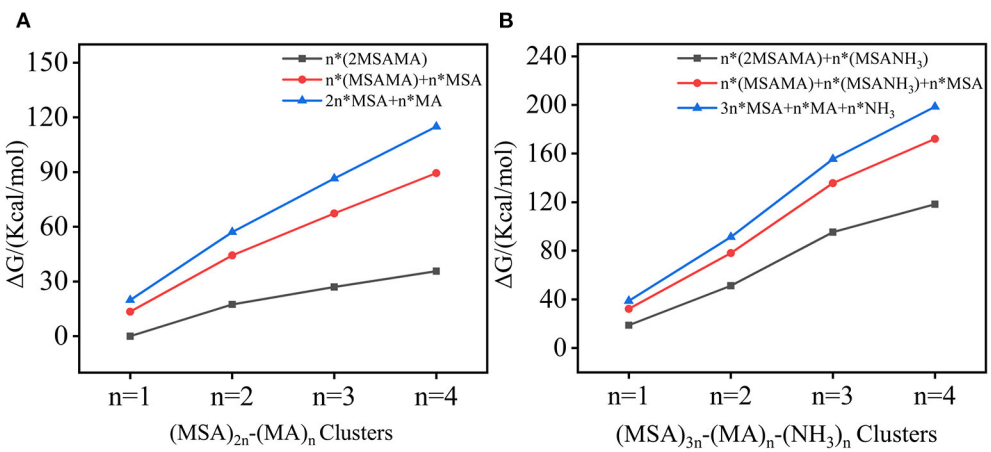

FIGURE 4 | Dissociation free energies (ΔG, 298.15 K) of $(MSA)_{2n}$-$(MA)_n$ and $(MSA)_{3n}$-$(MA)_n$ -$(NH_3)_n$ (n =1–4) clusters through three reaction paths.

also be detected. The excess MSA molecules enhance the stability of clusters and provide additional hydrogen binding sites for further growth.

CONCLUSION

In this work, we explored the microscopic formation mechanism of methanesulfonic acid–methylamine–ammonia particles under acid-rich conditions. Structures, energies, properties and stabilities of binary $(MSA)_{2n}$-$(MA)_n$ and ternary $(MSA)_{3n}$-$(MA)_n$-$(NH_3)_n$, ($n = 1$–4) systems were calculated at the level of B3LYP-D3/6-311+G(2d,2p)//B3LYP-D3/6-31G(d). The most stable clusters have a cage-like skeleton, which are composed of the ion pairs formed by proton transfer from the acid to the base molecule. According to the dissociation energy and dynamic simulation at 300 K, these eight acid-rich clusters possess considerable thermodynamic and dynamic stabilities. Like in other acid–base systems, proton transfer plays an important role on charge transfer and the stability of clusters. Moreover, MA and NH_3, which are both abundant vapor molecules in many atmospheric locations, have a synergistic effect on NPF under acid-rich conditions. The excess of MSA molecules can promote the stability of clusters, and also provide potential sites for HBs to further connect with other molecules, which is favorable for particle growth. This work does not only increase the molecular-level understanding of the MSA-MA-NH_3 particle formation, but also reveals the importance of acid-rich conditions and acidic particles.

Considering the decline in sulfur dioxide (precursor of sulfuric acid in the air) associated with the burning of fossil fuels (Jefferson et al., 1998; Klimont et al., 2013; Perraud et al., 2015; Murphy et al., 2017) and higher gas concentration of MSA in coastal areas (Berresheim et al., 1993, 2013; Eisele and Tanner, 1993; Jefferson et al., 1998; Berresheim, 2002; Bardouki et al., 2003), it can be predicted that the aerosol particles produced by MSA may become more important in the future. Thus, more experimental and theoretical studies focusing on MSA-rich conditions should be conducted to estimate the climatic impact of multi-component MSA aerosol particles. Especially in the ever-changing and complex atmospheric environment, the ubiquitous water molecules and various volatile acidic compounds from natural sources, and climatic phenomena such as acid mist and acid rain caused by anthropogenic sources will all affect the formation rate of new particles. The measurement of atmospheric composition in a higher acid state and its theoretical research are essential to understand acidizing deposition and to formulate economic and effective control strategies in the future.

DATA AVAILABILITY STATEMENT

The original contributions presented in the study are included in the article/**Supplementary Material**, further inquiries can be directed to the corresponding author/s.

AUTHOR CONTRIBUTIONS

ML: conceptualization, formal analysis, investigation, methodology, data curation, visualization, and writing—original draft. NM: resources, supervision, validation, and writing—review and editing. YH: data curation and visualization. ZW: investigation and methodology. LC: funding acquisition and writing—review and editing. WL: conceptualization, funding acquisition, investigation, project administration, resources, supervision, validation, and writing—review and editing. JX: conceptualization, funding acquisition, investigation, project administration, resources, supervision, validation, and writing—review and editing. All authors contributed to the article and approved the submitted version.

FUNDING

This work was supported by the Zhejiang Provincial Natural Science Foundation of China (No. LQ20B030002), and the National Natural Science Foundation of China (Nos. 12075211, 11975206, and 11875236).

SUPPLEMENTARY MATERIAL

The Supplementary Material for this article can be found online at: https://www.frontiersin.org/articles/10.3389/fevo.2022.875585/full#supplementary-material

REFERENCES

Almeida, J., Schobesberger, S., Kürten, A., Ortega, I. K., Kupiainen-Määttä, O., and Praplan, A. P. (2013). Molecular understanding of sulphuric acid–amine particle nucleation in the atmosphere. *Nature* 502, 359–363. doi: 10.1038/nature12663

Bardouki, H., Berresheim, H., Vrekoussis, M., Sciare, J., Kouvarakis, G., and Oikonomou, K. (2003). Gaseous (DMS, MSA, SO_2, H_2SO_4 and DMSO) and particulate (sulfate and methanesulfonate) sulfur species over the northeastern coast of Crete. *Atmos. Chem. Phys.* 3, 1871–1886. doi: 10.5194/acp-3-1871-2003

Barnes, I., Hjorth, J., and Mihalopoulos, N. (2006). Dimethyl sulfide and dimethyl sulfoxide and their oxidation in the atmosphere. *ChemInform* 37. doi: 10.1002/chin.200624259

Berndt, T., Sipilä, M., Stratmann, F., Petäjä, T., Vanhanen, J., and Mikkilä, J. (2013). *Enhancement of Atmospheric H2SO4/H2O Nucleation: Organic Oxidation Products vs. Amines.* Gases/Laboratory Studies/Troposphere/Chemistry (chemical composition and reactions) [Preprint]. Available online at: https://doi.org/10.5194/acpd-13-16301-2013

Berresheim, H. (2002). Gas-aerosol relationships of H_2SO_4, MSA, and OH: Observations in the coastal marine boundary layer at Mace Head, Ireland. *J. Geophys. Res.* 107:8100. doi: 10.1029/2000JD000229

Berresheim, H., Adam, M., Monahan, C., ODowd, C., Plane, J. M. C., and Bohn, B. (2013). Missing SO_2 oxidant in the coastal atmosphere? - Evidence from high resolution measurements of OH and atmospheric sulfur compounds. *Atmosp. Chem. Phys.* 14, 12209–12223. doi: 10.5194/acp-14-12209-2014

Berresheim, H., Eisele, F. L., Tanner, D. J., Mcinnes, L. M., Ramsey-Bell, D. C., and Covert, D. S. (1993). Atmospheric sulfur chemistry and cloud condensation nuclei (CCN) concentrations over the northeastern Pacific Coast. *J. Geophys. Res.* 98:12701. doi: 10.1029/93JD00815

Bzdek, B. R., Zordan, C. A., Pennington, M. R., Luther, G. W., and Johnston, M. V. (2012). Quantitative assessment of the sulfuric acid contribution to new particle growth. *Environ. Sci. Technol.* 46, 4365–4373. doi: 10.1021/es204556c

Chan, T., and Mozurkewich, M. (2001). Measurement of the coagulation rate constant for sulfuric acid particles as a function of particle size using tandem differential mobility analysis. *J. Aerosol Sci.* 32, 321–339. doi: 10.1016/S0021-8502(00)00081-1

Charlson, R. J., Schwartz, S. E., Hales, J. M., Cess, R. D., Coakley, J. A., and Hansen, J. E. (1992). Climate forcing by anthropogenic aerosols. *Science* 255, 423–430. doi: 10.1126/science.255.5043.423

Chee, S., Barsanti, K., Smith, J. N., and Myllys, N. (2021). A predictive model for salt nanoparticle formation using heterodimer stability calculations. *Atmos. Chem. Phys.* 21, 11637–11654. doi: 10.5194/acp-21-11637-2021

Chee, S., Myllys, N., Barsanti, K. C., Wong, B. M., and Smith, J. N. (2019). An experimental and modeling study of nanoparticle formation and growth from dimethylamine and nitric acid. *J. Phys. Chem. A* 123, 5640–5648. doi: 10.1021/acs.jpca.9b03326

Chen, H., Chee, S., Lawler, M. J., Barsanti, K. C., Wong, B. M., and Smith, J. N. (2018). Size resolved chemical composition of nanoparticles from reactions of sulfuric acid with ammonia and dimethylamine. *Aerosol Sci. Technol.* 52, 1120–1133. doi: 10.1080/02786826.2018.1490005

Chen, H., Ezell, M. J., Arquero, K. D., Varner, M. E., Dawson, M. L., and Finlayson-Pitts, B. J. (2015). New particle formation and growth from methanesulfonic acid, trimethylamine and water. *Phys. Chem. Chem. Phys.* 17, 13699–13709. doi: 10.1039/c5cp00838g

Chen, H., and Finlayson-Pitts, B. J. (2017). New particle formation from methanesulfonic acid and amines/ammonia as a function of temperature. *Environ. Sci. Technol.* 51, 243–252. doi: 10.1021/acs.est.6b04173

Chen, H., Varner, M. E., Gerber, R. B., and Finlayson-Pitts, B. J. (2016). Reactions of methanesulfonic acid with amines and ammonia as a source of new particles in air. *J. Phys. Chem. B* 120, 1526–1536. doi: 10.1021/acs.jpcb.5b07433

Dawson, M. L., Varner, M. E., Perraud, V., Ezell, M. J., Gerber, R. B., and Finlayson-Pitts, B. J. (2012). Simplified mechanism for new particle formation from methanesulfonic acid, amines, and water *via* experiments and ab initio calculations. *Proc. Natl. Acad. Sci. U.S.A.* 109, 18719–18724. doi: 10.1073/pnas.1211878109

Dawson, M. L., Varner, M. E., Perraud, V., Ezell, M. J., Wilson, J., and Zelenyuk, A. (2014). Amine–amine exchange in aminium–methanesulfonate aerosols. *J. Phys. Chem. C* 118, 29431–29440. doi: 10.1021/jp506560w

Dunne, E. M., Gordon, H., Kürten, A., Almeida, J., Duplissy, J., and Williamson, C. (2016). Global atmospheric particle formation from CERN CLOUD measurements. *Science* 354, 1119–1124. doi: 10.1126/science.aaf2649

Eisele, F. L., and Tanner, D. J. (1993). Measurement of the gas phase concentration of H_2SO_4 and methane sulfonic acid and estimates of H_2SO_4 production and loss in the atmosphere. *J. Geophys. Res. Atmos.* 98, 9001–9010. doi: 10.1029/93JD00031

Elm, J. (2017). Elucidating the limiting steps in sulfuric acid–base new particle formation. *J. Phys. Chem. A* 121, 8288–8295. doi: 10.1021/acs.jpca.7b08962

Elm, J., Kubečka, J., Besel, V., Jääskeläinen, M. J., Halonen, R., and Kurtén, T. (2020). Modeling the formation and growth of atmospheric molecular clusters: a review. *J. Aerosol Sci.* 149:105621. doi: 10.1016/j.jaerosci.2020.105621

Ezell, M. J., Chen, H., Arquero, K. D., and Finlayson-Pitts, B. J. (2014). Aerosol fast flow reactor for laboratory studies of new particle formation. *J. Aerosol Sci.* 78, 30–40. doi: 10.1016/j.jaerosci.2014.08.009

Finlayson-Pitts, B. J., Wingen, L. M., Perraud, V., and Ezell, M. J. (2020). Open questions on the chemical composition of airborne particles. *Commun. Chem.* 3:108. doi: 10.1038/s42004-020-00347-4

Foster, J. P., and Weinhold, F. (1980). Natural hybrid orbitals. *J. Am. Chem. Soc.* 102, 7211–7218. doi: 10.1021/ja00544a007

Frisch, M. J., Trucks, G. W., Schlegel, H. B., Scuseria, G. E., Robb, M. A., and Cheeseman, J. R. (2016). *Gaussian 16, Revision A.03*. Wallingford, CT: Gaussian, Inc.

Ge, X., Wexler, A. S., and Clegg, S. L. (2011). Atmospheric amines – Part I. A review. *Atmos. Environ.* 45, 524–546. doi: 10.1016/j.atmosenv.2010.10.012

Glasow, R. V., and Crutzen, P. J. (2004). Model study of multiphase DMS oxidation with a focus on halogens. *Atmos. Chem. Phys.* 4, 589–608. doi: 10.5194/acp-4-589-2004

Hanson, D. R., McMurry, P. H., Jiang, J., Tanner, D., and Huey, L. G. (2011). Ambient pressure proton transfer mass spectrometry: detection of amines and ammonia. *Environ. Sci. Technol.* 45, 8881–8888. doi: 10.1021/es201819a

Hoover, W. G. (1985). Canonical dynamics: equilibrium phase-space distributions. *Phys. Rev. A* 31, 1695–1697. doi: 10.1103/PhysRevA.31.1695

Hostaš, J., Rezáč, J., and Hobza, P. (2013). On the performance of the semiempirical quantum mechanical PM6 and PM7 methods for noncovalent interactions. *Chem. Phys. Lett.* 568–569, 161–166. doi: 10.1016/j.cplett.2013.02.069

Humphrey, W., Dalke, A., and Schulten, K. (1996). VMD: visual molecular dynamics. *J. Mol. Graph.* 14, 33–38. doi: 10.1016/0263-7855(96)00018-5

Hunt, S. W., Higgins, K. J., Craddock, M. B., Brauer, C. S., and Leopold, K. R. (2003). Influence of a polar near-neighbor on incipient proton transfer in a strongly hydrogen bonded complex. *J. Am. Chem. Soc.* 125, 13850–13860. doi: 10.1021/ja030435x

Illinois, U. (2014). *Visual Molecular Dynamics.* Available online at: http://www.mendeley.com/research/visual-molecular-dynamics/ (accessed August 5, 2021).

Jefferson, A., Tanner, D. J., Eisele, F. L., Davis, D. D., Chen, G., and Crawford, J. (1998). OH photochemistry and methane sulfonic acid formation in the coastal Antarctic boundary layer. *J. Geophys. Res. Atmos.* 103, 1647–1656. doi: 10.1029/97jd02376

Jen, C. N., McMurry, P. H., and Hanson, D. R. (2014). Stabilization of sulfuric acid dimers by ammonia, methylamine, dimethylamine, and trimethylamine. *J. Geophys. Res.* 119, 7502–7514. doi: 10.1002/2014JD021592

Johnson, E. R., Keinan, S., Mori-Sanchez, P., Contreras-Garcia, J., Cohen, A. J., and Yang, W. (2010). Revealing noncovalent interactions. *J. Am. Chem. Soc.* 132:6498. doi: 10.1021/ja100936w

Karaboga, D. (2005). *An Idea Based on Honey Bee Swarm for Numerical Optimization.* Available online at: http://www.researchgate.net/publication/255638348 (accessed October 5, 2009).

Kim, J., Ahlm, L., Yli-Juuti, T., Lawler, M., Keskinen, H., and Tröstl, J. (2016). Hygroscopicity of nanoparticles produced from homogeneous nucleation in the CLOUD experiments. *Atmos. Chem. Phys.* 16, 293–304. doi: 10.5194/acp-16-293-2016

Kirkby, J., Curtius, J., Almeida, J., Dunne, E., Duplissy, J., and Ehrhart, S. (2011). Role of sulphuric acid, ammonia and galactic cosmic rays in atmospheric aerosol nucleation. *Nature* 476, 429–433. doi: 10.1038/nature10343

Kittelson, D. B., Watts, W. F., and Johnson, J. P. (2004). Nanoparticle emissions on Minnesota highways. *Atmos. Environ.* 38, 9–19. doi: 10.1016/j.atmosenv.2003.09.037

Klimont, Z., Smith, S. J., and Cofala, J. (2013). The last decade of global anthropogenic sulfur dioxide: 2000–2011 emissions. *Environ. Res. Lett.* 8:014003. doi: 10.1088/1748-9326/8/1/014003

Knopf, D. A., Alpert, P. A., and Wang, B. (2018). The role of organic aerosol in atmospheric ice nucleation: a review. *ACS Earth Space Chem.* 2, 168–202. doi: 10.1021/acsearthspacechem.7b00120

Kuang, C., McMurry, P. H., McCormick, A. V., and Eisele, F. L. (2008). Dependence of nucleation rates on sulfuric acid vapor concentration in diverse atmospheric locations. *J. Geophys. Res.* 113:D10209. doi: 10.1029/2007JD009253

Kulmala, M. (2003). Atmospheric science: how particles nucleate and grow. *Science* 302, 1000–1001. doi: 10.1126/science.1090848

Kulmala, M., Kontkanen, J., Junninen, H., Lehtipalo, K., Manninen, H. E., and Nieminen, T. (2013). Direct observations of atmospheric aerosol nucleation. *Science* 339, 943–946. doi: 10.1126/science.1227385

Kulmala, M., Petäjä, T., Ehn, M., Thornton, J., Sipilä, M., and Worsnop, D. R. (2014). Chemistry of atmospheric nucleation: on the recent advances on precursor characterization and atmospheric cluster composition in connection with atmospheric new particle formation. *Annu. Rev. Phys. Chem.* 65, 21–37. doi: 10.1146/annurev-physchem-040412-110014

Kupiainen, O., Ortega, I. K., Kurtén, T., and Vehkamäki, H. (2012). Amine substitution into sulfuric acid – ammonia clusters. *Atmos. Chem. Phys.* 12, 3591–3599. doi: 10.5194/acp-12-3591-2012

Kurnig, I. J., and Scheiner, S. (1987). *Ab Initio* investigation of the structure of hydrogen halide-amine complexes in the gas phase and in a polarizable medium. *Int. J. Quant. Chem.* 32, 47–56. doi: 10.1002/qua.560320809

Kurten, T., Loukonen, V., Vehkamaki, H., and Kulmala, M. (2008). Amines are likely to enhance neutral and ion-induced sulfuric acid-water nucleation in the atmosphere more effectively than ammonia. *Atmos. Chem. Phys.* 8, 4095–4103. doi: 10.5194/acp-8-4095-2008

Lawler, M. J., Winkler, P. M., Kim, J., Ahlm, L., Tröstl, J., and Praplan, A. P. (2016). Unexpectedly acidic nanoparticles formed in dimethylamine–ammonia–sulfuric-acid nucleation experiments at CLOUD. *Atmos. Chem. Phys.* 16, 13601–13618. doi: 10.5194/acp-16-13601-2016

Lehtinen, K., and Kulmala, M. (2003). *Initial Steps of Particle Formation and Growth.* Washington, DC: AGU Fall Meeting Abstracts.

Lelieveld, J., Evans, J. S., Fnais, M., Giannadaki, D., and Pozzer, A. (2015). The contribution of outdoor air pollution sources to premature mortality on a global scale. *Nature* 525, 367–371. doi: 10.1038/nature15371

Ling, L., Li, H., Zhang, H., Zhong, J., Bai, Y., Ge, M., et al. (2018). The role of nitric acid in atmospheric new particle formation. *Phys. Chem. Chem. Phys.* 20, 17406–17414. doi: 10.1039/C8CP02719F

Makkonen, R., Asmi, A., Kerminen, V.-M., Boy, M., Arneth, A., and Hari, P. (2012). Air pollution control and decreasing new particle formation lead to strong climate warming. *Atmos. Chem. Phys.* 12, 1515–1524. doi: 10.5194/acp-12-1515-2012

McMurry, P. H. (2000). A review of atmospheric aerosol measurements. *Atmos. Environ.* 34, 1959–1999. doi: 10.1016/S1352-2310(99)00455-0

Merikanto, J., Spracklen, D. V., Mann, G. W., Pickering, S. J., and Carslaw, K. S. (2009). Impact of nucleation on global CCN. *Atmos. Chem. Phys.* 9, 8601–8616. doi: 10.5194/acp-9-8601-2009

Miller, Y., Chaban, G. M., Jia, Z., Asmis, K. R., Neumark, D. M., and Gerber, R. B. (2007). Vibrational spectroscopy of $(SO_4^{2-})\cdot(H_2O)_n$ clusters, n=1-5: Harmonic and anharmonic calculations and experiment. *J. Chem. Phys.* 127:250. doi: 10.1063/1.2764074

Murphy, J. G., Gregoire, P. K., Tevlin, A. G., Wentworth, G. R., Ellis, R. A., and Markovic, M. Z. (2017). Observational constraints on particle acidity using measurements and modelling of particles and gases. *Faraday Discuss.* 200, 379–395. doi: 10.1039/C7FD00086C

Myhre, G., Myhre, C. L., Samset, B., and Storelvmo, T. (2013). *Aerosols and their Relation to Global Climate and Climate Sensitivity*. Available online at: http://www.researchgate.net/publication/259117107_Aerosols_and_their_Relation_to_Global_Climate_and_Climate_Sensitivity

Myllys, N., Chee, S., Olenius, T., Lawler, M., and Smith, J. (2019). Molecular-level understanding of synergistic effects in sulfuric acid–amine–ammonia mixed clusters. *J. Phys. Chem. A* 123, 2420–2425. doi: 10.1021/acs.jpca.9b00909

Nishino, N., Arquero, K. D., Dawson, M. L., and Finlayson-Pitts, B. J. (2014). Infrared studies of the reaction of methanesulfonic acid with trimethylamine on surfaces. *Environ. Sci. Technol.* 48, 323–330. doi: 10.1021/es403845b

Nosé, S. (1984). A unified formulation of the constant temperature molecular dynamics methods. *J. Chem. Phys.* 81, 511–519. doi: 10.1063/1.447334

Olenius, T., Halonen, R., Kurtén, T., Henschel, H., Kupiainen-Määttä, O., Ortega, I. K., et al. (2017). New particle formation from sulfuric acid and amines: comparison of monomethylamine, dimethylamine, and trimethylamine. *J. Geophys. Res.* 122, 7103–7118. doi: 10.1002/2017JD026501

Perraud, V., Horne, J. R., Martinez, A. S., Kalinowski, J., Meinardi, S., Dawson, M. L., et al. (2015). The future of airborne sulfur-containing particles in the absence of fossil fuel sulfur dioxide emissions. *Proc. Natl. Acad. Sci. U.S.A.* 112, 13514–13519. doi: 10.1073/pnas.1510743112

Perraud, V., Li, X., Jiang, J., Finlayson-Pitts, B. J., and Smith, J. N. (2020a). Size-resolved chemical composition of sub-20 nm particles from methanesulfonic acid reactions with methylamine and ammonia. *ACS Earth Space Chem.* 4, 1182–1194. doi: 10.1021/acsearthspacechem.0c00120

Perraud, V., Xu, J., Gerber, R. B., and Finlayson-Pitts, B. J. (2020b). Integrated experimental and theoretical approach to probe the synergistic effect of ammonia in methanesulfonic acid reactions with small alkylamines. *Environ. Sci.* 22, 305–328. doi: 10.1039/C9EM00431A

Pope, C. A., and Dockery, D. W. (2006). Health effects of fine particulate air pollution: lines that connect. *J. Air Waste Manage. Assoc.* 56, 709–742. doi: 10.1080/10473289.2006.10464485

Putaud, J.-P., Van Dingenen, R., Alastuey, A., Bauer, H., Birmili, W., and Cyrys, J. (2010). A European aerosol phenomenology – 3: physical and chemical characteristics of particulate matter from 60 rural, urban, and kerbside sites across Europe. *Atmos. Environ.* 44, 1308–1320. doi: 10.1016/j.atmosenv.2009.12.011

Reed, A. E., and Weinhold, F. (1983). Natural bond orbital analysis of near-Hartree–Fock water dimer. *J. Chem. Phys.* 78, 4066–4073. doi: 10.1063/1.445134

Riccobono, F., Schobesberger, S., Scott, C. E., Dommen, J., Ortega, I. K., and Rondo, L. (2014). Oxidation products of biogenic emissions contribute to nucleation of atmospheric particles. *Science* 344, 717–721. doi: 10.1126/science.1243527

Saxon, A., and Diaz-Sanchez, D. (2005). Air pollution and allergy: you are what you breathe. *Nat. Immunol.* 6, 223–226. doi: 10.1038/ni0305-223

Schobesberger, S., Franchin, A., Bianchi, F., Rondo, L., Duplissy, J., and Kürten, A. (2015). On the composition of ammonia–sulfuric-acid ion clusters during aerosol particle formation. *Atmos. Chem. Phys.* 15, 55–78. doi: 10.5194/acp-15-55-2015

Sebastianelli, P., Cometto, P. M., and Pereyra, R. G. (2018). Systematic characterization of gas phase binary pre-nucleation complexes containing H_2SO_4 + X, [X = NH_3, $(CH_3)NH_2$, $(CH_3)_2NH$, $(CH_3)_3N$, H_2O, $(CH_3)OH$, $(CH_3)_2O$, HF, CH_3F, PH_3, $(CH_3)PH_2$, $(CH_3)_2PH$, $(CH_3)_3P$, H_2S, $(CH_3)SH$, $(CH_3)_2S$, HCl, $(CH_3)Cl$]. A computational study. *J. Phys. Chem. A* 122, 2116–2128. doi: 10.1021/acs.jpca.7b10205

Sipila, M., Berndt, T., Petaja, T., Brus, D., Vanhanen, J., Stratmann, F., et al. (2010). The role of sulfuric acid in atmospheric nucleation. *Science* 327, 1243–1246. doi: 10.1126/science.1180315

Spracklen, D. V., Carslaw, K. S., and Kulmala, M. (2006). The contribution of boundary layer nucleation events to total particle concentrations on regional and global scales. *Atmos. Chem. Phys.* 6, 5631–5648. doi: 10.5194/acp-6-5631-2006

Steinfeld, J. I. (1998). Atmospheric chemistry and physics: from air pollution to climate change. *Environment* 40, 26–26. doi: 10.1080/00139157.1999.10544295

Stewart, J. (2007). Optimization of parameters for semiempirical methods V: modification of NDDO approximations and application to 70 elements. *J. Mol. Model.* 13, 1173–1213. doi: 10.1007/s00894-007-0233-4

Stolzenburg, M. R., and McMurry, P. H. (1991). An ultrafine aerosol condensation nucleus counter. *Aerosol Sci. Technol.* 14, 48–65. doi: 10.1080/02786829108959470

Takayanagi, T., Yoshikawa, T., Kakizaki, A., Shiga, M., and Tachikawa, M. (2008). Molecular dynamics simulations of small glycine–$(H_2O)_n$ (n=2–7) clusters on semiempirical PM6 potential energy surfaces. *J. Mol. Struct.* 869, 29–36. doi: 10.1016/j.theochem.2008.08.016

Tian, L., and Chen, F. (2012). Multiwfn: a multifunctional wavefunction analyzer. *J. Comput. Chem.* 33, 580–592. doi: 10.1002/jcc.22885

Tosso, R. D., Andujar, S. A., Gutierrez, L., Angelina, E., Rodríguez, R., Nogueras, M., et al. (2013). Molecular modeling study of dihydrofolate reductase inhibitors. Molecular dynamics simulations, quantum mechanical calculations, and experimental corroboration. *J. Chem. Inform. Model.* 53, 2018–2032. doi: 10.1021/ci400178h

VandeVondele, J., Krack, M., Mohamed, F., Parrinello, M., Chassaing, T., and Hutter, J. (2005). Quickstep: fast and accurate density functional calculations using a mixed Gaussian and plane waves approach. *Comput. Phys. Commun.* 167, 103–128. doi: 10.1016/j.cpc.2004.12.014

von Schneidemesser, E., Monks, P. S., Allan, J. D., Bruhwiler, L., Forster, P., and Fowler, D. (2015). Chemistry and the linkages between air quality and climate change. *Chem. Rev.* 115, 3856–3897. doi: 10.1021/acs.chemrev.5b00089

Wang, L., Khalizov, A. F., Zheng, J., Xu, W., Ma, Y., and Lal, V. (2010). Atmospheric nanoparticles formed from heterogeneous reactions of organics. *Nat. Geosci.* 3, 238–242. doi: 10.1038/ngeo778

Wang, M., Mei, Y., and Ryde, U. (2019). Host–guest relative binding affinities at density-functional theory level from semiempirical molecular dynamics simulations. *J. Chem. Theory Comput.* 15, 2659–2671. doi: 10.1021/acs.jctc.8b01280

Weber, R. J., Marti, J. J., McMurry, P. H., Eisele, F. L., Tanner, D. J., and Jefferson, A. (1996). Measured atmospheric new particle formation rates: implications for nucleation mechanisms. *Chem. Eng. Commun.* 151, 53–64. doi: 10.1080/00986449608936541

Weber, R. J., McMurry, P. H., Eisele, F. L., and Tanner, D. J. (1995). Measurement of expected nucleation precursor species and 3-500-nm diameter particles at mauna loa observatory. *Hawaii. J. Atmos. Sci.* 52, 2242–2257. Available online at: https://journals.ametsoc.org/view/journals/atsc/52/12/1520-0469_1995_052_2242_moenps_2_0_co_2.xml (accessed April 5, 2022).

Xantheas, S. S. (1995). *Ab initio* studies of cyclic water clusters (H_2O)n, n=1–6. III. Comparison of density functional with MP2 results. *J. Chem. Phys.* 102, 4505–4517. doi: 10.1063/1.469499

Xu, J., Finlayson-Pitts, B. J., and Gerber, R. B. (2017). Nanoparticles grown from methanesulfonic acid and methylamine: microscopic structures and formation mechanism. *Phys. Chem. Chem. Phys.* 19, 31949–31957. doi: 10.1039/C7CP06489F

Yu, F., Wang, Z., Luo, G., and Turco, R. (2008). Ion-mediated nucleation as an important global source of tropospheric aerosols. *Atmos. Chem. Phys.* 8, 2537–2554. doi: 10.5194/acp-8-2537-2008

Yu, H., and Lee, S.-H. (2012). Chemical ionisation mass spectrometry for the measurement of atmospheric amines. *Environ. Chem.* 9:190. doi: 10.1071/EN12020

Zhang, J., and Dolg, M. (2015). ABCluster: the artificial bee colony algorithm for cluster global optimization. *Phys. Chem. Chem. Phys.* 17, 24173-24181. doi: 10.1039/c5cp04060d

Zhang, J., and Dolg, M. (2016). Global optimization of clusters of rigid molecules using the artificial bee colony algorithm. *Phys. Chem. Chem. Phys.* 18, 3003–3010. doi: 10.1039/c5cp06313b

Zhang, R. (2010). Getting to the critical nucleus of aerosol formation. *Science* 328, 1366–1367. doi: 10.1126/science.1189732

Zhang, R., Khalizov, A., Wang, L., Hu, M., and Xu, W. (2012). Nucleation and growth of nanoparticles in the atmosphere. *Chem. Rev.* 112, 1957–2011. doi: 10.1021/cr2001756

Zhao, F., Feng, Y.-J., Liu, Y.-R., Jiang, S., Huang, T., and Wang, Z.-H. (2019). Enhancement of atmospheric nucleation by highly oxygenated organic molecules: a density functional theory study. *J. Phys. Chem. A* 123, 5367–5377. doi: 10.1021/acs.jpca.9b03142

Zhao, Y., Liu, Y.-R., Jiang, S., Huang, T., Wang, Z.-H., and Xu, C.-X. (2020). Volatile organic compounds enhancing sulfuric acid-based ternary homogeneous nucleation: the important role of synergistic effect. *Atmos. Environ.* 233:117609. doi: 10.1016/j.atmosenv.2020.117609

Zollner, J. H., Glasoe, W. A., Panta, B., Carlson, K. K., McMurry, P. H., and Hanson, D. R. (2012). Sulfuric acid nucleation: power dependencies, variation with relative humidity, and effect of bases. *Atmos. Chem. Phys.* 12, 4399–4411. doi: 10.5194/acp-12-4399-2012

Conflict of Interest: The authors declare that the research was conducted in the absence of any commercial or financial relationships that could be construed as a potential conflict of interest.

Publisher's Note: All claims expressed in this article are solely those of the authors and do not necessarily represent those of their affiliated organizations, or those of the publisher, the editors and the reviewers. Any product that may be evaluated in this article, or claim that may be made by its manufacturer, is not guaranteed or endorsed by the publisher.

frontiers | Frontiers in Environmental Science

ORIGINAL RESEARCH
published: 25 April 2022
doi: 10.3389/fenvs.2022.872249

Evaluation of Long-Term Modeling Fine Particulate Matter and Ozone in China During 2013–2019

*Jianjiong Mao, Lin Li, Jingyi Li, Ishaq Dimeji Sulaymon, Kaili Xiong, Kang Wang, Jianlan Zhu, Ganyu Chen, Fei Ye, Na Zhang, Yang Qin, Momei Qin and Jianlin Hu**

Jiangsu Key Laboratory of Atmospheric Environment Monitoring and Pollution Control, Collaborative Innovation Center of Atmospheric Environment and Equipment Technology, Nanjing University of Information Science and Technology, Nanjing, China

Air quality in China has been undergoing significant changes due to the implementation of extensive emission control measures since 2013. Many observational and modeling studies investigated the formation mechanisms of fine particulate matter ($PM_{2.5}$) and ozone (O_3) pollution in the major regions of China. To improve understanding of the driving forces for the changes in $PM_{2.5}$ and O_3 in China, a nationwide air quality modeling study was conducted from 2013 to 2019 using the Weather Research and Forecasting/Community Multiscale Air Quality (WRF/CMAQ) modeling system. In this study, the model predictions were evaluated using the observation data for the key pollutants including O_3, sulfur dioxide (SO_2), nitrogen dioxide (NO_2), and $PM_{2.5}$ and its major components. The evaluation mainly focused on five major regions, that is , the North China Plain (NCP), the Yangtze River Delta (YRD), the Pearl River Delta (PRD), the Chengyu Basin (CY), and the Fenwei Plain (FW). The CMAQ model successfully reproduced the air pollutants in all the regions with model performance indices meeting the suggested benchmarks. However, over-prediction of $PM_{2.5}$ was noted in CY. NO_2, O_3, and $PM_{2.5}$ were well simulated in the north compared to the south. Nitrate (NO_3^-) and ammonium (NH_4^+) were the most important $PM_{2.5}$ components in heavily polluted regions. For the performance on different pollution levels, the model generally over-predicted the clean days but underpredicted the polluted days. O_3 was found increasing each year, while other pollutants gradually reduced during 2013–2019 across the five regions. In all of the regions except PRD (all seasons) and YRD (spring and summer), the correlations between $PM_{2.5}$ and O_3 were negative during all four seasons. Low-to-medium correlations were noted between the simulated $PM_{2.5}$ and NO_2, while strong and positive correlations were established between $PM_{2.5}$ and SO_2 during all four seasons across the five regions. This study validates the ability of the CMAQ model in simulating air pollution in China over a long period and provides insights for designing effective emission control strategies across China.

Keywords: fine particulate matter, ozone, long-term simulations, spatiotemporal variations, WRF-CMAQ, China

OPEN ACCESS

Edited by:
Yuqiang Zhang,
the University of North Carolina at Chapel Hill, United States

Reviewed by:
Dan Chen,
China Meteorological Administration, China
Kaiyu Chen,
The University of Utah, United States

****Correspondence:***
Jianlin Hu
jianlinhu@nuist.edu.cn

Specialty section:
This article was submitted to Atmosphere and Climate, a section of the journal Frontiers in Environmental Science

Received: *09 February 2022*
Accepted: *22 March 2022*
Published: *25 April 2022*

Citation:
Mao J, Li L, Li J, Sulaymon ID, Xiong K, Wang K, Zhu J, Chen G, Ye F, Zhang N, Qin Y, Qin M and Hu J (2022) Evaluation of Long-Term Modeling Fine Particulate Matter and Ozone in China During 2013–2019. Front. Environ. Sci. 10:872249. doi: 10.3389/fenvs.2022.872249

INTRODUCTION

Due to rapid population growth, industrialization, economic advancement, and urbanization, China has been experiencing severe air pollution problems in recent decades (de Leeuw et al., 2021; Zhao et al., 2021). In 2013, the Ministry of Ecology and Environment of China initiated the setting up of nationwide air pollution monitoring networks. Subsequently, the Air Pollution Prevention and Control Action Plan (APPCAP) was issued and implemented in September 2013 with a series of clean air policies, which has led to decrease in the concentrations of fine particulate matter with aerodynamic diameters less than or equal to 2.5 μm ($PM_{2.5}$) as well as improved air quality (Qiang Zhang et al., 2019). Several studies have used various air quality models (Chen et al., 2014; Chen et al., 2018) in forecasting air pollution levels in China. The three-dimensional chemical transport models (CTMs) can provide detailed gaseous and particulate matter (PM) concentrations and their sources, as well as their chemical compositions (Bell, 2006). The Community Multiscale Air Quality (CMAQ) model, being one of the CTMs, has been widely used in predicting air quality in recent years (Luo and Cao, 2012; Zhang et al., 2014; Hu et al., 2016, 2017; Liu et al., 2020; Sulaymon et al., 2021a, 2021b; Wang et al., 2021). For instance, Zhang et al. (2014) applied the Weather Research and Forecasting (WRF) and CMAQ model (WRF-CMAQ) to simulate air quality in eastern United States during a 7-year period. Hu et al. (2016) carried out a 1-year simulation of ozone (O_3) and PM in China using the WRF-CMAQ model. With the WRF-CMAQ model, Shi et al. (2020) analyzed the sensitivity of O_3 and $PM_{2.5}$ to meteorological variables in China, and the results revealed that surface O_3 and $PM_{2.5}$ concentrations could change significantly due to changes in meteorological parameters. Sulaymon et al. (2021a) utilized the WRF-CMAQ model to evaluate the regional transport of $PM_{2.5}$ during severe atmospheric pollution episodes in the western Yangtze River Delta (YRD), China. The results of the study revealed the dominant transport pathways and the heights at which they occurred. Also, Sulaymon et al. (2021b) employed the WRF-CMAQ model to investigate the remote causes of $PM_{2.5}$ pollution in the Beijing–Tianjin–Hebei (BTH) region during the COVID-19 lockdown period. The results showed that the high $PM_{2.5}$ concentrations in BTH during the lockdown were caused by unfavorable meteorological conditions and suggested that the roles of both chemistry and meteorology in the formation of air pollution must be taken into consideration while designing effective emission control strategies in the region. In addition, Yang et al. (2019) used the WRF-CMAQ model to assess $PM_{2.5}$ in Xi'an during the winter periods of 2014–2017. Furthermore, Hu et al. (2017) employed the WRF-CMAQ model in predicting air quality for health effect studies in China and found that the model performed much better in more developed regions compared to underdeveloped regions such as western China.

Following the establishment of pollutant observation networks across China, it was found that the pollution events show regional differences based on the observation data in recent years. Liu et al. (2020) found emission reduction as the major driving force for the $PM_{2.5}$ change in the YRD region during the COVID-19 lockdown period. Tan et al. (2015) elucidated and reported the effects of spatial resolution on air quality simulation in a highly industrialized area in the city of Shanghai, China. Li et al. (2017) found improvement in both meteorology and air quality simulations during a high O_3 event in the YRD in 2013 by incorporating satellite-derived land surface parameters. Sun et al. (2016) employed the WRF-Chem model to investigate a severe haze episode that occurred over the YRD in 2013. Wang et al. (2021) investigated the impacts of meteorological inputs (by using different reanalysis data in the WRF model) and grid resolutions on air quality simulations in the YRD. Gong et al. (2021) quantified the influence of inter-city transport on air quality in the YRD region and suggested regional cooperative controls of $PM_{2.5}$ and O_3 in the region. Qin et al. (2021) investigated the spatial distribution and trend of double high pollution ($PM_{2.5}$ and O_3) in the YRD during 2015–2019. While some studies (Wang et al., 2015; Chen et al., 2017; Xueshun Chen et al., 2019; Tao et al., 2020) majorly focused on the North China Plain (NCP) region, Xiaoju Li et al. (2021) overviewed the air quality models on air pollution in the Sichuan Basin, a highly humid and foggy area.

In this study, a long-term (2013–2019) air quality simulation was conducted over China using the WRF-CMAQ model. China was divided into five regions for model evaluation, and the simulated results were compared with observation data. All of the cities' data were averaged in each area for regional analysis. The critical gas- and particulate-phase pollutants were O_3, SO_2, NO_2, and $PM_{2.5}$. The three major components (sulfate (SO_4^{2-}), nitrate (NO_3^-), and ammonium (NH_4^+)) of $PM_{2.5}$ were further analyzed in cities with sufficient observation data in each region. In addition, the model performances during different pollution levels were discussed. Furthermore, the correlations between $PM_{2.5}$ and other pollutants (O_3, SO_2, and NO_2) were investigated.

MATERIALS AND METHODS

Model Configurations

The meteorological fields were simulated using the WRF (version 4.2.1) model with the FNL reanalysis dataset. The FNL data were obtained from the U.S. National Centre for Atmospheric Research (NCAR), with a spatial resolution of 1.0° × 1.0° (http://rda.ucar.edu/datasets/ds083.2/, last accessed on 15 November 2021). The physical parameterizations used in this study include the Thompson microphysical process, RRTMG longwave/shortwave radiation scheme; Noah land-surface scheme; MYJ boundary layer scheme; and modified Tiedtke cumulus parameterization scheme. The detailed configuration settings could be found in the work of Hu et al. (2016) and Wang et al. (2021).

The CMAQ version 5.2 (CMAQv5.2) model (Fahey et al., 2017), configured with the gas-phase mechanism of SAPRC07tic and the aerosol module of AERO6i, was employed in this study to simulate the air quality over China during 2013–2019. Air quality simulations were performed for a period of 7 years (2013–2019) using a horizontal resolution of 36 km. The corresponding domain covered China and the surrounding countries and

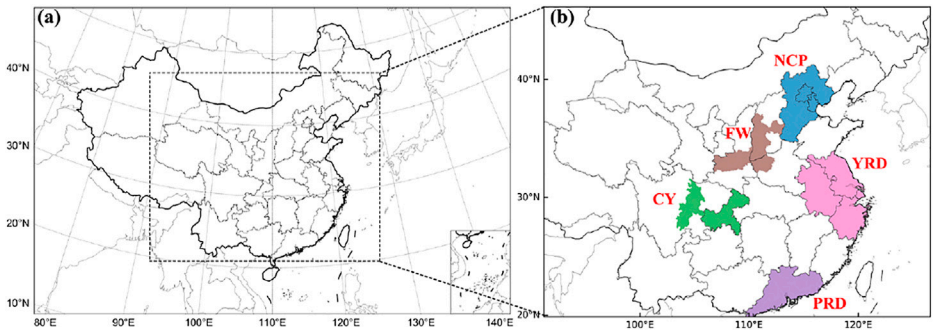

FIGURE 1 | (A) WRF/CMAQ modeling domain. **(B)** The studied five regions (North China Plain (NCP), Yangtze River Delta (YRD), Pearl River Delta (PRD), Chengyu (CY), and Fenwei Plain (FW)).

regions with 197 × 127 grids (**Figure 1A**). The vertical resolution had 18 layers. The initial and boundary conditions were provided by the default profiles of the CMAQ model. The simulated results of the first three days were not included in the model analysis, thus serving as a spin-up and reducing the effects of the initial conditions on the simulated results.

Emission Inventory

The Multi-resolution Emission Inventory for China version 1.3 (MEICv1.3) (http://www.meicmodel.org) and Regional Emission inventory in ASia (REASv3.2) (https://www.nies.go.jp/REAS/) were used to provide the anthropogenic emissions. MEIC served as the anthropogenic emissions from China, while REAS served as the anthropogenic emissions from neighboring countries and regions. The MEICv1.3 emissions of the year 2017 were used for the simulations of the years 2018 and 2019, as no reliable sources for emission changes in China were currently available. For REAS, since no emission inventory was released for the years after 2015, we used the emission inventory in the year 2015 for 2016–2019. Although emission inventories are usually released 2–3 years behind, we acknowledge that this may cause additional uncertainties in the simulation for 2018 and 2019. Biogenic emissions were generated using the Model for Emissions of Gases and Aerosols from Nature (MEGANv2.1) (Guenther et al., 2012) for the whole simulation period. The open biomass burning emissions were processed using the Fire Inventory for NCAR (FINN) during the entire study period (Wiedinmyer et al., 2011). The spatiotemporal variations of the total emission of $PM_{2.5}$, SO_2, NOx, NH_3, and VOC across the five regions are shown in **Supplementary Table S3**.

Observation Data

The daily observation data of meteorological variables (wind speed, wind direction, relative humidity, and temperature) for the selected regions were downloaded from the Chinese Meteorological Agency (http://data.cma.cn/en, last accessed on 30 November 2021). There were 18, 11, 14, 14, and 11 meteorological stations considered in the NCP, YRD, PRD, CY, and FW regions, respectively. In addition, the hourly observation data of air pollutants ($PM_{2.5}$, O_3, NO_2, and SO_2) were obtained from the Chinese Ministry of Ecology and Environment (https://www.mee.gov.cn/, last accessed on 20 December 2021). In this study, five regions in China were selected as target areas (**Figure 1B**), and they include the North China Plain (NCP, with 70 air quality monitoring stations), Yangtze River Delta (YRD, with 107 air quality monitoring stations), Pearl River Delta (PRD, with 54 air quality monitoring stations), Chengyu (CY, with 40 air quality monitoring stations), and Fenwei Plain (FW, with 60 air quality monitoring stations) regions. Besides the NCP and YRD, most of the cities in other regions had a month observation data in 2013. The cities with data of more than 3 months in each region were selected for citywide analysis in 2013, while all of the data in each region were selected for regional analysis. In the subsequent years (2014–2019), the observation data of the monitoring stations in each of the cities were used citywide, while the observation data of all the cities located in each region were used to estimate the average observation value of the region (Hu et al., 2016; Sulaymon et al., 2021c). The 21 cities selected in 2013 in the five regions are as follows: Beijing, Tianjin, Shijiazhuang, Qinhuangdao, Chengde, and Zhangjiakou in the NCP; Shanghai, Wuxi, Nanjing, Suzhou, Xuzhou, and Hangzhou in the YRD; Guangzhou, Dongguan, and Shenzhen in the PRD; Chengdu, Mianyang, and Chongqing in the CY; and Xi'an, Xianyang, and Baoji in the FW. The details about the selected cities in each region are shown in **Supplementary Table S1**. Furthermore, the predicted major chemical components of $PM_{2.5}$ (SO_4^{2-}, NO_3^-, and NH_4^+) were evaluated using the daily observation data in nine cities (Beijing, Shijiazhuang, Nanjing, Suzhou, Xuzhou, Hangzhou, Guangzhou, Shenzhen, and Chengdu) during the study period.

RESULTS AND DISCUSSION

WRF Model Performance

Previous studies have investigated and documented the impacts of meteorological conditions on the formation, transportation, and dissipation of air pollutants (Hu et al., 2016; Hua et al., 2021; Sulaymon et al., 2021c, 2021d). In

TABLE 1 | Model performance of meteorological factors in the five regions during 2013–2019.

Area	T2, °C			RH, %			WS, m/s			WD, °		
	MB	**ME**	**RMSE**	**MB**	**ME**	**RMSE**	**MB**	**ME**	**RMSE**	**MB**	**ME**	**RMSE**
NCP	-0.02	1.28	1.62	-4.76	9.23	11.50	**0.56**	0.84	1.04	**13.48**	**38.12**	50.02
YRD	**1.25**	1.90	2.41	3.50	7.28	9.56	**0.60**	0.94	1.21	**-21.48**	**48.83**	186.81
PRD	**-0.64**	1.27	1.61	1.69	5.53	7.33	**1.77**	1.87	**2.18**	**-43.53**	**68.98**	92.34
CY	**-2.15**	**2.38**	2.85	3.38	7.35	9.67	0.41	0.77	0.98	**-19.08**	**47.63**	108.49
FW	**0.91**	1.66	2.29	-1.34	8.64	11.07	**0.69**	0.92	1.17	7.10	**45.84**	59.09
Benchmarks	≤±0.5	≤2.0					≤±0.5	≤2.0	≤2.0	≤±10	≤±30	

MB: mean bias; ME: mean error; RMSE: root mean square error. The benchmarks were suggested by Boylan and Russell (2006). The values that do not meet the benchmarks are highlighted in bold.

addition, the influences of some meteorological parameters (such as wind speed, wind direction, temperature, and relative humidity) on air quality modeling have been elucidated (Hu et al., 2016; Sulaymon et al., 2021b; Wang et al., 2021). Therefore, the evaluation of the WRF model performance was carried out prior to the usage of its meteorological fields in the air quality simulations. The evaluation of the WRF model was achieved by comparing the predicted wind speed (WS) and wind direction (WD) at 10 m above the surface, as well as the simulated relative humidity (RH) and temperature (T2) at 2 m above the ground level to their corresponding observed values in each region during the entire study period. The statistical indices used in evaluating the WRF model were the mean bias (MB), mean error (ME), and root mean square error (RMSE) (**Table 1**). The benchmarks of statistical indices employed in this study were suggested by Emery et al. (2017). T2 was generally over-predicted in all the regions except the NCP, whose MB value fell below the suggested benchmark (≤±0.5), while the ME values in all the regions, except the CY (the southeast basin of the Tibetan Plateau, with poor terrain and complicated weather conditions), were found below the suggested benchmark (≤2.0). With low ME indices (≤2.0) in four out of the five regions, it is shown that T2 was well simulated in the four regions. Previous studies have reported over-prediction of T2 in the YRD (Ma et al., 2021; Sulaymon et al., 2021a; Wang et al., 2021) and PRD (Wang N. et al., 2016). The results of this study are consistent with previously reported ones in the studied regions. However, no benchmarks were suggested for the MB and ME values of RH, and RH was underestimated in the NCP and FW, while it was overestimated in the other three regions. The MB values of WS in all the regions except the CY greatly exceeded the recommended criterion (≤±0.5), while the ME values in all the five regions were below the benchmark (≤2.0). In addition, the RMSE values of WS met the benchmark (≤2.0) in all the regions except the PRD. Considering the ME and RMSE values, the simulated WS reasonably captured the observations in all the regions. Over-prediction of WS has been previously found in the PRD (Wang N. et al., 2016; Qing Chen et al., 2019), NCP (Hanyu Zhang et al., 2019; Sulaymon et al., 2021b; Mengmeng Li et al., 2021), and YRD (Sulaymon et al., 2021a; Ma et al., 2021; Wang et al., 2021; Yu et al., 2021). Except in FW, the MB indices of WD in other regions were greater than the suggested benchmark (≤±10), while the ME values in all the regions greatly exceeded the recommended criterion (≤±30), especially in the PRD (68.98), YRD (48.83), CY (47.63), and FW (45.84). The model performance of WD in this study was consistent with previous studies in the YRD (Sulaymon et al., 2021a; Wang et al., 2021; Yu et al., 2021) and NCP (Sulaymon et al., 2021b) regions. Generally, the WRF model in this study performed better when compared to previous studies across China (Hu et al., 2016, 2017; Wang H. L. et al., 2016; Hanyu Zhang et al., 2019; Qing Chen et al., 2019; Sulaymon et al., 2021a, 2021b; Ma et al., 2021; Mengmeng Li et al., 2021; Yu et al., 2021), and the simulated meteorological fields were further utilized in driving the CMAQ model.

CMAQ Model Performance

Supplementary Figures S1-S5 show the comparison of the simulated daily mean concentrations of O_3, NO_2, SO_2, and $PM_{2.5}$ with the observations in 21 cities during 2013–2019. The time series of pollutants' concentrations in six major cities in the NCP region are illustrated in **Supplementary Figure S1**. In the NCP, the observed O_3 was about 200 μg/m^3 in summer and 50 μg/m^3 in winter; NO_2 was 100 μg/m^3 in winter and 20 μg/m^3 in summer; SO_2 was 100 μg/m^3 in winter and 10 μg/m^3 in summer before 2016 and 10 μg/m^3 without seasonal change after 2016; and $PM_{2.5}$ was 200 μg/m^3 in winter and 10 μg/m^3 in summer. The simulated O_3 and $PM_{2.5}$ were captured well with the observation data; SO_2 was well simulated on monthly trends at Beijing, Tianjin, and Shijiazhuang sites than in other cities such as Qinhuangdao, Chengde, and Zhangjiakou, where it was high in winter and low in summer before 2016. NO_2 was underestimated by over 20 μg/m^3, without obvious seasonal change after 2016. **Supplementary Figure S2** shows the six megacities in the YRD region. The monthly trend and simulated results of O_3, NO_2, and $PM_{2.5}$ were the same as in the NCP; the predicted SO_2 was better in Shanghai, Wuxi, and Hangzhou compared to Nanjing, Suzhou, and Xuzhou, which was near the observed data within 10 μg/m^3. **Supplementary Figure S3** shows the three cities in the PRD region. The monthly trends of O_3 and $PM_{2.5}$ were the same as those of the NCP and YRD. SO_2 was well simulated in Guangzhou and Dongguan sites relative to Shenzhen, which was overestimated by more than 20 μg/m^3; NO_2 was well simulated in Shenzhen with a little seasonal change. **Supplementary Figure S4** shows the three urban stations in

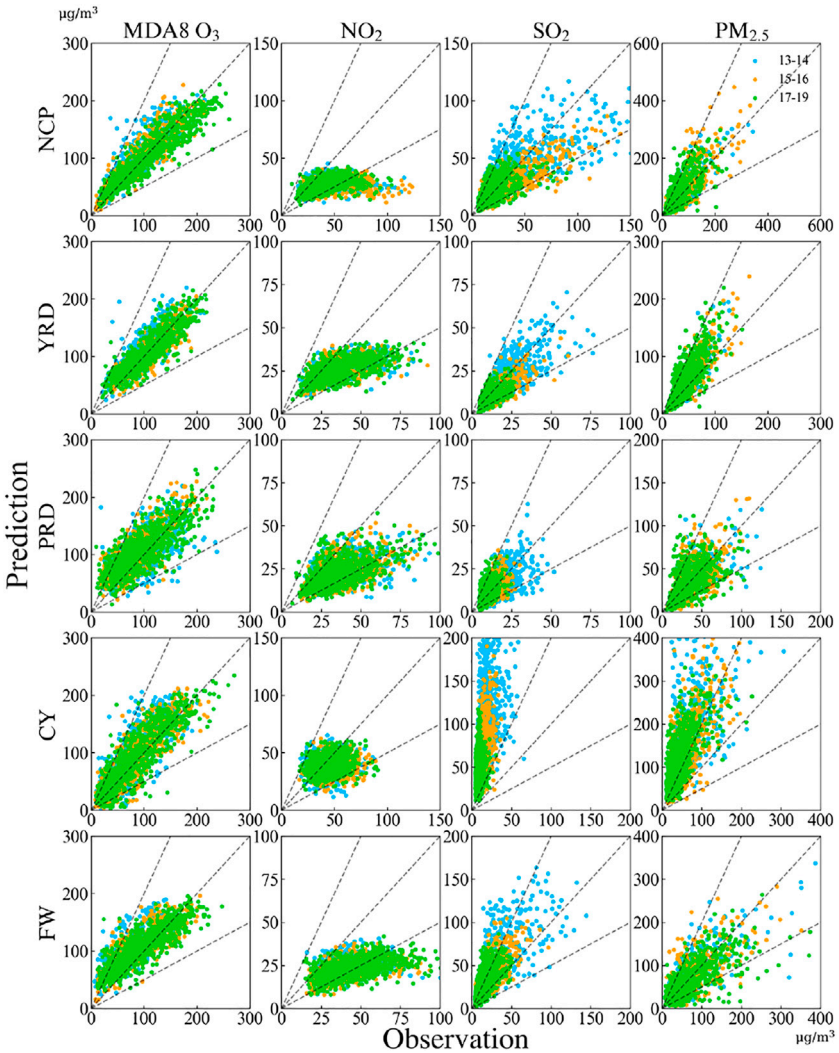

FIGURE 2 | Model performance of O_3, NO_2, SO_2, and $PM_{2.5}$ in the five regions during the 2013–2014, 2015–2016, and 2017–2019 periods.

the CY region. The simulated O_3 was close to the observation data; NO_2 was well simulated in Chengdu without seasonal changes; $PM_{2.5}$ and SO_2 were generally overestimated. FW (**Supplementary Figure S5**) was similar to CY on monthly trend, and both O_3 and $PM_{2.5}$ were well predicted, while NO_2 and SO_2 were underestimated.

Figure 2 shows the comparison of simulated pollutants with observed data in the five regions. The observed data of all stations and the simulated results in the five regions were grouped into three (2013–2014, 2015–2016, and 2017–2019) for model evaluation. The statistical metrics of normalized mean bias (NMB), normalized mean error (NME), and the correlation coefficient (R) were calculated to evaluate the pollutant predictions in each region (**Table 2**). The model performance criteria for O_3 and $PM_{2.5}$ were suggested by Emery et al. (2017). In the NCP, O_3 was slightly overpredicted during 2013–2014 (NMB: 0.19), while it was well predicted during the 2015–2016 and 2017–2019 periods (NMB less than the benchmark), and the model performance improved with an increase in years as observed in R-values. The model performance in predicting $PM_{2.5}$ and SO_2 also improved significantly with an increase in years with higher R-values during 2015–2016 and 2017–2019 compared to the 2013–2014 period and with the statistical metrics of $PM_{2.5}$ meeting the suggested benchmarks (**Table 2**). NO_2 was underestimated, but the model performance also improved with increased R-value as the years increased. Similar to the NCP, O_3 was slightly overpredicted in the YRD during 2013–2014 (NMB: 0.16), while it was well predicted during the 2015–2016 (NMB: 0.02) and 2017–2019 (NMB: 0.02) periods. The model performance improved with higher R-values with an increase in years. In terms of NMB and R-values, the model performance of SO_2 in the YRD decreased with an increase in years. $PM_{2.5}$ was well estimated with the NMB and R-values of 0.22–0.30 and 0.83–0.87, respectively, while NO_2 was underestimated with fluctuating R-values, a similar scenario to what was found in the

TABLE 2 | Model performance of the air pollutants in the five regions during the 2013–2014, 2015–2016, and 2017–2019 periods.

Area		2013–2014					2015–2016					2017–2019					Benchmarks
		NCP	**YRD**	**PRD**	**CY**	**FW**	**NCP**	**YRD**	**PRD**	**CY**	**FW**	**NCP**	**YRD**	**PRD**	**CY**	**FW**	
MDA8 O_3	PRE	100.14	101.47	100.20	85.47	86.10	98.28	98.60	101.47	87.65	103.22	102.16	105.05	107.26	88.62	104.69	
	OBS	83.22	87.44	89.57	73.10	55.22	88.70	108.79	83.87	84.56	85.02	109.67	105.57	96.62	84.68	93.41	
	NMB	**0.19**	**0.16**	0.14	**0.21**	**0.58**	0.08	-0.02	**0.20**	0.09	**0.21**	-0.03	0.02	0.11	0.09	0.11	<***±0.15***
	NME	0.23	0.21	0.31	0.34	**0.60**	0.16	0.13	0.28	0.22	0.29	0.15	0.13	0.24	0.23	0.22	<***0.35***
	R	0.90	0.86	0.64	0.82	0.80	0.92	0.87	0.80	0.88	0.87	0.92	0.88	0.78	0.88	0.85	>***0.5***
NO_2	PRE	28.56	26.67	23.33	38.74	26.31	26.78	25.60	22.15	38.80	22.68	27.68	25.59	22.06	39.54	23.14	
	OBS	44.00	36.21	34.73	41.96	42.40	48.37	33.85	33.50	46.29	39.53	41.36	35.96	34.72	43.31	44.68	
	NMB	-0.34	-0.26	-0.33	-0.08	-0.38	-0.44	-0.25	-0.34	-0.16	-0.42	-0.33	-0.28	-0.36	-0.08	-0.48	
	NME	0.37	0.29	0.36	0.27	0.39	0.45	0.28	0.35	0.26	0.42	0.35	0.32	0.39	0.24	0.48	
	R	0.10	0.53	0.48	0.07	0.08	0.19	0.52	0.58	0.12	0.43	0.42	0.60	0.55	0.26	0.54	
SO_2	PRE	46.20	23.61	16.57	131.68	71.80	27.52	14.13	11.79	72.56	30.57	19.89	9.35	10.49	49.85	23.82	
	OBS	48.20	24.86	19.11	22.68	40.31	36.21	18.65	12.35	14.96	18.92	19.57	10.92	9.13	9.40	14.20	
	NMB	0.00	-0.04	-0.13	4.79	0.74	-0.21	-0.28	-0.04	3.78	0.62	0.07	-0.10	0.19	4.38	0.82	
	NME	0.36	0.24	0.29	4.79	0.81	0.31	0.30	0.27	3.78	0.66	0.36	0.29	0.36	4.38	0.87	
	R	0.73	0.72	0.53	0.23	0.64	0.81	0.70	0.62	0.32	0.79	0.78	0.64	0.59	0.25	0.79	
$PM_{2.5}$	PRE	105.40	69.46	38.82	186.94	106.51	83.44	61.15	31.83	138.85	59.36	68.80	52.95	31.12	116.92	55.34	
	OBS	89.94	63.92	47.60	71.46	114.68	75.08	47.10	33.14	57.87	59.94	56.67	40.98	31.51	42.95	61.32	
	NMB	0.02	0.28	-0.08	**1.71**	0.00	0.14	0.22	-0.04	**1.38**	0.01	0.21	0.30	0.01	**1.66**	-0.09	<***±0.3***
	NME	0.34	0.35	0.30	**1.73**	0.29	0.34	0.33	0.32	**1.39**	0.38	0.41	0.40	0.34	**1.67**	0.34	<***0.5***
	R	0.56	0.87	0.67	0.42	0.79	0.82	0.85	0.71	0.66	0.74	0.78	0.83	0.64	0.69	0.75	>***0.4***
	PRE	100.14	101.47	100.20	85.47	86.10	98.28	98.60	101.47	87.65	103.22	102.16	105.05	107.26	88.62	104.69	

NMB: normalized mean bias; NME: normalized mean error; R: correlation coefficient. The performance criteria were suggested by Emery et al. (2017). The values in bold were above the benchmarks.

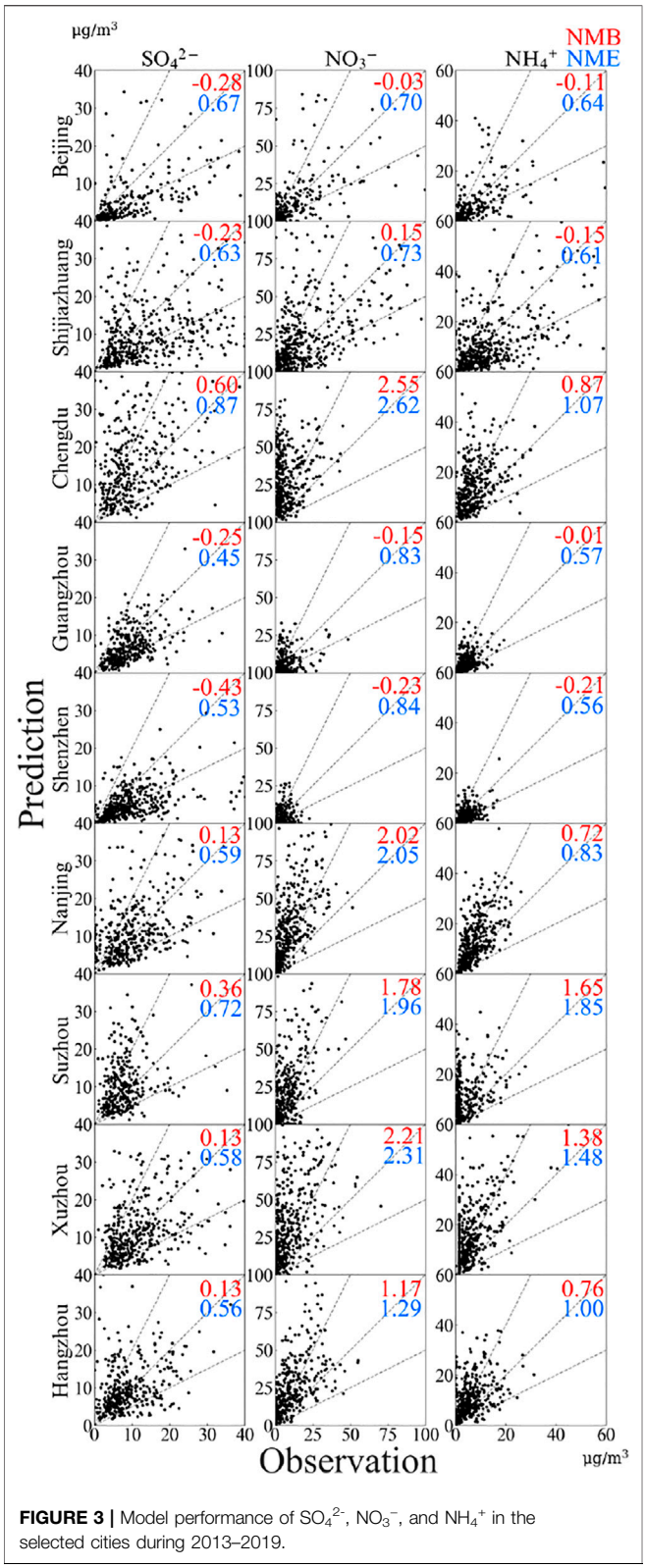

FIGURE 3 | Model performance of SO_4^{2-}, NO_3^-, and NH_4^+ in the selected cities during 2013–2019.

NCP. The trio of O_3, SO_2, and $PM_{2.5}$ was well predicted in the PRD region with their NMB values found below the suggested benchmarks during the grouped study periods, except for O_3 with NMB value slightly higher than the criterion during 2015–2016. The model performance of O_3, SO_2, and $PM_{2.5}$ significantly improved with higher R-values as the years increased. NO_2 was underestimated during the three periods, and the bias increased with an increase in years. It should be noted that the four pollutants (O_3, NO_2, SO_2, and $PM_{2.5}$) had their highest R-values during the 2015–2016 period. In the CY region, O_3 was slightly overpredicted during 2013–2014 (NMB: 0.21), while it was well predicted during the 2015–2016 and 2017–2019 (NMB: 0.09) periods. The model performance of O_3 improved with higher R-values with an increase in years. NO_2 was underestimated while SO_2 and $PM_{2.5}$ were highly overestimated, with the NMB and NME values of $PM_{2.5}$ greatly exceeding the suggested criteria during the three periods. The R-values of $PM_{2.5}$ also increased with the increase in years, while fluctuation was noted in the R-values of SO_2. $PM_{2.5}$ in the FW region was well predicted with very low NMB values. The R-value decreased as the years increased, an indication that the best model performance occurred during the 2013–2014 period (**Table 2**). NO_2 was underestimated throughout the three periods, while O_3 was overestimated during the 2013–2014 and 2015–2016 periods. The overall model performance improved as the years increased. Above all, the model exhibited better performances in reproducing O_3, SO_2, and $PM_{2.5}$ in the NCP, YRD, and PRD regions.

Figure 3 shows the results of the model performance of SO_4^{2-}, NO_3^-, and NH_4^+ in the nine selected cities across the five regions. In Beijing and Shijiazhuang, SO_4^{2-} had an NMB value of ~ -0.2, an indication of underprediction, while NO_3^- and NH_4^+ were well simulated. The NMB value of NO_3^- (0.15) in Shijiazhuang was relatively the same as that of $PM_{2.5}$ in the NCP (**Figure 2**), indicating that NO_3^- was more dominant in the NCP. In Nanjing, Suzhou, Xuzhou, and Hangzhou (YRD), SO_4^{2-} was well simulated, while NO_3^- and NH_4^+ were overestimated. The NMB of $PM_{2.5}$ in the YRD (**Figure 2**) was similar to the NMB of SO_4^{2-} in the selected four cities in the YRD (**Figure 3**), suggesting that SO_4^{2-} significantly dominated $PM_{2.5}$ in the YRD compared to NO_3^- and NH_4^+. NO_3^- and NH_4^+ in Guangzhou and Shenzhen were also well simulated, while SO_4^{2-} was underestimated. All of the three major components dominated $PM_{2.5}$ in the PRD. In Chengdu, NO_3^- and NH_4^+ were overestimated with NMB values of 2.55 and 0.87, respectively. This feature was also observed in $PM_{2.5}$ in the CY (overprediction) (**Figure 2**), and this shows that NO_3^- and NH_4^+ were the important components of $PM_{2.5}$ in the CY.

The analysis of the spatial and temporal variations shows that effective emissions control strategies are needed in eastern China. The control of $PM_{2.5}$ is always complicated as it is related to its major components. For instance, it was found that NO_3^- was significant in the NCP and SO_4^{2-} was dominant in the YRD, while all of the three components equally influenced $PM_{2.5}$ in the PRD region. In addition, NO_3^- and NH_4^+ were more dominant than SO_4^{2-} in the CY. From the abovementioned analysis, it can be concluded that NO_3^- and NH_4^+ were the main components of $PM_{2.5}$ in heavily polluted regions, where the maximum $PM_{2.5}$ concentration was above 250 μg/m^3. However, in clean regions such as the PRD (with high temperature and precipitation), where the maximum $PM_{2.5}$ concentration was below 150 μg/m^3, each component equally influenced $PM_{2.5}$.

TABLE 3 | Model performance of O_3 and $PM_{2.5}$ during different pollution levels in the five regions.

Area	Components	Statistics	Good	Moderate	Lightly polluted	Moderately polluted	Heavily polluted	Severely polluted	Benchmarks
NCP	MDA8 O_3	NMB	**0.19**	0.03	-0.09	**-0.16**	-	-	<±0.15
		NME	0.25	0.14	0.12	0.16	-	-	<0.35
		R	0.80	**0.49**	**0.39**	**0.23**	-	-	>0.5
	$PM_{2.5}$	NMB	**0.37**	0.20	0.16	0.05	0.06	-0.02	<±0.3
		NME	**0.53**	0.39	0.38	0.33	0.26	0.19	<0.5
		R	0.47	**0.39**	**0.35**	**0.14**	**0.33**	**0.33**	>0.4
YRD	MDA8 O_3	NMB	0.15	-0.001	-0.07	-0.10	-	-	<±0.15
		NME	0.21	0.12	0.10	0.10	-	-	<0.35
		R	0.65	0.58	**0.39**	**-0.83**	-	-	>0.5
	$PM_{2.5}$	NMB	0.28	0.24	0.28	0.21	-	-	<±0.3
		NME	0.41	0.35	0.35	0.30	-	-	<0.5
		R	0.58	0.57	**0.35**	**-0.11**	-	-	>0.4
PRD	MDA8 O_3	NMB	**0.35**	0.003	-0.08	**-0.18**	-	-	<±0.15
		NME	**0.40**	0.17	0.15	0.20	-	-	<0.35
		R	0.53	**0.43**	**0.22**	**-0.22**	-	-	>0.5
	$PM_{2.5}$	NMB	0.08	-0.07	-0.25	-0.30	-	-	<±0.3
		NME	0.39	0.28	0.32	0.30	-	-	<0.5
		R	0.55	**0.27**	**0.33**	**0.19**	-	-	>0.4
CY	MDA8 O_3	NMB	**0.20**	0.08	-0.04	**-0.15**	-	-	<±0.15
		NME	**0.37**	0.18	0.10	0.15	-	-	<0.35
		R	0.69	**0.47**	**0.20**	0.50	-	-	>0.5
	$PM_{2.5}$	NMB	**2.64**	**1.64**	**1.36**	**0.83**	**0.68**	-	<±0.3
		NME	**2.64**	**1.65**	**1.38**	**0.84**	**0.72**	-	<0.5
		R	**0.20**	**0.23**	**0.24**	**-0.09**	**0.09**	-	>0.4
FW	MDA8 O_3	NMB	**0.47**	0.04	-0.11	**-0.28**	-	-	<±0.15
		NME	**0.49**	0.14	0.12	0.28	-	-	<0.35
		R	0.67	**0.31**	0.50	0.58	-	-	>0.5
	$PM_{2.5}$	NMB	**0.32**	0.03	-0.11	-0.15	-0.26	**-0.40**	<±0.3
		NME	**0.51**	0.34	0.34	0.30	0.30	0.40	<0.5
		R	**0.18**	**0.38**	**0.23**	**0.10**	**0.16**	**0.15**	>0.4

NMB: normalized mean bias; NME: normalized mean error; R: correlation coefficient. The performance criteria were suggested by Emery et al. (2017). The values in bold were above the benchmarks.

Model Performance During Different Pollution Levels

The model performance during different pollution levels was also evaluated. The pollution levels used in this study were based on ambient air quality standards of the Chinese Ministry of Ecology and Environment. **Table 3**, **Supplementary Table S2**, and **Figure 4** show the model performance during different pollution levels in different regions. O_3 was overestimated during the "Good" level and underestimated during the "Lightly Polluted" and "Moderately Polluted" levels in all regions (**Table 3**). $PM_{2.5}$ was overestimated in the NCP, YRD, and CY. NCP was overpredicted (<10 μg/m^3) during low-pollution and underestimated (<10 μg/m^3) during high-pollution events. In the YRD and CY, $PM_{2.5}$ was overestimated (>20 μg/m^3). In the CY, $PM_{2.5}$ was highly overpredicted as all of the statistical metrics breached the suggested standards for all the pollution levels. This could be attributed to the poor terrain and complicated weather conditions in the CY region. In the PRD and FW, $PM_{2.5}$ was generally underpredicted (>20 μg/m^3), especially during the four pollution stages. As shown in **Supplementary Table S2**, NO_2 was underestimated in all the five regions (>10 μg/m^3) with different pollution levels except in the CY. SO_2 in the NCP, YRD, and PRD regions was underestimated (>5 μg/m^3), while it was overestimated in the CY and FW (>10 μg/m^3).

Monthly and Annual Trends of Pollutants During the Study Period

Supplementary Figure S6 illustrates the monthly trends and the highest and lowest concentrations of the pollutants (O_3, NO_2, SO_2, and $PM_{2.5}$), while **Figure 5** shows the annual trends of the pollutants in the five regions during 2013–2019. In addition, **Figure 6** shows the total trends of the pollutants, which were obtained as the difference between 2019 and 2013 annual average concentrations in each region. Considering the model performance of the pollutants, NO_2 was generally underpredicted on a monthly basis in all the regions during the whole study period except in the CY, while other pollutants exhibited better monthly predictions as illustrated in **Supplementary Figure S6**. It should be noted that SO_2 was also overpredicted in the CY region.

In the NCP, the changes in the four pollutants during the study period followed the same pattern (**Figure 5**). Overall, the

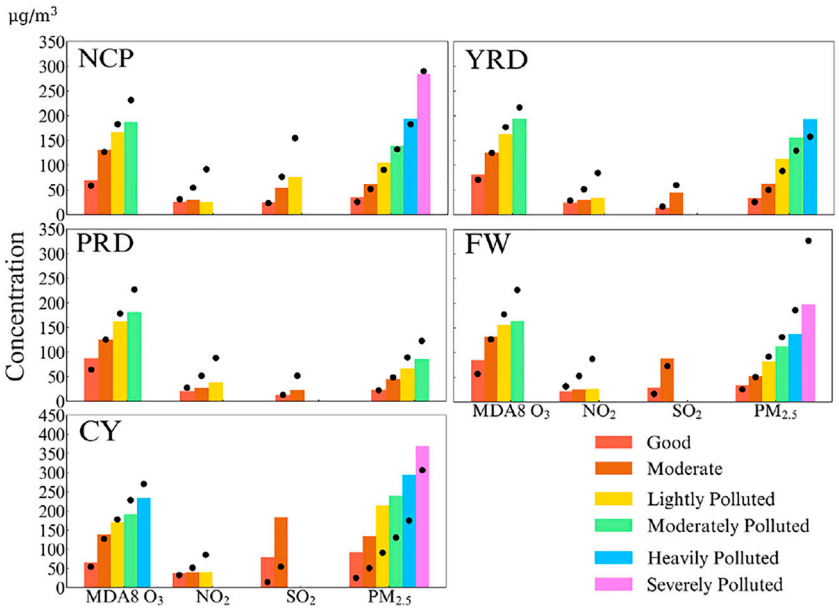

FIGURE 4 | Comparison of the predicted (column) and observed (black dot) O_3, NO_2, SO_2, and $PM_{2.5}$ in the five regions for different pollution levels during the 2013–2019 period. Units are $\mu g/m^3$.

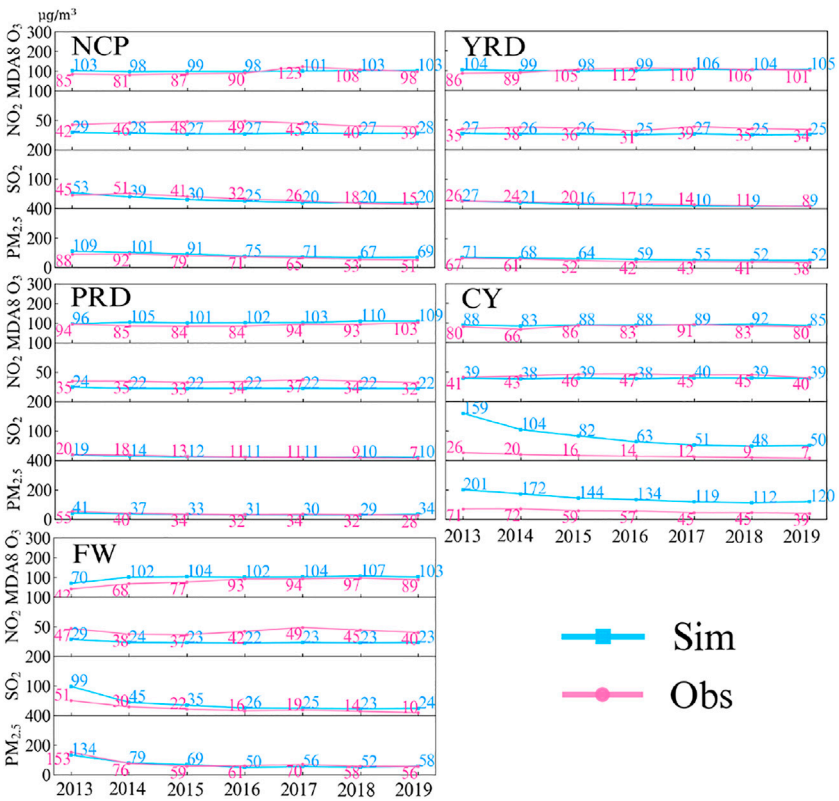

FIGURE 5 | Comparison of the predicted (in blue) and observed (in red) annual averaged concentrations of O_3, NO_2, SO_2, and $PM_{2.5}$ in the five regions. Units are $\mu g/m^3$.

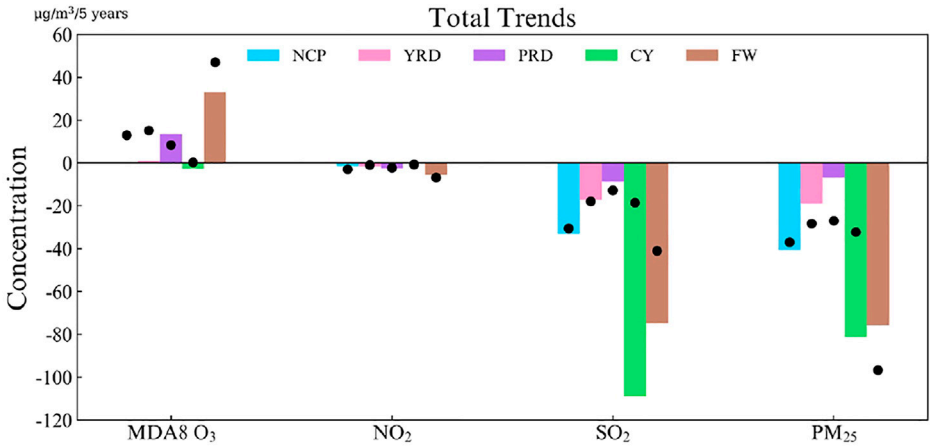

FIGURE 6 | Changes in the predicted (column) and observed (black dot) O_3, NO_2, SO_2, and $PM_{2.5}$ in the five regions during the 2013–2019 period. Units are μg/m^3.

observed and simulated SO_2 and $PM_{2.5}$ decreased by about 40 μg/m^3 (**Figure 6**), while they both decreased by ~8 μg/m^3 per year. NO_2 and O_3 also decreased by 3 μg/m^3 per year. It can be observed from the monthly average variation (**Supplementary Figure S6**) that O_3 had high concentrations in summer (~200 μg/m^3) and low concentrations in winter (~20 μg/m^3). Contrary to O_3, other pollutants exhibited high and low concentrations in winter and summer, respectively. The difference between the simulated and observed O_3, SO_2, and $PM_{2.5}$ was less than 10 μg/m^3.

In the YRD, the trio of O_3, SO_2, and $PM_{2.5}$ followed the same trends as observed in the NCP (**Figure 6**). The observed value of NO_2 decreased to 31 μg/m^3 in 2017 and later increased in the subsequent year (**Figure 5**). Similar to the NCP, O_3 had high concentrations in summer (~140 μg/m^3) and low concentrations in winter (~50 μg/m^3), while the reverse was the case for other pollutants. Regarding the model performance, NO_2 was underestimated (>10 μg/m^3) while other pollutants were well simulated with better model performances. The annual trends of observed pollutants in the PRD were not different from those of NCP and YRD (**Figure 6**). It can be observed from the monthly average variation (**Supplementary Figure S6**) that O_3 had high concentrations in summer (~140 μg/m^3) and low concentrations in winter (~80 μg/m^3). Contrarily, other pollutants displayed high and low concentrations in winter and summer, respectively. The simulated O_3 was overestimated (~10 μg/m^3) (**Figure 5**) and increased during the study period (**Figure 6**). NO_2 was underestimated, while $PM_{2.5}$ and SO_2 were well simulated with minimum bias (**Figure 5**).

The trends of the observed SO_2 and $PM_{2.5}$ in the CY were similar to the previously discussed regions (**Figure 6**). SO_2 decreased by 55 μg/m^3 between 2013 and 2014 (**Figure 5**). During the entire study period (**Figure 5**), SO_2 and $PM_{2.5}$ were overpredicted and NO_2 was underpredicted, while O_3 was well simulated with minimum bias. The simulated SO_2 during the first 4 years (2013–2016) exhibited apparent seasonal variations, while the levels of observed SO_2 were generally the same with no significant changes during the entire study period. In the FW region, the observed O_3 increased steadily (**Figures 5**, **6**), while SO_2 and $PM_{2.5}$ showed a decreasing trend during 2013–2019. Similar to other regions, high and low concentrations of O_3 were observed in summer and winter, respectively, while the other three pollutants had their high and low concentrations during winter and summer, respectively. $PM_{2.5}$ and SO_2 were well simulated (**Figure 5**), NO_2 was underpredicted (**Supplementary Figure S5, S6**), and O_3 was highly overestimated during 2013–2015 (**Figure 5**), while the model performance for O_3 greatly improved during 2016–2019.

Generally, O_3 in the PRD and FW increased significantly during the study period and was about 110 μg/m^3. No significant change was found in NO_2 during 2013–2019. SO_2 and $PM_{2.5}$ decreased on yearly basis. All of the pollutants were well predicted in 2019 except SO_2 and $PM_{2.5}$ in the CY region.

Correlations Between $PM_{2.5}$ and Other Pollutants

Figure 7 shows the correlation coefficients (R) between $PM_{2.5}$ and O_3, while the correlation coefficients between $PM_{2.5}$, NO_2, and SO_2 are illustrated in **Supplementary Figure S8**. Considering the simulated concentrations, there was an apparent seasonal change between $PM_{2.5}$ and O_3 across the five regions (**Supplementary Figure S7**). The seasonality and correlation gradually weakened from north to south, with the difference of the NCP being more obvious than that of the YRD in different seasons. In the NCP, there was no correlation between $PM_{2.5}$ and O_3 in spring (**Figure 7**). $PM_{2.5}$ was positively correlated to O_3 in summer (0.2) and negatively correlated in autumn (-0.3) and winter (-0.8). The observed concentrations also exhibited similar correlations, but the correlations were closer to zero compared to the simulated concentrations (**Figure 7**). In the YRD, the simulated $PM_{2.5}$ was positively correlated with simulated O_3 during spring and summer, while negative correlations were found between them in autumn and winter. The correlation coefficients were all below 0.5. For the observed concentrations, positive correlations (<0.5)

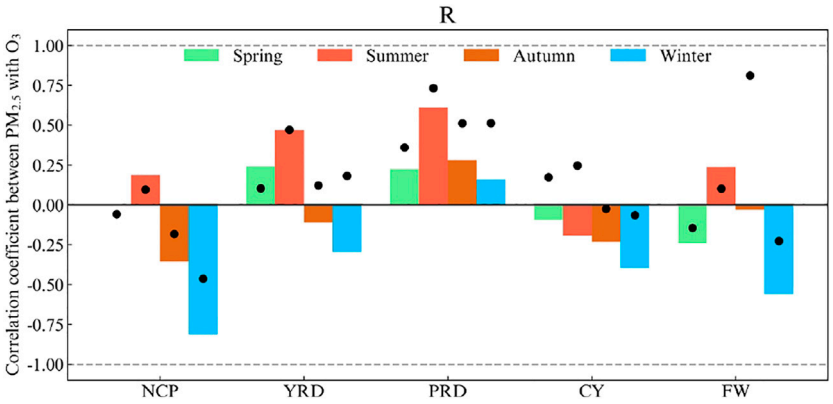

FIGURE 7 | Correlation coefficients (R) between $PM_{2.5}$ and O_3 during the four seasons in the five regions. The columns represent the predicted, while the black dots represent the observed.

were found between the two pollutants during the four seasons. The difference between the correlation coefficients of the simulated and observed concentrations might be attributed to the overprediction of $PM_{2.5}$ as O_3 was well simulated (**Figure 4**). In the PRD, positive correlations were found between $PM_{2.5}$ and O_3 during the four seasons for both simulated and observed concentrations. In the CY and FW regions, the relationships between the simulated $PM_{2.5}$ and O_3 were all negative during the four seasons except in summer in the FW, which was positive. The poor correlations found with the simulated concentrations might be attributed to the location of the CY and FW in an inland area. Considering the observed concentrations, positive correlations were noted in spring and summer, while negative correlations were found during autumn and winter in the CY. In the FW, however, the observed $PM_{2.5}$ and O_3 displayed positive relationships during summer and autumn and negative correlations in both spring and winter.

In addition to the relationship between $PM_{2.5}$ and O_3, the correlations between $PM_{2.5,}$ $NO_{2,}$ and SO_2 were also assessed (**Supplementary Figures S7, S8**). Low-to-medium correlation coefficients were noted between the simulated $PM_{2.5}$ and NO_2, while high coefficients were found between the observed $PM_{2.5}$ and NO_2 during the four seasons across the five regions, an indication of the strong relationship between $PM_{2.5}$ and NO_2 across China during the study period. The low correlation between the simulated $PM_{2.5}$ and NO_2 could be associated with the underestimation of NO_2 across the five regions during the four seasons. In addition, in both simulation and observation scenarios, there were strong and positive correlations between $PM_{2.5}$ and SO_2 during the four seasons in all five regions, and the correlation coefficients for the two scenarios were relatively similar.

CONCLUSION

In this study, the WRF-CMAQ model was employed to simulate the concentrations of O_3, NO_2, SO_2, and $PM_{2.5}$ in China during 2013–2019. The WRF model showed better performance in predicting reasonable and acceptable meteorological fields, which were used in driving the CMAQ model. O_3 was well simulated, while NO_2 was underestimated in the five selected regions. The model performance of SO_2 improved with an increase in years except in the CY region, which is an inland characterized by complex terrain and complicated weather conditions. $PM_{2.5}$ was well simulated in the NCP, YRD, and PRD, while it was overestimated in the CY and FW regions with NMB and NME values greatly exceeding the suggested criteria. NO_3^- and NH_4^+ were the main components that dominated $PM_{2.5}$ in heavily polluted regions, while $PM_{2.5}$ was influenced by SO_4^{2-} in moderately polluted regions. In clean regions, such as the PRD with high temperature and precipitation, $PM_{2.5}$ was equally dominated by each of NO_3^-, SO_4^{2-}, and NH_4^+. During different pollution levels, all of the pollutants were overpredicted and underpredicted for clean and polluted levels, respectively. The concentrations of O_3 were found increasing in each year, while those of other pollutants gradually reduced during 2013–2019 across the five regions. Substantive reductions were observed in SO_2 and $PM_{2.5}$ in the CY and FY regions during the 2013–2019 period. The reductions in the concentrations of the pollutants could be attributed to China's strict emission control policies, which were implemented across the country in 2013. Considering the correlations between $PM_{2.5}$ and other pollutants, $PM_{2.5}$ and O_3 showed seasonal variations in each region, while the variations reduced from north to south. Generally, in all of the regions except the PRD (all seasons) and YRD (spring and summer), the correlations between $PM_{2.5}$ and O_3 were negative during the four seasons. Low-to-medium correlations were noted between the simulated $PM_{2.5}$ and NO_2, while high coefficients were found between the observed $PM_{2.5}$ and NO_2 during the four seasons across the five regions, an indication of the strong relationship between $PM_{2.5}$ and NO_2 across China during the study period. In addition, in both simulation and observation scenarios, there were strong and positive correlations between $PM_{2.5}$ and SO_2 during the four seasons in all five regions. The results of this study improve the understanding of the ability of the CMAQ model in simulating air pollution in China over a long period and provide useful information for designing effective emission control

policies toward abating the levels of pollutants in the five regions and China as a country.

DATA AVAILABILITY STATEMENT

The original contributions presented in this study are included in the article/**Supplementary Material**; further inquiries can be directed to the corresponding author.

AUTHOR CONTRIBUTIONS

JM, and JH designed research. JM, LL, KX, KW, JZ, and GC conducted the simulations, JL, IS, FY, NZ, MQ, YQ and JH contributed to model development and configuration. JM, LL, IS, and JH analyzed the data. JM prepared the manuscript and all coauthors helped improve the manuscript.

FUNDING

This work was supported by the National Natural Science Foundation of China (42007187 and 92044302).

SUPPLEMENTARY MATERIAL

The Supplementary Material for this article can be found online at: https://www.frontiersin.org/articles/10.3389/fenvs.2022.872249/full#supplementary-material

REFERENCES

Bell, M. (2006). The Use of Ambient Air Quality Modeling to Estimate Individual and Population Exposure for Human Health Research: a Case Study of Ozone in the Northern Georgia Region of the United States. *Environ. Int.* 32, 586–593. doi:10.1016/j.envint.2006.01.005

Boylan, J. W., and Russell, A. G. (2006). PM and Light Extinction Model Performance Metrics, Goals, and Criteria for Three-Dimensional Air Quality Models. *Atmos. Environ.* 40 (26), 4946–4959. doi:10.1016/j.atmosenv.2005.09.087

Chen, Q., Sheng, L., Gao, Y., Miao, Y., Hai, S., Gao, S., et al. (2019). The Effects of the Trans-regional Transport of $PM_{2.5}$ on a Heavy Haze Event in the Pearl River Delta in January 2015. *Atmosphere* 10, 237. doi:10.3390/atmos10050237

Chen, X., Wang, Z., Li, J., and Yu, F. (2014). Development of a Regional Chemical Transport Model with Size-Resolved Aerosol Microphysics and its Application on Aerosol Number Concentration Simulation over China. *Sola* 10, 83–87. doi:10.2151/sola.2014-017

Chen, X., Wang, Z., Li, J., Chen, H., Hu, M., Yang, W., et al. (2017). Explaining the Spatiotemporal Variation of fine Particle Number Concentrations over Beijing and Surrounding Areas in an Air Quality Model with Aerosol Microphysics. *Environ. Pollut.* 231, 1302–1313. doi:10.1016/j.envpol.2017.08.103

Chen, X., Wang, Z., Li, J., Yang, W., Chen, H., Wang, Z., et al. (2018). Simulation on Different Response Characteristics of Aerosol Particle Number Concentration and Mass Concentration to Emission Changes over mainland China. *Sci. Total Environ.* 643, 692–703. doi:10.1016/j.scitotenv.2018.06.181

Chen, X., Yang, W., Wang, Z., Li, J., Hu, M., An, J., et al. (2019). Improving New Particle Formation Simulation by Coupling a Volatility-Basis Set (VBS) Organic Aerosol Module in NAQPMS+APM. *Atmos. Environ.* 204, 1–11. doi:10.1016/j.atmosenv.2019.01.053

de Leeuw, G., Ronald, V. D., Bai, J., Xue, Y., Varotsos, C., Li, Z., et al. (2021). Air Quality over China. *Remote Sens.* 13, 3542. doi:10.3390/rs13173542

Emery, C., Liu, Z., Russell, A. G., Odman, M. T., Yarwood, G., and Kumar, N. (2017). Recommendations on Statistics and Benchmarks to Assess Photochemical Model Performance. *J. Air Waste Manage. Assoc.* 67, 582–598. doi:10.1080/10962247.2016.1265027

Fahey, K. M., Carlton, A. G., Pye, H. O. T., Baek, J., Hutzell, W. T., Stanier, C. O., et al. (2017). A Framework for Expanding Aqueous Chemistry in the Community Multiscale Air Quality (CMAQ) Model Version 5.1, Geosci1. *Geosci. Model. Dev.* 10, 1587–1605. doi:10.5194/gmd-10-1587-2017

Gong, K., Li, L., Li, J., Qin, M., Wang, X., Ying, Q., et al. (2021). Quantifying the Impacts of Inter-city Transport on Air Quality in the Yangtze River Delta Urban Agglomeration, China: Implications for Regional Cooperative Controls of $PM_{2.5}$ and O_3. *Sci. Total Environ.* 779, 146619. doi:10.1016/j.scitotenv.2021.146619

Guenther, A. B., Jiang, X., Heald, C. L., Sakulyanontvittaya, T., Duhl, T., Emmons, L. K., et al. (2012). The Model of Emissions of Gases and Aerosols from Nature Version 2.1 (MEGAN2.1): an Extended and Updated Framework for Modeling Biogenic Emissions. *Geosci. Model. Dev.* 5, 1471–1492. doi:10.5194/gmd-5-1471-2012

Hu, J., Chen, J., Ying, Q., and Zhang, H. (2016). One-year Simulation of Ozone and Particulate Matter in China Using WRF/CMAQ Modeling System. *Atmos. Chem. Phys.* 16, 10333–10350. doi:10.5194/acp-16-10333-2016

Hu, J., Li, X., Huang, L., Ying, Q., Zhang, Q., Zhao, B., et al. (2017). Ensemble Prediction of Air Quality Using the WRF/CMAQ Model System for Health Effect Studies in China. *Atmos. Chem. Phys.* 17, 13103–13118. doi:10.5194/acp-17-13103-2017

Hua, J., Zhang, Y., de Foy, B., Shang, J., Schauer, J. J., Mei, X., et al. (2021). Quantitative Estimation of Meteorological Impacts and the COVID-19 Lockdown Reductions on NO_2 and $PM_{2.5}$ over the Beijing Area Using Generalized Additive Models (GAM)). *J. Environ. Manage.* 291, 112676. doi:10.1016/j.jenvman.2021.112676

Li, M., Wang, T., Xie, M., Zhuang, B., Li, S., Han, Y., et al. (2017). Improved Meteorology and Ozone Air Quality Simulations Using MODIS Land Surface Parameters in the Yangtze River Delta Urban Cluster, China. *J. Geophys. Res. Atmos.* 122, 3116–3140. doi:10.1002/2016jd026182

Liu, T., Wang, X., Hu, J., Wang, Q., An, J., Gong, K., et al. (2020). Driving Forces of Changes in Air Quality during the COVID-19 Lockdown Period in the Yangtze River Delta Region, China. *Environ. Sci. Technol. Lett.* 7, 779–786. doi:10.1021/acs.estlett.0c00511

Li, M., Zhang, Z., Yao, Q., Wang, T., Xie, M., Li, S., et al. (2021). Nonlinear Responses of Particulate Nitrate to NOx Emission Controls in the Megalopolises of China. *Atmos. Chem. Phys.* 21 (19), 15135–15152. doi:10.5194/acp-21-15135-2021

Luo, X., and Cao, H. (2012). Evaluation of Air Quality Using the CMAQ Modeling System. *Proced. Environ. Sci.* 12, 159–165. doi:10.1016/j.proenv.2012.01.261

Li, X., Hussain, S. A., Sobri, S., and Md Said, M. S. (2021). Overviewing the Air Quality Models on Air Pollution in Sichuan Basin, China. *Chemosphere* 271, 129502. doi:10.1016/j.chemosphere.2020.129502

Ma, J., Shen, J., Wang, P., Zhu, S., Wang, Y., Wang, P., et al. (2021). Modeled Changes in Source Contributions of Particulate Matter during the COVID-19 Pandemic in the Yangtze River Delta, China. *Atmos. Chem. Phys.* 21 (9), 7343–7355. doi:10.5194/acp-21-7343-2021

Qin, Y., Li, J., Gong, K., Wu, Z., Chen, M., Qin, M., et al. (2021). Double High Pollution Events in the Yangtze River Delta from 2015 to 2019: Characteristics, Trends, and Meteorological Situations. *Sci. Total Environ.* 792, 148349. doi:10.1016/j.scitotenv.2021.148349

Shi, Z., Huang, L., Li, J., Ying, Q., Zhang, H., and Hu, J. (2020). Sensitivity Analysis of the Surface Ozone and Fine Particulate Matter to Meteorological Parameters in China. *Atmos. Chem. Phys.* 20, 13455–13466. doi:10.5194/acp-20-13455-2020

Sulaymon, I. D., Zhang, Y., Hu, J., Hopke, P. K., Zhang, Y., Zhao, B., et al. (2021a). Evaluation of Regional Transport of $PM_{2.5}$ during Severe Atmospheric Pollution Episodes in the Western Yangtze River Delta, China. *J. Environ. Manage.* 293, 112827. doi:10.1016/j.jenvman.2021.112827

Sulaymon, I. D., Zhang, Y., Hopke, P. K., Hu, J., Zhang, Y., Li, L., et al. (2021b). Persistent High $PM_{2.5}$ Pollution Driven by Unfavorable Meteorological Conditions during the COVID-19 Lockdown Period in the Beijing-Tianjin-

Hebei Region, China. *Environ. Res.* 198, 111186. doi:10.1016/j.envres.2021.111186

Sulaymon, I. D., Zhang, Y., Hopke, P. K., Hu, J., Rupakheti, D., Xie, X., et al. (2021c). Influence of Transboundary Air Pollution and Meteorology on Air Quality in Three Major Cities of Anhui Province, China. *J. Clean. Prod.* 329, 129641. doi:10.1016/j.jclepro.2021.129641

Sulaymon, I. D., Zhang, Y., Hopke, P. K., Zhang, Y., Hua, J., and Mei, X. (2021d). COVID-19 Pandemic in Wuhan: Ambient Air Quality and the Relationships between Criteria Air Pollutants and Meteorological Variables before, during, and after Lockdown. *Atmos. Res.* 250, 105362. doi:10.1016/j.atmosres.2020.105362

Sun, K., Liu, H., Ding, A., and Wang, X. (2016). WRF-Chem Simulation of a Severe Haze Episode in the Yangtze River Delta, China. *Aerosol Air Qual. Res.* 16, 1268–1283. doi:10.4209/aaqr.2015.04.0248

Tan, J., Zhang, Y., Ma, W., Yu, Q., Wang, J., and Chen, L. (2015). Impact of Spatial Resolution on Air Quality Simulation: A Case Study in a Highly Industrialized Area in Shanghai, China. *Atmos. Pollut. Res.* 6, 322–333. doi:10.5094/apr.2015.036

Tao, H., Xing, J., Zhou, H., Pleim, J., Ran, L., Chang, X., et al. (2020). Impacts of Improved Modeling Resolution on the Simulation of Meteorology, Air Quality, and Human Exposure to $PM_{2.5}$, O_3 in Beijing, China. *J. Clean. Prod.* 243, 118574. doi:10.1016/j.jclepro.2019.118574

Wang, H. L., Qiao, L. P., Lou, S. R., Zhou, M., Chen, J. M., Wang, Q., et al. (2015). $PM_{2.5}$ Pollution Episode and its Contributors from 2011 to 2013 in Urban Shanghai, China. *Atmos. Environ.* 123, 298–305. doi:10.1016/j.atmosenv.2015.08.018

Wang, H., Wang, Q., Gao, Y., Zhou, M., Jing, S., Qiao, L., et al. (2020a). Estimation of Secondary Organic Aerosol Formation during a Photochemical Smog Episode in Shanghai, China. *J. Geophys. Res. Atmos.* 125, 7. doi:10.1029/2019jd032033

Wang, H., Yan, R., Xu, T., Wang, Y., Wang, Q., Zhang, T., et al. (2020b). Observation Constrained Aromatic Emissions in Shanghai, China. *J. Geophys. Res. Atmos.* 125, 6. doi:10.1029/2019jd031815

Wang, X., Li, L., Gong, K., Mao, J., Hu, J., Li, J., et al. (2021). Modeling Air Quality during the EXPLORE-YRD Campaign–Part I. Model Performance Evaluation and Impacts of Meteorological Inputs and Grid Resolutions. *Atmos. Environ.* 246, 118131. doi:10.1016/j.atmosenv.2020.118131

Wang, H. L., Qiao, L. P., Lou, S. R., Zhou, M., Ding, A. J., Huang, H. Y., et al. (2016). Chemical Composition of $PM_{2.5}$ and Meteorological Impact Among Three Years in Urban Shanghai, China. *J. Clean. Prod.* 112, 1302–1311. doi:10.1016/j.jclepro.2015.04.099

Wang, N., Lyu, X. P., Deng, X. J., Guo, H., Deng, T., Li, Y., et al. (2016). Assessment of Regional Air Quality Resulting from Emission Control in the Pearl River Delta Region, Southern China. *Sci. Total Environ.* 573, 1554–1565. doi:10.1016/j.scitotenv.2016.09.013

Wiedinmyer, C., Akagi, S. K., Yokelson, R. J., Emmons, L. K., Al-Saadi, J. A., Orlando, J. J., et al. (2011). The Fire Inventory from NCAR (FINN): A High-Resolution Global Model to Estimate the Emissions from Open Burning. *Geosci. Model. Dev.* 4, 625–641. doi:10.5194/gmd-4-625-2011

Yang, X., Wu, Q., Zhao, R., Cheng, H., He, H., Ma, Q., et al. (2019). New Method for Evaluating winter Air Quality: PM2.5 Assessment Using Community Multi-Scale Air Quality Modeling (CMAQ) in Xi'an. *Atmos. Environ.* 211, 18–28. doi:10.1016/j.atmosenv.2019.04.019

Yu, Y., Xu, H., Jiang, Y., Chen, F., Cui, X., He, J., et al. (2021). A Modeling Study of $PM_{2.5}$ Transboundary during a winter Severe Haze Episode in Southern Yangtze River Delta, China. *Atmos. Res.* 248, 105159. doi:10.1016/j.atmosres.2020.105159

Zhang, H., Chen, G., Hu, J., Chen, S.-H., Wiedinmyer, C., Kleeman, M., et al. (2014). Evaluation of a Seven-Year Air Quality Simulation Using the Weather Research and Forecasting (WRF)/Community Multiscale Air Quality (CMAQ) Models in the Eastern United States. *Sci. Total Environ.* 473-474, 275–285. doi:10.1016/j.scitotenv.2013.11.121

Zhang, H., Cheng, S., Yao, S., Wang, X., and Zhang, J. (2019). Multiple Perspectives for Modeling Regional $PM_{2.5}$ Transport across Cities in the Beijing-Tianjin-Hebei Region during Haze Episodes. *Atmos. Environ.* 212, 22–35. doi:10.1016/j.atmosenv.2019.05.031

Zhang, Q., Zheng, Y., Tong, D., Shao, M., Wang, S., Zhang, Y., et al. (2019). Drivers of Improved $PM_{2.5}$ Air Quality in China from 2013 to 2017. *Proc. Natl. Acad. Sci. U.S.A.* 116, 24463–24469. doi:10.1073/pnas.1907956116

Zhao, X., Wang, G., Wang, S., Zhao, N., Zhang, M., and Yue, W. (2021). Impacts of COVID-19 on Air Quality in Mid-eastern China: An Insight into Meteorology and Emissions. *Atmos. Environ.* 266, 118750. doi:10.1016/j.atmosenv.2021.118750

Conflict of Interest: The authors declare that the research was conducted in the absence of any commercial or financial relationships that could be construed as a potential conflict of interest.

Publisher's Note: All claims expressed in this article are solely those of the authors and do not necessarily represent those of their affiliated organizations, or those of the publisher, the editors, and the reviewers. Any product that may be evaluated in this article, or claim that may be made by its manufacturer, is not guaranteed or endorsed by the publisher.

frontiers | Frontiers in Ecology and Evolution

ORIGINAL RESEARCH
published: 26 April 2022
doi: 10.3389/fevo.2022.897410

Effective Air Purification *via* Pt-Decorated N_3-CNT Adsorbent

Yinli Yang[1†], Sitong Liu[1†], Kai Guo[1], Liang Chen[1,2], Jing Xu[1] and Wei Liu[1*]*

[1] *Department of Optical Engineering, College of Optical, Mechanical and Electrical Engineering, Zhejiang A&F University, Hangzhou, China,* [2] *School of Physical Science and Technology, Ningbo University, Ningbo, China*

Effectively removal of air pollutants using adsorbents is one of the most important methods to purify the air. In this work, we proposed for the first time that PtN_3-CNT is an effective adsorbent for air purification. Its air purification performance was studied by calculating the adsorption behaviors and electronic structures of 12 gas molecules, including the main components of air (N_2, O_2, H_2O, CO_2) and the most common air pollutants (NO, NO_2, SO_3, SO_2, CO, O_3, NH_3, H_2S), on the surface of PtN_3-CNT using first-principles calculations. The results showed that these gases were adsorbed stably *via* the coordination between Pt and the coordinated atoms (C, N, O, and S atoms) in the gas molecules, and the adsorption energies vary in the range of −0.81∼−4.28 eV. The obvious chemical interactions between PtN_3-CNT and the adsorbed gas molecules are mainly determined by the apparent overlaps between the Pt *5d* orbitals and the outmost *p* orbitals of the coordination atoms. PtN_3-CNT has strong adsorption capacity for the toxic gas molecules, while relatively weaker adsorption performance for the main components of the air except oxygen. The recovery time of each adsorbed molecule calculated at different temperatures showed that, CO_2, H_2O, and N_2 can be desorbed gradually at 298∼498 K, while the toxic gases are always adsorbed stably on the surface of PtN_3-CNT. Considering the excellent thermal stability of PtN_3-CNT at up to 1000 K proved by AIMD, PtN_3-CNT is very suitable to act as an adsorbent to remove toxic gases to achieve the purpose of air purification. Our findings in this report would be beneficial for exploiting possible carbon-based air purification adsorbents with excellent adsorbing ability and good recovery performance.

Keywords: air pollution, gas separation, carbon nanotube, transition metal doping, density functional theory

OPEN ACCESS

Edited by:
Shupeng Zhu,
University of California, Irvine, United States

Reviewed by:
Lei Zhao,
Southwest Petroleum University, China
Haifeng Zheng,
State Key Laboratory of Rare Earth Resources Utilization, Changchun Institute of Applied Chemistry (CAS), China

***Correspondence:**
Wei Liu
weiliu@zafu.edu.cn
Jing Xu
jingxu@zafu.edu.cn

[†] *These authors have contributed equally to this work*

Specialty section:
This article was submitted to Interdisciplinary Climate Studies, a section of the journal Frontiers in Ecology and Evolution

Received: *16 March 2022*
Accepted: *06 April 2022*
Published: *26 April 2022*

Citation:
Yang Y, Liu S, Guo K, Chen L, Xu J and Liu W (2022) Effective Air Purification via Pt-Decorated N_3-CNT Adsorbent. Front. Ecol. Evol. 10:897410. doi: 10.3389/fevo.2022.897410

INTRODUCTION

In recent years, more and more attention has been paid to the impact of air pollution on human health. The effective purification of the air has become a research hotspot in both academia and industry (Zhao and Yang, 2003; Ren et al., 2017). One of the most important ways to purify the air is to adsorb the pollutants through adsorbents (DeCoste and Peterson, 2014; Perreault et al., 2015; Liu et al., 2020). The rapid development of low-dimensional carbon materials provides more options for the detection and separation of atmospheric pollutants (Samaddar et al., 2018; Teng et al., 2018; Cai et al., 2021). Single-walled carbon nanotubes (CNTs) are often used as adsorbents to adsorb certain harmful gases due to their unique tubular structures, huge effective surfaces, high thermal stability and high chemical stability (Li et al., 2018; Poudel and Li, 2018). However, the

pristine CNTs have some disadvantages of few detection gas types, poor recovery performance, low sensitivity, and poor selectivity (Tabtimsai et al., 2020). Therefore, a variety of methods have been proposed to improve the adsorption performance of CNTs, mainly including functional group modification (Guo et al., 2021; Lim et al., 2021), metal doping (Zhou X. et al., 2010; Cui et al., 2018), non-metal doping (Esrafili and Heydari, 2019; Liu et al., 2019), plasma treatment (Babu et al., 2013; Cui et al., 2020; Sun et al., 2021), molecular sieve treatment, and so on (Niimura et al., 2012; Hou et al., 2018).

Noble metals are commonly used catalysts in chemical reactions (Zhang et al., 2021), and they can also serve as active centers for interaction with gas molecules (Tabtimsai et al., 2018). Novel gas sensors have been fabricated and reported by doping metal atoms on the surfaces of transition metal dichaldogenides (Zhang D. et al., 2017; Zhang et al., 2019, 2020). When noble metals are embedded on the surfaces of CNTs, the physical and chemical properties of CNTs will be significantly changed, thus enhancing the adsorption capacity of CNTs to various gas molecules (Zhang et al., 2014). However, the binding of metal atoms with CNTs is often weak and the anchored metal atoms are easy to desorb. Due to the strong coordination interaction between nitrogen atoms and many metal atoms (Wang H. et al., 2021; Wang L. et al., 2021) N_x (x = 3 or 4) groups have been introduced into the surfaces of CNTs to stabilize the adsorption of metal atoms (Feng et al., 2010). The doping of N atoms in CNTs will also introduce novel states near the Fermi level, thus improving the adsorption selectivity and sensitivity of CNTs to gas molecules (Zhou Y. et al., 2010; Gao et al., 2018; Tabtimsai et al., 2020). Hence, the combination of the electron-donating properties of noble metals and electron-attracting properties of N_x groups will result in significant electron localization, which is helpful to promote the stable chemisorption behavior of gas molecules on the surfaces of CNTs (Peng and Cho, 2003; Li et al., 2009).

In this work, the air purification performance of Pt-decorated N_3-CNT as adsorbent was studied using first-principles calculations. The adsorption behaviors and electronic structures of 12 gas molecules on the surface of PtN_3-CNT were investigated. The calculated results confirmed that the N_3 group could effectively enhance the adsorption performance of metal-doped CNTs toward gas molecules through the improvement of electron mobility and chemical activity. The adsorption capacity of PtN_3-CNT to common air pollutants and the main components of the air varies greatly. The recovery time for the gas molecules to desorb from the PtN_3-CNT surface were further calculated at different temperatures.

COMPUTATIONAL METHODS

The Vienna Ab initio Simulation Package (VASP) (Kresse and Furthmüller, 1996) based on density functional theory was used for all the first-principles calculations. The Perdew-Burke-Ernzerhof (PBE) (Perdew et al., 1996) functional in generalized gradient approximation (GGA) (Kohn and Sham, 1965) was used to describe the exchange-correlation interactions. The kinetic energy cutoff was set to 550 eV. The convergence criteria for energy and force in all the calculations were 1×10^{-5} eV and −0.01 eV/Å, respectively. The first Brillouin zone was represented using the Monkhorst-Pack scheme (Chadi, 1977) with a $1 \times 1 \times 2$ K-point mesh. Vacuum layers of 25Å were set in the radial directions of the CNTs to avoid interactions between adjacent structures. The Gaussian smearing method and a denser K-point mesh ($1 \times 1 \times 8$) were used in all the electronic properties calculations. In addition, the van der Waals interaction was considered using DFT-D3 correction method of Grimme et al. (2010). Ab initio molecular dynamics (AIMD) simulations in the canonical ensemble (NVT) with the Nosé-Hoover thermostat (Hoover, 1985) were performed for 5.0 ps with a time-step of 1.0 fs at 1000 K. The stress tensor was calculated every time-step.

To evaluate the adsorption behaviors of gas molecules, we use the adsorption energy (E_{ad}) as the descriptor which is defined as follows:

$$E_{ad} = E_{PtN_3-CNT/gas} - E_{PtN_3-CNT} - E_{gas} \quad (1)$$

where $E_{PtN_3-CNT/gas}$, E_{PtN_3-CNT}, E_{gas} represent the total energy of the adsorption system, PtN_3-CNT and isolated gas molecules, respectively. In addition, the bader charge (Bader and Beddall, 1972) is used to analyze the charge transfer between the gas molecules and the modified surface. The charge transfer can be defined as the number of electrons carried by the gas molecules after adsorption, because the electron value carried by the molecule is always zero before adsorption. Positive values indicate charge transfer from PtN_3-CNT to gas molecules, while negative values indicate the reverse charge transfer path.

RESULTS

Geometric and Electronic Structures of PtN_3-CNT

Zigzag (8,0) single-walled carbon nanotube was chosen as the substrate to construct the PtN_3-CNT structure by firstly deleting one carbon atom to form a single-vacancy defect, secondly substitutional doping of three carbon atoms possessing dangling bonds with nitrogen atoms, and finally adsorbing one Pt atom at the center of the N_3 group. The geometric and electronic structures of PtN_3-CNT were investigated. **Figure 1A** shows the top and side views of the geometric configuration of the optimized PtN_3-CNT. The Pt atom is captured by the N_3 group, and the lengths of Pt-N bonds are 1.96 and 2.08Å, respectively. The binding energies (E_b) for one Pt atom on the surface of CNTs were calculated using the following formula:

$$E_b = E_{PtN_3-CNT} - E_{N_3-CNT} - E_{Pt} \quad (2)$$

where E_{PtN_3-CNT}, E_{N_3-CNT}, E_{Pt} represent the energies of PtN_3-CNT, pure N_3-CNT and Pt atom, respectively. The obtained negative E_b (−3.20 eV) value demonstrates that the binding of Pt atom on the surface of CNT *via* N_3 groups is thermodynamically preferable. Furthermore, to investigate the thermal stability of PtN_3-CNT, ab initio molecular dynamics (AIMD) simulations

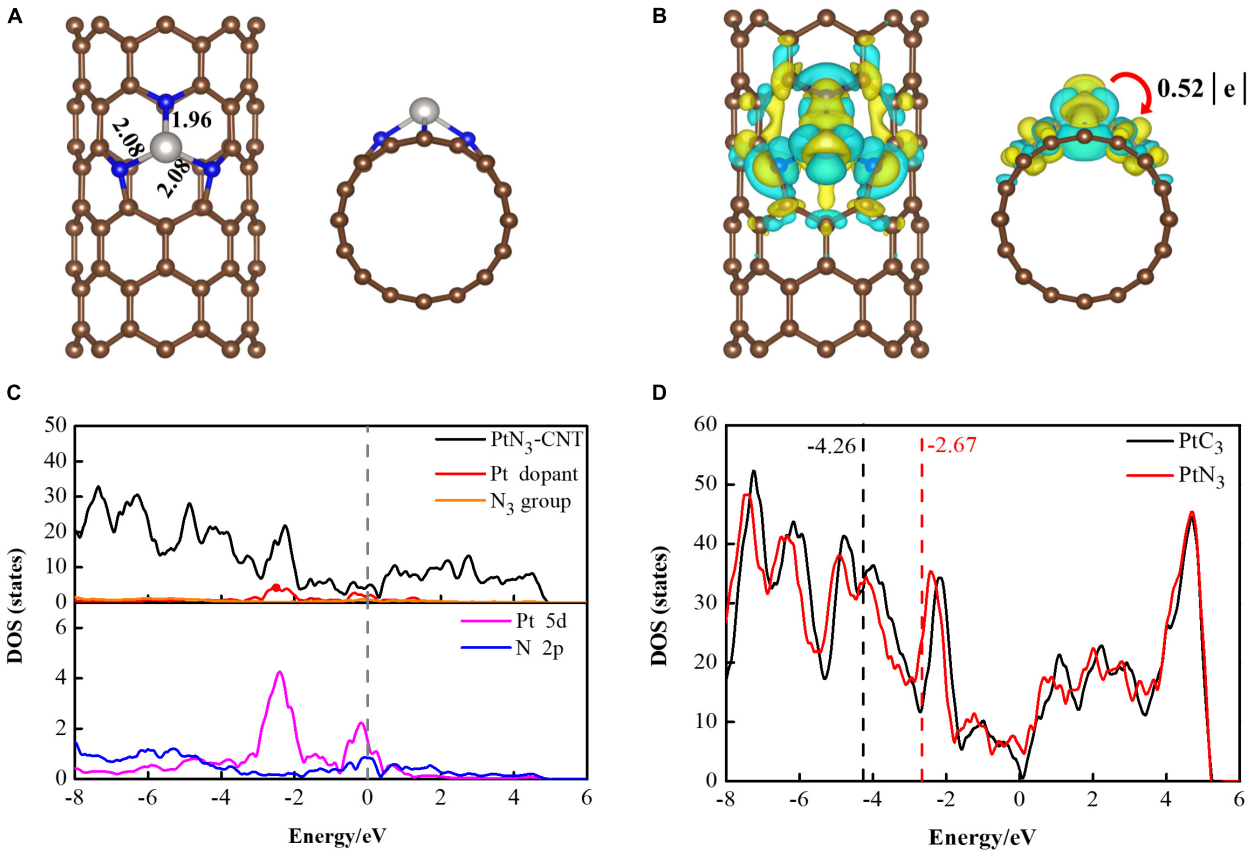

FIGURE 1 | (A) The top and side views of the optimized geometries of PtN_3-CNT; **(B)** Deformation charge distribution of PtN_3-CNT. The yellow area and cyan area represent the accumulation and consumption of electrons, respectively. The value of the isosurface level is 0.0011 e/Å^3. **(C)** DOS and PDOS of PtN_3-CNT; **(D)** *d*-band centers of PtN_3-CNT and PtC_3-CNT. Brown, blue, gray balls represent C, N, and Pt atoms, respectively.

were performed at 1000 K. The obtained results were shown in **Supplementary Figure 1**. No reconstruction of the PtN_3-CNT structure was found, implying that PtN_3-CNT can withstand temperatures up to 1000 K.

The result of deformation charge distribution (DCD) of PtN_3-CNT are shown in **Figure 1B**, which indicates that the N_3 group could act as the electron active center to withdraw electrons from the carbon nanotube and Pt atom. The Pt atom acts as an electron donor to release 0.52 *e* to N_3-CNT, and the three N atoms obtain 0.14 *e*, 0.13 *e* and 0.12 *e*, respectively. This is because the lone pair electrons and non-bonded electrons carried on the sp^2 orbitals of the three N atoms produce highly localized acceptor-like states at the Fermi level (Rangel and Sansores, 2014), and the strong electron withdrawing properties of the N_3 center further enhance the electron distribution.

Next, the density of states (DOS) and the projected density of states (PDOS) of PtN_3-CNT and PtC_3-CNT were calculated to further understand the electronic behaviors and the effect of the N_3 group. As shown in **Figure 1C**, the partial DOS curve of the metal dopant and the N_3 group are in good agreement with the total DOS curve of PtN_3-CNT, especially in the region close to the Fermi level. In the PtN_3-CNT system, it can be seen that due to the doping of N atoms in carbon nanotubes, the electron-donating properties of Pt are combined with the electron-absorbing properties of N_3 group, leading to significant electron localization, thus forming a new state near the Fermi level, which will improve the adsorption selectivity and sensitivity of carbon nanotubes to gas molecules. The contribution of the Pt dopant to the total DOS in PtN_3-CNT is greater than that in PtC_3-CNT (shown in **Supplementary Figure 2**), which endows the doped Pt atom a greater regulatory effect on the electronic behavior of PtN_3-CNT. From the PDOS, it is shown that there exists a large-area overlap between the Pt 5*d* orbital and the N 2*p* orbital. This means that the Pt atom chemically interacts with N_3-CNT, leading to significant electron transfer and making PtN_3-CNT more active (Zhao and Wu, 2018).

We also calculated the *d*-band center structures and positions of PtN_3-CNT and PtC_3-CNT to evaluate whether the N_3 group has enhanced the gas adsorption ability of Pt-decorated CNT (shown in **Figure 1D**). The result illustrates that the *d*-band center value of the PtC_3-CNT system is −4.26 eV, while the value of the PtN_3-CNT system is −2.67 eV, which is closer to the Fermi level than the PtC_3-CNT system. As the position of the *d*-band center increases, the anti-bonding orbital formed by the system to adsorb gas molecules will be pushed up. The higher the anti-bonding orbital position is, the more stable the

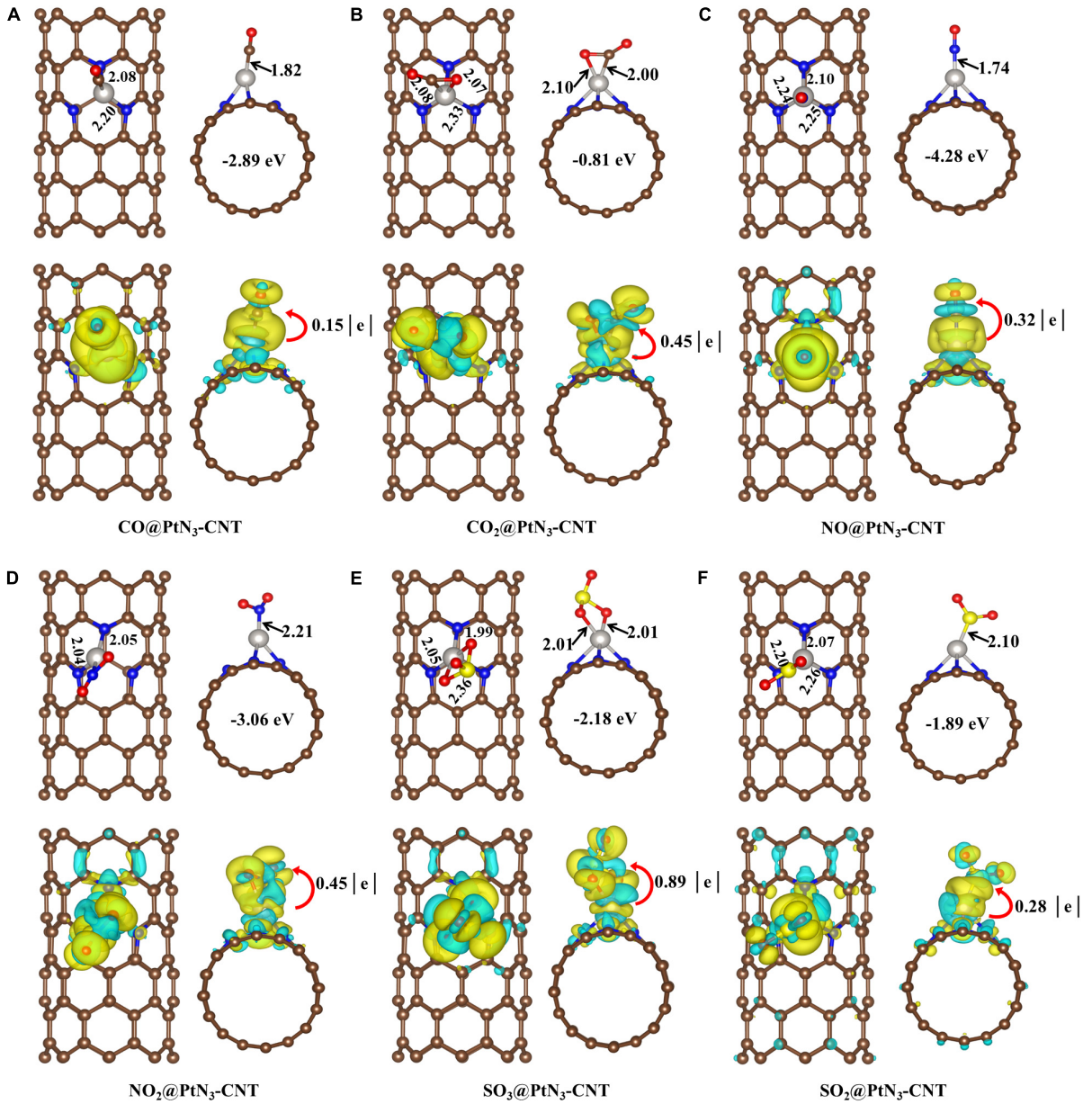

FIGURE 2 | Adsorption structures and deformation charge distribution of **(A)** CO@PtN_3-CNT system; **(B)** CO_2@PtN_3-CNT system; **(C)** NO@PtN_3-CNT system; **(D)** NO_2@PtN_3-CNT system; **(E)** SO_3@PtN_3-CNT system; and **(F)** SO_2@PtN_3-CNT system. In the middle of the side views are the adsorption energies of the gas molecules. Yellow and red balls represent S and O atoms, respectively. The yellow area and cyan area represent the accumulation and consumption of electrons, respectively.

system is after adsorbing gas molecules. Therefore, the PtN_3-CNT system is more favorable for gas adsorption than the PtC_3-CNT system, and the adsorption ability of Pt-decorated CNT toward gas molecules is effectively enhanced.

Adsorption of Gas Molecules on the Surface of PtN_3-CNT

The adsorption of 12 kinds of gas molecules on the surface of PtN_3-CNT were investigated, including the main components of the air (N_2, O_2, H_2O, and CO_2), the most common air pollutants nitrous oxides (NO, NO_2), sulfur oxides (SO_2, SO_3), CO, O_3, NH_3, and H_2S. For each adsorbed gas molecule, a variety of different adsorption structures were obtained and only the most stable geometric structures are discussed in the following sections. These 12 gas molecules are divided into three categories for discussion, namely the oxides, the hydrides and the elemental gases.

The optimized structures for the oxides adsorption on PtN_3-CNT and the DCD figures are shown in **Figure 2**. CO, NO, NO_2,

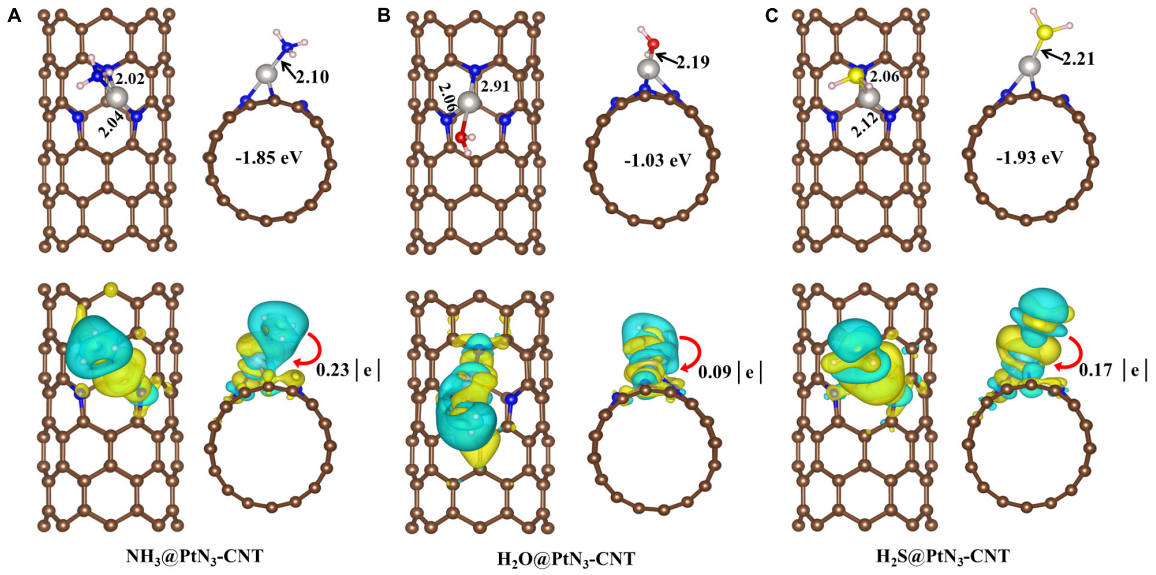

FIGURE 3 | Adsorption structures and deformation charge distribution of **(A)** NH_3@PtN_3-CNT system; **(B)** H_2O@PtN_3-CNT system; **(C)** H_2S@PtN_3-CNT system. Light pink ball represents H atom. The yellow area and cyan area represent the accumulation and consumption of electrons, respectively.

and SO_2 molecules interact with the dopant Pt atoms through a single atom forming new Pt-C (1.82Å), Pt-N (1.74Å for NO, and 2.21Å for NO_2), and Pt-S (2.10Å) bonds while CO_2 and SO_3 are adsorbed on the surface by forming two bonds. The newly formed Pt-C, Pt-N, and Pt-S bonds in the adsorption structures of CO, NO, and SO_2 are shorter than the sum of the covalent bond radius of Pt and C (1.98Å), Pt and N (1.94Å), Pt and S (2.26Å), indicating that the noble metal dopant (Pt) has a strong binding force to CO, NO, and SO_2 molecules, resulting in the chemisorption properties of these systems. The adsorption energies of these oxides vary in the range of −0.81∼−4.28 eV, and 0.15∼0.89 electrons are transferred from the adsorbent surfaces to the gas molecules. Among these oxides, the adsorption of CO_2 on the surface of PtN_3-CNT is the weakest.

As shown in **Figure 3**, the three hydrides (NH_3, H_2O, and H_2S) are adsorbed stably on PtN_3-CNT with adsorption energies of −1.85, −1.03, and −1.93 eV, respectively. The adsorption of H_2O has the smallest adsorption energy in the considered hydrides. In the adsorption structures, Pt atoms coordinate with the N, O, and S atoms as in the adsorption of oxides, and the newly formed Pt-N, Pt-O, and Pt-S bonds are 2.10, 2.19, and 2.21Å, respectively. Moreover, unlike the adsorption of oxides, 0.23, 0.09, and 0.17 e are transferred from the gas molecules to the adsorbent PtN_3-CNT, which is because that the electronegativity of hydrogen atoms is much weaker.

The adsorption structures of the three elemental gases (O_3, O_2, N_2) on PtN_3-CNT are shown in **Figure 4**. The adsorption energies of O_3 and O_2 (−3.59 and −3.24 eV, respectively) on PtN_3-CNT are much larger than that of N_2 (−1.36 eV), which may be due to the fact that two oxygen atoms are coordinated with the dopant Pt in the adsorption structures of O_3 and O_2. The newly formed Pt-O bonds in O_3@PtN_3-CNT and O_2@PtN_3-CNT are 1.99, 1.95, and 2.07Å, respectively. The newly formed Pt-N bond in N_2@PtN_3-CNT (1.89Å) is smaller than the sum of the covalent bond radius of Pt and N (1.94Å), indicating that the adsorption of N_2 molecules on the surface of PtN_3-CNT is chemical adsorption. 0.70, 0.59, and 0.22 e are transferred from the elemental gas molecules to the adsorbent surfaces, respectively.

In all the adsorption structures discussed above, the chemical Pt-N bonds in PtN_3-CNT are stretched by 0.01–0.29Å after adsorption, and one Pt-N is even broken in some adsorption structures (CO, NO_2, NH_3, H_2O, H_2S, O_2, and N_2). After adsorption, the chemical bonds in the gas molecules are all elongated relative to free molecules, indicating that these gas molecules are activated after adsorption on the PtN_3-CNT surfaces. Moreover, the adsorption energies of some gas molecules on Pt-CNT (−1.73 eV for CO, −3.53 eV for NO, −1.37 eV for NH_3, −1.06 eV for N_2, respectively) have been reported previously. These E_{ad} are 0.30∼1.16 eV smaller than the corresponding adsorption energies on PtN_3-CNT, confirming that the N_3 dopant have effectively improved the reactivity of CNTs, thereby enhancing the adsorption performance of the system for gas molecules.

Next, the electronic structures of gas@PtN_3-CNT systems are investigated. From the above discussion, it can be found that the gas molecules are adsorbed on the surface of PtN_3-CNT through the coordination of Pt with C, N, O, and S atoms, respectively. The DOS and PDOS of the gas molecules with the largest E_{ad} (CO, NO, O_3, and H_2S) in each coordination mode are shown in **Figure 5**, and those of the other gases are shown in **Supplementary Figure 3**. Generally, the total DOS curves of gas@PtN_3-CNT are very similar with that of isolated PtN_3-CNT, except that the total DOS curves of the adsorbed systems shift to the high energy region. This could be attributed to the electron-withdrawing behavior of PtN_3-CNT that results

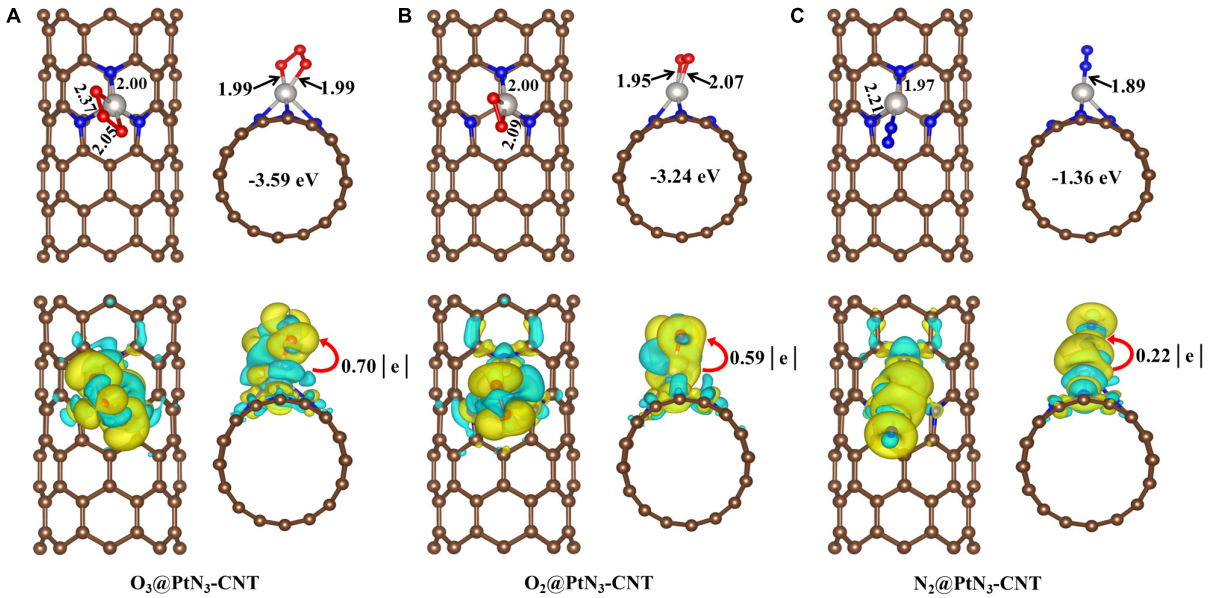

FIGURE 4 | Adsorption structures and deformation charge distribution of **(A)** O_3@PtN_3-CNT system; **(B)** O_2@PtN_3-CNT system; **(C)** N_2@PtN_3-CNT system. The yellow area and cyan area represent the accumulation and consumption of electrons, respectively.

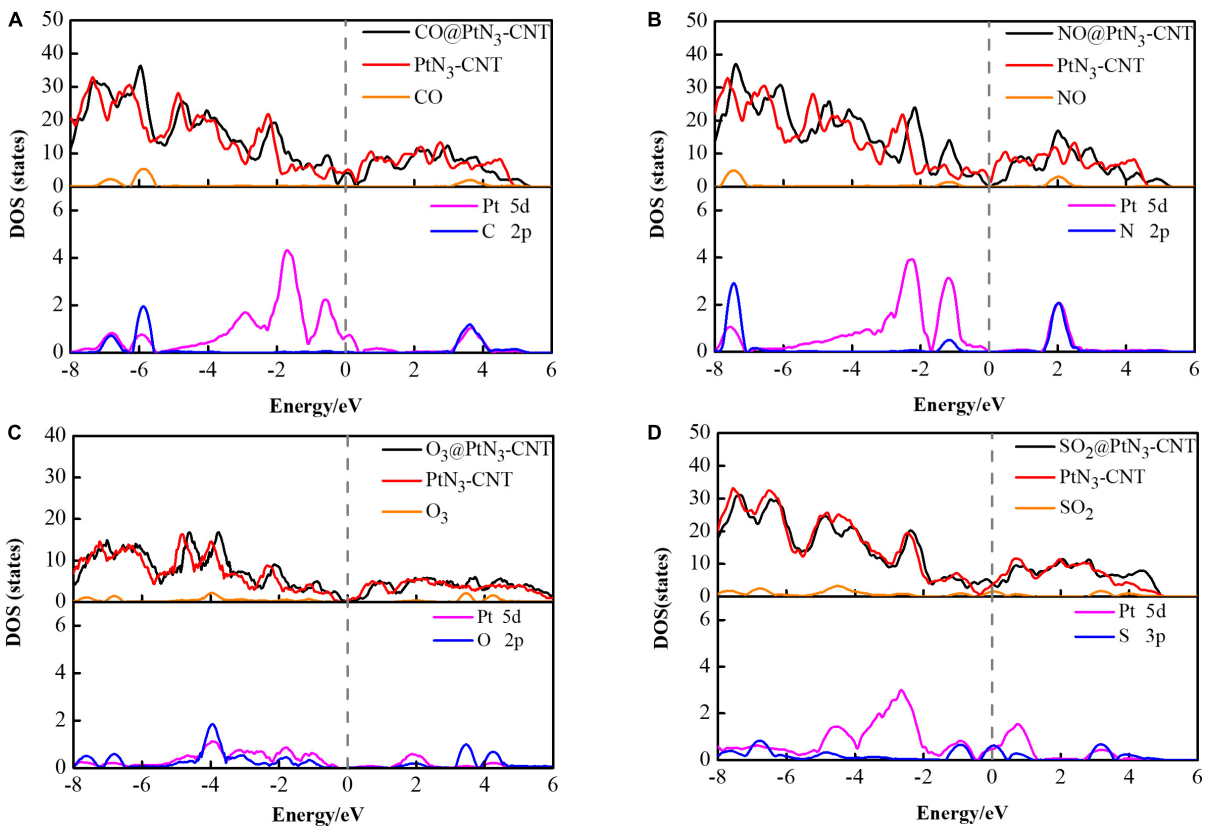

FIGURE 5 | DOS and PDOS of **(A)** CO@PtN_3-CNT system; **(B)** NO@PtN_3-CNT system; **(C)** O_3@PtN_3-CNT system; and **(D)** H_2S@PtN_3-CNT system. The dashed line represents the Fermi level.

TABLE 1 | Adsorption energies (E_{ad}), distances between Pt and the coordinated atoms (D), and the charge transferred between PtN_3-CNT and the gas molecules for Gas@PtN_3-CNT systems (Q_T).

Gas	E_{ad} (eV)	D (Å)	Q_T (e)	Gas	E_{ad} (eV)	D (Å)	Q_T (e)
CO	−2.89	1.82	0.15	NH_3	−1.85	2.10	−0.23
CO_2	−0.81	2.00 2.10	0.45	H_2S	−1.93	2.21	−0.17
NO	−4.28	1.74	0.32	H_2O	−1.03	2.19	−0.09
NO_2	−3.06	2.21	0.45	O_3	−3.59	1.99	0.70
SO_3	−2.18	2.01	0.89	O_2	−3.24	1.95 2.07	0.59
SO_2	−1.89	2.10	0.28	N_2	−1.36	1.89	0.22

in an increase of the effective Coulomb potential (Zhang et al., 2018). The adsorbed gas molecules contribute dramatically to the total DOS in some specific areas (for CO, near 3.75, −5.82, and −6.85 eV; for NO, near 2.01, −1.15, and −7.42 eV; for O_3, near 4.25, 3.45, −4.15, −6.75, and −7.71 eV; for H_2S, near 2.85 and −7.68 eV), which are derived from the outermost *p* orbitals of the coordinated atoms in the gas molecules. And obvious deformations have taken place at these areas in the total DOS curves. Meanwhile, there exist apparent overlaps between the Pt *5d* and the outmost *p* orbitals of the coordination atoms, indicating the obvious chemical interactions between PtN_3-CNT and the adsorbed gas molecules. It can also be concluded that these outermost *p* orbitals of the coordinated atoms in the adsorbed gas molecules play an important role in the adsorption of gases on PtN_3-CNT.

Application of PtN_3-CNT in Air Purification

Previous calculated results show that PtN_3-CNT has strong adsorption capacity for the toxic gas molecules (NO, NO_2, SO_3, SO_2, CO, NH_3, H_2S, and O_3) with E_{ad} in the range of −1.85∼−4.28 eV, while relatively weaker adsorption performance for the main components of the air except oxygen (N_2, H_2O, and CO_2) with E_{ad} in the range of −0.81∼−1.36 eV. If these gas molecules were adsorbed on the surface of PtN_3-CNT, it would be very difficult for the toxic gas molecules to desorb, but the main components of the air may be desorbed by heating. Therefore, we assume that PtN_3-CNT possess the potential as an excellent gas adsorbent for the air purification.

To prove this hypothesis, the recovery time for the gas molecules to desorb from the PtN_3-CNT surface was investigated based on the transition state theory and van't Hoff-Arrhenius expression (Zhang et al., 2009) as below:

$$\tau = A^{-1} e^{(-E_a / K_B T)} \quad (3)$$

where A, K_B, and T represent the attempt frequency (10^{12} s^{-1}) (Peng et al., 2004), the Boltzmann constant [8.318×10^{-3} kJ (mol K)$^{-1}$] and the temperature, respectively. E_a is the desorption potential barrier and can be considered the same as E_{ad}. From Equation (3), it can be concluded that the recovery time increases exponentially with the increase of E_{ad}. The larger the E_{ad} is, the more difficult the gas desorption process is. And increasing the temperature can effectively accelerate this process (Schedin et al., 2007; Yang et al., 2017; Zhang X. et al., 2017). According to the previously obtained E_{ad} as shown in **Table 1**,

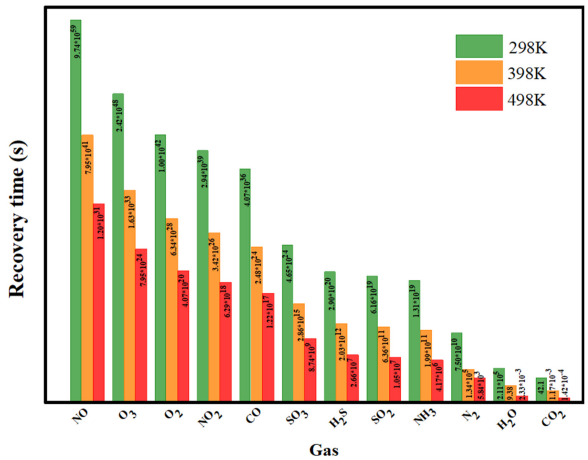

FIGURE 6 | Recovery time for the Gas@PtN_3-CNT systems at various temperatures.

the recovery time for the desorption of all the gas molecules from the PtN_3-CNT surface at 298, 398, 498 K were calculated (listed in **Supplementary Table 1**) and plotted in **Figure 6**. The results showed that the desorption of all the gas molecules is very unrealistic at room temperature, except for CO_2 which requires only 42.10 s to desorb from the surface of PtN_3-CNT. The good adsorption performance and short recovery time at ambient temperature make PtN_3-CNT an excellent candidate for CO_2 sensing. When the temperature is increased by 100–398 K, H_2O can be desorbed with a recovery time of 9.38 s. When the temperature is increased again by 100–498 K, N_2 will be desorbed with a recovery time of 1.62 h, while all the toxic gas molecules and O_2 are still adsorbed stably on the surface of PtN_3-CNT. Therefore, considering the excellent thermal stability of PtN_3-CNT at up to 1000 K proved by AIMD previously, and the adsorption and desorption behavior at different temperature, PtN_3-CNT structure is very suitable to act as an adsorbent to remove toxic gases to achieve the purpose of air purification.

CONCLUSION

In summary, we proposed that PtN_3-CNT is an excellent adsorbent for air purification in this work. The adsorption of four main components of the air (N_2, O_2, H_2O, CO_2) and eight common air pollutants (NO, NO_2, SO_3, SO_2, CO,

O_3, NH_3, H_2S) on the surface of PtN_3-CNT were studied using first-principles calculations. The calculation results about *d*-band centers and adsorption energies confirmed that the N_3 dopant have effectively improved the reactivity of CNTs, thereby enhancing the adsorption performance of PtN_3-CNT for gas molecules. All the considered gases can be adsorbed stably on PtN_3-CNT, and the adsorption energies for the toxic gas molecules (−1.85∼−4.28 eV) are larger than those for the main components of the air except oxygen (−0.81∼−1.36 eV). The recovery time for the desorption of all the gas molecules from the PtN_3-CNT surface at 298, 398, 498 K were calculated. The obtained results showed that CO_2, H_2O, and N_2 can be desorbed at 298, 398, and 498 K, respectively, while all the air pollutants and O_2 are always adsorbed stably. Therefore, PtN_3-CNT can be used to purify the air by firstly adsorbing the gas mixture and then gradually releasing the air by heating.

DATA AVAILABILITY STATEMENT

The raw data supporting the conclusions of this article will be made available by the authors, without undue reservation.

AUTHOR CONTRIBUTIONS

WL, JX, YY, and SL conceived the research. YY, KG, and SL performed the calculations and analyzed the data. WL, JX, and YY wrote the manuscript. LC helped to revise the manuscript. All authors discussed and commented on the manuscript and approved the submitted version.

FUNDING

This work was supported by the Zhejiang Provincial Natural Science Foundation of China (No. LQ20B030002) and the National Natural Science Foundation of China (Nos. 12075211, 11975206, 11875236, and U1832150).

SUPPLEMENTARY MATERIAL

The Supplementary Material for this article can be found online at: https://www.frontiersin.org/articles/10.3389/fevo.2022.897410/full#supplementary-material

REFERENCES

Babu, D. J., Lange, M., Cherkashinin, G., Issanin, A., Staudt, R., and Schneider, J. J. (2013). Gas adsorption studies of CO_2 and N_2 in spatially aligned double-walled carbon nanotube arrays. *Carbon* 61, 616–623. doi: 10.1016/j.carbon.2013.05.045

Bader, R. F. W., and Beddall, P. M. (1972). Virial field relationship for molecular charge distributions and the spatial partitioning of molecular properties. *J. Chem. Phys.* 56, 3320–3329. doi: 10.1063/1.1677699

Cai, G., Yan, P., Zhang, L., Zhou, H.-C., and Jiang, H.-L. (2021). Metal–Organic framework-based hierarchically porous materials: synthesis and applications. *Chem. Rev.* 121, 12278–12326. doi: 10.1021/acs.chemrev.1c00243

Chadi, D. J. (1977). Special points for brillouin-zone integrations. *Phys. Rev. B* 16, 1746–1747. doi: 10.1103/PhysRevB.16.1746

Cui, H., Zhang, X., Chen, D., and Tang, J. (2018). Adsorption mechanism of SF_6 decomposed species on pyridine-like PtN_3 embedded CNT: a DFT study. *Appl. Surf. Sci.* 447, 594–598. doi: 10.1016/j.apsusc.2018.03.232

Cui, J., Zhang, K., Zhang, X., and Lee, Y. (2020). A computational study to design zeolite-templated carbon materials with high performance for CO_2/N_2 separation. *Microporous Mesoporous Mater.* 295:109947. doi: 10.1016/j.micromeso.2019.109947

DeCoste, J. B., and Peterson, G. W. (2014). Metal–Organic frameworks for air purification of toxic chemicals. *Chem. Rev.* 114, 5695–5727. doi: 10.1021/cr4006473

Esrafili, M. D., and Heydari, S. (2019). B-doped C_3N monolayer: a robust catalyst for oxidation of carbon monoxide. *Theor. Chem. Acc.* 138:57. doi: 10.1007/s00214-019-2444-z

Feng, H., Ma, J., and Hu, Z. (2010). Nitrogen-doped carbon nanotubes functionalized by transition metal atoms: a density functional study. *J. Mater. Chem.* 20:1702. doi: 10.1039/b915667d

Gao, Z., Sun, Y., Li, M., Yang, W., and Ding, X. (2018). Adsorption sensitivity of Fe decorated different graphene supports toward toxic gas molecules (CO and NO). *Appl. Surf. Sci.* 456, 351–359. doi: 10.1016/j.apsusc.2018.06.112

Grimme, S., Antony, J., Ehrlich, S., and Krieg, H. (2010). A consistent and accurate ab initio parametrization of density functional dispersion correction (DFT-D) for the 94 elements H-Pu. *J. Chem. Phys.* 132:154104. doi: 10.1063/1.3382344

Guo, K., Liu, S., Tu, H., Wang, Z., Chen, L., Lin, H., et al. (2021). Crown ethers in hydrogenated graphene. *Phys. Chem. Chem. Phys.* 23, 18983–18989. doi: 10.1039/D1CP03069H

Hoover, W. G. (1985). Canonical dynamics: equilibrium phase-space distributions. *Phys. Rev. A* 31, 1695–1697. doi: 10.1103/PhysRevA.31.1695

Hou, J., Zhang, H., Hu, Y., Li, X., Chen, X., Kim, S., et al. (2018). Carbon nanotube networks as nanoscaffolds for fabricating ultrathin carbon molecular sieve membranes. *ACS Appl. Mater. Interfaces* 10, 20182–20188. doi: 10.1021/acsami.8b04481

Kohn, W., and Sham, L. J. (1965). Self-Consistent equations including exchange and correlation effects. *Phys. Rev.* 140, A1133–A1138. doi: 10.1103/PhysRev.140.A1133

Kresse, G., and Furthmüller, J. (1996). Efficiency of ab-initio total energy calculations for metals and semiconductors using a plane-wave basis set. *Comput. Mater. Sci.* 6, 15–50. doi: 10.1016/0927-0256(96)00008-0

Li, Y., Chen, J., Cai, P., and Wen, Z. (2018). An electrochemically neutralized energy-assisted low-cost acid-alkaline electrolyzer for energy-saving electrolysis hydrogen generation. *J. Mater. Chem. A* 6, 4948–4954. doi: 10.1039/C7TA10374C

Li, Y.-H., Hung, T.-H., and Chen, C.-W. (2009). A first-principles study of nitrogen- and boron-assisted platinum adsorption on carbon nanotubes. *Carbon* 47, 850–855. doi: 10.1016/j.carbon.2008.11.048

Lim, N., Kim, K. H., and Byun, Y. T. (2021). Preparation of defected SWCNTs decorated with en-APTAS for application in high-performance nitric oxide gas detection. *Nanoscale* 13, 6538–6544. doi: 10.1039/D0NR08919B

Liu, D., Li, C., Wu, J., and Liu, Y. (2020). Novel carbon-based sorbents for elemental mercury removal from gas streams: a review. *Chem. Eng. J.* 391:123514. doi: 10.1016/j.cej.2019.123514

Liu, P., Liang, J., Xue, R., Du, Q., and Jiang, M. (2019). Ruthenium decorated boron-doped carbon nanotube for hydrogen storage: a first-principle study. *Int. J. Hydrog. Energy* 44, 27853–27861. doi: 10.1016/j.ijhydene.2019.09.019

Niimura, S., Fujimori, T., Minami, D., Hattori, Y., Abrams, L., Corbin, D., et al. (2012). Dynamic quantum molecular sieving separation of D_2 from H_2 –D_2 mixture with nanoporous materials. *J. Am. Chem. Soc.* 134, 18483–18486. doi: 10.1021/ja305809u

Peng, S., and Cho, K. (2003). Ab initio study of doped carbon nanotube sensors. *Nano Lett.* 3, 513–517. doi: 10.1021/nl034064u

Peng, S., Cho, K., Qi, P., and Dai, H. (2004). Ab initio study of CNT NO2 gas sensor. *Chem. Phys. Lett.* 387, 271–276. doi: 10.1016/j.cplett.2004.02.026

Perdew, J. P., Burke, K., and Ernzerhof, M. (1996). Generalized gradient approximation made simple. *Phys. Rev. Lett.* 77, 3865–3868. doi: 10.1103/PhysRevLett.77.3865

Perreault, F., Fonseca de Faria, A., and Elimelech, M. (2015). Environmental applications of graphene-based nanomaterials. *Chem. Soc. Rev.* 44, 5861–5896. doi: 10.1039/C5CS00021A

Poudel, Y. R., and Li, W. (2018). Synthesis, properties, and applications of carbon nanotubes filled with foreign materials: A review. *Mater. Today Phys.* 7, 7–34. doi: 10.1016/j.mtphys.2018.10.002

Rangel, E., and Sansores, E. (2014). Theoretical study of hydrogen adsorption on nitrogen doped graphene decorated with palladium clusters. *Int. J. Hydrog. Energy* 39, 6558–6566. doi: 10.1016/j.ijhydene.2014.02.062

Ren, H., Koshy, P., Chen, W.-F., Qi, S., and Sorrell, C. C. (2017). Photocatalytic materials and technologies for air purification. *J. Hazard. Mater.* 325, 340–366. doi: 10.1016/j.jhazmat.2016.08.072

Samaddar, P., Son, Y.-S., Tsang, D. C. W., Kim, K.-H., and Kumar, S. (2018). Progress in graphene-based materials as superior media for sensing, sorption, and separation of gaseous pollutants. *Coord. Chem. Rev.* 368, 93–114. doi: 10.1016/j.ccr.2018.04.013

Schedin, F., Geim, A. K., Morozov, S. V., Hill, E. W., Blake, P., Katsnelson, M. I., et al. (2007). Detection of individual gas molecules adsorbed on graphene. *Nat. Mater.* 6, 652–655. doi: 10.1038/nmat1967

Sun, X., Bao, J., Li, K., Argyle, M. D., Tan, G., Adidharma, H., et al. (2021). Advance in using plasma technology for modification or fabrication of carbon-based materials and their applications in environmental, material, and energy fields. *Adv. Funct. Mater.* 31:2006287. doi: 10.1002/adfm.202006287

Tabtimsai, C., Rakrai, W., Phalinyot, S., and Wanno, B. (2020). Interaction investigation of single and multiple carbon monoxide molecules with Fe-, Ru-, and Os-doped single-walled carbon nanotubes by DFT study: applications to gas adsorption and detection nanomaterials. *J. Mol. Model.* 26:186. doi: 10.1007/s00894-020-04457-7

Tabtimsai, C., Somtua, T., Motongsri, T., and Wanno, B. (2018). A DFT study of H_2CO and HCN adsorptions on 3d, 4d, and 5d transition metal-doped graphene nanosheets. *Struct. Chem.* 29, 147–157. doi: 10.1007/s11224-017-1013-0

Teng, W., Bai, N., Chen, Z., Shi, J., Fan, J., and Zhang, W. (2018). Hierarchically porous carbon derived from metal-organic frameworks for separation of aromatic pollutants. *Chem. Eng. J.* 346, 388–396. doi: 10.1016/j.cej.2018.04.051

Wang, H., Li, J., Li, K., Lin, Y., Chen, J., Gao, L., et al. (2021). Transition metal nitrides for electrochemical energy applications. *Chem. Soc. Rev.* 50, 1354–1390. doi: 10.1039/D0CS00415D

Wang, L., Zhu, C., Xu, M., Zhao, C., Gu, J., Cao, L., et al. (2021). Boosting activity and stability of metal single-atom catalysts via regulation of coordination number and local composition. *J. Am. Chem. Soc.* 143, 18854–18858. doi: 10.1021/jacs.1c09498

Yang, A.-J., Wang, D.-W., Wang, X.-H., Chu, J.-F., Lv, P.-L., Liu, Y., et al. (2017). Phosphorene: a promising candidate for highly sensitive and selective sf6 decomposition gas sensors. *IEEE Electron Device Lett.* 38, 963–966. doi: 10.1109/LED.2017.2701642

Zhang, A., Liang, Y., Zhang, H., Geng, Z., and Zeng, J. (2021). Doping regulation in transition metal compounds for electrocatalysis. *Chem. Soc. Rev.* 50, 9817–9844. doi: 10.1039/D1CS00330E

Zhang, D., Cao, Y., Yang, Z., and Wu, J. (2020). Nanoheterostructure construction and DFT study of Ni-Doped In_2O_3 Nanocubes/WS_2 hexagon nanosheets for formaldehyde sensing at room temperature. *ACS Appl. Mater. Interfaces* 12, 11979–11989. doi: 10.1021/acsami.9b15200

Zhang, D., Wu, J., Li, P., and Cao, Y. (2017). Room-temperature SO_2 gas sensing properties based on metaldoped MoS_2 nanoflower: an experimental and density functional theory Investigation. *J. Mater. Chem. A* 5, 20666–20677. doi: 10.1039/C7TA07001B

Zhang, D., Yang, Z., Li, P., Pang, M., and Xue, Q. (2019). Flexible self-powered high-performance ammonia sensor based on Au-decorated MoSe2 nanoflowers driven by single layer MoS_2-flake piezoelectric nanogenerator. *Nano Energy* 65:103974. doi: 10.1016/j.nanoen.2019.103974

Zhang, X., Cui, H., Chen, D., Dong, X., and Tang, J. (2018). Electronic structure and H_2S adsorption property of Pt_3 cluster decorated (8, 0) SWCNT. *Appl. Surf. Sci.* 428, 82–88. doi: 10.1016/j.apsusc.2017.09.084

Zhang, X., Dai, Z., Chen, Q., and Tang, J. (2014). A DFT study of SO_2 and H_2S gas adsorption on Au-doped single-walled carbon nanotubes. *Phys. Scr.* 89:065803. doi: 10.1088/0031-8949/89/6/065803

Zhang, X., Gao, B., Creamer, A. E., Cao, C., and Li, Y. (2017). Adsorption of VOCs onto engineered carbon materials: a review. *J. Hazard. Mater.* 338, 102–123. doi: 10.1016/j.jhazmat.2017.05.013

Zhang, Y.-H., Chen, Y.-B., Zhou, K.-G., Liu, C.-H., Zeng, J., Zhang, H.-L., et al. (2009). Improving gas sensing properties of graphene by introducing dopants and defects: a first-principles study. *Nanotechnology* 20:185504. doi: 10.1088/0957-4484/20/18/185504

Zhao, C., and Wu, H. (2018). A first-principles study on the interaction of biogas with noble metal (Rh, Pt, Pd) decorated nitrogen doped graphene as a gas sensor: a DFT study. *Appl. Surf. Sci.* 435, 1199–1212. doi: 10.1016/j.apsusc.2017.11.146

Zhao, J., and Yang, X. (2003). Photocatalytic oxidation for indoor air purification: a literature review. *Build. Environ.* 38, 645–654. doi: 10.1016/S0360-1323(02)00212-3

Zhou, X., Tian, W. Q., and Wang, X.-L. (2010). Adsorption sensitivity of Pd-doped SWCNTs to small gas molecules. *Sens. Actuators B: Chem.* 151, 56–64. doi: 10.1016/j.snb.2010.09.054

Zhou, Y., Neyerlin, K., Olson, T. S., Pylypenko, S., Bult, J., Dinh, H. N., et al. (2010). Enhancement of Pt and Pt-alloy fuel cell catalyst activity and durability via nitrogen-modified carbon supports. *Energy Environ. Sci* 3:1437. doi: 10.1039/c003710a

Conflict of Interest: The authors declare that the research was conducted in the absence of any commercial or financial relationships that could be construed as a potential conflict of interest.

Publisher's Note: All claims expressed in this article are solely those of the authors and do not necessarily represent those of their affiliated organizations, or those of the publisher, the editors and the reviewers. Any product that may be evaluated in this article, or claim that may be made by its manufacturer, is not guaranteed or endorsed by the publisher.

frontiers | Frontiers in Environmental Science

ORIGINAL RESEARCH
published: 29 April 2022
doi: 10.3389/fenvs.2022.894887

Assessing the Impacts of Climate Change on Meteorology and Air Stagnation in China Using a Dynamical Downscaling Method

Anqi Hu[1], Xiaodong Xie[1], Kangjia Gong[1], Yuhui Hou[2], Zhan Zhao[3] and Jianlin Hu[1]*

[1]Jiangsu Key Laboratory of Atmospheric Environment Monitoring and Pollution Control, Collaborative Innovation Center of Atmospheric Environment and Equipment Technology, Nanjing University of Information Science and Technology, Nanjing, China, [2]Tongxiang Meteorological Bureau, Jiaxing, China, [3]California Air Resources Board, Sacramento, CA, United States

This study utilizes the Weather Research and Forecasting model with a higher resolution (36 km × 36 km) to dynamically downscale the Community Earth System Model results forced by the three representative concentration pathways (RCP) scenarios (RCP4.5, RCP6.0, and RCP8.5) over China. The goal was to compare meteorological fields during the present (2006–2015) and future (2046–2055) climatological periods. An appropriate air stagnation judgment index was selected to explore the effect of climate change on air quality-related meteorological conditions. The results show that the occurrence of wintertime air stagnation over China in the middle of this century (2046–2055) will reduce slightly, with the largest reduction projected under the RCP8.5 scenario (–4 times). However, long-lasting air stagnation events (ASE) are projected to increase in the future, and this increasing trend is more obvious under the RCP8.5 scenario. The projected increase in the long-lasting ASE in different regions of China ranges from 3 to 11 times. Among these, Central China has the largest increase, followed by East and Northeast China, while South China has the lowest increase in ASE. Our results indicate that more attention should be dedicated to extreme pollution events that may potentially be caused by long-lasting air stagnation events in the future.

Keywords: climate change, air stagnation events, downscaling, RCP scenarios, China

OPEN ACCESS

Edited by:
Yuqiang Zhang, University of North Carolina at Chapel Hill, United States

Reviewed by:
Yang Gao, Ocean University of China, China
Jian Sun, University Corporation for Atmospheric Research (UCAR), United States

****Correspondence:***
Xiaodong Xie
xiaodong.xie@nuist.edu.cn

Specialty section:
This article was submitted to Atmosphere and Climate, a section of the journal Frontiers in Environmental Science

Received: *12 March 2022*
Accepted: *13 April 2022*
Published: *29 April 2022*

Citation:
Hu A, Xie X, Gong K, Hou Y, Zhao Z and Hu J (2022) Assessing the Impacts of Climate Change on Meteorology and Air Stagnation in China Using a Dynamical Downscaling Method. Front. Environ. Sci. 10:894887. doi: 10.3389/fenvs.2022.894887

1 INTRODUCTION

With the rapid development of the Chinese economy and the accelerated process of industrialization, air pollution events of long durations and high concentrations occur frequently over China (Horton et al., 2012; Wang et al., 2019; Qin et al., 2021). The Chinese government has actively taken preventive measures to strictly control air pollutant emissions nationwide. Although the annual mean $PM_{2.5}$ (fine particle matter with aerodynamic diameter ≤2.5 μm) concentrations have continued to decrease in recent years, severe haze pollution events still occur frequently during the winters, especially in North China (Chen and Wang, 2015; Sun et al., 2019). Therefore, in addition to strictly controlling emission sources, other factors, such as meteorological conditions, need to be considered to improve air quality. The interactions between climate change and air pollution have been hot topics in recent years. Climate and weather conditions strongly influence the spatial and temporal distribution of air pollutants concentrations (Kinney, 2018). When emission sources are relatively stable, diffusion, transmission, and transformation of atmospheric pollutants in

a given region majorly depend on local meteorological conditions (Shi et al., 2020). The impact of meteorological conditions on the concentration of air pollutants can vary dozens of times (Zhang et al., 2010). Therefore, to improve air quality, it is not only necessary to control emission sources, but also to combine meteorological conditions and climate change.

A factor that causes deterioration in air quality is atmospheric stagnation under high-pressure systems and the resultant weak near-surface winds, compounded by stable vertical temperature profiles (inversion) (Lee et al., 2020). In addition to intensive emissions, stagnant meteorological conditions, characterized by slow winds, strong inversion, and shallow boundary layer, are key to the formation of severe haze pollution events (Mu and Liao, 2014; Zhang et al., 2014; Zhang et al., 2015; Cai et al., 2017; Wang et al., 2018; Xu et al., 2020). Many studies have assessed the association between air stagnation and haze pollution in China (Zhao et al., 2013; Wang et al., 2014; Zhang et al., 2014; Cai et al., 2017; Jing et al., 2017; Liao et al., 2018; Wang et al., 2018). Previous research has shown that a lower boundary layer creates covered pot-like conditions, limiting the vertical diffusion of pollutants (Yang et al., 2021). The weakening effect of quiet wind on the horizontal diffusion capacity of the atmosphere makes it difficult for pollutants to diffuse (Rigby and Toumi, 2008; Fu et al., 2014). The continuous absence of precipitation also reduces the wet deposition of pollutants, thereby deteriorating air quality (Guo et al., 2016). Extreme pollution events are thus often caused by long-lasting stagnation conditions (Cai et al., 2017).

To objectively measure stagnation conditions and their impacts on air pollution, several air stagnation indices (ASI) were proposed (Horton et al., 2012; Mu and Liao, 2014; Zhang et al., 2014; Huang et al., 2018; Li et al., 2020). The most used ASI was proposed by Horton et al. (2012), which is based on the wind speed at 10 m (WS10) and 500 hPa, while considering total precipitation (PCP). Collectively, these parameters are used as indicators of horizontal atmospheric dispersion capacity and wet deposition, respectively. However, this index has a weak correspondence with pollutants such as $PM_{2.5}$ and O_3 (Li et al., 2014; Kerr and Waugh, 2018; Garrido-Perez et al., 2019). Huang et al. (2018) replaced the 10 m and 500 hPa wind velocity fields with wind flux in the boundary layer and added the available potential energy based on the convective available potential energy (CAPE) and convective inhibition (CIN). Wang et al. (2018) used atmospheric planetary boundary layer height (PBLH) instead of 500 hPa wind speed to characterize the vertical mixing of pollutants. Garrido-Perez et al. (2021) compared the performance of the three ASIs (Horton et al., 2012; Huang et al., 2018; Wang et al., 2018) and found that all three revealed similar spatial patterns in the stagnation frequency. Furthermore, the response of PM_{10} concentrations to stagnation varied with ASI and depended on location and season. The main exceptions occurred in coastal areas, where the ASI defined by Wang et al. (2018) seemed to be more accurate than the other ASIs.

Climate change will lead to changes in air stagnation conditions, and global warming may increase the static stability of the lower troposphere by reducing near-surface wind speed, which means air stagnation events (ASE) will be more frequent in the future (Lee et al., 2020). Horton et al. (2012) reported that highly industrialized areas, such as eastern China, are more sensitive to climate warming and the incidence of air stagnation in such regions was expected to increase by 12%–25% in the late-21st century (2081–2100) as compared to the late-20th century (1981–2000). Wang et al. (2018) calculated ASI from observational data to find strong air stagnation conditions from autumn to winter over China, especially in the Sichuan basin and the Beijing-Tianjin-Hebei (BTH) region (more than 40% of the whole year).

The Global Climate Model (GCM) has been used widely in previous studies for climate change projections (Hewitson and Crane, 2006). However, the spatial resolution of GCMs is coarse and they cannot predict regional-scale weather patterns well, and thus, are not suitable for high-resolution regional climate, air quality, and health impact research. Dynamical downscaling is a kind of downscaling technique that converts coarse resolution outputs from GCM to fine spatial resolution by developing regional climate models (Lee et al., 2014). This study uses climate projections from the Community Earth System Model (CESM) provided by the Coupled Model Intercomparision Project 5 (CMIP5) to obtain initial and boundary conditions for the Weather Research and Forecasting (WRF) model. We have generated regional-scale meteorological fields for the present (2006–2015) and future (2046–2055) climatological periods under the three RCP scenarios (RCP4.5, RCP6.0, and RCP8.5). As mentioned above, we choose the ASI defined by Wang et al. (2018) to calculate atmospheric stagnation in this study and explore the impacts of climate change on air stagnation. This paper is organized as follows. **Section 2** describes the data and methods used in this study, while the results are presented and discussed in **Section 3**. **Section 4** comprises a summary and conclusions.

2 METHODS

2.1 Data Description and Experimental Setup

Global bias-corrected data produced by CESM version 1 that participated in the CMIP5 was obtained from the website of the Research Data Archive (https://rda.ucar.edu/datasets/ds316.1/ #! description). The dataset was provided in the Intermediate File Format specific to WRF and contained all the variables needed for the initial and boundary conditions for WRF simulations. This dataset had already been bias-corrected using the European Centre for Medium-Range Weather Forecasts (ECMWF) Interim Reanalysis (ERA-Interim) fields for 1981–2005, following the method of Bruyère et al. (2014). All the variables had 26 pressure levels and were provided in files at 6-hourly intervals. Files were available for a simulation for the present (1951–2005) and three future scenarios (RCP4.5, RCP6.0, and RCP8.5) spanning 2006–2100.

We ran the WRF model to generate hourly meteorological fields of the "Basecase" (2006–2015) and the three RCP cases (RCP4.5, RCP6.0, RCP8.5) for the winter months (December, January, and

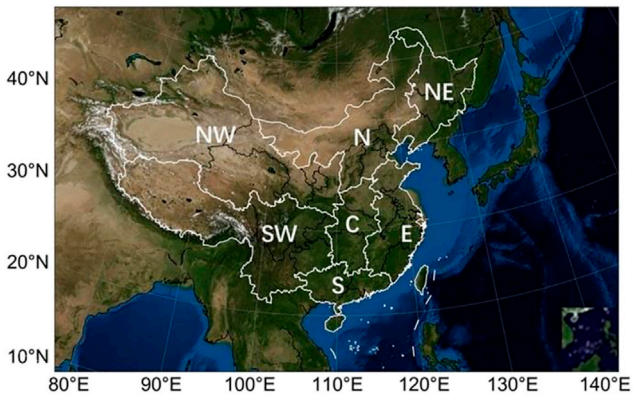

FIGURE 1 | Model domain and sub-regions used for analysis. E: East China, N: North China, C: Central China, S: South China, SW: Southwest China, NW: Northwest China, NE: Northeast China.

February) of 2046–2055. The simulation domain covered the entirety of China with a spatial resolution of 36 km × 36 km (**Figure 1**). The physical options used to drive the WRF simulations are listed in **Table 1** (Hu et al., 2016), including the new Thompson microphysics scheme (Thompson et al., 2008), Rapid Radiative Transfer Model (RRTM) longwave radiation (Mlawer et al., 1997), and Yonsei University PBL parameterization (Hong et al., 2006). Due to corrupted data caused by a modelling bug in CESM, bias-corrected data was unavailable for RCP2.6. Thus, we chose three scenarios (RCP4.5, RCP6.0, and RCP8.5), spanning the winter of 2046–2055, to drive WRF v3.8 for future analyses. Results from the CESM model using the RCP6.0 emission scenario were used as the meteorological boundary and initial fields of the WRF model for the 2006–2015 periods. The WRF model was configured with 44 vertical layers from surface to 50 hPa (**Supplementary Figure S1**). Because of the vast territory of China, climate and air quality vary in the different regions. To better compare and summarize changes in different regions, we divided China into seven regions based on differences in climate and administration (**Figure 1**), including East China (E), North China (N), Central China (C), South China (S), Southwest China (SW), Northwest China (NW), and Northeast China (NE).

2.2 Air Stagnation Days and Events

We adopt the ASI definition proposed by Wang et al. (2018), which is shown in **Eq. 1**. This parameterization is derived using PBLH and WS10 data to fit the normalized daily $PM_{2.5}$ concentrations during the winter. This could better explain haze events and has been used in other studies (Zhang et al., 2019; Gao et al., 2020). For each grid cell (i, j), if the daily cumulative precipitation is <1 mm and the daily average PBLH and WS10 satisfy **Eq. 1**, the air is considered stagnant and the given day is considered to be an air stagnation day (ASD). We define an ASE as an event in which air stagnation lasts for 3 days or more.

$$\boldsymbol{PBLH_{i,j} < 0.759 * exp\left(-0.6 * WS10_{i,j}\right) + 0.264} \quad (1)$$

2.3 Model Performance Evaluation

Evaluation of model performance is an important step to verify the reliability of modelling results and to establish confidence for further application. The WRF simulations were validated using the fifth-generation European Centre for Medium-Range Weather Forecasts (ECMWF) reanalysis data for global climate and weather (ERA5). Monthly averaged data (Hersbach et al., 2019) from ERA5 for 2006 to 2015 were obtained from the website https://cds.climate.copernicus.eu/cdsapp#!/dataset/. In this study, statistical metrics and benchmarks recommended by the United States EPA were used. The normalized mean deviation (NMB), normalized mean error (NME), and the Pearson correlation coefficient (R) of the observed and simulated values were calculated to quantitatively evaluate model performance (Emery et al., 2017). The corresponding equations are shown below:

$$\boldsymbol{NMB = \sum \frac{(P_j - O_j)}{O_j} \times 100} \quad (2)$$

$$\mathbf{NME = \sum \frac{|P_j - O_j|}{O_j} \times 100} \quad (3)$$

$$\mathbf{R = \frac{\sum\left[\left(P_j - \bar{P}\right) \times \left(O_j - \bar{O}\right)\right]}{\sqrt{\sum\left(P_j - \bar{P}\right)^2 \times \sum\left(O_j - \bar{O}\right)^2}}} \quad (4)$$

3 RESULTS AND DISCUSSION

3.1 Evaluation of Present Climatological Simulation

Figure 2 shows the spatial distribution of wintertime (DJF) meteorological fields from the Basecase and the corresponding ERA5 reanalysis data. Detailed statistical metrics are listed in

TABLE 1 | Major physics options for WRF simulations.

Physics	Option	Meaning
Microphysics	mp_physics = 8	New Thompson et al. scheme
Long wave radiation	ra_lw_physics = 1	RRTM scheme
Shortwave radiation	ra_sw_physics = 2	Goddard shortwave
Surface layer	sf_sfclay_physics = 1	Monin-Obukhov similarity theory
Land surface	sf_surface_physics = 2	MM5 Land surface model
Planetary boundary layer	bl_pbl_physics = 1	Yonsei University scheme
Cumulus parameterization	cu_physics = 3	Grell-Devenyi ensemble scheme
Urban surface	sf_urban_surface = 0	Not enabled

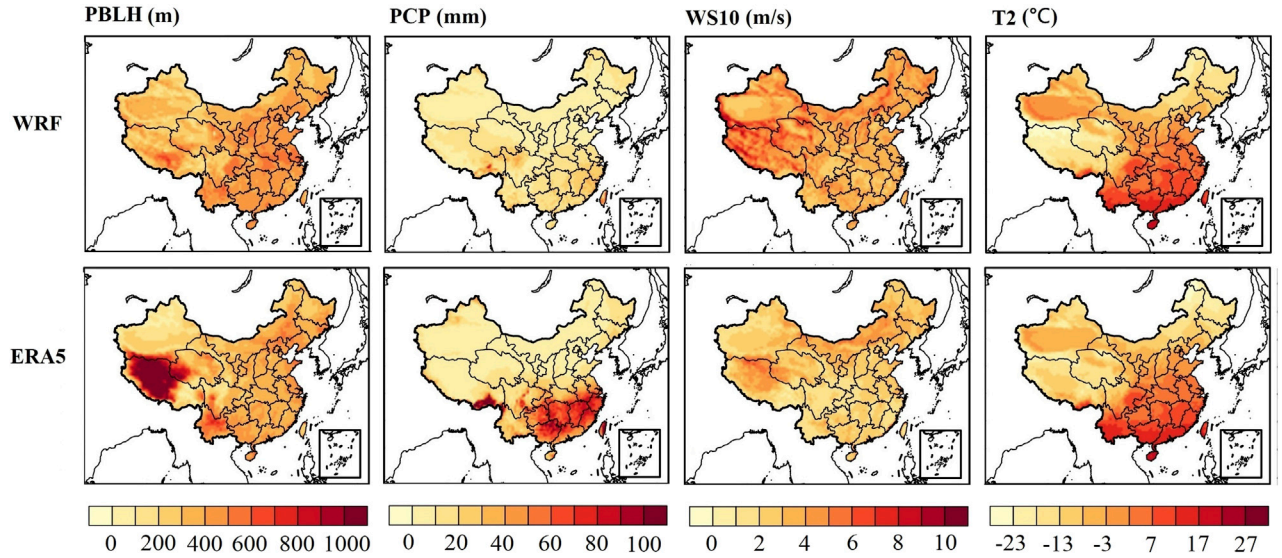

FIGURE 2 | Comparisons of meteorological fields from Basecase simulations and ERA5 data.

TABLE 2 | Statistical parameters for simulated meteorology at all grid cells within the model domain.

	ERA5	WRF	Bias	ME	NMB	NME	RMSE	R	IoA
PBLH (m)	490.40	477.92	−12.48	115.87	−0.03	0.24	172.22	0.84	0.90
PCP (mm)	38.54	16.79	−21.75	26.80	−0.56	0.70	45.57	0.47	0.55
WS10 (m/s)	3.91	4.87	0.95	1.10	0.24	0.28	1.60	0.85	0.88
T2 (K)	275.57	276.58	1.01	1.94	0.00	0.01	2.79	0.99	0.99

Table 2. Note that PBLH, WS10, and T2 were averaged from 2006 to 2015, while PCP was calculated as the average of cumulative winter precipitation. As can be seen from **Figure 2**, the simulated PBLH in the Tibetan Plateau and its surrounding areas was significantly underestimated, which might be due to the complex terrain in the region (Wang et al., 2021). Combined with **Table 2**, the mean PBLH within the model domain was 490.4 m in the ERA5 data, while it was 477.92 m according to WRF. The WRF model underestimated PBLH with a mean bias of −12.48 m, while the RMSE was as large as 172.22 m. This indicated that model performances may vary a lot across the different regions. Nevertheless, the simulated PBLH showed a strong positive correlation of 0.84 with ERA5 data, suggesting that the overall model performance was acceptable. The WRF model successfully captured the general pattern of PCP as compared to the ERA5 data, but underestimated PCP in southern China. Previous studies have reported that ERA5 precipitation data are relatively higher than the ground observations over China in winters, with a mean bias of 35% (Jiang et al., 2021; Jiao et al., 2021), which partly explains the discrepancy between WRF simulations and ERA5 data. A comparison of the simulated PCP with the Tropical Rainfall Measuring Mission (TRMM) satellite data for 2006–2015 (**Supplementary Figure S2**) revealed that the WRF-simulated PCP had similar spatial patterns to that of TRMM data. The WRF-simulated mean PCP within the model domain was 15.0 mm, which was close to that of TRMM data (15.5 mm), giving us confidence in the simulated PCP.

The WS10 and T2 (the temperature at 2 m) predicted by WRF showed relatively consistent spatial patterns with those from ERA5 data. WS10 was slightly overestimated with a mean bias of 0.95 m/s. The ME and RMSE of WS10 were both less than 2 m/s, and thus, met the performance criteria suggested by Emery et al. (2001). The model performance for T2 was the best among the selected meteorological factors with correlation coefficients as high as 0.99. To explore the differences in modelling results before and after downscaling, we compared the CESM output with ERA5 data and WRF simulations (**Supplementary Figure S3**; **Supplementary Table S1**). Because bias-corrected CESM output does not provide PBLH and PCP (Bruyère et al., 2014; Bruyère et al., 2015), only projected WS10 and T2 obtained. As **Supplementary Figure S3** shows, both WRF and CESM exhibited good spatial agreement with the ERA5 data. As compared to CESM, WRF could reproduce more regional scale details for both WS10 and T2, especially in the Tibetan Plateau and the Sichuan Basin. Previous studies have indicated that CESM cannot capture topography-induced temperature patterns (Liu et al., 2013; Chen et al., 2018), which is consistent with our results. The biases between CESM and ERA5 were 1.07 m/s and 0.95 K for WS10 and T2,

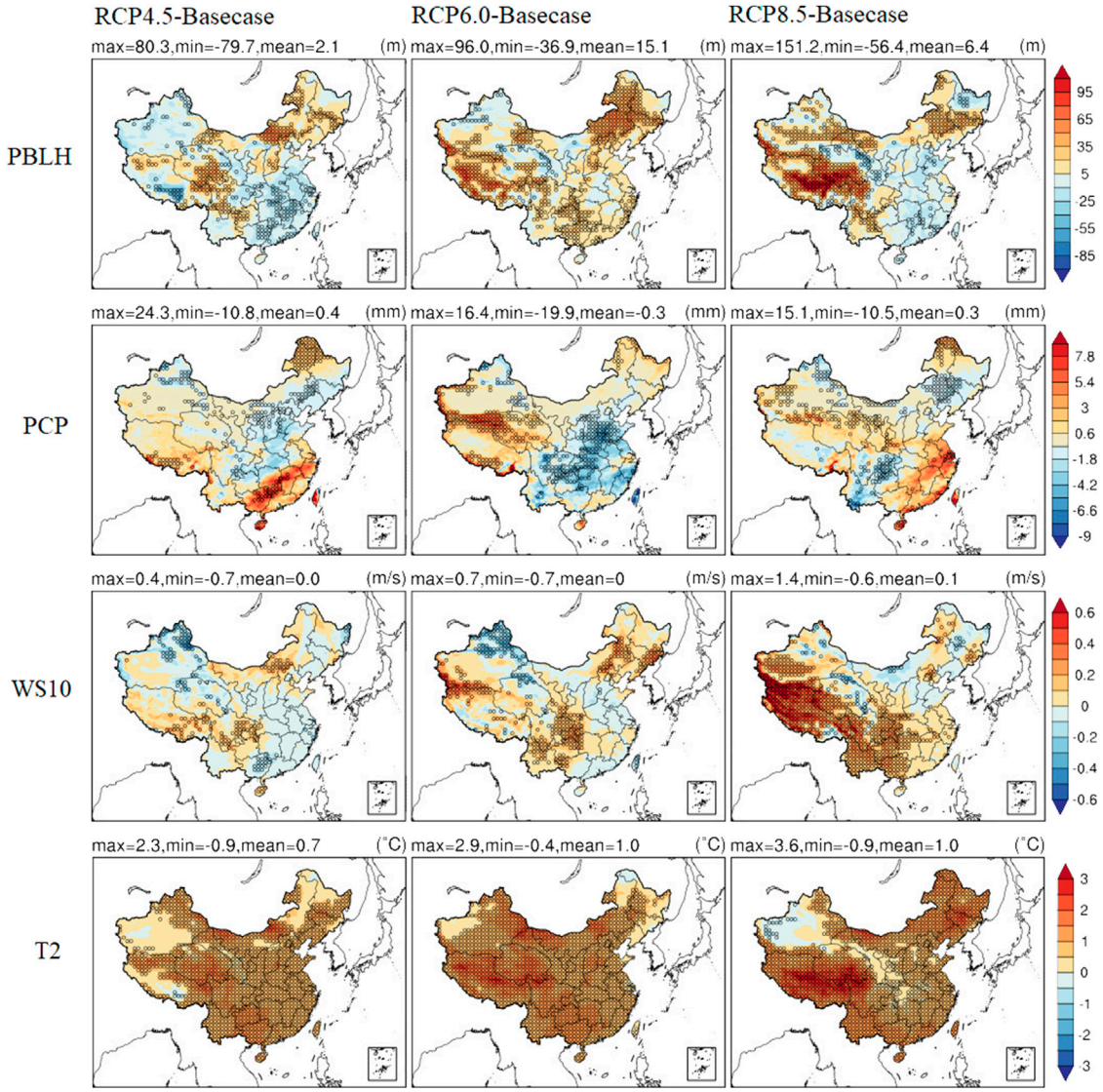

FIGURE 3 | Spatial distributions of the projected changes in meteorological fields for the 2046–2055 period relative to the 2006–2015 period. Significant changes (confidence level of 95%) are marked with circles.

respectively, which was slightly larger than those between WRF and ERA5.

3.2 Changes in Meteorological Conditions Under Different Scenarios

The decadal mean values of PBLH, WS10, T2, and PCP under the three RCP scenarios were calculated and compared with the Basecase to obtain their spatial and temporal variations due to climate change. Note that PCP was calculated as the average cumulative winter precipitation. **Figure 3** shows the WRF-projected changes in PBLH, WS10, T2, and PCP under RCP4.5, RCP6.0, and RCP8.5 scenarios relative to the present period; relative changes in these parameters in the different regions are depicted in **Figure 4**. Wintertime PBLH at the national scale was projected to increase for the 2046–2055 period under the three RCP scenarios. The increase in PBLH was more obvious for the RCP6.0 scenario (15.1 m), followed by RCP8.5 (6.4 m) and RCP4.5 (2.1 m). A significant increase mainly occurred in the Tibetan Plateau and some parts of North and Northeast China under the three RCP scenarios. For Central, East, and South China, the WRF-RCP4.5 and WRF-RCP8.5 projected generally shallow PBLH, while WRF-RCP6.0 showed a weak increase.

The projected changes in PCP in China were more varied among different scenarios. The WRF-RCP4.5 projected wetter conditions in South and East China and slightly drier conditions in Central, North, and Northeast China for the 2046–2055 period. Under RCP6.0, PCP showed a decreasing trend in most of China except Northwest and Northeast China. A significant decrease

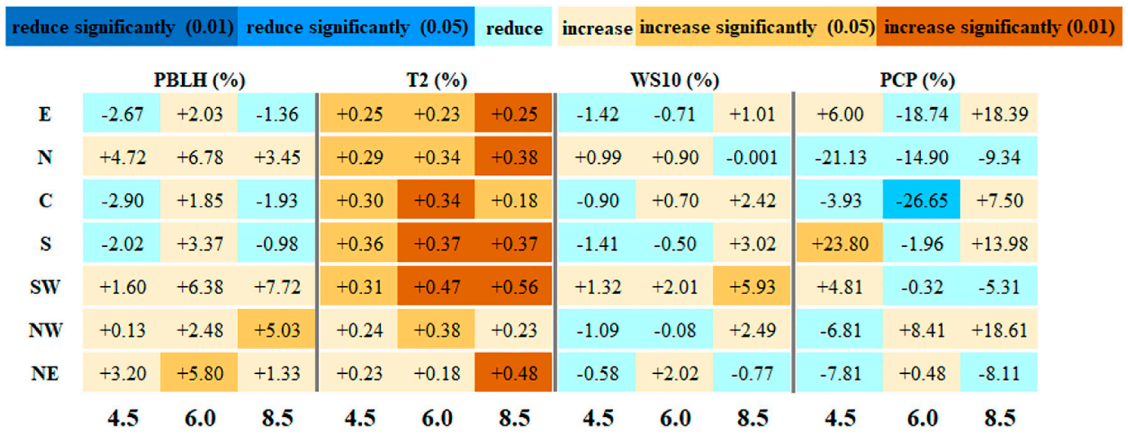

	PBLH (%)			T2 (%)			WS10 (%)			PCP (%)		
E	-2.67	+2.03	-1.36	+0.25	+0.23	+0.25	-1.42	-0.71	+1.01	+6.00	-18.74	+18.39
N	+4.72	+6.78	+3.45	+0.29	+0.34	+0.38	+0.99	+0.90	-0.001	-21.13	-14.90	-9.34
C	-2.90	+1.85	-1.93	+0.30	+0.34	+0.18	-0.90	+0.70	+2.42	-3.93	-26.65	+7.50
S	-2.02	+3.37	-0.98	+0.36	+0.37	+0.37	-1.41	-0.50	+3.02	+23.80	-1.96	+13.98
SW	+1.60	+6.38	+7.72	+0.31	+0.47	+0.56	+1.32	+2.01	+5.93	+4.81	-0.32	-5.31
NW	+0.13	+2.48	+5.03	+0.24	+0.38	+0.23	-1.09	-0.08	+2.49	-6.81	+8.41	+18.61
NE	+3.20	+5.80	+1.33	+0.23	+0.18	+0.48	-0.58	+2.02	-0.77	-7.81	+0.48	-8.11
	4.5	6.0	8.5	4.5	6.0	8.5	4.5	6.0	8.5	4.5	6.0	8.5

FIGURE 4 | The relative changes (2046–2055 relative to 2006–2015) in meteorological fields for different regions of China. Statistical significance is marked with color.

was projected for Central China with a regional mean of 26.65% (−14.13 mm). Under RCP8.5, however, wetter conditions were projected for Central, East, and South China, with a maximum increase of 23.80% (15.1 mm). Significant decreases were found for Southwest and Northeast China, with the regional mean value changes of −2.35 and −1.38 mm, respectively. The PCP in North China showed a consistent decreasing trend under the three RCP scenarios, however, the changes were different for other regions.

For WS10, the national mean value for the 2046–2055 period remained largely unchanged relative to the present 2006–2015 period under the RCP4.5 and RCP6.0 scenarios, while it increased slightly under RCP8.5. The projected WS10 showed an increasing trend under all three scenarios over Southwest China, while the largest increase was found under RCP8.5 (5.93%). For other regions, the projected changes in WS10 were less than 2.02% under the RCP4.5 and RCP6.0 scenarios. As can be seen from **Figure 3**, the projected wintertime temperatures showed a significantly increasing trend over China under all three scenarios. Due to the highest anthropogenic greenhouse gas emissions in RCP8.5, the projected T2 showed the greatest increase, followed by RCP6.0 and RCP4.5. The projected changes in temperature presented obvious regional differences. The largest warming was found in the Tibetan Plateau, with a maximum of 3.6°C increase in average temperature under RCP8.5. The regional mean relative changes in T2 ranged from 0.18% to 0.56%, and the maximum occurred in Southwest China (0.56%).

The CESM-projected WS10 and T2 distributions over China under the three scenarios for the 2046–2055 period were also compared with distributions for the 2006–2015 period (**Supplementary Figures S4, S5**). Generally, there are no obvious differences between the CESM and WRF projections. The WRF-projected mean values of changes in WS10 and T2 under the three scenarios were comparable to those obtained from CESM; however, the latter covered a wider range, which is attributable to the finer spatial resolution of WRF that allowed it to better capture regional-scale climate patterns. As compared to the CESM simulations, the WRF projections showed a decrease in WS10 in South and Northeast China under the RCP6.0 and RCP8.5 scenarios.

3.3 Changes in Air Stagnation Under Different Scenarios

The spatial distributions of ASD and ASE in the Basecase and their changes under the three RCPs over China are shown in **Figure 5**. The projected total ASD during the 2006–2015 period was 167 days, while the changes during the 2046–2055 period under the three RCPs aere 6 days (RCP4.5), −9 days (RCP6.0), and −7 days (RCP8.5), respectively. The maximum (minimum) changes projected were 55 (−43), 37 (−83), and 49 (−68) days under RCP4.5, RCP6.0, and RCP8.5, respectively. Under the RCP4.5 scenario, the projected number of ASD increased in most of China, while it decreased significantly in Northwest, Southwest, and Northwest China under the RCP6.0 and RCP8.5 scenarios. Significant reductions in the number of ASD were also found in Sichuan Basin under RCP8.5, with a minimum of about −68 days. The projected ASE exhibited an increasing trend from south to north during the 2006–2015 period, with a national mean value of 56.9. The changes in ASE under the three scenarios showed similar spatial distributions to those of ASD. Positive changes were mainly projected for East and Central China, and the eastern part of Northwest and Southwest China under RCP4.5. Negative changes were found in most of China under the RCP6.0 and RCP8.5 scenarios. At the national scale, the projected ASE decreased in the future for the three scenarios, with the maximum decrease occurring in RCP8.5 (−4.0), followed by RCP6.0 (−2.9) and RCP4.5 (−0.5).

The probability distribution of ASE and the changes in ASE over the 2046–2055 period relative to 2006–2015 was calculated using the total ASE during the winter of the 10 years for each grid cell in China; the distribution is shown in **Figure 6** to identify the changes of air stagnation under the different scenarios. The numbers of ASE occurrence in China during the winter of the 10 years were mainly concentrated in 30–75 events (for points with a frequency greater than 1%). The projected frequency of

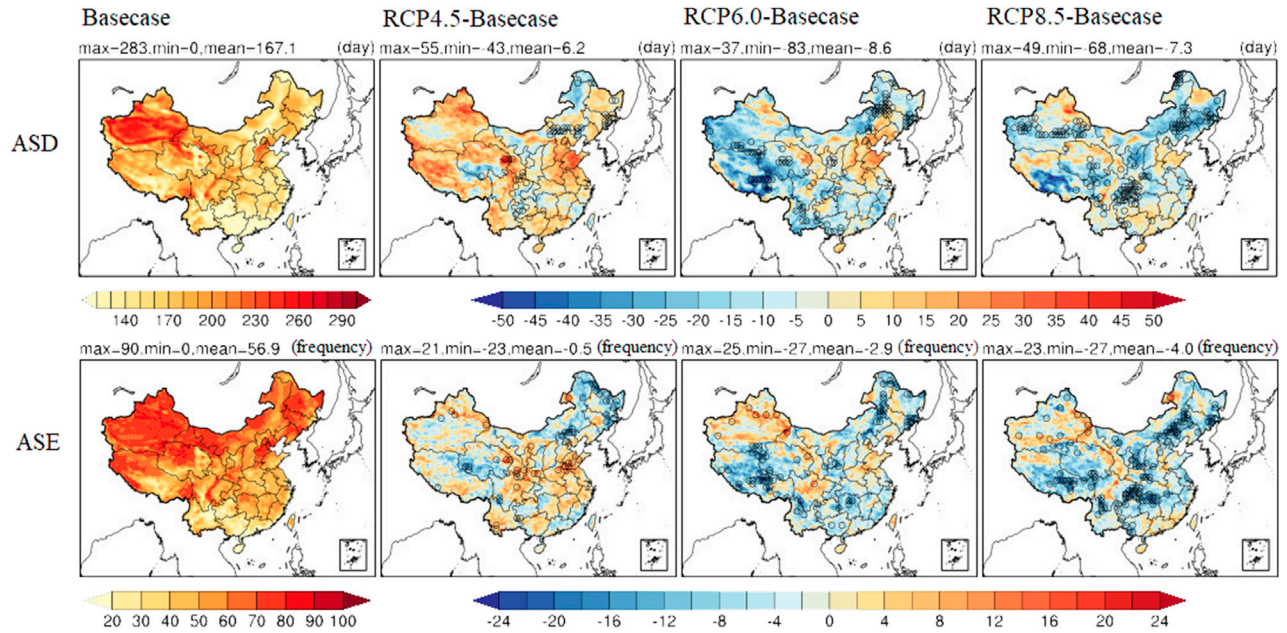

FIGURE 5 | Spatial distribution of atmospheric stagnation days, (ASD) and air stagnation events (ASE) in Basecase and their changes under the three RCPs over China. Significant changes (confidence level of 95%) are marked with circles.

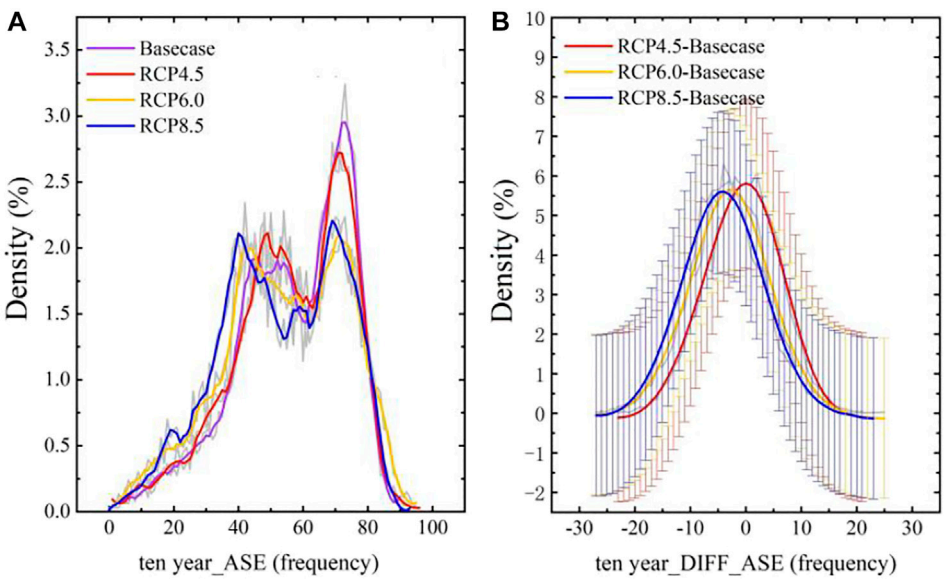

FIGURE 6 | Probability distribution of ASE **(A)** and ASE difference (2046–2055 relative to 2006–2015) **(B)**.

ASE occurrence exhibited a bimodal distribution, with a major peak at around 65–75 times and a minor peak at around 40–55 times. Both the peaks shifted to a less frequent ASE under the three RCP scenarios, which means that the number of wintertime ASE occurrences in China may decrease in the future. As can be seen from **Figure 6B**, the changes in ASE in the 2046–2055 period relative to the 2006–2015 period follow a normal distribution under the three RCP scenarios. The mean changes of winter ASE are −1, −3, and −4 times for RCP4.5, RCP6.0, and RCP8.5, respectively. This is related to the fact that the mean value of PBLH shows an increasing trend in the future, while the mean values of WS10 and PCP change slightly.

Long-lasting air stagnation events can increase the risk of public exposure to high concentrations of air pollutants. **Figure 7** shows the relative frequency distribution of the duration of ASD under the different scenarios for all grid cells over China. For

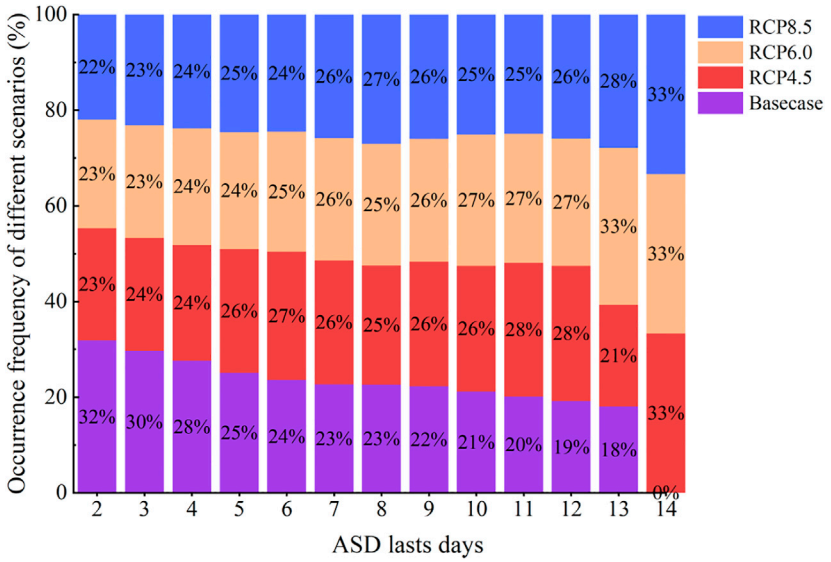

FIGURE 7 | The probability distribution of the number of days that ASE lasted under different representative concentration pathway, (RCP) scenarios.

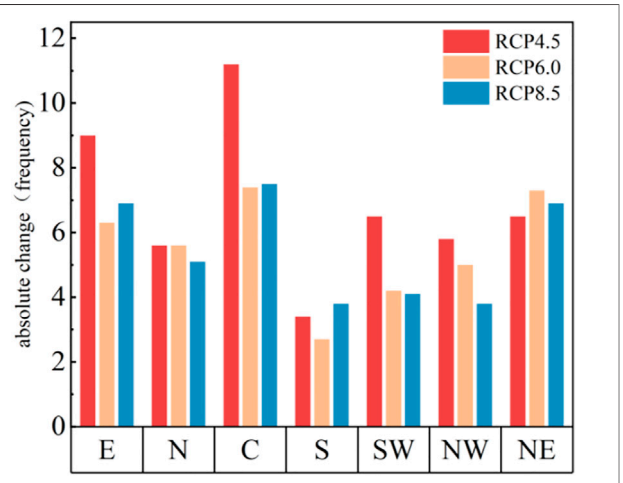

FIGURE 8 | The projected changes in ASE lasted for more than 5 days in the different regions.

example, assuming that an ASE would last for 3 days, the occurrence under different scenarios was in the order of Basecase (28%) > RCP6.0 (26%) > RCP8.5 (23%) > RCP4.5 (22%). As can be seen from **Figure 7**, the longest duration of winter ASE in China was projected to be 14 days. The frequency of ASE lasting 2–4 days was the highest (27%–29%) in the Basecase, but with the increase in duration, the proportion of Basecase gradually decreased. The proportion of the RCP scenario gradually increases, especially under the RCP8.5 scenario, which means that the probability of the occurrence of long-lasting ASE will increase in the future.

The changes in ASE lasted for more than 5 days for the 2046–2055 period relative to the present 2006–2015 period in different regions are given in **Figure 8**. Generally, the occurrence of long-lasting ASE in different regions of China increased by 3–11 times in the mid-century decade. The largest increase was projected unser the RCP4.5 scenario for most regions. Central China was found to have the largest increase among the different regions, followed by East China and Northeast China. The lowest increase was projected for South China and was majorly ascribed to a significant increase in PCP.

4 DISCUSSION

Our results indicate that long-lasting ASE will increase in the mid-century winter (2046–2055) over China due to climate change. Zou et al. (2017) projected that the forcing effect of arctic sea ice will cause more extreme atmospheric static stability in China. Using CMIP5 single-forcing experiments, Lee et al. (2020) suggested that global warming caused by anthropogenic greenhouse gases has likely increased the static stability of the lower troposphere, implying more stagnant conditions in the future. Huang et al. (2017) assessed changes in China's atmospheric stagnation from 1985 to 2014 and reported an upward trend. Based on a multi-model ensemble analysis under RCP8.5, Gao et al. (2020) found that by the end of this century, climate change may lead to an increase in both the duration and frequency of wintertime stagnation events over the North China Plain. Our results are consistent with the above-mentioned studies, providing confidence in our in-depth research on future projections.

This study used a dynamic downscaling method to generate high-resolution regional climate projects based on the outputs from the GCM. Such methods can provide more detailed information about regional or local synoptic patterns as compared to CESM data (**Supplementary Figure S3**). The results from the dynamic downscaling method predicted air

stagnation in various regions over China more suitably. However, results also depend on the choice of ASI as different ASIs may lead to different conclusion for different regions (Garrido-Perez et al., 2021). The ASI used in this study was based on empirical statistical analysis methods (Wang et al., 2018). To compare the differences between ASIs, we calculated the ASI based on atmospheric dynamic methods (Feng et al., 2018). The results are shown in **Supplementary Figure S7**. The projected ASI exhibited an increasing trend under RCP4.5, while it decreased under RCP6.0 and RCP8.5, which is consistent with changes in the projected ASD (**Figure 5**).

Note that only one model is used in this study, although use of multiple model sets may be more representative. In future work, we will evaluate the results of other models to make our findings more representative. In addition, the accuracy of the simulations also influences the credibility of the projections of air stagnation but considering that we have used data from 10 years, we believe that trends delineated in our results will not be affected. Moreover, due to limitations in computation and storage resources, nested simulations were not conducted in our study, such simulations could provide finer spatial resolution. In our follow-up study, we aim to apply the nested WRF simulations with a 12- or 4-km horizontal resolution for key regions, such as the North China Plain and the Yangtze River Delta.

5 CONCLUSION

This study uses future climate projections under three RCP scenarios (RCP4.5, RCP6.0, and RCP8.5) provided by the CESM model based on CMIP5 to drive the WRF model to obtain regional climate projections with a higher resolution (36 km × 36 km) over China. The ERA5 reanalysis data were used to evaluate the performance of WRF projections. The results indicate that the dynamic downscaling method used in this study can generate reasonable regional climate processes. The simulated WS10 and T2 were in good agreement with the ERA5 data. However, PBLH and PCP were underestimated in the Tibetan Plateau and South China, respectively. According to our projections, the occurrence of wintertime ASE will reduce slightly in the future, with the largest reduction (−4 times) expected under the RCP8.5 scenario. Nonetheless, the occurrence of long-lasting ASE will increase in the future, where the increasing trend is more obvious under the RCP8.5 scenario. The projected increase in long-lasting ASE ranged from 3 to 11 times in the different regions, among which Central China had the largest increase, followed by East and Northeast China. The increase in ASE frequency was projected to be the lowest in South China, which is likely attributed to a significant increase in PCP. Our results suggest that atmospheric stagnation in Central and East China should be given more attention in future research and analysis.

DATA AVAILABILITY STATEMENT

The original contributions presented in the study are included in the article/**Supplementary Material**, further inquiries can be directed to the corresponding author.

AUTHOR CONTRIBUTIONS

AH, XX, and JH designed the research. AH wrote the first draft of the manuscript. XX and JH reviewed and modified the manuscript. KG and YH analyzed the results. ZZ downloaded CMIP5 data and set up models. All authors contributed to manuscript revision, and read and approved the submitted version.

FUNDING

This work was supported by the National Key R&D Program of China (2019YFA0606802), the National Natural Science Foundation of China (41975162, 42021004), the Jiangsu Environmental Protection Research Project (2016015).

SUPPLEMENTARY MATERIAL

The Supplementary Material for this article can be found online at: https://www.frontiersin.org/articles/10.3389/fenvs.2022.894887/full#supplementary-material

REFERENCES

Bruyère, C. L., Done, J. M., Holland, G. J., and Fredrick, S. (2014). Bias Corrections of Global Models for Regional Climate Simulations of High-Impact Weather. *Clim. Dyn.* 43, 1847–1856. doi:10.1007/s00382-013-2011-6

Bruyère, C., Monaghan, A. J., Steinhoff, D. F., and Yates, D. (2015). *Bias-Corrected CMIP5 CESM Data in WRF/MPAS Intermediate File Format. No. NCAR/TN-515+STR*. Boulder, CO: NCAR. doi:10.5065/D6445JJ7

Cai, W., Li, K., Liao, H., Wang, H., and Wu, L. (2017). Weather Conditions Conducive to Beijing Severe Haze More Frequent under Climate Change. *Nat. Clim. Change* 7, 257–262. doi:10.1038/nclimate3249

Chen, H., and Wang, H. (2015). Haze Days in North China and the Associated Atmospheric Circulations Based on Daily Visibility Data from 1960 to 2012. *J. Geophys. Res. Atmos.* 120, 5895–5909. doi:10.1002/2015JD023225

Chen, L., Ma, Z., Li, Z., Wu, L., Flemke, J., and Li, Y. (2018). Dynamical Downscaling of Temperature and Precipitation Extremes in China under Current and Future Climates. *Atmos. Ocean* 56, 55–70. doi:10.1080/07055900.2017.1422691

Emery, C., Tai, E., and Yarwood, G. (2001). *Enhanced Meteorological Modeling and Performance Evaluation for Two Texas Ozone Episodes*. Report to the Texas Natural Resources Conservation Commission. Novato, CA: ENVIRON International Corporation.

Emery, C., Liu, Z., Russell, A. G., Odman, M. T., Yarwood, G., and Kumar, N. (2017). Recommendations on Statistics and Benchmarks to Assess Photochemical Model Performance. *J. Air Waste Manag. Assoc.* 67, 582–598. doi:10.1080/10962247.2016.1265027

Feng, J., Quan, J., Liao, H., Li, Y., and Zhao, X. (2018). An Air Stagnation Index to Qualify Extreme Haze Events in Northern China. *J. Atmos. Sci.* 75, 3489–3505. doi:10.1175/JAS-D-17-0354.1

Fu, G. Q., Xu, W. Y., Yang, R. F., Li, J. B., and Zhao, C. S. (2014). The Distribution and Trends of Fog and Haze in the North China Plain over the Past 30 Years. *Atmos. Chem. Phys.* 14, 11949. doi:10.5194/acp-14-11949-2014

Gao, Y., Zhang, L., Zhang, G., Yan, F., Zhang, S., Sheng, L., et al. (2020). The Climate Impact on Atmospheric Stagnation and Capability of Stagnation Indices in Elucidating the Haze Events over North China Plain and Northeast China. *Chemosphere* 258, 127335. doi:10.1016/j.chemosphere.2020.127335

Garrido-Perez, J. M., Ordóñez, C., García-Herrera, R., and Schnell, J. L. (2019). The Differing Impact of Air Stagnation on Summer Ozone across Europe. *Atmos. Environ.* 219, 117062. doi:10.1016/j.atmosenv.2019.117062

Garrido-Perez, J. M., García-Herrera, R., and Ordóñez, C. (2021). Assessing the Value of Air Stagnation Indices to Reproduce PM10 Variability in Europe. *Atmos. Res.* 248, 105258. doi:10.1016/j.atmosres.2020.105258

Guo, J., Deng, M., Lee, S. S., Wang, F., Li, Z., Zhai, P., et al. (2016). Delaying Precipitation and Lightning by Air Pollution over the Pearl River Delta. Part I: Observational Analyses. *J. Geophys. Res. Atmos.* 121, 6472–6488. doi:10.1002/2015jd023257

Hersbach, H., Bell, B., Berrisford, P., Biavati, G., Horányi, A., Muñoz Sabater, J., et al. (2019). ERA5 Monthly Averaged Data on Single Levels from 1979 to Present. *Copernicus Climate Change Service (C3S) Climate Data Store (CDS).* doi:10.24381/cds.f17050d7

Hewitson, B. C., and Crane, R. G. (2006). Consensus between GCM Climate Change Projections with Empirical Downscaling: Precipitation Downscaling over South Africa. *Int. J. Climatol.* 26, 1315–1337. doi:10.1002/joc.1314

Hong, S. Y., Noh, Y., and Dudhia, J. (2006). A New Vertical Diffusion Package with an Explicit Treatment of Entrainment Processes. *Mon. Weather Rev.* 134, 2318. doi:10.1175/mwr3199.1

Horton, D. E., Harshvardhan, H., and Diffenbaugh, N. S. (2012). Response of Air Stagnation Frequency to Anthropogenically Enhanced Radiative Forcing. *Environ. Res. Lett.* 7, 044034. doi:10.1088/1748-9326/7/4/044034

Hu, J., Chen, J., Ying, Q., and Zhang, H. (2016). One-year Simulation of Ozone and Particulate Matter in China Using WRF/CMAQ Modeling System. *Atmos. Chem. Phys.* 16, 10333–10350. doi:10.5194/acp-16-10333-2016

Huang, Q., Cai, X., Song, Y., and Zhu, T. (2017). Air Stagnation in China (1985-2014): Climatological Mean Features and Trends. *Atmos. Chem. Phys.* 17, 7793–7805. doi:10.5194/acp-17-7793-2017

Huang, Q., Cai, X., Wang, J., Song, Y., and Zhu, T. (2018). Climatological Study of the Boundary-Layer Air Stagnation Index for China and its Relationship with Air Pollution. *Atmos. Chem. Phys.* 18, 7573–7593. doi:10.5194/acp-18-7573-2018

Jiang, Q., Li, W., Fan, Z., He, X., Sun, W., Chen, S., et al. (2021). Evaluation of the ERA5 Reanalysis Precipitation Dataset over Chinese Mainland. *J. Hydrol.* 595, 125660. doi:10.1016/j.jhydrol.2020.125660

Jiao, D., Xu, N., Yang, F., and Xu, K. (2021). Evaluation of Spatial-Temporal Variation Performance of ERA5 Precipitation Data in China. *Sci. Rep.* 11, 20216. doi:10.1038/s41598-021-97432-y

Jing, P., Lu, Z., and Steiner, A. L. (2017). The Ozone-Climate Penalty in the Midwestern U.S. *Atmos. Environ.* 170, 130–142. doi:10.1016/j.atmosenv.2017.09.038

Kerr, G. H., and Waugh, D. W. (2018). Connections between Summer Air Pollution and Stagnation. *Environ. Res. Lett.* 13, 084001. doi:10.1088/1748-9326/aad2e2

Kinney, P. L. (2018). Interactions of Climate Change, Air Pollution, and Human Health. *Curr. Envir Health Rpt.* 5, 179–186. doi:10.1007/s40572-018-0188-x

Lee, J.-W., Hong, S.-Y., Chang, E.-C., Suh, M.-S., and Kang, H.-S. (2014). Assessment of Future Climate Change over East Asia Due to the RCP Scenarios Downscaled by GRIMs-RMP. *Clim. Dyn.* 42, 733–747. doi:10.1007/s00382-013-1841-6

Lee, D., Wang, S.-Y., Zhao, L., Kim, H. C., Kim, K., and Yoon, J.-H. (2020). Long-term Increase in Atmospheric Stagnant Conditions over Northeast Asia and the Role of Greenhouse Gases-Driven Warming. *Atmos. Environ.* 241, 117772. doi:10.1016/j.atmosenv.2020.117772

Li, L., Qian, J., Ou, C.-Q., Zhou, Y.-X., Guo, C., and Guo, Y. (2014). Spatial and Temporal Analysis of Air Pollution Index and its Timescale-dependent Relationship with Meteorological Factors in Guangzhou, China, 2001-2011. *Environ. Pollut.* 190, 75–81. doi:10.1016/j.envpol.2014.03.020

Li, J., Zhang, H., Ying, Q., Wu, Z., Zhang, Y., Wang, X., et al. (2020). Impacts of Water Partitioning and Polarity of Organic Compounds on Secondary Organic Aerosol over Eastern China. *Atmos. Chem. Phys.* 20, 7291–7306. doi:10.5194/acp-20-7291-2020

Liao, T., Gui, K., Jiang, W., Wang, S., Wang, B., Zeng, Z., et al. (2018). Air Stagnation and its Impact on Air Quality during Winter in Sichuan and Chongqing, Southwestern China. *Sci. Total Environ.* 635, 576–585. doi:10.1016/j.scitotenv.2018.04.122

Liu, S., Gao, W., and Liang, X.-Z. (2013). A Regional Climate Model Downscaling Projection of China Future Climate Change. *Clim. Dyn.* 41, 1871–1884. doi:10.1007/s00382-012-1632-5

Mlawer, E. J., Taubman, S. J., Brown, P. D., Iacono, M. J., and Clough, S. A. (1997). Radiative Transfer for Inhomogeneous Atmospheres: RRTM, a Validated Correlated-K Model for the Longwave. *J. Geophys. Res.* 102, 16663–16682. doi:10.1029/97JD00237

Mu, Q., and Liao, H. (2014). Simulation of the Interannual Variations of Aerosols in China: Role of Variations in Meteorological Parameters. *Atmos. Chem. Phys.* 14, 9597–9612. doi:10.5194/acp-14-9597-2014

Qin, Y., Li, J., Gong, K., Wu, Z., Chen, M., Qin, M., et al. (2021). Double High Pollution Events in the Yangtze River Delta from 2015 to 2019: Characteristics, Trends, and Meteorological Situations. *Sci. Total Environ.* 792, 148349. doi:10.1016/j.scitotenv.2021.148349

Rigby, M., and Toumi, R. (2008). London Air Pollution Climatology: Indirect Evidence for Urban Boundary Layer Height and Wind Speed Enhancement. *Atmos. Environ.* 42, 4932–4947. doi:10.1016/j.atmosenv.2008.02.031

Shi, Z., Huang, L., Li, J., Ying, Q., Zhang, H., and Hu, J. (2020). Sensitivity Analysis of the Surface Ozone and Fine Particulate Matter to Meteorological Parameters in China. *Atmos. Chem. Phys.* 20, 13455–13466. doi:10.5194/acp-20-13455-2020

Sun, J., Liang, M., Shi, Z., Shen, F., Li, J., Huang, L., et al. (2019). Investigating the PM2.5 Mass Concentration Growth Processes during 2013-2016 in Beijing and Shanghai. *Chemosphere* 221, 452–463. doi:10.1016/j.chemosphere.2018.12.200

Thompson, G., Field, P. R., Rasmussen, R. M., and Hall, W. D. (2008). Explicit Forecasts of Winter Precipitation Using an Improved Bulk Microphysics Scheme. Part II: Implementation of a New Snow Parameterization. *Mon. Weather Rev.* 136, 5095–5115. doi:10.1175/2008MWR2387.1

Wang, Y., Yao, L., Wang, L., Liu, Z., Ji, D., Tang, G., et al. (2014). Mechanism for the Formation of the January 2013 Heavy Haze Pollution Episode over Central and Eastern China. *Sci. China Earth Sci.* 57, 14–25. doi:10.1007/s11430-013-4773-4

Wang, X., Dickinson, R. E., Su, L., Zhou, C., and Wang, K. (2018). PM2.5 Pollution in China and How it Has Been Exacerbated by Terrain and Meteorological Conditions. *Bull. Am. Meteorol. Soc.* 991, 105–119. doi:10.1175/BAMS-D-16-030110.1175/bams-d-16-0301.1

Wang, P., Guo, H., Hu, J., Kota, S. H., Ying, Q., and Zhang, H. (2019). Responses of PM2.5 and O3 Concentrations to Changes of Meteorology and Emissions in China. *Sci. Total Environ.* 662, 297–306. doi:10.1016/j.scitotenv.2019.01.227

Wang, X., Tolksdorf, V., Otto, M., and Scherer, D. (2021). WRF-based Dynamical Downscaling of ERA5 Reanalysis Data for High Mountain Asia: Towards a New Version of the High Asia Refined Analysis. *Int. J. Climatol.* 41, 743–762. doi:10.1002/joc.6686

Xu, Z., Chen, S. X., and Wu, X. (2020). Meteorological Change and Impacts on Air Pollution: Results from North China. *J. Geophys. Res. Atmos.* 125, e2020JD032423. doi:10.1029/2020jd032423

Yang, H., Fang, Z., Xie, C., Cohen, J., and Cao, Y. (2021). Two Trans-boundary Aerosol Transport Episodes in the Western Yangtze River Delta, China: A Perspective from Ground-Based Lidar Observation. *Atmos. Pollut. Res.* 12, 370–380. doi:10.1016/j.apr.2021.01.004

Zhang, Y., Wen, X.-Y., and Jang, C. J. (2010). Simulating Chemistry-Aerosol-Cloud-Radiation-Climate Feedbacks over the Continental U.S. Using the Online-Coupled Weather Research Forecasting Model with Chemistry (WRF/Chem). *Atmos. Environ.* 44, 3568–3582. doi:10.1016/j.atmosenv.2010.05.056

Zhang, R., Qiang, L. I., and Zhang, R. N. (2014). Meteorological Conditions for the Persistent Severe Fog and Haze Event over Eastern China in January 2013. *Sci. China Earth Sci.* 57, 26–35. doi:10.1007/s11430-013-4774-3

Zhang, H., Wang, Y., Hu, J., Ying, Q., and Hu, X.-M. (2015). Relationships between Meteorological Parameters and Criteria Air Pollutants in Three Megacities in China. *Environ. Res.* 140, 242–254. doi:10.1016/j.envres.2015.04.004

Zhang, Q., Zheng, Y., Tong, D., Shao, M., Wang, S., Zhang, Y., et al. (2019). Drivers of Improved $PM_{2.5}$ Air Quality in China from 2013 to 2017. *Proc. Natl. Acad. Sci. U.S.A.* 116, 24463–24469. doi:10.1073/pnas.1907956116

Zhao, X. J., Zhao, P. S., Xu, J., Meng, W., Pu, W. W., Dong, F., et al. (2013). Analysis of a Winter Regional Haze Event and its Formation Mechanism in the North China Plain. *Atmos. Chem. Phys.* 13, 5685–5696. doi:10.5194/acp-13-5685-2013

Zou, Y., Wang, Y., Zhang, Y., and Koo, J. H. (2017). Arctic Sea Ice, Eurasia Snow, and Extreme Winter Haze in China. *Sci. Adv.* 3, e1602751. doi:10.1126/sciadv.1602751

Conflict of Interest: The authors declare that the research was conducted in the absence of any commercial or financial relationships that could be construed as a potential conflict of interest.

frontiers | Frontiers in Ecology and Evolution

ORIGINAL RESEARCH
published: 31 May 2022
doi: 10.3389/fevo.2022.845801

Impact of Urbanization on Meteorology and Air Quality in Chengdu, a Basin City of Southwestern China

Haofan Wang[1], Zhihong Liu[1], Kai Wu[2], Jiaxin Qiu[3], Yang Zhang[1], Bangping Ye[4] and Min He[1]*

[1] College of Resources and Environment, Chengdu University of Information Technology, Chengdu, China, [2] Department of Land, Air, and Water Resources, University of California, Davis, Davis, CA, United States, [3] College of New Energy and Environment, Jilin University, Changchun, China, [4] Sichuan Meteorological Observatory, Chengdu, China

Rapid urbanization has the potential to fundamentally perturb energy budget and alter urban air quality. While it is clear that urban meteorological parameters are sensitive to urbanization-induced changes in landscapes, a gap exists in our knowledge about how changes in land use and land cover affect the dynamics of urban air quality. Herein, we simulated a severe O_3 episode (10–16 July 2017) and a highly polluted $PM_{2.5}$ episode (25–30 December 2017) and assessed the changes of meteorological phenomenon and evolution of air pollutants induced by urbanization. We found that the urban expansion area (i.e., land use transition from natural to urban surfaces between 2000 and 2017, UEA) has a significant increase in nocturnal 2-m temperature (T2) with maximum values reaching 3 and 4°C in summer and winter, respectively. In contrast, UEA experienced cooling in the daytime with stronger reductions of T2 in winter than in summer. The T2 variability is primarily attributed to the intense thermal inertia and high heat capacity of the urban canopy and the shadowing effect caused by urbanization. Owing to increased surface roughness and decreased surface albedo as well as shadowing effects, the ventilation index (VI) of UEA increased up to 1,200 m^2/s in winter while decreased up to 950 m^2/s in summer. Changes in meteorological phenomenon alter physical and chemical processes associated with variations in $PM_{2.5}$ and O_3 concentrations. Urbanization leads to enhanced vertical advection process and weakened aerosol production, subsequently causing $PM_{2.5}$ levels to decrease by 33.2 $\mu g/m^3$ during the day and 4.6 $\mu g/m^3$ at night, respectively. Meanwhile, O_3 levels increased by 61.4 $\mu g/m^3$ at 20:00 due to the reduction of horizontal advection induced by urbanization, while O_3 concentrations changed insignificantly at other times. This work provides valuable insights into the effects of urbanization on urban meteorology and air quality over typical megacities, which support informed decision-making for urban heat and air pollution mitigation.

Keywords: urbanization, air quality, land use, land cover, complex terrain

OPEN ACCESS

Edited by:
Yuzhong Zhang,
Westlake University, China

Reviewed by:
Shan Yin,
Shanghai Jiao Tong University, China
Lei Chen,
Nanjing University of Information Science and Technology, China

****Correspondence:***
Yang Zhang
zhangyang@cuit.edu.cn

Specialty section:
This article was submitted to Interdisciplinary Climate Studies, a section of the journal Frontiers in Ecology and Evolution

Received: *30 December 2021*
Accepted: *05 May 2022*
Published: *31 May 2022*

Citation:
Wang H, Liu Z, Wu K, Qiu J, Zhang Y, Ye B and He M (2022) Impact of Urbanization on Meteorology and Air Quality in Chengdu, a Basin City of Southwestern China. Front. Ecol. Evol. 10:845801. doi: 10.3389/fevo.2022.845801

INTRODUCTION

Urbanization is an ubiquitous trend worldwide driven by rapid industrialization and socioeconomic development. More than 60% of the world population resided in urban areas in 2018 and it is projected to increase by 80% by 2030 (Grimm et al., 2008; Seto et al., 2012). Since 2000s, environmental issues including heatwaves, flooding, and poor air quality accompanied by urbanization have become public concerns which puts the environmental quality of cities under pressure (Fang et al., 2022). In particular, air pollution featured by high levels of ozone and particulate matter is recognized as a major environmental issue in highly urbanized megacities and city clusters in Asia. Urbanization leads to dramatic land use and land cover (LULC) alteration, which generally results in lower albedo, higher roughness, and higher thermal inertia (Fan et al., 2017). These changes could significantly impact surface energy budget and further influence regional meteorology (Vahmani and Hogue, 2014). Moreover, the street canyon and the gaps between buildings change the radiative forcing (Vahmani and Ban-Weiss, 2016). Changes in radiative forcing can lead to changes in near-surface temperatures, affecting the dispersion of pollutants and having a profound impact on air quality (Vahmani et al., 2016).

Prior studies that examine urbanization effects on local and regional-scale city environment were generally based on coupled urban canopy models (UCM) to mesoscale weather forecast models and air quality models (Lin et al., 2016; Lian et al., 2018). Over Los Angeles, Li et al. (2019) used WRF-Chem model to explore the effects of urbanization on meteorology and air quality and reported that nighttime 2-m temperature (T2) rise by up to 1.7°C and $PM_{2.5}$ concentrations fall by up to 2.5 $\mu g/m^3$ at night. In South Korea, Kim et al. (2021) found that urbanization in metropolitan Ulsan caused PM_{10} concentrations drop by up to 3 $\mu g/m^3$ and 5 $\mu g/m^3$ in the daytime and nighttime, respectively. Wang K. et al. (2021) found that LULC change in the Beijing-Tianjin-Hebei region had significant effects on meteorological conditions and air quality at urban stations, and UCM can improve the performance of meteorological simulation. With a focus on the Yangtze River Delta (YRD) in eastern China, Liao et al. (2014) investigated the performance of different urban canopy models in YRD by WRF-Chem model and pointed out that urbanization process significantly influences wind speeds (reduced by 0.7–2.6 m/s) across YRD. For Sichuan Basin situated in western China, Wang H. et al. (2021) found that increased roughness had a significant effect on reducing near-surface wind speeds, leading to the accumulation of $PM_{2.5}$ in urban areas of Chengdu. In prior work, only a few studies have focused on identifying the land cover changes over Chengdu based on satellite image and examined the variations of meteorological parameters over time, while modeling assessment on meteorology and air quality changes attributed to urbanization has been rarely conducted, which limits the understanding of environmental consequences induced by urbanization over time (Yang et al., 2020a).

Chengdu is the capital city of Sichuan province with 16.7 million residents and suffers from severe O_3 pollution in summer and experiences episodes of $PM_{2.5}$ pollution in winter (Yang et al., 2020b; Wu et al., 2021). Substantial anthropogenic emissions of oxides of nitrogen (NO_x), primary $PM_{2.5}$, and volatile organic compounds (VOCs) are emitted from on-road vehicles and industrial infrastructures, significantly contributing to the formation of O_3 and $PM_{2.5}$ in urban areas (Wu et al., 2022). Based on inventory analysis, the Sichuan Academy of Environmental Sciences (SCAES) estimated that emissions of NO_x, primary $PM_{2.5}$, and volatile organic compounds (VOCs) over Chengdu in 2017 were 140×10^6, 70×10^6, and 160×10^6 kg, respectively (Xu et al., 2020). Therefore, it is of utmost importance to quantify the magnitude changes of meteorological phenomenon and air quality attributed to rapid urbanization in Chengdu, the typical basin city located on western China.

In this study, we explicitly address the impacts of urbanization on meteorology and air quality by integrating urban canopy model within the WRF-CMAQ modeling system over Chengdu city. The model framework includes historical and current urban land cover datasets obtained from Moderate Resolution Imaging Spectroradiometer (MODIS) in combination with advanced urban parameterizations. Comparisons of meteorological parameters and air pollutants levels are made between model simulations configured with different land use and land cover data from MODIS. The findings of this work are useful in improving understanding on how urbanization modulate various aspects of meteorology and subsequently influence urban environment.

DATA AND METHODS

WRF-UCM-CMAQ Model Framework and Configurations

The WRFv4.1.1 model (Salamanca et al., 2011; Skamarock et al., 2019) and the CMAQv5.3.1 model (Appel et al., 2021), are both compiled and operated on a server with Linux environment. WRFv4.1.1 model was used to simulate meteorological conditions with meteorological initial and boundary conditions taken from NCEP 1° × 1° Final (FNL) reanalysis dataset. As shown in **Figure 1**, three nested domains were adopted with horizontal resolutions of 27, 9, and 3 km, respectively. The outermost domain covers southwest China and the innermost domain focuses on Chengdu. The physical parameterizations configured to be used in WRF are listed in **Table 1**. CMAQv5.3.1 was driven by meteorological fields provided by WRF to model trace gases and aerosols. The initial and boundary conditions for CMAQ were derived from the default profiles which represent a clean atmosphere. BVOC emissions were calculated by The Model of Emissions of Gases and Aerosols from Nature version 2.1 (MEGANv2.1) (Guenther et al., 2012; Wu et al., 2020). CMAQ was configured with the Carbon Bond chemical mechanism (CB06) and AERO6. The model simulation was performed over a 15 days period from 1 July 2017 to 16 July 2017 (summer period), which covers the evolution of a typical summertime O_3 episode in Chengdu and a 15 days period from 15 January

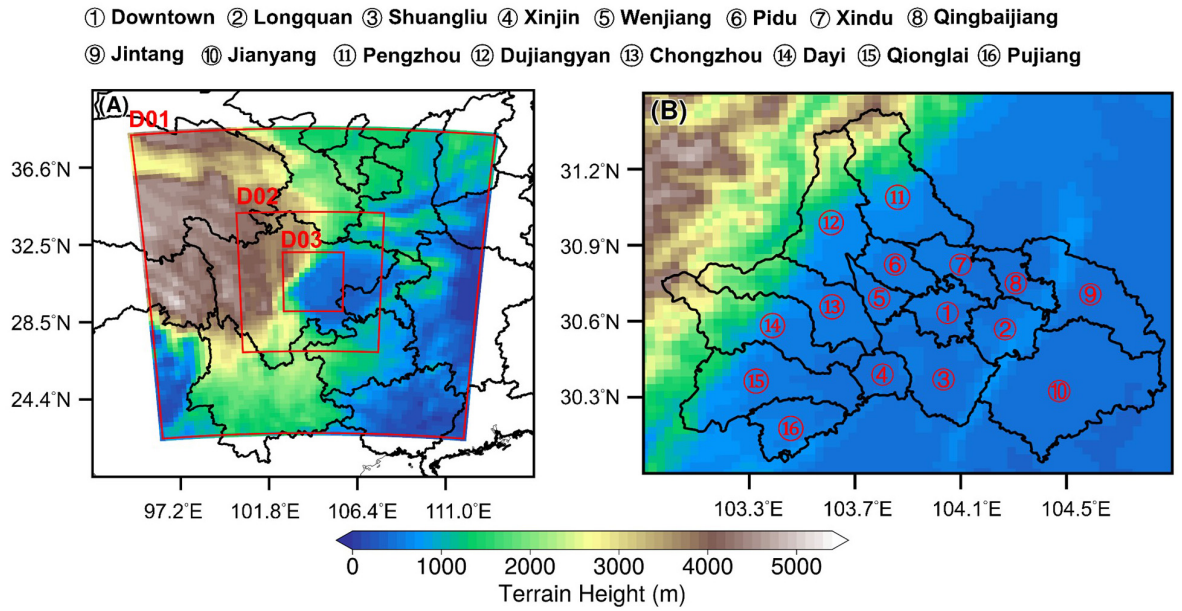

FIGURE 1 | Terrain map of the triple nested model domain **(A)** and subdistricts in Chengdu **(B)**.

2017 to 30 January 2017 (winter period), which covers the evolution of a typical wintertime $PM_{2.5}$ episode in Chengdu. To reduce bias from meteorological drift, the first 10 days in both simulations were treated as spin-up and were not analyzed in this study.

To probe the magnitude change modulated by advection, deposition, and chemical production/loss changes, process analysis module (PA) in the CMAQ model is activated in simulations (Yang et al., 2021). The physical and chemical processes in PA includes vertical advection (ZADV), horizontal advection (HADV), horizontal diffusion (HDIF), vertical diffusion (VDIF), primary emissions (EMIS), dry deposition (DDEP), cloud processes (CLDS), gas-phase chemistry (CHEM), and aerosol processes (AERO).

TABLE 1 | Summary of configurations in WRF-CMAQ modeling system.

Model attribution	Configuration
Land use/cover data	MODIS land cover data in 2000 and 2017
Meteorological initial conditions and boundary conditions	NCEP Final (FNL) reanalysis data
Anthropogenic emissions	MEIC in 2017
Biogenic emissions	MEGANv2.1 (Guenther et al., 2012)
Microphysics	Purdue Lin (Chen and Sun, 2002)
PBL physics scheme	MYJ (Janjić, 1994)
Shortwave and longwave radiation	Goddard (Chou et al., 2001) and Rapid Radiative Transfer Model (RRTM) (Mlawer et al., 1997)
Land surface model	Noah land surface model (LSM) (Ek et al., 2003)
Urban scheme	Single-layer urban canopy model (UCM) (Kusaka and Kimura, 2004)
Gas-phase chemistry	CB06 (Yarwood et al., 2010)
Aerosol module	AERO6 (Murphy et al., 2017; Pye et al., 2017)

MODIS, moderate-resolution Imaging spectroradiometer; NCEP, National Centers for Environmental Prediction; MEIC, multiresolution emission inventory for China.

Simulation Scenarios

To investigate the impact of land use and land cover changes induced by urbanization on regional meteorology and air quality over Chengdu, we conducted WRF-UCM-CMAQ simulations with two scenarios: 2000 LULC and 2017 LULC. The LULC data was obtained from the MODIS MCD12Q1 product. As seen in **Figure 2**, the urban areas of metropolitan Chengdu significantly expanded and there are considerable transitions from suburban areas to urban areas from 2000 to 2017, reflecting the rapid urbanization processes that occurred in Chengdu. The obvious changes between these two scenarios could result in changes in land surface properties and influence BVOC emissions from vegetation.

Ambient Monitoring Data

We use hourly ground-level meteorological observations [including 2-m temperature (T2), 10-m wind speed (WS10) and 10-m wind direction(WD10)] from 4 national basic meteorological stations [Chongzhou (CZ), Shuangliu (SL), Xindu (XD), and Wenjiang (WJ)] provided by the Sichuan Provincial Meteorological Service. Hourly ambient levels of air pollutants ($PM_{2.5}$ and O_3) from three monitoring stations are collected from the China National Environmental Monitoring Centre (CNEMC). The locations of these stations are shown in **Figure 3**. These data undergo rigorous

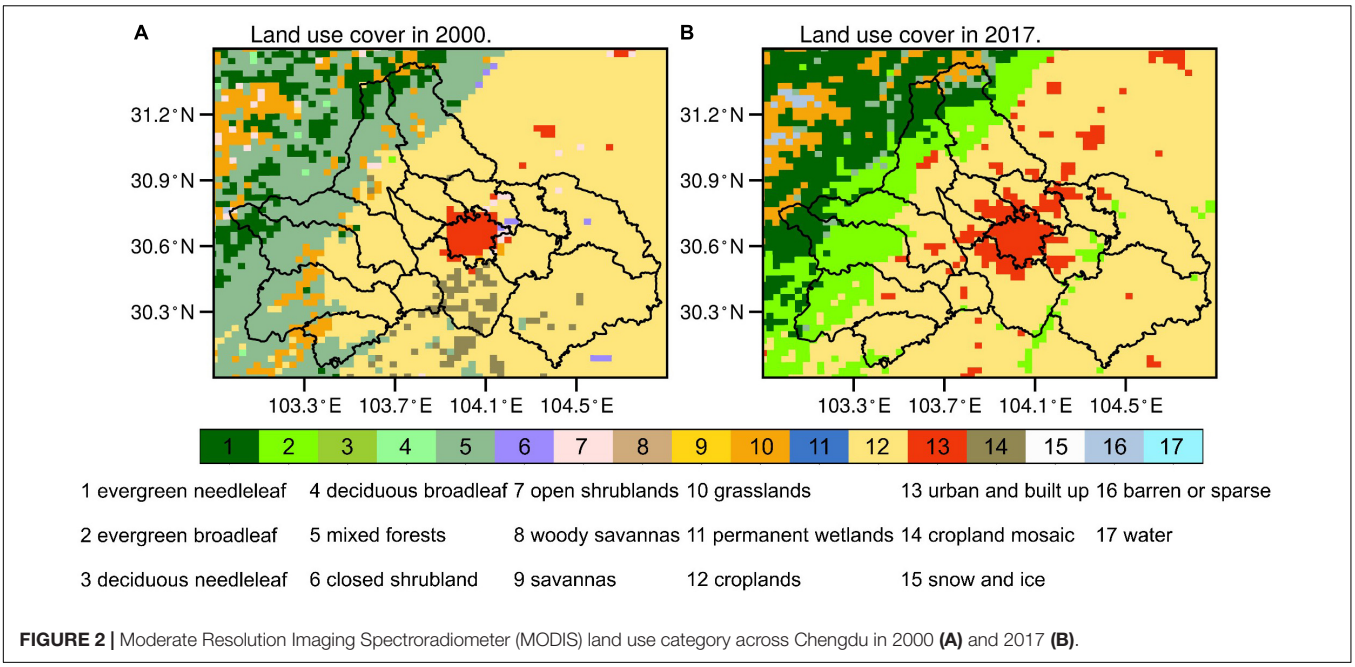

FIGURE 2 | Moderate Resolution Imaging Spectroradiometer (MODIS) land use category across Chengdu in 2000 **(A)** and 2017 **(B)**.

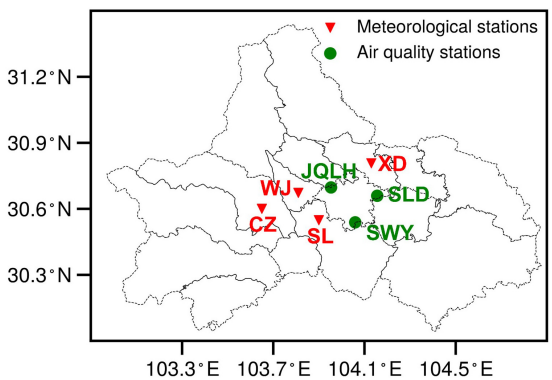

FIGURE 3 | Locations of air quality monitoring stations and meteorological sites in Chengdu.

quality control and are further used to assess the model performance of WRF-CMAQ.

Statistical Analysis

To assess the modeling performance, hourly output data from the WRF-CMAQ model was interpolated to the observation site (**Figure 3**). The model performance was quantified using statistical metrics including Pearson correlation coefficient (R), mean bias (MB), root mean square error (RMSE), normalized mean bias (NMB), the mean fractional error (MFE), and the mean fractional bias (MFB). The criteria values reported in Emery et al. (2017) and Boylan and Russell (2006) are adopted for comparing the statistical metrics. In previous studies, we assessed the model performance on meteorology and found that it can accurately reflect the diurnal pattern and fluctuation. It should be noted that the model performance evaluation on the wintertime meteorology has been described in detail previously (Wang H. et al., 2021), and thus will not be discussed here.

$$R = \frac{\sum_{i=1}^{n}\left(M_i - \bar{M}_i\right)\left(O_i - \bar{O}_i\right)}{\sqrt{\sum_{i=1}^{n}\left(M_i - \bar{M}_i\right)^2}\sqrt{\sum_{i=1}^{n}\left(O_i - \bar{O}_i\right)^2}}$$

$$MB = \frac{1}{n}\sum_{i=1}^{n}\left(M_i - O_i\right)$$

$$RMSE = \sqrt{\frac{\sum_{i=1}^{n}\left(O_i - M_i\right)^2}{n}}$$

$$NMB = \frac{\sum_{i=1}^{n}\left(M_i - O_i\right)}{\sum_{i=1}^{n} O_i}$$

$$MFE = \frac{2}{n}\sum_{i=1}^{n}\left|\frac{M_i - O_i}{M_i + O_i}\right|$$

$$MFB = \frac{2}{n}\sum_{i=1}^{n}\left(\frac{M_i - O_i}{M_i + O_i}\right)$$

Where M_i and O_i are the simulated and observed data, respectively. $\bar{M}_i$ and $\bar{O}_i$ are the average of the simulated and observed data, respectively. n is the number of samples.

Model Evaluation

Evaluation of the WRF-CMAQ model performance is undertaken through comparison against ground-level observations, as shown in **Supplementary Figure 1** and **Supplementary Table 1**. It can be clearly seen that the WRF model reasonably reproduces the diurnal pattern and variability of T2, with R values, ranged 0.73–0.83 and MB less than

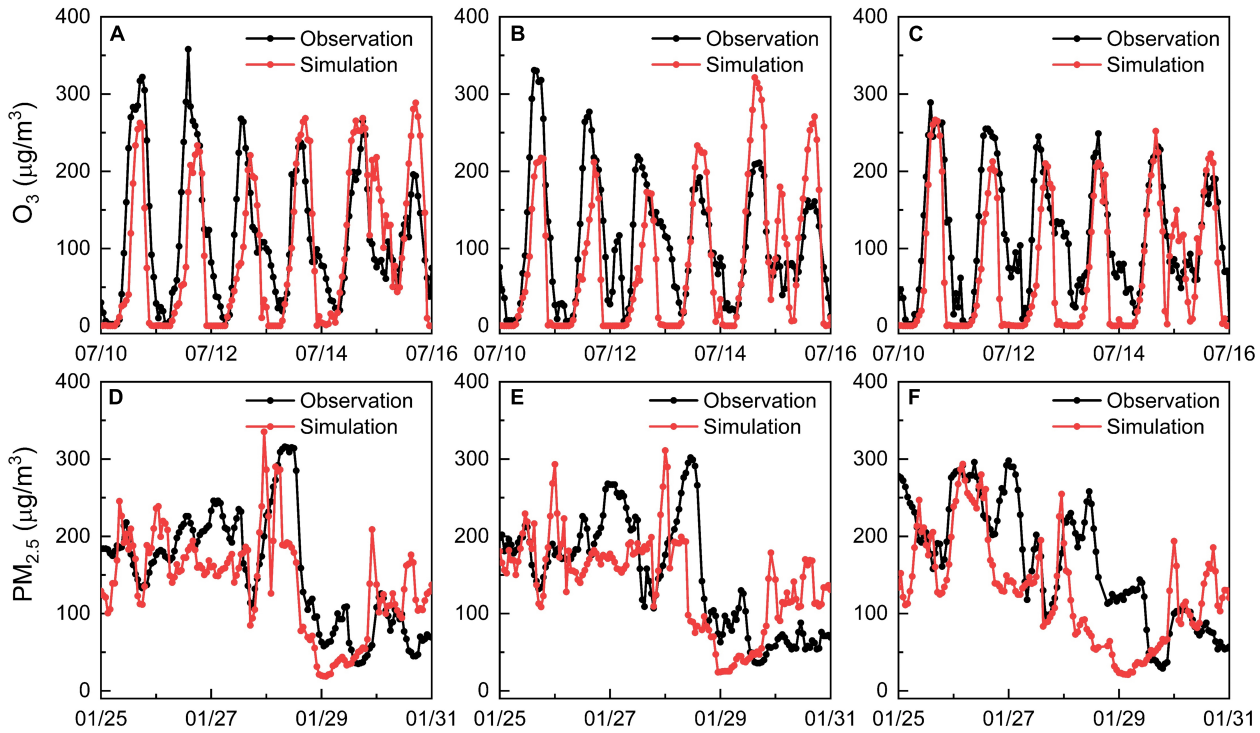

FIGURE 4 | Time series of simulated and observed hourly concentrations of O_3 at the **(A)** JQLH, **(B)** SLD, and **(C)** SWY stations over 10-16 July, 2017 and time series of simulated and observed hourly concentrations of $PM_{2.5}$ at the **(D)** JQLH, **(E)** SLD, and **(F)** SWY stations over 25–31 December, 2017.

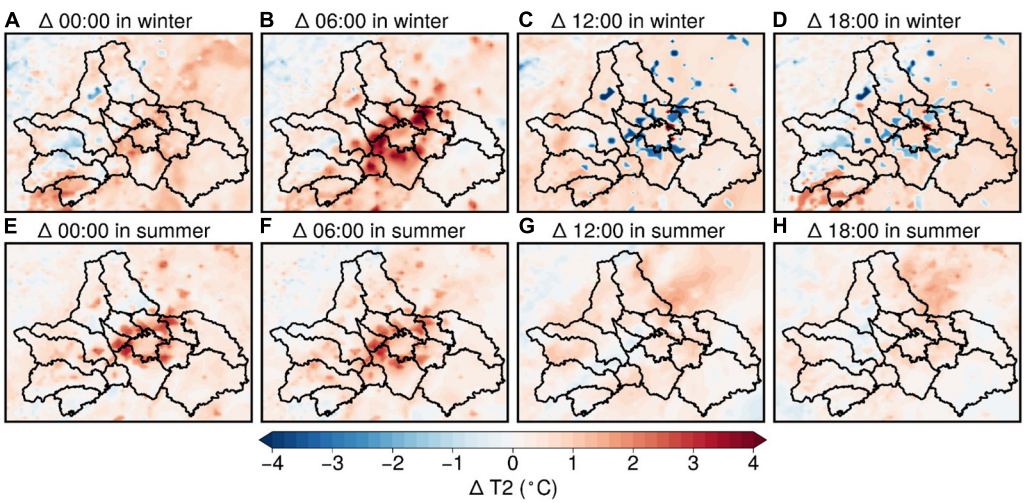

FIGURE 5 | Spatial map of T2 variations induced by land use change between 2000 and 2017 at 00:00, 06:00, 12:00, and 18:00 LST in winter **(A–D)** and summer **(E–H)**.

1.22°C. For WS10, while WRF tends to overestimate nighttime wind speed, the simulated wind fields are broadly consistent with observations.

Figure 4 depicts the comparison of simulated and observed O_3 and $PM_{2.5}$ concentrations at hourly intervals. The model accurately replicated the O_3 diurnal cycle, with R values ranging from 0.70 to 0.78 (**Supplementary Table 2**). The statistical measures of the model performance were reported in **Supplementary Table 2**. The simulated O_3 concentrations at JQLH, SLD, and SWY with MB are −7.04, −12.14, and 18.33 μg/m^3, respectively. Furthermore, the statistical metrics for O_3 are within the acceptable standards (NMB < ± 15%) when compared to established benchmarks (Emery et al., 2017) using hourly O_3 values.

In terms of $PM_{2.5}$ concentrations, the model captures $PM_{2.5}$ variations with R values ranging from 0.53-0.60 (**Supplementary Table 3**) and the MFB (MFE) of −14.9% (40.1%), −5.7% (34.2%), and 0.6% (33.2%), respectively, which attain the criteria standards (−30% ≤ MFB ≤ 30% and MFE ≤ 50%) reported by Boylan and Russell (2006) for model performance.

RESULTS AND DISCUSSION

Spatial Patterns Changes of Temperature and Process Drivers

Figure 5 presents spatial changes of T2 induced by LULC alteration via urbanization across Chengdu in winter and summer. Evidently, the most prominent effects are seen in metropolitan Chengdu where dominated by the anthropogenic land surface. Suburban and rural areas exhibit slight warming over time with T2 changes less than 1°C, indicating the impacts of urbanization at regional-scale. In addition, it is found that nocturnal T2 across UEA (i.e., land use transition from natural to urban surfaces between 2000 and 2017) increases significantly with maximum values reaching 3 and 4°C in summer and winter, respectively. In contrast, UEA experiences cooling in the daytime with a remarkably reduced T2 in winter than in summer. This pattern is mainly caused by intense thermal inertia and high heat capacity of the urban canopy, which is primarily attributed to manmade materials (e.g., pavements and buildings).

Urbanization turns natural land surface into anthropogenic land surface, thus leading to an increase in heat capacity and a reduction in surface albedo. Furthermore, the intense thermal inertia of the urban canopy hinders the cooling process during nighttime. Therefore, the cooling process of the urban surface is slower than that of the natural surface. Meanwhile, the increasing PBLH (**Supplementary Figure 2**) can also lead to warming because of lower air cooling rates at night (Li et al., 2019).

In the daytime, T2 in UEA decreases by about 2–3°C in winter due to the higher thermal inertia of the urban canopy while the change in summer is insignificant. This is mainly attributed to the perturbation of energy balance in urban areas induced by buildings within the city, namely, the shadow effects (SE). SE is explained by the low solar zenith angle in the winter period leading to less amount of solar radiation reaching the ground and subsequently resulting in less radiation shaded by the buildings, while the high solar zenith angle in the summer period causes much solar radiation to reach the ground and a large portion of it blocked by buildings. In summer, T2 increases due to the absorption of solar radiation, and the higher thermal inertia of the urban canopy hinders the process of temperature increase during the day. The temperature difference between the urban surface and the natural surface is insignificant because of the minor SE due to the high solar zenith angle in the summer period. In winter, while the urban canopy has thermal inertia, SE is more pronounced and shade most of the radiation, offsetting the warming and causing the temperature to decrease by 2–3°C over the UEA.

Spatial Patterns Changes of Ventilation and Process Drivers

Changes in ventilation conditions due to urbanization are discussed in this section. The changes in PBLH affect the vertical diffusion capacity of air pollutants, while the changes in WS10 affect the horizontal transport of ground-level air pollutants. Here, we use the ventilation index (VI) calculated as the product of PBLH and WS10 for illustrating the variations of diffusion capacity over Chengdu (Li et al., 2019). The equation for VI can be written as follow.

$$Ventilation\ index\ =\ PBLH\ \times\ WS10$$

where PBLH is the planetary boundary layer height (m) and WS10 is the 10-m wind speed (m/s).

Figure 6 presents spatial changes of VI induced urbanization across Chengdu in winter and summer. In winter, it is found that VI across UEA increases significantly with maximum values reaching 1,400 m^2/s and 1,300 m^2/s during the daytime and nighttime, respectively. In contrast, UEA has a significant diurnal variation of VI in summer, with a significant decrease in VI during the nighttime (maximum of 1,400 m^2/s) and a significant increase during the daytime (maximum of 1,500 m^2/s).

In winter, during the 00:00-06:00 period (**Supplementary Figure 4**), UEA exhibited stronger WS10 (**Supplementary Figure 3**) and higher PBLH (**Supplementary Figure 2**) in 2017, which can be attributed to the mechanism that SE causes long-wave radiation in the street valley to be repeatedly reflected and absorbed at night. The urban surface temperature increased due to the accumulation of long-wave radiation and anthropogenic heat rejection, which increases the aerodynamic energy of atmospheric turbulence and increase the WS10 and PBLH. Increasing PBLH is also related to increased surface roughness since shear production dominates turbulent kinetic energy (TKE) at night (Li et al., 2019). During 12:00–18:00 (**Supplementary Figure 4**), WS10 increased by 0.24 m/s and PBLH slightly increased by 47.3 m. The decrease of PBLH is mainly associated with air temperature changes because buoyancy production dominates TKE during the day. Reduced buoyancy production of TKE occurs when air temperature decreases (**Figures 5C,D**), resulting in a shallower PBLH. Ultimately, the increased WS10 resulted in a 1,400 m^2/s increase at 12:00 and a 1,300 m^2/s increase at 18:00 in VI.

In summer, during the 00:00–06:00 period (**Supplementary Figure 5**), UEA shows weaker WS10 (**Supplementary Figure 3**) and higher PBLH (**Supplementary Figure 2**) in 2017. The decrease in WS10 is mostly caused by the dragging force, which increases as the friction effect enhances. Additionally, SE causes the urban surface to heat up due to multiple reflections and absorptions of long-wave radiation in the street valley, delaying the heat dissipation process, and subsequently leading to an increase in PBLH. Consequently, the reduction of WS10 caused the VI to decrease by 500 m^2/s at 00:00 and 1,200 m^2/s at 06:00 (**Supplementary Figure 5**), which is beneficial to confine pollutants near the surface. At 12:00 (**Supplementary Figure 5**), the increased air temperature enhances the atmospheric turbulence and drives the daytime PBL

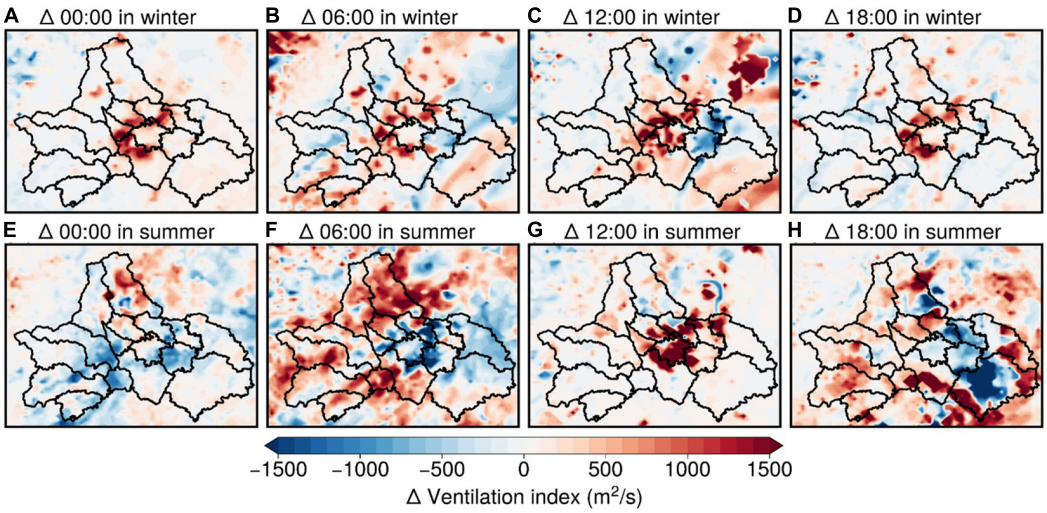

FIGURE 6 | Spatial map of VI variations induced by land use change between 2000 and 2017 at 00:00, 06:00, 12:00, and 18:00 in winter **(A–D)** and summer **(E–H)** periods.

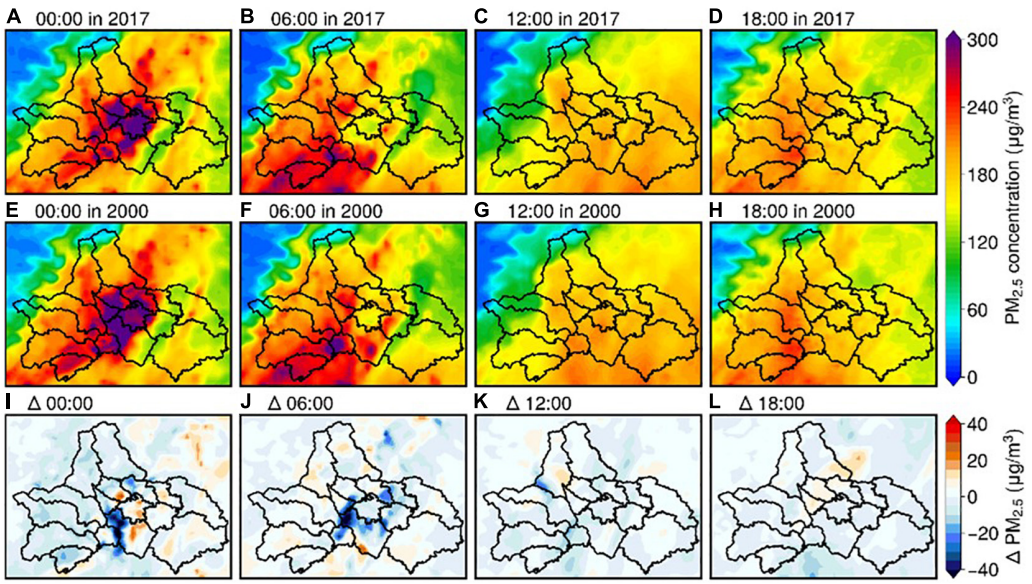

FIGURE 7 | Spatial map of simulated $PM_{2.5}$ levels and $PM_{2.5}$ variations induced by land use change between 2000 and 2017 at 00:00, 06:00, 12:00, and 18:00.

growth, resulting in an increase of 1,300 m^2/s in VI. In summary, WS10 acts as the dominant factor in altering VI in summer, while variability in PBLH governs the changes of VI in daytime and WS10 contributes to variations of VI at night in winter.

Temporal and Spatial Patterns of $PM_{2.5}$ Concentration Changes and Process Drivers

Figure 7 shows spatial distribution of $PM_{2.5}$ concentrations in 2000 and 2017 LULC at 00:00, 06:00, 12:00, and 18:00. There are $PM_{2.5}$ hotspots over UEA and southern Chengdu at 00:00, with peak levels spike to 313.4 and 283.3 $\mu g/m^3$ in 2017 and 2000, respectively. In the morning (06:00), $PM_{2.5}$ levels over downtown Chengdu drop to 126.3 $\mu g/m^3$ and elevated $PM_{2.5}$ concentrations are found over rural areas. It is worth noting that urbanization leads to considerable decrease of $PM_{2.5}$ concentrations (>40 $\mu g/m^3$) across UEA at night. However, the change of $PM_{2.5}$ is insignificant in the daytime over the study domain, implying varied effects induced by urbanization for different time periods.

To further examine the dominant contributor that leads to variations of $PM_{2.5}$, the chemical components of $PM_{2.5}$ are classified into the following three categories: secondary inorganic

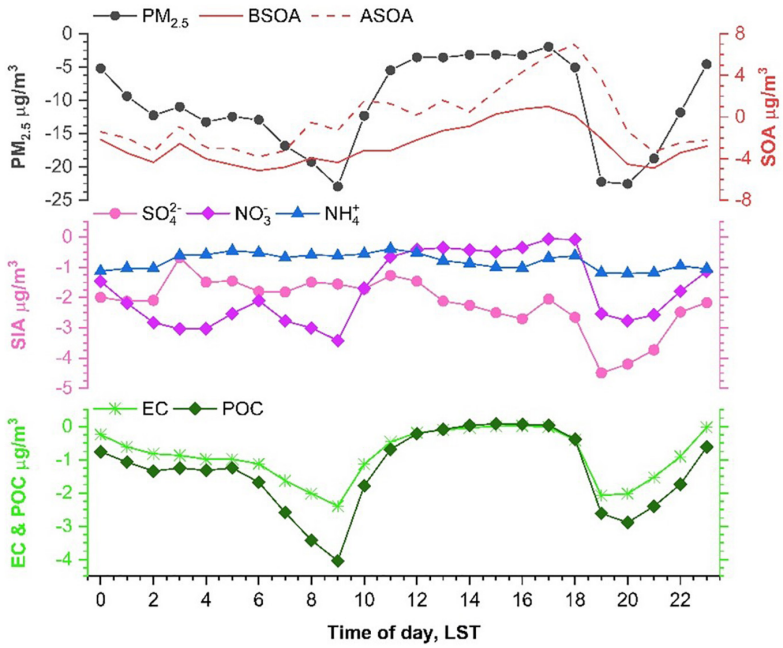

FIGURE 8 | Diurnal pattern of $PM_{2.5}$ and chemical components over UEA of Chengdu between 2000 and 2017. The average data was calculated from the value of UEA.

aerosols (SIA), including nitrate (NO_3^-), sulfate (SO_4^{2-}), and ammonium (NH_4^+); carbonaceous aerosols, including elemental carbon (EC) and primary organic carbon (POC); and secondary organic aerosol (SOA), including SOA formed from anthropogenic VOC precursors (ASOA) and biogenic VOC precursors (BSOA). **Figure 8** depicts the diurnal changes of $PM_{2.5}$ components and total $PM_{2.5}$ concentrations over UEA. The primary carbonaceous aerosols have similar temporal changes with WS10. During the daytime, the slight changes of WS10 do not substantially affect primary carbonaceous aerosols concentrations. In addition, the shift of land cover dominated by vegetation to anthropogenic land surface leads to reductions of BVOC emissions and subsequently results in reduced BSOA concentrations (by 3.4 $\mu g/m^3$). Some semi-volatile compounds species in ASOA increase by 2.85 $\mu g/m^3$ due to the changes in gas-particle phase partitioning from the temperature reduction. The concentrations of nocturnal nitrate and sulfate aerosols decreased by 2.8 $\mu g/m^3$ and 1.3 $\mu g/m^3$, respectively. It is worth mentioning that reductions of nitrate and sulfate account for approximately 40% of the decline in $PM_{2.5}$ concentrations. As sulfate is non-volatile, weakened atmospheric oxidation rates induced by reduced temperature and enhanced ventilation are dominant contributors to declined sulfate. Unlike large reductions in nitrate and sulfate, CMAQ predicts the changes of NH_4^+ to a lesser extent due to relatively low level of ammonia emissions in Chengdu.

The impact of urbanization on $PM_{2.5}$ concentrations in winter results exhibited the $PM_{2.5}$ concentrations over UEA significantly increased at night while slightly decreased during the daytime. In 2017, AERO process had a daytime impact of -28.3 $\mu g/m^3$, compared to -19.4 $\mu g/m^3$ in 2000 (**Figure 9**). AERO process enhanced since the temperature decreases during the day, reducing air oxidation rate and hence the SOA level decreased. CHEM and DDEP processes were insignificantly affected by urbanization, while HADV and ZADV processes had remarkable impacts from urbanization due to the increase of VI. HADV process in 2017 resulted in $PM_{2.5}$ concentrations increased by 26.3 $\mu g/m^3$ at night and increased by 5.2 $\mu g/m^3$ during the day, whereas HADV process in 2000 resulted in $PM_{2.5}$ concentrations increased by 13.8 $\mu g/m^3$ at night and decrease by 2.2 $\mu g/m^3$ during the day. According to ZADV process, $PM_{2.5}$ concentrations over UEA decreased by 33.4 $\mu g/m^3$ and 29.3 $\mu g/m^3$ during the nighttime in 2017 and 2000, respectively. This discrepancy could be attributed to the increased T2 from more anthropogenic heat and the higher heat storage capacity, which enhanced vertical convection. Because of the lower WS10 during the nighttime in 2017, HDIF process led to a 0.15 $\mu g/m^3$ increase in $PM_{2.5}$ concentrations, whereas HDIF caused $PM_{2.5}$ concentrations to decrease by 0.15 $\mu g/m^3$ during the night in 2000 due to the higher WS10. In addition, owing to the increase in T2, the UEA acquired a higher temperature gradient, making VDIF process stronger in 2017 than it was in 2000.

Temporal and Spatial Patterns of O_3 Concentration Changes and Process Drivers

Figure 10 shows the spatial distribution of simulated O_3 at 00:00, 06:00, 12:00, and 18:00 during the summer episode. It is worth

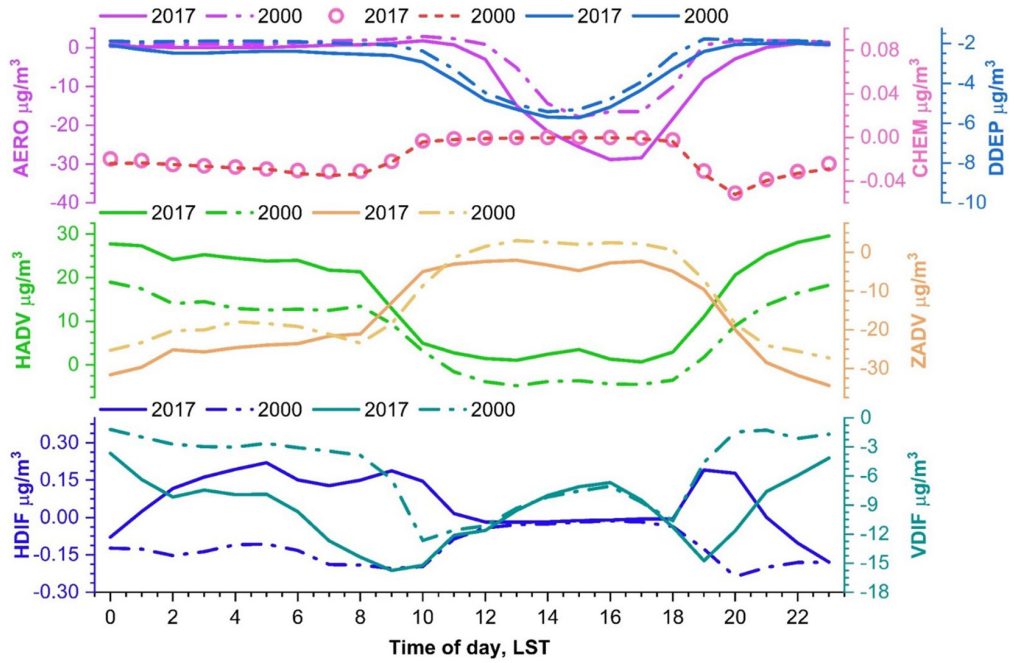

FIGURE 9 | Diurnal pattern of physical and chemical processes for $PM_{2.5}$ in 2000 and 2017. The average data was calculated from the value of UEA.

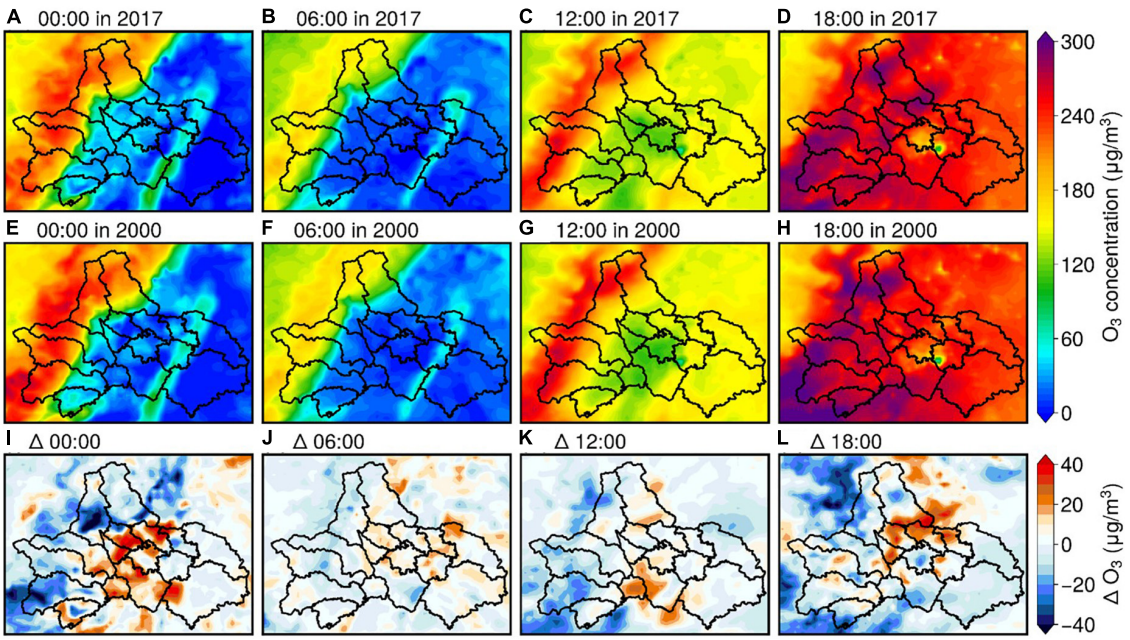

FIGURE 10 | Spatial map of simulated O_3 levels and O_3 variations induced by land use change between 2000 and 2017 at 00:00, 06:00, 12:00, and 18:00.

noting that the Mountain Range area situated in the northwestern Chengdu exhibited elevated O_3 levels between 00:00 and 06:00 with peak O_3 concentrations spiking above 200 $\mu g/m^3$, which is mainly attributed to weak NO_x titration at night due to the relatively low anthropogenic NO_x emissions over this region. In contrast, O_3 levels in metropolitan Chengdu showed a typical diurnal pattern which is characterized by peak concentrations occurring in the afternoon and decreasing to a low level (less than 30 $\mu g/m^3$) at night due to sufficient NO_x titration.

In comparison to the difference in O_3 concentrations between 2000 and 2017, O_3 levels in UEA increase significantly at midnight (00:00) with an enhancement magnitude reaching

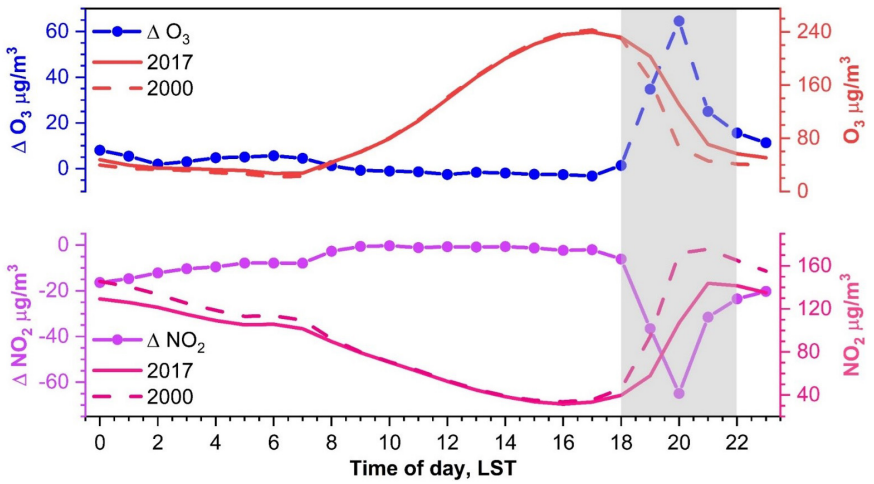

FIGURE 11 | Diurnal pattern of O_3 and NO_2 over UEA of Chengdu between 2000 and 2017. The average data was calculated by the value over UEA.

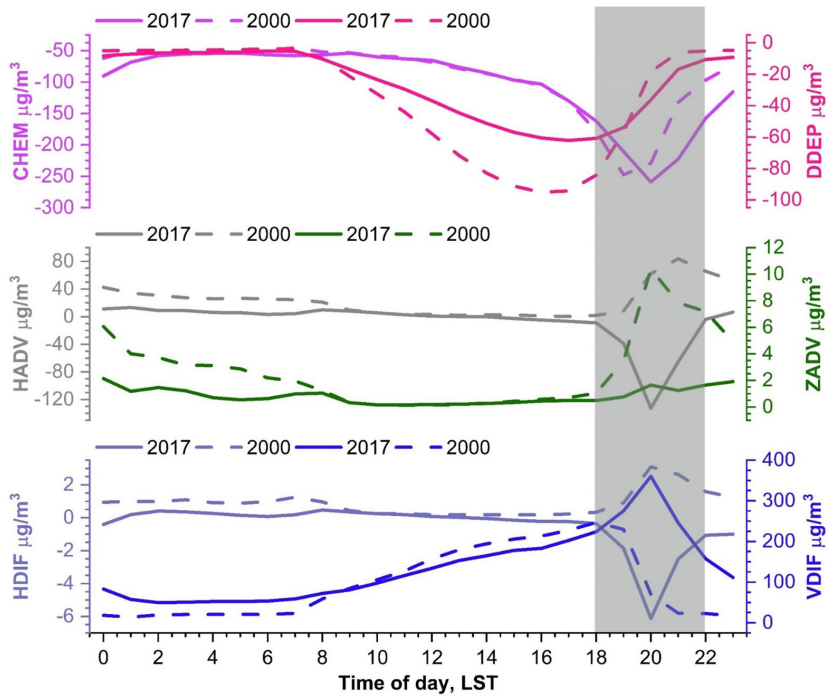

FIGURE 12 | Diurnal pattern of physical and chemical processes for O_3 in 2000 and 2017. The average data was calculated from the value of UEA.

40 μg/m^3, which is consistent with the variation of nocturnal temperature in **Supplementary Figure 5B**. This pattern implies that the impacts of the thermal inertia of urban buildings govern this phenomenon, as the cooling rates over anthropogenic land surface are lower than natural LULC. Furthermore, there is a notable increase in O_3 concentrations at 18:00 throughout the UEA with a similar spatial pattern and magnitude as 00:00. **Figure 11** demonstrates that O_3 and NO_2 concentrations increased significantly at 20:00 with values of 61.4 and 62.3 μg/m^3, respectively, while the concentrations of O_3 and NO_2 did not change significantly during the daytime, which is due to that VI had remarkable increase around 20:00 while VI changed marginally during the daytime. Thus, regions with lower NO_2 levels (i.e., UEA) would accumulate more O_3 concentrations due to the weaker titration during the nighttime.

Changes in O_3 concentrations are mainly caused by HADV and VDIF processes, as seen in **Figure 12**. Accumulated contribution from VDIF increase to 323.4 μg/m^3 becasuse PBLH and vertical wind speed both increase induced by urbanization. In terms of HADV process, the increase of WS10 facilitates

the dispersion and transport outflow of O_3, which cause O_3 concentrations to decrease by 133.7 $\mu g/m^3$ in 2017 while to increase 43.3 $\mu g/m^3$ in 2000. Higher plant fraction in 2000 leads to stronger DDEP process during the daytime because vegetation could consume O_3 through plant stomata. However, during the nighttime, the intensity of DDEP process in 2000 is weaker than that in 2017 which is due to that O_3 concentrations in 2000 is much lower than that in 2017 at this time.

CONCLUSION

In this study, we use parallel WRF-UCM-CMAQ modeling with LULC data in 2000 and 2017 to investigate the effects of urbanization on regional meteorology and air quality in Chengdu, a typical megacity in the southwestern China. Changes in key meteorological parameters and air pollutants levels are compared in a summertime high O_3 event and a winter $PM_{2.5}$ episode.

Our results find that land surface alteration induced by urbanization exhibits profound effects on meteorological parameters across UEA. In winter, urbanization leads to reduced T2 (by −1.1°C) and increased VI (by 819 m^2/s) during the daytime, while increasing T2 (by 0.46°C) and VI (by 328 m^2/s) at night in summer, urbanization increased T2 throughout the day (0.55°C during the day and 2.0°C at night) while VI increased by 1,161 m^2/s during 18:00-20:00 and decreased by 355 m^2/s during the other times. The magnitude difference in nocturnal T2 between winter and summer is mainly because the intense solar radiation in summer lead urban surface to store more heat, which can raise T2 at night. The differences in VI can be attributed to changes in PBLH and WS10 caused by increased surface roughness and reduced surface albedo, as well as energy changes in atmospheric turbulence caused by SE.

Changes in regional meteorology have an impact on gaseous pollutants concentrations and particulate pollution. $PM_{2.5}$ concentrations are dictated by the various competing processes, including (a) the gas-particle phase partitioning, (b) the atmospheric oxidation rate, and (c) ventilation. In addition, urbanization caused the LULC from vegetation dominated shift to the anthropogenic land surface, which results in reduced BSOA concentrations (by 3.4 $\mu g/m^3$). These processes lead to $PM_{2.5}$ decrease by 33.2 and 4.6 $\mu g/m^3$ during the daytime and nighttime, respectively. For O_3, it is found that urbanization leads to insignificant changes in daytime O_3 levels while nocturnal O_3 concentrations in 2017 substantially increase as compared with 2000, which is attributed to VDIF process at night bringing in more concentrations.

Here, we demonstrate the crucial effects of urbanization on urban meteorological parameters and its subsequent influence on air quality by taking the megacity of Chengdu as an example. The findings of this work contribute insight into developing climate adaptation and air pollution mitigation strategies for megacities and heavily urbanized areas.

DATA AVAILABILITY STATEMENT

Publicly available datasets were analyzed in this study. This data can be found here: http://meicmodel.org/, https://earthdata.nasa.gov/, and https://rda.ucar.edu/datasets/ds083.2/index.html.

AUTHOR CONTRIBUTIONS

HW: conceptualization, methodology, formal analysis, investigation, writing—original draft, visualization, and project administration. ZL: conceptualization and project administration. KW: conceptualization and writing—review and editing. JQ: review and editing. YZ: conceptualization, writing—review and editing, and project administration. BY and MH: resources and data curation. All authors contributed to the article and approved the submitted version.

FUNDING

This study was funded by the National Natural Science Foundation of China (No. 41901294), the Scientific Research Foundation of CUIT (No. KYTZ201909), the Science and Technology Department of Sichuan Province Foundation (No. 21YYJC3604), the Key Research and Development Projects of Sichuan Science and Technology (No. 2022YFS0482), Sichuan Science and Technology Program (No. 2020YFG0144), and FengYun Application Pioneering Project (No. FY-APP-2021.0208).

ACKNOWLEDGMENTS

We thank the MEIC team from Tsinghua University for providing the Multiscale Emission Inventory of China (MEIC).

SUPPLEMENTARY MATERIAL

The Supplementary Material for this article can be found online at: https://www.frontiersin.org/articles/10.3389/fevo.2022.845801/full#supplementary-material

REFERENCES

Appel, K. W., Bash, J. O., Fahey, K. M., Foley, K. M., Gilliam, R. C., Hogrefe, C., et al. (2021). The Community Multiscale Air Quality (CMAQ) model versions 5.3 and 5.3.1: system updates and evaluation. *Geosci. Model Dev.* 14, 2867–2897. doi: 10.5194/gmd-14-2867-2021

Boylan, J. W., and Russell, A. G. (2006). PM and light extinction model performance metrics, goals, and criteria for three-dimensional air quality models. *Atmosph. Env.* 40, 4946–4959. doi: 10.1016/j.atmosenv.2005.09.087

Chen, S.-H., and Sun, W.-Y. (2002). A One-dimensional Time Dependent Cloud Model. *J. Meteorol. Soc. Jap.* 80, 99–118. doi: 10.2151/jmsj.80.99

Chou, M.-D., Suarez, M. J., Liang, X.-Z., Yan, M. M.-H., and Cote, C. (2001). *A Thermal Infrared Radiation Parameterization for Atmospheric Studies. NASA Technique Report NASA/TM-2001-104606*. Greenbelt, MD: National Aeronautics and Space Administration, Goddard Space Flight Center.

Ek, M. B., Mitchell, K. E., Lin, Y., Rogers, E., Grunmann, P., Koren, V., et al. (2003). Implementation of Noah land surface model advances in the National Centers for Environmental Prediction operational mesoscale Eta model. *J. Geophys. Res.* 108:2002JD003296. doi: 10.1029/2002JD003296

Emery, C., Liu, Z., Russell, A. G., Odman, M. T., Yarwood, G., and Kumar, N. (2017). Recommendations on statistics and benchmarks to assess photochemical model performance. *J. Air Waste Manag. Assoc.* 67, 582–598. doi: 10.1080/10962247.2016.1265027

Fan, C., Myint, S., Kaplan, S., Middel, A., Zheng, B., Rahman, A., et al. (2017). Understanding the Impact of Urbanization on Surface Urban Heat Islands—A Longitudinal Analysis of the Oasis Effect in Subtropical Desert Cities. *Remote Sens.* 9:672. doi: 10.3390/rs9070672

Fang, C., Qiu, J., Li, J., and Wang, J. (2022). Analysis of the meteorological impact on $PM_{2.5}$ pollution in Changchun based on KZ filter and WRF-CMAQ. *Atmospheric Env.* 271:118924. doi: 10.1016/j.atmosenv.2021.118924

Grimm, N. B., Faeth, S. H., Golubiewski, N. E., Redman, C. L., Wu, J., Bai, X., et al. (2008). Global Change and the Ecology of Cities. *Science* 319, 756–760. doi: 10.1126/science.1150195

Guenther, A. B., Jiang, X., Heald, C. L., Sakulyanontvittaya, T., Duhl, T., Emmons, L. K., et al. (2012). The Model of Emissions of Gases and Aerosols from Nature version 2.1 (MEGAN2.1): an extended and updated framework for modeling biogenic emissions. *Geosci. Model Dev.* 5, 1471–1492. doi: 10.5194/gmd-5-1471-2012

Janjić, Z. I. (1994). The Step-Mountain Eta Coordinate Model: Further Developments of the Convection, Viscous Sublayer, and Turbulence Closure Schemes. *Mon. Wea. Rev.* 122, 927–945. doi: 10.1175/1520-04931994122<0927:TSMECM<2.0.CO;2

Kim, G., Lee, J., Lee, M.-I., and Kim, D. (2021). Impacts of urbanization on atmospheric circulation and aerosol transport in a coastal environment simulated by the WRF-Chem coupled with urban canopy model. *Atmosph. Env.* 249:118253. doi: 10.1016/j.atmosenv.2021.118253

Kusaka, H., and Kimura, F. (2004). Coupling a Single-Layer Urban Canopy Model with a Simple Atmospheric Model: impact on Urban Heat Island Simulation for an Idealized Case. *J. Meteorol. Soc. J.* 82, 67–80. doi: 10.2151/jmsj.82.67

Li, Y., Zhang, J., Sailor, D. J., and Ban-Weiss, G. A. (2019). Effects of urbanization on regional meteorology and air quality in Southern California. *Atmos. Chem. Phys.* 19, 4439–4457. doi: 10.5194/acp-19-4439-2019

Lian, J., Wu, L., Bréon, F.-M., Broquet, G., Vautard, R., Zaccheo, T. S., et al. (2018). Evaluation of the WRF-UCM mesoscale model and ECMWF global operational forecasts over the Paris region in the prospect of tracer atmospheric transport modeling. *Elementa: Sci. Anthrop.* 6:64. doi: 10.1525/elementa.319

Liao, J., Wang, T., Wang, X., Xie, M., Jiang, Z., Huang, X., et al. (2014). Impacts of different urban canopy schemes in WRF/Chem on regional climate and air quality in Yangtze River Delta, China. *Atmosph. Res.* 145–146, 226–243. doi: 10.1016/j.atmosres.2014.04.005

Lin, C.-Y., Su, C.-J., Kusaka, H., Akimoto, Y., Sheng, Y.-F., Huang, J.-C., et al. (2016). Impact of an improved WRF urban canopy model on diurnal air temperature simulation over northern Taiwan. *Atmos. Chem. Phys.* 16, 1809–1822. doi: 10.5194/acp-16-1809-2016

Mlawer, E. J., Taubman, S. J., Brown, P. D., Iacono, M. J., and Clough, S. A. (1997). Radiative transfer for inhomogeneous atmospheres: RRTM, a validated correlated-k model for the longwave. *J. Geophys. Res.* 102, 16663–16682. doi: 10.1029/97JD00237

Murphy, B. N., Woody, M. C., Jimenez, J. L., Carlton, A. M. G., Hayes, P. L., Liu, S., et al. (2017). Semivolatile POA and parameterized total combustion SOA in CMAQv5.2: impacts on source strength and partitioning. *Atmos. Chem. Phys.* 17, 11107–11133. doi: 10.5194/acp-17-11107-2017

Pye, H. O. T., Murphy, B. N., Xu, L., Ng, N. L., Carlton, A. G., Guo, H., et al. (2017). On the implications of aerosol liquid water and phase separation for organic aerosol mass. *Atmos. Chem. Phys.* 17, 343–369. doi: 10.5194/acp-17-343-2017

Salamanca, F., Martilli, A., Tewari, M., and Chen, F. (2011). A Study of the Urban Boundary Layer Using Different Urban Parameterizations and High-Resolution Urban Canopy Parameters with WRF. *J. Appl. Meteorol. Climat.* 50, 1107–1128. doi: 10.1175/2010JAMC2538.1

Seto, K. C., Guneralp, B., and Hutyra, L. R. (2012). Global forecasts of urban expansion to 2030 and direct impacts on biodiversity and carbon pools. *Proc. Natl. Acad. Sci.* 109, 16083–16088. doi: 10.1073/pnas.1211658109

Skamarock, W. C., Klemp, J. B., Dudhia, J., Gill, D. O., Liu, Z., Berner, J., et al. (2019). *A Description of the Advanced Research WRF Model Version 4. UCAR/NCAR*. doi: 10.5065/1DFH-6P97

Vahmani, P., and Ban-Weiss, G. A. (2016). Impact of remotely sensed albedo and vegetation fraction on simulation of urban climate in WRF-urban canopy model: A case study of the urban heat island in Los Angeles: Satellite-supported urban climate model. *J. Geophys. Res. Atmos.* 121, 1511–1531. doi: 10.1002/2015JD023718

Vahmani, P., and Hogue, T. S. (2014). Incorporating an Urban Irrigation Module into the Noah Land Surface Model Coupled with an Urban Canopy Model. *J. Hydromet.* 15, 1440–1456. doi: 10.1175/JHM-D-13-0121.1

Vahmani, P., Sun, F., Hall, A., and Ban-Weiss, G. (2016). Investigating the climate impacts of urbanization and the potential for cool roofs to counter future climate change in Southern California. *Environ. Res. Lett.* 11, 124027. doi: 10.1088/1748-9326/11/12/124027

Wang, H., Liu, Z., Zhang, Y., Yu, Z., and Chen, C. (2021). Impact of different urban canopy models on air quality simulation in Chengdu, southwestern China. *Atmosph. Env.* 267:118775. doi: 10.1016/j.atmosenv.2021.118775

Wang, K., Tong, Y., Gao, J., Gao, C., Wu, K., Yue, T., et al. (2021). Impacts of LULC, FDDA, Topo-wind and UCM schemes on WRF-CMAQ over the Beijing-Tianjin-Hebei region, China. *Atmosph. Pollut. Res.* 12, 292–304. doi: 10.1016/j.apr.2020.11.011

Wu, K., Wang, Y., Qiao, Y., Liu, Y., Wang, S., Yang, X., et al. (2022). Drivers of 2013–2020 ozone trends in the Sichuan Basin China: Impacts of meteorology and precursor emission changes. *Env. Pollut.* 300:118914. doi: 10.1016/j.envpol.2022.118914

Wu, K., Yang, X., Chen, D., Gu, S., Lu, Y., Jiang, Q., et al. (2020). Estimation of biogenic VOC emissions and their corresponding impact on ozone and secondary organic aerosol formation in China. *Atmosph. Res.* 231:104656. doi: 10.1016/j.atmosres.2019.104656

Wu, K., Zhu, S., Liu, Y., Wang, H., Yang, X., Liu, L., et al. (2021). Modeling Ammonia and Its Uptake by Secondary Organic Aerosol Over China. *Geophys. Res. Atmos.* 126:34109. doi: 10.1029/2020JD034109

Xu, C.-X., Chen, J.-H., Li, Y., He, M., Feng, X.-Q., and Han, L. (2020). Emission Inventory and Characteristics of Anthropogenic Air Pollution Sources Based on Second Pollution Source Census Data in Sichuan Province. *Huan Jing Ke Xue* 41, 4482–4494. doi: 10.13227/j.hjkx.202002162

Yang, X., Wu, K., Wang, H., Liu, Y., Gu, S., Lu, Y., et al. (2020a). Summertime ozone pollution in Sichuan Basin, China: Meteorological conditions, sources and process analysis. *[J]. Atmos. Environ.* 226:117392.

Yang, X., Lu, Y., Zhu, X., He, J., Jiang, Q., Wu, K., et al. (2020b). Formation and Evolution Mechanisms of Severe Haze Pollution in the Sichuan Basin, Southwest China. *Aerosol. Air. Qual. Res.* 20, 2557–2567. doi: 10.4209/aaqr.2020.04.0173

Yang, X., Wu, K., Lu, Y., Wang, S., Qiao, Y., Zhang, X., et al. (2021). Origin of regional springtime ozone episodes in the Sichuan Basin, China: Role of synoptic forcing and regional transport. *Environ. Poll.* 278:116845. doi: 10.1016/j.envpol.2021.116845

Yarwood, G., Jung, J., Whitten, G. Z., Heo, G., Mellberg, J., and Estes, M. (2010). "Updates to the Carbon Bond mechanism for version 6 (CB6)," in *9th Annual CMAS Conference*, (Chapel Hill, NC), 11–13.

Conflict of Interest: The authors declare that the research was conducted in the absence of any commercial or financial relationships that could be construed as a potential conflict of interest.

Publisher's Note: All claims expressed in this article are solely those of the authors and do not necessarily represent those of their affiliated organizations, or those of the publisher, the editors and the reviewers. Any product that may be evaluated in this article, or claim that may be made by its manufacturer, is not guaranteed or endorsed by the publisher.

frontiers | Frontiers in Environmental Science

ORIGINAL RESEARCH
published: 06 June 2022
doi: 10.3389/fenvs.2022.907868

Unexpected Methane Emissions From Old Small Fishing Vessels in China

Lizhi Wang[1,2,3], Wei Du[2,4], Huizhong Shen[5,6], Yuanchen Chen[7], Xi Zhu[2], Xiao Yun[2], Guofeng Shen[2], Yilin Chen[5,6], Junfeng Liu[2], Xuejun Wang[2] and Shu Tao[2,5,6]*

[1]Key Laboratory of Agro-Forestry Environmental Processes and Ecological Regulation of Hainan Province, Hainan University, Haikou, China, [2]Laboratory for Earth Surface Processes, College of Urban and Environmental Sciences, Sino-French Institute for Earth System Science, Peking University, Beijing, China, [3]College of Ecology and Environment, Hainan University, Haikou, China, [4]Key Laboratory of Geographic Information Science of the Ministry of Education, School of Geographic Sciences, East China Normal University, Shanghai, China, [5]School of Environmental Science and Engineering, Southern University of Science and Technology, Shenzhen, China, [6]Guangdong Provincial Observation and Research Station for Coastal Atmosphere and Climate of the Greater Bay Area, Southern University of Science and Technology, Shenzhen, China, [7]College of Environment, Research Centre of Environmental Science, Zhejiang University of Technology, Hangzhou, China

Diesel-fueled ships have long been considered to contribute a marginal fraction of the global methane (CH_4) emission budget compared to liquified natural gas (LNG)-fueled ships. Here, based on real-world measurements, we find that a specific yet-overlooked group of diesel-fueled ships–the old small fishing vessels (OSFVs)–is associated with high levels of CH_4 emissions. The emission factors of CH_4 from OSFVs is on average 5.2 ± 6.4 g CH_4 per 1 kg fuel consumed, approaching EF_{CH4} of LNG-fueled ships (5.3–30.1 g/kg) and being at least six times EF_{CH4} of other types of diesel-fueled ships (0.0–0.9 g/kg). We estimate that CH_4 emissions from OSFVs in China amount to 570–2,240 t per year, which is comparable to the total CH_4 emission from all LNG-fueled ships worldwide. Our results thus call for revision of the global CH_4 emission inventory for shipping.

Keywords: methane emission, old small fishing vessel, emission factor, climate change, China

OPEN ACCESS

Edited by:
Haofei Yu,
University of Central Florida, United States

Reviewed by:
Junwen Liu,
Jinan University, China
Congmeng Lyu,
University of Colorado Boulder, United States

***Correspondence:**
Huizhong Shen
shenhz@sustech.edu.cn

Specialty section:
This article was submitted to Atmosphere and Climate, a section of the journal Frontiers in Environmental Science

Received: *30 March 2022*
Accepted: *11 May 2022*
Published: *06 June 2022*

Citation:
Wang L, Du W, Shen H, Chen Y, Zhu X, Yun X, Shen G, Chen Y, Liu J, Wang X and Tao S (2022) Unexpected Methane Emissions From Old Small Fishing Vessels in China. Front. Environ. Sci. 10:907868. doi: 10.3389/fenvs.2022.907868

INTRODUCTION

Methane (CH_4) is a powerful greenhouse gas with radiative forcing on average 80.8–82.5 times that of carbon dioxides of an equal mass over 20 years and 27.2–29.8 times over 100 years. (Forster et al., 2021). CH_4 is an important precursor of tropospheric ozone which has adverse effects on human health and vegetation growth (Crutzen, 1973). CH_4 emissions from shipping have gained growing attention due to the expansion of maritime transportation in the context of globalization (Olmer et al., 2017; Ushakov et al., 2019). Past studies on shipping emissions of CH_4 have been focused on liquified natural gas (LNG)-powered ships because substantial CH_4 can escape unburned at the exhaust from low-pressure LNG-fueled engines of these ships, as is called "CH_4 slip" (Ushakov et al., 2019). Diesel-powered ships, on the other hand, have typically much lower levels of CH_4 slip (two orders of magnitude lower than LNG-powered ships) (Nielsen and Stenersen, 2010), and their CH_4 emissions are considered to be negligible (Nielsen and Stenersen, 2010).

However, not all the diesel engines are CH_4 free. Engines subject to old technology or under poor maintenance may release high levels of CH_4 because, in addition to direct slip, CH_4 is produced by incomplete combustion that occurs more frequently in old engines or during abnormal engine operation (Nam et al., 2004; Amous, 2000; Karakurt et al., 2012). It was found, for example, that emission factors of CH_4 (EF_{CH4}, i.e., the amount of CH_4 emitted per unit mass of fuel consumed) for on-road vehicles with a model year of 1980 were six times the EF_{CH4} for those with a model year of 2000 (Nam et al., 2004). Similar differences are expected for ships, with poorly-maintained old ships

being associated with higher levels of CH_4. However, investigations on CH_4 emissions from old ships are scarce.

Old small fishing vessels (OSFVs, defined as small fishing vessels over ten-year age) in China are a typical group of vessels privately owned by local fishermen in low-income community. Most OSFVs are under poor maintenance conditions and absent from regular official emission inspection. China Fishery Statistical Yearbook reported a total of 370 thousand small fishing vessels which account for half of the fishing fleet in China (Ministry of Agriculture and Rural Affairs of the People's Republic of China, 2020), but their aging rate (i.e., the fraction of OSFVs among the small fishing vessels) is not known. Assuming an aging rate between 12 and 47% based on other types of ships on record (including dry bulk cargo ship, container vessel, and liquid cargo) (Ministry of Transport of the People's Republic of China, 2021a), OSFVs may account for 6–24% of the fishing fleet in China—the top fishery country of the world. The tonnage of China's OSFVs (140,000–550,000 tonnes) could be comparable with that of the entire fishing fleet in some world's leading fishery countries, such as the United States (271,000 tonnes), Norway (392,000 tonnes), Vietnam (445,000 tonnes), Korea (512,000 tonnes), Philippines ($495,000 tonnes), or Japan (936,000 tonnes) (Organisation for Economic Co-operation and Development, 2019). Despite the large number and high emission potentials, EF_{CH4} of OSFVs have not yet been investigated, and their share of China's total shipping emission is unclear.

In this study, we measured EF_{CH4} of typical OSFVs in China. To the best of our knowledge, this is the first time to report EF_{CH4} of OSFVs. We further compared OSFVs' EF_{CH4} with EF_{CH4} of other ships that were measured in this study or reported in literature. Based on our measurements, we estimated the CH_4 emissions from OSFVs and discussed the importance of OSFVs for CH_4 emissions from shipping in China.

METHODS

On-Site Measurements

On-site measurements were conducted on three OSFVs which were all more than 10 years old and less than 12 m in length (**Supplementary Table S1**). The OSFVs were all wooden boats whose tonnages ranged from 10 to 15 t. Each OSFV was equipped with a diesel engine. The engine capacities of these three OSFVs were 8.8, 16, and 108 kW, respectively. For comparison, other types of marine vessels were also tested, including three medium fishing boats, three tug boats, one ferry, one cargo, and two engineering vessels. The tonnages of these vessels were much larger than those of OSFVs, ranging from 69 t for medium fishing boats to 6,000 t for one of the engineering vessels. All vessels were fueled with marine light diesel. The compositions and properties of light diesel from local gas stations were analyzed and summarized in **Supplementary Table S2**. Note that the light diesel used by the vessels may not meet the China's national standards because inferior cheap diesel may be provided and distributed by illegal suppliers in local areas (Long and Shi, 2020). More details about the OSFVs and other tested vessels, including their age, tonnage, engine power, length, etc., are provided in **Supplementary Table S1** with the vessels' photographs shown in **Supplementary Figure S1**.

On-site emission sampling was conducted in May 2016 and August 2017 in three harbors, i.e., Yangpu, Haikou, and Sanya in Hainan Province, China (**Supplementary Figure S2**). The on-site sampling system consisted of a sampling probe (with the inner diameter of 10 mm), a residence chamber, a particulate matter pre-filter, a gas sensor box, an online nondispersive infrared analyzer (GXH-3051, Beijing Junfang Lihua Institute of Science & Technology, China), and an active pump (SKC, PA, United States) (**Supplementary Figure S3**). During sampling, the gas pump was operated at a flow rate of ~2.0 L/min. Exhaust gases were extracted through the sampling probe placed near the centers of the engine exhaust ports (or chimneys for large vessels). The sampled gases were then directed into the residence chamber to facilitate better mixing and subsequently went through the particulate matter filter to avoid excessive particulate loading and through silica gel to remove water vapor. Filtered dry gases were collected in the gas sensor box where CH_4, carbon dioxide (CO_2), and carbon monoxide (CO) concentrations were measured using the online nondispersive infrared analyzer. All the instruments were checked and calibrated prior every sampling cycle. The flow of the gas pump was calibrated both before and after sampling, using a primary flow calibrator (Bios Defender 510, United States). The layout of the sampling system is shown in **Supplementary Figure S3**. Similar sampling systems have been used to measure shipping emissions of particulate- and gaseous-phase pollutants, as described in detail in previous studies (Wang et al., 2022a; Wang et al., 2022b).

The on-site measurements covered an array of driving modes, including cruising, operating, manoeuvring, and berthing. For cruising and berthing modes, each sampling cycle lasted for about 10 minutes when the vessels ran under stable engine loads. For maneuvering and operating modes, each sampling cycle covered a whole activity period. During most sampling cycles, repetitive samples were collected simultaneously, from which the averages and variations of the measurement results were taken.

Calculation of Emission Factors

We calculated fuel-based EF_{CH4} in the unit of g × (kg fuel)$^{-1}$ based on the widely-used carbon mass balance method (Zhang et al., 2000), assuming that carbon in fuel is mainly emitted in the form of CO_2, CO, and CH_4. EF_{CH4} is calculated as follows,

$$EF_{CH_4} = \frac{1000 \times C_{CH_4} \times f_{C-fuel}}{C_{CO_2} \times f_{C-CO_2} + C_{CO} \times f_{C-CO} + C_{C-CH_4} \times f_{CH_4}}$$

where C_{CH4}, C_{CO2}, and C_{CO} are measured concentrations of CH_4, CO_2, and CO in exhaust gas, respectively; $f_{C\text{-}CH4}$, $f_{C\text{-}CO2}$, and f_{CO} denote carbon contents in CH_4, CO_2, and CO, respectively, and are 12/16, 12/44, and 12/28, respectively; $f_{C\text{-}fuel}$ denotes the carbon content in fuel and was measured to be 86.5% in this study. Following previous studies, (Zhang et al., 2018; Wang et al., 2022b) integrated EF_{CH4} of each type of vessel, representing a daily average level, was calculated by integrating EF_{CH4} under different driving modes with corresponding time-driving mode patterns. Detailed procedures for calculating integrated EF can be found in previous studies. (Zhang et al., 2018; Wang et al., 2022b)

TABLE 1 | Integrated emission factors of methane (EF_{CH4}) from different types of vessels measured in this study.

Vessel type	Number of vessels	Number of sampling cycles	EF_{CH4}, g/kg
			Mean (Standard deviation)
OSFV	3	8	5.23 (6.40)
Fishing vessel, median	5	12	0.02 (0.03)
Tug boat	3	20	0.05 (0.11)
Ferry	1	2	0.93 (1.21)
Cargo	1	3	0.00 (0.00)
Engineering vessel	2	13	0.04 (0.13)

Note: The EF_{CH4} listed in this table integrates EF_{CH4} under different driving modes with corresponding time-driving mode patterns (Zhang et al., 2018; Wang et al., 2022b). "OSFV" denotes old small fishing vessel.

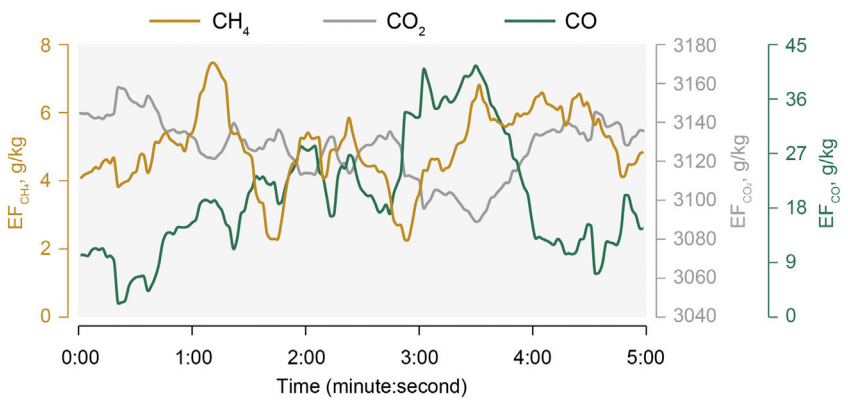

FIGURE 1 | The measured temporal variation in instantaneous EF_{CH4}, EF_{CO2}, and EF_{CO} of a typical OSFV during cruising.

RESULTS AND DISCUSSION

Average EF_{CH4} of OSFVs and Variations

The average EF_{CH4} of the 58 measurements is 0.9 g/kg (g CH_4 emitted per kg fuel burned), varying among individual measurements from 0 to 14.8 g/kg. When considering time-driving mode patterns, the integrated EF_{CH4} range from 0 g/kg for cargoes to 5.2 g/kg for OSFVs. **Table 1** shows the integrated EF_{CH4} values and standard deviations of different types of vessels, which reveals considerable differences in EF_{CH4} levels. Median fishing vessels (0.02 g/kg), tugs (0.05 g/kg), cargoes (0.00 g/kg), and engineering ships (0.04 g/kg) have much lower EF_{CH4} than ferries (0.9 g/kg) and OSFVs (5.2 g/kg).

Factors Affecting EF_{CH4}

The average EF_{CH4} of the 58 measurements (0.90 g/kg) was more than one order of magnitude higher than the EF_{CH4} proposed by the International Maritime Organization (IMO) in their latest GHG study (0.04–0.05 g/kg) (Faber et al., 2020). This difference was mainly driven by the high levels of EF_{CH4} from OSFVs which were on average over 100 times the IMO proposed levels. Note that the IMO's EF_{CH4} (0.04–0.05 g/kg) was used to represent a fleet-average level for estimating global emissions from diesel-fueled ships and was based on measurements conducted on four ships only (Cooper and Gustafsson, 2004; Faber et al., 2020). Among the four ships, none were OSFVs.

Despite the high average of OSFVs' EF_{CH4}, EF_{CH4} of individual OSFVs vary widely and fluctuate in time during each driving cycle. The three OSFVs we measured have EF_{CH4} of 0.0, 1.6, and 12.3 g/kg, respectively. The near-zero EF_{CH4} of the first OSFV is likely associated with its installation of a different type of engine which has a much higher capacity (108 kW) than those of the other two OSFVs (16 and 8.8 kW, respectively). The third OSFV shows the highest EF_{CH4}, which may be a result of its being the oldest (15 years) among the three OSFVs (10 years for the other two). High temporal resolution of the measurement data allows for further investigation into the instantaneous EF_{CH4} during sailing. **Figure 1** shows the temporal variation of EF_{CH4} over 5 minutes in the middle of a typical sailing cycle. EF_{CH4} are found to be changing by a factor of three (from 2.3 to 7.2 g/kg) within this short period, which are more variable than the EFs of CO_2, as expected, but less variable than the EFs of CO (varying by a factor of 18) (**Figure 1**). The ratio of CH_4/CO_2 in OSFV exhaust is on average 1.5×10^{-3}, which is much larger than the other types of diesel-fueled ships measured in this study (6.1×10^{-4} on average) but lower than LNG-fueled ships as reported in literature (typically 0.6–0.9%) (Ushakov et al., 2019).

CH_4 emissions from LNG-fueled ships have been of great concern due to substantial CH_4 slipping from LNG-fueled ships—LNG typically contains more than 90% CH_4 which is subject to potential leakage during engine operation (Guo and Ghalambor, 2014; Ushakov et al., 2019). CH_4 content in diesel, on the other hand, is neglectable, and diesel-fueled ships are

associated with EF_{CH4} levels typically two orders of magnitude lower than those of LNG-fueled ships (Faber et al., 2020). Surprisingly, the average measured EF_{CH4} of OSFVs (5.2 g/kg) in this study, which are fueled by diesel, is over six times EF_{CH4} of other diesel-fueled ships measured in this study and approaches those of LNG-fueled ships reported in literature (5.3–30.1 g/kg) (Ushakov et al., 2019; Faber et al., 2020). As we measured, the composition of fuel collected from nearby gas stations represents common diesel composition (**Supplementary Table S2**). Therefore, such high levels of CH_4 are very likely a result of combustion by-products under abnormal engine operation rather than slipping of unburned fuel. This presumption is strengthened by similarly higher levels of emissions from OSFVs of other incomplete by-products reported in previous studies (Wang et al., 2022a; Wang et al., 2022b). Nevertheless, the underlying mechanisms leading to the high EF_{CH4} of OSFVs warrant further investigation.

CH_4 Emissions From Domestic OSFVs and Implications

Assuming that the fraction of OSFVs among small fishing vessels fall within the range of 12–47% (note that the range is based on the reported aging rates of other types of ships in China) (Ministry of Transport of the People's Republic of China, 2021a), we estimate that the oil consumption by OSFVs in China is 4.7–18.3 PJ $year^{-1}$ in 2020. In comparison, the global consumption of LNG by shipping estimated by the International Energy Agency is 12.7 PJ $year^{-1}$ in the same year (International Energy Agency, 2019). OSFVs in China alone amounts to an annual CH_4 emission of approximately 570–2,240 t, which is similar in magnitude to the CH_4 emission from all LNG-fueled ships globally (2,610 t) (Faber et al., 2020).

The robustness of the current study is affected by both the limited number of ships investigated and the high variability of EF_{CH4} among OSFVs. As for the OSFVs monitored, only one exceeds significantly from the average EF_{CH4} (0.90 g/kg), reaching a mean value of 12.3 g/kg, while the other two show limited emissions (0.0 and 1.6 g/kg), which warrants more measurements for further investigation. We also note that the literature-reported EF_{CH4} data for diesel-fueled ships are very scarce. For example, IMO uses data from merely four ships to approximate the average EF_{CH4} of the global diesel-fueled fleet. The measured EF_{CH4} of the three OSFVs and 12 diesel-fueled ships of other types in this study, therefore, represent a significant addition to the current EF_{CH4} dataset.

In recent years, China has made great efforts to reduce pollutants emissions from various sources (Zheng et al., 2018; Xie, 2020), including domestic shipping (Ministry of Ecology and Environment of the People's Republic of China, 2018). OSFVs are being phased out due to stringent regulations and incentives to promote replacement of OSFVs (Ministry of Agriculture and Rural Affairs, 2019; Ministry of Transport of the People's Republic of China, 2021b). In a follow-up investigation, we conducted an expanded survey on the actual share of OSFVs operating in Hainan in 2021, 4 years after our emission measurements were carried out. The survey investigated 67 small fishing vessels in eight main harbors in Hainan and revealed an aging rate of 16% among the small fishing vessels, which is close to the lower bound of our estimated aging rate (12–47%). The difference between the survey-based local aging rate and the estimated nationwide aging rate is reasonable, given that Hainan together with some other leading ocean fishing provinces pioneers the phasing-out of OSFVs (Department of Agriculture and Rural Affairs of Hainan Province, 2018). Considering the high emission levels of CH_4, as revealed in this study, and other incomplete combustion by-products (Wang et al., 2022a; Wang et al., 2022b), the phasing-out of OSFVs driven by stringent regulations may yield significant climate and health cobenefits.

DATA AVAILABILITY STATEMENT

The original contributions presented in the study are included in the article/**Supplementary Material**, further inquiries can be directed to the corresponding author.

AUTHOR CONTRIBUTIONS

LW: Methodology, Investigation, Formal analysis, Writing—review and editing. WD: Methodology, Investigation, Writing—review and editing. HS: Investigation, Formal analysis, Writing—original draft, Writing—review and editing, Funding acquisition. YC: Methodology, Investigation. XZ: Methodology, Investigation. XY: Methodology, Investigation. GS: Methodology, Investigation, Funding acquisition. YC: Methodology, Investigation, Formal analysis. JL: Conceptualization, Methodology. XW: Methodology, Investigation. ST: Conceptualization, Methodology, Writing—review and editing, Funding acquisition.

FUNDING

This research is supported by the National Natural Science Foundation of China (Grants 41991312, 41821005, 41922057, 41830641, and 42192510), Department of Science and Technology of Guangdong Province (Grant 2021B1212050024), Department of Education of Guangdong Province (2021KCXTD004), Shenzhen Environmental Monitoring Center (Grant 0722-216FE4812SZF-2), and Center for Computational Science and Engineering at Southern University of Science and Technology.

SUPPLEMENTARY MATERIAL

The Supplementary Material for this article can be found online at: https://www.frontiersin.org/articles/10.3389/fenvs.2022.907868/full#supplementary-material

Supplementary Figure S1 | On-site photographs of the old small fishing vessels **(A)**, medium fishing boats **(B)**, tug boats **(C)**, ferries **(D)**, cargo **(E)**, and engineering vessels **(F)** tested in this study.

Supplementary Figure S2 | The map of the sampling locations.

Supplementary Figure S3 | Schematic of the on-site sampling system.

Supplementary Table S1 | Summary of the key information on the tested vessels.

Supplementary Table S2 | Summary of the content of carbon (C), hydrogen (H), nitrogen (N), and sulfur (S) in local light diesel at Yangpu port.

REFERENCES

Amous, S. (2000). "Non-CO_2 Emissions From Stationary Combustion," in *Good Practice Guidance and Uncertainty Management in National Greenhouse Gas Inventories*. IPCC, 41–54.

Cooper, D., and Gustafsson, T. (2004). *Methodology for Calculating Emissions from Ships: 1. Update of Emission Factors*. Norrköping, Sweden: SMHI Swedish Meteorological and Hydrological Institute.

Crutzen, P. (1973). A Discussion of the Chemistry of Some Minor Constituents in the Stratosphere and Troposphere. *Pageoph* 106-108 (1), 1385–1399. doi:10.1007/bf00881092

Department of Agriculture and Rural Affairs of Hainan Province (2018). Announcement of the Proposed Subsidy for the Renewal and Transformation of Marine Fishing Fishing Vessels in Hainan Province in 2018. Available at: https://agri.hainan.gov.cn/hnsnyt/xxgk/0200/0202/201901/t20190124_2267113.html (accessed 2021/8/13).

Faber, J., Hanayama, S., Zhang, S., Pereda, P., Comer, B., Hauerhof, E., et al. (2020). Reduction of GHG Emissions from Ships—Fourth IMO GHG Study 2020—Final Report. *IMO MEPC* 75 (7), 15.

Forster, P., Storelvmo, T., Armour, K., Collins, W., Dufresne, J.-L., Frame, D., et al. (2021). "The Earth's Energy Budget, Climate Feedbacks, and Climate Sensitivity," in *Climate Change 2021: The Physical Science Basis. Contribution of Working Group I to the Sixth Assessment Report of the Intergovernmental Panel on Climate Change*. Editors V. Masson-Delmotte, P. Zhai, A. Pirani, S. L. Connors, C. Péan, S. Berger, et al. (Cambridge, United Kingdom, New York, NY: Cambridge University Press), 923–1054. doi:10.1017/9781009157896.009

Guo, B., and Ghalambor, A. (2014). *Natural Gas Engineering Handbook*. Houston, TX: Gulf Publishing Company.

International Energy Agency (2019). World Energy Statistics 2019. Available at: https://www.iea.org/data-and-statistics/data-product/world-energy-statistics (Accessed 05/04/2021).

Karakurt, I., Aydin, G., and Aydiner, K. (2012). Sources and Mitigation of Methane Emissions by Sectors: A Critical Review. *Renew. energy* 39 (1), 40–48. doi:10.1016/j.renene.2011.09.006

Long, W., and Shi, J. (2020). *Hainan Investigated and Punished 13 Cases of Illegal Use of Over-standard Fuel Oil in a Year*. Wuhan, China: China Water Transport News. Available at: http://www.zgsyb.com/news.html?aid=533559 (accessed 11 202113.

Ministry of Agriculture and Rural Affairs (2019). Fishing Vessel Renovation Subsidy Standard. Available at: https://www.sohu.com/a/348651794_769126 (accessed 2021/12/25).

Ministry of Agriculture and Rural Affairs of the People's Republic of China (2020). *China Fishery Statistical Yearbook*. Beijing, China: China Agriculture Press.

Ministry of Ecology and Environment of the People's Republic of China (2018). *Limits and Measurement Methods for Exhaust Pollutants from Marine engines (CHINA I, II)*. Available at: http://www.mee.gov.cn/ywgz/fgbz/bz/bzwb/dqhjbh/dqydywrwpfbz/201608/t20160830_363272.shtml (Accessed 05/04/2021).

Ministry of Transport of the People's Republic of China (2021). An Analysis Report on the Capacity of Coastal Inter-provincial Freight Ships in 2020. Available at: https://xxgk.mot.gov.cn/2020/jigou/syj/202102/t20210219_3526026.html (accessed 2021 07/08/2021).

Ministry of Transport of the People's Republic of China (2021). Decision of the Ministry of Transport on Amending the "Regulations on the Administration of Old Transport Ships. Available at: http://www.gov.cn/zhengce/zhengceku/2021-08/26/content_5633472.htm?_zbs_baidu_bk (accessed 2021/12/25).

Nam, E. K., Jensen, T. E., and Wallington, T. J. (2004). Methane Emissions from Vehicles. *Environ. Sci. Technol.* 38 (7), 2005–2010. doi:10.1021/es034837g

Nielsen, J., and Stenersen, D. (2010). Emission Factors for CH_4, NOX, Particulates and Black Carbon for Domestic Shipping in Norway, Revision 1. *Marinted Report MT22 A10-199* (Marintek: Klima og forurensningsdirektoratet). Available at: https://www.miljodirektoratet.no/globalassets/publikasjoner/klif2/publikasjoner/2746/ta2746.pdf (Accessed 05/04/2021).

Olmer, N., Comer, B., Roy, B., Mao, X., and Rutherford, D. (2017). *Greenhouse Gas Emissions from Global Shipping, 2013–2015 Detailed Methodology*. Washington, DC, USA: International Council on Clean Transportation, 1–38.

Organisation for Economic Co-operation and Development (2019). *OECD.Stat: Fisheries and Aquaculture Statistics*. Available at: https://stats.oecd.org/ (Accessed 05/04/2021).

Ushakov, S., Stenersen, D., and Einang, P. M. (2019). Methane Slip from Gas Fuelled Ships: A Comprehensive Summary Based on Measurement Data. *J. Mar. Sci. Technol.* 24 (4), 1308–1325. doi:10.1007/s00773-018-00622-z

Wang, L., Du, W., Chen, Y., Wang, W., Chen, Y., Zhu, X., et al. (2022). High PM2.5 Emission from Typical Old, Small Fishing Vessels in China. *Environ. Sci. Technol. Lett.* 9 (3), 199–204. doi:10.1021/acs.estlett.1c00927

Wang, L., Du, W., Yun, X., Chen, Y., Zhu, X., Shen, H., et al. (2022). On-site Measured Emission Factors of Polycyclic Aromatic Hydrocarbons for Different Types of Marine Vessels. *Environ. Pollut.* 297, 118782. doi:10.1016/j.envpol.2021.118782

Xie, Z. (2020). China's Historical Evolution of Environmental Protection along with the Forty Years' Reform and Opening-Up. *Environ. Sci. Ecotechnology* 1, 100001. doi:10.1016/j.ese.2019.100001

Zhang, F., Chen, Y., Chen, Q., Feng, Y., Shang, Y., Yang, X., et al. (2018). Real-world Emission Factors of Gaseous and Particulate Pollutants from Marine Fishing Boats and Their Total Emissions in China. *Environ. Sci. Technol.* 52 (8), 4910–4919. doi:10.1021/acs.est.7b04002

Zhang, J., Smith, K. R., Ma, Y., Ye, S., Jiang, F., Qi, W., et al. (2000). Greenhouse Gases and Other Airborne Pollutants from Household Stoves in China: A Database for Emission Factors. *Atmos. Environ.* 34 (26), 4537–4549. doi:10.1016/s1352-2310(99)00450-1

Zheng, B., Tong, D., Li, M., Liu, F., Hong, C., Geng, G., et al. (2018). Trends in China's Anthropogenic Emissions since 2010 as the Consequence of Clean Air Actions. *Atmos. Chem. Phys.* 18 (19), 14095–14111. doi:10.5194/acp-18-14095-2018

Conflict of Interest: The authors declare that the research was conducted in the absence of any commercial or financial relationships that could be construed as a potential conflict of interest.

frontiers | Frontiers in Ecology and Evolution

ORIGINAL RESEARCH
published: 27 June 2022
doi: 10.3389/fevo.2022.924944

Modeling Biogenic Volatile Organic Compounds Emissions and Subsequent Impacts on Ozone Air Quality in the Sichuan Basin, Southwestern China

Shaobo Zhang[1], Yaqiong Lyu[2], Xianyu Yang[1], Liang Yuan[1], Yurun Wang[3], Lei Wang[1], Yuxin Liang[1], Yuhong Qiao[4,5] and Shigong Wang[1]*

[1] Plateau Atmosphere and Environment Key Laboratory of Sichuan Province, School of Atmospheric Sciences, Chengdu University of Information Technology, Chengdu, China, [2] Institute of Mountain Hazards and Environment, Chinese Academy of Sciences, Chengdu, China, [3] Department of Land, Air and Water Resources, University of California, Davis, Davis, CA, United States, [4] Chongqing Institute of Eco-Environmental Science, Chongqing, China, [5] Chongqing Key Laboratory of Urban Atmospheric Environment Observation and Pollution Control, Chongqing, China

OPEN ACCESS

Edited by:
Shupeng Zhu,
University of California, Irvine, United States

Reviewed by:
Haolin Wang,
Sun Yat-sen University, China
Ryan Wu,
University of California, Irvine, United States

***Correspondence:**
Yaqiong Lyu
yaqiong@imde.ac.cn

Specialty section:
This article was submitted to Interdisciplinary Climate Studies, a section of the journal Frontiers in Ecology and Evolution

Received: *20 April 2022*
Accepted: *18 May 2022*
Published: *27 June 2022*

Citation:
Zhang S, Lyu Y, Yang X, Yuan L, Wang Y, Wang L, Liang Y, Qiao Y and Wang S (2022) Modeling Biogenic Volatile Organic Compounds Emissions and Subsequent Impacts on Ozone Air Quality in the Sichuan Basin, Southwestern China. Front. Ecol. Evol. 10:924944. doi: 10.3389/fevo.2022.924944

Biogenic volatile organic compounds (BVOCs) impact atmospheric oxidation capacity and regional air quality through various biogeochemistry processes. Accurate estimation of BVOC emissions is crucial for modeling the fate and transport of air pollutants in chemical transport models. Previous modeling characterizes the spatial variability of BVOCs while estimated BVOC emissions show large uncertainties, and the impacts of BVOC emissions on ozone (O_3) air quality are not well understood. In this study, we estimate the BVOC emissions by model of emissions of gases and aerosols from nature (MEGAN) v2.1 and MEGAN v3.1 over the Sichuan Basin (SCB) situated in southwestern China for 2017. Further, the critical role of BVOC emissions on regional O_3 pollution is illustrated with a CMAQ modeled O_3 episode in summer 2017. Annual BVOC emissions over the SCB in 2017 are estimated to be 1.8×10^6 tons with isoprene emissions as high as 7.3×10^5 tons. Abundant BVOC emissions are depicted over the southern and southeastern SCB, in contrast to the relatively low emissions of BVOC over the Chengdu Plain and northeastern SCB. CMAQ simulations depict a strong influence of BVOC on ambient O_3 formation over densely forested regions including southern SCB and Chongqing city, accounting for 10% of daily maximum hourly O_3 concentration (DM1h O_3) and 6% of daily maximum 8-h average O_3 (MDA8h O_3) concentrations in July 2017. Over the severe O_3 episode in summer 2017, sensitivity experiments indicate that enhanced BVOC emissions contribute substantially to basin-wide O_3 concentrations and elevate peak O_3 levels by 36.5 and 31.2 $\mu g/m^3$ for the southern SCB and Chengdu Plain, respectively. This work identifies robustly important effects of BVOC emissions on O_3 exceedance events over the SCB and contributes insight into pursuing an O_3 abatement strategy with full consideration of potential contributions from BVOC emissions.

Keywords: BVOCs, air quality, MEGAN, ozone, Sichuan basin

INTRODUCTION

Biogenic volatile organic compounds (BVOCs) emitted by terrestrial ecosystems have multiple effects on the earth's system through altering the global carbon cycle and shaping tropospheric composition due to their large quantity and high chemical reactivity (Peñuelas and Staudt, 2010; Unger, 2014). Globally, BVOC emissions are about 10 times higher than the anthropogenic VOC (AVOC) emissions (Messina et al., 2016). BVOCs are predominantly composed of isoprene, monoterpenes, and sesquiterpenes and these species undergo rapid oxidation reactions in the atmosphere, which then form air pollutants including ozone (O_3) and particulate matter (PM), which are harmful to human health and vegetation growth (Carlton et al., 2010; Shrivastava et al., 2017; Xu et al., 2021). Substantial evidence from field, modeling, and laboratory works has shown that BVOCs actively participate in photochemical oxidation and influence urban O_3 formation (Churkina et al., 2017; Gu et al., 2021). A better understanding of the estimation of BVOC is thus critical to assess the environmental impacts of BVOC and develop effective O_3 control strategies.

Accurately estimating BVOC emissions is challenging due to limitations associated with spatial heterogeneity of land cover, multiple environmental stresses, and rapidly changing driving factors (Jiang et al., 2018; Demetillo et al., 2019). In recent years, BVOC emissions have been estimated on regional and global scales by various models, including the model of emissions of gases and aerosols from nature (MEGAN) and the biogenic emission inventory system (BEIS) (Carlton and Baker, 2011; Wu et al., 2020). Among numerical BVOC estimation models, MEGAN version 2.1 has been extensively used in previous studies due to its advanced algorithm and performance in capturing the magnitude and variations of BVOC emissions (Guenther et al., 2012). However, prior studies have revealed that environmental stress, particularly drought and ambient O3 concentrations, significantly influences the magnitude of BVOC emissions, while these mechanistic effects are not well represented in MEGANv2.1 (Jiang et al., 2018; Demetillo et al., 2019). To date, MEGANv3.1 has incorporated the parameterization of BVOC response to environment stress and Berkeley-Dalhousie Soil NOx Parameterization (BDSNP) for optimizing soil NOx emissions, which illustrates improved accuracy and enhanced capability in characterizing BVOC emissions (Guenther et al., 2017). Nonetheless, potential limitations in existing studies involve the lack of urban LAI in satellite-derived LAI products [typically from the moderate resolution imaging spectroradiometer (MODIS)]. As a result, BVOC emissions in urban areas could be significantly underestimated by numerical models and further lead to substantial uncertainty in assessing the impacts of BVOC emissions on urban air quality (Alonzo et al., 2015; Ghirardo et al., 2016). Given the growing urban green space in densely populated city clusters, urban BVOC emissions may be considerably higher than currently estimated and therefore can have an essential impact on urban atmospheric chemistry (Connop et al., 2016; Ren et al., 2017).

Strict regulation of NO_x, SO_2, and primary $PM_{2.5}$ emissions by the Air Pollution Prevention and Control Action Plan (APPCAP) have resulted in declining ambient $PM_{2.5}$ concentrations across China, which has effectively mitigated wintertime haze pollution (Zheng et al., 2018). Despite considerable achievements in reducing ambient $PM_{2.5}$ concentrations, deteriorated O_3 levels have emerged as a prominent concern in China, which raises a new challenge for air quality management (Liu and Wang, 2020). Highly developed city clusters including the North China Plain (NCP), Yangtze River Delta (YRD), Pearl River Delta (PRD), and Sichuan Basin (SCB) have turned out to be the most polluted regions throughout China (Wu et al., 2019; Wang et al., 2021; Yang et al., 2021). While several explanations have been proposed for the degraded O_3 air quality over China including the transition of the O_3-NO_x-VOCs sensitivity regime attributed to disproportionately reductions in NO_x and VOCs emissions, climate-driven unfavorable meteorological conditions, and the impacts of reduced PM emissions that influence O_3 production, the crucial role of BVOC emissions on O_3 pollution still lack of attention and BVOC emissions may be far more than currently thought. Furthermore, limited case studies are insufficient to demonstrate the sensitivity of BVOC emissions to model parameters and how these changes impact O_3 production during extreme O_3 episodes, particularly for the SCB where elevated BVOC emissions are estimated (Ma et al., 2019; Yang et al., 2020).

Located in the southwestern China, the SCB is the most developed economic zone in China and has approximately 110 million residents within an area of 260,000 km^2. O_3 attainment in SCB is challenging because of widely distributed industrial infrastructures, intense BVOC emissions, and a complex distribution of anthropogenic sources (Wu et al., 2022). The SCB is influenced by subtropical and temperate climates, featured by persistent high temperatures through the warm season. The vegetation types in this region are mainly subtropical evergreen broadleaf trees and subtropical evergreen coniferous trees, which exhibit high BVOC emission potentials (Wu et al., 2020). These features are in favor of BVOC emissions in the SCB. The national biogenic emission inventory reported in previous studies has shown that BVOC emissions in the SCB are much higher than in the NCP and YRD regions (Li et al., 2012). Though BVOCs are highly reactive in the atmosphere, their oxidation products have longer lifetime which can persist for a few days, allowing regional transport of secondary products under prevailing wind fields (Jeon et al., 2014). Measurements in the SCB indicate that urban BVOC emissions significantly contribute to O_3 episodes and thus cannot be neglected (Tan et al., 2018). While prior studies have assessed the effects of BVOC emissions on O_3 formation in SCB, most previous studies in SCB only focused on a specific short period and adopted a coarse spatial resolution that was not enough to fully quantify how BVOC emissions affect surface O_3 spatiotemporally (Yang et al., 2020). Therefore, further detailed assessment of the unique and changing BVOC profiles in the SCB is urgently needed to formulate an effective O_3 mitigation strategy.

In this study, we quantify the BVOC emission budget and examine BVOC profiles for 2017 over the SCB based on the MEGAN model, and quantitatively assess the impacts of BVOC emissions on O_3 concentrations over the warm season in 2017 through the WRF-CMAQ modeling system. Further, a regional

extreme O_3 episode that occurred in July 2017 was simulated to probe the effects of heat wave induced BVOC enhancement on O_3 episodes across the SCB. The article is organized as follows. In section "Methodology," the configurations of the WRF-CMAQ system, the set-up of MEGAN and the ambient measurements of air pollutants are presented. The spatial pattern and seasonal variability of BVOC emissions and the contribution of BVOC to the basin-wide O_3 episode are investigated in section "Results and Discussion." In section "Conclusion," we discuss the findings and implications for regulatory measures.

METHODOLOGY

Ambient Observations

Two observation datasets were adopted in this study for exploring the spatial pattern and magnitude of air pollutants and evaluating the model performance. For meteorology, hourly observation of meteorological parameters was acquired from the China Meteorological Data Service Center (CMDSC) which have made bias-correction for ensuring data accuracy. Hourly gaseous pollutants concentrations were obtained from the monitoring network operated by the China National Environmental Monitoring Center (CNEMC) with rigorous data quality control following the guidance of Sichuan environmental monitoring center.

Air Quality Modeling

Meteorological fields are simulated by the Weather Research and Forecasting (WRFv3.9.1) model. The model is set-up for three nested domains centered over SCB with horizontal resolution of 27, 9, and 3 km, respectively (as seen in **Figure 1**). The model simulation spans the time period for the whole year of 2017 with hourly output. To minimize the impact of initial conditions, we run the WRF model month by month with the first 3 days in each simulation excluded as spin-up. Meteorological initial and boundary conditions for driving WRF are acquired from the National Centers for Environmental Prediction (NCEP) Final (FNL) 1.0° × 1.0° reanalysis data.[1] The vertical structure of the WRF model contains 30 layers of which 10 layers are within the boundary layer height. The four-dimensional data assimilation technique (FDDA) is applied to the outermost domain to nudge 3-D winds, temperature, and humidity at 3 h intervals with strengths of 5×10^{-5}, 1×10^{-5}, and 1×10^{-5} s^{-1}, respectively (Yang et al., 2020). In addition, NCEP Automated Data Processing (ADP) global surface (ds461.0) and upper observational data[2] are assimilated to WRF. Model configurations including physical parameterizations are summarized in **Table 1**.

CMAQ v5.3.1 is used to simulate gaseous pollutants and aerosols (Appel et al., 2021). The simulation period spans from June 28 to July 30 in 2017, with the simulation results for June discarded as spin-up. Chemical boundary and initial conditions for the outermost domain were generated by default profiles within CMAQ which represent a clean atmosphere, while the initial and boundary conditions for the nested domains are extracted from model outputs of the outer domain. Gas-phase chemistry and aerosol mechanism were represented with the Carbon-Bond (CB06) and the Aerosol 06 (AERO6) (Pye et al., 2017). Anthropogenic emissions are based upon the Multi-resolution Emission Inventory for China (MEIC) in 2017 and

[1]https://rda.ucar.edu/datasets/ds083.2/

[2]https://rda.ucar.edu/datasets/ds461.0/

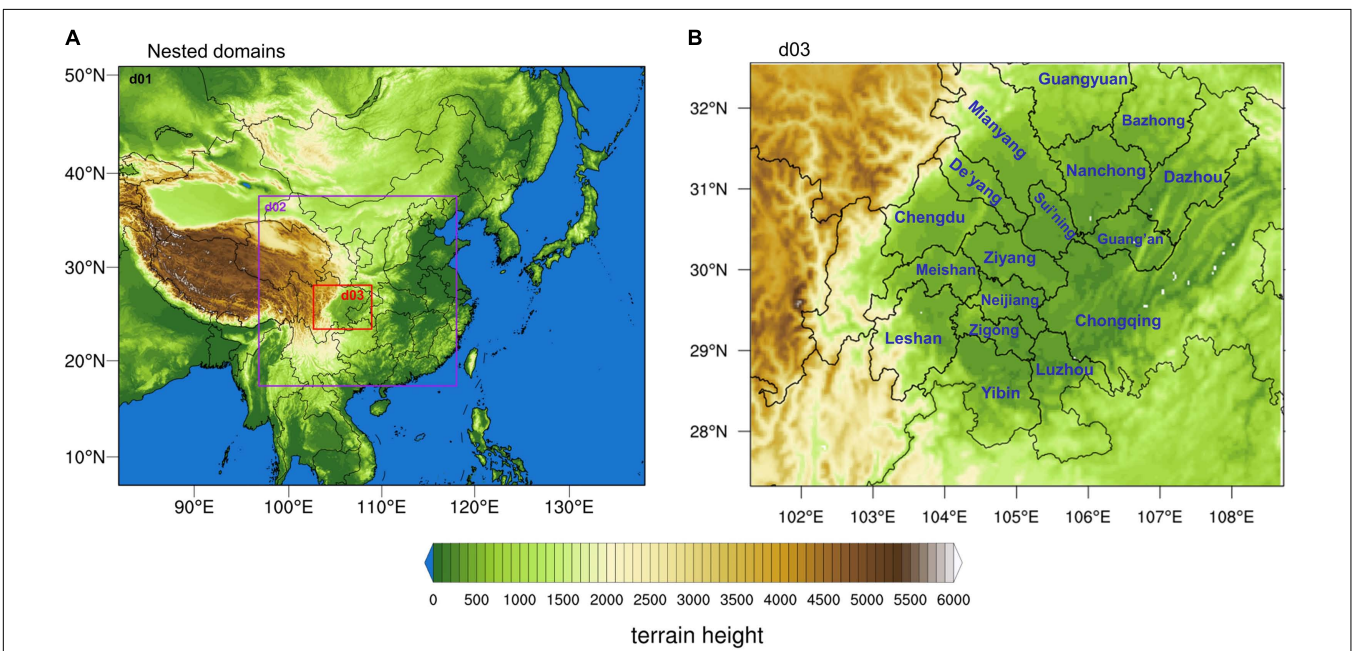

FIGURE 1 | Three nested WRF domains with terrain height (m) **(A)** domain configurations, **(B)** innermost domain.

TABLE 1 | Configurations of WRF model.

WRF version	ARW v3.9.1
Horizontal	Three nested with 27 km/9 km/3 km
Vertical layers	30 layers
Initial and boundary conditions	NCEP-FNL 1°×1°
Microphysics	Morrison
PBL scheme	YSU scheme
Longwave radiation	RRTMG scheme
Shortwave radiation	RRTMG scheme
Surface layer physics	Noah LSM scheme
Cumulus	Kain-fritsch scheme

TABLE 2 | CMAQ sensitivity experiments.

Abbreviation	Anthropogenic emissions	Biogenic emissions
Baseline	Y	Y
Nobio	Y	N

undergo spatial and temporal allocation based on high resolution spatial surrogates (Zheng et al., 2018). Biogenic emissions are calculated from MEGAN, as discussed in section "Model of Emissions of Gases and Aerosols From Nature Model." Here, two sensitivity experiments were conducted to examine the effects of BVOC emissions on summer O_3 levels over the SCB, as summarized in **Table 2**. In the baseline scenario, both anthropogenic and biogenic emissions are included, while biogenic emissions are eliminated in the Nobio scenario to represent the pure contribution of anthropogenic emissions.

Model of Emissions of Gases and Aerosols From Nature Model

Biogenic emissions were calculated by using the MEGANv2.1 and MEGANv3.1 models, respectively (Guenther et al., 2012). For MEGANv2.1, the model inputs include leaf area index (LAI) based on the Moderate Resolution Imaging Spectroradiometer (MODIS) MOD15A2H LAI product and plant function types (PFTs) obtained from the MODIS MCD12Q1 product for 2017. A global emission factor database based on ecoregion-averaged PFT was used to reflect the BVOC emission rate under standard canopy conditions. The meteorological fields used for driving MEGAN were provided by the WRF model described in section "Air Quality Modeling."

In the parameterization of MEGANv2.1, the emission rate of BVOCs is determined by the product of emission factor and emission activity factor, as shown in Eq. (1):

$$Emission = \varepsilon \cdot \gamma \cdot \rho \tag{1}$$

where ε represents the emission factor (emission rate at standard conditions) and ρ denotes the change within the canopy (generally set to 1). The emission activity factor for each compound class (γi) takes the changes in environmental conditions into account, which is formulated as Eq. (2):

$$\gamma_i = C_{CE} \cdot LAI \cdot \gamma_{P,i}\gamma_{T,i}\gamma_{A,i}\gamma_{SM,i}\gamma_{C,i} \tag{2}$$

where each parameter represents the emission response to light (γP), temperature (γT), leaf age (γA), soil moisture (γSM), leaf area index (LAI), and CO_2 inhibition (γ C).

Unlike MEGANv2.1, MEGANv3.1 introduces a J-rating scheme for representing the data quality of emission factors with a J-rating of 4 denoting the highest quality data while J-rating of 0 corresponding to lowest quality data (Guenther et al., 2017). Herein, we only use the data with a J-rating of 4 with parameterizations for environmental stress turned on in the experiment for MEGANv3.1.

RESULTS AND DISCUSSION

Evaluation of Model Performance

To evaluate the model performance over the innermost domain, statistical metrics including mean bias (MB), normalized mean bias (NMB), normalized mean error (NME), and root-mean-square error (RMSE), were quantified based on ambient measurements and modeled parameters (including 2-m temperature, 2-m relative humidity, 10-m wind speed, 10-m wind direction, O_3 levels, and NO_2 concentrations). The definitions of these statistical metrics are presented in Eqs. (3)–(6), where Pi and Oi denote the predicted values and observations, respectively. The evaluation of WRF and CMAQ model performance over the study period have been described in detail by Yang et al. (2020) and Wang et al. (2022). Briefly, WRF model broadly capture the day-to-day variability of 2-m temperature and 2-m relative humidity with *R* values ranging from 0.92–0.98 to 0.58–0.67, respectively. For gaseous pollutants, CMAQ simulations successfully reproduce the diurnal pattern and peak O3 concentrations (*R* values ranged 0.68–0.75) over warm season (April–September), particularly showing good agreement with observed O_3 in summer.

$$MB = \frac{1}{N}\sum_{i=1}^{N}(P_i - O_i) \tag{3}$$

$$NMB = \frac{\sum_{i=1}^{N}(P_i - O_i)}{\sum_{i=1}^{N} O_i} \tag{4}$$

$$NME = \frac{\sum_{i=1}^{N}|P_i - O_i|}{\sum_{i=1}^{N} O_i} \tag{5}$$

$$\mathrm{RMSE} = \left[\frac{1}{N}\sum_{i=1}^{N}(P_i - O_i)^2\right]^{\frac{1}{2}} \tag{6}$$

Spatial Pattern and Temporal Variability of Biogenic Volatile Organic Compounds Emissions

To identify spatially explicit BVOC emissions throughout the model domain, the SCB is divided into subregions based on geographic locations and air pollution zones (**Table 3**). The annual BVOC emissions for SCB in 2017 are 1.8×10^6 tons and 1.2×10^6 tons estimated by MEGANv2.1 and

TABLE 3 | Classification of city clusters in the SCB.

Cluster	City
Chengdu plain	Chengdu
	Deyang
	Mianyang
	Suining
	Leshan
	Meishan
	Ya'an
	Ziyang
Southern SCB	Zigong
	Luzhou
	Neijiang
	Yibin
Northeastern SCB	Guangyuan
	Nanchong
	Guang'an
	Dazhou
	Bazhong

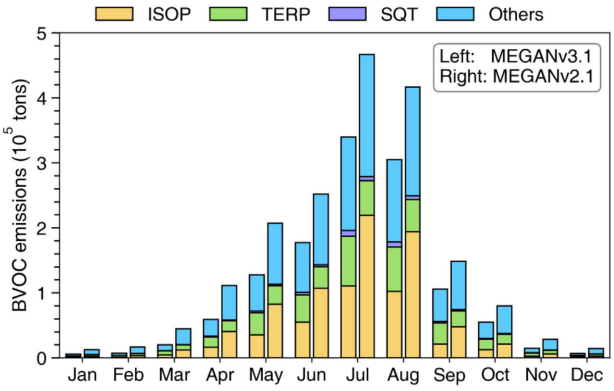

FIGURE 2 | Monthly emission budget of BVOC over SCB for 2017 estimated by MEGANv2.1 and MEGANv3.1.

MEGANv3.1, respectively (as seen in **Figure 2**). By source category, the emissions of isoprene (ISOP), monoterpenes (TERP), sesquiterpene (SESQ), and other BVOCs in MEGANv2.1 were 7.3×10^5 (41.1% of total BVOCs), 2.4×10^5 (13.5%), 2.3×10^4 (1.3%), and 7.9×10^5 (44.1%) tons, respectively. In contrast, MEGANv3.1 estimated 3.6×10^5 tons for ISOP (29.7% of total BVOCs), 3.0×10^5 tons for TERP (24.8%), 2.9×10^4 tons for SESQ (2.4%), and 5.3×10^5 tons for other BVOCs (43.2%), respectively. The significant decrease in ISOP emission amount, while a slight increase in TERP and SESQ emissions, imply that the profound heatwaves in summer 2017 had a significant impact on BVOC emissions across the SCB (Wu et al., 2022). Interestingly, while isoprene is the governing compound among all species, the sum of other BVOCs is in excess of the emissions of isoprene. For the abundance of other VOCs in MEGANv2.1, methanol is the dominant contributor with annual emissions of 4.9×10^5 tons, followed by acetone (6.2×10^4 tons), ethene (4.4×10^4 tons), propene (3.7×10^4 tons), and ethanol (2.1×10^4 tons). The amount of BVOC emissions is in good agreement with Wu et al. (2020) for the same period, while slightly lower than the value reported by Li et al. (2012), which could be partially attributed to input parameters and study period.

Figure 3 presents annual emissions of total BVOC, isoprene, monoterpenes, and sesquiterpenes across the SCB in MEGANv2.1. It can be clearly seen that emissions of BVOC are spatially heterogeneous over the study domain. Isoprene and monoterpenes emissions in Chengdu, Ziyang, Deyang, and Suining cities are relatively low because the PFTs in these cities are dominated by cropland rather than trees. In contrast, maximum BVOC emission fluxes are found in southern and southwestern SCB, particularly the cities of Luzhou, Yibin, Leshan, and Zigong exhibiting much higher BVOC emissions in comparison with the Chengdu Plain and central SCB. It is worth mentioning that BVOC emissions from southern SCB account for 56% of total BVOC budget, which is primarily driven by the combined effects of warm climate conditions and the high density of biomass in these regions (Ma et al., 2019). In MEGANv3.1, it can be clearly seen that TERP emissions are much higher than in MEGANv2.1, with strong enhancement (difference higher than 1 tons/km^2) in southern and northeastern SCB (**Figure 4**). However, ISOP emissions exhibit basin-wide reductions (magnitude larger than 4 tons/km^2) due to the response of vegetation to persistent drought conditions, thus leading to BVOC emissions in MEGANv3.1 significantly lower than in MEGANv2.1.

Figure 5 depicts the seasonal distribution of BVOC emissions across the SCB for 2017. As ambient BVOCs are mainly emitted from vegetation, BVOC emissions have a seasonal pattern that is notably consistent with the period of plant growth and evolution. In summer, BVOC emissions generally reach their peak due to the hot and sunny weather conditions in combination with high values of LAI. Similarly, the warm meteorological conditions and moderate precipitation in spring both favor vegetation growth, resulting in high BVOC emissions that are only slightly lower than in summer. In contrast, plants enter the senescence period in autumn and LAI gradually decrease, causing BVOC emissions substantially decrease compared with spring and summer. Winter has the lowest BVOC emissions of the four seasons, owing to weakened plant evolution and a drop in temperature and sunlight.

Impact of Biogenic Volatile Organic Compounds Emission on Ozone Air Quality in the Sichuan Basin

Previous studies have suggested that severe O_3 pollution over China in the year of 2017 is in large part due to protracted unfavorable meteorology (featured by hot and stagnant weather conditions) and climate-driven elevated BVOC emissions (Wu et al., 2020). In the summer of 2017, the SCB suffered profound heat waves that led to a substantial increase in O_3 exceedances (Yang et al., 2020). **Figure 6** presents the daily maximum hourly O_3 concentration (DM1h O_3) and daily maximum 8-h average O_3 (MDA8 O_3) concentrations in July 2017 for the SCB. The Chengdu Plain, the most densely populated area in SCB, exhibits

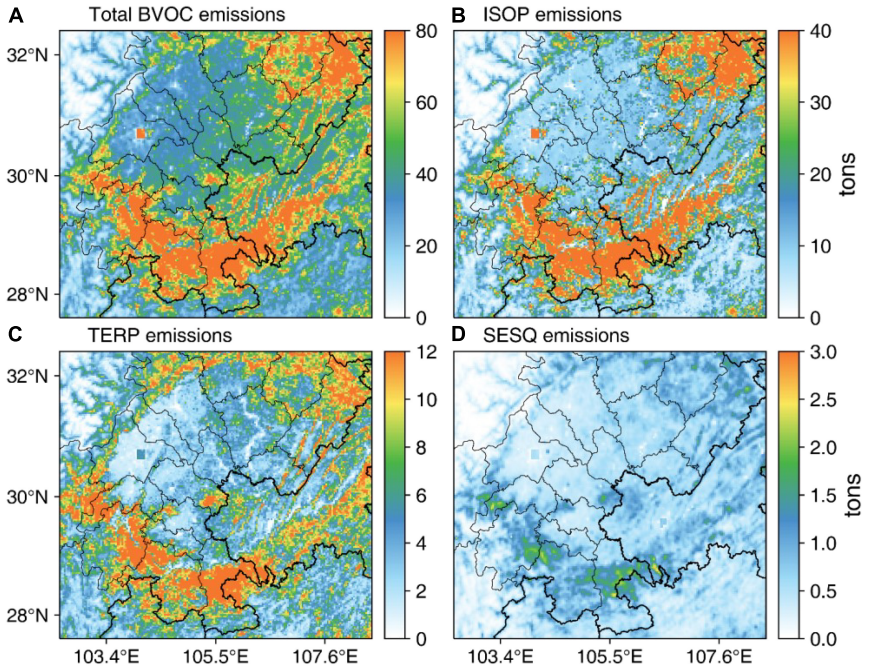

FIGURE 3 | Annual emissions of total BVOC **(A)**, isoprene **(B)**, monoterpenes **(C)**, and sesquiterpenes **(D)** for 2017 estimated by MEGAN2.1.

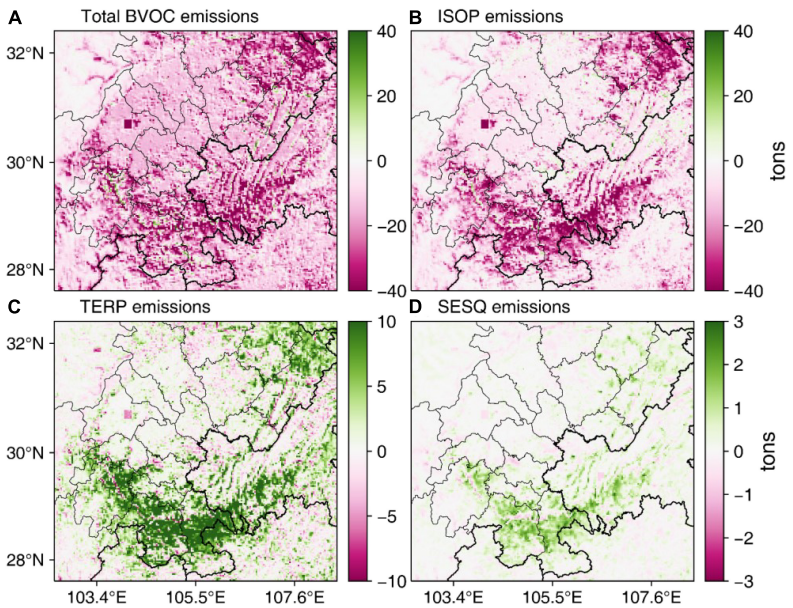

FIGURE 4 | Differences of annual total BVOC, isoprene, monoterpene, and sesquiterpenes emissions between the MEGAN2.1 and MEGAN3.1.

the highest O_3 levels in July (monthly average MDA8 O_3 reaching 140 $\mu g/m^3$). High levels of O_3 are also found in southern SCB and metropolitan Chongqing where monthly average MDA8 O_3 is higher than 120 $\mu g/m^3$. For DM1h O_3, the hotspots of O_3 are much more clearly distinguishable, particularly featured by a broader region under high O_3 exposure (DM1h O_3 higher than 200 $\mu g/m^3$).

To examine the effects of BVOC on ambient O_3 levels across the SCB, we calculated the difference in MDA8 O_3 concentrations for July 2017 between the baseline scenario and the nobio scenario (as discussed in section "Model of Emissions of Gases and Aerosols From Nature Model"), as seen in **Figure 7**. The domain-averaged contribution of BVOC to O_3 is found to be 5.6 $\mu g/m^3$ for DM1h O_3 and $\mu 4.2$ g/m^3 for MDA8h O_3,

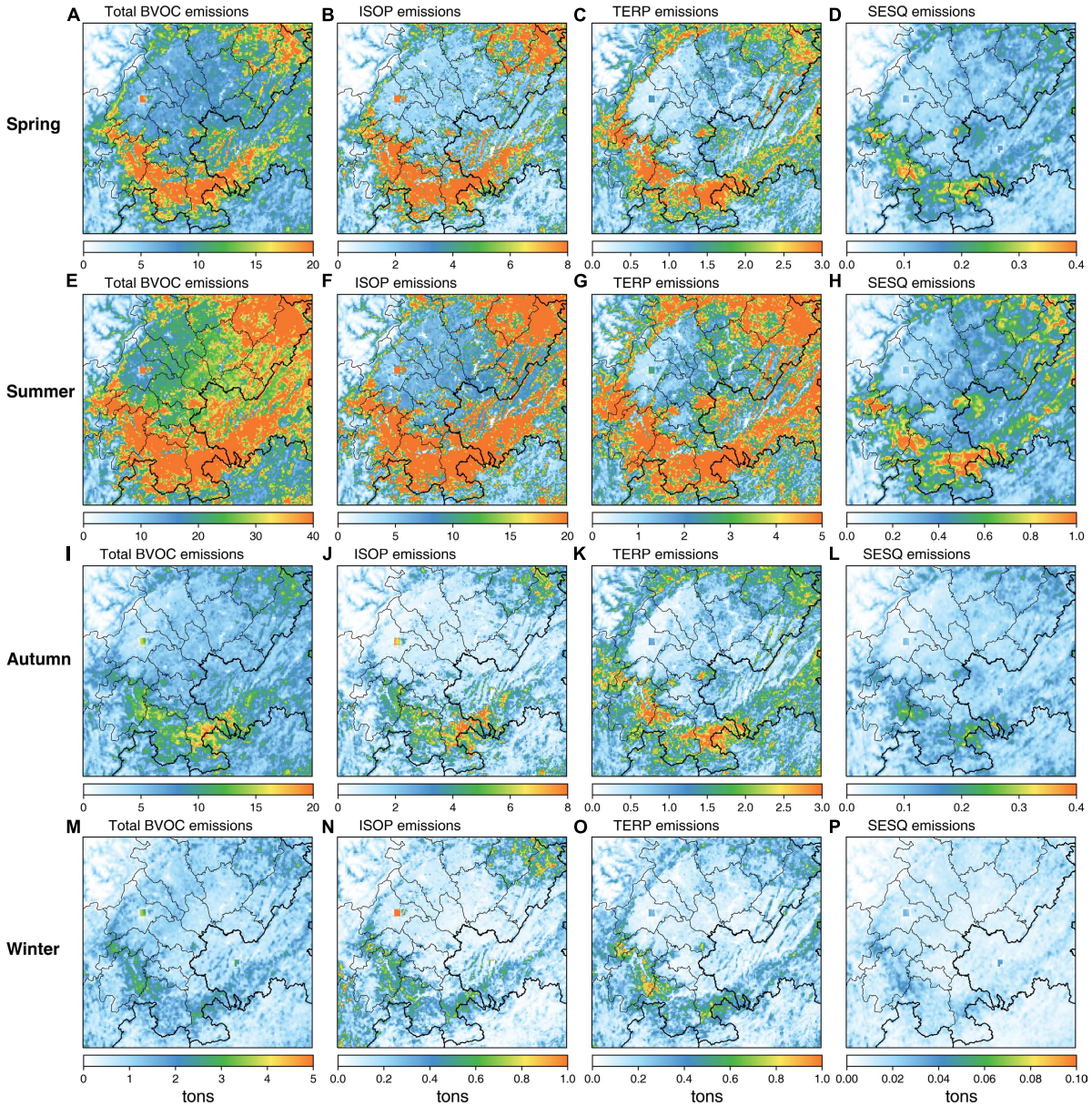

FIGURE 5 | Seasonal emissions of total BVOC, isoprene (ISOP), monoterpenes (TERP), and sesquiterpenes (SESQ) over the SCB in 2017 estimated by MEGAN2.1.

respectively. Spatially, the most prominent contribution of BVOC to ambient O_3 was found in southern SCB (Yibin, Luzhou, and Zigong cities) where the amount of BVOC emissions is highest across the model domain, with DM1h O_3 and MDA8h O_3 over 15 $\mu g/m^3$ and 11 $\mu g/m^3$, respectively. In addition, BVOC emissions show a distinct role in O_3 formation in Leshan and metropolitan Chongqing with a contribution ranged from 8 to 10 $\mu g/m^3$. This phenomenon is broadly consistent with the spatial distribution of BVOC emissions (as seen in **Figure 3**), implying the significant influence of biogenic precursors on local photochemical reactions. Interestingly, while BVOC emissions in Chengdu are comparatively low, there is a considerable impact on DM1h O_3 attributed to BVOCs in urban Chengdu. This behavior is largely due to regional transport of BVOC and its oxidation products under synoptic forcing that occurred in summer, which is coincident with findings reported by Tan et al. (2018) and Yang et al. (2020).

Episode of Intense Biogenic Volatile Organic Compounds Emission Triggered O_3 Pollution Over Sichuan Basin in July 2017

Although BVOC emissions are of minor importance for summertime mean O_3 concentrations, they may act as the key modulating factor which affects the intensity and severity of O_3

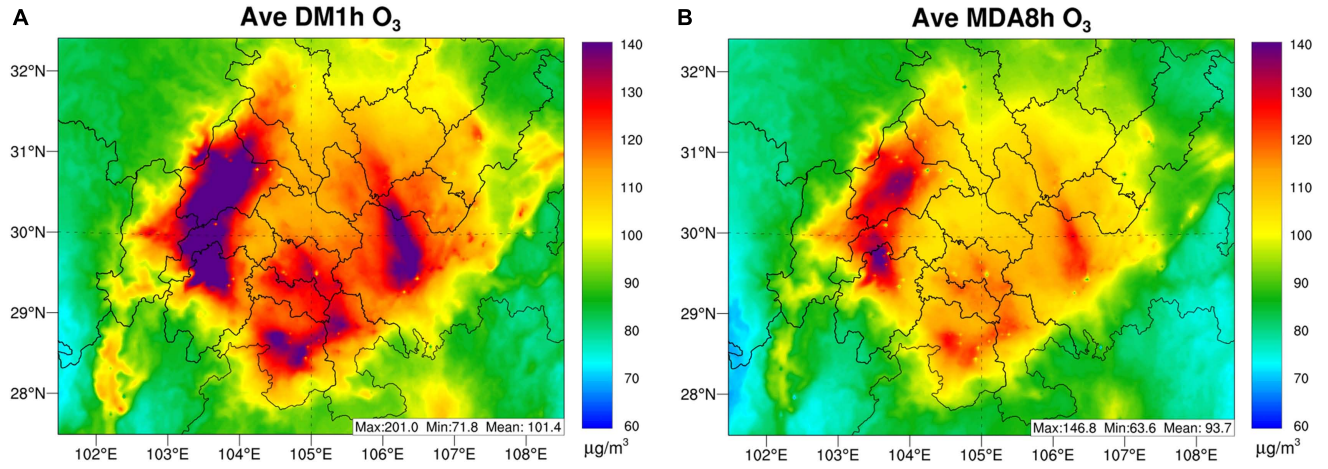

FIGURE 6 | Spatial map of daily maximum hourly O_3 concentrations (DM1h O_3) and daily maximum 8-h average (MDA8) O_3 concentrations in July 2017.

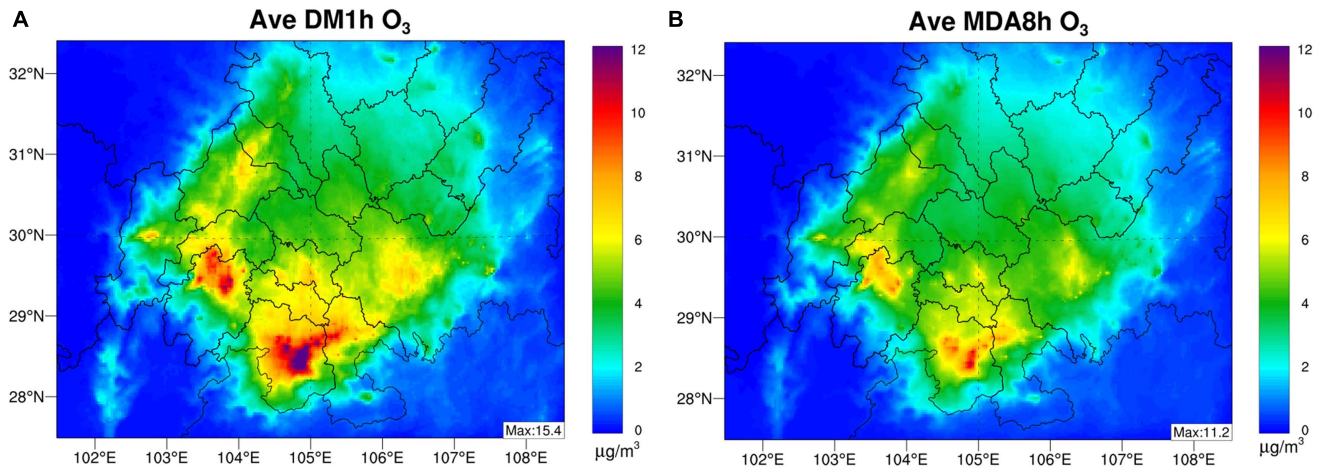

FIGURE 7 | Contribution of BVOC emissions on monthly average daily maximum hourly O_3 concentrations (DM1h O_3) and daily maximum 8-h average (MDA8) O_3 concentrations in July 2017.

episodes with a far larger contribution than average values. To probe the effects of enhanced BVOC emissions on extreme O_3 exceedance events over the SCB, the WRF-CMAQ model is used to simulate a basin-wide O_3 episode over 5–14 July 2017. The O_3 episode that took place on 8–13 July 2017 has turned out to be one of the most severe regional O_3 events through the SCB in terms of affected area and severity (Yang et al., 2020). It is worth noting that this episode was featured by widely recorded O_3 exceedance and extremely high O_3 concentrations observed in Chengdu and Deyang cities, which even spiked to 389 and 317 $\mu g/m^3$.

Figure 8 depicts the spatial pattern of BVOC contributions on MDA8 O_3 levels over the period of the episode, where the effects is quantified as the difference between baseline minus nobio. At the initial stage of the episode (8 July), MDA8 O_3 concentrations were comparatively low across the SCB and the effects of BVOCs were not significant, with basin-wide contribution of less than 6 $\mu g/m^3$, suggesting minor effects of BVOC emissions on ambient O_3 formation on clean days. On 9 July, the synoptic pattern characterized by a controlling high pressure system triggered a heat wave across the SCB, which caused O_3 levels to slightly increase compared with 8th July. It can be clearly seen that there was a hotspot of BVOC contribution (higher than 20 $\mu g/m^3$) situated on the southern SCB, corresponding to the O_3 exceedance in in Meishan and Leshan cities. From 10 to 12 July, the heat wave further intensified, with daytime 2-m temperatures reported in most cities in excess of 36°C. In response to the prolonged heat wave and the unusual dry conditions, estimated BVOC emissions dramatically increased by 60% as compared with 8th July, and subsequently exhibited considerable contributions to elevated O_3 concentrations over time, presenting a governing role in determining the distribution of O_3. Spatially, the most prominent BVOC impacts (36.5 $\mu g/m^3$) are found over the southern SCB, where BVOC emissions are most abundant throughout the model domain (as seen in **Figure 2**). In addition,

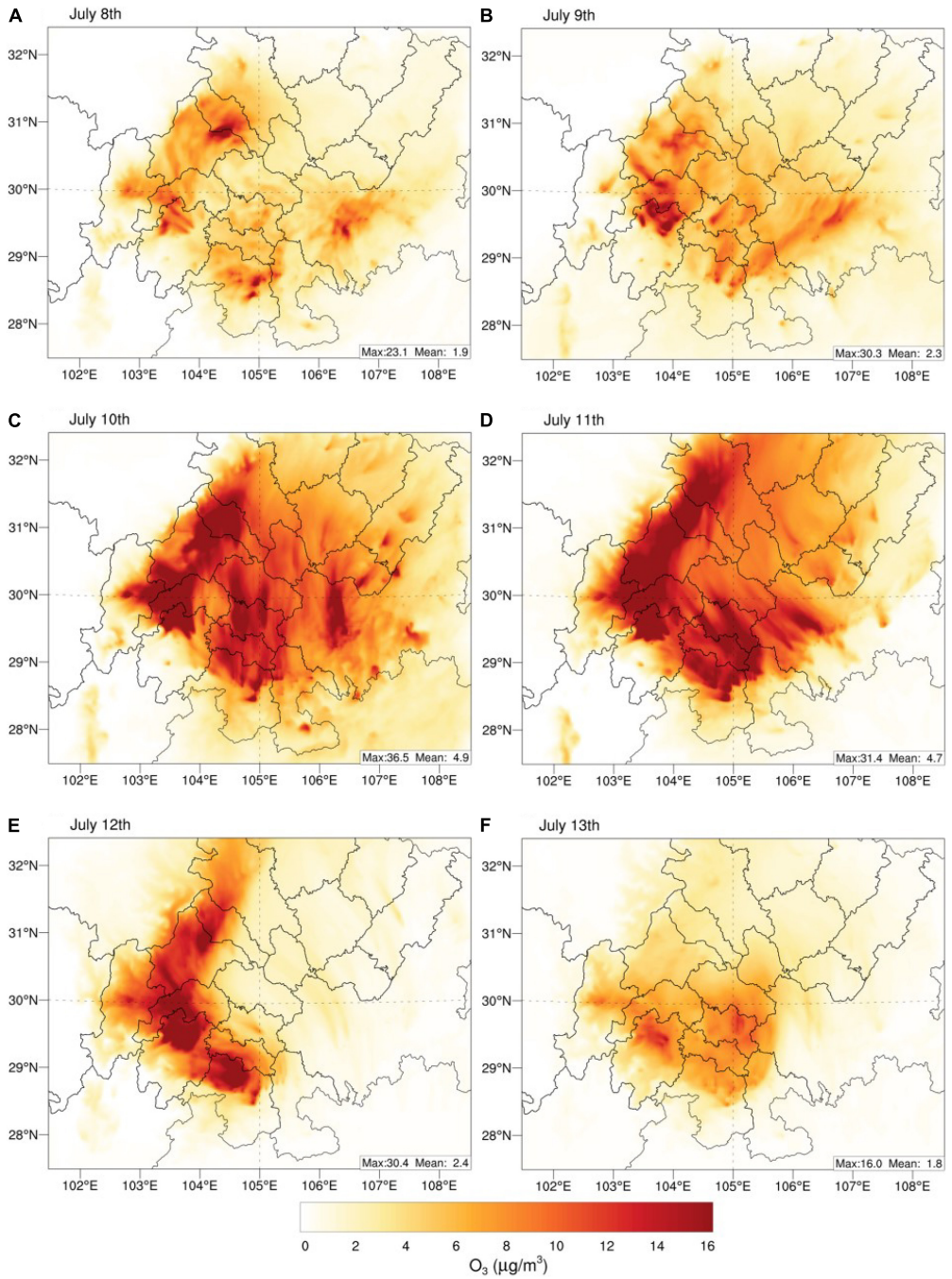

FIGURE 8 | Impacts of BVOC emissions on MDA8 O_3 concentrations (i.e., baseline minus nobio) simulated by CMAQ model over SCB during 8–13 July in 2017.

BVOC emissions significantly contribute to the O_3 formation over downwind regions, most notably in the Chengdu Plain with a maximum value reaching 31.2 $\mu g/m^3$. This phenomenon mainly arises from intense local anthropogenic emissions there, which interact with BVOC and its oxidation products. Under the strong southeasterly wind fields, the outflow from the southern SCB and Chongqing city was transported along the Chengdu Plain, leading to BVOC and its oxidation products originating from upwind areas advected to the downwind regions and reacted alongside the pathway, thus significantly enhancing regional MDA8 O_3 reaching 220 $\mu g/m^3$ in the Chengdu Plain. In contrast, the impacts of BVOC emissions on O_3 formation are comparatively low over the northeastern SCB (less than 6 $\mu g/m^3$) due to relatively low levels of anthropogenic emissions. On 13 July, the basin-wide wind speed slightly decreased and stagnant conditions dominated the Chengdu Plain, leading to a

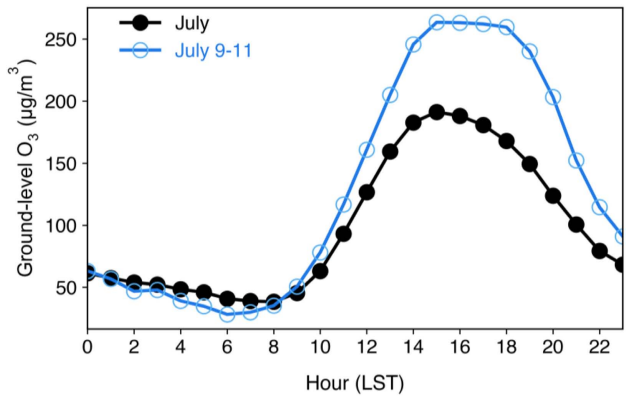

FIGURE 9 | Diurnal pattern of ground-level O_3 concentrations observed from CNEMC network in Chengdu.

smaller magnitude of BVOC contribution on O_3 and making the net effects of BVOC emissions largely limited on a local scale.

Figure 9 presents the diurnal pattern of O_3 levels in Chengdu city during the extreme O_3 episode and July. From a monthly perspective, O_3 concentrations peak in the afternoon, and MDA8 O_3 generally corresponds to 1,200–1,900 LST. O_3 levels decreased rapidly after 2,000 LST due to declining air temperature and a lack of solar radiation. In contrast, O_3 concentrations showed a distinctly different diurnal pattern during the severe O_3 episode that elevated O_3 levels persisted through 1,200–2,000 LST and exhibited an explosive increase with the magnitude of peak O_3 levels greatly enhanced, indicating that the importance of BVOC emissions increases dramatically on hot summer afternoons, coincident with periods of peak photochemical activity. This observation evidence further demonstrates that the regional transport of BVOCs and their oxidation products modulates the urban atmospheric chemistry with intensified photochemical reactions.

CONCLUSION

In this study, we adopted the MEGANv2.1 and MEGANv3.1 models for estimating the BVOC emissions across the SCB for 2017 and distinguished the critical role of BVOC on summer O_3 levels and the formation of region-wide O_3 episodes through WRF-CMAQ modeling. The annual BVOC emissions over the SCB were estimated to be at 1.8×10^6 tons and 1.2×10^6 tons by MEGANv2.1 and MEGANv3.1, respectively. The incorporation of environmental stress parameterizations and the J-rating scheme in MEGANv3.1 exert a profound influence on the estimated BVOC budget, featured by reduced isoprene emissions and enhanced monoterpene emissions. The spatial pattern of BVOC emissions is largely determined by local vegetation cover and climate conditions. Intense BVOC emissions are mainly found over southern SCB and Chongqing city, while BVOC emissions in the Chengdu Plain and northeastern SCB are comparatively low.

Results of CMAQ model simulations indicate that BVOC contribute considerably to monthly average DM1h O_3 (maximum 10%) and MDA8 O_3 (maximum 8%) with most prominent impacts on regions with high BVOC emission intensity. Episodic assessment demonstrates that the magnitude of BVOC effects on MDA8 O_3 could be substantially enhanced due to the elevated BVOCs emitted by vegetation in response to profound heat waves, subsequently contributing to a basin-wide O_3 episode with a peak contribution of 36.5 μg/m^3. Furthermore, the prevailing wind fields may amplify the effects of BVOC over downwind areas (Chengdu Plain) *via* BVOC transport and advection, modulating and facilitating the spike in O_3 levels.

The findings of this work provide a quantitative estimation for the SCB and emphasize the importance of biogenic precursors on ambient O_3 formation and region-wide O_3 episodes. Given the rapidly expanding urban green spaces, BVOC emissions are expected to substantially increase under a warming climate. However, existing O_3 mitigation strategies have mainly focused on anthropogenic VOCs and largely neglected these biogenic compounds, so the effectiveness of regulation measures based on cutting anthropogenic VOCs may be overestimated.

DATA AVAILABILITY STATEMENT

The raw data supporting the conclusions of this article will be made available by the authors, without undue reservation.

AUTHOR CONTRIBUTIONS

SZ designed this work and wrote the original draft. YQL, XY, YW, LY, and LW conducted formal analysis and edited the manuscript. YW, YXL, and YQ contributed to the methodology and software. SW supervised this work and provided project administration. All authors contributed to the manuscript and approved the submission.

FUNDING

This work was funded by the National Natural Science Foundation of China (Nos. 42175174 and 42005072), the Project (No. PAEKL-2020-C6) supported by the Open Research Fund Program of the Plateau Atmosphere and Environment Key Laboratory of Sichuan Province, and the Scientific Research Foundation of the Chengdu University of Information Technology (No. KYTZ201823).

ACKNOWLEDGMENTS

We acknowledge the MEIC team at Tsinghua University for providing the multiscale emission inventory of China. We would like to thank the Chengdu Plain Urban Meteorology and Environment Observation and Research Station of Sichuan Province for ambient monitoring data.

REFERENCES

Alonzo, M., Bookhagen, B., McFadden, J. P., Sun, A., and Roberts, D. A. (2015). Mapping urban forest leaf area index with airborne lidar using penetration metrics and allometry. *Remote Sens. Environ.* 162, 141–153. doi: 10.1016/j.rse.2015.02.025

Appel, K. W., Bash, J. O., Fahey, K. M., Foley, K. M., Gilliam, R. C., Hogrefe, C., et al. (2021). The community multiscale air quality (CMAQ) model versions 5.3 and 5.3.1: system updates and evaluation. *Geosci. Model Dev.* 14, 2867–2897. doi: 10.5194/gmd-14-2867-2021

Carlton, A. G., and Baker, K. R. (2011). Photochemical modeling of the ozark isoprene volcano: megan, beis, and their impacts on air quality predictions. *Environ. Sci. Technol.* 45, 4438–4445. doi: 10.1021/es200050x

Carlton, A. G., Pinder, R. W., Bhave, P. V., and Pouliot, G. A. (2010). To what extent can biogenic SOA be controlled? *Environ. Sci. Technol.* 44, 3376–3380. doi: 10.1021/es903506b

Churkina, G., Kuik, F., Bonn, B., Lauer, A., Grote, R., Tomiak, K., et al. (2017). Effect of VOC emissions from vegetation on air quality in Berlin during a heatwave. *Environ. Sci. Technol.* 51, 6120–6130. doi: 10.1021/acs.est.6b06514

Connop, S., Vandergert, P., Eisenberg, B., Collier, M. J., Nash, C., Clough, J., et al. (2016). Renaturing cities using a regionally-focused biodiversity-led multifunctional benefits approach to urban green infrastructure. *Environ. Sci. Policy* 62, 99–111. doi: 10.1016/j.envsci.2016.01.013

Demetillo, M. A. G., Anderson, J. F., Geddes, J. A., Yang, X., Najacht, E. Y., Herrera, S. A., et al. (2019). Observing severe drought influences on ozone air pollution in California. *Environ. Sci. Technol.* 53, 4695–4706. doi: 10.1021/acs.est.8b04852

Ghirardo, A., Xie, J., Zheng, X., Wang, Y., Grote, R., Block, K., et al. (2016). Urban stress-induced biogenic VOC emissions and SOA-forming potentials in Beijing. *Atmos. Chem. Phys.* 16, 2901–2920. doi: 10.5194/acp-16-2901-2016

Gu, S., Guenther, A., and Faiola, C. (2021). Effects of anthropogenic and biogenic volatile organic compounds on Los Angeles air quality. *Environ. Sci. Technol.* 55, 12191–12201. doi: 10.1021/acs.est.1c01481

Guenther, A. B., Jiang, X., Heald, C. L., Sakulyanontvittaya, T., Duhl, T., Emmons, L. K., et al. (2012). The model of emissions of gases and aerosols from nature version 2.1 (MEGAN2.1): an extended and updated framework for modeling biogenic emissions. *Geosci. Model Dev.* 5, 1471–1492. doi: 10.5194/gmd-5-1471-2012

Guenther, A., Tejas, S., Huang, L., Wentland, A., Jung, J., Beardsley, R., et al. (2017). "A Next Generation Modelling System for Estimating Texas Biogenic VOC Emissions," in *Project Report of Texas Commission on Environmental Quality*, (Austin: University of Texas).

Jeon, W.-B., Lee, S.-H., Lee, H., Park, C., Kim, D.-H., and Park, S.-Y. (2014). A study on high ozone formation mechanism associated with change of NOx/VOCs ratio at a rural area in the Korean Peninsula. *Atmos. Environ.* 89, 10–21. doi: 10.1016/j.atmosenv.2014.02.005

Jiang, X., Guenther, A., Potosnak, M., Geron, C., Seco, R., Karl, T., et al. (2018). Isoprene emission response to drought and the impact on global atmospheric chemistry. *Atmos. Environ.* 183, 69–83. doi: 10.1016/j.atmosenv.2018.01.026

Li, M., Huang, X., Li, J., and Song, Y. (2012). Estimation of biogenic volatile organic compound (BVOC) emissions from the terrestrial ecosystem in China using real-time remote sensing data. *Atmos. Chem. Phys. Discuss.* 12, 6551–6592. doi: 10.5194/acpd-12-6551-2012

Liu, Y., and Wang, T. (2020). Worsening urban ozone pollution in China from 2013 to 2017 – Part 1: the complex and varying roles of meteorology. *Atmos. Chem.Phys.* 20, 6305–6321. doi: 10.5194/acp-20-6305-2020

Ma, M., Gao, Y., Wang, Y., Zhang, S., Leung, L. R., Liu, C., et al. (2019). Substantial ozone enhancement over the North China Plain from increased biogenic emissions due to heat waves and land cover in summer 2017. *Atmos. Chem. Phys.* 19, 12195–12207. doi: 10.5194/acp-19-12195-2019

Messina, P., Lathière, J., Sindelarova, K., Vuichard, N., Granier, C., Ghattas, J., et al. (2016). Global biogenic volatile organic compound emissions in the ORCHIDEE and MEGAN models and sensitivity to key parameters. *Atmos. Chemis.Phys.* 16, 14169–14202. doi: 10.5194/acp-16-14169-2016

Peñuelas, J., and Staudt, M. (2010). BVOCs and global change. *Trends Plant Sci.* 15, 133–144. doi: 10.1016/j.tplants.2009.12.005

Pye, H. O. T., Murphy, B. N., Xu, L., Ng, N. L., Carlton, A. G., Guo, H., et al. (2017). On the implications of aerosol liquid water and phase separation for organic aerosol mass. *Atmos. Chem. Phys.* 17, 343–369. doi: 10.5194/acp-17-343-2017

Ren, Y., Qu, Z., Du, Y., Xu, R., Ma, D., Yang, G., et al. (2017). Air quality and health effects of biogenic volatile organic compounds emissions from urban green spaces and the mitigation strategies. *Environ. Pollut.* 230, 849–861. doi: 10.1016/j.envpol.2017.06.049

Shrivastava, M., Cappa, C. D., Fan, J., Goldstein, A. H., Guenther, A. B., Jimenez, J. L., et al. (2017). Recent advances in understanding secondary organic aerosol: implications for global climate forcing. *Rev. Geophys.* 55, 509–559. doi: 10.1002/2016RG000540

Tan, Z., Lu, K., Jiang, M., Su, R., Dong, H., Zeng, L., et al. (2018). Exploring ozone pollution in Chengdu, southwestern China: a case study from radical chemistry to O3-VOC-NOx sensitivity. *Sci. Total Environ.* 636, 775–786. doi: 10.1016/j.scitotenv.2018.04.286

Unger, N. (2014). On the role of plant volatiles in anthropogenic global climate change. *Geophys. Res. Lett.* 41, 8563–8569. doi: 10.1002/2014GL061616

Wang, H., Wu, K., Liu, Y., Sheng, B., Lu, X., He, Y., et al. (2021). Role of heat wave-induced biogenic VOC enhancements in persistent ozone episodes formation in pearl river delta . *J. Geophys. Res. Atmos.* 126. doi: 10.1029/2020JD034317

Wang, Y., Yang, X., Wu, K., Mei, H., Lu, Y., Smedt, I. D., et al. (2022). Long-term trends of ozone and precursors from 2013 to 2020 in a megacity (Chengdu), China: evidence of changing emissions and chemistry. *Atmos. Res.*

Wu, K., Kang, P., Tie, X., Gu, S., Zhang, X., Wen, X., et al. (2019). Evolution and assessment of the atmospheric composition in hangzhou and its surrounding areas during the G20 Summit. *Aerosol. Air Qual. Res.* 9, 2757–2769. doi: 10.4209/aaqr.2018.12.0481

Wu, K., Yang, X., Chen, D., Gu, S., Lu, Y., Jiang, Q., et al. (2020). Estimation of biogenic VOC emissions and their corresponding impact on ozone and secondary organic aerosol formation in China. *Atmos. Res.* 231:104656. doi: 10.1016/j.atmosres.2019.104656

Wu, K., Wang, Y., Qiao, Y., Liu, Y., Wang, S., Yang, X., et al. (2022). Drivers of 2013–2020 ozone trends in the Sichuan Basin, China. impacts of meteorology and precursor emission changes. *Environ. Pollut.* 300:118914. doi: 10.1016/j.envpol.2022.118914

Xu, L., Du, L., Tsona, N. T., and Ge, M. (2021). Anthropogenic effects on biogenic secondary organic aerosol formation. *Adv. Atmos. Sci.* 38, 1053–1084. doi: 10.1007/s00376-020-0284-3

Yang, X., Wu, K., Wang, H., Liu, Y., Gu, S., Lu, Y., et al. (2020). Summertime ozone pollution in Sichuan Basin, China: meteorological conditions, sources and process analysis. *Atmos. Environ.* 226:117392. doi: 10.1016/j.atmosenv.2020.117392

Yang, X., Wu, K., Lu, Y., Wang, S., Qiao, Y., Zhang, X., et al. (2021). Origin of regional springtime ozone episodes in the Sichuan Basin, China: role of synoptic forcing and regional transport. *Environ. Pollut.* 278:116845. doi: 10.1016/j.envpol.2021.116845

Zheng, B., Tong, D., Li, M., Liu, F., Hong, C., Geng, G., et al. (2018). Trends in China's anthropogenic emissions since 2010 as the consequence of clean air actions. *Atmos. Chem. Phys.* 18, 14095–14111. doi: 10.5194/acp-18-14095-2018

Conflict of Interest: The authors declare that the research was conducted in the absence of any commercial or financial relationships that could be construed as a potential conflict of interest.

frontiers | Frontiers in Environmental Science

ORIGINAL RESEARCH
published: 29 June 2022
doi: 10.3389/fenvs.2022.945658

Multiple Models Used to Deconstruct the Characteristics of Atmospheric Particles in Arid Region of Northwest China

Chao Liu[1†], Tianhao Zhang[1†], Bingqing Lu[1], Guozhong Zheng[2], Xiaoyan Liu[3], Ying Gao[2], Ying Chen[1] and Xiang Li[1*]*

[1]Department of Environmental Science and Engineering, Fudan University, Shanghai, China, [2]Jiuquan Ecological Environment Bureau of Gansu Province, Jiuquan, China, [3]Ecological Environment Monitoring Center of Jiuquan City, Jiuquan, China

OPEN ACCESS

Edited by:
Shupeng Zhu,
University of California, Irvine, United States

Reviewed by:
Xue Li,
Jinan University, China
Yan Lyu,
Zhejiang University of Technology, China

***Correspondence:**
Xiang Li
lixiang@fudan.edu.cn
Ying Chen
yingchen@fudan.edu.cn

†These authors have contributed equally to this work and share first authorship

Specialty section:
This article was submitted to Atmosphere and Climate, a section of the journal Frontiers in Environmental Science

Received: *16 May 2022*
Accepted: *06 June 2022*
Published: *29 June 2022*

Citation:
Liu C, Zhang T, Lu B, Zheng G, Liu X, Gao Y, Chen Y and Li X (2022) Multiple Models Used to Deconstruct the Characteristics of Atmospheric Particles in Arid Region of Northwest China. Front. Environ. Sci. 10:945658. doi: 10.3389/fenvs.2022.945658

Northwest China has a desert, arid and semi-arid climate that makes outdoor air sampling challenging. The region is also affected by intense dust storms. Monitoring challenges from the harsh climate have limited supplies of the data needed to inform appropriate regulatory actions to address air pollution in the region. Here we combine a comprehensive set of state-of-the-art offline analytical approaches and multiple models to deconstruct the chemical nature and sources of particulate matter at arid city in northwestern China. We collected 972 samples in Jiuquan during the period March 2019 through January 2020. The annual levels of PM_{10} (73.7 μg/m^3) exceeded the Chinese Ambient Air Quality Standard (CAAQS) Grade II of 70 μg/m^3. The percentages of the sum of sulfate, nitrate and ammonium, inorganic elements, organic carbon and elemental carbon in PM_{10} mass ranged 6.8–15.8%, 9.9–12.2%, 9.0–27.7%, and 1.5–4.7%, respectively. Analyses of sources indicated that soil dust was a major contributor to PM_{10} levels in Jiuquan city accounting for 24.8–30.5%. Fugitive dust and coal combustion were the second and third largest contributors to PM_{10}, respectively. Our results suggest that natural emissions can make air quality regulation futile. In this comprehensive particulate pollution analysis, we present the view that the sizeable regional particulate sources warrant national and regional mitigation strategies to ensure compliance with air quality requirements.

Keywords: arid region, particulate matter, chemical composition, source apportionment, dust, regional transport

INTRODUCTION

Studies have consistently shown that particulate matter (PM) can have significant deleterious effects on atmospheric quality and climate change in a region (Tsiouri et al., 2015; Tao et al., 2017b; Jiang et al., 2018; Javed and Guo, 2021). This effect has been verified to be directly related to PM level, size, and component (Almeida et al., 2009; Wang et al., 2013; Pui et al., 2014; Tao et al., 2017b). In consequence, a number of local governments have undertaken to regulate ambient PM concentrations for the benefit of air quality. To develop compliance strategies, we must pinpoint the major sources and measure their respective effects on ambient PM.

In Northwest China, attribution of emissions sources tends to prove difficult for a number of reasons: 1) a lack of integrated monitoring networks to gather comprehensive air pollution data; 2)

the pollution of most cities mostly drifts in either from nearby cities or from further afield (e.g., other countries); 3) many cities are involved in a multitudinous range of industrial activities pertaining to iron and steel smelting; and 4) the high quality emission datasets necessary for dispersion models tend not to be on offer.

Even in the face of such obstacles, several source apportionment studies have in fact taken place in Lanzhou. These works discerned three main types of sources of particulate matter—crustal, long range transport, and local emissions (Chu et al., 2008; Qiu et al., 2016; Wang et al., 2016; Guan et al., 2019; Jiang et al., 2021). Research performed using satellite measurements to probe atmospheric pollution in Xinjiang autonomous region showed that soil dust, fossil fuel burning, and local vehicle exhausts constituted most of the airborne particles (Wang et al., 2020).

One past air quality study taking place on the Silk Road, Northwest China, involved PM samples being collected from multiple sites during summer and winter, 2018. The work indicated that daily average PM_{10} and $PM_{2.5}$ concentrations in four cities were 112–152 and 70–81 μg/m^3, respectively (Zhou et al., 2021). These levels were over double the Grade I daily standard of CAAQS of 50 μg/m^3 for PM_{10} and 35 μg/m^3 for $PM_{2.5}$. Sand storms are commonplace in Hexi Corridor. The local climate is relatively arid most of the year, and the terrain is valley. Regrettably, these natural sands and dusts do not submit to human control or regulation, whereas the regional joint prevention and control can do some good. For example, weather warnings in advance of sand storms may prompt the population to remain inside to limit their exposure.

When samples taken on days during by extreme sand storms were factored out of previous analyses, the PM_{10} and $PM_{2.5}$ levels in most cities of Northwest China were found to be still quite high. Any suggestion that these levels can be blamed on these extreme sand storm events risks being false. The effect of sand dust on PM level in the Hexi Corridor is not one that has been subject to extensive study, meaning that the present study offers a chance to improve air quality by looking into contributions from other significant sources. Dust is nonetheless still expected be the main contributor to atmospheric particle levels.

Jiuquan, a typical arid city in northwestern China, is located in the Silk Road Economic Belt, and has undergone rapid growth in its economic and industrial development over the past few decades. Besides, the valley landform also makes it vulnerable to surrounding desert sources. Hence, the type of air pollution in this region is a composite pollution dominated by dust and coal-fired emissions. Here we selected Jiuquan for the research as representative of the arid region of northwest China, and used detailed observations and multiple models to identify and quantify the major sources. This study qualitatively and quantitatively analyzes the air particulate pollution law of a typical arid region in northwestern China and summarizes the regional sources of PM_{10}. The results from this study should avail for the government of northwest China in relation to the scientific and rational measures that should be used to effectively mitigate against environmental pollution from airborne particulate matter.

EXPERIMENTAL METHODS

Site and Sampling

Jiuquan experiences the four seasons of the year as very discrete in their manifestations in light of the local weather, in consequence of which a decision was made to likewise divide the sampling into four phases selected to represent spring–28 March to 4 May 2019, summer–14 July to 13 August 2019, fall–11 October to 7 November 2019, and winter–14 December 2019 to 9 January 2020, respectively. A total of 972 PM_{10} samples were collected from 3 sites in Jiuquan city. Additional particulars on the sampling locations can be seen in **Figure 1** and **Supplementary Table S1**. PM_{10} samples were collected on 90 mm quartz filters (Whatman, Maidstone, United Kingdom) using a particulate sampler (TH150F, Wuhan Tianhong Instruments, Wuhan, China) operating at a flow rate of 100 L/min. Three quartz filters were collected at each site at the same time. Sampling duration was 23 h, starting at 9:00 local time every day and ending at 8:00 local time the following day. Field blank filters enabled us to correct for any artifacts of gas absorption and filters' background levels. Before and after sampling, each filter was equilibrated at a relative humidity of 50% and a temperature of 25°C for 24 h and then weighed (precision 10 μg, Sartorius, Göttingen, Germany). PM_{10} mass concentrations were determined from the mass difference and the sampled air volume. The aerosol-loaded filter samples were stored in a freezer at −20°C prior to analysis to prevent volatilization of particles.

Chemical Analysis

Filter samples were applied to determine nine water-soluble ions (WSIs). They were sectioned and a quarter of the filter was put into 10 ml ultra-pure water (18.2 MΩ) for 40 min with ultrasonic agitation to complete extract these WSIs. The solutions thus extracted were filtered (0.22 μm, PTFE, Whatman, United States) and then was analyzed using an ion chromatography (Metrohm940, Metrohm, Switzerland). Anions (F^-, Cl^-, NO_3^-, and SO_4^{2-}) were separated by a Metrosep A supp5-150/4.0 column, using a mixed solution of 3.2 mmol/L Na_2CO_3 and 1.0 mmol/L $NaHCO_3$ as the eluent. Cation (Na^+, NH_4^+, K^+, Ca^{2+}, and Mg^{2+}) concentrations were determined with the use of a Metrosep C4-150/4.0 column, using a mixed solution of 1.7 mmol/L HNO_3 and 0.7 mmol/L $C_7H_5NO_4$ as an eluent. A calibration was performed for each analytical sequence. Procedural blank values were subtracted from sample concentrations.

Organic carbon (OC) and elemental carbon (EC) were analyzed using a DRI model 2001 carbon analyzer (Atmoslytic, Inc., Calabasas, United States), and the IMPROVE thermal/optical reflectance (TOR) protocol (Chow and Watson, 2002; Cao, 2003; Gu et al., 2010) was used for the carbon analysis. An area of 0.526 cm^2 was punched out of each filter and analyzed in the hope of detecting four OC fractions (OC_1, OC_2, OC_3, and OC_4 at 120°C, 250°C, 450°C, and 550°C, respectively, in a Helium atmosphere); PC (a pyrolyzed carbon fraction measured by finding when transmitted laser light regains

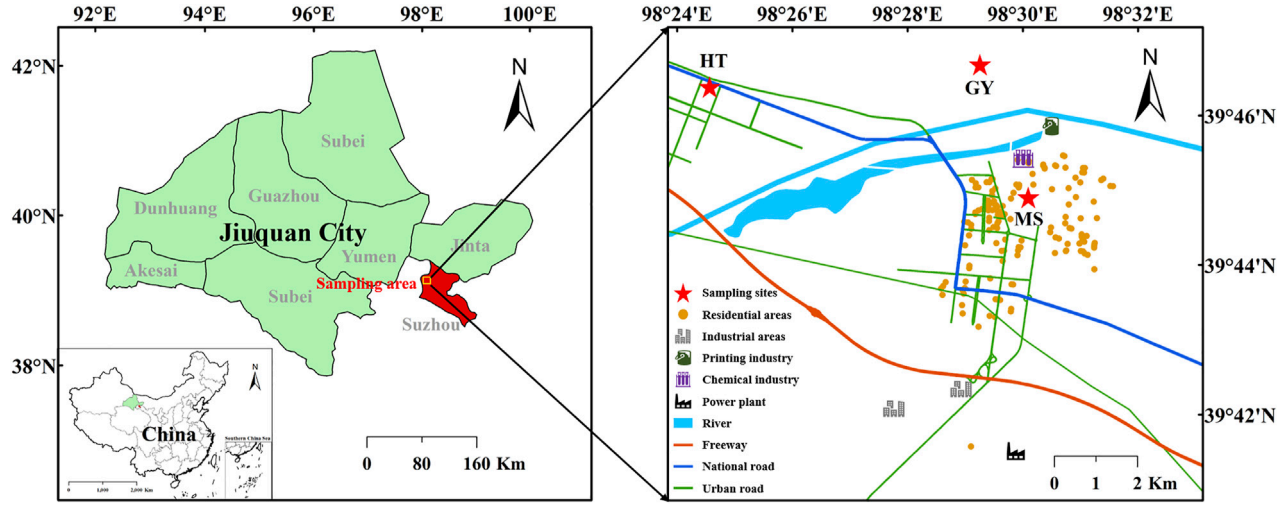

FIGURE 1 | Geographical location of study area as well as sampling sites in Jiuquan city. SZ, Suzhou District site; HT, High-tech Zone site; MS, Meteorological Station site.

its prior intensity upon addition of O_2 to the analytical air being probed); and three EC fractions (EC_1, EC_2, and EC_3 at 550°C, 700°C, and 800°C, respectively, in a 2% O_2/98% He atmosphere). The IMPROVE protocol defines OC as $OC_1 + OC_2 + OC_3 + OC_4$ + PC and EC as $EC_1 + EC_2 + EC_3 - PC$.

Following ion and carbonaceous species analysis, another quarter filter was chopped up finely and immersed in a mixed solution of concentrated HNO_3 and concentrated HF. Eleven inorganic elements (Mg, Al, Ca, Fe, V, Mn, Ni, Cu, Zn, Pb, and Ba) were extracted by microwave digestion and inductively coupled plasma mass spectrometer (ICP-MS, 7900, Agilent Technologies, United States) was then employed to find the concentrations of these metals. The mixed standard solution containing 5% HNO_3 was prepared into different concentration gradients, and a standard curve was established for quantitative analysis of inorganic elements.

Data Analysis

Positive Matrix Factorization (PMF) is a multivariate receptor model that employed to measure the contributions of various emissions sources to PM. More specifics regarding this model can be found elsewhere (Wang et al., 2015; Li et al., 2016; Alahmad et al., 2021; Zhou et al., 2021). In this paper, 6 WSIs (Cl^-, NO_3^-, SO_4^{2-}, Na^+, NH_4^+, and K^+), OC, EC and 11 elements (Mg, Al, Ca, Fe, V, Mn, Ni, Cu, Zn, Pb, and Ba) were included for the PMF analysis. All these species were categorized on the basis of their signal-to-noise ratio (S/N) as "bad" (S/N < 0.2), "weak" (0.2 ≤ S/N ≤ 2) and "strong" (S/N ≥ 2) species, and PM mass was chosen as the total variable.

In order to identify the origin and pathway of the air masses reaching Jiuquan and analyze its impact on air quality, back trajectory simulation was performed by using Hybrid Single-Particle Lagrangian Integrated Trajectory (HYSPLIT) model developed by the National Oceanic and Atmospheric Administration (NOAA) Air Resource Laboratory (Draxier and Hess, 1998). 48 h backwards trajectories were worked out with the HYSPLIT model, based on an elevation of 500 m. The meteorological data utilized for this back trajectory simulation are six-hourly archive values from the National Centre for Environmental Prediction (NCEP/NCAR) Global Data Assimilation System (GDAS) dataset (available at ftp://arlftp.arlhq.noaa.gov/ pub/archives/gdas1/).

RESULTS AND DISCUSSION

Temporal and Spatial Variations of PM

To better understand the variations of air pollutants in Hexi Corridor, five representative cities are selected for analysis according to geographical locations, including Jiuquan, Jia Yuguan, Wuwei, Jinchang, and Zhangye. **Supplementary Table S2** shows the levels of CO, O_3, SO_2, NO_2, $PM_{2.5}$, and PM_{10} over these cities in 2019, which were obtained from government reports. The 95th percentile of CO concentrations in five cities ranged from 0.9 to 1.2 mg/m^3, perfectly meeting the Grade I daily standard of CAAQS (4 mg/m^3). The 90th percentile of 8-h O_3 concentrations varied from 134 μg/m^3 to 138 μg/m^3, which is lower than the Grade II standard of CAAQS (160 μg/m^3). The annual mean concentrations varied from 8 to 17 μg/m^3 for SO_2, and from 15 to 25 μg/m^3 for NO_2, both meeting the Grade I annual standard of CAAQS (20 μg/m^3 for SO_2 and 40 μg/m^3 for NO_2). The annual average $PM_{2.5}$ concentrations were also lower than the Grade II annual standards of CAAQS (35 μg/m^3), which are 20–28 μg/m^3. The annual average PM_{10} concentrations in Jiuquan, Jia Yuguan, Wuwei, Jinchang, and Zhangye were 65, 61, 61, 58, and 55 μg/m^3, respectively. Among these cities, the annual average PM_{10} concentrations of Jiuquan closed the Grade II annual standard of CAAQS (70 μg/m^3), which may be explained by the valley landform and high emissions of particles from the surrounding deserts.

TABLE 1 | Annual mean and seasonal mean of $PM_{2.5}$ and PM_{10} mass concentrations and meteorological parameters in Jiuquan city during the entire sampling period (March 2019–January 2020). T: Temperature; RH: Relative Humidity; WS: Wind Speed; Prec: Precipitation.

	Annual	Spring	Summer	Fall	Winter
$PM_{2.5}$ (μg/m^3)	24.8	22.4	17.0	27.7	27.5
PM_{10} (μg/m^3)	73.7	87.3	55.2	89.3	65.7
$PM_{2.5}/PM_{10}$ (%)	33.6	25.7	30.8	31.0	41.9
T (°C)	8.8	13.2	23.0	7.1	-5.4
RH (%)	40.3	31.1	44.3	40.4	46.6
WS (m/s)	1.9	2.3	2.1	1.7	1.6
Prec (mm)	0.2	0.2	0.6	0.0	0.1

TABLE 2 | Seasonal distribution of water-soluble ions mass concentrations in four seasons in Jiuquan city during the entire sampling period (μg/m^3).

Season	Annual	Spring	Summer	Fall	Winter
F^-	0.07	0.08	0.02	0.06	0.10
Cl^-	0.83	0.85	0.30	1.23	0.95
NO_3^-	3.25	2.24	1.62	4.35	4.79
SO_4^{2-}	3.19	3.34	2.51	3.54	3.36
Na^+	1.35	0.93	0.42	1.90	2.14
NH_4^+	0.93	0.36	0.21	0.93	2.23
K^+	0.27	0.37	0.10	0.38	0.25
Ca^{2+}	2.02	1.85	1.24	2.80	2.20
Mg^{2+}	0.18	0.22	0.08	0.22	0.22
Total	12.09	10.23	6.50	15.41	16.24
WISs/PM_{10} (%)	16.4	11.7	11.8	17.3	24.7

Table 1 shows the seasonal variations of PM levels in Jiuquan during the sampling period (March 2019–January 2020). The annual average concentrations of $PM_{2.5}$ and PM_{10} were 24.8 and 73.7 μg/m^3, which were comparable with previous studies (Guan et al., 2019). It is worth nothing that the annual average concentration of PM_{10} exceeded the Grade II annual standard of CAAQS (70 μg/m^3). The seasonal average levels reach to the maximum in fall with mass concentrations of 27.7 ($PM_{2.5}$) and 89.3 μg/m^3 (PM_{10}), and minimum in summer with the PM mass as low as 17.0 ($PM_{2.5}$) and 55.2 μg/m^3 (PM_{10}). The trend of PM emissions is consistent with other cities (Gu et al., 2010; Ma and Jia, 2016). High PM concentrations often occur at the turn of the seasons, especially in late fall and early winter as well as late winter and early spring. Besides, the seasonal ratios of $PM_{2.5}$/PM_{10} were found to have decreased in the order of 41.9% in winter, 31.0% in fall, 30.8% in summer, and 25.7% in spring. These seasonal variations might be blamed on the cooperative effects of variations in emissions and seasonal meteorological conditions. In the spring, there was a tendency for windy and dry conditions, which favor for dispersion of PM, but the low humidity would tend to discourage secondary particle production. In the summertime, the precipitation was ample and the PM might tend to be efficiently taken away by wet scavenging. In the fall, the exposed soil after the harvest mainly caused higher concentration of PM. In the winter, the highest $PM_{2.5}/PM_{10}$ ratio could be attributed to the combination effect of both strong emissions of pollutants and relatively constant atmospheric condition, the former enhances the emissions of primary pollutants and their precursor gases, while the latter tends to militate against the dispersion of air pollutants and thus tends to lead to their accumulation over nearby surfaces.

Chemical Characteristics of PM_{10}

Water-Soluble Ions

The mass concentrations of WSIs and their relative effects on the PM_{10} levels for the present research are summarized in **Table 2**. We found that the WSIs concentration showed obvious seasonal variation in Jiuquan and was highest in winter (16.24 μg/m^3), followed by fall (15.41 μg/m^3), spring (10.23 μg/m^3), and summer (6.50 μg/m^3), accounting for 24.7%, 17.3%, 11.7% and 11.8% of PM_{10}, respectively. In winter, the high levels of WSIs might be attributed to the lower air temperature, significant temperature inversion, and stronger emission sources, particularly from coal combustion for domestic heating. Clearly, NO_3^-, SO_4^{2-}, and Ca^{2+} dominated the water-soluble inorganic species, being responsible for 8.5–15.8% of PM_{10} mass. F^- showed the lowest levels of the ionic species we detected. The primary ion composition in different seasons is jointly affected by the ion formation mechanism and meteorological conditions. In summer, high temperature and increased radiation are more likely to promote the chemical reaction rate of SO_2 and formation of SO_4^{2-}, and high temperature could lead NH_4NO_3 dissociating to gaseous HNO_3 and NH_3 (Chiwa, 2010; He et al., 2017), so that the concentration of SO_4^{2-} was higher than that of NO_3^-. The NO_3^- levels were enhanced in winter as compared to other seasons, which can be explained by the accumulation of pollutants under low temperature and stable synoptic conditions. The sulfur oxidation rates (SORs) for four seasons were all >0.1 and generally higher than the nitrogen oxidation rates (NORs) (**Supplementary Table S3**), implying that airborne photochemical oxidation of SO_2 and the conversion of SO_2 to sulfate was more likely to occur than the conversion of NO_2 to nitrate (Li et al., 2016; Qin et al., 2021). Some coal-related ions such as NH_4^+ were more abundant in winter than in other seasons, an observation mainly believed to be due to more coal combustion for power plants and domestic heating supply (He et al., 2017). **Supplementary Figure S1** shows the strong correlation between NH_4^+ and NO_3^-, which is higher than that between NH_4^+ and SO_4^{2-}, suggesting NH_4NO_3 to be the major chemical fraction of WSIs, followed by $(NH_4)_2SO_4$ and NH_4HSO_4 (He et al., 2017).

Anion equivalents (AE)/Cation equivalents (CE) ratios are often employed to discern the acidity of PM, and their calculation method is provided in the **Supplementary Material**. As shown in **Figure 2**, the CE/AE ratios have significant seasonal differences. Except for summer, the CE/AE ratios for spring, fall and winter were above 1, which indicated that the atmospheric particles in these three seasons were characterized as alkaline in nature. In summer, however, the CE/AE ratios was close to 1, and the particles were close to being neutral, which is associated with lower soil and industrial emissions in summer.

Carbonaceous Species

Carbonaceous chemicals in atmospheric aerosols are mostly made up of two species, namely, OC and EC (Zhou et al., 2021). The main origins of OC and EC include commercial coal burning, motor-

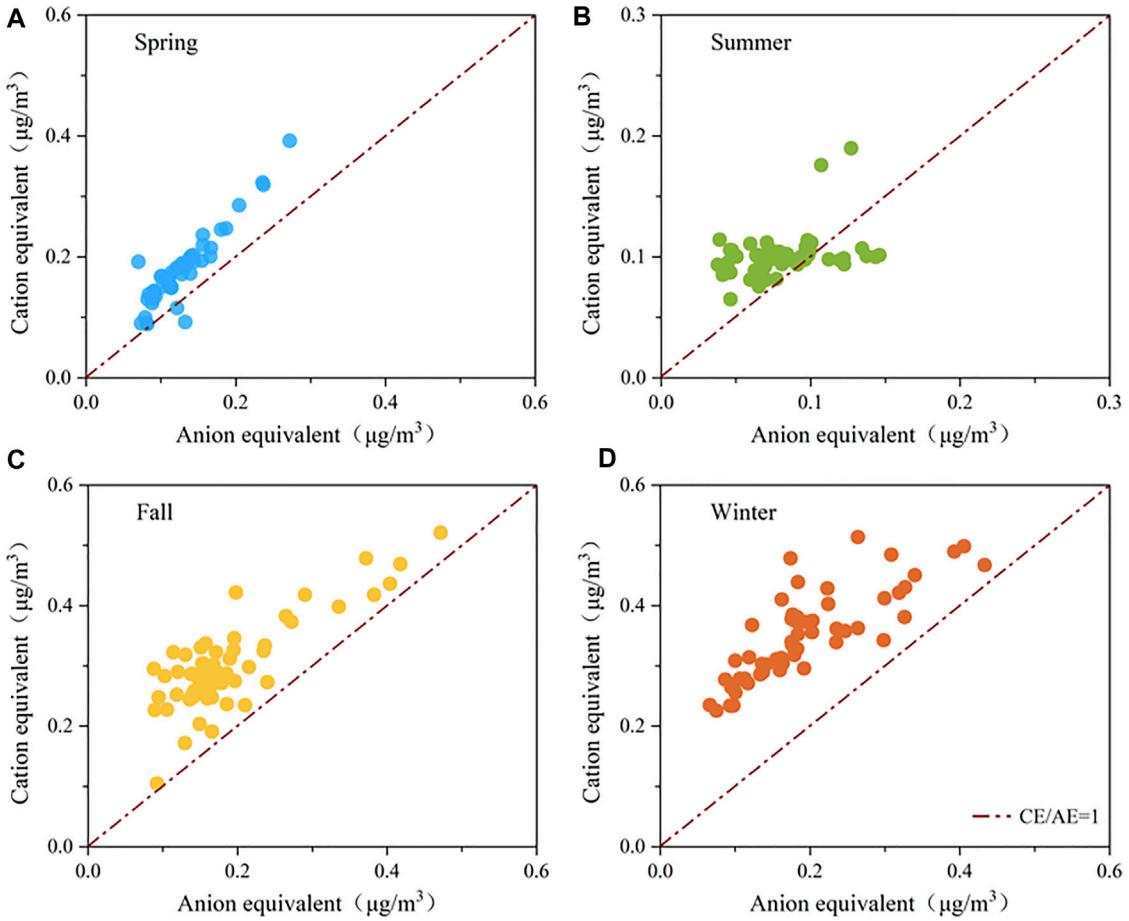

FIGURE 2 | Total cation versus anion micro-equivalents concentrations in four seasons: **(A)** spring, **(B)** summer, **(C)** fall and **(D)** winter.

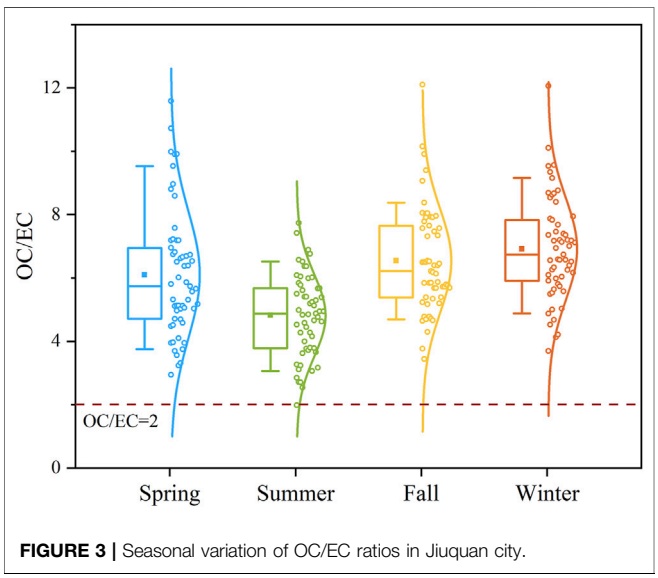

FIGURE 3 | Seasonal variation of OC/EC ratios in Jiuquan city.

vehicle exhausts and biomass combustion (Gu et al., 2010). OC can be divided into primary organic carbon (POC) that is directly emitted from anthropogenic and biogenic sources and secondary organic carbon (SOC) that is generated by atmospheric photochemical reactions. The OC/EC ratio is well regarded as an indicator of fractions attributable to primary and secondary organic aerosols (SOA). While the OC/EC ratio does depend on the length of time and methods used in the analysis, in general, an OC/EC value above 2.0–2.2 informs us that secondary organic carbon (SOC) may be produced (Zhang et al., 2013; Li et al., 2016). As shown in **Figure 3** and **Supplementary Table S4**, the seasonal average concentration varied from 7.0 (summer) to 18.2 μg/m^3 (winter) for OC and from 1.3 (spring) to 3.1 μg/m^3 (winter) for EC. The OC/EC ratio does here point in the direction of potential presence of SOA with annual mean OC/EC ratios of 5.7. In particular, higher OC/EC ratio and SOC (Calculation method is provided in the **Supplementary Material**) concentration were detected in the wintertime as contrasted with other seasons.

TABLE 3 | Seasonal distribution of inorganic elements mass concentrations in four seasons in Jiuquan city during the entire sampling period (ng/m^3).

Season	Annual	Spring	Summer	Fall	Winter	EF
Mg	1.8×10^3	2.0×10^3	9.9×10^2	2.4×10^3	1.6×10^3	2.4
Al	2.9×10^3	3.6×10^3	2.1×10^3	3.6×10^3	2.2×10^3	1.0
Ca	1.4×10^3	1.4×10^3	6.7×10^2	1.8×10^3	1.7×10^3	1.1
Fe	2.3×10^3	3.0×10^3	1.5×10^3	2.7×10^3	2.1×10^3	1.3
V	4.6	6.6	2.2	6.5	3.1	1.3
Mn	69.5	71.9	32.5	115.8	57.9	2.0
Ni	14.7	11.4	3.2	23.0	21.3	8.3
Cu	13.1	6.4	2.8	18.9	24.3	3.7
Zn	61.0	23.6	23.2	128.6	68.5	36.8
Pb	26.6	37.2	29.8	17.9	21.6	86.1
Ba	49.9	50.8	35.1	65.1	48.7	4.5
Total	8.6×10^3	10.1×10^3	5.4×10^3	10.9×10^3	7.9×10^3	—
Total/PM_{10} (%)	11.7	11.6	9.9	12.2	12.0	—

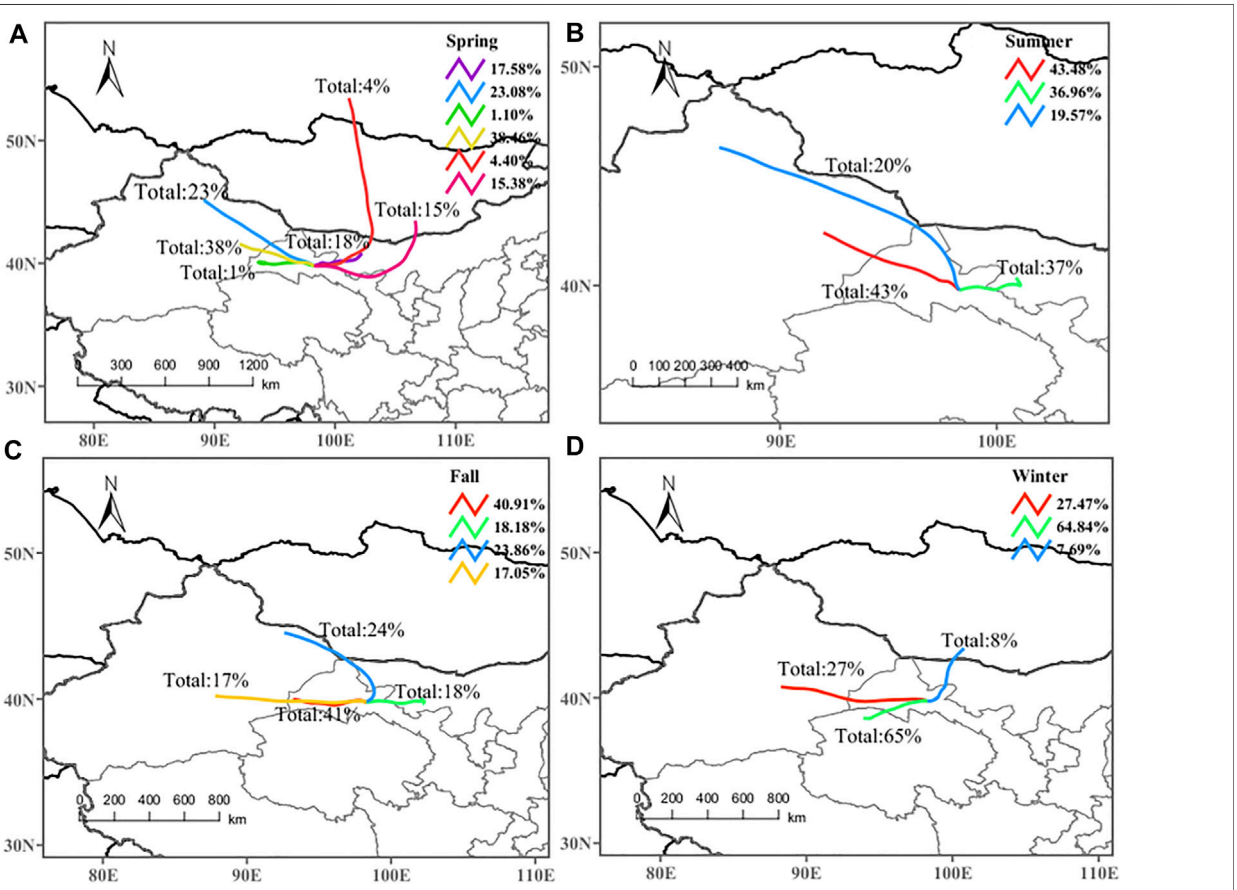

FIGURE 4 | Analytical results of 48 h air mass back trajectories arriving at 500 m elevation in four seasons in Jiuquan city. The percentage in the figure represents the proportion of the air mass to the total backward trajectory.

Inorganic Elements

The mass concentrations of inorganic elements in PM_{10} samples are shown in **Table 3**. We found that the total concentration of inorganic elements was highest in fall (10.9 μg/m^3), followed by spring (10.1 μg/m^3), winter (7.9 μg/m^3), and summer (5.4 μg/m^3), accounting for 12.2%, 11.6%, 12.0% and 9.9% of PM_{10} mass, respectively. Moreover, the comparatively high concentrations of inorganic elements were found in the order Al > Fe > Mg > Ca, the mass contributions of these four elements made up 9.6–11.8% for PM_{10}, and their concentration can be compared with Xi'an, Lanzhou, and other cities (Wang et al., 2013). To look into their main formation processes, the Enrichment factor (EF) method

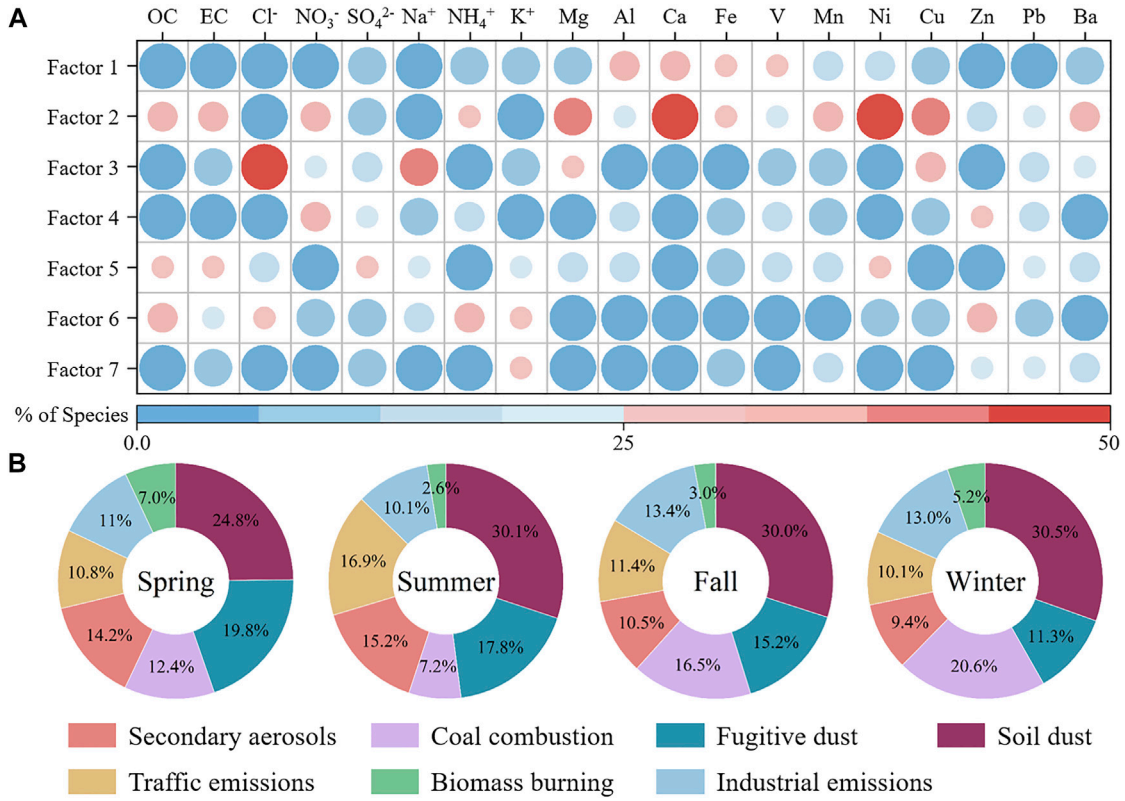

FIGURE 5 | The PMF model was used to analyze the source factor profiles **(A)** and their relative contributions to PM_{10} in four seasons **(B)** in Jiuquan city. The color gradient represents the contribution of a certain chemical component to the source.

availed to tell anthropogenic and natural sources apart (Zhou et al., 2021). We entertained the idea of using Al as the reference element and judge the anthropogenic and crustal origin of inorganic elements based on a critical EF value of 10 (Hsu et al., 2010). The EFs of those elements (Mg, Al, Ca, Fe, V, Mn, Ni, Cu, Zn, Pb and Ba) in PM_{10} are shown in **Table 3**. The EFs of Mg, Al, Ca, Fe, V, Mn, Ni, Cu and Ba were <10, indicating these inorganic elements were mainly from mineral dusts, whereas the EFs of Zn and Pb were >10, indicating they are mainly from anthropogenic sources.

Source Apportionment of PM_{10}

Influence of Air Masses Transport

To interpret the influence of regional sources and long-range movement of pollutants in Jiuquan, the 48-h air mass backward trajectories ending were determined by the HYSPLIT model. **Figure 4** shows the backward air mass trajectories in four seasons in Jiuquan city. We found that the seasonal differences of PM_{10} partially caused by the different air mass origins in different seasons. For example, the highest PM_{10} in Jiuquan in fall seems to be something that can be attributed to the air masses coming from many deserts (17% for the Taklimakan Desert, 18% for the Badain Jaran Desert) and the Gobi Desert. The lowest PM_{10} in summer was due to almost 80% of air masses from the edge of the Taklimakan Desert and the Badain Jaran Desert, and only 20% of the air masses being from the Gurbantunggut Desert. In spring, air masses were mainly from both the west (38%) and northwest (23%) and basically passed the dust storm source areas including the Taklimakan Desert and the Gurbantunggut Desert. Hence, dust storms generally occurred in the spring, at which time the $PM_{2.5}/PM_{10}$ ratio was the lowest (25.7%), indicating that PM_{10} mostly originated from natural sources. Most of the air masses during wintertime reaching this region were from the Gobi Desert of northwest Qinghai Province (65%) passing over the industrial city of Jia Yuguan, which may be the reason for the highest $PM_{2.5}/PM_{10}$ ratio in winter.

Positive Matric Factorization Analysis

PMF is commonly used to obtain the contributions of different source factors and their profiles. In the present study, PMF analysis employing many detected chemical species (*Data Analysis Section*) found seven major source factors in Jiuquan, including 1) soil dust, 2) fugitive dust, 3) coal combustion, 4) secondary aerosols, 5) traffic emissions, 6) industrial emissions, and 7) biomass burning. The profiles of these factors and their contributions to PM_{10} are shown in **Figure 5**. The details are elaborated below.

The first factor pertains to soil dust which includes significant concentrations of soil elements Ca, Fe, Al, and Mg in PM_{10} compared with other elements. These crustal elements are a known signature of soil dust (Khodeir et al., 2012; Grivas et al., 2018; Jain et al., 2020). The contribution from soil dust

to PM_{10} mass was 24.8–30.5%. This is in good concurrence with high PM_{10} levels detected in Lanzhou city (Wang et al., 2009) and high fractions of soil dust in PM_{10} as a consequence of the low rainfall in conjunction with exposed ground conditions.

The second factor accounted for about 11.3–19.8% of PM_{10} mass; this was separately classed as fugitive dust emission, comprising a mixture of re-suspended road dust, construction, and demolition dust. This source profile has high loadings of Mg and Ca, which have been detected before in the construction dust (Crilley et al., 2017). This source also showed significant levels of Mn, Ni, Cu, and NO_3^-, linked also with re-suspended road dust (Khodeir et al., 2012; Javed and Guo, 2021).

The third factor is coal combustion characterized by elevated levels of Cl^- and Pb. The concentrations of good marker of coal burning such as Cl^- increased by 3.2 times, from summer to winter due to wintertime indoor heating and stagnant weather. This source was responsible for 20.6% of the PM_{10} mass during the winter, as against only 7.2% in summer. Coal burning has proven one of the most important sources for atmospheric particles in many of China's cities (Song et al., 2006; Geng et al., 2013; Tao et al., 2014; Li et al., 2016; Liu et al., 2016).

The fourth factor is related to secondary aerosols characterized by high levels of SO_4^{2-}, NO_3^-, and NH_4^+ in PM_{10}, which are generated by photochemical or other chemical reaction processes. This factor contributed 9.4–15.2% to PM_{10} mass. Their levels show effects of precursor gases and atmospheric parameters, such as temperature, humidity, insolation, and solar radiation (Lurmann et al., 2006; Wang et al., 2016; Tan et al., 2017).

The fifth factor finds the cause of high fractions of OC, EC, Mn, and Pb in PM_{10}, a feature of traffic emissions. The contribution from traffic exhausts to PM_{10} was 10.1–16.9%. Past work has demonstrated that OC and EC are the most widespread species in traffic exhaust (Kim et al., 2003; Song et al., 2006; Wang et al., 2016; Tao et al., 2017a). Mn and Pb are sometimes also generated from lubricant oil, brake linings, and tires (Zhou et al., 2004; Lough et al., 2005; Yu et al., 2013).

The sixth source is the industrial emissions, where a host of metals such as K^+, Ni, and Zn, linked to iron and steel processing, serve as the signature (Song et al., 2001; Mooibroek et al., 2011). This factor contributed 13.4 and 13.0% to the PM_{10} mass in fall and winter, respectively. As referred to above, the majority of the air masses during fall and winter reaching this region travels across Jia Yuguan city (**Figure 4**), a major centre for the iron and steel industry northwestern China, which might make its mark felt on the air in Jiuquan.

The seventh factor corresponds to biomass burning, and shows high proportion of K^+. Prior studies have shown that soluble K^+ can be enriched in the aerosol by biomass burning (Chow et al., 2004; Duan et al., 2004; Shen et al., 2009). This factor accounted for 2.6–7.0% of PM_{10} mass, indicating the presence of burning vegetation and domestic wood combustion in the area.

CONCLUSION

Although PM pollution has to some extent been dealt with in the last few years in northwestern China, the annual average PM_{10} levels in Jiuquan were still exceeded the Grade II annual standard of CAAQS (70 $\mu g/m^3$), indicating the issue of atmospheric PM pollution in the area remains significant. The seasonal mean concentration of PM_{10} in fall was 1.6 times higher than in summer. The water-soluble ions were dominated by three ionic species (NO_3^-, SO_4^{2-}, and Ca^{2+}) accounting for 8.5–15.8% of PM_{10} mass. PM_{10} in Jiuquan was alkaline by the micro-equivalents concentration methods but nearly neutral in summer, and the chemical forms of WSIs were mainly NH_4NO_3, $(NH4)_2SO_4$ and NH_4HSO_4. In general, water-soluble ions showed a definite seasonal pattern, rising in winter and falling in summer. However, the highest inorganic elements were observed in the fall. It is also worth noting that the overall carbonaceous particle matter made up around 10.5–32.4% of PM_{10} mass.

The back trajectory analysis corroborated the view that the long-range transport of air masses from desert areas has an important impact on the level of particulate matter in Jiuquan. In addition, seven source factors were identified for PM_{10} through PMF model analysis. Soil dust, fugitive dust and coal combustion are the most important sources, accounting for 24.8–30.5%, 11.3–19.8%, and 7.2–20.6% of PM_{10}, respectively. The significant contributions of natural emissions and regional transport set a major challenge to achieving local PM standards, pointing in turn to how crucial regional collaboration is when seeking more effective control policies to reduce air pollution. The findings herein offer worthwhile initial analysis on the potential sources identified and their probable relative contributions to particulate pollution; this will thus be useful for policymakers when they advance local air quality improvement strategies and when they work on regional collaboration on pollution control policies.

DATA AVAILABILITY STATEMENT

The raw data supporting the conclusion of this article will be made available by the authors, without undue reservation.

AUTHOR CONTRIBUTIONS

CL wrote the manuscript. XL and YC reviewed and modified the manuscript. Sampling work was performed by GZ, XL, and YG. TZ and BL measured and analyzed the samples. CL and TZ provided the graphics. XL administered the project. All authors contributed to manuscript revision and read and approved the submitted version.

FUNDING

This work was supported by the National Natural Science Foundation of China (Nos. 42061134006 and 21876029). The authors declare no conflicts of interest.

SUPPLEMENTARY MATERIAL

The Supplementary Material for this article can be found online at: https://www.frontiersin.org/articles/10.3389/fenvs.2022.945658/full#supplementary-material

REFERENCES

Alahmad, B., Al-Hemoud, A., Kang, C.-M., Almarri, F., Kommula, V., Wolfson, J. M., et al. (2021). A Two-Year Assessment of Particulate Air Pollution and Sources in Kuwait. *Environ. Pollut.* 282, 117016. doi:10.1016/j.envpol.2021.117016

Almeida, S. M., Freitas, M. C., Repolho, C., Dionísio, I., Dung, H. M., Caseiro, A., et al. (2009). Characterizing Air Particulate Matter Composition and Sources in Lisbon, Portugal. *J. Radioanal. Nucl. Chem.* 281 (2), 215–218. doi:10.1007/s10967-009-0113-8

Cao, J. (2003). Characteristics of Carbonaceous Aerosol in Pearl River Delta Region, China during 2001 Winter Period. *Atmos. Environ.* 37 (11), 1451–1460. doi:10.1016/s1352-2310(02)01002-6

Chiwa, M. (2010). Characteristics of Atmospheric Nitrogen and Sulfur Containing Compounds in an Inland Suburban-Forested Site in Northern Kyushu, Western Japan. *Atmos. Res.* 96 (4), 531–543. doi:10.1016/j.atmosres.2010.01.001

Chow, J. C., Watson, J. G., Kuhns, H., Etyemezian, V., Lowenthal, D. H., Crow, D., et al. (2004). Source Profiles for Industrial, Mobile, and Area Sources in the Big Bend Regional Aerosol Visibility and Observational Study. *Chemosphere* 54 (2), 185–208. doi:10.1016/j.chemosphere.2003.07.004

Chow, J. C., and Watson, J. G. (2002). PM2.5 Carbonate Concentrations at Regionally Representative Interagency Monitoring of Protected Visual Environment Sites. *J. Geophys. Res.* 107 (D21), 6–1. doi:10.1029/2001jd000574

Chu, P. C., Chen, Y., Lu, S., Li, Z., and Lu, Y. (2008). Particulate Air Pollution in Lanzhou China. *Environ. Int.* 34 (5), 698–713. doi:10.1016/j.envint.2007.12.013

Crilley, L. R., Lucarelli, F., Bloss, W. J., Harrison, R. M., Beddows, D. C., Calzolai, G., et al. (2017). Source Apportionment of Fine and Coarse Particles at a Roadside and Urban Background Site in London during the 2012 Summer ClearfLo Campaign. *Environ. Pollut.* 220, 766–778. doi:10.1016/j.envpol.2016.06.002

Draxier, R. R., and Hess, G. D. (1998). An Overview of the HYSPLIT_4 Modelling System for Trajectories, Dispersion and Deposition. *Aust. Meteorol. Mag.* 47 (4), 295–308.

Duan, F., Liu, X., Yu, T., and Cachier, H. (2004). Identification and Estimate of Biomass Burning Contribution to the Urban Aerosol Organic Carbon Concentrations in Beijing. *Atmos. Environ.* 38 (9), 1275–1282. doi:10.1016/j.atmosenv.2003.11.037

Geng, N., Wang, J., Xu, Y., Zhang, W., Chen, C., and Zhang, R. (2013). PM2.5 in an Industrial District of Zhengzhou, China: Chemical Composition and Source Apportionment. *Particuology* 11 (1), 99–109. doi:10.1016/j.partic.2012.08.004

Grivas, G., Cheristanidis, S., Chaloulakou, A., Koutrakis, P., and Mihalopoulos, N. (2018). Elemental Composition and Source Apportionment of Fine and Coarse Particles at Traffic and Urban Background Locations in Athens, Greece. *Aerosol Air Qual. Res.* 18 (7), 1642–1659. doi:10.4209/aaqr.2017.12.0567

Gu, J., Bai, Z., Liu, A., Wu, L., Xie, Y., Li, W., et al. (2010). Characterization of Atmospheric Organic Carbon and Element Carbon of PM2.5 and PM10 at Tianjin, China. *Aerosol Air Qual. Res.* 10 (2), 167–176. doi:10.4209/aaqr.2009.12.0080

Guan, Q., Liu, Z., Yang, L., Luo, H., Yang, Y., Zhao, R., et al. (2019). Variation in PM2.5 Source over Megacities on the Ancient Silk Road, Northwestern China. *J. Clean. Prod.* 208, 897–903. doi:10.1016/j.jclepro.2018.10.199

He, Q., Yan, Y., Guo, L., Zhang, Y., Zhang, G., and Wang, X. (2017). Characterization and Source Analysis of Water-Soluble Inorganic Ionic Species in PM2.5 in Taiyuan City, China. *Atmos. Res.* 184, 48–55. doi:10.1016/j.atmosres.2016.10.008

Hsu, S. C., Liu, S. C., Tsai, F., Engling, G., Lin, I. I., Chou, C. K. C., et al. (2010). High Wintertime Particulate Matter Pollution Over an Offshore Island (Kinmen) off Southeastern China: An Overview. *J. Geophys. Res.* 115 (D17), D17309. doi:10.1029/2009jd013641

Jain, S., Sharma, S. K., Vijayan, N., and Mandal, T. K. (2020). Seasonal Characteristics of Aerosols (PM2.5 and PM10) and Their Source Apportionment Using PMF: A Four Year Study over Delhi, India. *Environ. Pollut.* 262, 114337. doi:10.1016/j.envpol.2020.114337

Javed, W., and Guo, B. (2021). Chemical Characterization and Source Apportionment of Fine and Coarse Atmospheric Particulate Matter in Doha, Qatar. *Atmos. Pollut. Res.* 12 (2), 122–136. doi:10.1016/j.apr.2020.10.015

Jiang, N., Yin, S., Guo, Y., Li, J., Kang, P., Zhang, R., et al. (2018). Characteristics of Mass Concentration, Chemical Composition, Source Apportionment of PM 2.5 and PM 10 and Health Risk Assessment in the Emerging Megacity in China. *Atmos. Pollut. Res.* 9 (2), 309–321. doi:10.1016/j.apr.2017.07.005

Jiang, H., Li, Z., Wang, F., Zhou, X., Wang, F., Ma, S., et al. (2021). Water-Soluble Ions in Atmospheric Aerosol Measured in a Semi-arid and Chemical-Industrialized City, Northwest China. *Atmosphere* 12 (4), 456. doi:10.3390/atmos12040456

Khodeir, M., Shamy, M., Alghamdi, M., Zhong, M., Sun, H., Costa, M., et al. (2012). Source Apportionment and Elemental Composition of PM2.5 and PM10 in Jeddah City, Saudi Arabia. *Atmos. Pollut. Res.* 3 (3), 331–340. doi:10.5094/apr.2012.037

Kim, E., Hopke, P. K., and Edgerton, E. S. (2003). Source Identification of Atlanta Aerosol by Positive Matrix Factorization. *J. Air & Waste Manag. Assoc.* 53 (6), 731–739. doi:10.1080/10473289.2003.10466209

Li, H., Wang, Q. g., Yang, M., Li, F., Wang, J., Sun, Y., et al. (2016). Chemical Characterization and Source Apportionment of PM2.5 Aerosols in a Megacity of Southeast China. *Atmos. Res.* 181, 288–299. doi:10.1016/j.atmosres.2016.07.005

Liu, B., Song, N., Dai, Q., Mei, R., Sui, B., Bi, X., et al. (2016). Chemical Composition and Source Apportionment of Ambient PM2.5 during the Non-heating Period in Taian, China. *Atmos. Res.* 170, 23–33. doi:10.1016/j.atmosres.2015.11.002

Lough, G. C., Schauer, J. J., Park, J.-S., Shafer, M. M., Deminter, J. T., and Weinstein, J. P. (2005). Emissions of Metals Associated with Motor Vehicle Roadways. *Environ. Sci. Technol.* 39 (3), 826–836. doi:10.1021/es048715f

Lurmann, F. W., Brown, S. G., McCarthy, M. C., and Roberts, P. T. (2006). Processes Influencing Secondary Aerosol Formation in the San Joaquin Valley during Winter. *J. Air & Waste Manag. Assoc.* 56 (12), 1679–1693. doi:10.1080/10473289.2006.10464573

Ma, X., and Jia, H. (2016). Particulate Matter and Gaseous Pollutions in Three Megacities over China: Situation and Implication. *Atmos. Environ.* 140, 476–494. doi:10.1016/j.atmosenv.2016.06.008

Mooibroek, D., Schaap, M., Weijers, E. P., and Hoogerbrugge, R. (2011). Source Apportionment and Spatial Variability of PM2.5 Using Measurements at Five Sites in the Netherlands. *Atmos. Environ.* 45 (25), 4180–4191. doi:10.1016/j.atmosenv.2011.05.017

Pui, D. Y. H., Chen, S.-C., and Zuo, Z. (2014). PM 2.5 in China: Measurements, Sources, Visibility and Health Effects, and Mitigation. *Particuology* 13, 1–26. doi:10.1016/j.partic.2013.11.001

Qin, Y., Li, J., Gong, K., Wu, Z., Chen, M., Qin, M., et al. (2021). Double High Pollution Events in the Yangtze River Delta from 2015 to 2019: Characteristics, Trends, and Meteorological Situations. *Sci. Total Environ.* 792, 148349. doi:10.1016/j.scitotenv.2021.148349

Qiu, X., Duan, L., Gao, J., Wang, S., Chai, F., Hu, J., et al. (2016). Chemical Composition and Source Apportionment of PM10 and PM2.5 in Different Functional Areas of Lanzhou, China. *J. Environ. Sci.* 40, 75–83. doi:10.1016/j.jes.2015.10.021

Shen, Z., Cao, J., Arimoto, R., Han, Z., Zhang, R., Han, Y., et al. (2009). Ionic Composition of TSP and PM2.5 during Dust Storms and Air Pollution Episodes at Xi'an, China. *Atmos. Environ.* 43 (18), 2911–2918. doi:10.1016/j.atmosenv.2009.03.005

Song, X.-H., Polissar, A. V., and Hopke, P. K. (2001). Sources of Fine Particle Composition in the Northeastern US. *Atmos. Environ.* 35 (31), 5277–5286. doi:10.1016/s1352-2310(01)00338-7

Song, Y., Zhang, Y., Xie, S., Zeng, L., Zheng, M., Salmon, L. G., et al. (2006). Source Apportionment of PM2.5 in Beijing by Positive Matrix Factorization. *Atmos. Environ.* 40 (8), 1526–1537. doi:10.1016/j.atmosenv.2005.10.039

Tan, J., Zhang, L., Zhou, X., Duan, J., Li, Y., Hu, J., et al. (2017). Chemical Characteristics and Source Apportionment of PM 2.5 in Lanzhou, China. *Sci. Total Environ.* 601-602, 1743–1752. doi:10.1016/j.scitotenv.2017.06.050

Tao, J., Gao, J., Zhang, L., Zhang, R., Che, H., Zhang, Z., et al. (2014). PM_{2.5} Pollution in a Megacity of Southwest China: Source Apportionment and Implication. *Atmos. Chem. Phys.* 14 (16), 8679–8699. doi:10.5194/acp-14-8679-2014

Tao, J., Zhang, L., Cao, J., and Zhang, R. (2017a). A Review of Current Knowledge Concerning PM_{2. 5} Chemical Composition, Aerosol Optical Properties and Their Relationships across China. *Atmos. Chem. Phys.* 17 (15), 9485–9518. doi:10.5194/acp-17-9485-2017

Tao, J., Zhang, L., Cao, J., Zhong, L., Chen, D., Yang, Y., et al. (2017b). Source Apportionment of PM2.5 at Urban and Suburban Areas of the Pearl River Delta Region, South China - with Emphasis on Ship Emissions. *Sci. Total Environ.* 574, 1559–1570. doi:10.1016/j.scitotenv.2016.08.175

Tsiouri, V., Kakosimos, K. E., and Kumar, P. (2015). Concentrations, Sources and Exposure Risks Associated with Particulate Matter in the Middle East Area-A Review. *Air Qual. Atmos. Health* 8 (1), 67–80. doi:10.1007/s11869-014-0277-4

Wang, S., Feng, X., Zeng, X., Ma, Y., and Shang, K. (2009). A Study on Variations of Concentrations of Particulate Matter with Different Sizes in Lanzhou, China. *Atmos. Environ.* 43 (17), 2823–2828. doi:10.1016/j.atmosenv.2009.02.021

Wang, J., Hu, Z., Chen, Y., Chen, Z., and Xu, S. (2013). Contamination Characteristics and Possible Sources of PM10 and PM2.5 in Different Functional Areas of Shanghai, China. *Atmos. Environ.* 68, 221–229. doi:10.1016/j.atmosenv.2012.10.070

Wang, Q. Q., Huang, X. H. H., Zhang, T., Zhang, Q., Feng, Y., Yuan, Z., et al. (2015). Organic Tracer-Based Source Analysis of PM 2.5 Organic and Elemental Carbon: A Case Study at Dongguan in the Pearl River Delta, China. *Atmos. Environ.* 118, 164–175. doi:10.1016/j.atmosenv.2015.07.033

Wang, Y., Jia, C., Tao, J., Zhang, L., Liang, X., Ma, J., et al. (2016). Chemical Characterization and Source Apportionment of PM2.5 in a Semi-arid and Petrochemical-Industrialized City, Northwest China. *Sci. Total Environ.* 573, 1031–1040. doi:10.1016/j.scitotenv.2016.08.179

Wang, W., Samat, A., Abuduwaili, J., and Ge, Y. (2020). Spatio-Temporal Variations of Satellite-Based PM2.5 Concentrations and its Determinants in Xinjiang, Northwest of China. *Int. J. Environ. Res. Public Health* 17 (6), 2157. doi:10.3390/ijerph17062157

Yu, L., Wang, G., Zhang, R., Zhang, L., Song, Y., Wu, B., et al. (2013). Characterization and Source Apportionment of PM2.5 in an Urban Environment in Beijing. *Aerosol Air Qual. Res.* 13 (2), 574–583. doi:10.4209/aaqr.2012.07.0192

Zhang, R., Jing, J., Tao, J., Hsu, S.-C., Wang, G., Cao, J., et al. (2013). Chemical Characterization and Source Apportionment of PM_{2.5} in Beijing: Seasonal Perspective. *Atmos. Chem. Phys.* 13 (14), 7053–7074. doi:10.5194/acp-13-7053-2013

Zhou, L., Hopke, P. K., Paatero, P., Ondov, J. M., Pancras, J. P., Pekney, N. J., et al. (2004). Advanced Factor Analysis for Multiple Time Resolution Aerosol Composition Data. *Atmos. Environ.* 38 (29), 4909–4920. doi:10.1016/j.atmosenv.2004.05.040

Zhou, X., Li, Z., Zhang, T., Wang, F., Tao, Y., Zhang, X., et al. (2021). Chemical Nature and Predominant Sources of PM10 and PM2.5 from Multiple Sites on the Silk Road, Northwest China. *Atmos. Pollut. Res.* 12 (1), 425–436. doi:10.1016/j.apr.2020.10.001

Conflict of Interest: The authors declare that the research was conducted in the absence of any commercial or financial relationships that could be construed as a potential conflict of interest.

Publisher's Note: All claims expressed in this article are solely those of the authors and do not necessarily represent those of their affiliated organizations, or those of the publisher, the editors and the reviewers. Any product that may be evaluated in this article, or claim that may be made by its manufacturer, is not guaranteed or endorsed by the publisher.

frontiers | Frontiers in Environmental Science

ORIGINAL RESEARCH
published: 04 July 2022
doi: 10.3389/fenvs.2022.929449

Chemical Composition, Optical Properties and Sources of $PM_{2.5}$ From a Highly Urbanized Region in Northeastern Mexico

Karim Acuña Askar[1], Lucy T. González[2], Alberto Mendoza[2], Oxana V. Kharissova[3], Andrea Rodríguez-Garza[2], Eleazar M. Lara[4], Alfredo Campos[5], D. López-Serna[4], Lilia M. Bautista-Carrillo[6], J. M. Alfaro-Barbosa[4] and F. E. Longoria-Rodríguez[6]*

[1]Universidad Autónoma de Nuevo León, Facultad de Medicina, Laboratorio de Biorremediación Ambiental, Monterrey, México, [2]Tecnologico de Monterrey, Escuela de Ingeniería y Ciencias, Monterrey, México, [3]Universidad Autónoma de Nuevo León, Facultad de Fisicomatemáticas, Centro de Innovación, Investigación y Desarrollo en Ingeniería y Tecnología, Monterrey, México, [4]Universidad Autónoma de Nuevo León, Facultad de Ciencias Químicas, Laboratorio de Química Analítica Ambiental, Monterrey, México, [5]Centro de Investigación en Materiales Avanzados S.C. (CIMAV), Chihuahua, México, [6]Centro de Investigación en Materiales Avanzados S.C. (CIMAV), Unidad Monterrey, Apodaca, México

OPEN ACCESS

Edited by:
Michael MacKinnon,
University of California, Irvine,
United States

Reviewed by:
Bighnaraj Sarangi,
University of Puerto Rico, Puerto Rico
Beatrice Moroni,
University of Perugia, Italy

***Correspondence:**
Lucy T. González
lucy.gonzalez@tec.mx

Specialty section:
This article was submitted to Toxicology, Pollution and the Environment, a section of the journal Frontiers in Environmental Science

Received: 26 April 2022
Accepted: 08 June 2022
Published: 04 July 2022

Citation:
Acuña Askar K, González LT, Mendoza A, Kharissova OV, Rodríguez-Garza A, Lara EM, Campos A, López-Serna D, Bautista-Carrillo LM, Alfaro-Barbosa JM and Longoria-Rodríguez FE (2022) Chemical Composition, Optical Properties and Sources of $PM_{2.5}$ From a Highly Urbanized Region in Northeastern Mexico. Front. Environ. Sci. 10:929449. doi: 10.3389/fenvs.2022.929449

Here, we report the chemical composition and optical properties of the fine particles ($PM_{2.5}$) and water-soluble organic carbon (WSOC) of these particles. Additionally, the potential sources of WSOC emission were determined through the study on fluorescence excitation–emission matrix spectra and parallel factor analysis (EEM-PARAFAC). Samples were collected in an urban site of the Monterrey Metropolitan Area in Mexico during summer and winter and characterized using attenuated total reflectance-Fourier-transform infrared spectroscopy (ATR-FTIR), ultraviolet-visible-near infrared-diffuse reflectance spectroscopy (UV–Vis-NIR-DRS), fluorescence spectroscopy, X-ray photoelectron spectroscopy (XPS), and X-ray diffraction (XRD) techniques. The ATR-FTIR analyses allowed the identification of inorganic ions (e.g., CO_3^{2-}, SO_4^{2-}, and NO_3^-), organic functional groups [e.g., carbonyls (C=O), organic hydroxyl (C-OH), carboxylic acid (COOH)], and aromatic and unsaturated aliphatic hydrocarbons. The results obtained by XRD and XPS revealed the presence of organic and inorganic chemical species in $PM_{2.5}$. The diffuse reflectance spectra of $PM_{2.5}$ provided the absorption bands in the UV region for $CaSO_4$, $CaCO_3$, and aluminosilicates. The absorption coefficient at 365 nm (Abs_{365}) and Ångström absorption exponent (AAE) values obtained for the aqueous extracts suggest that many of the water-soluble organic compounds corresponded to brown carbon (BrC) chromophores. The mass absorption efficiency values at 365 nm (MAE_{365}) were higher in the winter than summer samples, suggesting the presence of more BrC compounds in the winter samples. The fluorescence indices combined with

Abbreviations: ATR, Attenuated total reflection; DOM, Dissolved organic matter; DRS, Diffuse reflectance spectroscopy; EC, Elemental carbon; FI, Fluorescence index; HULIS, Humic-like substances; MAE, Mass absorption efficiency; MMA, Monterrey metropolitan area; MS, Mass spectrometry; NIST, National institute of standards and technology; OC, Organic carbon; PM, Particulate matter; SIMA, Sistema integral de monitoreo ambiental; TOC, Total organic carbon; VOC, Volatile organic compounds; WSOC, Water-soluble organic carbon; XPS, X-ray photoelectron spectroscopy; XRD, X-ray diffraction.

EEM-PARAFAC analysis showed that the WSOC fraction was mainly composed of humic-like substances (HULIS) which are both of terrestrial and microbial origin.

Keywords: PM2.5, mass absorption efficiency (MAE)., water-soluble organic carbon (WSOC), parallel factor analysis (PARAFAC), Ångström absorption exponent

1 INTRODUCTION

The extensive atmospheric pollution occurring in large cities as a result of fast-growing urban and industrial development has caused an increase in the number of people to be continuously exposed to low-quality ambient air. Particulatematter (PM) is a common atmospheric pollutant, which has been widely studied because of its adverse effects on both the public health and global climate. Particularly, fine PM ($PM_{2.5}$) has been considered more dangerous because it is able to penetrate the deep parts of the human lung. Indeed, numerous studies have associated the components of $PM_{2.5}$ to many respiratory (e.g., lung cancer) and cardiovascular diseases. These components have also been found to cause genetic mutations in animals (Lippmann et al., 2006; Happo et al., 2010). In addition to the adverse effects on animal and human health, $PM_{2.5}$ influences both local and global climates. Several $PM_{2.5}$ components have been shown to cause the dispersion and absorption of light (including infrared light). These effects on light disturb the radiation balance of the atmosphere, which may then cause unexpected variations in the atmospheric heating-cooling cycles (Jacobson, 2004; Huo et al., 2016; Chen et al., 2019). Our present knowledge related to the influence of $PM_{2.5}$ on radiative forcing (change in energy flux in the atmosphere) and climate change is still limited. Moreover, there are difficulties associated with the current atmospheric models, which are used to measure the magnitude of both capture and release of radiation by $PM_{2.5}$. For example, different types of aerosols may exert a large range of contrasting effects on the net cooling or heating of an atmosphere. This is caused by the high variability of the $PM_{2.5}$ properties in the atmospheric aerosols as a function of the region.

$PM_{2.5}$ is composed of a wide variety of chemical substances of both organic and inorganic origin, being carbonaceous material the component that have attracted the most attention because they contribute between 10% and 70% of the total mass of $PM_{2.5}$, with concentrations found in selected areas ranged from a few pg/m^3 to hundreds of ng/m^3 (Tsapakis et al., 2002; Hecobian et al., 2010; Khare et al., 2011). Black carbon (BC) is the main light-absorbing carbonaceous material in the range from visible to near infrared light. However, the fraction of organic carbon (OC) that is often called "Brown Carbon (BrC)" has also been found to significantly absorb ultraviolet (UV) and shorter wavelength visible (Vis) light (Jacobson, 2001; Bond et al., 2004). The contribution of BrC to climate change is not limited to its impact to the atmosphere due to its ability and capacity to absorb solar radiation. Recent studies have shown that BrC has accelerated the melting of snow and decreased the Earth's albedo (Andreae and Ramanathan, 2013; Qian et al., 2015; Yan et al., 2018; Leskinen et al., 2020). Some researchers have classified OC based on its water solubility, i.e., the water-soluble organic carbon (WSOC) and water-insoluble organic carbon (Kondo et al., 2007; Miyazaki et al., 2009). The analyses of the optical properties of WSOC have allowed the identification of its probable emission sources, and thus provided helpful strategies to control emission. In the literature it has been reported that WSCOC originate from either primary sources (biomass burning, fossil fuel combustion) or atmospheric secondary processes, including gas-to-particle conversion and gas deposition onto the surface of a PM (Graber and Rudich, 2006; Sullivan and Weber, 2006; Duarte et al., 2007).

The study of the optical properties of atmospheric particles requires a variety of analytical techniques, including Fourier-transform infrared (FTIR) and UV–Vis spectroscopy, fluorescence, mass spectrometry (MS), and chromatography. Hecobian et al. (2010) characterized the optical properties of the water-soluble fraction of $PM_{2.5}$ samples using various analytical techniques. Their samples were collected in the southeastern United States throughout different seasons of a year. They found that the WSOC absorption was higher in the samples obtained during the cold months. The WSOC content was closely related to the presence of levoglucosan in the sample, suggesting that biomass burning was the main source of the emission. Moreover, Chen et al. (2016a) studied the relationship between the optical properties and chemical composition of total suspended PM in samples using FTIR, UV-Vis, fluorescence spectroscopy, electrospray ionization mass spectrometry (ESI-MS) and high-resolution accurate mass spectrometry (HR-AMS). They found that the mass absorption efficiency (MAE) was higher for the less polar organic compounds in the sample. In addition, the nitrogen and oxygen containing organic compounds contributed significantly to the total absorption of light and fluorescence of PM.

The Monterrey Metropolitan Area (MMA) has been considered the most polluted city in Mexico and one of the most polluted cities in Latin America (Clean Air Institute, 2012; INECC, 2014). The elevated emissions in the MMA originate mainly from the high industrial activity and vehicle traffic. However, studies on the chemical composition of atmospheric PM and optical properties of $PM_{2.5}$ in the MMA have been limited (Mancilla et al., 2015; Mancilla et al., 2016; Mancilla et al., 2019; González et al., 2016; González et al., 2017; González et al., 2018; López-Ayala et al., 2019; Longoria-Rodríguez et al., 2020; Longoria-Rodríguez et al., 2021). There is also limited information on the absorption response and light emission of $PM_{2.5}$ in Mexico after exposure to variable wavelengths of radiation (Liñán-Abanto et al., 2019; Carmona et al., 2021). Furthermore, studies on the chemical and optical characteristics of WSOC in $PM_{2.5}$ in Mexico and other Latin American countries have not been done. Therefore, this research focuses on three main objectives; 1) determine the chemical composition and optical properties of $PM_{2.5}$ collected in the MMA during winter and summer, 2) determine the effect of seasonal variation on the chemical composition and optical properties of the $PM_{2.5}$, and 3) establish possible sources of

TABLE 1 | Statistical summary of the meteorological variables recorded during both study periods. SD: Standard deviation.

Meteorological parameter	Winter		Summer	
	Average	SD	Average	SD
Pressure (mmHg)	719.7	7.2	708.5	4.1
Relative humidity (%)	59.5	20.6	56.9	16.3
Solar radiation (W/m^2)	145.4	222.8	238.9	273.1
Room temperature (°C)	21.1	6.3	35.9	2.9
Wind speed (km/h)	8.6	4.7	14.4	0.6
Wind Direction (degree)	15.0	67.0	136.9	83.2

WSOC emissions in MMA by applying the parallel factor analysis (PARAFAC) model. The analytical techniques including attenuated total reflection (ATR)-FTIR, UV/VIS-diffuse reflectance spectroscopy (DRS), fluorescence, x-ray diffraction (XRD), and x-ray photoelectron spectroscopy (XPS) were used to determine the optical properties and chemical composition of the $PM_{2.5}$ samples.

2 METHODOLOGY

2.1 Sampling of $PM_{2.5}$

The sampling site was in the northwestern region of the MMA in Nuevo Leon, Mexico. $PM_{2.5}$ sampling was performed at the routine monitoring station of the Integral Environmental Monitoring System [Sistema Integral de Monitoreo Ambiental (SIMA), the initials in Spanish] located in the San Bernabé suburb (25° 45' 24.86"N, 100° 21' 56.95"W, 551 m. a.s.l.) near the Talleres subway station. This station is surrounded by a highly populated urban area and located alongside the westward winds, which is coming from the highest density industrial area of MMA. In addition, it lies near a natural reserve Mount del Topo Chico. $PM_{2.5}$ samples were collected during July to August 2019 and January to February 2020 following the Method IO-2.1 USEPA method (U.S. EPA. Environmental Protection Agency Methods, 1999), where sampling temperature, relative humidity, and atmospheric pressure conditions were recorded (**Table 1**). The samples were collected every 6 days, collecting a total of 8 samples in each period.

A high-volume sampler HiVol 3000 from Ecotech, which was previously calibrated according to Method IO-2.1 USEPA (U.S. EPA. Environmental Protection Agency Methods, 1999) was placed at the SIMA station. $PM_{2.5}$ samples were collected for 24 h on fiberglass filters (EPM 2000 of $8'' \times 10''$), with a mean airflow of 67 m^3/h. For the sampling, glass fiber filters were chosen instead of quartz filters since glass is a material that does not interfere with the analyzes by the XRD technique. The mass of a loaded filter was determined using an analytical balance XS205 dual range from Mettler Toledo under a controlled relative humidity. The filter was stored at−15°C when not in use.

2.2 Optical Analysis of $PM_{2.5}$ Samples

2.2.1 ATR-FTIR Analysis

Chemical functional groups present in the $PM_{2.5}$ were identified by ATR-FTIR using a Nicolet omnic iS50 FTIR spectrophotometer from Thermo Fisher Scientific. Measurements were made in ATR mode using an ATR Smart Orbit accessory supplied with a diamond crystal. All spectra were recorded at a resolution of 4 cm^{-1} over the spectral range from 4,000 to 400 cm^{-1}. The absorption path length and total data points were 1 cm and 7,468, respectively. A scan was performed with the sample placed upside down on the ATR crystal (diameter = 3 mm). The background correction was performed by subtracting the absorption spectrum of the filter without sample from that obtained for the loaded filters. Samples did not require any pre-treatment and were analyzed directly on the fiberglass filters. The resulting set of data with baseline correction was analyzed using the SpectraGryph 1.2 Spectroscopy software (Menges, 2020).

2.2.2 UV–Vis Absorption Profiles of $PM_{2.5}$

$PM_{2.5}$ samples were characterized using the UV–Vis-NIR-DRS technique. The UV–Vis-NIR-DRS spectra were obtained with an Agilent Model Cary 5000 spectrometer equipped with an external integration sphere DRA 2500 from Agilent Technologies. The analysis was carried out directly on a filter at an area of 0.3 cm^2. The absorption path length was 1 nm. The filter blank was measured before the analysis. Prior to each measurement, baseline corrections were performed at both 0% and 100% transmittance. Samples were analyzed over the range from 200 to 2,500 nm with a resolution of 2 nm, which resulted in 2,301 data points.

2.2.2.1 Analysis of Water-Soluble Organic Carbon Fraction by UV–Vis

For WSOC fraction extraction, 10% of the total area of a filter (and filter blanks) was extracted with 30 ml of purified water in an ultrasonic bath for 15 min. The purified water was obtained from a Milli-Q system from Merck Millipore (Burlington, MA, United States). The extraction procedure was repeated twice. The extract was filtered through a 25-mm outer diameter polytetrafluoroethylene (PTFE) syringe filter of 0.22 μm pore size from Tisch Scientific. Approximately 3 ml of the filtered extract (WSOC solution) was placed in a 1-cm quartz cuvette and scanned from 200 to 800 nm in 1 nm increments using the Agilent Model Cary 5000. Purified water was used as both blank reference and baseline source of data.

The light absorption coefficient (Abs_λ, Mm^{-1}) was determined by **Eq. 1** (Teich et al., 2017):

$$Abs_\lambda = (A_\lambda - A_{700}) \frac{Vl}{Va \times L} \times \ln(10) \quad (1)$$

where A_λ and A_{700} corresponded to the absorption of the extracts at the wavelengths of λ and 700 nm, respectively. *Vl* was the volume of the solvent that the sample extract removed from the filter, *Va* was the air volume, and *L* was the absorption path length (i.e., 1 cm). The light absorption coefficient at 365 nm (Abs_{365}) was used as the indicator of BrC (Wu et al., 2019; Mo et al., 2021). Furthermore, the mass absorption efficiency at 365 nm (MAE_{365}, m^{2}g^{-1}C) was measured. MAE is a parameter that described the

light absorbing ability of WSOC. This parameter was determined by **Eq. 2** (Chen et al., 2018):

$$MAE_{365} = \frac{Abs_{365}}{C_{WSOC}} \quad (2)$$

where Cwsoc represented the WSOC concentration in μgC/m^3. The WSOC concentration was determined using a total organic carbon (TOC) analyzer model TOC-VCSH from Shimadzu (Kyoto, Japan). During the analysis, the supply gas pressure, carrier gas flow, and furnace temperature were set at 200–250 kPa, 150 ml min^{-1}, and 680°C, respectively. The sample was acidified and injected into the analyzer oven. In the oven, the carbon was catalytically oxidized to CO_2 at 680°C and the produced CO_2 was detected by the sensitive Nondispersive Infrared (NDIR) detector (2,500 cm^{-1}). Moreover, the wavelength dependence and light absorption of a water extract was investigated by the Ångström absorption exponent (AAE) in the wavelength range from 300 to 600 nm by **Eq. 3** (Moosmüller et al., 2011).

$$AAE = \frac{\ln(Abs\lambda 2) - \ln(Abs\lambda 1)}{\ln(\lambda 2) - \ln(\lambda 1)} \quad (3)$$

2.2.3 Analysis of $PM_{2.5}$ by Fluorescence Spectroscopy

The fluorescence of $PM_{2.5}$ particles was measured by placing a small portion of a filter (0.5 cm^2) in the sample holder of a spectrofluorometer Model FluoroMax-4 from Horiba, which was supplied with a vertically assembled xenon-arc lamp set at 150 W without ozone. The excitation wavelength was 355 nm and the emission wavelength ranged from 400 to 700 nm, with slit set to 5 nm for both the excitation and emission monochromators and using a 0.1 s integration time. The detected signals were provided by a photon-counting detector R928P PMT (185–850 nm). A photodiode array was used to monitor the lamp output.

The excitation–emission matrices (EEMs) of the WSOC fractions were measured in the range from 200 to 600 nm for excitation and 220–600 nm for emission. The band passes for excitation and emission were 20 and 1 nm, respectively. Three fluorescence indices were evaluated including the fluorescence index (FI), biological index (BIX), and humification index (HIX). These indexes have been implemented in studies involving DOM in both soil and aquatic systems and aerosol due to the similarities in the optical aspects of WSOC and aquatic DOM. Indeed, these indexes have been shown to provide some information on the nature of the organic compounds present in the water-soluble fraction of aerosols (McKnight et al., 2001; Huguet et al., 2009; Birdwell and Engel, 2010). The fluorescence parameters FI, BIX, and HIX were evaluated by **Eqs 4–6**, respectively.

$$FI = \frac{F(Ex = 370\,nm, Em = 450\,nm)}{F(Ex = 370\,nm, Em = 500\,nm)} \quad (4)$$

$$BIX = \frac{F(Ex = 310\,nm, Em = 380\,nm)}{F(Ex = 310\,nm, Em = 430\,nm)} \quad (5)$$

$$HIX = \frac{F(Ex = 255\,nm, Em = 434 - 480\,nm)}{F(Ex = 255\,nm, Em = 300 - 345\,nm)} \quad (6)$$

where F represents the fluorescence intensity and Ex and Em the excitation and emission wavelengths, respectively. In the literature, FI <1.4 has been attributed to the fluorophores of terrestrial fulvic acid with greater aromaticity, while values higher than 1.9 correspond to fluorophores from microbial emissions of lower aromaticity (McKnight et al., 2001; Wu et al., 2021). The BIX value is used to assess the contributions from microbial activities, BIX >1 indicates the predominant biological or microbial formation, while BIX <0.6 corresponds to an autochthonous component with smaller contribution from biological materials (Huguet et al., 2009; Wen et al., 2021; Wu et al., 2021). HIX value represents the degree of humification of organic matter, higher values (HIX ˃10) are attributed to more humic or aromatic organic matter associated with terrestrial sources, while lower values (HIX ˂5) are associated with organic matter freshly formed (Yang et al., 2020). Finally, to support the information provided by the fluorescence indices, the PARAFAC model was applied. Recently, some researchers have reported the importance of using fluorescence indices and the PARAFAC model to establish possible sources of emission of carbonaceous material in the aqueous fraction. PARAFAC is a statistical model approach that extracts independent fluorophores from EEMs under ideal conditions (Bro, 1997). The determination of the component number and the treatment of the spectroscopic data, which included the biases correction, scattering remove and normalization, was carried out by applying the staRdom software ["spectroscopic analysis of dissolved organic matter (DOM) in R"]. (Pucher et al., 2019).

2.3 Mineralogical and Chemical Analysis

2.3.1 Chemical Surface Analysis of $PM_{2.5}$ Using X-Ray Photoelectron Spectroscopy

The XPS technique was used to determine the surface chemical composition of $PM_{2.5}$. For this purpose, a Thermo Scientific Escalab 250Xi spectrometer with both a six-channel (channeltron) detector and a monochromatic X-ray Al Kα source (1486.68 eV) was used. A selected 1 cm^2 piece from the center of each filter was cut and placed on the sample holder using carbon tape. Measurements were read while keeping ultrahigh vacuum conditions (10^{-10} torr). Survey spectra for all the samples were collected over the 1100 eV range at a resolution of 1 eV per step, 100 ms, and 150 eV of pass energy. For the chemical species of interest, high-resolution spectra were collected at a resolution of 0.1 eV per step and 20 eV of pass energy. For data treatment, Avantage software (Thermo Scientific version 5.9) was used, and the assignment of signals was made based on the literature reports and the standards database of the National Institute of Standards and Technology (NIST).

2.3.2 Characterization of Crystalline Phases by X-Ray Diffraction

The mineralogical composition of $PM_{2.5}$ was determined through XRD by using a PANalytical Empyrean X-ray diffractometer with Cu radiation (Kα = 1.5405 Å), and an X'Celerator ultra-fast

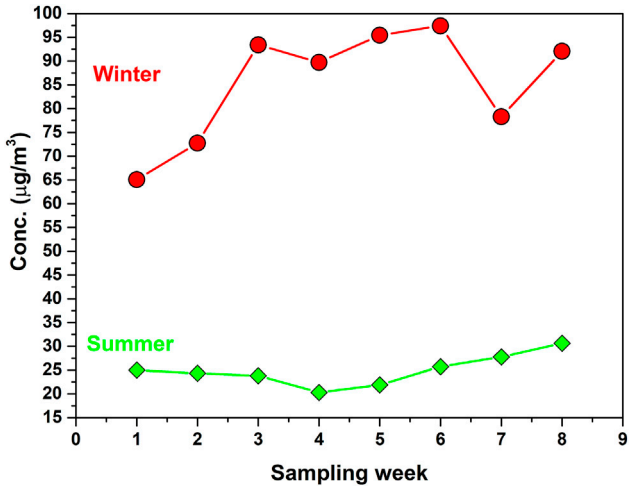

FIGURE 1 | Temporal evolution of $PM_{2.5}$ during the summer and winter seasons at the San Bernabé station.

detector based on real-time multiple-step technology with Bragg–Brentano geometry. The diffractometer (operating at 45 kV and 40 mA) collected the scans in the 2θ range of 5°–90° with a step size of 0.016° and 59 s per step. For structural refinements, both the Rietveld method and the crystalline phase identification approach were performed by using the High Score Plus software version 3.0.5 and the ICDD PDF+4 plus database as well (ICDD, International Center for Diffraction Data, Newtown Square, PA, United States).

3 RESULTS AND DISCUSION

3.1 $PM_{2.5}$ in the Monterrey Metropolitan Area During the Winter and Summer Seasons

The daily variation of $PM_{2.5}$ concentrations found in the MMA during the two study periods is shown in **Figure 1**. The average concentrations of $PM_{2.5}$ in winter were much higher (three times higher) than in summer. The concentrations found in winter and summer were 84.39 ± 11.67 and 25.04 ± 3.05 μg/m^3, respectively. A similar seasonal trend has been observed in other studies, which were conducted in different cities (Zhou et al., 2020; Duan et al., 2021). According to the regulation by Mexican Norm NOM-025-SSA1-2014 (SSA, 2014), the maximum allowed limit of $PM_{2.5}$ in the air is 45 μg/m^3 (24 h average). Therefore, the levels found in the winter samples from the San Bernabé station was above the maximum allowed limit, suggesting the poor air quality and potential health risk to the exposed population. The high levels found during the winter season was attributed to the increase in both fossil fuels and biomass burning, which was from the high energy demands by both industries and residences during this season. Similar

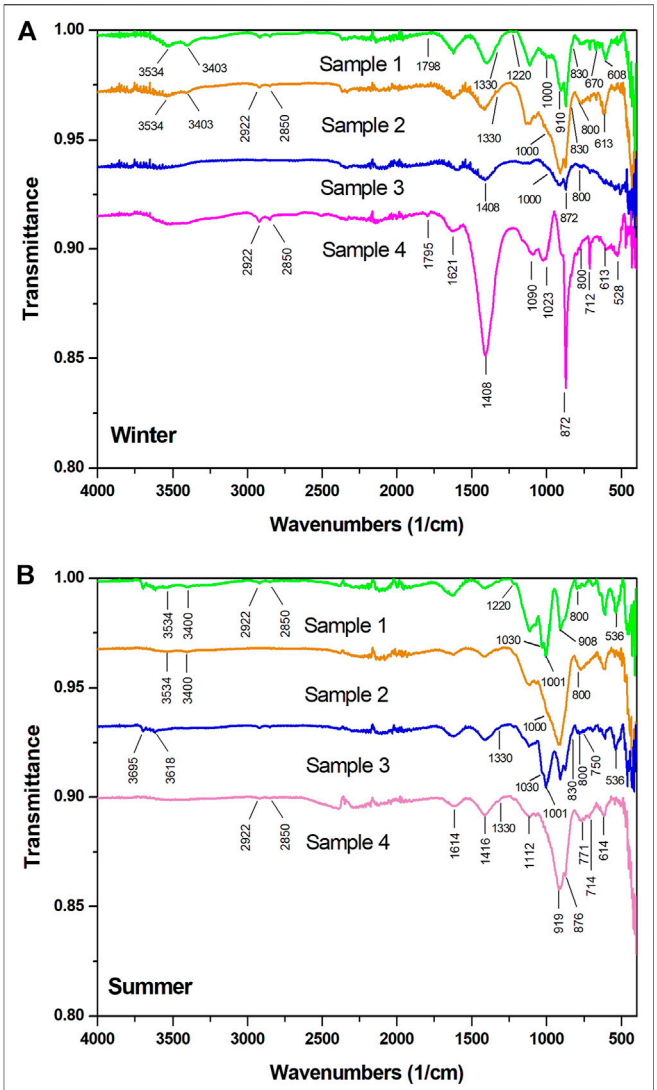

FIGURE 2 | ATR-FTIR spectrum of selected $PM_{2.5}$ samples collected on fiberglass filters, **(A)** winter, samples: 1(W6), 2(W5), 3(W3), 4(W8) and **(B)** summer, samples: 1(S1), 2(S3), 3(S6), 4(S8).

results have been reported by different researchers (Ravindra et al., 2022; Wang et al., 2022). In addition, low wind speeds and rainfalls were registered during the winter (**Table 1**). These conditions favored the stagnation of particles in the area.

3.2. Functional Groups, Light-Absorbing and Fluorescent Properties of $PM_{2.5}$

3.2.1 Identification of Chemical Functional Groups by ATR-FTIR

The infrared spectra of the $PM_{2.5}$ samples that were collected in winter and summer are shown in **Figure 2**. In the two study period, the absorption bands between 612 and 615 cm^{-1}and 1,080 and 1,135 cm^{-1}was attributed to the sulfate ions, which

TABLE 2 | Summary of the functional groups identified by FT-IR on the $PM_{2.5}$ samples collected in both seasons.

Functional group	Wavelenght (cm^{-1})	Winter samples	Summer samples
Sulfate	613, 1,080–1,135	ALL	ALL
Nitrate	820–830, 1,320–1,330, 1,760–1,800	W4, W5, W6, W8	S5, S6, S7, S8
Si-O	800, 1,000–1,044	W1, W2, W3, W5, W6, W7, W8	S1, S2, S3, S6, S7, S8
Al-OH	900–920, 3,618–3,700	W5, W6, W7	S1, S3, S6, S8
Carbonate ions CO_3^{2-}	712, 872, 1,412	ALL	ALL
Aromatic	772, 870, 910, 1,030,	ALL	ALL
OH stretching (water and/or hydroxylated compounds such as alcohols, polyols)	1,617, 1,640, 3,400	W1, W2, W4, W5, W6, W8	ALL
Aliphatic stretching	2,850, 2,920	W1, W2, W4, W5, W6, W7, W8	S1, S2, S4, S5, S6, S7, S8
O-H groups associated with alcohols, phenols, and carboxylic acids	3,534, 3,560	W1, W2, W4, W5, W6 W8	S1, S3, S5, S6, S7, S8
Carbonyl	1,798–1,800	W4, W6	S6, S7, S8

were likely as $CaSO_4$ (Allen et al., 1994; Maria et al., 2002; Radulescu et al., 2017; Yu et al., 2018; Zeb et al., 2018). It is of further importance to notice that $CaSO_4$ particles has a cooling effect on the atmosphere, which causes a negative radiative forcing and alters the troposphere temperature balance (Buseck and Pósfai, 1999; Martin et al., 2004). A summary of the chemical species that were found in the samples is found in **Table 2**. In majority of the collected samples, CO_3^{2-}signals (i.e., at 1,412 cm^{-1} and 872 cm^{-1}) were predominant in the $PM_{2.5}$ samples (Shaka' and Saliba, 2004; Bahadur et al., 2010; Siciliano et al., 2018). Moreover, the band found between 710 and 719 cm^{-1} was related to the asymmetric vibrations of $CaCO_3$ (Varrica et al., 2019). Recent studies indicated that both carbonate ion and its products from atmospheric aging can affect the climate directly by dispersing and absorbing solar and terrestrial radiation (Crowley et al., 2010; Tang et al., 2015). They can affect the climate indirectly by changing the microphysics, albedo, and useful life of clouds.

The weak shoulder signals between the ranges from 1,320 to 1,330 cm^{-1} and 820–830 cm^{-1} in some samples suggested the presence of NO_3^- species (**Figure 2B**). These signals overlapped with the strong CO_3^{2-} signals between 1,412 and 870 cm^{-1}. In addition, in some summer and winter samples, the absorption signals between 1,760 and 1,800 cm^{-1} were observed, which indicated the presence of inorganic nitrate Previous studies on the MMA have reported the presence of NO_3^- in $PM_{2.5}$ (Martinez et al., 2012; Mancilla et al., 2019). Meanwhile, the peaks between 1,000 and 1,044 cm^{-1} and peak at 800 cm^{-1} were due to Si-O bonds (samples: S1, S3, S6, W6, W5, and W3) The peak between 1,000 and 1,044 $cm^{-1}$was due to the asymmetric stretching vibrations of the O-Si-O, while the peak at 800 $cm^{-1}$was due to bending vibrations of the O-Si-O bond in the silicates (Maria et al., 2002; Shaka' and Saliba, 2004; Simonsen et al., 2009; Radulescu et al., 2017; Zeb et al., 2018). In addition, in both summer and winter samples, a peak was observed between 900 and 920 cm^{--1}, which was indicative of Al-(OH) bond vibrations. Compounds with Al-(OH) are usually present in aluminosilicate minerals such as kaolinite ($Al_2Si_2O_5(OH)_4$) (Ravisankar et al., 2010). It should be noted that this peak appeared more intense in the summer samples and in some cases this peak overlapped with the carbonate band at ~877 cm^{-1}. The absorption signals found between 3,618 and 3,700 cm^{-1}as well as 3,695 and 3,700 cm^{-1} corresponded to the vibrations of the OH functional groups, which are typically located between the tetrahedral and octahedral layers of clay minerals (aluminosilicates). These functional groups have been shown to interact with the Si-O-Si layers to produce bonds, which produce characteristic absorptions at 3,620 and 3,695 cm^{-1} (Davarcioglu, 2011; Varrica et al., 2019). Additionally, the absorption bands at lower frequencies of around 540 cm^{-1} and the small peak at 750 cm^{-1}, which appeared in some samples were attributed to the Al-O-Si bonds in silicates (Chou et al., 2005; Coury and Dillner, 2008).

The OH stretching vibrations around 3,400 cm^{-1}observed in our samples (**Figure 2**) indicated the presence of water and/or hydroxylated compounds such as alcohols and polyols from biogenic sources and biomass burning (Gipson et al., 2015; Siciliano et al., 2018; Zapata-Hernandez et al., 2020). The broad band observed between 1,617 and 1,640 cm^{-1}confirmed the presence of water in the samples. The broad band signal between 1,617 and 1,640 cm^{-1} indicated of an overlap of the signals from different chemical functional groups including the stretching vibration absorptions for C=C aromatic and C=O bonds. Some authors have attributed this broad band signal to the functional groups found in organonitrates, aromatic amides, and organic amines (Ji et al., 2015; Radulescu et al., 2017; Siciliano et al., 2018; Zapata-Hernandez et al., 2020). Meanwhile, the appearance of the weak shoulder signals at around 1,220 cm^{-1} in most of the samples supported the presence of organ nitrated compounds (Shaka' and Saliba, 2004).

The broad band observed between 3,534 and 3,560 cm^{-1} in our samples (**Figure 2**) were due to the vibrations of the O-H groups in alcohols, phenols, and carboxylic acids (Allen et al., 1994; Coury and Dillner, 2008; Shaka' and Saliba, 2004). A weak peak between 1,798 and 1,800 cm^{-1} was observed in three and five of the summer and winter samples, respectively. This

peak corresponded to the vibrations of the carbonyl functional group (C=O) in carboxylic acids. The amounts of carboxylic acids seemed to be higher in the winter samples suggested in **Figure 2A** (Siciliano et al., 2018). In most of the collected samples, peaks were observed between 2,920 and 2,850 cm^{-1}, which were associated to the CH_2 in aliphatic compounds (Shaka' and Saliba, 2004; Zapata-Hernández et al., 2020).

3.2.2 Analysis of $PM_{2.5}$ Samples by X-Ray Diffraction and X-Ray Photoelectron Spectroscopy

3.2.2.1 Chemical Analysis of the Crystalline Phases by X-Ray Diffraction

The XRD diffractograms obtained for the $PM_{2.5}$ samples in the two study periods are shown in **Figure 3**. Several reflections with different intensities were observed in the diffractograms. Most of the signals corresponded to the crystalline phases of $CaCO_3$ (index number or ICDD No. 010721937), SiO_2 (ICDD No. 010781252), and $CaSO_4{\cdot}2H_2O$ (ICDD No. 010741433). Signals with lower intensities corresponded to the aluminosilicates including kyanite (ICDD No. 000110046), albite (ICDD No. 010831658), leucite (ICDD No. 010768736), sillimanite (ICDD No. 000380471), pyrophyllite dehydroxylated (ICDD No. 010734051), and NaCl (ICDD No. 010763457). In the literature it is reported that in the study region there are some mineral deposits related to these crystalline phases (such as muscovite, sillimanite, kaolin, albite, quartz, plagioclase, feldspars, and micas), only some of them are commercially exploited (nl.gob.mx, 2020). On the other hand, it is known that these mineral phases are used in the refractory and ceramic industry, which are abundant in the area and therefore it is not ruled out that they also contribute to the emission of these crystalline compounds (Bradt, 2008). Adjustments on the reflection profiles were carried out by the Rietveld method, which allowed us to perform semiquantitative analysis on each of the crystalline phases detected (Rietveld, 1969). The refinement of the signals provided the mass percentage of each crystalline phase in the diffractograms. The results showed that the most abundant crystalline phases were $CaCO_3$ and SiO_2 (**Table 3**). $CaSO_4$ was also abundant while aluminosilicates and NaCl were the least abundant. These phases have been extensively reported in the literature (Ahmady-birgani et al., 2015; Zarasvandi et al., 2011). The average percentage of $CaCO_3$ was slightly higher in summer (73.9%) than in winter (71.1%). These findings were consistent with the ATR-FTIR results, which showed the carbonate absorption bands at 1,412, 872, and 710–719 cm^{-1}, in all samples collected in both seasonal periods. These crystalline phases may have emerged from natural sources (resuspension of crust material) and anthropogenic sources. We note that MMA is a semiarid region with many ceramic, glass and, cement industrial facilities, as well as quarries inserted within the expanding metropolitan area.

On the other hand, the average percentage of $CaSO_4$ found was significantly higher in winter (10.2%; min: 0% and max: 30%) than in summer (4.5%; min: 0% and max: 12%), which was consistent with the findings by the ATR-FTIR technique. In ATR-FTIR, we found more frequent and greater intensity signals for SO_4^{-2} (1,080–1,135 and 612–615 cm^{-1}) in the winter samples. This finding is relevant as most of the previous studies in the MMA have assumed that sulfate associated to the $PM_{2.5}$ is mainly in the form of $(NH_4)_2SO_4$ (Martinez et al., 2012; Mancilla et al., 2019). The higher percentage of $CaSO_4$ found in the winter samples is likely more related to the meteorological parameters and concentration of SO_2 in the atmosphere, since we have

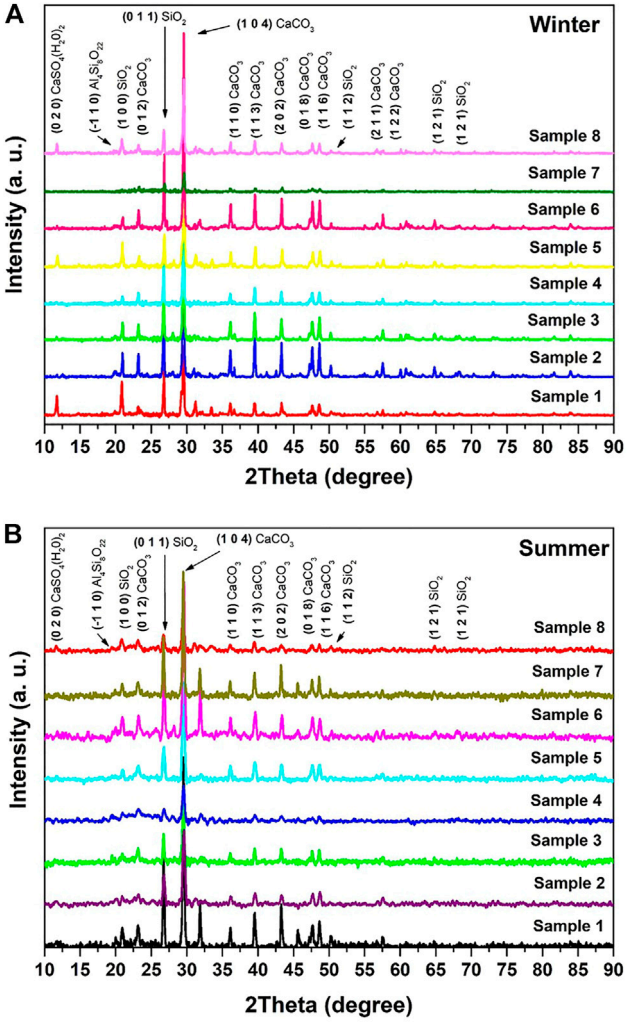

FIGURE 3 | X-ray diffraction patterns of $PM_{2.5}$ collected in **(A)** winter and **(B)** summer.

TABLE 3 | Contents of the most important crystalline mineral phases present in the $PM_{2.5}$ samples, which were obtained by x-ray powder diffractometry.

% Phases	Season	
	Summer	Winter
Calcite	73.9	71.1
Quartz	16.9	15.2
Gypsum	4.5	10.2
Aluminosilicates	3.4	3.2
Halite	1.2	0.3

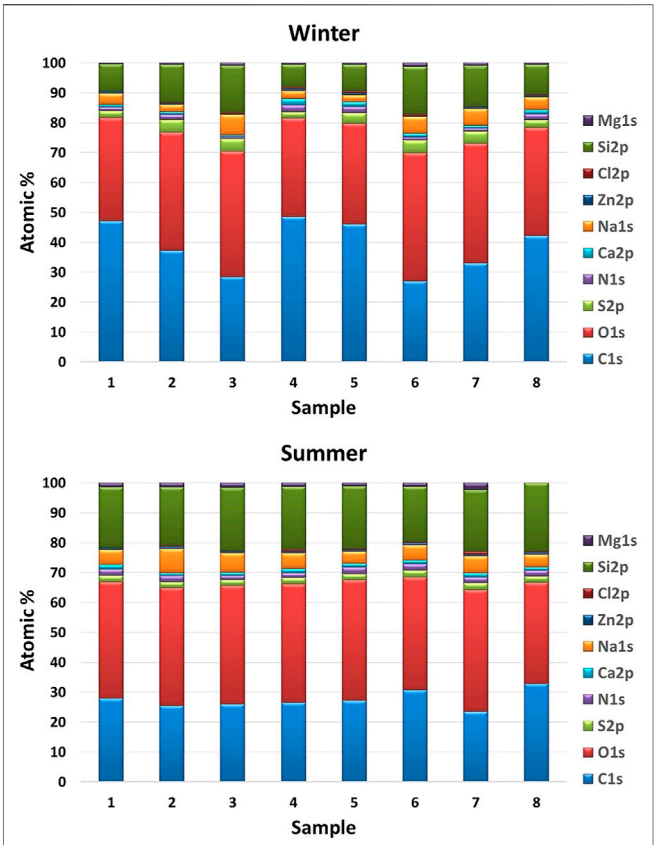

FIGURE 4 | Surface elemental composition obtained by XPS of $PM_{2.5}$ samples for the two study periods.

considered $CaSO_4$ as a phase of secondary origin. Sulfates are formed by photochemical reactions that occur between their main precursor (SO_2) and oxidizing species such as O_3 and NOx (Xu et al., 2016). Unfortunately, SO_2 is not monitored in the San Bernabé station. However, further exploration of available ground-level SO_2 data from the local air quality monitoring network resulted in identifying that the nearby North 2 station had a complete dataset for the periods of interest. The North 2 station is approximately 6 km to the southeast of the Northwest (San Bernabé) station, in a very similar landuse and main emission sources setup. Assuming that the North 2 station is a good proxy for the Northwest station, we retrieved SO_2 data for the North 2 station for the months of interest (**Supplementary Table S2**). The data confirms that SO_2 levels are higher during the winter period, which could contribute to the formation of sulfates in this season. Another factor to consider is the changes in the meteorological parameters, where several studies have shown the dependency of sulfate levels to relative humidity and wind speed (Banerjee et al., 2015; Pant et al., 2015; Lu et al., 2016). For example, Song et al. (2014) attributed the high percentages of sulfate found in their PM_{10} samples to the higher humidity and low wind speed in the collection/sampling area (Henan, China). Moreover, Yue et al. (2022) found that the reaction between SO_2 and $CaCO_3$ particles in the atmosphere was favored by relative humidity values of greater than 40%. Therefore, the low wind speed, high relative humidity, as well as the abundance of SO_2 y $CaCO_3$ during the winter sampling (**Table 1**) in the MMA explained the higher proportions of $CaSO_4$ found in the winter samples. It should be noted that there is no known primary source of $CaSO_4$ near the study area. In addition, in some samples it is not possible to detect the presence of this mineral phase, it is only detected when the meteorological parameters are favorable for the photochemical reaction to take place. For everything described above, it can be thought that the $CaSO_4$ found in the PM is of secondary origin

Similar amounts of SiO_2 were found in all the samples. Several reports have associated SiO_2 with natural sources (Adamo et al., 2008; Saitoh et al., 2008; Song et al., 2014). Thus, it was not surprising to find SiO_2 in our samples, since the overall soil composition of the MMA falls within a sandy profile with numerous deposits that are rich with SiO_2. Nonetheless, the contributions from anthropogenic sources were not overlooked. For example, there is a large glass industry in MMA, which uses crystalline SiO_2 as raw material. Finally, we note that the XRD and ATR-FTIR results of this investigation complemented each other.

3.2.2.2 Determination of Surface Elemental Composition by X-Ray Photoelectron Spectroscopy

High-resolution XPS spectra of the elements identified in the survey scan were corrected using the C_{1s} signal (285 eV) as reference. The assignment of signals was carried out by considering the data from the literature and National Institute of Standards and Technology (NIST) database. The atomic percentage of silicon was corrected by the method described by Atzei and Rossi (2004) and Gilham et al. (2008). In both winter and summer samples, high-intensity bands related to C and O was found along with low-intensity bands related to Si, Na, N, and S. Additional elements identified through their high- and low-resolution spectra were Ca, Mg, Zn, Cl, and F. The surface elemental composition of the $PM_{2.5}$ samples are shown in **Figure 4**. The most abundant elements found were C, O, and Si followed by Na, S, N, and Ca. Similar results have been reported in studies by Guascito et al. (2015), Atzei et al. (2014) and Huertas et al. (2012). In these previous studies, C and O were the predominant elements found on the $PM_{2.5}$ samples. The average percentage of C were higher in the winter sample, which can be attributed to the higher consumption of fossil fuels due to e.g., increased use of heating both at the industrial and residential level in the MMA (**Figure 4**).

Signal speciation of C, N, S, and Ca was performed by deconvolution of the high-resolution spectrum of each element. For example, consider the high-resolution spectra of C, N, and S shown in **Figure 5**. For C_{1s} (280–295 eV), the deconvolutions showed eight different states of oxidized carbon found in all samples. These were the aliphatic (C-C, 285 eV), aromatic (C=C, 284.7 eV), EC (284 eV), carbonyl (C=O, 288 eV), carbides (283.6 eV), carboxylics (O-C=O, 289 eV), carbonates (289.5 eV), and ether/alcohol (C-O, 296.5 eV). Several researchers have reported these contributing functional groups on PM (Gaddam and Vander Wal, 2013; Atzei et al., 2014). The atomic percentages of each contributing

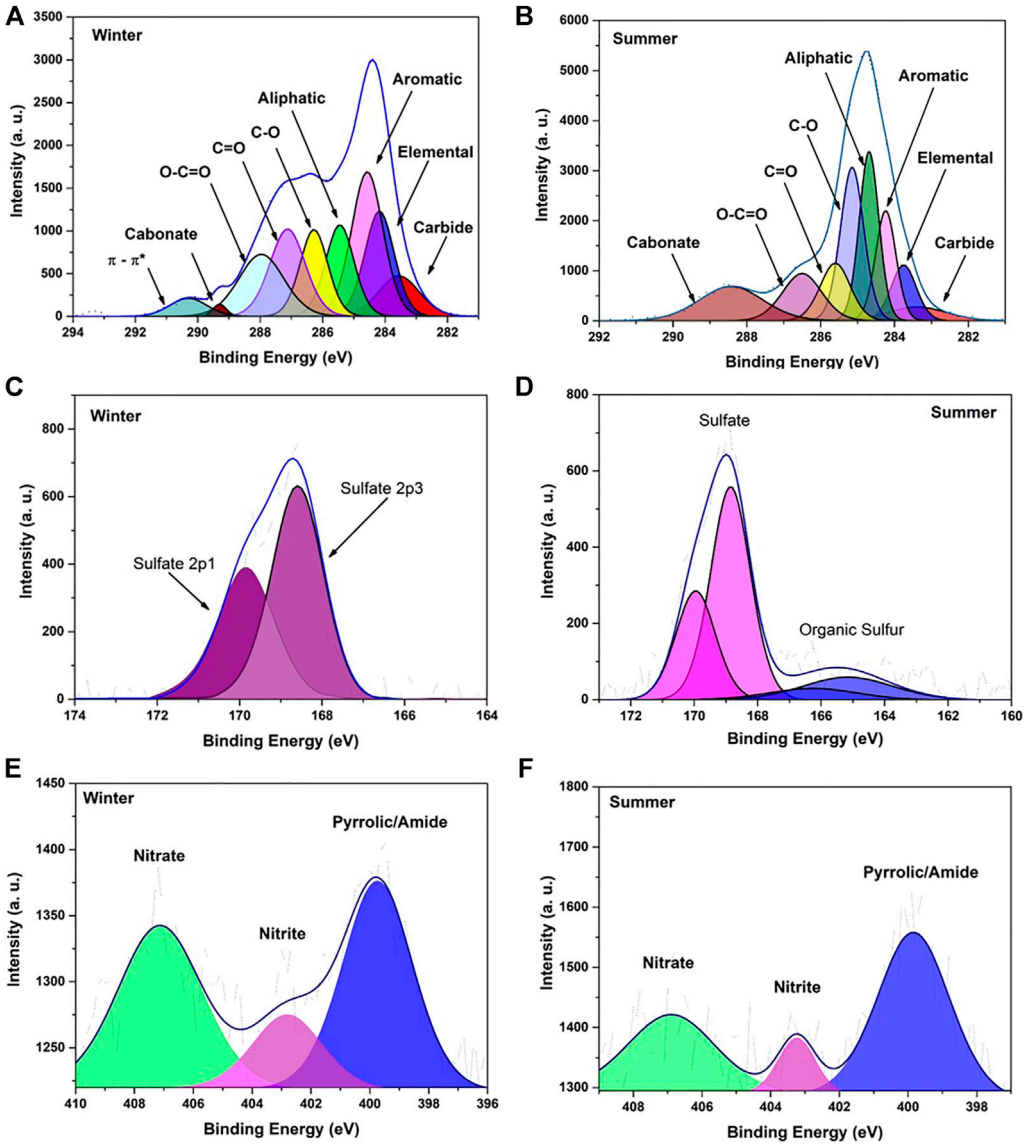

FIGURE 5 | Deconvolution of high-resolution spectra in the region of the signal **(A,B)** C_{1s}, **(C,D)** S_{2p}, and **(E,F)** N_{1s} of $PM_{2.5}$ collected in winter and summer.

functional group to the C_{1s} signal are summarized in **Table 4**. The aromatic hydrocarbons in all the samples were considered as the highest component to the C_{1s} signals. This was followed by the EC and aliphatic hydrocarbons chains. The least contributing component in the winter and summer samples were carbonates and carbides, respectively. The atomic percentages of highly oxidized species such as ether, alcohol, carboxylic acids and/or carbonyl groups were significantly higher in the winter samples. These were consistent with the results of the ATR-FTIR spectra. The higher proportion of these functional groups in winter could be related to an increase in coal burning, in addition to a greater atmospheric oxidation caused by changes in meteorological parameters (Domínguez et al., 1999; Ahlers et al., 2000; Siciliano et al., 2018). In contrast, the decrease in oxidized species observed in summer could explain the higher proportion of aromatic and aliphatic groups recorded in this season. On the other hand, average area percentage of EC in all samples did not show any significant variation.

For the observed N_{1s} signal in the samples, three contributors were identified including amide/pyrrole groups, nitrites, and nitrates, positioned at bonding energies of 399.2 and 402 eV and 407, respectively. The results obtained for the winter and summer samples showed a similar trend, where amide/pyrrole groups predominated at the surface level on $PM_{2.5}$ followed by nitrates and nitrites. These were consistent with the ATR-FTIR findings where organic amides and amines, as well as inorganic nitrate were found in the samples. The abundance of amide/pyrrole groups was associated to the burning of fossil fuels. The nitrates and nitrites were of secondary origin from the photo-oxidation reactions of gaseous nitrogenous precursors in the

TABLE 4 | Atomic percentage of each contributing functional group to the C1s signals (n = 8).

Sample	Element (atomic %)							
	Carbide	Elemental	Aromatic C-H	Aliphatic C-H	C-O	C=O	O-C=O	Carbonate
Winter samples								
1	0.1	13.7	23.7	20.6	17.4	17.0	5.7	1.9
2	6.2	21.9	19.7	16.3	14.2	14.2	2.0	5.5
3	7.9	14.7	24.8	12.4	11.5	14.7	13.4	0.8
4	13.4	20.1	10.3	16.7	12.5	13.5	8.3	5.3
5	14.2	21.6	14.5	13.3	13.6	15.1	4.8	2.9
6	0.1	24.8	22.6	23.1	19.7	5.0	3.1	1.6
7	14.0	29.8	22.1	15.3	8.9	6.2	2.5	1.3
8	0.1	22.3	35.5	14.7	7.9	16.3	3.0	0.2
Summer samples								
1	2.7	21.7	25.1	26.7	10.3	5.6	6.6	1.4
2	0.5	22.1	19.5	20.5	8.4	14.7	13.1	1.3
3	1.3	13.1	28.9	25.5	18.8	3.8	5.4	3.1
4	4.7	13.6	42.6	11.9	15.0	—	—	12.2
5	—	17.6	40.8	18.7	7.1	6.5	1.6	7.7
6	15.8	22.9	22.8	15.7	13.8	—	—	9.0
7	—	20.2	27.8	19.7	12.7	5.9	—	13.7
8	—	36.9	26.0	27.0	—	—	—	10.2

atmosphere. In the literature, it has been reported that some ions of secondary origin, such as nitrites, are more stable under conditions of low solar radiation, which is consistent with the lower solar radiation recorded in winter(Paoletti et al., 2003). The atomic percentages obtained for the amide/pyrrole groups and nitrates in the two seasons were similar. This confirmed that seasonal variation had no significant effect on the amounts of these species in the atmosphere. Interestingly, the concentrations of nitrite were significantly higher in the winter samples (**Table 5**), which was attributed to the typically lower solar radiation during the cold months (Hoek et al., 1996; Lee et al., 1999; Paoletti et al., 2003).

Two components for the Ca_{2p} signal were identified, where one was located at a binding energy of 347 eV, which corresponded to $CaCO_3$. The other was at 347.8 eV, which was associated with $CaSO_4$ (Guascito et al., 2015). Our results showed that $CaCO_3$ was the main signal contributor in all samples, while the highest percentages of $CaCO_3$ were found in the summer samples (e.g., 74.6%). Notably, the deconvolution of the C_{1s} signals suggested a higher percentage of $CaCO_3$ in the summer samples. This was explained by the summer activities related to the extraction of limestone from local quarries and its use as a raw material in the cement binder industry. The deconvolution of S_{2p} signals showed that the sulfates and organic sulfur compounds dominated the winter (68.4%) and summer (65.9%) samples, respectively. The higher levels of $CaSO_4$ found in the winter samples were related to the changes in meteorological conditions and possibly higher concentrations of SO_2 in the atmosphere during the sampling. In summer, the meteorological conditions did not favor the formation of the $CaSO_4$, which led to an increase in the percentages of organic sulfur in this season.

3.2.3 Diffuse Reflectance Spectroscopy Analysis

The DRS technique has been widely used for the characterization of solid materials (Zwinkels et al., 2014; Bock et al., 2019), since it is a tool useful to determine the electronic transitions from the valence to conduction band (band gap) of semiconductor oxide powders (Escobedo-Morales et al., 2019). In the environmental sciences, has been applied mainly for the analysis of minerals in soils (Sellitto et al., 2009; Szalai et al., 2013), however, we have found a few studies that used DRS for the characterization of atmospheric particulate material. For example, Wonaschütz et al. (2009) used this technique for the characterization of BC and BrC in atmospheric aerosols. In another study, Morozzi et al. (2021) used DRS to characterize the diverse mineral phases of the Sahara dust that were present in the PM samples obtained from the Mediterranean area.

The diffuse reflectance spectra obtained from the $PM_{2.5}$ samples are shown in **Figures 6A,B**. Significant attenuation of the signal response in the visible region (400–800 nm) were observed in all the spectra, indicating the presence of chromophores that were likely from the carbonaceous materials in the samples. On the other hand, the UV region spectra showed some noticeable changes in the slopes of the curves. These were associated to the electronic transitions in the inorganic materials present in the samples (Makuła et al., 2018). The spectra were converted by the Kubleka–$132#? Munk function. To better define the processes involved, the second derivative was obtained by following the methodology proposed by Torrent and Barrón (2015) and the results are shown in **Figures 6C,D**. In the spectra, the absorption band near 250 nm was related to the presence of $CaSO_4$, whose absorption range was previously reported to be between 250 and 350 nm (Nagabhushana et al., 2010). The absorption band

TABLE 5 | Atomic percentage of each contributing functional group to the (a) N_{1s}, (b) Ca_{2p}, and (c) S_{2p} signals.

N_{1s}						
Sample	**Winter**			**Summer**		
	Atomic %			**Atomic %**		
	Pyrrolic/Amide	**Nitrite**	**Nitrate**	**Pyrrolic/Amide**	**Nitrite**	**Nitrate**
1	29.0	50.6	20.5	66.0	-	34.0
2	60.9	24.5	14.6	57.2	10.1	32.7
3	53.2	27.4	19.3	65.1	0.0	34.9
4	66.3	—	33.7	55.1	11.9	33.0
5	48.9	29.8	21.3	72.8	—	27.2
6	71.7	13.3	15.0	62.7	8.7	28.6
7	44.1	15.7	40.3	49.8	21.8	28.4
8	50.6	14.4	50.6	48.1	41.1	10.9

Ca_{2p}				
Sample	**Winter**		**Summer**	
	Atomic %		**Atomic %**	
	Carbonate	**Sulfate**	**Carbonate**	**Sulfate**
1	41.0	59.0	87.6	12.4
2	48.7	51.3	68.1	31.9
3	51.3	48.8	72.3	27.7
4	48.2	51.8	72.9	27.1
5	53.5	46.6	79.7	20.3
6	39.4	60.6	76.3	23.7
7	34.4	65.6	72.2	27.8
8	83.9	16.1	67.7	32.3

S_{2p}				
Sample	**Winter**		**Summer**	
	Atomic %		**Atomic %**	
	Sulfate	**Organic sulfur**	**Sulfate**	**Organic sulfur**
1	80.0	20.0	29.5	70.5
2	74.7	25.3	100.0	—
3	57.4	42.6	20.3	79.7
4	72.1	27.9	27.3	72.8
5	92.8	7.2	21.9	78.1
6	56.2	43.8	19.9	80.1
7	58.2	41.8	23.9	76.1
8	55.7	44.3	29.7	70.3

between 210 and 230 nm corresponded to the $CaCO_3$ electronic transition from the valence to conduction band (Al Omari et al., 2016). The additional absorptions observed between 330–400 nm in some samples are possibly related to electronic transitions of the aluminosilicates containing transition metals (Zent et al., 2008; Tarantola et al., 2019). The above demonstrates the application of the DRS technique to characterize the inorganic fraction present in PM. In addition, it is versatile, simple and low cost since the analysis of the sample is done directly in the filter, without the need to use reagents or solvents for its

3.2.3.1 UV–Vis Analyses of Water-Soluble Organic Carbon

To fully understand the optical properties of the water-soluble fraction, UV–Vis analyses were performed on the aqueous extracts of the $PM_{2.5}$ samples collected in the San Bernabé monitoring station. The variation of the Abs_λ with respect to the wavelength of radiation in the range of 300–600 nm is shown in **Figure 7A**. In both seasons studied, the absorption intensities decreased notably at longer wavelengths, suggesting a strong dependence with the radiation wavelength, which is characteristic of BrC (Cheng et al., 2016; Wu et al., 2020). Furthermore, the absorption coefficients of the winter samples were higher than the summer samples. Similar results have been reported by Chen et al. (2018) for samples obtained in Nanjing, China. Prior studies have associated the Abs_{365} with the absorption coefficient of BrC (not inorganic salts) (Hecobian et al., 2010). The values for Abs_{365} and temporal variation are shown in **Table 6** and **Figure 7B**, respectively. The Abs_{365} values were higher in the winter ($1.15 \pm 0.49\ Mm^{-1}$) than summer ($0.66 \pm 0.19\ Mm^{-1}$) samples, which has been a seasonal trend confirmed by other researchers (Kim et al., 2016; Chen et al., 2020). The values we found were comparable to those reported by

Liu et al. (2018) for samples obtained in Guangzhou City, China, and by Liu et al. (2013) in Atlanta, United States. However, our values were lower than those reported by Satish et al. (2017) for samples obtained from the cities of Indo-Gangeti Plain, India Satish et al. (2017) and Huang et al. (2018) for samples obtained from Xi'an, China. Strong correlations of the Abs_{365} of water extracts with WSOC concentrations for both winter ($r = 0.89$) and summer ($r = 0.93$) were found (**Figure 7C**), which is indicative that WSOC contains BrC (Chen et al., 2020). The difference in the Abs_{365} values found in both seasons could be attributed to differences in the emission sources that predominate in each season (Chen et al., 2018; Zhan et al., 2022).

On the other hand, the average MAE_{365} values in the winter and summer samples were $0.23 \pm 0.05\ m^2g^{-1}$ and $0.19 \pm 0.04\ m^2g^{-1}$, respectively (**Table 6** and **Figure 8A**). These results indicate that BrC in winter has a higher absorption capacity compared to summer. This could be attributed to a higher concentration of BrC chromophores in winter and/or to differences in the chemical nature of chromophores that predominate in the cold season as a result of differences in emission sources. In this study, the observed MAE_{365} values were lower than those reported for cities with higher pollution indices such as Beijing, China (Yan et al., 2015), Xi'an, China (Yuan et al., 2020), and New Delhi, India (Kirillova et al., 2014). In addition, our values were closer to the values reported for Seoul, Korea (Kim et al., 2016) and Atlanta, United States (Hecobian et al., 2010).

The AAE is a very important parameter that provides information on the spectral dependence of the aerosol and the absorption of light in bulk (e.g., extracts) (Moosmüller et al., 2011). In the literature, it has been reported that BC from the burning of fossil fuels generally has AAE values that were close to 1 (Fraund et al., 2020). This means that the refractive index values of BC are independent of the wavelength. AAE values slightly higher than one indicated the presence of BC or a mixture of BrC and BC (Pokhrel et al., 2017). Meanwhile, high AAE values between 5 and 9 revealed the predominance of BrC in the aerosol samples (Chakraborty et al., 2016; Lin et al., 2017). The AAE values calculated for WSOC of our samples in the wavelength range from 300 to 600 nm are summarized in **Table 6**. The average values obtained for the winter and summer samples were 6.32 ± 0.78 and 7.33 ± 1.02, respectively (**Figure 8B**). The high AAE values in all samples as well as the high correlations found between Abs_{365} and WSOC concentration demonstrated an important contribution of BrC chromophores in the WSOC (Lin et al., 2017; Yuan et al., 2020). The AAE

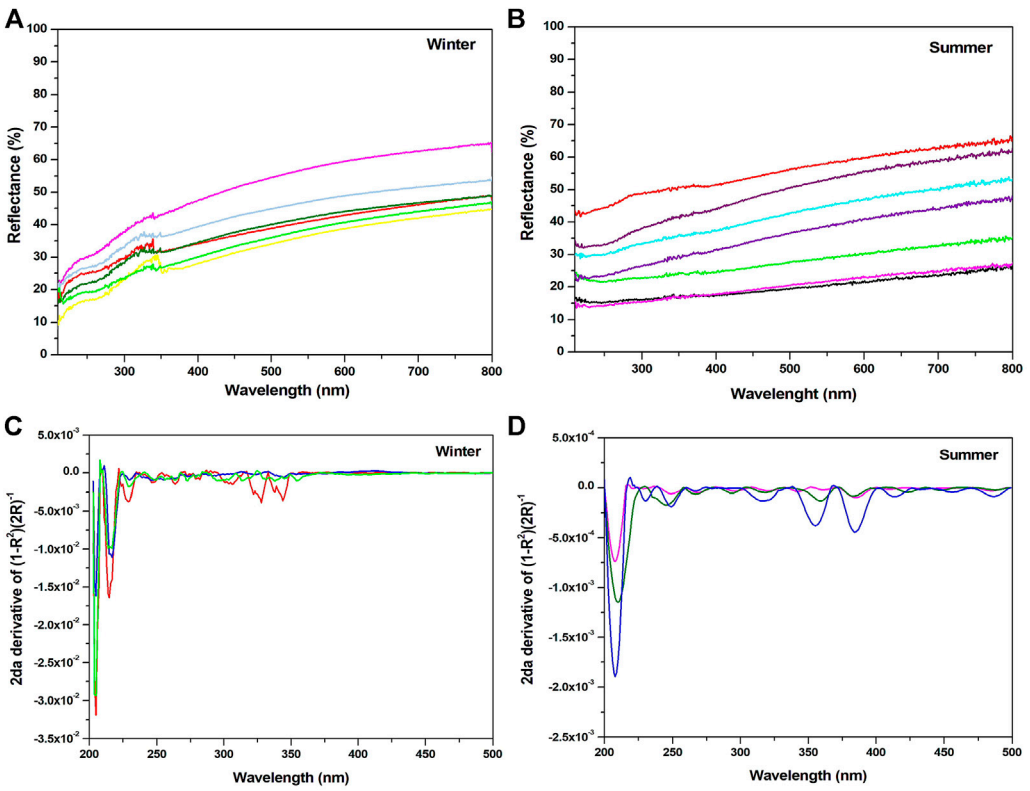

FIGURE 6 | Diffuse reflectance spectra of representative $PM_{2.5}$samples obtained during **(A)** winter and **(B)** summer. Derivative of second order of the Kubelka–Munk function of the same samples collected in **(C)** winter and **(D)** summer.

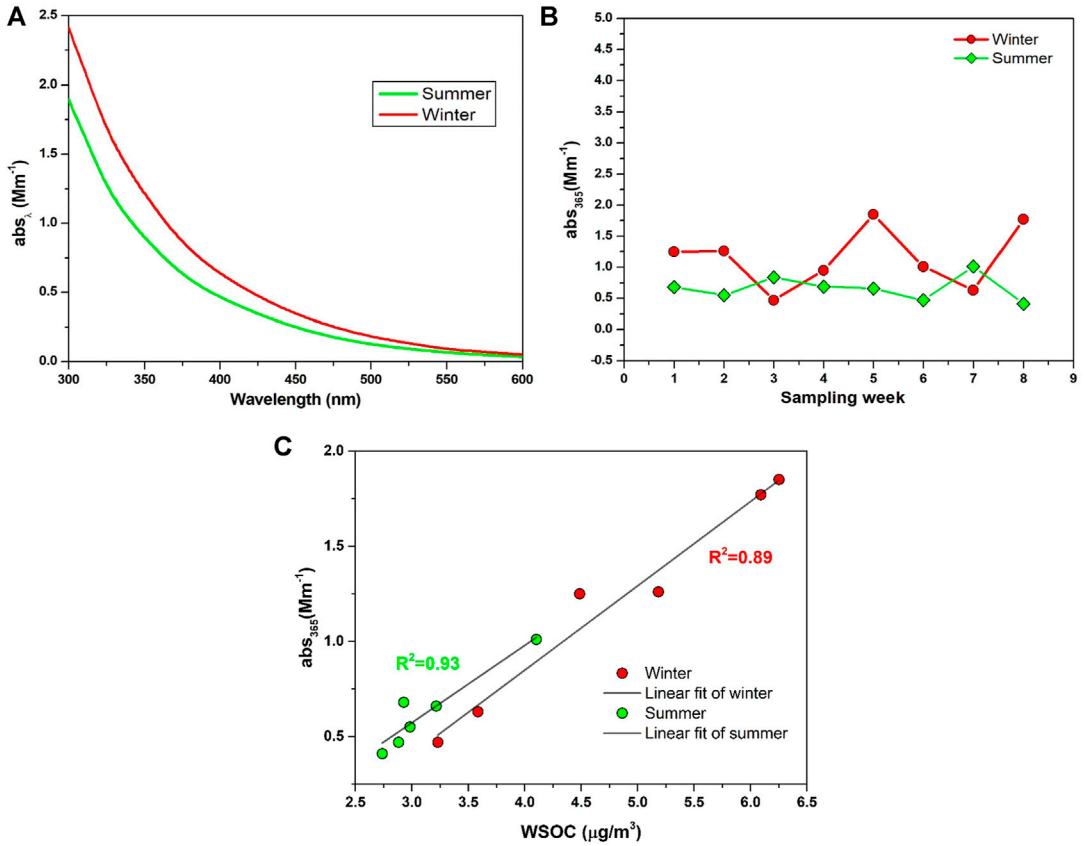

FIGURE 7 | (A) Averaged light absorption spectra of the WSOC for the samples obtained in winter and summer. **(B)** Time series of light absorption coefficient at 365 nm (Abs_{365}) for the two study periods. **(C)** Scatter plots of Abs365 versus WSOC.

values were higher in the summer samples, indicating a greater contribution of compounds that absorb at shorter wavelengths in these samples. Similarly, Chen et al. (2018) reported that the highest and lowest values of AAE for $PM_{2.5}$ samples collected throughout the year from Nanjing, China was obtained from the summer and winter samples, respectively. The results were explained by the difference in the chemical composition or emission sources in these seasons. Likewise, Kim et al. (2016) reported a similar seasonal variation, where the higher values of AAE in summer was attributed to the presence of metals that come from the Earth's crust

3.2.4 Analysis of $PM_{2.5}$ by Fluorescence Spectroscopy

The fluorescence emission spectra (with excitation at 355 nm) of the filters collected during winter and summer are shown in **Supplementary Figure S1**. The maximum wavelength intensity of the spectra from the winter and summer samples ranged from 440 to 464 nm and 439–449 nm, respectively. Similar ranges have been reported by other researchers for highly oxygenated carbonaceous and humic-like substances (HULIS) (McKnight et al., 2001; Chen et al., 2016b; Qin et al., 2021). Barsotti et al. (2016) reported that HULIS derived from the oligomerization of phenolic compounds exhibited a strong fluorescence emission in the vicinity of 450 nm. On the other hand, it is known that ozone and hydroxyl radicals are able to cause the oxidation of volatile organic compounds (VOCs) such as limonene and α-pinene. The oxidation generated HULIS that showed strong fluorescence emissions within the range of 437–513 nm. The average of maximum emission intensities was higher in the winter ($1.6 \times 10^6 \pm 7.8 \times 10^5$ a.u.) than summers ($1.4 \times 10^6 \pm 6.3 \times 10^5$ a.u.) samples. This was attributed to the greater amounts of oxygenated carbonaceous species found in the winter samples. Through XPS analyses, we also found slightly higher values for the total percentage of carbon and extent of functionalization by oxidized species on the C_{1s} signal in the winter samples.

An exploratory EEM study was conducted to gain insights on the fluorescent compounds found in the samples. The aqueous extracts of the samples obtained during both seasons were used. The fluorescence indexes HIX, BIX, and FI were determined. These indexes have been implemented in studies involving DOM in both soil and aquatic systems and aerosol due to the similarities in the optical aspects of WSOC and aquatic DOM. Indeed, these indexes have been shown to provide some information on the nature of the organic compounds present in the water-soluble fraction of aerosols (McKnight et al., 2001; Huguet et al., 2009; Birdwell and Engel, 2010). The FI values are summarized in **Supplementary Table S1**, where 40% of the samples showed FI ~

TABLE 6 | WSOC mass concentration and light absorption parameters (Abs_{365}, MAE_{365}, and AAE), measured during winter and summer in the two study periods.

Sample	Winter				Sample	Summer			
	Abs_{365} Mm^{-1}	AAE	WSOC $\mu g/m^3$	MAE_{365} m^2g^{-1}		Abs_{365} Mm^{-1}	AAE	WSOC $\mu g/m^3$	MAE_{365} m^2g^{-1}
1	1.25	6.93	4.49	0.28	1	0.68	7.23	2.93	0.23
2	1.26	5.36	5.18	0.24	2	0.55	7.59	2.98	0.18
3	0.47	6.72	3.23	0.15	3	0.84	5.69	—	—
4	0.95	6.06	—	—	4	0.69	6.10	—	—
5	1.85	5.06	6.25	0.30	5	0.66	7.96	3.22	0.21
6	1.01	6.31	—	—	6	0.47	8.49	2.88	0.16
7	0.63	6.99	3.58	0.18	7	1.01	7.11	4.10	0.25
8	1.77	7.14	6.09	0.29	8	0.41	8.43	2.74	0.15

1.5 values. This suggested the presence of fulvic acid-like substances with high aromaticity and of terrestrial origin. Meanwhile, 60% of the remaining samples produced FI values >2. This indicated the strong presence of fluorescent compounds with low aromaticity and of microbial origin. Similar results have been reported by Lee et al. (2013) in their EEM analysis of fresh and aged organic aerosols. They suggested that aerosols with FI values near 1.4 and 1.9 were associated with fulvic acids of terrestrial and microbial origin, respectively. The presence of this acid in our samples was verified by the FTIR and XPS results, where C = O (1798–1800 cm^{-1}) and OH (3500–3650 cm^{-1}) vibrations for the carboxylic acid group and OC = O, 289 eV to the C_{1s} signal for the carboxyl group, respectively were observed. The autochthonous contribution index value (BIX near 0.4) also suggested that fulvic acid came from nonbiological sources. In addition, the HIX index found in the aerosols of ~0.6 can be associated with the low-grade humification fluorescent components.

The PARAFAC model was applied to identify the possible sources of emission for the water-soluble carbonaceous substances that were present in the collected samples (Murphy et al., 2013). Recently, this model has been used to characterize the water-soluble organic matter in atmospheric aerosols (Mladenov et al., 2011; Matos et al., 2015; Chen et al., 2021) and organic matter in various aqueous matrices (Ishii and Boyer, 2012; Dittmar and Stubbins, 2014; Wünsch and Murphy, 2021). It is important to mention that in Mexico and possibly in Latin America, fluorescence indices and the PARAFAC model had not yet been used in the study of atmospheric aerosols. The results obtained are shown in **Figure 9**. The model was fixed for three components and helped determine 99.1% the data set variance and delivered central consistency values higher than 87%. Additionally, the model was validated through the analysis of divided halves (**Supplementary Figure S2**) and Tucke r´s congruence coefficient for both excitation and emission spectra The coefficients were found to be higher than the similarity threshold (0.95) proposed by Murphy et al. (2014). Component 1 (C1) revealed the primary and secondary signals (λex/λem) of 340/433 nm and 340/394 nm, respectively. Component (C2) gave the primary and secondary signals of 300/410 nm and 360/410 nm, respectively. Component 3 (C3) showed one signal of 360/398 nm. The signals for C1 were similar to those reported for highly oxygenated HULIS of terrestrial and dust origin, which were found in aerosol samples from urban areas and organic matter dissolved in water samples (Fu et al., 2015; Yan and Kim, 2017; Qin et al., 2018; Wang et al., 2020). Moreover, Wen et al. (2021) applied the PARAFAC model to samples collected from three sites with different environments in northern China. One of the components presented signals of 245 and 360/476 nm, which were associated with highly oxygenated HULIS from terrestrial sources. In

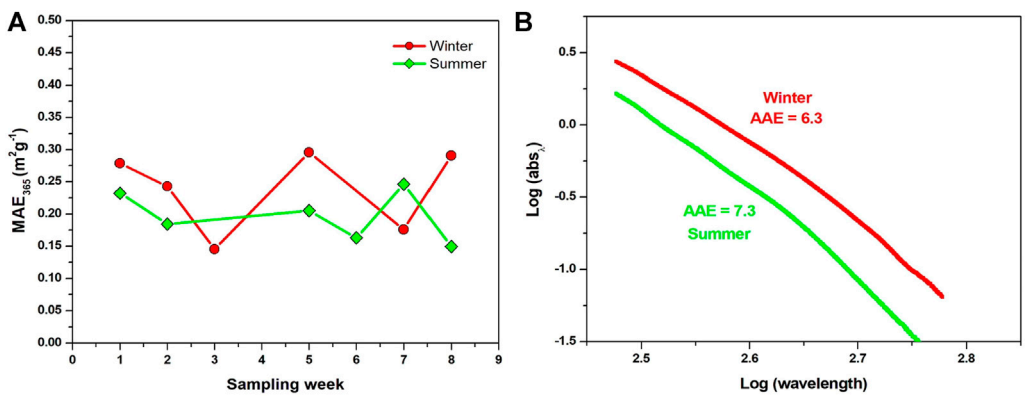

FIGURE 8 | (A) Time series of mass absorption efficiency at 365 nm (MAE_{365}) for the two study periods, **(B)** linear regression fit log(abs_{365}) versus log(λ) in the wavelength range of 300–600 nm for both study periods.

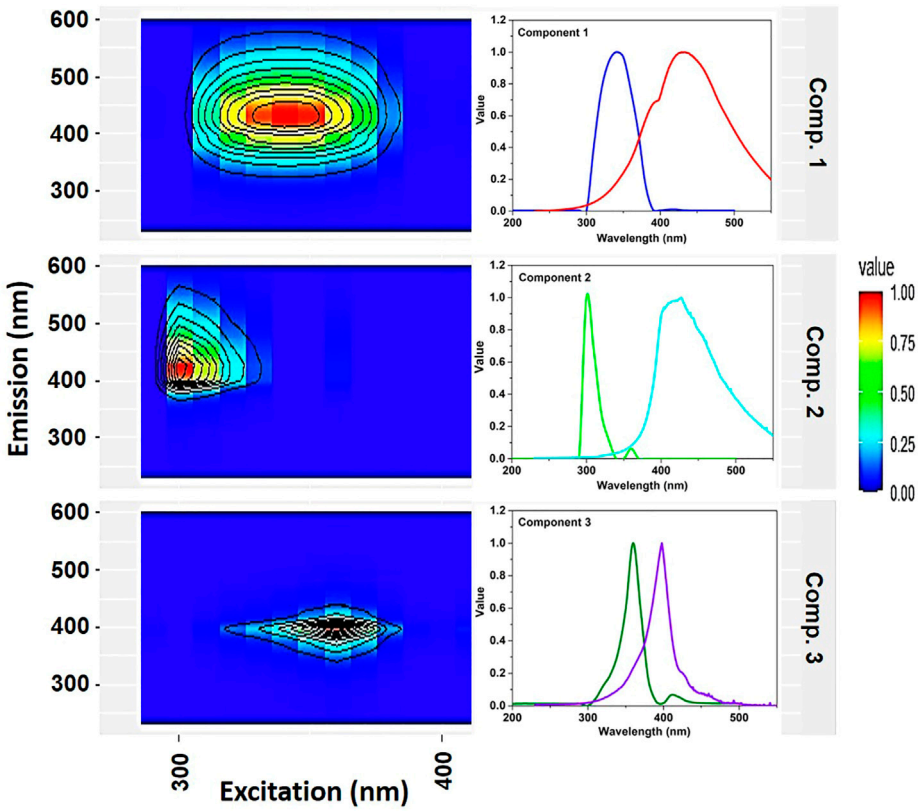

FIGURE 9 | Comparison of the final models with three normalized components according to the maximum fluorescence (Fmax) emission.

addition, Murphy et al. (2011) attributed the signal of 349/431 nm to terrestrial humic- and fulvic-like fluorescent compounds in their samples of organic matter dissolved in water.

In the case of C2, the fluorescence was associated to HULIS of microbial origin (Søndergaard et al., 2003; Zhuo et al., 2010; Murphy et al., 2011). Similar fluorescent compounds have been identified in the DOM of groundwater (Chen et al., 2010). On the other hand, C3 was similar to those found for humic fluorophores present in wastewater (Stedmon and Markager, 2005; D'Andrilli et al., 2013). Here, the results of the PARAFAC study were fully consistent with those obtained from the fluorescence indices study. These studies revealed the contribution of HULIS of terrestrial and microbial origin in the samples. It is important to emphasize that the emission sources and chemical composition of the fluorophores in the PM may not be the same as those found in the DOM. Moreover, only a few studies have used the fluorescence indices and PARAFAC method to characterize the fluorophore components in PM samples. Therefore, it was not possible to compare the detected components that may be found in different sources of atmospheric aerosols, such as biomass burning, fossil sources, secondary aerosols of biogenic, and anthropogenic VOCs, among others. In this sense, the present work, although an exploratory study, may serve as a basis to deepen the study of the fluorophore components present in atmospheric aerosols in Mexico.

4 CONCLUSION

This study investigated the light absorption characteristics and chemical composition of $PM_{2.5}$ particles and their water-soluble fraction. In winter, the concentration of $PM_{2.5}$ recorded at the San Bernabé station exceeded the limits in Mexico (NOM-025-SSA1-2014), which was a potential health risk to the exposed population. The presence of inorganic species in the samples collected during winter and summer, such as $CaCO_3$, $CaSO_4$, SiO_2, and aluminosilicates were identified by ATR-FTIR, XRD, and XPS techniques. The DRS spectra showed that most of the detected constituents of the sample absorbed mainly in the UV region (200–350 nm). The highest percentages of $CaSO_4$ were found in the winter samples (both at the surface level and in the bulk). This was attributed to the higher concentration of SO_2 in the atmosphere, as well as the higher humidity and low wind speed that were recorded during the winter months of sample collection. The speciation of the C_{1s} signal showed eight different oxidation states for carbon in all samples, with aromatic hydrocarbons, EC, and aliphatic hydrocarbons as the main contributors to the overall signal.

The light absorption by the water extracts exhibited a strong dependence with the wavelengths in the ranges 300 and 600 nm. Optical parameters, such as ABs_{365} and AAE, as well as the high correlation found between Abs_{365} and WSOC, showed that a fraction of WSOC corresponds to BrC chromophores. The Abs_{365}

and MAE_{365} were found to be higher in the winter than in summer samples. This was attributed to the differences in the chemical nature of the BrC compounds and/or to a higher concentration of these compounds in the winter samples. EEM-PARAFAC analysis showed that the water-soluble BrC compounds were mainly HULIS that come from terrestrial (C1), microbial origin (C2) and humic fluorophores (C3). A high correlation was found between the fluorescence indices (FI, HIX, and BIX) and EMM-PARAFAC, which suggested the importance of both approaches in establishing the possible sources of emission for the BrC compounds in the aqueous extracts. We believe that it is necessary to continue the global studies on the molecular characterization of BrC compounds and fluorescence properties of atmospheric WSOC. These studies will allow us to establish a database on atmospheric aerosols for more accurate identification of possible emission sources.

DATA AVAILABILITY STATEMENT

The original contributions presented in the study are included in the article/**Supplementary Material**, further inquiries can be directed to the corresponding author.

AUTHOR CONTRIBUTIONS

Conceptualization, LG; Writing—original draft preparation, LG, AM, FL, and KA; Writing—review and editing, LG, JA, AM, and FL; Characterization, LB-C, DL-S, AR-G, and AC; Data curation, EL, Investigation, JA-B and OK; Supervision, LG.

ACKNOWLEDGMENTS

The authors thank Ing. Armandina Valdez for the use of the monitoring stations of the Sistema Integral de Monitoreo Ambiental (SIMA). The valuable support of Dr. Alonso Concha and M. C. Gerardo Silva Vidaurri from CIMAV.

SUPPLEMENTARY MATERIAL

The Supplementary Material for this article can be found online at: https://www.frontiersin.org/articles/10.3389/fenvs.2022.929449/full#supplementary-material

REFERENCES

Adamo, P., Giordano, S., Naimo, D., and Bargagli, R. (2008). Geochemical Properties of Airborne Particulate Matter (PM10) Collected by Automatic Device and Biomonitors in a Mediterranean Urban Environment. *Atmos. Environ.* 42, 346–357. doi:10.1016/j.atmosenv.2007.09.018

Ahlers, F., Bubert, H., Steuernage, S., and Wiermann, R. (2000). The Nature of Oxygen in Sporopollenin from the Pollen of Typha Angustifolia L. *Z. Naturforsch. C* 55, 129–136. doi:10.1515/znc-2000-3-401

Ahmady-birgani, H., Mirnejad, H., Feiznia, S., and Mcqueen, K. G. (2015). Mineralogy and Geochemistry of Atmospheric Particulates in Western. *Atmos. Environ.* 119, 262–272. doi:10.1016/j.atmosenv.2015.08.021

Al Omari, M. M. H., Rashid, I. S., Qinna, N. A., Jaber, A. M., and Badwan, A. A. (2016). "Calcium Carbonate," in *Profiles of Drug Substances, Excipients and Related Methodology*. Editor H. G. Brittain (Amman: Academic Press), 31–132. doi:10.1016/bs.podrm.2015.11.003

Allen, D. T., Palen, E. J., Haimov, M. I., Hering, S. V., and Young, J. R. (1994). Fourier Transform Infrared Spectroscopy of Aerosol Collected in a Low Pressure Impactor (LPI/FTIR): Method Development and Field Calibration. *Aerosol Sci. Technol.* 21, 325–342. doi:10.1080/02786829408959719

Andreae, M. O., and Ramanathan, V. (2013). Climate's Dark Forcings. *Science* 340, 280–281. doi:10.1126/science.1235731

Atzei, D., Fantauzzi, M., Rossi, A., Fermo, P., Piazzalunga, A., Valli, G., et al. (2014). Surface Chemical Characterization of PM10 Samples by XPS. *Appl. Surf. Sci.* 307, 120–128. doi:10.1016/j.apsusc.2014.03.178

Atzei, D., and Rossi, A. (2004). Quantitative Surface Analysis of Urban Airborne Particles by X-Ray Photoelectron Spectroscopy. *Ann. Chim.* 94, 123–133. doi:10.1002/adic.200490016

Bahadur, R., Uplinger, T., Russell, L. M., Sive, B. C., Cliff, S. S., Millet, D. B., et al. (2010). Phenol Groups in Northeastern U.S. Submicrometer Aerosol Particles Produced from Seawater Sources. *Environ. Sci. Technol.* 44, 2542–2548. doi:10.1021/es9032277

Banerjee, T., Murari, V., Kumar, M., and Raju, M. P. (2015). Source Apportionment of Airborne Particulates through Receptor Modeling: Indian Scenario. *Atmos. Res.* 164-165, 167–187. doi:10.1016/j.atmosres.2015.04.017

Barsotti, F., Ghigo, G., and Vione, D. (2016). Computational Assessment of the Fluorescence Emission of Phenol Oligomers: A Possible Insight into the Fluorescence Properties of Humic-like Substances (HULIS). *J. Photochem. Photobiol. A Chem.* 315, 87–93. doi:10.1016/j.jphotochem.2015.09.012

Birdwell, J. E., and Engel, A. S. (2010). Characterization of Dissolved Organic Matter in Cave and Spring Waters Using UV-Vis Absorbance and Fluorescence Spectroscopy. *Org. Geochem.* 41, 270–280. doi:10.1016/j.orggeochem.2009.11.002

Bock, S., Kijatkin, C., Berben, D., and Imlau, M. (2019). Absorption and Remission Characterization of Pure, Dielectric (Nano-)powders Using Diffuse Reflectance Spectroscopy: An End-To-End Instruction. *Appl. Sci.* 9, 4933. doi:10.3390/APP9224933

Bond, T. C., Streets, D. G., Yarber, K. F., Nelson, S. M., Woo, J. H., and Klimont, Z. (2004). A Technology-Based Global Inventory of Black and Organic Carbon Emissions from Combustion. *J. Geophys. Res.* 109, 1–43. doi:10.1029/2003JD003697

Bradt, R. C. (2008). "The Sillimanite Minerals: Andalusite, Kyanite, and Sillimanite," in *Ceramic and Glass Materials: Structure, Properties and Processing*. Editors J. F. Shackelford and R. H. Doremus (Boston, MA: Springer US), 41–48. doi:10.1007/978-0-387-73362-3_3

Bro, R. (1997). PARAFAC. Tutorial and Applications. *Chemom. Intelligent Laboratory Syst.* 38, 149–171. doi:10.1016/S0169-7439(97)00032-4

Buseck, P. R., and Pósfai, M. (1999). Airborne Minerals and Related Aerosol Particles: Effects on Climate and the Environment. *Proc. Natl. Acad. Sci. U.S.A.* 96, 3372–3379. doi:10.1073/pnas.96.7.3372

Carmona, J. M., Gupta, P., Lozano-García, D. F., Vanoye, A. Y., Hernández-Paniagua, I. Y., and Mendoza, A. (2021). Evaluation of Modis Aerosol Optical Depth and Surface Data Using an Ensemble Modeling Approach to Assess pm2.5 Temporal and Spatial Distributions. *Remote Sens.* 13, 3102. doi:10.3390/rs13163102

Chakraborty, A., Ervens, B., Gupta, T., and Tripathi, S. N. (2016). Characterization of Organic Residues of Size-resolved Fog Droplets and Their Atmospheric Implications. *J. Geophys. Res. Atmos.* 121, 4317–4332. doi:10.1002/2015JD024508

Chen, M., Price, R. M., Yamashita, Y., and Jaffé, R. (2010). Comparative Study of Dissolved Organic Matter from Groundwater and Surface Water in the Florida Coastal Everglades Using Multi-Dimensional Spectrofluorometry Combined

with Multivariate Statistics. *Appl. Geochem.* 25, 872–880. doi:10.1016/j.apgeochem.2010.03.005

Chen, P., Kang, S., Li, C., Zhang, Q., Guo, J., Tripathee, L., et al. (2019). Carbonaceous Aerosol Characteristics on the Third Pole: A Primary Study Based on the Atmospheric Pollution and Cryospheric Change (APCC) Network. *Environ. Pollut.* 253, 49–60. doi:10.1016/j.envpol.2019.06.112

Chen, Q., Chen, Q., Hua, X., Guan, D., and Chang, T. (2021). Gas-phase Brown Carbon: Absorbance and Chromophore Types. *Atmos. Environ.* 264, 118646. doi:10.1016/j.atmosenv.2021.118646

Chen, Q., Ikemori, F., and Mochida, M. (2016a). Light Absorption and Excitation-Emission Fluorescence of Urban Organic Aerosol Components and Their Relationship to Chemical Structure. *Environ. Sci. Technol.* 50, 10859–10868. doi:10.1021/acs.est.6b02541

Chen, Q., Miyazaki, Y., Kawamura, K., Matsumoto, K., Coburn, S., Volkamer, R., et al. (2016b). Characterization of Chromophoric Water-Soluble Organic Matter in Urban, Forest, and Marine Aerosols by HR-ToF-AMS Analysis and Excitation-Emission Matrix Spectroscopy. *Environ. Sci. Technol.* 50, 10351–10360. doi:10.1021/acs.est.6b01643

Chen, Y., Ge, X., Chen, H., Xie, X., Chen, Y., Wang, J., et al. (2018). Seasonal Light Absorption Properties of Water-Soluble Brown Carbon in Atmospheric Fine Particles in Nanjing, China. *Atmos. Environ.* 187, 230–240. doi:10.1016/j.atmosenv.2018.06.002

Chen, Y., Xie, X., Shi, Z., Li, Y., Gai, X., Wang, J., et al. (2020). Brown Carbon in Atmospheric Fine Particles in Yangzhou, China: Light Absorption Properties and Source Apportionment. *Atmos. Res.* 244, 105028. doi:10.1016/j.atmosres.2020.105028

Cheng, Y., He, K.-b., Du, Z.-y., Engling, G., Liu, J.-m., Ma, Y.-l., et al. (2016). The Characteristics of Brown Carbon Aerosol during Winter in Beijing. *Atmos. Environ.* 127, 355–364. doi:10.1016/j.atmosenv.2015.12.035

Chou, C. C.-K., Huang, S.-H., Chen, T.-K., Lin, C.-Y., and Wang, L.-C. (2005). Size-segregated Characterization of Atmospheric Aerosols in Taipei during Asian Outflow Episodes. *Atmos. Res.* 75, 89–109. doi:10.1016/j.atmosres.2004.12.002

Clean Air Institute (2012). *Air Quality in Latin America: An Overview*. Washington, DC: Clean Air Institute.

Coury, C., and Dillner, A. M. (2008). A Method to Quantify Organic Functional Groups and Inorganic Compounds in Ambient Aerosols Using Attenuated Total Reflectance FTIR Spectroscopy and Multivariate Chemometric Techniques. *Atmos. Environ.* 42, 5923–5932. doi:10.1016/j.atmosenv.2008.03.026

Crowley, J. N., Ammann, M., Cox, R. A., Hynes, R. G., Jenkin, M. E., Mellouki, A., et al. (2010). Evaluated Kinetic and Photochemical Data for Atmospheric Chemistry: Volume V - Heterogeneous Reactions on Solid Substrates. *Atmos. Chem. Phys.* 10, 9059–9223. doi:10.5194/acp-10-9059-2010

D'Andrilli, J., Foreman, C. M., Marshall, A. G., and McKnight, D. M. (2013). Characterization of IHSS Pony Lake Fulvic Acid Dissolved Organic Matter by Electrospray Ionization Fourier Transform Ion Cyclotron Resonance Mass Spectrometry and Fluorescence Spectroscopy. *Org. Geochem.* 65, 19–28. doi:10.1016/j.orggeochem.2013.09.013

Davarcioglu, B. (2011). Spectral Characterization of Non-clay Minerals Found in the Clays (Central Anatolian-Turkey). *Int. J. Phys. Sci.* 6, 511–522. doi:10.5897/IJPS10.615

Dittmar, T., and Stubbins, A. (2014). "Dissolved Organic Matter in Aquatic Systems," in *Treatise on Geochemistry*. Editors H. D. Holland and K. K. Turekian. Second Edition (Oxford: Elsevier), 125–156. doi:10.1016/B978-0-08-095975-7.01010-X

Domínguez, E., Mercado, J. A., Quesada, M. A., and Heredia, A. (1999). Pollen Sporopollenin: Degradation and Structural Elucidation. *Sex. Plant Reprod.* 12, 171–178. doi:10.1007/s004970050189

Duan, X., Yan, Y., Li, R., Deng, M., Hu, D., and Peng, L. (2021). Seasonal Variations, Source Apportionment, and Health Risk Assessment of Trace Metals in PM2.5 in the Typical Industrial City of Changzhi, China. *Atmos. Pollut. Res.* 12, 365–374. doi:10.1016/j.apr.2020.09.017

Duarte, R. M. B. O., Santos, E. B. H., Pio, C. A., and Duarte, A. C. (2007). Comparison of Structural Features of Water-Soluble Organic Matter from Atmospheric Aerosols with Those of Aquatic Humic Substances. *Atmos. Environ.* 41, 8100–8113. doi:10.1016/j.atmosenv.2007.06.034

Escobedo-Morales, A., Ruiz-López, I. I., Ruiz-Peralta, M. d., Tepech-Carrillo, L., Sánchez-Cantú, M., and Moreno-Orea, J. E. (2019). Automated Method for the Determination of the Band Gap Energy of Pure and Mixed Powder Samples Using Diffuse Reflectance Spectroscopy. *Heliyon* 5, e01505–19. doi:10.1016/j.heliyon.2019.e01505

Fraund, M., Bonanno, D. J., China, S., Pham, D. Q., Veghte, D., Weis, J., et al. (2020). Optical Properties and Composition of Viscous Organic Particles Found in the Southern Great Plains. *Atmos. Chem. Phys.* 20, 11593–11606. doi:10.5194/acp-20-11593-2020

Fu, P., Kawamura, K., Chen, J., Qin, M., Ren, L., Sun, Y., et al. (2015). Fluorescent Water-Soluble Organic Aerosols in the High Arctic Atmosphere. *Sci. Rep.* 5, 1–8. doi:10.1038/srep09845

Gaddam, C. K., and Vander Wal, R. L. (2013). Physical and Chemical Characterization of SIDI Engine Particulates. *Combust. Flame* 160, 2517–2528. doi:10.1016/j.combustflame.2013.05.025

Gilham, R. J. J., Spencer, S. J., Butterfield, D., Seah, M. P., and Quincey, P. G. (2008). On the Applicability of XPS for Quantitative Total Organic and Elemental Carbon Analysis of Airborne Particulate Matter. *Atmos. Environ.* 42, 3888–3891. doi:10.1016/j.atmosenv.2008.01.007

Gipson, K., Stevens, K., Brown, P., and Ballato, J. (2015). Infrared Spectroscopic Characterization of Photoluminescent Polymer Nanocomposites. *J. Spectrosc.* 2015, 1–9. doi:10.1155/2015/489162

González, L. T., Longoria Rodríguez, F. E., Sánchez-Domínguez, M., Cavazos, A., Leyva-Porras, C., Silva-Vidaurri, L. G., et al. (2017). Determination of Trace Metals in TSP and PM 2.5 Materials Collected in the Metropolitan Area of Monterrey, Mexico: A Characterization Study by XPS, ICP-AES and SEM-EDS. *Atmos. Res.* 196, 8–22. doi:10.1016/j.atmosres.2017.05.009

González, L. T., Longoria-Rodríguez, F. E., Sánchez-Domínguez, M., Leyva-Porras, C., Acuña-Askar, K., Kharissov, B. I., et al. (2018). Seasonal Variation and Chemical Composition of Particulate Matter: A Study by XPS, ICP-AES and Sequential Microanalysis Using Raman with SEM/EDS. *J. Environ. Sci.* 74, 32–49. doi:10.1016/j.jes.2018.02.002

González, L. T., Rodríguez, F. E. L., Sánchez-Domínguez, M., Leyva-Porras, C., Silva-Vidaurri, L. G., Acuna-Askar, K., et al. (2016). Chemical and Morphological Characterization of TSP and PM2.5 by SEM-EDS, XPS and XRD Collected in the Metropolitan Area of Monterrey, Mexico. *Atmos. Environ.* 143, 249–260. doi:10.1016/j.atmosenv.2016.08.053

Graber, E. R., and Rudich, Y. (2006). Atmospheric HULIS: How Humic-like Are They? A Comprehensive and Critical Review. *Atmos. Chem. Phys.* 6, 729–753. doi:10.5194/acp-6-729-2006

Guascito, M. R., Cesari, D., Chirizzi, D., Genga, A., and Contini, D. (2015). XPS Surface Chemical Characterization of Atmospheric Particles of Different Sizes. *Atmos. Environ.* 116, 146–154. doi:10.1016/j.atmosenv.2015.06.028

Happo, M. S., Salonen, R. O., Hälinen, A. I., Jalava, P. I., Pennanen, A. S., Dormans, J. A. M. A., et al. (2010). Inflammation and Tissue Damage in Mouse Lung by Single and Repeated Dosing of Urban Air Coarse and Fine Particles Collected from Six European Cities. *Inhal. Toxicol.* 22, 402–416. doi:10.3109/08958370903527908

Hecobian, A., Zhang, X., Zheng, M., Frank, N., Edgerton, E. S., and Weber, R. J. (2010). Water-soluble Organic Aerosol Material and the Light-Absorption Characteristics of Aqueous Extracts Measured over the Southeastern United States. *Atmos. Chem. Phys.* 10, 5965–5977. doi:10.5194/acp-10-5965-2010

Hoek, G., Mennen, M. G., Allen, G. A., Hofschreuder, P., and Van Der Meulen, T. (1996). Concentrations of Acidic Air Pollutants in The Netherlands. *Atmos. Environ.* 30, 3141–3150. doi:10.1016/1352-2310(96)00032-5

Huang, R.-J., Yang, L., Cao, J., Chen, Y., Chen, Q., Li, Y., et al. (2018). Brown Carbon Aerosol in Urban Xi'an, Northwest China: The Composition and Light Absorption Properties. *Environ. Sci. Technol.* 52, 6825–6833. doi:10.1021/acs.est.8b02386

Huertas, J. I., Camacho, D. A., and Huertas, M. E. (2012). Standardized Emissions Inventory Methodology for Open-Pit Mining Areas. *Environ. Sci. Pollut. Res.* 19, 2784–2794. doi:10.1007/s11356-012-0778-3

Huguet, A., Vacher, L., Relexans, S., Saubusse, S., Froidefond, J. M., and Parlanti, E. (2009). Properties of Fluorescent Dissolved Organic Matter in the Gironde Estuary. *Org. Geochem.* 40, 706–719. doi:10.1016/j.orggeochem.2009.03.002

Huo, M. Q., Sato, K., Ohizumi, T., Akimoto, H., and Takahashi, K. (2016). Characteristics of Carbonaceous Components in Precipitation and Atmospheric Particle at Japanese Sites. *Atmos. Environ.* 146, 164–173. doi:10.1016/j.atmosenv.2016.07.017

INECC (2014). Informe nacional de calidad del aire 2013, méxico. 52.

Ishii, S. K. L., and Boyer, T. H. (2012). Behavior of Reoccurring PARAFAC Components in Fluorescent Dissolved Organic Matter in Natural and Engineered Systems: A Critical Review. *Environ. Sci. Technol.* 46, 2006–2017. doi:10.1021/es2043504

Jacobson, M. Z. (2004). Climate Response of Fossil Fuel and Biofuel Soot, Accounting for Soot's Feedback to Snow and Sea Ice Albedo and Emissivity. *J. Geophys. Res.* 109, a–n. doi:10.1029/2004JD004945

Jacobson, M. Z. (2001). Strong Radiative Heating Due to the Mixing State of Black Carbon in Atmospheric Aerosols. *Nature* 409, 695–697. doi:10.1038/35055518

Ji, Z., Dai, R., and Zhang, Z. (2015). Characterization of Fine Particulate Matter in Ambient Air by Combining TEM and Multiple Spectroscopic Techniques - NMR, FTIR and Raman Spectroscopy. *Environ. Sci. Process. Impacts* 17, 552–560. doi:10.1039/c4em00678j

Khare, P., Baruah, B. P., and Rao, P. G. (2011). Water-soluble Organic Compounds (WSOCs) in PM2.5 and PM10 at a Subtropical Site of India. *Tellus, Ser. B Chem. Phys. Meteorol.* 63, 990–1000. doi:10.1111/j.1600-0889.2011.00564.x

Kim, H., Kim, J. Y., Jin, H. C., Lee, J. Y., and Lee, S. P. (2016). Seasonal Variations in the Light-Absorbing Properties of Water-Soluble and Insoluble Organic Aerosols in Seoul, Korea. *AtmosEnviron* 129, 234–242. doi:10.1016/j.atmosenv.2016.01.042

Kirillova, E. N., Andersson, A., Tiwari, S., Srivastava, A. K., Bisht, D. S., and Gustafsson, Ö. (2014). Water-soluble Organic Carbon Aerosols during a Full New Delhi Winter: Isotope-Based Source Apportionment and Optical Properties. *J. Geophys. Res. Atmos.* 119, 3476–3485. doi:10.1002/2013JD020041

Kondo, Y., Miyazaki, Y., Takegawa, N., Miyakawa, T., Weber, R. J., Jimenez, J. L., et al. (2007). Oxygenated and Water-Soluble Organic Aerosols in Tokyo. *J. Geophys. Res. Atmos.* 112, D01203. doi:10.1029/2006JD007056

Lee, H. J., Julie)Laskin, A., Laskin, J., and Nizkorodov, S. A. (2013). Excitation–Emission Spectra and Fluorescence Quantum Yields for Fresh and Aged Biogenic Secondary Organic Aerosols. *Environ. Sci. Technol.* 47, 5763–5770. doi:10.1021/es400644c

Lee, H. S., Kang, C.-M., Kang, B.-W., and Kim, H.-K. (1999). Seasonal Variations of Acidic Air Pollutants in Seoul, South Korea. *Atmos. Environ.* 33, 3143–3152. doi:10.1016/S1352-2310(98)00382-3

Leskinen, A., Ruuskanen, A., Kolmonen, P., Zhao, Y., Fang, D., Wang, Q., et al. (2020). The Contribution of Black Carbon and Non-BC Absorbers to the Aerosol Absorption Coefficient in Nanjing, China. *Aerosol Air Qual. Res.* 20, 590–605. doi:10.4209/aaqr.2019.06.0326

Lin, P., Bluvshtein, N., Rudich, Y., Nizkorodov, S. A., Laskin, J., and Laskin, A. (2017). Molecular Chemistry of Atmospheric Brown Carbon Inferred from a Nationwide Biomass Burning Event. *Environ. Sci. Technol.* 51, 11561–11570. doi:10.1021/acs.est.7b02276

Liñán-Abanto, R. N., Peralta, O., Salcedo, D., Ruiz-Suárez, L. G., Arnott, P., Paredes-Miranda, G., et al. (2019). Optical Properties of Atmospheric Particles over an Urban Site in Mexico City and a Peri-Urban Site in Queretaro. *J. Atmos. Chem.* 76, 201–228. doi:10.1007/s10874-019-09394-1

Lippmann, M., Ito, K., Hwang, J.-S., Maciejczyk, P., and Chen, L.-C. (2006). Cardiovascular Effects of Nickel in Ambient Air. *Environ. Health Perspect.* 114, 1662–1669. doi:10.1289/ehp.9150

Liu, C., Chung, C. E., Yin, Y., and Schnaiter, M. (2018). The Absorption Ångström Exponent of Black Carbon: from Numerical Aspects. *Atmos. Chem. Phys.* 18, 6259–6273. doi:10.5194/acp-18-6259-2018

Liu, J., Bergin, M., Guo, H., King, L., Kotra, N., Edgerton, E., et al. (2013). Size-resolved Measurements of Brown Carbon in Water and Methanol Extracts and Estimates of Their Contribution to Ambient Fine-Particle Light Absorption. *Atmos. Chem. Phys.* 13, 12389–12404. doi:10.5194/acp-13-12389-2013

Longoria-Rodríguez, F. E., González, L. T., Mancilla, Y., Acuña-Askar, K., Arizpe-Zapata, J. A., González, J., et al. (2021). Sequential SEM-EDS, PLM, and MRS Microanalysis of Individual Atmospheric Particles: A Useful Tool for Assigning Emission Sources. *Toxics* 9, 37. doi:10.3390/toxics9020037

Longoria-Rodríguez, F. E., González, L. T., Mendoza, A., Leyva-Porras, C., Arizpe-Zapata, A., Esneider-Alcalá, M., et al. (2020). Environmental Levels, Sources, and Cancer Risk Assessment of PAHs Associated with PM2.5 and TSP in Monterrey Metropolitan Area. *Arch. Environ. Contam. Toxicol.* 78, 377–391. doi:10.1007/s00244-019-00701-1

López-Ayala, O., González-Hernández, L.-T., Alcantar-Rosales, V.-M., Elizarragaz-de la Rosa, D., Heras-Ramírez, M.-E., Silva-Vidaurri, L.-G., et al. (2019). Levels of Polycyclic Aromatic Hydrocarbons Associated with Particulate Matter in a Highly Urbanized and Industrialized Region in Northeastern Mexico. *Atmos. Pollut. Res.* 10, 1655–1662. doi:10.1016/j.apr.2019.06.006

Lu, S., Hao, X., Liu, D., Wang, Q., Zhang, W., Liu, P., et al. (2016). Mineralogical Characterization of Ambient Fine/ultrafine Particles Emitted from Xuanwei C1 Coal Combustion. *Atmos. Res.* 169, 17–23. doi:10.1016/j.atmosres.2015.09.020

Makuła, P., Pacia, M., and Macyk, W. (2018). How to Correctly Determine the Band Gap Energy of Modified Semiconductor Photocatalysts Based on UV-Vis Spectra. *J. Phys. Chem. Lett.* 9, 6814–6817. doi:10.1021/acs.jpclett.8b02892

Mancilla, Y., Herckes, P., Fraser, M. P., and Mendoza, A. (2015). Secondary Organic Aerosol Contributions to PM2.5 in Monterrey, Mexico: Temporal and Seasonal Variation. *Atmos. Res.* 153, 348–359. doi:10.1016/j.atmosres.2014.09.009

Mancilla, Y., Hernandez Paniagua, I. Y., and Mendoza, A. (2019). Spatial Differences in Ambient Coarse and Fine Particles in the Monterrey Metropolitan Area, Mexico: Implications for Source Contribution. *J. Air & Waste Manag. Assoc.* 69, 548–564. doi:10.1080/10962247.2018.1549121

Mancilla, Y., Mendoza, A., Fraser, M. P., and Herckes, P. (2016). Organic Composition and Source Apportionment of Fine Aerosol at Monterrey, Mexico, Based on Organic Markers. *Atmos. Chem. Phys.* 16, 953–970. doi:10.5194/acp-16-953-2016

Maria, S. F., Russell, L. M., Turpin, B. J., and Porcja, R. J. (2002). FTIR Measurements of Functional Groups and Organic Mass in Aerosol Samples over the Caribbean. *Atmos. Environ.* 36, 5185–5196. doi:10.1016/S1352-2310(02)00654-4

Martin, S. T., Hung, H.-M., Park, R. J., Jacob, D. J., Spurr, R. J. D., Chance, K. V., et al. (2004). Effects of the Physical State of Tropospheric Ammonium-Sulfate-Nitrate Particles on Global Aerosol Direct Radiative Forcing. *Atmos. Chem. Phys.* 4, 183–214. doi:10.5194/acp-4-183-2004

Martinez, M. A., Caballero, P., Carrillo, O., Mendoza, A., and Mejia, G. M. (2012). Chemical Characterization and Factor Analysis of PM2.5 in Two Sites of Monterrey, Mexico. *J. Air & Waste Manag. Assoc.* 62, 817–827. doi:10.1080/10962247.2012.681421

Matos, J. T. V., Freire, S. M. S. C., Duarte, R. M. B. O., and Duarte, A. C. (2015). Natural Organic Matter in Urban Aerosols: Comparison between Water and Alkaline Soluble Components Using Excitation-Emission Matrix Fluorescence Spectroscopy and Multiway Data Analysis. *Atmos. Environ.* 102, 1–10. doi:10.1016/j.atmosenv.2014.11.042

McKnight, D. M., Boyer, E. W., Westerhoff, P. K., Doran, P. T., Kulbe, T., and Andersen, D. T. (2001). Spectrofluorometric Characterization of Dissolved Organic Matter for Indication of Precursor Organic Material and Aromaticity. *Limnol. Oceanogr.* 46, 38–48. doi:10.4319/lo.2001.46.1.0038

Menges, F. (2020). "Spectragryph–Optical Spectroscopy Software," Version 1.2.15, 2020. Available at: http://www.effemm2.de/spectragryph/.

Miyazaki, Y., Kondo, Y., Shiraiwa, M., Takegawa, N., Miyakawa, T., Han, S., et al. (2009). Chemical Characterization of Water-Soluble Organic Carbon Aerosols at a Rural Site in the Pearl River Delta, China, in the Summer of 2006. *J. Geophys. Res.* 114. doi:10.1029/2009JD011736

Mladenov, N., Alados-Arboledas, L., Olmo, F. J., Lyamani, H., Delgado, A., Molina, A., et al. (2011). Applications of Optical Spectroscopy and Stable Isotope Analyses to Organic Aerosol Source Discrimination in an Urban Area. *Atmos. Environ.* 45, 1960–1969. doi:10.1016/j.atmosenv.2011.01.029

Mo, Y., Li, J., Cheng, Z., Zhong, G., Zhu, S., Tian, C., et al. (2021). Dual Carbon Isotope-Based Source Apportionment and Light Absorption Properties of Water-Soluble Organic Carbon in $PM_{2.5}$ over China. *JGR Atmos.* 126, 1–13. doi:10.1029/2020JD033920

Moosmüller, H., Chakrabarty, R. K., Ehlers, K. M., and Arnott, W. P. (2011). Absorption Ångström Coefficient, Brown Carbon, and Aerosols: Basic Concepts, Bulk Matter, and Spherical Particles. *Atmos. Chem. Phys.* 11, 1217–1225. doi:10.5194/acp-11-1217-2011

Morozzi, P., Ballarin, B., Arcozzi, S., Brattich, E., Lucarelli, F., Nava, S., et al. (2021). Ultraviolet-Visible Diffuse Reflectance Spectroscopy (UV-Vis DRS), a Rapid and Non-destructive Analytical Tool for the Identification of Saharan Dust Events in Particulate Matter Filters. *Atmos. Environ.* 252, 118297. doi:10.1016/j.atmosenv.2021.118297

Murphy, K. R., Hambly, A., Singh, S., Henderson, R. K., Baker, A., Stuetz, R., et al. (2011). Organic Matter Fluorescence in Municipal Water Recycling

Schemes: Toward a Unified PARAFAC Model. *Environ. Sci. Technol.* 45, 2909–2916. doi:10.1021/es103015e

Murphy, K. R., Stedmon, C. A., Graeber, D., and Bro, R. (2013). Fluorescence Spectroscopy and Multi-Way Techniques. PARAFAC. *Anal. Methods* 5, 6557–6566. doi:10.1039/c3ay41160e

Murphy, K. R., Stedmon, C. A., Wenig, P., and Bro, R. (2014). OpenFluor- an Online Spectral Library of Auto-Fluorescence by Organic Compounds in the Environment. *Anal. Methods* 6, 658–661. doi:10.1039/c3ay41935e

Nagabhushana, H., Nagaraju, G., Nagabhushana, B. M., Shivakumara, C., and Chakradhar, R. P. S. (2010). Hydrothermal Synthesis and Characterization of CaSO4pseudomicrorods. *Philos. Mag. Lett.* 90, 289–298. doi:10.1080/09500831003636051

nl.gob.mx (2020). Atlas de Georrecursos del Estado de Nuevo León, Región Sur 1.

Pant, P., Shukla, A., Kohl, S. D., Chow, J. C., Watson, J. G., and Harrison, R. M. (2015). Characterization of Ambient PM2.5 at a Pollution Hotspot in New Delhi, India and Inference of Sources. *Atmos. Environ.* 109, 178–189. doi:10.1016/j.atmosenv.2015.02.074

Paoletti, L., Berardis, B. D. E., and Arrizza, L. (2003). Inquinamento da polveri e da particolato fino in siti con differenti caratteristiche ambientali. *Ann. Ist. Super. Sanità* 39, 381–385. doi:10.1049/el:20031096

Pokhrel, R. P., Beamesderfer, E. R., Wagner, N. L., Langridge, J. M., Lack, D. A., Jayarathne, T., et al. (2017). Relative Importance of Black Carbon, Brown Carbon, and Absorption Enhancement from Clear Coatings in Biomass Burning Emissions. *Atmos. Chem. Phys.* 17, 5063–5078. doi:10.5194/acp-17-5063-2017

Pucher, M., Wünsch, U., Weigelhofer, G., Murphy, K., Hein, T., and Graeber, D. (2019). StaRdom: Versatile Software for Analyzing Spectroscopic Data of Dissolved Organic Matter in R. *Water* 11, 2366. doi:10.3390/w11112366

Qian, Y., Yasunari, T. J., Doherty, S. J., Flanner, M. G., Lau, W. K. M., Ming, J., et al. (2015). Light-absorbing Particles in Snow and Ice: Measurement and Modeling of Climatic and Hydrological Impact. *Adv. Atmos. Sci.* 32, 64–91. doi:10.1007/s00376-014-0010-0

Qin, J., Tan, J., Zhou, X., Yang, Y., Qin, Y., Wang, X., et al. (2021). Measurement Report: Particle-size-dependent Fluorescence Properties of Water-Soluble Organic Compounds (WSOCs) and Their Atmospheric Implications for the Aging of WSOCs. *Atmos. Chem. Phys.* 22, 465–479. doi:10.5194/acp-22-465-2022

Qin, J., Zhang, L., Zhou, X., Duan, J., Mu, S., Xiao, K., et al. (2018). Fluorescence Fingerprinting Properties for Exploring Water-Soluble Organic Compounds in PM2.5 in an Industrial City of Northwest China. *Atmos. Environ.* 184, 203–211. doi:10.1016/j.atmosenv.2018.04.049

Radulescu, C., Stihi, C., Iordache, S., Dunea, D., and Dulama, I. D. (2017). Characterization of Urban Atmospheric PM2.5 by ATR-FTIR, ICP-MS and SEM-EDS Techniques. *Rev. Chim.* 68, 805–810. doi:10.37358/rc.17.4.5557

Ravindra, K., Singh, T., Mandal, T. K., Sharma, S. K., and Mor, S. (2022). Seasonal Variations in Carbonaceous Species of PM2.5 Aerosols at an Urban Location Situated in Indo-Gangetic Plain and its Relationship with Transport Pathways, Including the Potential Sources. *J. Environ. Manag.* 303, 114049. doi:10.1016/j.jenvman.2021.114049

Ravisankar, R., Kiruba, S., Eswaran, P., Senthilkumar, G., and Chandrasekaran, A. (2010). Mineralogical Characterization Studies of Ancient Potteries of Tamilnadu, India by FT-IR Spectroscopic Technique. *E-Journal Chem.* 7, S185–S190. doi:10.1155/2010/643218

Rietveld, H. M. (1969). A Profile Refinement Method for Nuclear and Magnetic Structures. *J. Appl. Cryst.* 2, 65–71. doi:10.1107/s0021889869006558

Saitoh, K., Sera, K., and Shirai, T. (2008). Characterization of Atmospheric Aerosol Particles in a Mountainous Region in Northern Japan. *Atmos. Res.* 89, 324–329. doi:10.1016/j.atmosres.2008.03.007

Satish, R., Shamjad, P., Thamban, N., Tripathi, S., and Rastogi, N. (2017). Temporal Characteristics of Brown Carbon over the Central Indo-Gangetic Plain. *Environ. Sci. Technol.* 51, 6765–6772. doi:10.1021/acs.est.7b00734

Sellitto, V. M., Fernandes, R. B. A., Barrón, V., and Colombo, C. (2009). Comparing Two Different Spectroscopic Techniques for the Characterization of Soil Iron Oxides: Diffuse versus Bi-directional Reflectance. *Geoderma* 149, 2–9. doi:10.1016/j.geoderma.2008.11.020

Secretaría de Salud (2014). "NORMA Oficial Mexicana NOM-025-SSA1-2014, Salud Ambiental," in Valores límite permisibles para la concentración de partículas suspendidas PM10 y PM2.5 en el aire ambiente y criterios para su evaluación, México, DF.

Shaka', H., and Saliba, N. A. (2004). Concentration Measurements and Chemical Composition of PM10-2.5 and PM2.5 at a Coastal Site in Beirut, Lebanon. *Atmos. Environ.* 38, 523–531. doi:10.1016/j.atmosenv.2003.10.009

Siciliano, T., Siciliano, M., Malitesta, C., Proto, A., Cucciniello, R., Giove, A., et al. (2018). Carbonaceous PM10 and PM2.5 and Secondary Organic Aerosol in a Coastal Rural Site Near Brindisi (Southern Italy). *Environ. Sci. Pollut. Res.* 25, 23929–23945. doi:10.1007/s11356-018-2237-2

Simonsen, M. E., Sønderby, C., Li, Z., and Søgaard, E. G. (2009). XPS and FT-IR Investigation of Silicate Polymers. *J. Mat. Sci.* 44, 2079–2088. doi:10.1007/s10853-009-3270-9

Søndergaard, M., Stedmon, C. A., and Borch, N. H. (2003). Fate of Terrigenous Dissolved Organic Matter (DOM) in Estuaries: Aggregation and Bioavailability. *Ophelia* 57, 161–176. doi:10.1080/00785236.2003.10409512

Song, X., Shao, L., Zheng, Q., and Yang, S. (2014). Mineralogical and Geochemical Composition of Particulate Matter (PM10) in Coal and Non-coal Industrial Cities of Henan Province, North China. *Atmos. Res.* 143, 462–472. doi:10.1016/j.atmosres.2014.03.015

Stedmon, C. A., and Markager, S. (2005). Resolving the Variability in Dissolved Organic Matter Fluorescence in a Temperate Estuary and its Catchment Using PARAFAC Analysis. *Limnol. Oceanogr.* 50, 686–697. doi:10.4319/lo.2005.50.2.0686

Sullivan, A. P., and Weber, R. J. (2006). Chemical Characterization of the Ambient Organic Aerosol Soluble in Water: 2. Isolation of Acid, Neutral, and Basic Fractions by Modified Size-Exclusion Chromatography. *J. Geophys. Res.* 111, 1–19. doi:10.1029/2005JD006486

Szalai, Z., Kiss, K., Jakab, G., Sipos, P., Belucz, B., and Németh, T. (2013). The Use of UV-VIS-NIR Reflectance Spectroscopy to Identify Iron Minerals. *Astron. Nachr.* 334, 940–943. doi:10.1002/asna.201211965

Tang, M. J., Whitehead, J., Davidson, N. M., Pope, F. D., Alfarra, M. R., McFiggans, G., et al. (2015). Cloud Condensation Nucleation Activities of Calcium Carbonate and its Atmospheric Ageing Products. *Phys. Chem. Chem. Phys.* 17, 32194–32203. doi:10.1039/c5cp03795f

Tarantola, A., Voudouris, P., Eglinger, A., Scheffer, C., Trebus, K., Bitte, M., et al. (2019). Metamorphic and Metasomatic Kyanite-Bearing Mineral Assemblages of Thassos Island (Rhodope, Greece). *Minerals* 9, 252. doi:10.3390/MIN9040252

Teich, M., Van Pinxteren, D., Wang, M., Kecorius, S., Wang, Z., Müller, T., et al. (2017). Contributions of Nitrated Aromatic Compounds to the Light Absorption of Water-Soluble and Particulate Brown Carbon in Different Atmospheric Environments in Germany and China. *Atmos. Chem. Phys.* 17, 1653–1672. doi:10.5194/acp-17-1653-2017

Torrent, J., and Barrón, V. (2015). "Diffuse Reflectance Spectroscopy," in *Methods of Soil Analysis Part 5—Mineralogical Methods, 5.5*. Wisconsin: Soil Science Society of America, 5, 367–385. doi:10.2136/sssabookser5.5.c13

Tsapakis, M., Lagoudaki, E., Stephanou, E. G., Kavouras, I. G., Koutrakis, P., Oyola, P., et al. (2002). The Composition and Sources of PM2.5 Organic Aerosol in Two Urban Areas of Chile. *Atmos. Environ.* 36, 3851–3863. doi:10.1016/S1352-2310(02)00269-8

U.S. EPA. Environmental Protection Agency Methods (1999). *Compendium Method IO-2.1*.

Varrica, D., Tamburo, E., Vultaggio, M., and Di Carlo, I. (2019). ATR-FTIR Spectral Analysis and Soluble Components of PM10 and PM2.5 Particulate Matter over the Urban Area of Palermo (Italy) during Normal Days and Saharan Events. *Ijerph* 16, 2507. doi:10.3390/ijerph16142507

Wang, H., Zhang, L., Huo, T., Wang, B., Yang, F., Chen, Y., et al. (2020). Application of Parallel Factor Analysis Model to Decompose Excitation-Emission Matrix Fluorescence Spectra for Characterizing Sources of Water-Soluble Brown Carbon in PM2.5. *Atmos. Environ.* 223, 117192. doi:10.1016/j.atmosenv.2019.117192

Wang, Z., Wang, R., Wang, J., Wang, Y., McPherson Donahue, N., Tang, R., et al. (2022). The Seasonal Variation, Characteristics and Secondary Generation of PM2.5 in Xi'an, China, Especially during Pollution Events. *Environ. Res.* 212, 113388. doi:10.1016/j.envres.2022.113388

Wen, H., Zhou, Y., Xu, X., Wang, T., Chen, Q., Chen, Q., et al. (2021). Water-soluble Brown Carbon in Atmospheric Aerosols along the Transport Pathway

of Asian Dust: Optical Properties, Chemical Compositions, and Potential Sources. *Sci. Total Environ.* 789, 147971. doi:10.1016/j.scitotenv.2021.147971

Wonaschütz, A., Hitzenberger, R., Bauer, H., Pouresmaeil, P., Klatzer, B., Caseiro, A., et al. (2009). Application of the Integrating Sphere Method to Separate the Contributions of Brown and Black Carbon in Atmospheric Aerosols. *Environ. Sci. Technol.* 43, 1141–1146. doi:10.1021/es8008503

Wu, C., Wang, G., Li, J., Li, J., Cao, C., Ge, S., et al. (2020). The Characteristics of Atmospheric Brown Carbon in Xi'an, Inland China: Sources, Size Distributions and Optical Properties. *Atmos. Chem. Phys.* 20, 2017–2030. doi:10.5194/acp-20-2017-2020

Wu, G., Fu, P., Ram, K., Song, J., Chen, Q., Kawamura, K., et al. (2021). Fluorescence Characteristics of Water-Soluble Organic Carbon in Atmospheric Aerosol☆☆. *Environ. Pollut.* 268, 115906. doi:10.1016/j.envpol.2020.115906

Wu, G., Ram, K., Fu, P., Wang, W., Zhang, Y., Liu, X., et al. (2019). Water-Soluble Brown Carbon in Atmospheric Aerosols from Godavari (Nepal), a Regional Representative of South Asia. *Environ. Sci. Technol.* 53, 3471–3479. doi:10.1021/acs.est.9b00596

Wünsch, U. J., and Murphy, K. (2021). A Simple Method to Isolate Fluorescence Spectra from Small Dissolved Organic Matter Datasets. *Water Res.* 190, 116730. doi:10.1016/j.watres.2020.116730

Xu, P., Xu, J., He, M., Song, L., Chen, D., Guo, G., et al. (2016). Morphology and Chemical Characteristics of Micro- and Nano-Particles in the Haze in Beijing Studied by XPS and TEM/EDX. *Sci. Total Environ.* 565, 827–832. doi:10.1016/j.scitotenv.2016.03.042

Yan, C., Zheng, M., Sullivan, A. P., Bosch, C., Desyaterik, Y., Andersson, A., et al. (2015). Chemical Characteristics and Light-Absorbing Property of Water-Soluble Organic Carbon in Beijing: Biomass Burning Contributions. *Atmos. Environ.* 121, 4–12. doi:10.1016/j.atmosenv.2015.05.005

Yan, G., and Kim, G. (2017). Speciation and Sources of Brown Carbon in Precipitation at Seoul, Korea: Insights from Excitation-Emission Matrix Spectroscopy and Carbon Isotopic Analysis. *Environ. Sci. Technol.* 51, 11580–11587. doi:10.1021/acs.est.7b02892

Yan, J., Wang, X., Gong, P., Wang, C., and Cong, Z. (2018). Review of Brown Carbon Aerosols: Recent Progress and Perspectives. *Sci. Total Environ.* 634, 1475–1485. doi:10.1016/j.scitotenv.2018.04.083

Yang, Y., Qin, J., Qi, T., Zhou, X., Chen, R., Tan, J., et al. (2020). Fluorescence Characteristics of Particulate Water-Soluble Organic Compounds Emitted from Coal-Fired Boilers. *Atmos. Environ.* 223, 117297. doi:10.1016/j.atmosenv.2020.117297

Yu, X., Song, W., Yu, Q., Li, S., Zhu, M., Zhang, Y., et al. (2018). Fast Screening Compositions of PM2.5 by ATR-FTIR: Comparison with Results from IC andOC/EC Analyzers. *J. Environ. Sci.* 71, 76–88. doi:10.1016/j.jes.2017.11.021

Yuan, W., Huang, R.-J., Yang, L., Guo, J., Chen, Z., Duan, J., et al. (2020). Characterization of the Light-Absorbing Properties, Chromophore Composition and Sources of Brown Carbon Aerosol in Xi'an, Northwestern China. *Atmos. Chem. Phys.* 20, 5129–5144. doi:10.5194/acp-20-5129-2020

Yue, Y., Cheng, J., Lee, K. S., Stocker, R., He, X., Yao, M., et al. (2022). Effects of Relative Humidity on Heterogeneous Reaction of SO2 with CaCO3 Particles and Formation of CaSO4·2H2O Crystal as Secondary Aerosol. *Atmos. Environ.* 268, 118776. doi:10.1016/j.atmosenv.2021.118776

Zarasvandi, A., Carranza, E. J. M., Moore, F., and Rastmanesh, F. (2011). Spatio-Temporal Occurrences and Mineralogical-Geochemical Characteristics of Airborne Dusts in Khuzestan Province (Southwestern Iran). *J. Geochemical. Explor.* 111, 138–151. doi:10.1016/j.gexplo.2011.04.004

Zapata-Hernandez, C., Durango-Giraldo, G., Tobón, C., and Buitrago-Sierra, R. (2020). Physicochemical Characterization of Airborne Particulate Matter in Medellín, Colombia, and its Use in an In Silico Study of Ventricular Action Potential. *Water. Air. Soil Pollut.* 231, 508. doi:10.1007/s11270-020-04884-5

Zeb, B., Alam, K., Sorooshian, A., Blaschke, T., Ahmad, I., and Shahid, I. (2018). On the Morphology and Composition of Particulate Matter in an Urban Environment. *Aerosol Air Qual. Res.* 18, 1431–1447. doi:10.4209/aaqr.2017.09.0340

Zent, A. P., Ichimura, A. S., Quinn, R. C., and Harding, H. K. (2008). The Formation and Stability of the Superoxide Radical (O2−) on Rock-Forming Minerals: Band Gaps, Hydroxylation State, and Implications for Mars Oxidant Chemistry. *J. Geophys. Res.* 113, 1–13. doi:10.1029/2007JE003001

Zhan, Y., Tsona, N. T., Li, J., Chen, Q., and Du, L. (2022). Water-soluble Matter in PM2.5 in a Coastal City over China: Chemical Components, Optical Properties, and Source Analysis. *J. Environ. Sci.* 114, 21–36. doi:10.1016/j.jes.2021.07.011

Zhou, Y., Xiao, H., Guan, H., Zheng, N., Zhang, Z., Tian, J., et al. (2020). Chemical Composition and Seasonal Variations of PM2.5 in an Urban Environment in Kunming, SW China: Importance of Prevailing Westerlies in Cold Season. *Atmos. Environ.* 237, 117704. doi:10.1016/j.atmosenv.2020.117704

Zhuo, J. F., Guo, W. D., Deng, X., Zhang, Z. Y., Xu, J., and Huang, L. F. (2010). [Fluorescence Excitation-Emission Matrix Spectroscopy of CDOM from Yundang Lagoon and its Indication for Organic Pollution]. *Guang Pu Xue Yu Guang Pu Fen Xi* 30, 1539–1544.

Zwinkels, J., Germer, T., and Tsai, B. (2014). *Experimental Methods in the Physical Sciences Spectrophotometry: Accurate Measurement of Optical Properties of Materials*, 1–10. Amsterdam, Netherlands: Elsevier.

Conflict of Interest: The authors declare that the research was conducted in the absence of any commercial or financial relationships that could be construed as a potential conflict of interest.

Publisher's Note: All claims expressed in this article are solely those of the authors and do not necessarily represent those of their affiliated organizations, or those of the publisher, the editors and the reviewers. Any product that may be evaluated in this article, or claim that may be made by its manufacturer, is not guaranteed or endorsed by the publisher.

frontiers | Frontiers in Environmental Science

TYPE Original Research
PUBLISHED 22 July 2022
DOI 10.3389/fenvs.2022.915531

OPEN ACCESS

EDITED BY
Yuzhong Zhang,
Westlake University, China

REVIEWED BY
Shixian Zhai,
Harvard University, United States
Zhijiong Huang,
Jinan University, China

*CORRESPONDENCE
Ja-Ho Koo,
zach45@yonsei.ac.kr

SPECIALTY SECTION
This article was submitted to Atmosphere and Climate, a section of the journal Frontiers in Environmental Science

RECEIVED 08 April 2022
ACCEPTED 28 June 2022
PUBLISHED 22 July 2022

CITATION
Lee T, Go S, Lee YG, Park SS, Park J and Koo J-H (2022), Temporal variability of surface air pollutants in megacities of South Korea.
Front. Environ. Sci. 10:915531.
doi: 10.3389/fenvs.2022.915531

Temporal variability of surface air pollutants in megacities of South Korea

Taegyung Lee[1], Sujung Go[2], Yun Gon Lee[3], Sang Seo Park[4], Jinsoo Park[5] and Ja-Ho Koo[1]*

[1]Department of Atmospheric Sciences, Yonsei University, Seoul, South Korea, [2]Joint Center for Earth Systems Technology, University of Maryland Baltimore Country, Baltimore, MD, United States, [3]Department of Atmospheric Sciences, Chungnam National University, Daejeon, South Korea, [4]School of Urban and Environmental Engineering, Ulsan National Institute of Science and Technology, Ulsan, South Korea, [5]Air Quality Research Division, Climate and Air Quality Research Department, National Institute of Environmental Research, Incheon, South Korea

This study investigated the various temporal (weekly, monthly, and inter-annual) variability of air pollutants (PM_{10}, SO_2, NO_2, O_3, CO) in seven megacities in South Korea (Seoul, Busan, Incheon, Daegu, Gwangju, Daejeon, and Ulsan). We found that the general decreasing trend of PM_{10}, SO_2, NO_2, and CO. An exceptional pollutant is O_3, showing a clear increasing trend consistently in all seven megacities. Seasonally PM_{10}, SO_2, NO_2, and CO have the highest level in winter due to the large fossil-fuel combustion for the heating demand, but O_3 shows the maximum peak in summer related to the intensified photochemistry. Based on the analysis for percentile values of air pollutants, we recognized that some patterns of air pollutants in Korean megacities are overlooked: O_3 increase is not perfectly related to the NO_2 pattern, somewhat high SO_2 in the coastal cities, ambiguous weekly pattern on Monday (as a weekday) and Sunday (as a weekend). Through this comprehensive analysis of multiple air pollutants using the percentile values, the characteristic for various temporal change of air pollutants in Korean megacities can be better understood, and some useful ideas for the air quality control in the urban region can be also excavated.

KEYWORDS

South Korea, megacity, PM10, NO2, ozone, SO2, carbon monoxide

Introduction

Air pollutants have adverse health effects, leading to respiratory and cardiovascular diseases (Xing et al., 2016; Wang et al., 2017). Moreover, they widely influence the ecosystem such as the crop damage (Wang et al., 2017). The air pollution level is also associated with the extent of absorption and scattering of solar radiation, resulted in the change of short-term radiative forcing (Huang et al., 2009; Che et al., 2014). To assess these situations, the analysis of long-term dataset of air pollutants is crucial. In this context, a number of countries basically started to manage the surface networks for the long-term observation of some key air pollutants. For example, Republic of Korea (South

Korea) started the measurements of the mass density of particulate matter (PM) with the diameter < 10 μm (PM_{10}), ozone (O_3), nitrogen dioxide (NO_2), sulfur dioxide (SO_2), and carbon monoxide (CO) with some volatile organic compounds (VOCs) from the year 1973 (SS, 2022). These measurements of air pollutants are generally provided through the national data archive, AIRKOREA, for the diagnosis of regional air quality.

Using the multiple datasets in a country range, there have been a number of studies for examining the long-term variation of air pollutants. For South Korea, Yoo et al. (2015) was the representative research showing the spatiotemporal properties of air pollutants in the Korean peninsula. They examined the daily, weekly, and annual concentration distributions of AIRKOREA air pollutants in four land types (residential, commercial, greenbelt, and industrial areas), and found that the levels of PM_{10} and SO_2 were high in industrial areas, NO_2 and CO levels were high in commercial areas, and O_3 level was high in greenbelt areas. Namely, this study suggested that the local pattern of air pollutants is much affected by the land type. However, the air pollutant pattern is not always identical in a same land type. For example, there were some different patterns of air pollutants among provincial capital cities in China (Xie et al., 2015; Zhao et al., 2016), indicating the necessity of deeper analysis about the air pollutant pattern in the urban area where most of monitoring sites were located. The pattern analysis of urban air pollution will be also helpful idea for the diagnosis of human health, which is vulnerable to the high level of air pollutants (Kim et al., 2011; Lee S. W. et al., 2019).

Thus, here we investigated the various temporal variations of urban air pollutants in the Korean peninsula, using the surface measurement dataset in seven megacities of South Korea where high air pollution is generally found: Seoul, Busan, Incheon, Daegu, Gwangju, Daejeon, and Ulsan. Moreover, the air quality index was calculated based on the level of multiple pollutants for the comprehensive examination of the long-term air quality change. Understanding the local characteristics of air pollution at these megacities will be practically helpful for diagnosing the air pollution damage to the population living in each city, and the analysis of the long-term trend can be used as a reference to identify the degree of air quality improvement in each city. Based on these ideas, effective air pollution mitigation policies can be established for the urban region in South Korea. To get over the limitation of mean pattern analysis, this study also examined the percentile analysis, particularly temporal pattern of 10th and 90th percentile of air pollutant level, implying the characteristic of background and highly polluted conditions.

Data and methods

The Ministry of Environment in South Korea has established the nationwide surface measurement network for monitoring the level of representative air pollutants such as PM, O_3, NO_2, SO_2, and CO, which are measured by β-ray absorption method, ultraviolet (UV) photometric method, Chemiluminescent method, pulse UV fluorescence method, and non-dispersive infrared method, respectively (ME·NIER, 2021). Raw measured data from this monitoring network have been inspected and validated by the National Ambient air quality Monitoring Information System (NAMIS), then the final quality-confirmed data were prepared and provided through the AIRKOREA data archive (ME·NIER, 2021; KECO, 2022b). This study analyzed the hourly median value of PM_{10} (units: $\mu g/m^3$), O_3 (unit: ppb), NO_2 (unit: ppb), SO_2 (unit: ppb), CO (unit: ppb) from 2002 to 2020 in seven megacities of South Korea where population is higher than at least 1 million: Seoul, Busan, Daegu, Incheon, Gwangju, Dajeon, and Ulsan (KOSIS, 2021) (Supplementary Figure S1). As shown in Figure 1, there are total 120 monitoring sites in these seven megacities (27 for Seoul, 22 for Busan, 14 for Daegu, 21 for Incheon, 9 for Gwangju, 10 for Daejeon, and 17 for Ulsan). The median pattern among all sites in each megacity was basically analyzed in this study. While the local difference definitely exists in each megacity (e.g., Vuong et al., 2022), the analysis based on the median value, not affected by outliers different from mean value, can be a significant signal to show the general pattern of each city.

$PM_{2.5}$ data were not considered in this study because of the short monitoring history (started since 2015). While the

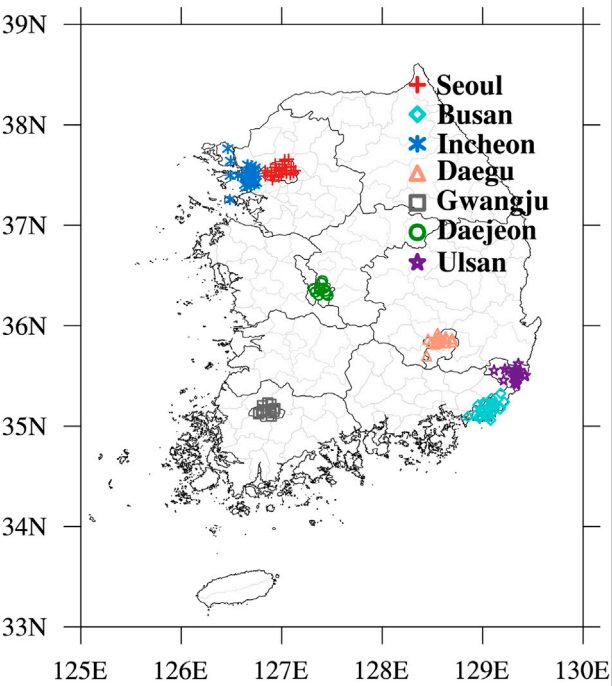

FIGURE 1
Location of AIRKOREA urban air quality monitoring stations in seven megacities: Seoul, Busan, Incheon, Daegu, Gwangju, Daejeon, and Ulsan.

AIRKOREA performs the quality control/assurance process regularly and releases the quality-confirmed data as mentioned, sometimes there can be ambiguous cases founded by the manual data quality check. For example, we are not sure if the CO levels in Gwangju from February to March 2003 reflects the real situation based on our own assessment of data quality (Supplementary Figure S2). We did not include these cases for our study.

For the purpose to provide the adverse effects of air pollution on human health to the non-expert public, the comprehensive air-quality index (CAI) was designed and widely used in South Korea (ME, 2006; ME·NIER, 2021). CAI is a unitless proxy showing the degree of local air pollution in general. CAI is calculated through several steps, which are described in the AIRKOREA webpage (KECO, 2022a). Based on this guideline, we calculated the CAI using the level of five pollutants (PM_{10}, O_3, NO_2, SO_2, and CO). In brief, the level of each air pollutant is normalized to an individual index, and finally a CAI is determined by the highest index among five normalized indices from normalized PM_{10}, O_3, NO_2, SO_2, and CO. The range of CAI (0–500) was divided into four categories for depicting the degree of air pollution: Good (0–50), Moderate (51–100), Unhealthy (101–250), and Very unhealthy (251–500). As the CAI becomes closer to the Unhealthy category, even a short-term exposure can have a serious and adverse impact on the public regardless of a kind of air pollutants (e.g., Pope et al., 2006; Choi et al., 2018). Since CAI value can be an easy and intuitive information to the non-expert public people, the long-term variation of CAI in South Korea was also examined in this study.

In the analysis for the temporal variability of the regional air pollutants in South Korea, it is necessary to filter out the influence of Asian dust events, which are the natural events happened occasionally. Namely, the effect of Asian dust can screen other meaningful signals of regional air pollution associated with a number of urban activities. South Korea is frequently impacted by the long-range transported Asian dust (Tsai and Chen, 2006; Lee, 2014; Ghim et al., 2017). Thus, the Asian dust days were generally excluded for the spatiotemporal analysis of PM (Ghim et al., 2015). We also did not use air pollutant data for the days of Asian dust, which was determined according to visual observations and instrumental observations by the Korea Meteorological Administration. The number of Asian dust days in each city is summarized in Supplementary Table S1.

Long-term trend analysis was performed based on the linear regression method. The trend value is estimated using Eq. 1 where x is year, y is the level of each air pollutants, and n means 19 years (from 2002 to 2020). For each trend, the significance test was also conducted based on *p* value from the Student's *t*-test. We obtain the t value from *t* test (Eq. 2, where b is the slope from the linear regression method, μ is the specified mean, and σ is the standard deviation), then *p* value can be finally achieved from the t distribution table. All trend values and significant test results (*p* values and determination of significance) were summarized in Supplementary Tables S2–S8.

$$Trend = \frac{n\sum_{i=1}^{n} x_i y_i - \sum_{i=1}^{n} x_i \sum_{i=1}^{n} y_i}{n\sum_{i=1}^{n} (x_i)^2 - \left(\sum_{i=1}^{n} x_i\right)^2} \quad (1)$$

$$t = \frac{b - \mu}{\sigma} \quad (2)$$

TABLE 1 Median concentrations of PM_{10} (μg m^{-3}), O_3 (ppb), NO_2 (ppb), SO_2 (ppb), and CO (ppb) in the study areas.

Cities	PM_{10}	O_3	NO_2	SO_2	CO
Seoul	42.1 ± 31.0	16.3 ± 16.8	30.7 ± 15.5	4.4 ± 2.3	487.0 ± 265.6
Busan	41.9 ± 24.5	25.8 ± 14.4	19.4 ± 10.4	5.1 ± 2.8	387.5 ± 163.6
Incheon	44.6 ± 29.1	21.1 ± 15.7	24.4 ± 14.0	5.9 ± 3.0	520.0 ± 264.0
Daegu	41.4 ± 25.4	20.8 ± 18.4	19.3 ± 12.9	3.8 ± 2.9	472.7 ± 281.7
Gwangju	36.2 ± 25.0	23.0 ± 16.6	16.8 ± 11.0	3.0 ± 2.0	460.0 ± 252.2
Daejeon	37.2 ± 25.2	19.8 ± 18.1	17.1 ± 10.9	3.0 ± 2.4	466.7 ± 292.0
Ulsan	38.8 ± 23.7	23.6 ± 15.0	19.4 ± 10.6	6.0 ± 5.2	471.4 ± 193.0

The SDs are presented with the ± values (2002–2020).

Result and discussion

Overall pattern of air pollutants in megacities

At first, we examined the patterns of PM_{10}, O_3, NO_2, SO_2, and CO in seven megacities during whole measurement period (2002–2020) using the median value (Table 1). PM_{10} is generally higher in Seoul, Busan, Incheon, and Daegu compared to PM_{10} in Gwangju, Daejeon, and Ulsan. NO_2, typically related to the traffic amounts (Park et al., 2021b), shows similar pattern to PM_{10} pattern. O_3 pattern is reverse to the NO_2 pattern, supporting the previous findings that the ozone production in Korean peninsula is chemically located in the VOC-limited regime (Kim et al., 2018; Bae et al., 2020). SO_2 level is highest in Busan, Incheon, and Ulsan that are harbor regions, showing that the ship-plume still much degrades the air quality in the industrialized megacities near the coast (Chen et al., 2017; Sorte et al., 2020). This simple median pattern analysis let us know the differences among the seven targeted megacities, and necessity to develop the multiple policies matching to each individual situation suitably.

We then investigated the monthly variation of air pollutants using median values. Figure 2 shows the monthly median of PM_{10}, O_3, NO_2, SO_2, and CO in seven megacities. Mainly there is large contrast between the winter (December, January, and February, hereafter DJF) and summer (June, July, and August, hereafter JJA) season; The level of air pollutants is generally high in winter but low in summer, except O_3 and SO_2 in Busan and Ulsan. These air pollutants (PM_{10}, NO_2, O_3, and CO) are mainly

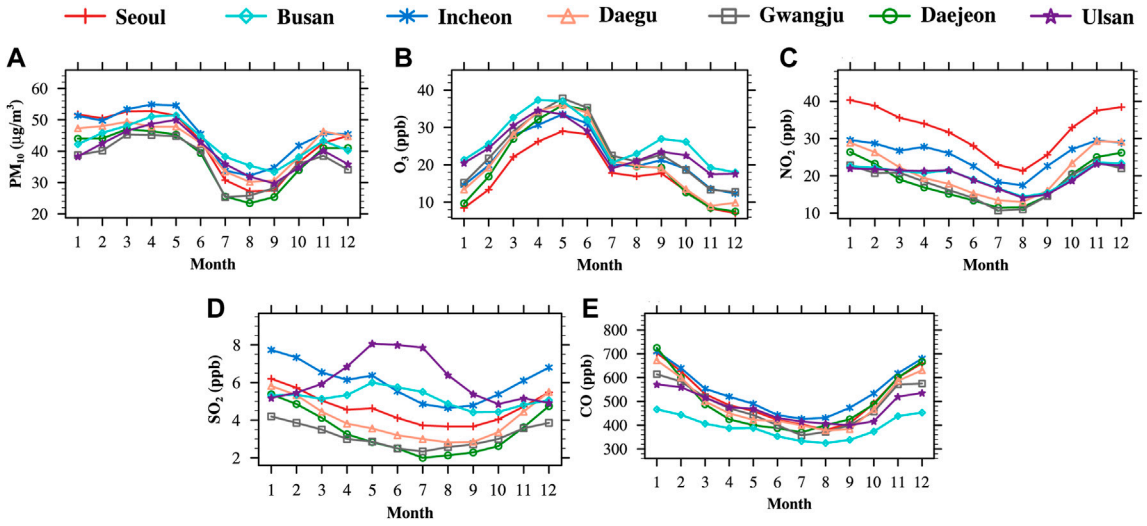

FIGURE 2
Monthly variations of median level **(A)** PM_{10} (μg m^{-3}), **(B)** O_3 (ppb), **(C)** NO_2 (ppb), **(D)** SO_2 (ppb), and **(E)** CO (ppb) in seven megacities, South Korea. Monthly median was estimated in the period from 2002 to 2020.

emitted from the fuel combustion and relevant processes, which is typically high in the cold season (i.e., winter) due to the large heating demand (Masiol et al., 2014; Zhang and Cao, 2015). Lower level in summer is contributed by the wash-out effect in the rainy season (Kim et al., 2014; Luo et al., 2014) and the strong vertical mixing in the deepened boundary layer due to the large surface heating (Su et al., 2018). In spring (March, April, and May, hereafter MAM), the monthly pattern of aerosol is a little different from that of gaseous pollutants. The maximum of aerosol mass density (PM_{10}) occurs in spring (Figure 2A), implying that the long-range transport of mineral dust particle largely enhances the median level of regional aerosol loading although we excluded serious Asian dust event days as mentioned.

In contrast to PM_{10}, NO_2, O_3, and CO, the O_3 level shows the reverse seasonal pattern: high in summer but low in winter (Figure 2B). Since the O_3 production is strongly affected by the photochemical processes, the amount of O_3 increases rapidly in summer when the solar radiation is intensified (Seo et al., 2014; Zhao et al., 2016). One more thing to underline is the exceptional monthly pattern of SO_2 in Busan and Ulsan (Figure 2D). It is well known that the ship plume is one of dominant sources of anthropogenic SO_2 (Yang et al., 2016), and our analysis revealed same result: higher SO_2 in coastal megacities (Ulsan, Busan, and Incheon). Also, these coastal cities have a large industrial area, therefore the high SO_2 emission is also expected from the manufacturing and industrial processes (Choi et al., 2020). The unique summer peak of SO_2 in Ulsan located in the eastern coast (Figure 1) seems associated with the emission of local industrial area (Vuong et al., 2022) where the southeastern seasonal-wind is prevailing in summer (Clarke et al., 2014), resulted in the inland accumulation of emitted air pollutants. Higher SO_2 in summer, Busan (nearby Ulsan) can be explained in a similar way. Incheon does not show a summer SO_2 peak by the southeastern wind due to the location (western coast of Korean peninsula).

Additionally, we investigated the mean pattern of each day of the week (Figure 3), which is associated with the weekend effect (e.g., decrease of anthropogenic activity). In general, air pollution analysis based on the day of the week is conducted to see how much the anthropogenic emission from the urban activity degrades the local air quality (Xia et al., 2008; Chen et al., 2015). We found that PM_{10} and NO_2 in Korean megacities show the clear difference between the weekend (Saturday and Sunday) and weekday (other days except the weekend): 10% higher on weekdays than weekends (Figures 3A,C). This characteristic in Korean megacities is similar to the weekly pattern in other urban area (Gong et al., 2007; Stavrakou et al., 2020). As shown in the monthly variation, weekly pattern of O_3 is also opposite to that of NO_2: higher in the weekend and lower in the weekdays (Figure 3B). Considering that both aerosol and ozone are harmful to the respiratory health, weekend is also not a period of safety for residents having the respiratory symptom, especially asthma patients who are seriously vulnerable to the high O_3 (Li et al., 2019). SO_2 also shows some weekday-weekend difference but its quantity is quite smaller than PM_{10} and NO_2 (Figure 3D) because most of fuel utilized in South Korea was already much desulfurized (Kim and Lee, 2018). CO does not have a significant weekday-weekend difference (Figure 3E) due to its long lifetime (Yoo et al., 2015).

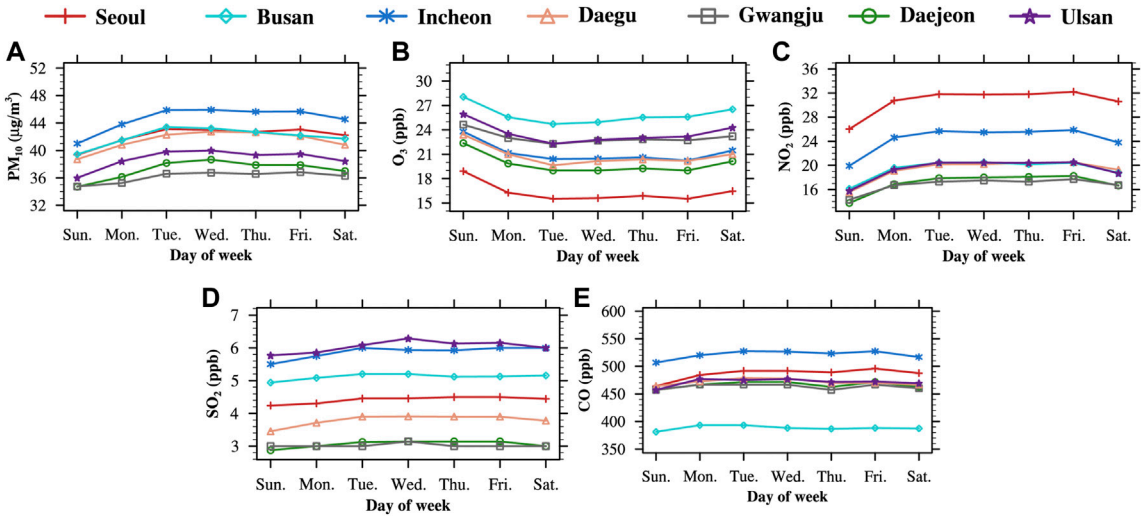

FIGURE 3
Weekly variations of median level **(A)** PM_{10} (μg m^{-3}), **(B)** O_3 (ppb), **(C)** NO_2 (ppb), **(D)** SO_2 (ppb), and **(E)** CO (ppb) in seven megacities, South Korea. Weekly median was estimated in the period from 2002 to 2020.

Typically, the weekday-weekend difference of air pollution becomes larger as the urban region has higher pollution (Huryn and Gough, 2014) or lower greenish area (Elansky et al., 2020), which can be confirmed here by the larger weekday-weekend difference in higher populated megacities (i.e., Seoul).

Another interesting feature is the difference of air pollution level among each day of week. As known, weekday-weekend difference of urban air pollution has been examined in the world (Marr and Harley, 2002; Almeida et al., 2006). We generally define the "weekday" as the period from Monday to Friday, and the "weekend" as the period from Saturday and Sunday. But it seems that Monday in weekday and Saturday in weekend are in the sort of transition regime. For example, PM_{10} and NO_2 on Saturday is not small as shown on Sunday, and those on Monday is not high as shown in other weekdays (Tuesday to Thursday) (Figures 3A,C). In other words, it is hard to categorize Monday as the weekday and Saturday as the weekend, whereas Tuesday to Friday have a consistent pattern of air pollution as the weekday and Sunday clearly shows the property of weekend. This feature probably comes from the life and working style in South Korean megacities. Recently, Monday and Saturday seem the moving day of urban people in South Korea: Travel to their suburban residence area on Saturday and return to the working place on Monday. For the proper application of these situation to the weekly variation of urban air pollutants in South Korea, the social activity pattern will be more investigated for the weekday and weekend separately. So far, it looks better to define the weekday based on the period from Tuesday to Friday and the weekend based on Sunday for the weekday-weekend difference of air pollutants.

Long-term trend of air pollutants in megacities

After the analysis of general pattern, we investigated the long-term trend of PM_{10}, O_3, NO_2, SO_2, and CO in seven megacities, South Korea. In this work, we basically analyzed the trend of median (50th percentile) value, and also compare the trend of 10th and 90th percentile values, which typically describe the background and high polluted air condition (Yoon et al., 2016). We performed the long-term trend analysis of annual percentiles first then carried on the analysis for the monthly and day of week percentiles.

The trends of annual 10th, 50th (median), and 90th percentile for PM_{10}, O_3, NO_2, SO_2, and CO in seven megacities were compared as shown in Figure 4; Time-series were provided in Supplementary Figures S3–S5. PM_{10} trend is consistently negative in all seven megacities, and the magnitude is the largest for the 90th percentile trends, implying the decrease of serious haze cases. Trends of annual NO_2 percentiles are also consistently decreasing and the magnitude is large for the 90th percentile, similar to trends of PM_{10}. Decreasing trend of both PM_{10} and NO_2 is the strongest in Seoul and becomes weaker as the city population (Supplementary Figure S1) is getting lower. It seems that the effort to reduce air pollutants emission in highly populated megacities works for the steady improvement of Korean urban air quality. There are some exceptions that are

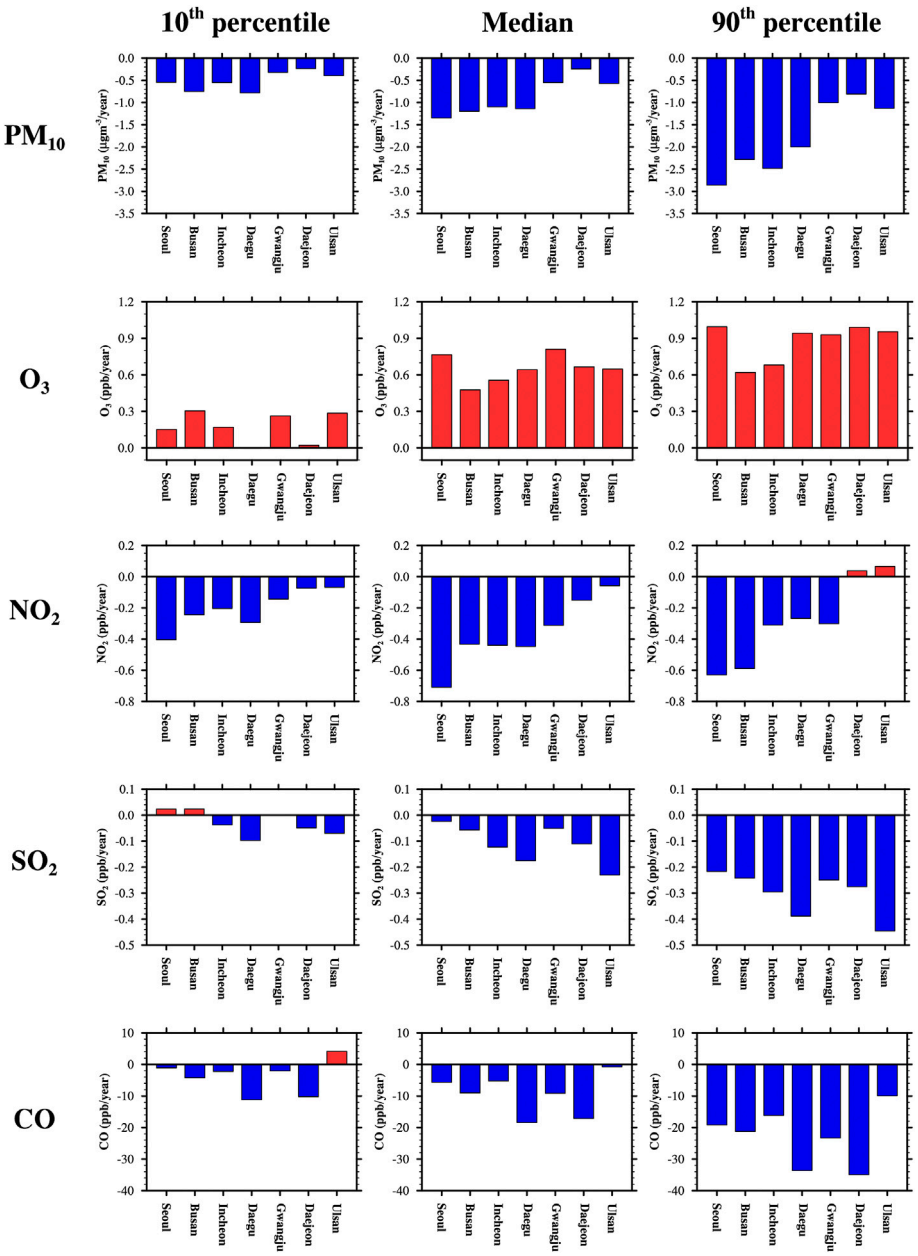

FIGURE 4
Long-term (2002-2020) trends of PM_{10} (μg m^{-3}/year), O_3 (ppb/year), NO_2 (ppb/year), SO_2 (ppb/year), and CO (ppbl/year) using 10th, 50th (median), and 90th percentile levels in seven megacities, South Korea.

increasing trend of 90th percentiles of NO_2 in Daejeon and Ulsan, but these do not hurt the finding above because of its small and insignificant magnitude.

SO_2 also shows the decreasing trend but the pattern is a little different: larger decrease in less-populated megacities. Seoul and Busan even have increasing trend of SO_2 when 10th percentiles were analyzed, implying that the control of manufacturing activities and industrial processes, the main sources of SO_2 emission (Choi et al., 2020), in large megacities of South Korea is still significantly monitored. Despite the small magnitude of this increase, increasing trends of background SO_2 cannot be easily neglected in these high populated megacities (Supplementary Figure S1). CO trend is generally all negative, consistent with well-known recent CO decrease in other Asian regions (Liu et al., 2019; Zhang et al., 2020).

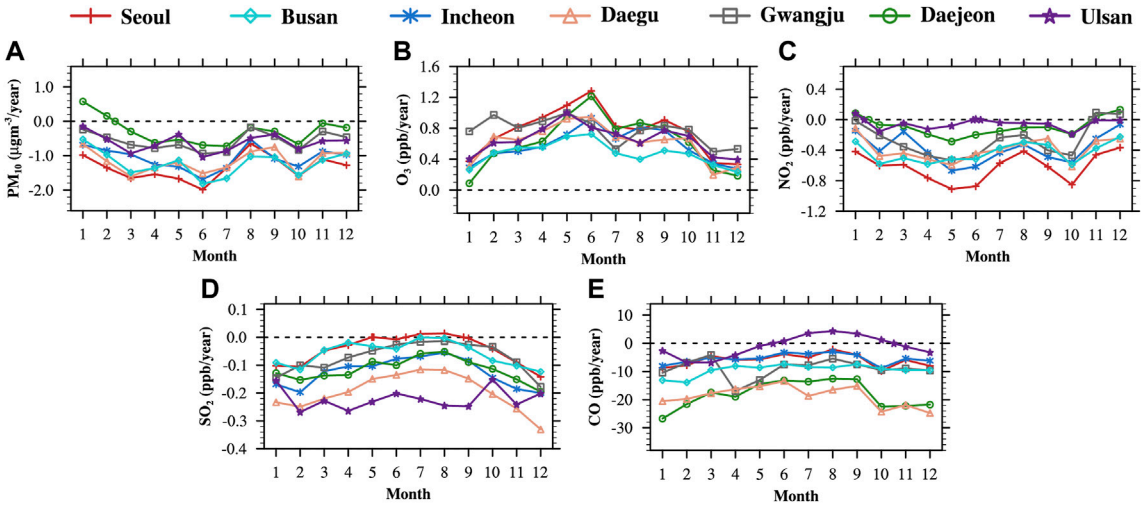

FIGURE 5
Long-term (2002-2020) trends of **(A)** monthly median PM_{10} (μg m^{-3}/year), **(B)** O_3 (ppb/year), **(C)** NO_2 (ppb/year), **(D)** SO_2 (ppb/year), and **(E)** CO (ppb/year) levels in seven megacities, South Korea.

In contrast, O_3 level becomes worsened. O_3 trends are consistently increasing in all megacities, and the magnitude is the largest for the 90th percentile trends. Different from PM_{10} and NO_2 trends, the increasing trend is not proportional to the city population. These features suggest that cases of high O_3 pollution have significantly contributed to the deterioration of urban air quality in South Korea, and this situation is not simply related to the level of other air pollutants or the scale of megacities. While the O_3 increase in the whole Korean peninsula has been reported (Yoo et al., 2015; Yeo and Kim, 2021), the main influencing factor is still not understood clearly. There were some trials to explain the O_3 increase in South Korea based on the meteorological effect (Seo et al., 2014), land use pattern (Yoo et al., 2015), and local emission effect (Shin et al., 2012; Yeo and Kim, 2021). The contribution of transboundary transport was also discussed (Oh et al., 2010; Choi et al., 2014). There is also a possibility that the photochemical production of ozone is getting larger by the increasing pattern of insolation and temperature in the Korean peninsula (Seo et al., 2014). In addition, the existence of stratospheric ozone intrusion may be associated with the O_3 increasing trend by considering the consistent O_3 increase in all seven megacities and the report of high ozone level above the boundary layer (Crawford et al., 2021).

Next, the long-term trend of air pollutants was investigated for each month. The difference of monthly trends between summer and winter is the first impression of this analysis, except CO (Figure 5). PM_{10} in seven megacities have a large decreasing trend in summer, but this decrease is not clearly shown in winter (Figure 5A). The decreasing trend of wintertime PM_{10} can be weakened by the long-term increase of stagnant condition in East Asia (Lee et al., 2020) because the stagnant air condition facilitates the high loading of local airborne aerosols, as recent studies indicated the anti-relationship between PM_{10} and wind speed (Kim et al., 2017). Considering that the high PM_{10} in Korean megacities generally happens in winter (Figure 2), the massive effort looks still required to avoid the threat of aerosol pollution to the public health in winter. In summer, aerosol pollution in the Korean peninsula usually relates to the large condensation and coagulation of particles (hygroscopic growth) under the stagnant air condition (Koo et al., 2016; Eck et al., 2020). Thus, the large negative trend in summer is explained by the situation that the stagnant air condition in summer is getting weaker, supported by the previous findings (Lee et al., 2020; Cho et al., 2021). The decrease of PM_{10} in spring is associated with the weaker Asian dust events recently (Lee et al., 2015; Zong et al., 2021).

While the signal is less obvious, the monthly pattern of long-tern NO_2 trends looks similar to that of PM_{10} (Figure 5C): larger decreasing in spring and summer, but almost no trend in winter. Reversely, O_3 trend is largely positive in summer but small in winter (Figure 5B). Focusing on the O_3 trend in Seoul and Busan, we found both large decreasing NO_2 and increasing O_3, similar to their anti-relationship associated with the NOx titration as shown in Figures 2, 3. In Gwangju, however, NO_2 decreasing rate is very small, but O_3 increasing rate is still quite large for all months. This is the difficult part to understand the ozone pattern in South Korea; Compared to the trends of other air pollutants, O_3 increasing trend is very consistent in all seven megacities regardless of regional difference. The reason is not clear at this present moment, but the influence of larger

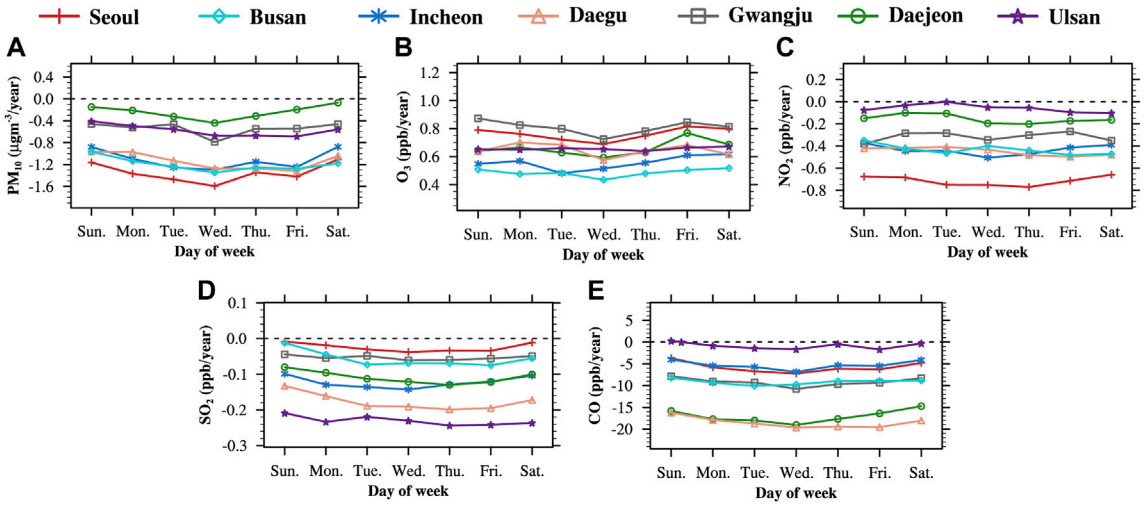

FIGURE 6
For each day of week, long-term (2002–2020) trends of median **(A)** PM_{10} (μgm^{-3}/year), **(B)** O_3 (ppb/year), **(C)** NO_2 (ppb/year), **(D)** SO_2 (ppb/year), and **(E)** CO (ppb/year) levels in seven megacities, South Korea.

scale forcing may be resulted in this consistent and significant O_3 increase. Future research will be significantly requested for better understanding of O_3 trend in Korean megacities.

Although SO_2 mean pattern is analogous to the NO_2 mean pattern (Figures 2, 3), monthly variation of SO_2 trend is a little different: Larger negative trend in winter. Decreasing SO_2 in cold winter season means that the environmental policy for SO_2 sources has been working well, which is good news to the domestic air quality. In addition, recent large SO_2 reduction in China (Sun et al., 2018; Bhardwaj et al., 2019) can be related to the large decrease of wintertime SO_2 in South Korea. Summertime SO_2 also has the decreasing trend but its magnitude is smaller than wintertime. The irregular pattern in summer is the small SO_2 increasing trend in Seoul and Busan, which are two main megacities in South Korea. Considering the increasing trend of 10th percentile SO_2 levels in Seoul and Busan (Figure 4), there may exist the increase of background SO_2 level in summer for Seoul and Busan, which is not well understood yet. CO trend does not depict the meaningful monthly variation. All seven megacities have clear decreasing trends of CO in all months.

For deeper analyses of median trends in each month, we also compared the trends of 10th and 90th percentile of air pollutants (Supplementary Figures S6, S7). One main finding is that the magnitude of long-term trends become more obvious if 90th percentile values are considered, but less significant with 10th percentile values. In other words, 90th percentile values more significantly illustrate decreasing trends of PM_{10}, NO_2, SO_2, and CO, and increasing trend of O_3 in all months, meaning that the change (i.e., improvement or degradation) of high polluted condition (meaning of 90th percentile values of air pollutants) is a dominant determining factor of long-term trends. This finding supports the previous studies addressing the necessity to control the high polluted condition mainly for better air quality (Park et al., 2021a). If the direction of trends (i.e., increase or decrease) is not identical in accordance with the choice of percentiles, the trend analysis should be performed more carefully. This feature was found in SO_2 trend pattern; 10th percentiles of SO_2 in Seoul and Busan show the consistent increasing trend, but 90th percentiles show the decreasing trends in all months. In other words, high SO_2 cases in Seoul and Busan is getting lesser, but the background SO_2 level is slightly increasing. This opposite pattern reveals the complex characteristics of sulfur pollution in the urban region. We do not clearly figure out this difference at this present moment, but anyhow, at least we can recognize the necessity of percentile trend analysis, providing the additional important information in detail.

Finally, we performed the analysis of trends in each day of week. This analysis enables us to check if there is a different trend of urban air pollution between the weekday and weekend period. Although the median trend of air pollutants between weekday and weekend periods is not much different (Figure 6), an interesting feature can be found; decreasing (increasing) trends tend to be stronger (weaker) in the middle of weekdays, but weaker (stronger) in the weekend. Considering that the higher concentration of air pollutants was usually detected in the middle of weekday as reported in some previous studies (e.g., Jin et al., 2005; Gong et al., 2007), urban activities degrading the air quality (e.g., manufacturing and industrial process) looks to be well controlled in South Korea.

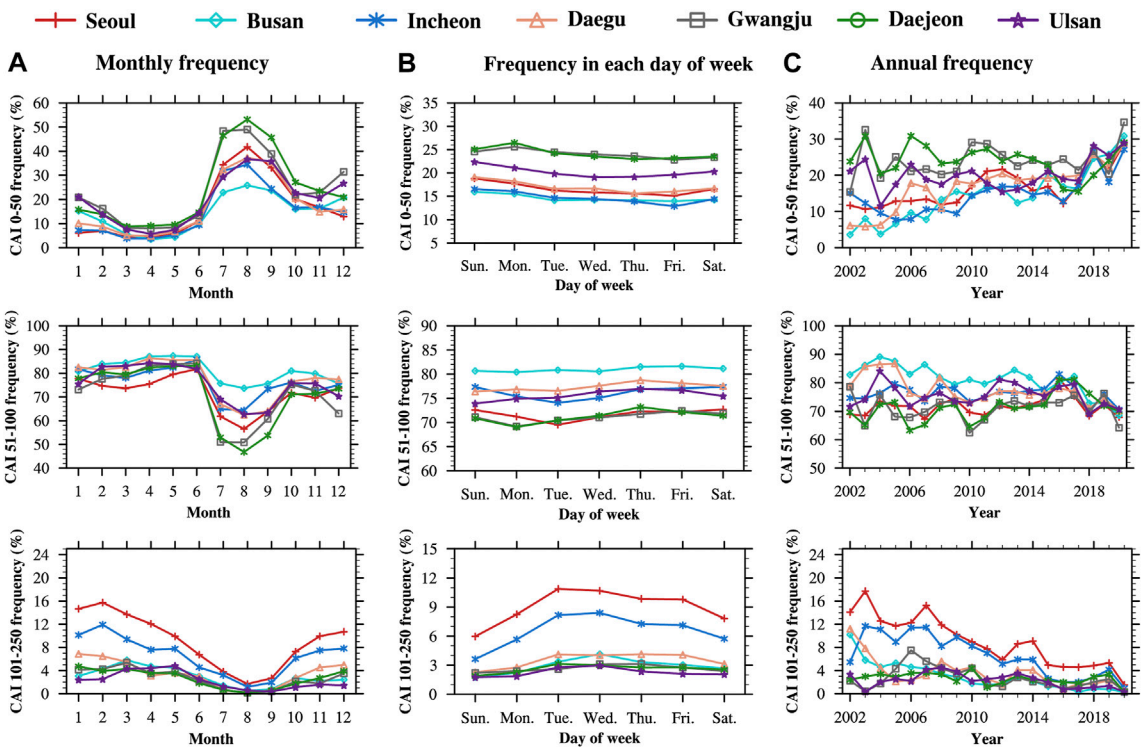

FIGURE 7
During the research period (2002–2020), frequency of CAI grades (CAI "good" for 0-50, CAI "moderate for 51–100, and CAI "unhealthy" for 101–250) in multiple time scale: **(A)** monthly frequency, **(B)** frequency in each day of week, and **(C)** annual frequency in seven megacities, South Korea.

Trends of 10th and 90th percentiles are rather different from the median trend patterns; They are opposite between Saturday and Sunday (Supplementary Figures S8, S9). Decrease of 10th and 90th PM_{10} and NO_2 percentiles is rather clear on Saturday but not on Sunday, in general. In contrast, decrease of 10th and 90th SO_2 and CO percentiles is strong in Sunday, but weaker in Saturday. Considering that SO_2 and CO tend to be more emitted from the fossil fuel combustion rather than the emission of aerosol (PM_{10}) and NO_2, we guess that fuel combustion-related industrial activities and manufacturing process may be still active on Saturday, resulted in weak decrease of SO_2 and CO. On Sunday, SO_2 and CO can be diminished but PM_{10} and NO_2 cannot have a large decrease if industrial activities are really ceased much but private activities are large enough. But this is just conjecture and the reason to induce this Saturday-Sunday difference is not clearly understood yet. Further study will be strongly required for better interpretation.

CAI patterns in Korean megacities

Lastly, we assessed the mean pattern and long-term variation of air quality in Korean megacities based on CAI values estimated by the combined evaluation of PM_{10}, O_3, NO_2, SO_2, and CO used in this study. As mentioned in chapter 3.1, there are four grades of CAI: Good (CAI from 0 to 50), Moderate (CAI from 51 to 100), Unhealthy (CAI from 101 to 250), and Very unhealthy (CAI > 250). Fortunately, there was no case classified in "Very unhealthy" in our study period. Thus, we examined how many cases were categorized into "Good," "Moderate," and "Unhealthy" grades, and how their frequencies have varied (Figure 7).

The monthly variation of CAI frequencies (Figure 7A) shows that the frequency of "Unhealthy" is the highest in winter (DJF) when the aerosol and its precursor species is largely emitted and accumulated. Reversely, the frequency of "Good" is generally high in summer (JJA). But there is the large difference among seven megacities; Daejeon and Gwangju show higher, but Busan and Incheon show relatively lower frequency of "Good" grade. In every year of South Korea, the rainy season (called Jangma) occurs from late June to middle of August. Therefore, the air pollutants are much washed out (Kim et al., 2014; Yoo et al., 2014), resulted in high number of "Good" grade. Nevertheless, we can see a weird difference of "Good" grade among seven cities. An interesting feature here is the lower number of "Good"

grade in Busan, Incheon, and Ulsan that are located in the coastal region, and these megacities usually have a large number of visitors who enjoy the summer vacation. Probably the anthropogenic emission from these visitors' activities and accompanying high traffic can disturb the improvement of local air quality. When CAI frequencies were compared among days of week (Figure 7B), there are not many significant features. The only obvious pattern is the weekday-weekend difference of "Unhealthy" frequency, which is about ~5% at maximum. Here the difference between Saturday and Sunday, and the difference between Monday and other weekdays was also found, as discussed with Figure 3.

In terms of the long-term trends of CAI (Figure 7C), the number of "Moderate" grade is most frequent every year in all seven cities, and its annual variation is consistent from 2002 to 2020, meaning that the normal condition has been well maintained. The number of "Unhealthy" grade is the least in Korean megacities. Different from "Moderate" grade, the number of "Good" and "Unhealthy" shows long-term change: increase of "Good" cases but decrease of "Unhealthy" cases. Specifically, the number of "Good" generally becomes higher, particularly in high-populated megacities (Seoul, Busan, Incheon, and Daegu). In contrast, "Unhealthy" cases tend to decrease, particularly Seoul and Incheon. These results well describe the steady improvement of air quality in Korean megacities during recent ~20 years. For example, the frequency of "Unhealthy" days in Seoul is higher than "Good" days in 2002, but this pattern becomes totally opposite in 2020. As examined so far, it seems that the decreasing pattern of PM_{10} and NO_2 dominantly leads the advanced air quality in Korean megacities. Nevertheless, Korean megacities still experience ~5% "Unhealthy" air quality condition in a year. These air quality conditions are determined by the high ozone level that is the only air pollutants showing the increasing trend at this present moment. Korean government will definitely conduct a dense preparation to avoid the health damage from the ozone pollution (Hwang et al., 2016) in the future.

Summary and conclusion

This study investigated several temporal (inter-annual, monthly, and weekly variation) patterns of air pollutants (PM_{10}, O_3, NO_2, SO_2, and CO) in seven megacities in South Korea. Most of air pollutants fortunately show the long-term decrease, but O_3 only has the strong increasing trend, meaning that the control of ozone pollution is the urgent issue to mitigate the future urban air pollution in South Korea. From a seasonal point of view, wintertime air pollution is still most serious in Korean cities. Considering the weaker monsoon effect can exacerbate the air pollution over the Korean peninsula and East Asia (Jeong and Park, 2017; Zou et al., 2017), the stronger reduction of local emission is required in the Korean megacities. Also, our analysis of weekly pattern suggested the air quality on Monday and Saturday seems located in the transition between the weekday and weekend. Since the weekly transportation between urban and suburban area becomes invigorative due to the enlargement of megacity area, we may need to examine the air quality in these transition days of week separately from the typical weekday and weekend period. One more point that we would underline in this study is the usefulness of percentile analysis, enabling us to assess the temporal variation of urban air quality in the background and high-polluted condition. We believe that the percentile analysis provides the meaningful idea additionally for the urban air quality diagnosis, not found in the mean-pattern based analysis. Some deeper analyses should be continued with the usage of social information related to the urban activity (e.g., traffic amount, power sources, *etc.*).

The number and size of megacity is continuously increasing in a global scale, and more people will live in the urban area. Although the governmental policy is prepared for whole country, this is why the environmental policy for the urban region is usually considered more significantly. In spite of recent findings for the large influence of long-range transboundary transport (Lee S. et al., 2019; Lee et al., 2021), synoptic meteorology (Bae et al., 2021; Ku et al., 2021), and climate variability (Jeong et al., 2018; Kim et al., 2021) to the air quality in South Korea, basic tactics to reduce the urban air pollution still lie on the control of local emission and anthropogenic activity. We confirmed this effect based on the COVID-19 period, showing the air quality enhancement by smaller anthropogenic activities (Koo et al., 2020; Park et al., 2021b). The analysis for temporal properties of air pollutants reveals which efforts are urgently requested. Based on this study, we can discover some unwatched features of air quality in Korean megacities; The ozone pollution is consistently serious in all seven megacities for a long time regardless of the local level of NO_2, the attention to the SO_2 pollution looks still needed for the coastal cities, and air quality on Saturday is not quite clean different from the typical expectation. We hope that these findings will be useful in the policy making processes for the improvement of air quality in Korean megacities.

Data availability statement

Publicly available datasets were analyzed in this study. This data can be found here: The surface measurement air pollutants datasets analyzed for this study can be found in the AIRKOREA https://www.airkorea.or.kr/index. The population census datasets analyzed for this study can be found in KOrean Statistical Information Service (KOSIS) https://kosis.kr/index/index.do.

Author contributions

J-HK designed the whole structure of this research, supervised the whole process of this research, and prepared the fund for this research. TL and J-HK performed the analysis mainly with the significant assistance from SG and SP for the establishment of dataset and methodology. YL and JP put the weight on the literature review of this research topic and excavated issues that this research need to examine. All authors participated the repeated discussion based on the results. TL and J-HK wrote the manuscript mainly, and SG, YL, SP, and JP improved the draft manuscript.

Funding

This work was supported by the National Research Foundation of Korea (NRF) grant funded by the Korea government (MSIT) (No. NRF-2020R1C1C1011624). This work was also supported from the National Institute of Environmental Research (NIER), funded by the Ministry of Environment (MOE) of the Republic of Korea (NIER 2022-01-01-001).

Conflict of interest

The authors declare that the research was conducted in the absence of any commercial or financial relationships that could be construed as a potential conflict of interest.

Publisher's note

All claims expressed in this article are solely those of the authors and do not necessarily represent those of their affiliated organizations, or those of the publisher, the editors and the reviewers. Any product that may be evaluated in this article, or claim that may be made by its manufacturer, is not guaranteed or endorsed by the publisher.

Supplementary material

The Supplementary Material for this article can be found online at: https://www.frontiersin.org/articles/10.3389/fenvs.2022.915531/full#supplementary-material

References

Almeida, S., Pio, C., Freitas, M., Reis, M., and Trancoso, M. (2006). Source apportionment of atmospheric urban aerosol based on weekdays/weekend variability: Evaluation of road re-suspended dust contribution. *Atmos. Environ.* 40, 2058–2067. doi:10.1016/j.atmosenv.2005.11.046

Bae, C., Kim, H. C., Kim, B.-U., and Kim, S. (2020). Surface ozone response to satellite-constrained NOx emission adjustments and its implications. *Environ. Pollut.* 258, 113469. doi:10.1016/j.envpol.2019.113469

Bae, M., Kim, B.-U., Kim, H. C., Kim, J., and Kim, S. (2021). Role of emissions and meteorology in the recent $PM_{2.5}$ changes in China and South Korea from 2015 to 2018. *Environ. Pollut.* 270, 116233. doi:10.1016/j.envpol.2020.116233

Bhardwaj, P., Ki, S. J., Kim, Y. H., Woo, J. H., Song, C. K., Park, S. Y., et al. (2019). Recent changes of trans-boundary air pollution over the yellow sea: Implications for future air quality in South Korea. *Environ. Pollut.* 247, 401–409. doi:10.1016/j.envpol.2019.01.048

Che, H., Xia, X., Zhu, J., Li, Z., Dubovik, O., Holben, B., et al. (2014). Column aerosol optical properties and aerosol radiative forcing during a serious haze-fog month over North China Plain in 2013 based on ground-based sunphotometer measurements. *Atmos. Chem. Phys.* 14, 2125–2138. doi:10.5194/acp-14-2125-2014

Chen, W., Tang, H., and Zhao, H. (2015). Diurnal, weekly and monthly spatial variations of air pollutants and air quality of Beijing. *Atmos. Environ.* 119, 21–34. doi:10.1016/j.atmosenv.2015.08.040

Chen, D., Wang, X., Nelson, P., Li, Y., Zhao, N., Zhao, Y., et al. (2017). Ship emission inventory and its impact on the PM2. 5 air pollution in Qingdao Port, North China. *Atmos. Environ.* 166, 351–361. doi:10.1016/j.atmosenv.2017.07.021

Cho, J., Kim, H., and Chung, Y. (2021). Spatio-temporal changes of PM10 trends in South Korea caused by East Asian atmospheric variability. *Air Qual. Atmos. Health* 14, 1001–1016. doi:10.1007/s11869-021-00995-y

Choi, K.-C., Lee, J.-J., Bae, C. H., Kim, C.-H., Kim, S., Chang, L.-S., et al. (2014). Assessment of transboundary ozone contribution toward South Korea using multiple source–receptor modeling techniques. *Atmos. Environ.* 92, 118–129. doi:10.1016/j.atmosenv.2014.03.055

Choi, Y., Kim, H., and Lee, J.-T. (2018). Temporal variability of short term effects of PM10 on mortality in Seoul, Korea. *Sci. total Environ.* 644, 122–128. doi:10.1016/j.scitotenv.2018.06.275

Choi, S.-W., Kim, T., Lee, H.-K., Kim, H.-C., Han, J., Lee, K.-B., et al. (2020). Analysis of the national air pollutant emission inventory (CAPSS 2016) and the major cause of change in republic of Korea. *Asian J. Atmos. Environ* 14, 422–445. doi:10.5572/ajae.2020.14.4.422

Clarke, K., Kwon, H.-O., and Choi, S.-D. (2014). Fast and reliable source identification of criteria air pollutants in an industrial city. *Atmos. Environ.* 95, 239–248. doi:10.1016/j.atmosenv.2014.06.040

Crawford, J. H., Ahn, J.-Y., Al-Saadi, J., Chang, L., Emmons, L. K., Kim, J., et al. (2021). The Korea–United States air quality (KORUS-AQ) field study. *Elementa* 9, 1–27. doi:10.1525/elementa.2020.00163

Eck, T., Holben, B., Kim, J., Beyersdorf, A., Choi, M., Lee, S., et al. (2020). Influence of cloud, fog, and high relative humidity during pollution transport events in South Korea: Aerosol properties and $PM_{2.5}$ variability. *Atmos. Environ.* 232, 117530. doi:10.1016/j.atmosenv.2020.117530

Elansky, N., Shilkin, A., Ponomarev, N., Semutnikova, E., and Zakharova, P. (2020). Weekly patterns and weekend effects of air pollution in the Moscow megacity. *Atmos. Environ.* 224, 117303. doi:10.1016/j.atmosenv.2020.117303

Ghim, Y. S., Chang, Y.-S., and Jung, K. (2015). Temporal and spatial variations in fine and coarse particles in Seoul, Korea. *Aerosol Air Qual. Res.* 15, 842–852. doi:10.4209/aaqr.2013.12.0362

Ghim, Y. S., Kim, J. Y., and Chang, Y.-S. (2017). Concentration variations in particulate matter in Seoul associated with Asian dust and smog episodes. *Aerosol Air Qual. Res.* 17, 3128–3140. doi:10.4209/aaqr.2016.09.0414

Gong, D. Y., Ho, C. H., Chen, D., Qian, Y., Choi, Y. S., Kim, J., et al. (2007). Weekly cycle of aerosol-meteorology interaction over China. *J. Geophys. Res.* 112, D22202. doi:10.1029/2007jd008888

Huang, W., Tan, J., Kan, H., Zhao, N., Song, W., Song, G., et al. (2009). Visibility, air quality and daily mortality in Shanghai, China. *Sci. Total Environ.* 407, 3295–3300. doi:10.1016/j.scitotenv.2009.02.019

Huryn, S. M., and Gough, W. A. (2014). Impact of urbanization on the ozone weekday/weekend effect in Southern Ontario, Canada. *Urban Clim.* 8, 11–20. doi:10.1016/j.uclim.2014.03.005

Hwang, S. H., Choi, Y.-H., Paik, H. J., Wee, W. R., Kim, M. K., Kim, D. H., et al. (2016). Potential importance of ozone in the association between outdoor air pollution and dry eye disease in South Korea. *JAMA Ophthalmol.* 134, 503. doi:10.1001/jamaophthalmol.2016.0139

Jeong, J. I., and Park, R. J. (2017). Winter monsoon variability and its impact on aerosol concentrations in East Asia. *Environ. Pollut.* 221, 285–292. doi:10.1016/j.envpol.2016.11.075

Jeong, J. I., Park, R. J., and Yeh, S.-W. (2018). Dissimilar effects of two el niño types on $PM_{2.5}$ concentrations in East Asia. *Environ. Pollut.* 242, 1395–1403. doi:10.1016/j.envpol.2018.08.031

Jin, M., Shepherd, J. M., and King, M. D. (2005). Urban aerosols and their variations with clouds and rainfall: A case study for New York and houston. *J. Geophys. Res.* 110, D10S20. doi:10.1029/2004jd005081

KECO (2022a). *Introduction to comprehensive air-quality index (CAI)*. Incheon, Republic of Korea Korea Environmental Corporation. [Online]. Available at: https://www.airkorea.or.kr/eng/khaiInfo?pMENU_NO=166 (Accessed March 13, 2022).

KECO (2022b). *NIER (National Institute of Environmental Research) dataset from air quality monitoring sites*. Incheon, Republic of Korea Korea Environmental Corporation. [Online]. Available at: https://www.airkorea.or.kr/web/last_amb_hour_data?pMENU_NO=123 (Accessed March 13, 2022).

Kim, B.-J., Kwon, J.-W., Seo, J.-H., Kim, H.-B., Lee, S.-Y., Park, K.-S., et al. (2011). Association of ozone exposure with asthma, allergic rhinitis, and allergic sensitization. *Ann. Allergy, Asthma & Immunol.* 107, 214–219.e1. doi:10.1016/j.anai.2011.05.025

Kim, S., Hong, K.-H., Jun, H., Park, Y.-J., Park, M., Sunwoo, Y., et al. (2014). Effect of precipitation on air pollutant concentration in Seoul, Korea. *Asian J. Atmos. Environ.* 8, 202–211. doi:10.5572/ajae.2014.8.4.202

Kim, H. C., Kim, S., Kim, B.-U., Jin, C.-S., Hong, S., Park, R., et al. (2017). Recent increase of surface particulate matter concentrations in the Seoul Metropolitan Area, Korea. *Sci. Rep.* 7, 4710. doi:10.1038/s41598-017-05092-8

Kim, S., Jeong, D., Sanchez, D., Wang, M., Seco, R., Blake, D., et al. (2018). The controlling factors of photochemical ozone production in Seoul, South Korea. *Aerosol Air Qual. Res.* 18, 2253–2261. doi:10.4209/aaqr.2017.11.0452

Kim, J.-H., Kim, S.-J., Youn, D., Kim, M.-K., Kim, J.-H., Kim, J., et al. (2021). Impact of north atlantic-East Asian teleconnections on extremely high january PM10 cases in Korea. *Environ. Pollut.* 290, 118051. doi:10.1016/j.envpol.2021.118051

Kim, Y. P., and Lee, G. (2018). Trend of air quality in Seoul: Policy and science. *Aerosol Air Qual. Res.* 18, 2141–2156. doi:10.4209/aaqr.2018.03.0081

Koo, J.-H., Kim, J., Lee, J., Eck, T. F., Lee, Y. G., Park, S. S., et al. (2016). Wavelength dependence of Ångström exponent and single scattering albedo observed by skyradiometer in Seoul, Korea. *Atmos. Res.* 181, 12–19. doi:10.1016/j.atmosres.2016.06.006

Koo, J.-H., Kim, J., Lee, Y. G., Park, S. S., Lee, S., Chong, H., et al. (2020). The implication of the air quality pattern in South Korea after the COVID-19 outbreak. *Sci. Rep.* 10, 22462. doi:10.1038/s41598-020-80429-4

KOSIS. 2021. *Population census [online]*. Daejeon, Republic of Korea Korean Statistical Information Service. Available at: https://kosis.kr/statHtml/statHtml.do?orgId=101&tblId=DT_1IN1502&vw_cd=MT_ZTITLE&list_id=A11_2015_1_10_10&scrId=&seqNo=&lang_mode=ko&obj_var_id=&itm_id=&conn_path=MT_ZTITLE&path=%252FstatisticsList%252FstatisticsListIndex.do [Accessed 13 March 2022].

Ku, H.-Y., Noh, N., Jeong, J.-H., Koo, J.-H., Choi, W., Kim, B.-M., et al. (2021). Classification of large-scale circulation patterns and their spatio-temporal variability during High-PM_{10} events over the Korean Peninsula. *Atmos. Environ.* 262, 118632. doi:10.1016/j.atmosenv.2021.118632

Lee, M. (2014). An analysis on the concentration characteristics of PM2. 5 in Seoul, Korea from 2005 to 2012. *Asia. Pac. J. Atmos. Sci.* 50, 585–594. doi:10.1007/s13143-014-0048-z

Lee, Y. G., Ho, C.-H., Kim, J.-H., and Kim, J. (2015). Quiescence of Asian dust events in South Korea and Japan during 2012 spring: Dust outbreaks and transports. *Atmos. Environ.* 114, 92–101. doi:10.1016/j.atmosenv.2015.05.035

Lee, S., Kim, J., Choi, M., Hong, J., Lim, H., Eck, T. F., et al. (2019a). Analysis of long-range transboundary transport (LRTT) effect on Korean aerosol pollution during the KORUS-AQ campaign. *Atmos. Environ.* 204, 53–67. doi:10.1016/j.atmosenv.2019.02.020

Lee, S. W., Yon, D. K., James, C. C., Lee, S., Koh, H. Y., Sheen, Y. H., et al. (2019b). Short-term effects of multiple outdoor environmental factors on risk of asthma exacerbations: Age-stratified time-series analysis. *J. Allergy Clin. Immunol.* 144, 1542–1550.e1. e1. doi:10.1016/j.jaci.2019.08.037

Lee, D., Wang, S.-Y. S., Zhao, L., Kim, H. C., Kim, K., Yoon, J.-H., et al. (2020). Long-term increase in atmospheric stagnant conditions over northeast Asia and the role of greenhouse gases-driven warming. *Atmos. Environ.* 241, 117772. doi:10.1016/j.atmosenv.2020.117772

Lee, S., Kim, M., Kim, S.-Y., Lee, D.-W., Lee, H., Kim, J., et al. (2021). Assessment of long-range transboundary aerosols in Seoul, South Korea from geostationary ocean color imager (GOCI) and ground-based observations. *Environ. Pollut.* 269, 115924. doi:10.1016/j.envpol.2020.115924

Li, X., Chen, Q., Zheng, X., Li, Y., Han, M., Liu, T., et al. (2019). Effects of ambient ozone concentrations with different averaging times on asthma exacerbations: A meta-analysis. *Sci. Total Environ.* 691, 549–561. doi:10.1016/j.scitotenv.2019.06.382

Liu, S., Fang, S., Liang, M., Sun, W., and Feng, Z. (2019). Temporal patterns and source regions of atmospheric carbon monoxide at two background stations in China. *Atmos. Res.* 220, 169–180. doi:10.1016/j.atmosres.2019.01.017

Luo, Y., Zheng, X., Zhao, T., and Chen, J. (2014). A climatology of aerosol optical depth over China from recent 10 years of MODIS remote sensing data. *Int. J. Climatol.* 34, 863–870. doi:10.1002/joc.3728

Marr, L. C., and Harley, R. A. (2002). Modeling the effect of weekday–weekend differences in motor vehicle emissions on photochemical air pollution in central California. *Environ. Sci. Technol.* 36, 4099–4106. doi:10.1021/es020629x

Masiol, M., Agostinelli, C., Formenton, G., Tarabotti, E., and Pavoni, B. (2014). Thirteen years of air pollution hourly monitoring in a large city: Potential sources, trends, cycles and effects of car-free days. *Sci. Total Environ.* 494, 84–96. doi:10.1016/j.scitotenv.2014.06.122

ME (2006). *Comprehensive Air-Quality index (CAI) development·dissemination for air quality evaluation*. Sejong, Republic of Korea: Ministry of Envrionment. [Online]. Available at: http://www.me.go.kr/home/web/board/read.do;jsessionid=AMjygdihuvFIT8wbEhB7SOdeVHrMwgmZ6cxfrxLtzSaAcD2mgGXhzHak2FOnDAwS.meweb2vhost_servlet_engine1?pagerOffset=7650&maxPageItems=10&maxIndexPages=10&searchKey=&searchValue=&menuId=&orgCd=&boardMasterId=1&boardCategoryId=&boardId=149437&decorator= (Accessed March 13, 2022).

ME·NIER (2021). Instruction of installation and management for ir quality monitoring network *[Online]*. Ministry of Environment·National Institute of Environmental Research. Available: https://www.airkorea.or.kr/web/board/3/267/?pMENU_NO=145 (Accessed March 13, 2022).

Oh, I.-B., Kim, Y.-K., Hwang, M.-K., Kim, C.-H., Kim, S., Song, S.-K., et al. (2010). Elevated ozone layers over the Seoul Metropolitan Region in Korea: Evidence for long-range ozone transport from eastern China and its contribution to surface concentrations. *J. Appl. Meteorology Climatol.* 49, 203–220. doi:10.1175/2009jamc2213.1

Park, D.-H., Kim, S.-W., Kim, M.-H., Yeo, H., Park, S. S., Nishizawa, T., et al. 2021a. Impacts of local versus long-range transported aerosols on PM10 concentrations in Seoul, Korea: an estimate based on 11-year PM10 and lidar observations. *Science of the Total Environment* 750, 141739. doi:10.1016/j.scitotenv.2020.141739

Park, H., Jeong, S., Koo, J.-H., Sim, S., Bae, Y., Kim, Y., et al. (2021b). Lessons from COVID-19 and Seoul: Effects of reduced human activity from social distancing on urban CO_2 concentration and air quality. *Aerosol Air Qual. Res.* 21, 200376. doi:10.4209/aaqr.2020.07.0376

Pope, C. A., III, Muhlestein, J. B., May, H. T., Renlund, D. G., Anderson, J. L., Horne, B. D., et al. (2006). Ischemic heart disease events triggered by short-term exposure to fine particulate air pollution. *Circulation* 114, 2443–2448. doi:10.1161/circulationaha.106.636977

Seo, J., Youn, D., Kim, J., and Lee, H. (2014). Extensive spatiotemporal analyses of surface ozone and related meteorological variables in South Korea for the period 1999–2010. *Atmos. Chem. Phys.* 14, 6395–6415. doi:10.5194/acp-14-6395-2014

Shin, H., Cho, K., Han, J., Kim, J., and Kim, Y. (2012). The effects of precursor emission and background concentration changes on the surface ozone concentration over Korea. *Aerosol Air Qual. Res.* 12, 93–103. doi:10.4209/aaqr.2011.09.0141

Sorte, S., Rodrigues, V., Borrego, C., and Monteiro, A. (2020). Impact of harbour activities on local air quality: A review. *Environ. Pollut.* 257, 113542. doi:10.1016/j.envpol.2019.113542

SS (2022). Key policy: Air pollution monitoring network *[online]*. Seoul, Republic of Korea: Seoul solution. Available at: https://seoulsolution.kr/en/node/6540 (Accessed March 22, 2022).

Stavrakou, T., MþLLER, J.-F., Bauwens, M., Boersma, K., and Van Geffen, J. (2020). Satellite evidence for changes in the NO_2 weekly cycle over large cities. *Sci. Rep.* 10, 10066. doi:10.1038/s41598-020-66891-0

Su, T., Li, Z., and Kahn, R. (2018). Relationships between the planetary boundary layer height and surface pollutants derived from lidar observations over China: Regional pattern and influencing factors. *Atmos. Chem. Phys.* 18, 15921–15935. doi:10.5194/acp-18-15921-2018

Sun, W., Shao, M., Granier, C., Liu, Y., Ye, C., Zheng, J., et al. (2018). Long-term trends of Anthropogenic SO_2, NOx, CO, and NMVOCs emissions in China. *Earth's. Future* 6, 1112–1133. doi:10.1029/2018ef000822

Tsai, Y. I., and Chen, C.-L. (2006). Characterization of Asian dust storm and non-Asian dust storm $PM_{2.5}$ aerosol in southern Taiwan. *Atmos. Environ.* 40, 4734–4750. doi:10.1016/j.atmosnv.2006.04.038

Vuong, Q. T., Park, M.-K., Van Do, T., Thang, P. Q., and Choi, S.-D. (2022). Driving factors to air pollutant reductions during the implementation of intensive

controlling policies in 2020 in Ulsan, South Korea. *Environ. Pollut.* 292. doi:10.1016/j.envpol.2021.118380

Wang, T., Xue, L., Brimblecombe, P., Lam, Y. F., Li, L., Zhang, L., et al. (2017). Ozone pollution in China: A review of concentrations, meteorological influences, chemical precursors, and effects. *Sci. Total Environ.* 575, 1582–1596. doi:10.1016/j.scitotenv.2016.10.081

Xia, X., Eck, T. F., Holben, B. N., Phillippe, G., and Chen, H. (2008). Analysis of the weekly cycle of aerosol optical depth using AERONET and MODIS data. *J. Geophys. Res.* 113, D14217. doi:10.1029/2007jd009604

Xie, Y., Zhao, B., Zhang, L., and Luo, R. (2015). Spatiotemporal variations of PM2. 5 and PM10 concentrations between 31 Chinese cities and their relationships with SO2, NO2, CO and O3. *Particuology* 20, 141–149. doi:10.1016/j.partic.2015.01.003

Xing, Y.-F., Xu, Y.-H., Shi, M.-H., and Lian, Y.-X. (2016). The impact of $PM_{2.5}$ on the human respiratory system. *J. Thorac. Dis.* 8, E69–E74. doi:10.3978/j.issn.2072-1439.2016.01.19

Yang, M., Bell, T. G., Hopkins, F. E., and Smyth, T. J. (2016). Attribution of atmospheric sulfur dioxide over the English Channel to dimethyl sulfide and changing ship emissions. *Atmos. Chem. Phys.* 16, 4771–4783. doi:10.5194/acp-16-4771-2016

Yeo, M. J., and Kim, Y. P. (2021). Long-term trends of surface ozone in Korea. *J. Clean. Prod.* 294, 125352. doi:10.1016/j.jclepro.2020.125352

Yoo, J.-M., Lee, Y.-R., Kim, D., Jeong, M.-J., Stockwell, W. R., Kundu, P. K., et al. (2014). New indices for wet scavenging of air pollutants (O_3, CO, NO_2, SO_2, and PM_{10}) by summertime rain. *Atmos. Environ.* 82, 226–237. doi:10.1016/j.atmosenv.2013.10.022

Yoo, J.-M., Jeong, M.-J., Kim, D., Stockwell, W. R., Yang, J.-H., Shin, H.-W., et al. (2015). Spatiotemporal variations of air pollutants (O_3, NO_2, SO_2, CO, PM_{10}, and VOCs) with land-use types. *Atmos. Chem. Phys.* 15, 10857–10885. doi:10.5194/acp-15-10857-2015

Yoon, J., Pozzer, A., Chang, D. Y., Lelieveld, J., Kim, J., Kim, M., et al. (2016). Trend estimates of AERONET-observed and model-simulated AOTs between 1993 and 2013. *Atmos. Environ.* 125, 33–47. doi:10.1016/j.atmosenv.2015.10.058

Zhang, X., Liu, J., Han, H., Zhang, Y., Jiang, Z., Wang, H., et al. (2020). Satellite-observed variations and trends in carbon monoxide over Asia and their sensitivities to biomass burning. *Remote Sens.* 12, 830. doi:10.3390/rs12050830

Zhang, Y.-L., and Cao, F. (2015). Fine particulate matter ($PM_{2.5}$) in China at a city level. *Sci. Rep.* 5, 14884. doi:10.1038/srep14884

Zhao, S., Yu, Y., Yin, D., He, J., Liu, N., Qu, J., et al. (2016). Annual and diurnal variations of gaseous and particulate pollutants in 31 provincial capital cities based on *in situ* air quality monitoring data from China National Environmental Monitoring Center. *Environ. Int.* 86, 92–106. doi:10.1016/j.envint.2015.11.003

Zong, Q., Mao, R., Gong, D.-Y., Wu, C., Pu, B., Feng, X., et al. (2021). Changes in dust activity in spring over East Asia under a global warming scenario. *Asia. Pac. J. Atmos. Sci.* 57, 839–850. doi:10.1007/s13143-021-00224-7

Zou, Y., Wang, Y., Zhang, Y., and Koo, J.-H. (2017). Arctic sea ice, Eurasia snow, and extreme winter haze in China. *Sci. Adv.* 3, e1602751. doi:10.1126/sciadv.1602751

frontiers | Frontiers in Ecology and Evolution

TYPE Original Research
PUBLISHED 03 August 2022
DOI 10.3389/fevo.2022.930569

OPEN ACCESS

EDITED BY
Yuzhong Zhang,
Westlake University, China

REVIEWED BY
Xianyu Yang,
Chengdu University of Information Technology, China
Haolin Wang,
Sun Yat-sen University, China

*CORRESPONDENCE
Guiqin Zhang
zhangguiqin@sdjzu.edu.cn

SPECIALTY SECTION
This article was submitted to Interdisciplinary Climate Studies, a section of the journal Frontiers in Ecology and Evolution

RECEIVED 28 April 2022
ACCEPTED 08 July 2022
PUBLISHED 03 August 2022

CITATION
Liang D, Yan H, Tian Y, Liu Y, Hao S, Bai H, Zhang G and Deng W (2022) Identification of key controlling factors of ozone pollution in Jinan, northern China over 2013–2020.
Front. Ecol. Evol. 10:930569.
doi: 10.3389/fevo.2022.930569

Identification of key controlling factors of ozone pollution in Jinan, northern China over 2013–2020

Di Liang[1], Huaizhong Yan[2], Yong Tian[3], Yalin Liu[3], Saimei Hao[4], Haoqiang Bai[4], Guiqin Zhang[4]* and Wei Deng[1]

[1]School of Science, Shandong Jianzhu University, Jinan, China, [2]Shandong Provincial Eco-Environment Monitoring Center, Jinan, China, [3]Shandong Provincial Jinan Eco-Environment Monitoring Center, Jinan, China, [4]School of Municipal and Environmental Engineering, Shandong Jianzhu University, Jinan, China

Urban ozone (O_3) pollution has become a prominent environmental threat to public health while the relationship between O_3 formation and driving factors remains elusive, particularly for megacities in the Shandong Peninsula of China. In this study, we use intensive ambient measurements of trace gases to comprehensively investigate the magnitude of O_3 pollution in Jinan city from 2013 to 2020. Further, emission inventory and OMI NO_2 columns are used for probing changes in precursor emissions. Ground-level measurements indicate degraded O_3 air quality afterward in 2015 and depict city-wide elevated O_3 levels (higher than 140 $\mu g/m^3$ in the warm season). For precursor emissions, it is found that NO_x emissions have decreased more than 30% due to successful regulation efforts, which is in excellent agreement with NO_2 columns from OMI. The method of objective synoptic weather pattern classification [T-Mode principal component analysis (PCT)] is adopted to distinguish the associated meteorological parameters under various synoptic patterns which govern the variability in regional O_3 levels. Among identified synoptic patterns, Type 2 and Type 8 featured by low sea level pressure (SLP), high temperature, and strong ultraviolet radiation are the most prevalent synoptic patterns in spring and summer, respectively, which are prone to the occurrence of O_3 exceedances. This work provides a detailed view of long-term O_3 levels and the relationship between precursors and meteorological conditions in a typical densely populated city in northern China, showing implications for developing O_3 mitigation strategies.

KEYWORDS

ozone (O_3), objective synoptic weather pattern classification, NO_x, air pollution, emission inventory

Introduction

Ozone (O_3) is a criteria air pollutant that forms by photochemical reactions of precursors [NO_x and volatile organic compounds (VOCs)] under the presence of sunlight. Exposure to elevated O_3 levels could induce a variety of adverse impacts on human health (Cromar et al., 2019; Lin et al., 2019; Yang et al., 2021) and affect the productivity of sensitive vegetation (Vlachokostas et al., 2010; Dong et al., 2021; Li et al., 2021a). With the rapid industrialization and urbanization in China, severe O_3 pollution has emerged as a pressing environmental concern in densely populated areas (Chan and Yao, 2008; Li and Huang, 2019; Dai et al., 2021; Li et al., 2021b; Xiong et al., 2021; Zhao et al., 2021), which is contrary to the steadily improved particle matter (PM) pollution over the past decade. In particular, Beijing-Tianjin-Hebei (BTH), Yangtze River Delta (YRD), Pearl River Delta (PRD), and Sichuan Basin (SCB) are recognized as the most polluted city clusters in China. Given the urgent demand to mitigate urban O_3 pollution, it is crucial to characterize O_3 variations and identify dominant factors that influence O_3 formation over major city clusters.

The fate, transport, and removal of O_3 in the atmosphere are largely determined by meteorological conditions (Wang et al., 2010; Pawlak and Jarosławski, 2014). Synoptic patterns act as the crucial factor which governs the variations of O_3 levels induced by meteorological processes. Prior studies have investigated the relationship between various synoptic patterns and associated O_3 changes in China through both modeling and statistical studies. Using a circulation classification method, Shu et al. (2016) found that the circulation pattern featured by stable western Pacific subtropical high could enhance O_3 production over the YRD and indicated that the frequency of this meteorological phenomenon showed a strong relationship with O_3 exceedance events. Wang et al. (2021) reported that synoptic forcing dominated by sea-land breeze contributed significantly to O_3 formation in PRD. Yang et al. (2020) distinguished two typical synoptic patterns which triggered O_3 episodes in the SCB based on the WRF-CMAQ model. Previous studies assessing the impacts of synoptic patterns on O_3 have been restricted to several typical O_3 episodes and mainly focused on BTH, YRD, PRD, and SCB, while little attention has been paid to megacities within these city clusters.

Jinan, the capital of Shandong Province, is recognized as one of the "2+26" cities of the channel of the BTH city cluster. While there have been considerable efforts in reducing air pollutants emissions, O_3 levels have increased by 17.3% in 2019 compared with 2013 in Jinan, posing a challenge to environmental management. The statistical assessment reported that O_3 exceedance is the major pollutant in 2020, accounting for 42.2% of air quality non-attainment in Jinan. The recent analysis by Lyu et al. (2019) demonstrated that O_3 episodes in Jinan are closely related to synoptic-driven dynamics. Therefore, a better understanding of dominant processes that affect O_3 levels in Jinan is required to design and implement effective O_3 regulation policies.

In this work, ambient measurements of trace gases from 2013 to 2020 are used to determine the magnitude of O_3 pollution in Jinan. Historical O_3 levels and occurrence of exceedance events in Jinan are revealed. Further, the trend of NO_x emissions is inferred from bottom-up emission inventory, as well as satellite observations, aimed at probing precursor emission changes from 2013 to 2020. Daily synoptic patterns are classified based on the objective T-Mode principal component analysis (PCT) method then combine with ground-level ambient measurements for examining the influence of different synoptic patterns on O_3 levels in Jinan. The findings of this study not only help understand long-term variations of O_3 levels but also have strong implications for designing and implementing effective regulatory policies in Jinan.

Materials and methods

Ambient air quality measurements

In this study, gaseous pollutants concentrations are collected from 14 national ambient air quality monitoring sites operated by China National Environmental Monitoring Center (CNEMC) and 11 local ambient air quality monitoring stations operated by Jinan Eco-environment Monitoring Center from 2013 to 2020 (locations shown in Figure 1). To identify variations among different type sites, ShiJianCeZhan (SJCZ), JiShuXueYuan (JSXY), PaoMaLing (PML), NongKeSuo (NKS), and ZhongZiCangKu (ZZKU) are selected for representing O_3 levels at urban, industry, rural, suburb, and near-road (traffic) conditions (marked in Figure 1).

Here, we use the maximum daily average 8 h (MDA8) O_3 concentration as the metric for assessing O_3 pollution and MDA8 values >160 $\mu g/m^3$ are identified as an exceedance day (which corresponds to National Ambient Air Quality Standards (NAAQS) (GB 3095-2012) for O_3 concentration). Daily average concentrations of CO, NO_2, and NO are calculated from hourly observations.

ERA5 reanalysis dataset

The ERA5 meteorological reanalysis from the European Center for Medium-Range Weather Forecasts (ECMWF) is adopted to represent meteorological phenomena over north China. The study domain is from 30°N to 42°N along the latitude and from 108°to 128°E along the longitude with a grid resolution of 0.25° × 0.25°. The daily sea level pressure (SLP) is used to classify the synoptic weather pattern

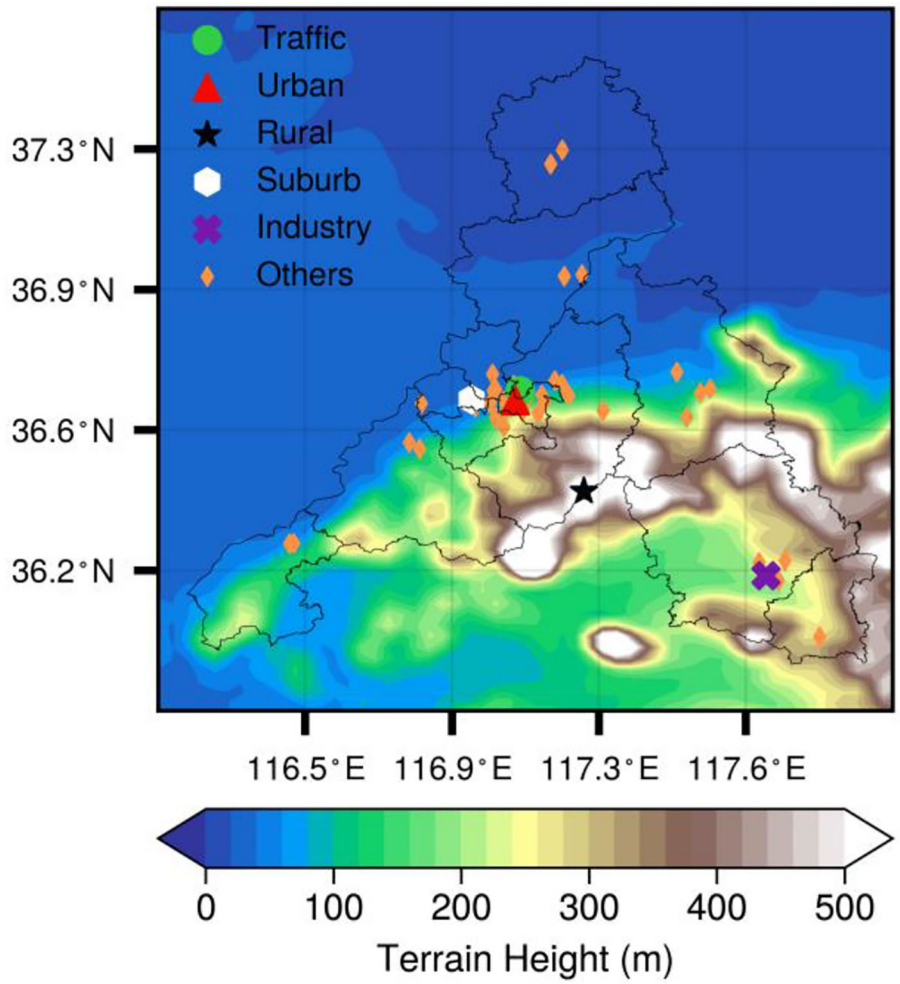

FIGURE 1
Locations of ambient air quality monitoring stations in Jinan city.

at 08:00 local solar time (LST) from 2013 to 2020 over North China (Li et al., 2017). Other meteorological factors include 2 m temperature (T2M), relative humidity at 1,000 Pa (RH), downward ultraviolet radiation (UVB), and 10 m of wind fields.

Objective synoptic pattern classification

The obliquely rotated principal components analysis (PCA) in T-mode (PCT) is a mathematical method based on data similarity and variance maximization (Huth, 1996; Huth et al., 2008). This method decomposes the original high-dimensional data into the principal component matrix and the loadings matrix then selects several principal components with large variance contributions and further rotates them obliquely. Finally, the classification of synoptic patterns is performed for each time period according to the calculated loadings. The synoptic classification software (http://www.cost733.org) (Philipp et al., 2010) is provided by the COST action 733, so as to obtain more accurate and stable synoptic patterns.

Anthropogenic emission inventory

The Multi-resolution Emission Inventory for China (MEIC) is a bottom-up inventory that has been widely used in quantifying anthropogenic emissions and chemical transport modeling (Wu et al., 2020; Yang et al., 2020; Wang et al., 2022). It provides monthly human-induced emissions across China, with a spatial resolution of $0.25^{\circ} \times 0.25^{\circ}$ (Zheng et al., 2018). Anthropogenic sectors in MEIC include power plants, agriculture, industrial, transportation, and residential.

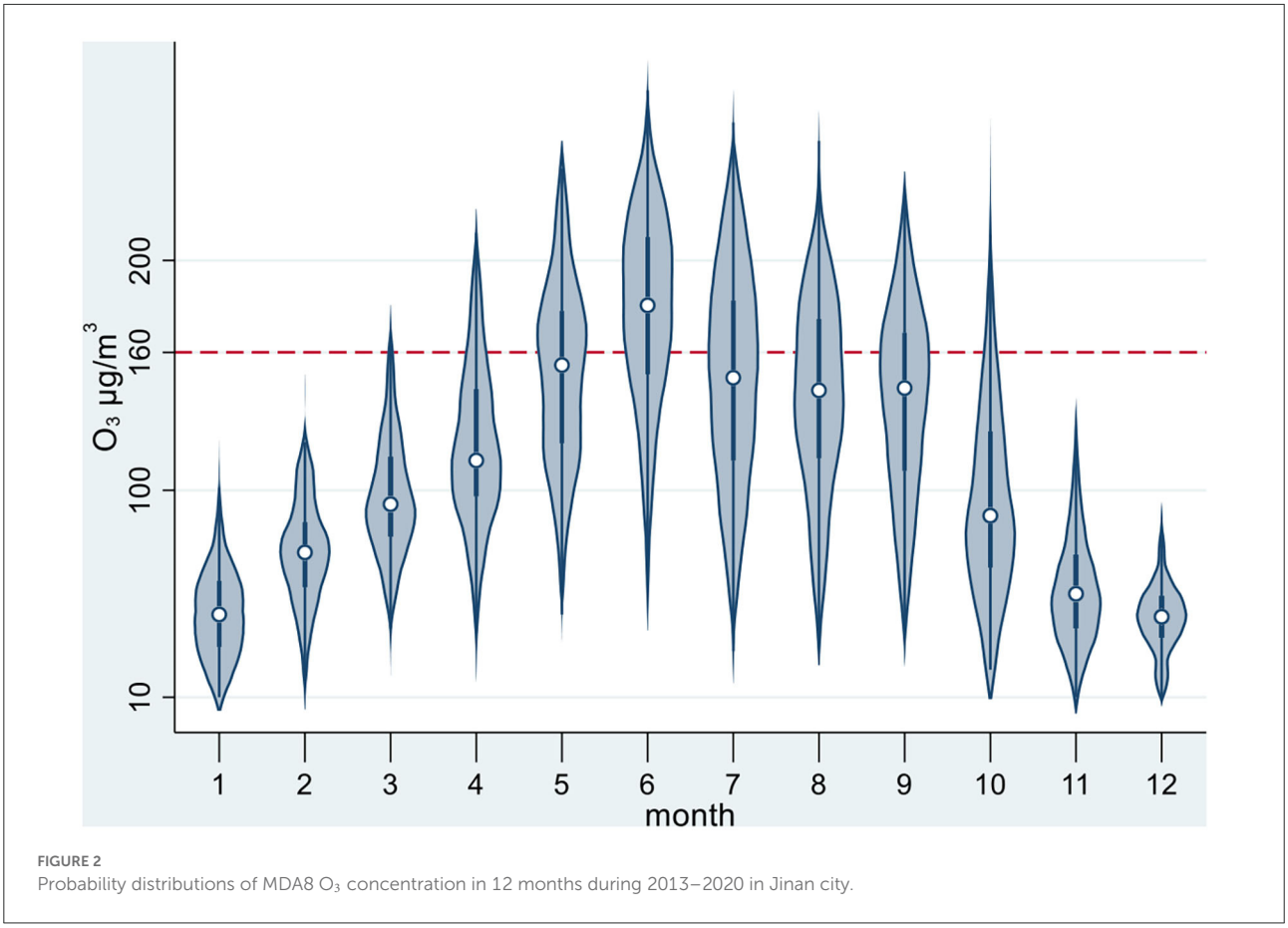

FIGURE 2
Probability distributions of MDA8 O_3 concentration in 12 months during 2013–2020 in Jinan city.

TABLE 1 O_3 exceedance events and annual average MDA8 O_3 concentrations from 2013 to 2020 in Jinan city.

Year	O_3 exceedance days	Proportion of O_3 alert day %	Annual average O_3 ($\mu g/m^3$)
2013	63	17.3	98.0
2014	81	22.2	106.6
2015	66	18.1	102.5
2016	71	19.4	105.2
2017	69	18.9	108.4
2018	92	25.2	114.2
2019	94	25.8	114.5
2020	73	20.0	111.5

TABLE 2 Average concentration of MDA8 O_3 over Jinan city during warm season (April–September) from 2013 to 2020.

Year	Industry	Traffic	Urban	Suburb	Rural
2013	137.5	156.1	129.4	117.8	122.0
2014	114.9	148.4	131.5	132.2	152.6
2015	104.6	118.1	123.9	132.6	147.8
2016	126.8	146.6	131.4	133.2	161.4
2017	128.4	140.6	146.7	134.0	131.8
2018	150.5	152.5	146.3	146.0	127.0
2019	162.2	161.9	159.6	149.4	132.0
2020	143.0	153. 7	157.4	145.4	139.8

OMI NO_2 columns

Ozone Monitoring Instrument (OMI) is an ultraviolet-visible spectrometer onboard the NASA Aura satellite, with a sun-synchronous orbit that crosses the Equator at around 13:45 local time (Levelt et al., 2006; Boersma et al., 2011). It has a 2,600 km cross-track swath length which enables daily coverage across the globe. Here, the tropospheric NO_2 retrieval product developed from Quality Assurance for Essential Climate Variables (QA4ECV) is used for inferring the trend in NO_2 columns and probing the spatial changes in NO_2 columns in Jinan over time (Zara et al., 2018). The development algorithm of QA4ECV NO_2 from OMI involves multi-step processes, including the calculation of air mass factor (AMF), conversion of NO_2 slant column to NO_2 vertical column, and data assimilation

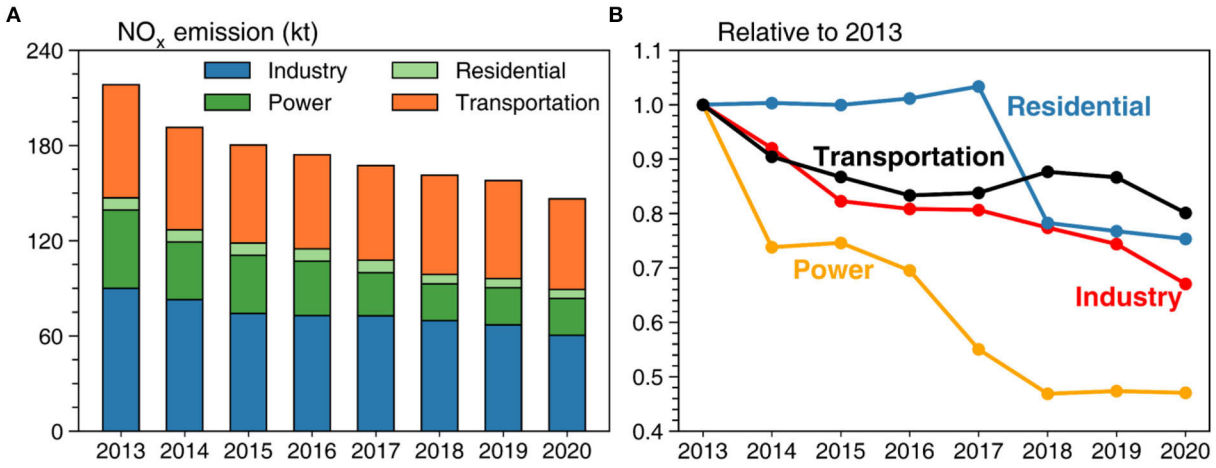

FIGURE 3
Sector-based anthropogenic NO*x* emissions derived from MEIC inventory during warm season (April-September) from 2013 to 2020 in Jinan city.

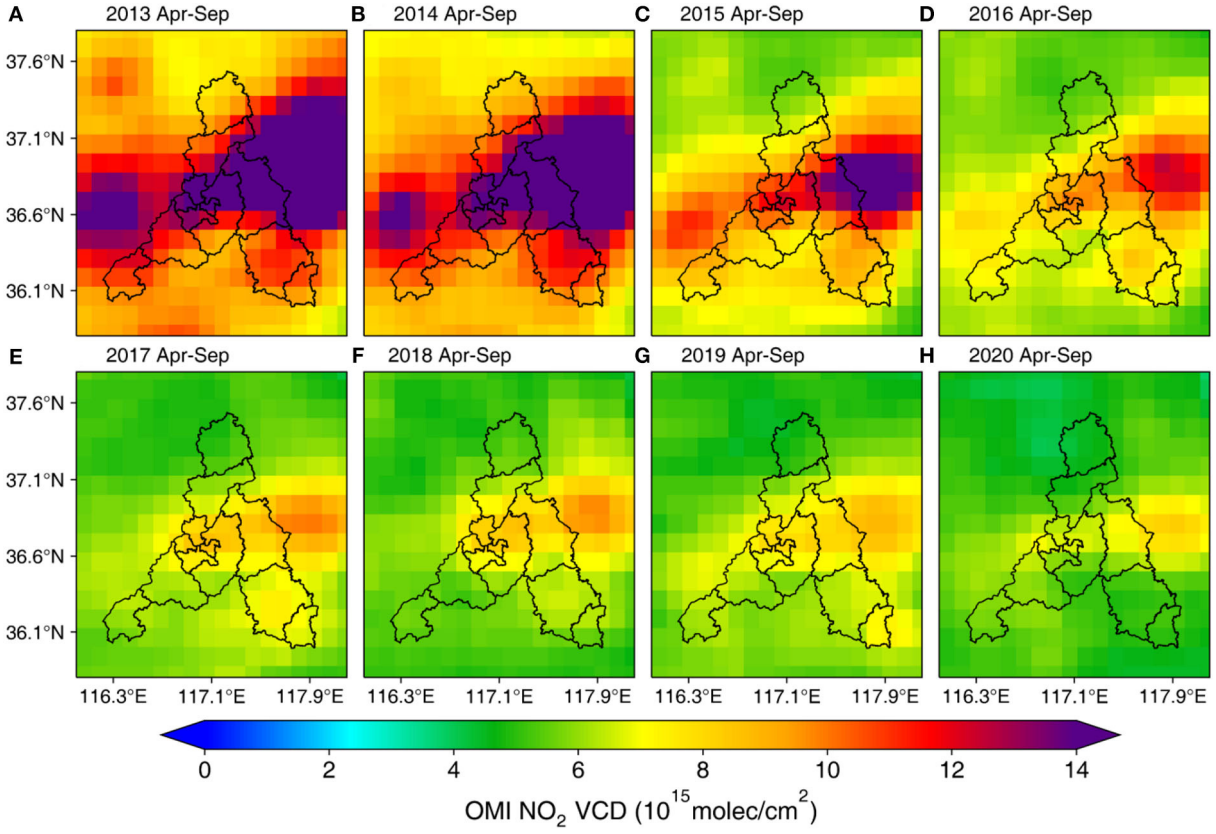

FIGURE 4
OMI mean tropospheric NO_2 vertical column density (VCD) during warm season (April–September) from 2013 to 2020 over Jinan city.

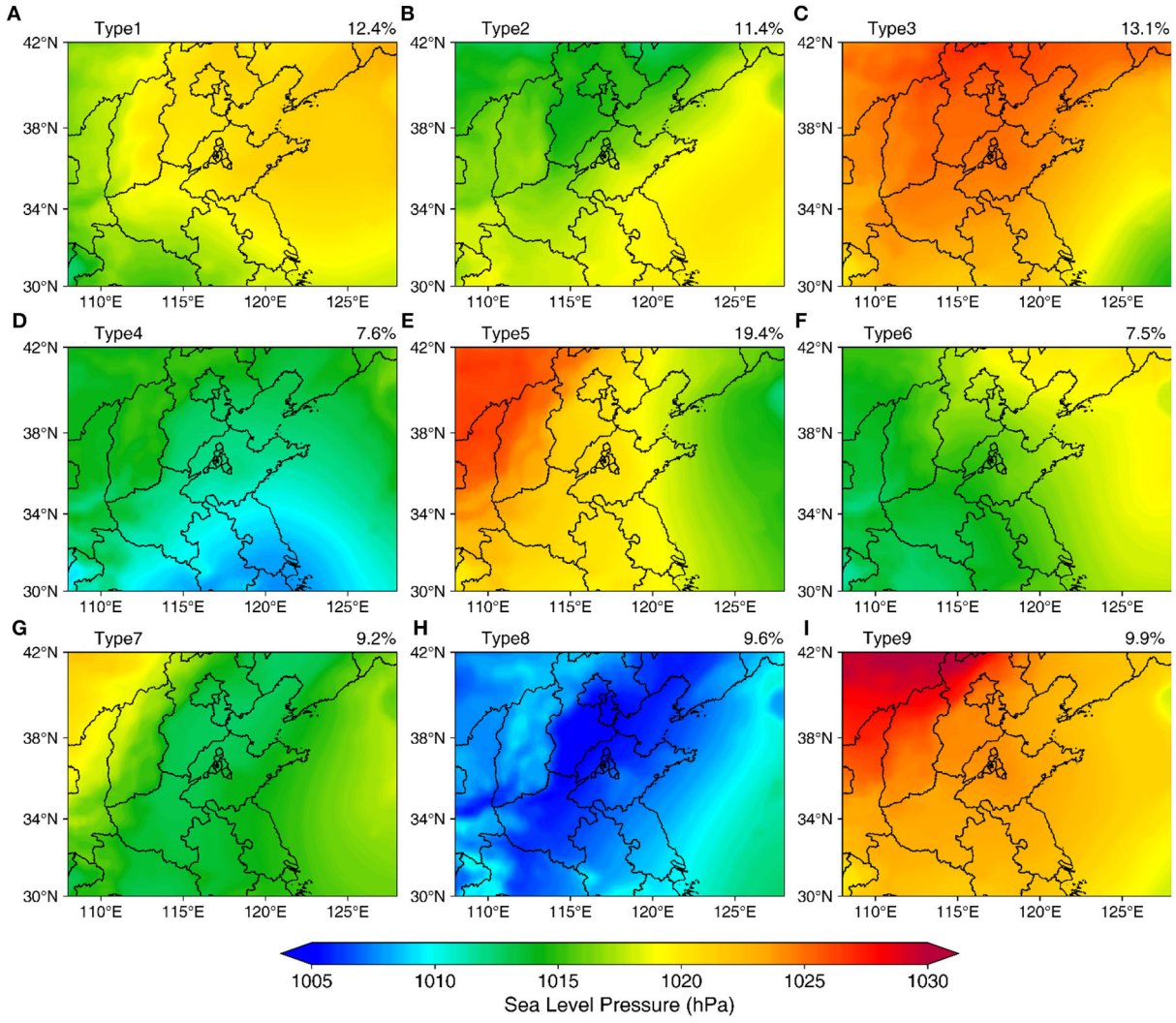

FIGURE 5
Sea level pressure distribution in 9 synoptic patterns during 2013–2020 in North China.

from global chemical transport model TM5. The accuracy of QA4ECV NO_2 has undergone rigorous validation against global differential optical absorption spectroscopy (DOAS) instrument networks (Compernolle et al., 2020).

Results and discussions

Characteristics of O_3 pollution in Jinan

As shown in Figure 2, summertime O_3 pollution in Jinan was quite severe which featured numerous O_3 exceedances and a progressively increase in the number of O_3 exceedance days was found over the study period (Table 1). The annual average MDA8 O_3 concentrations in Jinan were 98.0, 106.6, 102.5, 105.2, 108.4, 114.2, 114.5, and 111.5 $\mu g/m^3$ from 2013 to 2020, respectively. Since 2015, both O_3 exceedances and annual average MDA8 O_3 levels gradually increased and spiked to peak levels in 2019, implying that worsen O_3 air quality has become an emerging environmental concern in Jinan. Table 2 presents average MDA8 O_3 concentrations for different types of ambient monitoring stations during the warm season (April–September) from 2013 to 2020. Specifically, the trend in O_3 variations is broadly consistent among selected typical sites (industrial, traffic, urban, and suburban), which featured by descending trends between 2013 and 2015 while degraded O_3 levels afterward 2016. It is worth noting that both averaged MDA8 O_3 concentrations at industrial and traffic sites during the warm season were in excess of the O_3 standard (160 $\mu g/m^3$) in China's current National Ambient Air Quality Standards (NAAQS) in 2019, indicating the severity of O_3 pollution in Jinan.

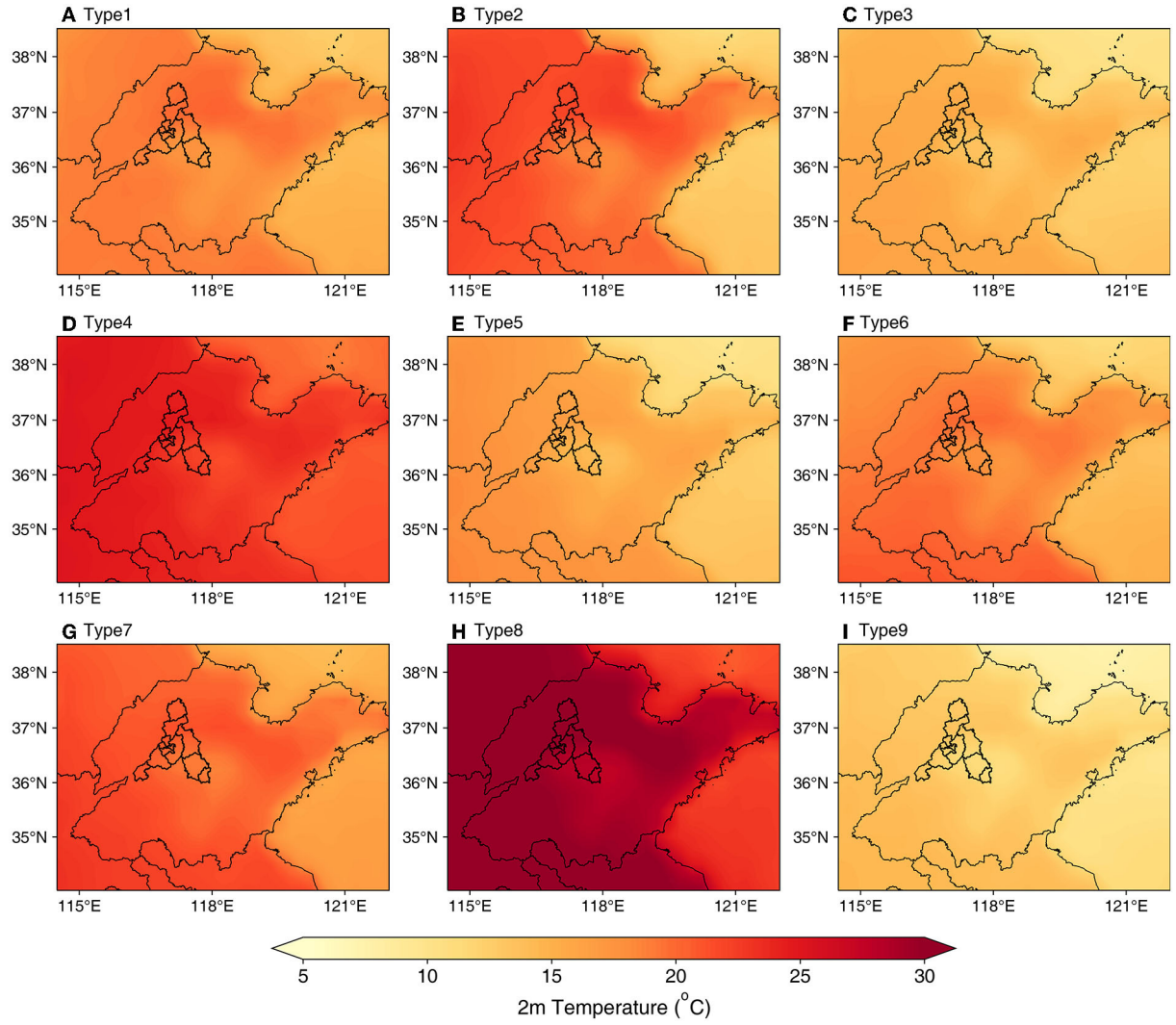

FIGURE 6
Air temperature at 2 m above the surface in 9 synoptic patterns during 2013–2020 in North China.

Trend of NO_x emissions in Jinan

Prior studies have demonstrated that urban O_3 formation is largely determined by the abundance of precursors which affects the O_3-VOCs-NO*x* sensitivity (Wu et al., 2022). To probe the variation of O_3 precursor emissions in Jinan, anthropogenic NO*x* emissions from MEIC inventory for the warm season (April–September) of 2013–2020 are derived, as shown in Figure 3. Starting in 2013, the MEIC inventory shows a continuous pattern of reductions in total NO*x* emissions due to the implementation of the Air Pollution Prevention and Control Action Plan (APPCAP), declining by 30.0% for the 2013–2020 period, whereas NO*x* emissions in each anthropogenic sector exhibit highly variable trend. Specifically, power plant emissions of NO*x* have declined more than 50.0% in 2020 compared with 2013, and industrial emissions show marked declines from 2013 to 2020. On the contrary, residential emissions persistently increased from 2013 to 2017, followed by a substantial decrease in 2018, implying the effectiveness of coal-to-gas initiatives in Jinan. Unlike power plants and industrial emissions, NO*x* emitted from traffic sources decreased from 2013 to 2016 followed by leveling off and even increased trend of NOx emissions afterward 2016, underlining the urgent need of taking action on regulating traffic NO*x* emissions in Jinan. It is worth mentioning that NO*x* emissions in 2020 significantly decreased compared with 2019, which could be linked to the reduced mobility attributed to COVID-19 lockdown measures (Zheng et al., 2021). In general, reductions in NO*x* emissions in Jinan from 2013 to 2020 are mainly contributed by regulation efforts on industrial and power

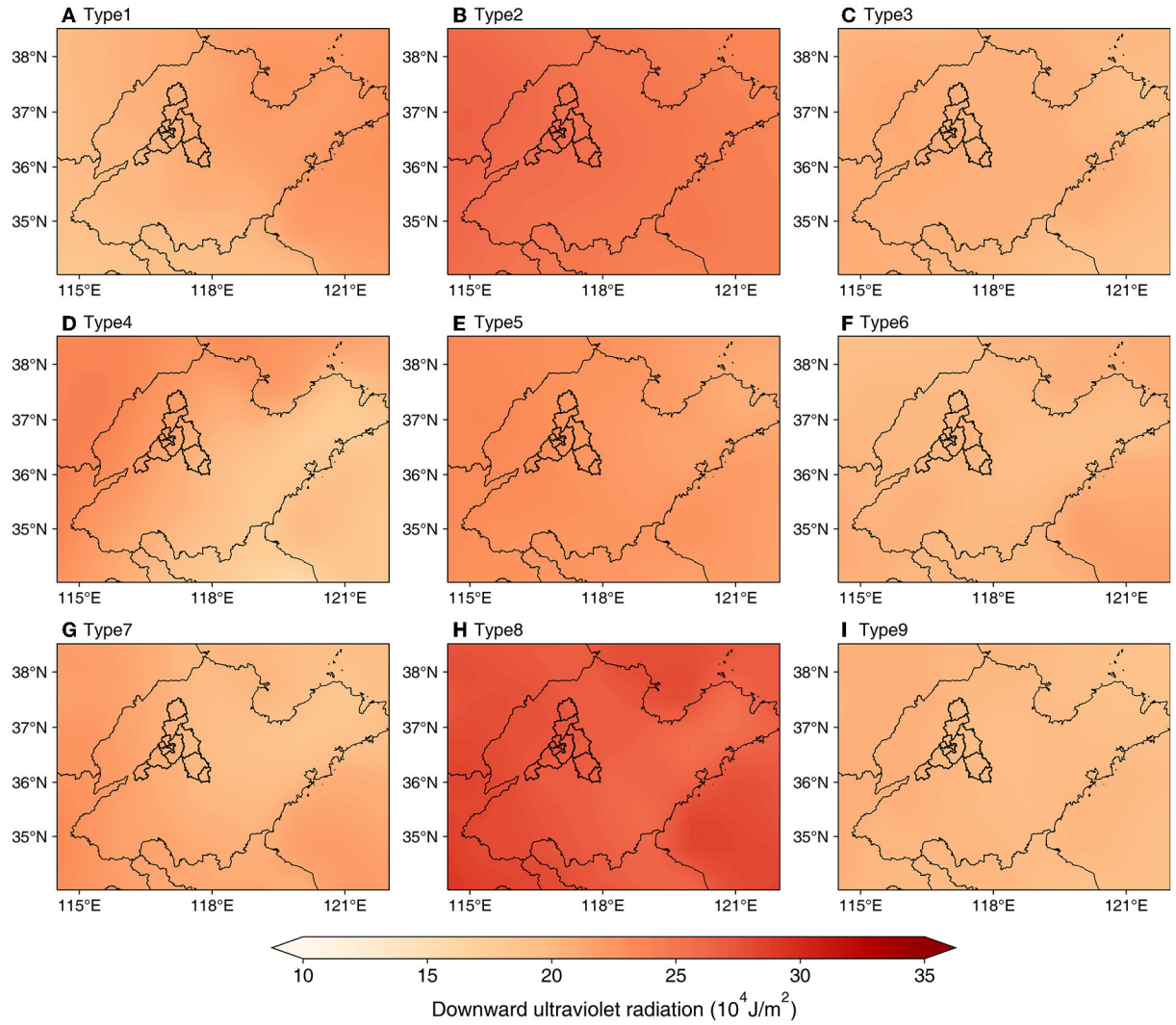

FIGURE 7
Downward UV radiation at the surface in 9 synoptic patterns during 2013–2020 in North China.

plant emissions, while traffic NO*x* emissions warrant further strict control.

Figure 4 presents tropospheric NO_2 columns from OMI during the warm season (April-September) from 2013 to 2020 over Jinan. For 2013, OMI depicts region-wide NO_2 spots, with peak levels higher than 14×10^{15} molec/cm^2. Interestingly, satellite observations indicate that emission control on NO_x introduced by APPCAP leads to substantial reductions in NO_x emissions over urban and suburban areas. As a result, NO_2 columns over urban areas of Jinan were even lower than 8×10^{15} molec/cm^2 for 2020. Compared with NO_x emissions estimated by MEIC, OMI NO_2 columns exhibit broadly consistent year-by-year changes and reduction magnitude. This phenomenon further confirms that control measures toward cutting NO_x emissions are effective for Jinan city from 2013 to 2020.

Relationship between synoptic patterns and ozone pollution

The synoptic weather pattern was classified into nine types by SLP based on the PCT method in North China (30° N–42°N, 108°E–128°E) from 2013 to 2020. Figure 5 depicts the spatial map of SLP among the identified 9 synoptic patterns. The spatial distribution of other key meteorological factors is presented in Figures 6–8. Furthermore, Table 3 lists monthly O_3 exceedances for Types 1–9 over the study period. Evidently, both the number of exceedance and the average MDA8 O_3 concentration in Type

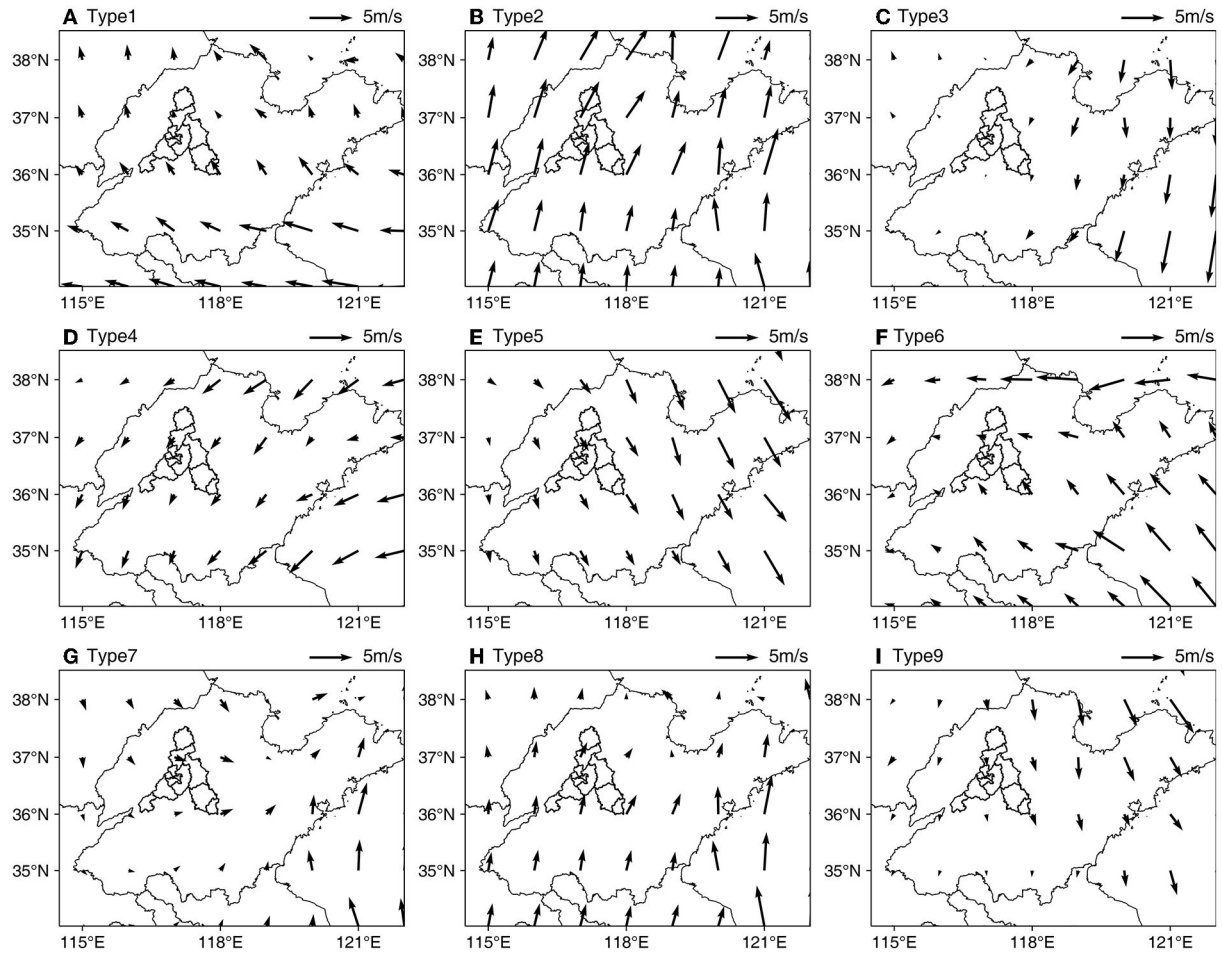

FIGURE 8
The 10-m wind in 9 synoptic patterns during 2013–2020 in North China.

8 is highest among identified synoptic patterns. In this cluster, the Shandong Peninsula, especially Jinan city, is situated in the center of the low-pressure system and is featured by low-pressure gradient and stagnant weather conditions, which are conducive to the accumulation of O_3 precursors. Furthermore, meteorological conditions in Type 8 are characterized by high temperatures (regional average higher than 30°C) and intense ultraviolet radiation. The combination of the abovementioned phenomenon modulated by synoptic patterns leads to severe O_3 pollution in Type 8. It is important to note that O_3 exceedances in the summer season (particularly June and July) largely correspond to the occurrence of Type 8.

Similarly, elevated O_3 levels are also depicted under the circulation pattern of Type 2. It can be clearly seen that this pattern is characterized by strong ultraviolet radiation and protracted higher temperature across Jinan and surrounding areas, which primes the landscape of O_3 formation. However, the strong southerly wind fields could carry some pollutants to downwind regions, which may enhance the ventilation across the study domain. Contrary to Type 8, the occurrence of Type 2 is mainly concentrated in the spring season. To a lesser extent, it can be clearly seen that Types 1, 4, and 5 also contribute to O_3 exceedances in summer. A detailed analysis shows that synoptic-driven weak wind fields in conjunction with stagnant conditions act as the governing factor in leading to the exceedances.

Conclusion

In this study, we adopt continuous ambient measurements from 2013 to 2020 for identifying variability in O_3 concentrations over Jinan city in Shandong Province. It is found that deteriorated O_3 pollution has emerged as a dominant environmental concern in the megacity, with a continuous increase in average MDA8 O_3 concentrations and exceedances events since 2015. Elevated O_3 levels are depicted across typical

TABLE 3 O_3 exceedance events in each month for Types 1–9 during 2013–2020.

Month	Type1	Type2	Type3	Type4	Type5	Type6	Type7	Type8	Type9
1	0	0	0	0	0	0	0	0	0
2	0	0	0	0	0	0	0	0	0
3	0	2	0	0	0	1	0	0	0
4	4	15	3	0	1	5	1	4	0
5	16	34	4	2	13	10	15	15	4
6	21	21	10	12	18	12	19	41	9
7	14	2	9	11	16	8	4	43	2
8	6	0	10	26	22	0	4	13	6
9	15	10	14	11	14	4	4	2	5
10	3	8	2	2	1	2	4	0	0
11	0	0	0	0	0	0	0	0	0
12	0	0	0	0	0	0	0	0	0

monitoring stations in each type, suggesting city-wide degraded O_3 air quality.

For precursor emissions, NO_x emissions from power plants (55%) and industrial (36%) sources substantially decreased over time due to the implementation of control strategies. However, traffic NO_x emissions remain a prominent concern which still maintains high levels of emissions. A persistent decrease of NO_2 columns is observed by OMI, adding support to the findings from the MEIC emission inventory. Given the continuous efforts on cutting NO_x emissions, quantification of VOCs emissions and joint regulation on NO_x and VOCs warrant further study.

Analysis of synoptic patterns shows that Type 2 and Type 8 are associated with higher O_3 concentrations, which correspond to a meteorological phenomenon, including low SLP, high temperature, and strong ultraviolet radiation. Under the influence of stagnant conditions in combination with meteorological conditions modulated by the synoptic pattern, these weather patterns govern the occurrence of exceedance events in spring and summer over Jinan from 2013 to 2020.

Overall, the characteristics and the influence of precursors and meteorological conditions on ozone in Jinan city were analyzed based on the mathematical models using the data of meteorological measurements and pollutant monitoring. This work provides insights into the magnitude of O_3 pollution in Jinan over time and distinguishes the trend of NO_x emissions through emission inventory and satellite data, which shapes a clear view of long-term O_3 variations. The classification of synoptic patterns clearly points to the relationship between O_3 pollution and distinct meteorological conditions driven by synoptic patterns, which shed light on the regulation of ambient O_3 in Jinan city.

Data availability statement

The original contributions presented in the study are included in the article/supplementary material, further inquiries can be directed to the corresponding author.

Author contributions

DL and GZ were responsible for the study concept and design. HY, YT, and YL contributed to the acquisition of the data. SH, HB, and WD assisted with the analyses and interpretation of the findings. DL drafted the initial manuscript. DL, GZ, HY, YT, YL, SH, HB, and WD critically reviewed the content and approved the final version of the manuscript for publication. All authors contributed to the article and approved the submitted version.

Funding

This work was supported by the Project Procurement of Atmospheric Source Apportionment of Jinan Government (No. 402015202000024-001), the Project of 20 Independent Training of Innovation Teams in Universities in Jinan (2020GXRC008), and the Planning Project of Commerce Statistical Society of China (2021STY30).

Conflict of interest

The authors declare that the research was conducted in the absence of any commercial or financial relationships that could be construed as a potential conflict of interest.

Publisher's note

References

Boersma, K. F., Eskes, H. J., Dirksen, R. J., van der A R. J., Veefkind, J. P., Stammes, P., et al. (2011). An improved tropospheric NO_2 column retrieval algorithm for the Ozone Monitoring Instrument. *Atmos. Meas. Tech.* 4, 1905–1928. doi: 10.5194/amt-4-1905-2011

Chan, C. K., and Yao, X. (2008). Air pollution in mega cities in China. *Atmos. Environ.* 42, 1–42. doi: 10.1016/j.atmosenv.2007.09.003

Compernolle, S., Verhoelst, T., Pinardi, G., Granville, J., Hubert, D., Keppens, A., et al. (2020). Validation of Aura-OMI QA4ECV NO2 climate data records with ground-based DOAS networks: the role of measurement and comparison uncertainties. *Atmos. Chem. Phys.* 20, 8017–8045. doi: 10.5194/acp-20-8017-2020

Cromar, K. R., Gladson, L. A., and Ewart, G. (2019). Trends in excess morbidity and mortality associated with air pollution above American thoracic society-recommended standards, 2008-2017. *Ann. Am. Thorac. Soc.* 16, 836–845. doi: 10.1513/AnnalsATS.201812-914OC

Dai, H., Zhu, J., Liao, H., Li, J., Liang, M., Yang, Y., et al. (2021). Co-occurrence of ozone and $PM_{2.5}$ pollution in the Yangtze River Delta over 2013-2019: spatiotemporal distribution and meteorological conditions. *Atmos. Res.* 249:105363. doi: 10.1016/j.atmosres.2020.105363

Dong, C., Gao, R., Zhang, X., Li, H., Wang, W., and Xue, L. (2021). Assessment of O_3-induced crop yield losses in Northern China during 2013–2018 using high-resolution air quality reanalysis data. *Atmos. Environ.* 259:118527. doi: 10.1016/j.atmosenv.2021.118527

Huth, R. (1996). An intercomparison of computer-assisted circulation classification methods. *Int. J. Climatol.* 16, 893–922. doi: 10.1002/(SICI)1097-0088(199608)16:8<893::AID-JOC51>3.0.CO;2-Q

Huth, R., Beck, C., Philipp, A., Demuzere, M., Ustrnul, Z., Cahynová, M., et al. (2008). Classifications of atmospheric circulation patterns: recent advances and applications. *Ann. N. Y. Acad. Sci.* 1146, 105–152. doi: 10.1196/annals.1446.019

Levelt, P. F., van den Oord, G. H. J., Dobber, M. R., Malkki, A., Visser, H., de Vries, J., et al. (2006). The ozone monitoring instrument. *IEEE Trans. Geosci. Remote Sens.* 44, 1093–1101. doi: 10.1109/TGRS.2006.872333

Li, C., Gu, X., Wu, Z., Qin, T., Guo, L., Wang, T., et al. (2021a). Assessing the effects of elevated ozone on physiology, growth, yield and quality of soybean in the past 40 years: a meta-analysis. *Ecotoxicol. Environ. Saf.* 208:111644. doi: 10.1016/j.ecoenv.2020.111644

Li, J., and Huang, X. (2019). Ground-level ozone concentration and landscape patterns in China's urban areas. *Photogramm. Eng. Remote Sensing* 85, 145–152. doi: 10.14358/PERS.85.2.145

Li, Y., Wang, X., Wu, Z., Li, L., Wang, C., Li, H., et al. (2021b). Atmospheric nitrous acid (HONO) in an alternate process of haze pollution and ozone pollution in urban Beijing in summertime: variations, sources and contribution to atmospheric photochemistry. *Atmos. Res.* 260:105689. doi: 10.1016/j.atmosres.2021.105689

Li, Z., Guo, J., Ding, A., Liao, H., Liu, J., Sun, Y., et al. (2017). Aerosol and boundary-layer interactions and impact on air quality. *Natl. Sci. Rev.* 4, 810–833. doi: 10.1093/nsr/nwx117

Lin, C. Y., Wang, C. M., Chen, M. L., and Hwang, B. F. (2019). The effects of exposure to air pollution on the development of uterine fibroids. *Int. J. Hyg. Environ. Health* 222, 549–555. doi: 10.1016/j.ijheh.2019.02.004

Lyu, X. P., Wang, N., Guo, H., Xue, L. K., Jiang, F., Zeren, Y. Z., et al. (2019). Causes of a continuous summertime O_3 pollution event in Jinan, a central city in the North China Plain. *Atmos. Chem. Phys.* 19, 3025–3042. doi: 10.5194/acp-19-3025-2019

Pawlak, I., and Jarosławski, J. (2014). *Analysis of Surface Ozone Variations Based on the Long-Term Measurement Series in Kraków (1854–1878), (2005–2013) and Belsk (1995–2012)*. Cham: Achievements, History and Challenges in Geophysics. doi: 10.1007/978-3-319-07599-0_18

Philipp, A., Bartholy, J., Beck, C., Erpicum, M., Esteban, P., Fettweis, X., et al. (2010). Cost733cat-A database of weather and circulation type classifications. *Phys. Chem. Earth* 35, 360–373. doi: 10.1016/j.pce.2009.12.010

Shu, L., Xie, M., Wang, T. J., Gao, D., Chen, P. L., Han, Y., et al. (2016). Integrated studies of a regional ozone pollution synthetically affected by subtropical high and typhoon system in the Yangtze River Delta region, China. *Atmos. Chem. Phys.* 16, 15801–15819. doi: 10.5194/acp-16-15801-2016

Vlachokostas, C., Nastis, S. A., Achillas, C., Kalogeropoulos, K., Karmiris, I., Moussiopoulos, N., et al. (2010). Economic damages of ozone air pollution to crops using combined air quality and GIS modelling. *Atmos. Environ.* 44, 3352–3361. doi: 10.1016/j.atmosenv.2010.06.023

Wang, H., Wu, K., Liu, Y., Sheng, B., Lu, X., He, Y., et al. (2021). Role of heat wave-induced biogenic VOC enhancements in persistent ozone episodes formation in Pearl River Delta. *J. Geophys. Res. Atmos.* 126:e2020JD034317. doi: 10.1029/2020JD034317

Wang, Y., Yang, X., Wu, K., Mei, H., Lu, Y., Smedt, I. D., et al. (2022). Long-term trends of ozone and precursors from 2013 to 2020 in a megacity (Chengdu), China: evidence of changing emissions and chemistry. *Atmos. Res.* 106309. doi: 10.1016/j.atmosres.2022.106309

Wang, Y., Zhang, Y., Hao, J., and Luo, M. (2010). Seasonal and spatial variability of surface ozone over China: contributions from background and domestic pollution. *Atmos. Chem. Phys. Discuss.* 10, 27853–27891. doi: 10.5194/acpd-10-27853-2010

Wu, K., Wang, Y., Qiao, Y., Liu, Y., Wang, S., Yang, X., et al. (2022). Drivers of 2013-2020 ozone trends in the Sichuan Basin, China: impacts of meteorology and precursor emission changes. *Environ. Pollut.* 300:118914. doi: 10.1016/j.envpol.2022.118914

Wu, K., Yang, X., Chen, D., Gu, S., Lu, Y., Jiang, Q., et al. (2020). Estimation of biogenic VOC emissions and their corresponding impact on ozone and secondary organic aerosol formation in China. *Atmos. Res.* 231:104656. doi: 10.1016/j.atmosres.2019.104656

Xiong, C., Wang, N., Zhou, L., Yang, F., Qiu, Y., Chen, J., et al. (2021). Component characteristics and source apportionment of volatile organic compounds during summer and winter in downtown Chengdu, Southwest China. *Atmos. Environ.* 258:118485. doi: 10.1016/j.atmosenv.2021.118485

Yang, J., Zhao, Y., Cao, J., and Nielsen, C. P. (2021). Co-benefits of carbon and pollution control policies on air quality and health till 2030 in China. *Environ. Int.* 152:106482. doi: 10.1016/j.envint.2021.106482

Yang, X., Wu, K., Wang, H., Liu, Y., Gu, S., Lu, Y., et al. (2020). Summertime ozone pollution in Sichuan Basin, China: Meteorological conditions, sources and process analysis. *Atmos. Environ.* 226:117392. doi: 10.1016/j.atmosenv.2020.117392

Zara, M., Boersma, K. F., De Smedt, I., Richter, A., Peters, E., Van Geffen, J. H. G. M., et al. (2018). Improved slant column density retrieval of nitrogen dioxide and formaldehyde for OMI and GOME-2A from QA4ECV: intercomparison, uncertainty characterization, and trends. *Atmos. Meas. Tech.* 11, 4033–4058. doi: 10.5194/amt-11-4033-2018

Zhao, H., Niu, Z., and Feng, X. (2021). Factors influencing improvements in air quality in Guanzhong cities of China, and variations therein for 2014-2020. *Urban Clim.* 38:10087. doi: 10.1016/j.uclim.2021.100877

Zheng, B., Tong, D., Li, M., Liu, F., Hong, C., Geng, G., et al. (2018). Trends in China's anthropogenic emissions since 2010 as the consequence of clean air actions. *Atmos. Chem. Phys.* 18, 14095–14111. doi: 10.5194/acp-18-14095-2018

Zheng, B., Zhang, Q., Geng, G., Chen, C., Shi, Q., Cui, M., et al. (2021). Changes in China's anthropogenic emissions and air quality during the COVID-19 pandemic in 2020. *Earth Syst. Sci. Data* 13, 2895–2907. doi: 10.5194/essd-13-2895-2021

frontiers | Frontiers in Environmental Science

TYPE Original Research
PUBLISHED 29 August 2022
DOI 10.3389/fenvs.2022.968507

OPEN ACCESS

EDITED BY
Haofei Yu,
University of Central Florida,
United States

REVIEWED BY
Ioannis Konstantinos Christodoulakis,
National and Kapodistrian University of Athens, Greece
Sampad Kumar Panda,
K L University, India

*CORRESPONDENCE
Jingyuan Li,
jingyuanli@nuist.edu.cn
Jianyong Lu,
jylu@nuist.edu.cn

SPECIALTY SECTION
This article was submitted to Atmosphere and Climate, a section of the journal Frontiers in Environmental Science

RECEIVED 14 June 2022
ACCEPTED 01 August 2022
PUBLISHED 29 August 2022

CITATION
Tian Y, Li J, Yang C, Cui J, Shen F, Lu J, Xiong S, Wei G, Li Z, Zhang H, Yang G, Wu Y, Wei Z, Jiang S, Yao J, Wang J and Zhu Z (2022), Effects of the annular eclipse on the surface O_3 in yunnan province, China.
Front. Environ. Sci. 10:968507.
doi: 10.3389/fenvs.2022.968507

Effects of the annular eclipse on the surface O_3 in yunnan province, China

Yufeng Tian[1,2], Jingyuan Li[1]*, Chaolei Yang[2], Jingqi Cui[1], Fuzhen Shen[3], Jianyong Lu[1]*, Shiping Xiong[1], Guanchun Wei[1], Zheng Li[1], Hua Zhang[1], Guanglin Yang[4,5], Yewen Wu[1], Zong Wei[2], Shuwen Jiang[1], Jingrui Yao[1], Jingye Wang[1] and Zhixin Zhu[1]

[1]Institute of Space Weather, School of Atmospheric Physics, Nanjing University of Information Science and Technology, Nanjing, China, [2]Kunming Comprehensive Survey Center of Natural Resources, China Geological Survey, Kunming, China, [3]Forschungszentrum Jülich, Institute of Energy and Climate Research, IEK-7: Stratosphere, Jülich, Germany, [4]Key Laboratory of Space Weather, National Center for Space Weather, China Meteorological Administration, Beijing, China., [5]Innovation Center for Feng Yun Meteorological Satellite (FYSIC), China Meteorological Administration, Beijing, China

The impact of the annual solar eclipse, starting on 21st June 2020, attributable to surface ozone concentration (O_3) has been investigated in this study. To estimate the influence of the solar eclipse on O_3 better, the variations of one reaction precursor of ozone production [nitrogen dioxide (NO_2)], coupled with the meteorological factors (including Total Solar Irradiance (TSI), Temperature (T), and Relative Humidity (RH)), were analyzed in Yunnan Province, China. The results show observed O_3 decreases from the beginning of the eclipse, reaching its minimum value when the eclipse left Yunnan province. During the period of the solar eclipse, the O_3 decrease lasted for 20 h with a reduction of more than 40%. The reduction of TSI lasted for 5 h with a maximum at -90%. Simultaneously, the temperature decreased but the relative humidity increased during the reduction in solar radiation. O_3 exhibits a significantly positive correlation with temperature and a negative correlation with relative humidity. However, NO_2 did not show a clear response with changes lasting for 4 h. O_3 and NO_2 show a negative correlation. The influence of CO on O_3 is minor except for Kunming. Thus, O_3 in seriously polluted cities is more sensitive to NO_2 and CO during the eclipse, such as in Kunming.

KEYWORDS

solar eclipse, surface ozone, total irradiance, CO, NO_2

Highlights

- (1) TSI decreases move from west to east with a reduction of more than 90% during the solar eclipse on June 21st, 2020, and last 3 h in Yunnan.
- (2) O_3 decreases more than 40% during solar eclipse, and starts to recover in Yunnan when the solar eclipse leaves Yunnan.
- (3) Both meteorological factors and precursors are important for affecting O_3 changes during solar eclipse.

1 Introduction

A moon shadow is cast in the Earth's atmosphere and surface when the Moon occurs between the Earth and the Sun. The moon's shadow moves through the Earth at thousands of kilometers per hour. The region marked by eclipse experiences a phenomenon similar to sunrise and sunset in a short time. The solar radiation in the moon's shadow sharply decreases and then recovers after the solar eclipse ends. The effects of different eclipse events on Earth are unique due to different paths and occurrence times (Baran et al., 2003). Therefore, the obscuration effects of the eclipse on the atmosphere are most attractive. The previous studies, although very limited due to rarely eclipse events, have shown the obscuration effects of the eclipse on the ionosphere, stratosphere, and surface, involving solar radiation, meteorological parameters, pollutants, and so on (e.g., Amiridis et al., 2007; Gerasopoulos et al., 2007; Kazadzis et al., 2007; Chung et al., 2010; Panda et al., 2015).

Significant reductions in global radiation, surface temperature, relative humidity, and wind speed can be observed during solar eclipses (e.g., Anderson et al., 1972; Founda et al., 2007; Pasachoff, 2009). The temperature in the Ahmedabad, India decreased by 0.5°C during a maximum solar obscuration on 11 August 1999, accompanied by a drop in the wind speed (Krishnan et al., 2004). A decrease of 0.7 m s^{-1} in wind speed and 3°C in temperature can be seen in southern England during the total solar eclipse on 11 August 1999 (Gray and Harrison 2012). Aplin et al. (2016) reviewed radiation changes during 44 solar eclipses from 1834 to 2006. They found that the radiation decreased to zero during total solar eclipses, whereas radiation was partly reduced during partial and annular eclipses.

The atmospheric photochemistry processes play an important role in ozone generation and elimination. O_3 is produced under photodissociation of NO_2 at wavelengths shorter than ~420 nm, etc., like $NO_2 + h\nu \rightarrow NO + O\ (\lambda < 420\,nm)$ and $O + O_2 + M \rightarrow O_3 + M$ (Nishanth et al., 2011). The decreases in solar radiation, coupled with varying meteorological conditions, have significant effects on photochemistry processes during a solar eclipse and thus affect the surface ozone concentration (O_3) (Chimonas and Hines, 1971; Reid et al., 1994; Zerefos et al., 2001; Tzanis et al., 2008; Subrahmanyam et al., 2011; Hanna et al., 2016; Hanna, 2018). Chakrabarty et al. (1997) reported that the total ozone column in Ahmedabad dropped sharply before the maximum obscuration of the eclipse on 24 October 1995, followed by a dramatic increase after 10 min of the maximum obscuration. Zerefos et al. (2001) found that the O_3 decreased by 10–15 ppbv and changed synchronously with solar radiation variations at Eptapirgio in Thessaloniki during the eclipse of 11 August 1999. They suggested that the reductions of O_3 were associated with both photochemical processes and winds. Kolev et al. (2005), using observations from different ground sites in Bulgaria, showed that the effects of the solar eclipse on O_3 had a certain delay of about 40 min and lasted for about 2 hours. Tzanis et al. (2007) observed that the effects of the total solar eclipse of 29 March 2006 on O_3 lasted almost 2 hours at four stations located in the Athens basin in Greece. The maximum changes of O_3 occurred after 1 hour of maximum obscuration at all stations, indicating that radiation decreases were responsible for the reductions of O_3. Sharma et al. (2010) reported that O_3 gradually dropped and have a certain delayed response to the solar eclipse. The O_3 changes lasted for 4 hours. They demonstrated that the O_3 variations were related to the photochemical reactions within the planetary boundary layer due to solar radiation changes. Using observations and simulations at Kannur in the southern region of India, Nishanth et al. (2011) found a reduction of 57.5% in O_3 induced by the eclipse on 15 January 2010 and suggested that the decrease of 59% in O_3 was associated with nitrogen dioxide (NO_2) photolysis rate drop. For the same eclipse event, Vyas et al. (2012) reported the same values and a slight depletion in a small range from −9 to −2 ppb on O_3 at Udaipur, India on the eclipse day. Overall, the previous studies proposed that the O_3 changes were related to photochemical processes with its precursor gases. At the same time, meteorological and boundary layer dynamics parameters also contributed a lot to O_3 concentration. Recently, the depletion of O_3 from 30% to 65% was observed by Pratap et al. (2021) in India during annular solar eclipses on 21st June 2020, in which the maximum O_3 variations of 65% appeared at Jaipur. However, the observed O_3 response to the eclipse is still inconclusive and lacks a global perspective.

The variations of O_3 have been focused on for several years as an important member of pollutants. The increase in O_3 can damage the respiratory and lungs (Wang et al., 2019). There are relationships between O_3 and short-term memory loss, immune system dysfunction, and lymphocyte chromosomal abnormalities (e.g., Monks et al., 2015). Thus, O_3 change should be focused on due to its hazard.

However, most of the previous studies are focused on North America, Europe, and South Asia, while there are few studies on the effect of the solar eclipse on ozone in China. Surface O_3 response to the eclipse is a complex process and varies by using observations due to the dynamic change of the meteorological condition, topography, and pollutant discharge in different regions. The annular solar eclipse on June 21st, 2020, a nearly total eclipse (99.5% of obscuration), is the only and fully visible in China in the past decade. Thus, the solar eclipse event provides a perfect opportunity to explore the O_3 variations response to eclipse in China. In this paper, using ground-based observations in Yunnan province, China, we investigate the effects of the solar eclipse on O_3, NO_2, Total Solar Irradiance (TSI), and

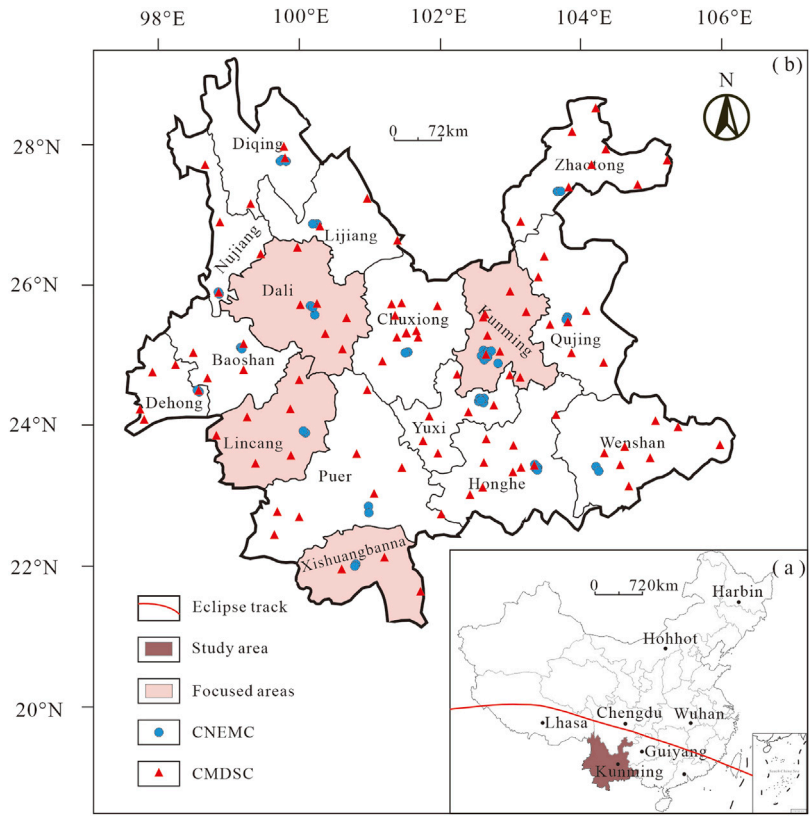

FIGURE 1
The study area (brown area), focused area (pink area) and observational sites from China National Environmental Monitoring Centre (CNEMC, blue circles) and China Meteorological Data Service Centre (CMDSC, red triangles). Brown lines represent the solar eclipse path.

meteorological data. The solar eclipse and observations are introduced in Section 2. We show results in Section 3 and discussion in Section 4. In Section 5 we illustrate the conclusions.

2 Solar eclipse event and data

2.1 Observations on solar eclipse

The annular solar eclipse, which occurred on 21 June 2020, began in central Africa, passed to South Asia, across China, and was last visible in the Pacific Ocean. The effects of the solar eclipse on the narrow strip were about 21.2 km. This annular solar eclipse began at 04:48 UT (Universal Time) in the eastern part of the Democratic Republic of the Congo and ended at 08: 32 UT in the Pacific Ocean. The process lasted 3 h and 45 min, spanning about 14,000 km across the Earth (https://eclipse.gsfc.nasa.gov). This solar eclipse was the only one that can be seen in its whole process and was close to total solar eclipses in China over the last decade. The annular solar eclipse entered from the sacred lake of Tibet, Ma Panyong, passed through the southern part of the Sichuan Basin, across Southern China, traversed Taiwan Strait, and finally left China.

The data in the study is from ground-based observation in Yunnan province. These sites are between 97°31′–106°11′E and 21°8′–29°15′N° in southern China and in the path of the solar eclipse on 21 June 2020. The solar eclipse started and ended slightly differently at different sites. The maximum obscuration of the eclipse was observed everywhere around 15:30:00 CST (Chinese Standard Time, Universal Time + 8 h). The eclipse in Kunming, the capital of Yunnan province, began at 14:02 CST and ended at 17:12 CST. The maximum obscuration of the eclipse in Kunming occurred at 15:45 CST and reached about 86.6%. The solar eclipse in Kunming lasted 3 h and 9 min. Figure 1 gives the full eclipse path in China during the annular solar eclipse on 21 June 2020.

2.2 Air quality and meteorology data

In this study, the air quality and meteorological datasets were released by the China National Environmental

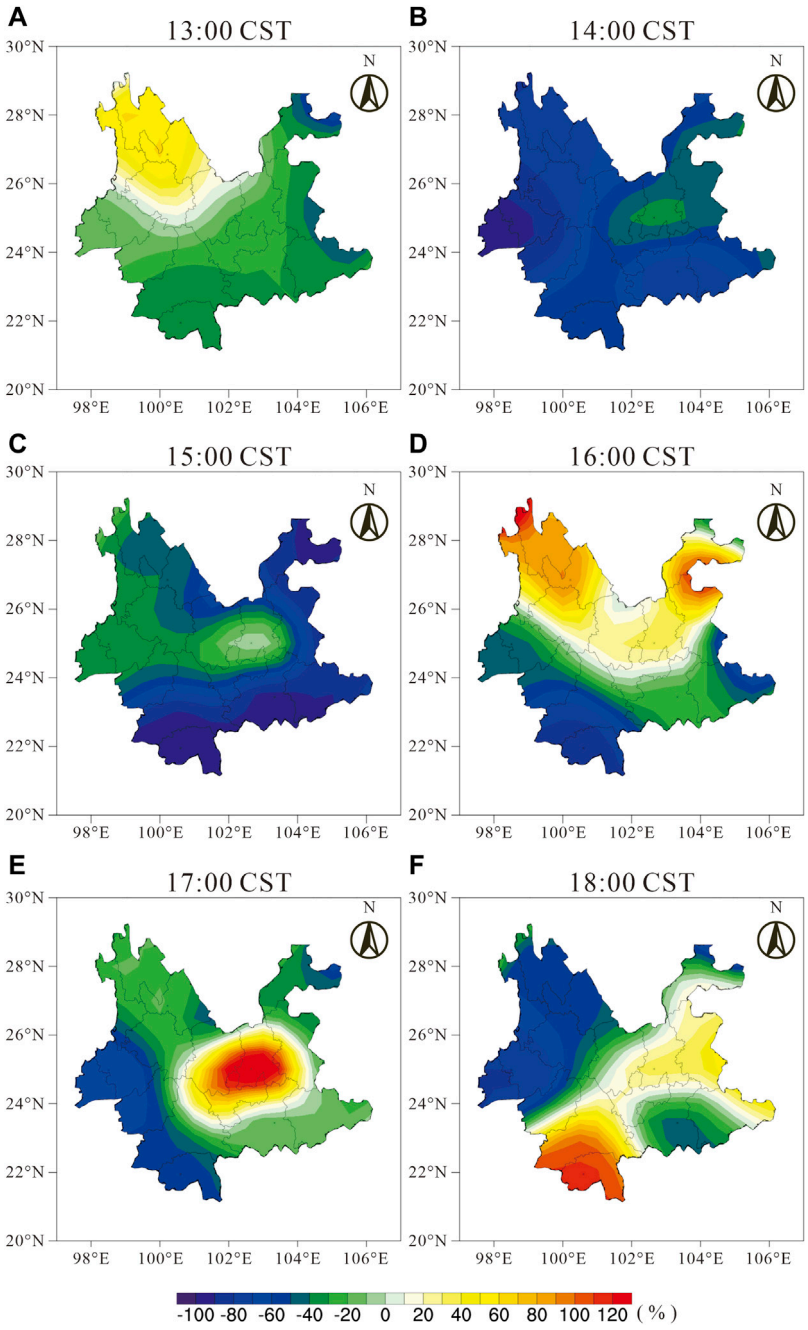

FIGURE 2
The variations in percentage of total solar irradiance at the ground station in Yunnan. The differences in percentage of irradiance are calculated by (hourly total irradiance-hourly total irradiance mean)/hourly total irradiance mean. Here the mean total irradiance between 18th and 20th is obtained to be solar irradiance during non-solar eclipse.

Monitoring Centre (CNEMC) and China Meteorological Data Service Centre (CMDSC), respectively. The meteorological data is hourly observations derived from the ground stations of the China Meteorological Data Network (http://data.cma.cn), mainly including Temperature (T), Relative Humidity (RH), and TSI. In addition, the sites measuring TSI are less, and the TSI data is available in the daytime from 06:00 CST to 18:00 CST. Hourly O_3 and NO_2 data were measured by 1,605 state-controlled monitoring stations of the China National Environmental Monitoring

Centre (http://106.37.208.233:20035). Blue circles and red triangles in Figure 1 represent the spatial distribution of 45 stations of the CNEMC and 103 stations of the CMDSC.

3 Results

3.1 Total solar irradiance variations

Figure 2 gives the variation percentage of TSI in Yunnan. The variation percentage of TSI is calculated by (hourly TSI—hourly TSI means)/hourly TSI means. Here the mean total irradiance between 18th and 20th is obtained to be quiet-time TSI. The percentage of hourly TSI eliminates the influences of diurnal variations. The changes in TSI percentage represent the effects of the solar eclipse on the TSI. The TSI significantly reduced as a response to the solar eclipse (Figure 1). The annular solar eclipse entered western Yunnan and traveled quickly eastward. The eclipse's effects on irradiance in Yunnan lasted for about 4 h. Before the solar eclipse (13:00 CST, Figure 2A), TSI was stepped distributed and gradually reduced from northwest to southeast, in which O_3 in the northwest was a slight increase in the range of 0%–40% and O_3 decreases were smaller than 40% in the southeast. When the solar eclipse entered Yunnan around 14: 00 CST (Figure 2B), O_3 in the central and eastern region decreased slightly, with a decrease from −30% to −60%. At this time, the TSI in the western region decreased significantly, with a decrease from −80% to −100%, which was clearly affected by the solar eclipse. At 15:00 CST (Figure 2C), as the solar eclipse gradually moved eastward, the areas of TSI decline also moved eastward. There is a slight decrease in the northwest region and a sharp decrease in the southeast region. The solar eclipse left Yunnan at 16:00 CST (Figure 2D) and then the TSI began to recover. TSI in the central and northern regions began to increase with increasing latitude, and the range of the increase is from 35% to 90%. However, the southern areas have been decreased in TSI, in which southwest irradiance was from −80% to −20% and southeast irradiance was from −20% to −10%. The solar eclipse would end in Yunnan at about 17: 00 CST. There were irradiance increases in the central and eastern regions, with an increase of nearly 150%. Whereas, the irradiance in the western regions decreased from −20% to −80% (Figure 2E). The irradiance changes were similar to that before the solar eclipse. At 18:00 CST (Figure 2F), the solar eclipse completely left Yunnan province. The irradiance enhancement in the southern region and reductions in the western region can be observed.

Kunming, the capital city of Yunnan province, is in the central and eastern part of Yunnan province (25°2′N, 102°39′E). The solar eclipse started in Kunming at 14: 02 CST and ended at 17:12 CST. The maximum obscuration of the eclipse was at 15:45 CST. Before the start of the solar eclipse, the TSI showed a slight decrease of −24%. The irradiance dropped to −36% after the eclipse started. Approaching the maximum obscuration, the TSI has little changed, and its changes were close to 0 compared to the eclipse beginning. After the eclipse's maximum obscuration, the TSI began to recover, with an increase of 35%. Approaching the eclipse ends, the irradiance increased up to 149%. After the eclipse completely left, the irradiance increased to 36% (Figure 2).

We find that the solar eclipse entered from the west of Yunnan, gradually traveled from west to east, and finally left from the east. While the solar radiation was closely related to the solar eclipse. Before the solar eclipse started, the solar radiation showed a slight change. During the maximum obscuration of the eclipse, the solar radiation changed with the solar eclipse moving and gradually decreased significantly from west to east. A drop of about 100% in reductions of TSI can be observed. After the maximum obscuration of the eclipse, the TSI fluctuated slightly during the recovery period. During the short recovery period, irradiance is recovered to normal., After the solar eclipse completely left Yunnan province, the impacts of the solar eclipse on the TSI had no obvious regularity, and the impact of the TSI on the whole Yunnan province lasted for about 4 h.

3.2 Surface ozone variations

Ozone in the stratosphere is the Earth's barrier, which can shield the Earth from the damage of the solar ultraviolet ray. However, surface ozone is a pollutant, which induces aggravating respiratory irritation and lung injury. The changes in O_3 affect air quality. Figure 3 shows the variation percentage of O_3 in Yunnan, which is calculated the same as TSI ((O_3-O_3 means)/O_3 means). Thus, Figure 3 gives the effects of the solar eclipse on O_3, which eliminates the effects of diurnal variations. At 13:00 CST on June 21 (Figure 3A), before the solar eclipse in Yunnan, a little change with a range between −10% and 10% in O_3 was observed in the northwest, central-eastern, and southern. The variations of O_3 in western Yunnan were about -20%. However, O_3 was reduced by 50% and 25% in the northeast and southeast Yunnan, respectively. The decreases in O_3 may be affected by the local meteorological condition. The increases in O_3 of 20%–50% can be observed in Dehong.

When the solar eclipse commenced at 14:00 CST (Figure 3B) in Yunnan, there was obvious depletion of O_3 by −10% to −30% in the western and central regions. The maximum depletion was located in Lincang. There is a strong connection between the O_3 depletion region and the TSI decrease region. The solar eclipse entered the western region of Yunnan at 14:00 CST. Thus, the changes of O_3 in the western were related to the solar eclipse. O_3 in the eastern region has no significant changes and was the same as that in quiet time at 13:00 CST.

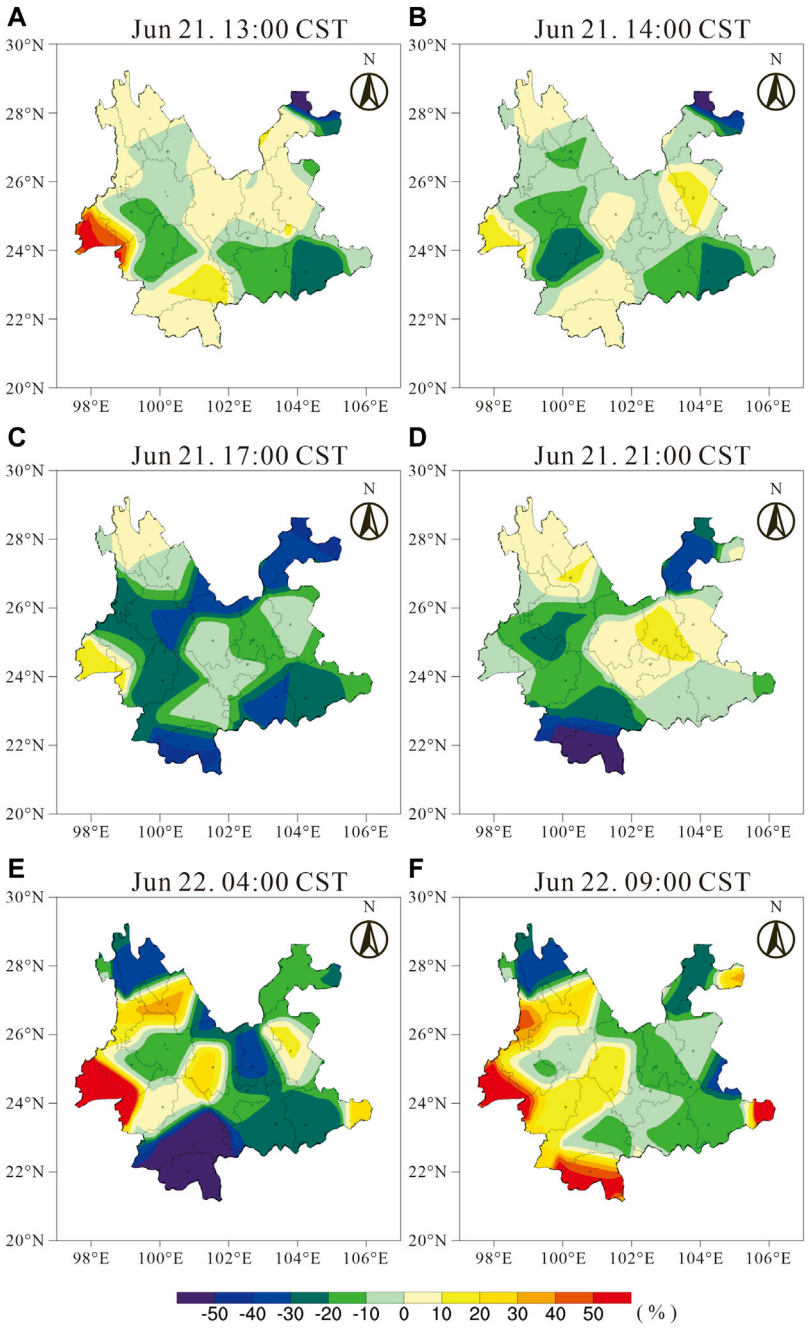

FIGURE 3
Same as Figure 2, but for surface ozone.

The solar eclipse ended at 17:00 CST (Figure 3C) in Yunnan. The O_3 decreases presented in the whole Yunnan province. The significant decreases from −10% to −40% in O_3 occurred in most of the region, while O_3 variations in the northwest and the central eastern region were relatively weak. The O_3 changes reached the maximum in most of the Yunnan, except for the southwest Yunnan.

During the recovery periods (Figure 3D), the effects of the solar eclipse on O_3 began to fade at 21:00 CST in most regions of Yunnan. The decline of O_3 in western and southeastern

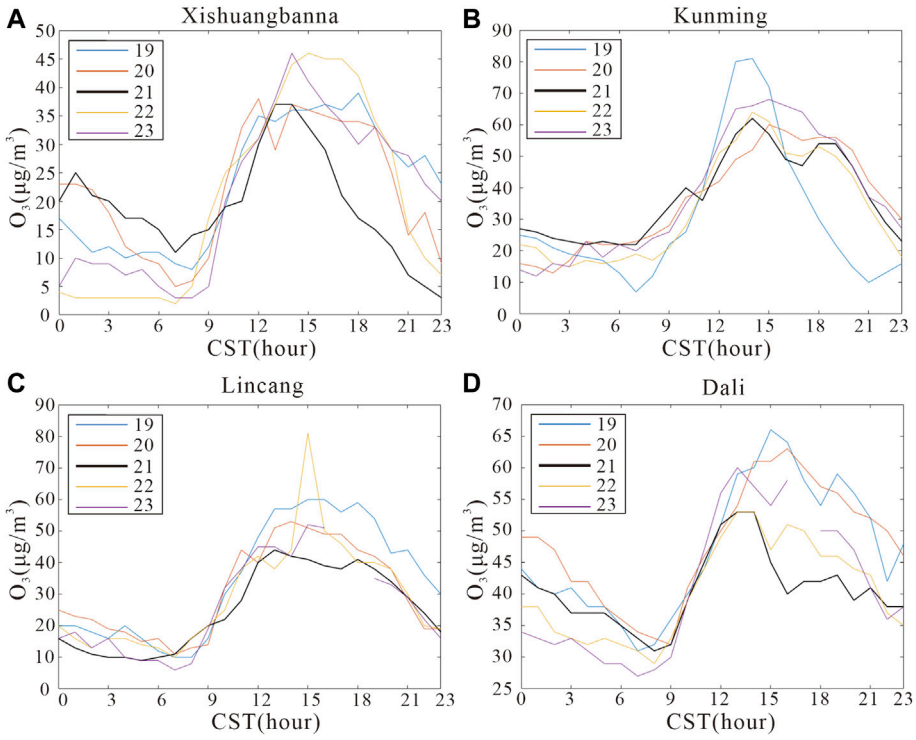

FIGURE 4
The variations of surface ozone concentration at different sites from 19th to 23rd June, 2020. The annular solar eclipse is on 21st June (black lines).

weakened significantly. O_3 increased from 10% to 30%. The northwest and central region recovered fully to normal., However, O_3 in Xishuangbanna continued to decrease from −30% to −50%. At 04:00 CST on June 22 (Figure 3E), the O_3 in the western region continued to rise with a range of 20%–50%. O_3 variations in the western and central regions were stable with a range of −15%–10%. The decrease of O_3 in Xishuangbanna reached the minimum value. Whereas, O_3 in the central and Diqing region began to decrease, which was associated with the meteorological condition and not caused by the eclipse. At this time, the effects of the solar eclipse on O_3 in most of the regions have finished, except for the Xishuangbanna region.

The influences of the solar eclipse on O_3 recovered completely at 09:00 CST on June 22 (Figure 3F). There were no significant changes in O_3, with a range of −15%–15%, in the northeast, central and southeast regions. The increases in O_3 ranging from 20% to 50% can be seen in the whole western region, except for Diqing. The O_3 in Diqing was the same as that at 04:00 CST. Compared with the O_3 before the eclipse (Figure 3A), the changes in O_3 at 09:00 CST were similar, which were mainly increases and relatively weak decreases. The effects of the solar eclipse on O_3 in Yunnan have vanished.

Compared to the observation of the other 4 days, a maximum depletion of 25 $\mu g \cdot m^{-3}$ in O_3 in Xishuangbanna can be observed (Figure 4A). The solar eclipse effects on O_3 began at 14:00 CST on 21st and ended at 07:00 CST on the 22nd, which lasted for 18 h. Figure 4B gives that the impacts of the solar eclipse on O_3 in Kunming were small. O_3 was reduced by 2 $\mu g \cdot m^{-3}$ compared with O_3 between 14:00 CST and 17:00 CST on non-eclipse days (20th, 22nd, and 23rd). The O_3 changes associated with the solar eclipse only lasted 4 h. The effects of the eclipse (June 21) on the concentration of O_3 in Lincang began after 13:00 CST compared with that before and after the eclipse (19th, 20th, 22nd, and 23rd, Figure 4C). The minimum value of O_3 reached 38 $\mu g \cdot m^{-3}$. The O_3 was reduced by 5 $\mu g \cdot m^{-3}$, and the result was eliminated diurnal variations and mainly caused by the eclipse. The influences of the eclipse lasted 6 h and recovered to normal at 18:00 CST. The O_3 concentration in Dali (Figure 4D) was affected by the solar eclipse, which began at 14:00 CST and ended at 21:00 CST on June 21. The process lasted for 8 h. O_3 decreased by 10 $\mu g \cdot m^{-3}$ associated with the eclipse.

The impacts of the solar eclipse on O_3 concentrations in different cities showed a different response. The solar eclipse had a significant impact on these three cities. The

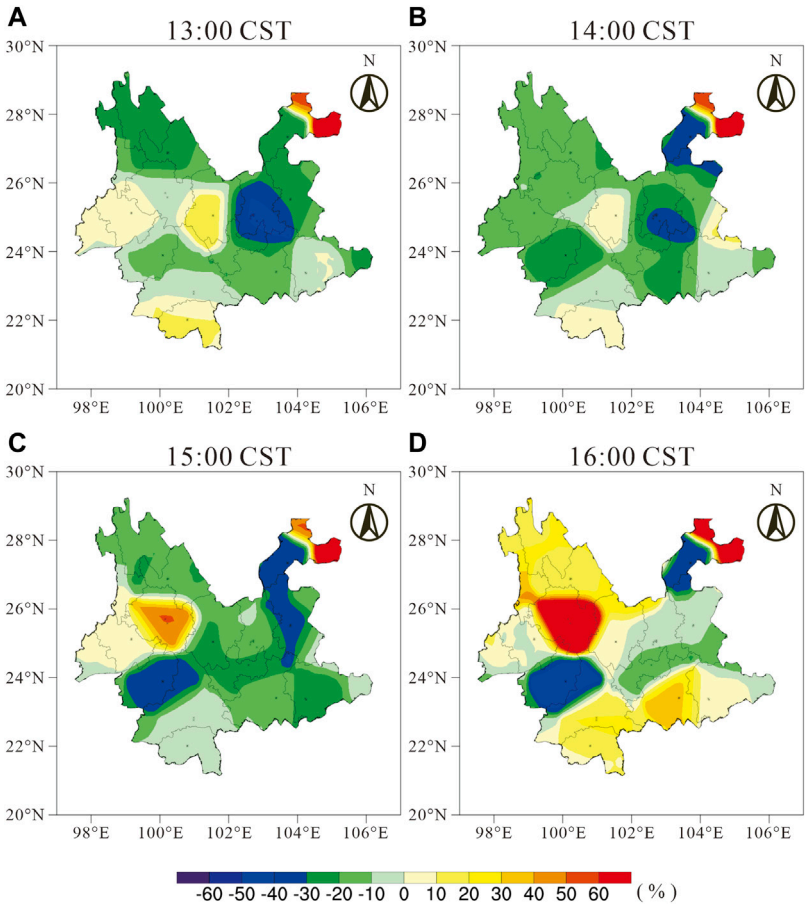

FIGURE 5
Same as Figure 2, but for NO_2.

concentration changes of O_3 in Dali, Xishuangbanna, and Lincang showed a significant decrease during the solar eclipse, then gradually returned to normal., The recovery periods of these three cities were different, with which the recovery period in Xishuangbanna was the longest. The effects of the eclipse on O_3 in Kunming were weak and had a short duration.

Therefore, O_3 changes were small before the solar eclipse. As the solar eclipse entered Yunnan, the O_3 gradually decreased. The decreases in O_3 became more and more significant until the solar eclipse left Yunnan. O_3 reached its minimum when the eclipse left Yunnan, and the O_3 depletion was from −10% to −40%. After the eclipse left Yunnan, O_3 began to recover, except for the southwest region. O_3 recovered after 8 h of eclipse occurrence, while O_3 in the southwest region continued to decrease and reached a minimum value of -60% until 04:00 CST on June 22. The effects of the solar eclipse on O3 recovered completely at 09: 00 CST on June 22. The influence of the solar eclipse on O_3 in Yunnan lasted for about 20 h. The results of O_3 caused by eclipse were similar to the previous study, while the O_3 reductions lasted significantly longer and the minimum value of O_3 occurred later than that in the previous study.

3.3 Surface NO_2 and carbonic oxide (CO) variations

As precursor gases, NO_2 and CO were important to the production of O_3 (e.g., Nishanth et al., 2011; Vyas et al., 2012). Figure 5 and Figure 6 give the variation percentage of NO_2 and CO in Yunnan, respectively. Before the solar eclipse (13:00 CST on June 21, Figure 5A), little changes in NO_2 can be observed in most regions, except for Kunming. There were significant decreases of -50% in Kunming. When the solar eclipse entered Yunnan (14:00 CST on June 21, Figure 5B), decreases and increases of NO_2 in Yunnan occurred. The NO_2 reduced by −10% to −20% in the western region. The

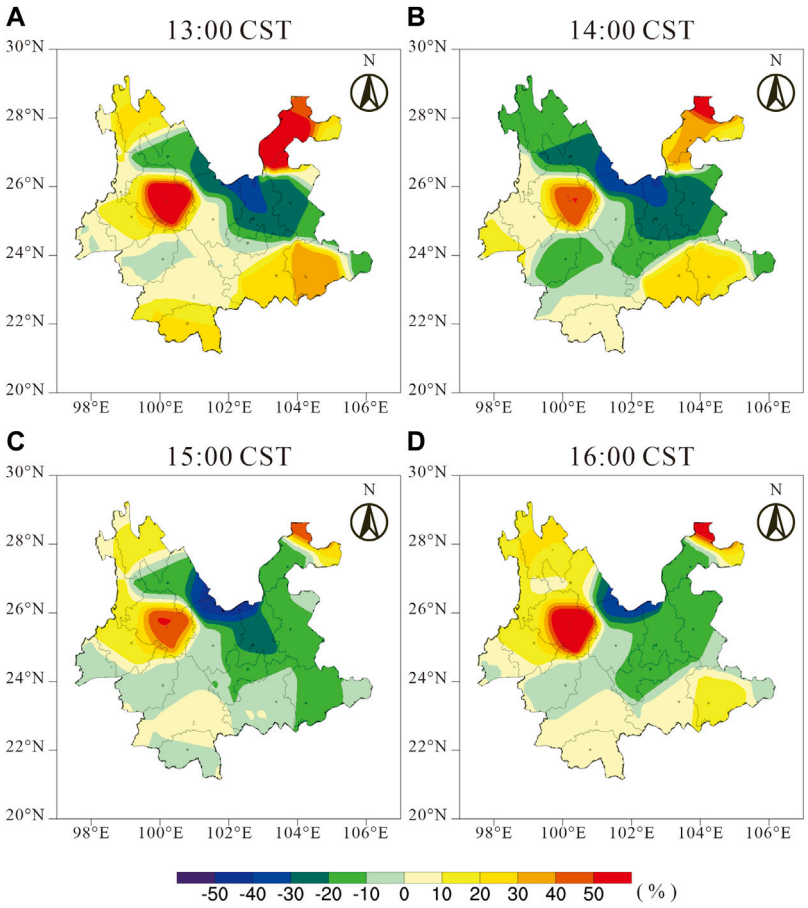

FIGURE 6
Same as Figure 2, but for CO.

TABLE 1 The correlation coefficients between surface O_3 and temperature, relative humidity, NO_2, and CO at different sites in Yunnan during solar eclipse (14:00 CST on 21st to 05:00 CST on 22nd) and quiet time from 18th to 24th June, 2020.

	City	Temperature	Relative humidity	NO_2	CO	TSI
Eclipse	Xishuangbanna	**0.99**	**−0.98**	−0.59	−0.15	**0.72**
	Kunming	**0.98**	**−0.97**	**−0.97**	**−0.81**	**0.64**
	Lincang	**0.97**	**−0.97**	**−0.8**	−0.23	**
	Dali	**0.88**	**−0.83**	−0.13	**	**
Quiet time	Xishuangbanna	**0.84**	**−0.83**	**−0.72**	−0.09	**0.39**
	Kunming	**0.74**	**−0.76**	**−0.52**	**−0.53**	**0.25**
	Lincang	**0.91**	**−0.88**	**−0.5**	−0.09	**
	Dali	**0.86**	**−0.81**	**−0.22**	−0.14	**

Bold means $p < 0.01$.
** means lack of measurement.
Correlation coefficients during quiet time removed the value affected by eclipse.

minimum value of NO_2 changes occurred in Zhaotong, which reached −40%. NO_2 increased by 10% compared to that at 13:00 CST in the northwest and central region. At 14:00 CST (Figure 5C), NO_2 in the southwest region continued to reduce,

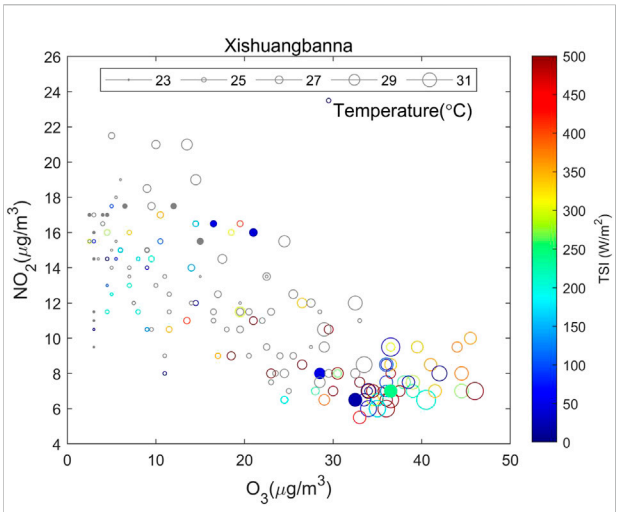

FIGURE 7
The relationships between O_3 and NO_2, temperature, and TSI at Xishuangbanna from 19th to 23rd June, 2020. The circle size and color represent temperature and total solar irradiance. Grey circles means missing TSI at night. Solid circles are affected by solar eclipse from 14:00 CST on 21st to 06:00 CST on 22nd June, 2020.

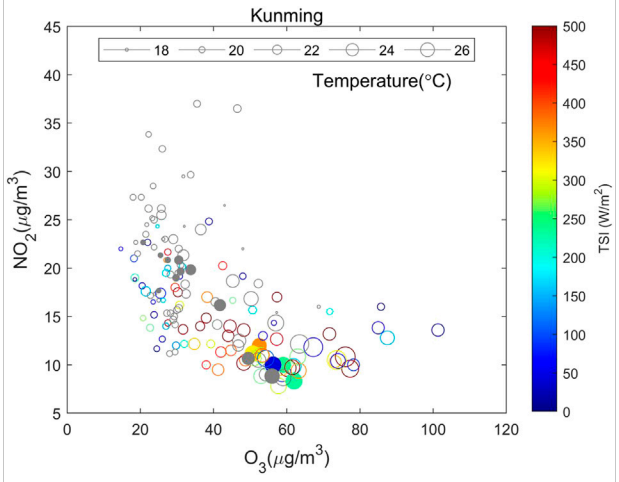

FIGURE 8
Same as Figure 7, but for Kunming.

especially decrease in 40% in Lincang. NO_2 in Baoshan and Dali have been recovered. NO_2 in Dali increased by 40%. NO_2 in the northeast region continued to decrease and penetrated to the central region. Increases in NO_2 can be observed at 16:00 CST (Figure 5D) in most of Yunnan. The NO_2 decreases of −40% in Lincang and Zhaotong have been maintained. Therefore, NO_2 in most of Yunnan has been recovered at 16:00 CST. The effects of the solar eclipse on NO_2 concentration only lasted for 3 h.

As another precursor gas, the changes of CO were smaller than that of NO_2 during the solar eclipse. The changes in CO were minor during the eclipse in Yunnan. CO reduced by −10% to −20% in the whole of Yunnan from 13:00 CST to 14:00 CST (Figures 6A,B), except Honghe maintained its previous state. At 15:00 CST (Figure 6C), CO increased by 10% in the central and northern regions of Yunnan. CO in the southern region decreased by 10%. A CO increase of 10% can be seen in the whole of Yunnan at 16:00 CST (Figure 6D). Thus, a slight CO variation of 10% can be observed.

3.4 The relationship between O_3 and precursors and meteorological conditons

To explore the reason causing the O_3 variation during the solar eclipse, we selected the four typical Yunnan cities (Same as Figure 4), Lincang, Xishuangbanna, Dali, and Kunming, respectively. The correlation coefficients between O_3 and temperature, relative humidity, NO_2, CO, and TSI were calculated from 18th to 24th (quiet time) and solar eclipse (21st) as shown in Table 1, in which R represented the correlation coefficients. The sites of TSI observation are far fewer than CNEMC sites, thus we selected two sites of the four sites in Figure 4, where TSI data was available in Xishuangbanna (Figure 7) and Kunming (Figure 8), to show multivariate analysis.

Xishuangbanna is a tropical and sunniest city, and TSI is generally above 350 W/m^2 (hollow circles in Figure 7). However, TSI was mostly below 100 W/m^2 in Xishuangbanna during the eclipse in the daytime except for one data was nearly 250 W/m^2. In the daytime, cold and high NO_2 caused lower O_3 in the daytime. On the contrary, warm and low NO_2 were related to high O_3. In addition, the higher temperature was associated with higher O_3 when NO_2 was invariant. At night, O_3 was controlled by temperature when NO_2 was above 14 $\mu m/m^3$. When NO_2 was smaller than 12 $\mu m/m^3$, O_3 did not depend on NO_2 concentration at night. O_3 was positively correlated with temperature and TSI, but negatively correlated with relative humidity, NO_2, and CO in Xishuangbanna (Figure 7; Table 1) during quiet time and eclipse. The rainforest of Xishuangbanna can provide better air quality, and reduce air pollution. Thus, CO and NO_2 concentrations were smaller than in a metropolis. The correlationship between O_3 and NO_2 and CO during the eclipse were weak and cannot pass significant tests ($p < 0.01$). Therefore, the temperature was the most important factor in affecting O_3 during the eclipse.

Kunming is a special city during this eclipse, TSI was similar to that during quiet time. Blue circles were less in Figure 8, which means TSI was similar to quiet time and the

effects of the eclipse on TSI were minor. In addition, the influences of TSI on O_3 were minor. Warm and low NO_2 were in the daytime, and cold and high NO_2 were in the nighttime. The correlation between O_3 and temperature was significantly positive and the correlation coefficient reached 0.98 during the eclipse (Figure 8; Table 1). O_3 and NO_2 have a negative correlation relationship (R = −0.97), passing the significance test ($p < 0.01$, Table 1). Therefore, there was higher O_3 in the daytime and lower O_3 in the nighttime. In the other three cities, CO has no significant effects on O_3. However, the O_3 in Kunming had a significant negative correlation with CO through a significant test during the solar eclipse and quiet time, in which the correlation coefficient was obviously larger during the eclipse. The increases in CO were observed in Kunming during the beginning and maximum obscuration. CO changes were minor due to the non-reaction of CO compared to NO_2. However, for Kunming, CO increases were associated with the chemical reaction of altering CO, etc., like $CO + 2O_2 + h\nu \rightarrow CO_2 + O_3$ (Sharma et al., 2010; Vyas et al., 2012). The reaction weakened and CO increased as solar radiation reduced. Kunming, as the capital city of Yunnan province, has a relatively serious air pollution problem compared to Xishuangbanna, thus NO_2 and CO play a vital role in affecting O_3 in Kunming during the eclipse.

O_3 in Lincang was positively correlated with temperature and the relationship was credible by the significance test ($p < 0.01$), which was 0.91 (0.97, where the R in parentheses was the correlation coefficient during the solar eclipses, the same as below). The O_3 was negatively correlated with the relative humidity and NO_2, passing the significance test ($p < 0.01$). R was −0.88 (−0.97) and −0.5 (−0.8). The correlation coefficient between the O_3 and CO did not pass the significance test. During the solar eclipse, temperature, relative humidity, and NO_2 in Lincang were more important for O_3 changes than that in quiet time, as the correlation coefficients were larger during a solar eclipse than that in quiet time.

O_3 in Dali and its temperature have a positive correlation relationship, passing the significance test ($p < 0.01$). R is 0.86 (0.88). O_3 and relative humidity are negatively correlated, passing the significance test ($p < 0.01$). R is −0.81 (−0.83). CO was invariant during the eclipse, which was unavailable. The correlation coefficients between O_3 and NO_2 failed in the significance test. The effects of temperature and relative humidity on O_3 were fairly weak during the solar eclipse. NO_2 and CO did not show significant importance for O_3 in Dali.

4 Discussion

As the solar eclipse occurred, reductions in solar irradiance were directly observed in different locations around the world. Founda et al. (2007) reported that solar irradiance was reduced by 89% and 100% over Thessaloniki and Kastelorizo, respectively. Girach et al. (2012) found that solar irradiance decline was most obvious over Thumba, India during the annular solar eclipse on 15 January 2010. During the solar eclipse events on 21 June 2020, due to the moon's shadow, the solar irradiance decreased by more than -90%, and the whole process lasted for about 5 h in Yunnan (Figure 2).

On the one hand, various meteorological conditions changed response to radiation variations. The temperature in Yunnan reduced during the solar eclipse, which is consistent with previous studies (Eaton et al., 1997; Anderson, 1999; Krishnan et al., 2004; Tzanis et al., 2008; Girach et al., 2012; Burt, 2018). O_3 and temperature in many cities in Yunnan are significantly and positively correlated (Table 1). Thus, the temperature is a greatly important factor in affecting the photochemical reaction of O_3. As the temperature decreased, O_3 also reduced which is consistent with previous studies (Sheehan and Bowman, 2001; Kleeman, 2008). An increasing trend in relative humidity changes is observed at most sites throughout the solar eclipse event (Table 1). Previous studies also reported an increase in relative humidity during solar eclipse events (Tzanis et al., 2008; Namboodiri et al., 2011; Prasad et al., 2019). Temperature and humidity were inversely proportional., The relative humidity would respond as the temperature changed. The radiation is further reduced due to the strong relative humidity and affects the photochemical reaction of O_3, thereby reducing O_3 which is consistent with previous studies (Kumar et al., 2014; Manju et al., 2018).

On the other hand, as a reaction precursor gas of ozone production, NO_2 changes can be observed during the solar eclipse. Sharma et al. (2010) observed NO_2 decreases from 2.52 to 0.78 ppb during a solar eclipse. However, Vyas et al. (2012) found that the differences in NO_2 increased slightly from −1.8 to 0.9 ppb during the maximum obscuration of the solar eclipse. After the maximum obscuration, there was a certain fluctuation in the range of 0.9–1.6 ppb. Nishanth et al. (2011) found that there are no changes in NO_x caused by the solar eclipse. During the solar eclipse on June 21, the effects of the solar eclipse on NO_2 in different cities of Yunnan are various. Decreases, increases, and invariance of NO_2 have been observed in response to eclipse. NO_2 in Kunming gradually increased from −40% to −10% with the solar radiation decreases. NO_2 in Dali and Xishuangbanna firstly decreased and then increased. NO_2 in Lincang decreased and minimum values can reach −40% during the entire eclipse (Figure 5). O_3 in Lincang and Kunming were negatively correlated with the NO_2 (Table 1), which means O_3 increased and NO_2 decreased. Whereas, there was no significant relationship between O_3 and NO_2 in Dali and Xishuangbanna (Table 1). O_3 is produced under photodissociation of NO_2 at wavelengths shorter than

~420 nm, etc., like $NO_2 + h\nu \rightarrow NO + O$ ($\lambda < 420\,nm$) and $O + O_2 + M \rightarrow O_3 + M$ (e.g., Nishanth et al., 2011). During a solar eclipse, the changes in meteorological conditions such as fewer radiations and colder could weaken the photolysis of NO_2, resulting in further weakening of the O_3 generation process. The consumption of NO_2 and production of O_3 have been weakened by solar radiation decreases. Thus, NO_2 and O_3 showed a negative correlation. Meanwhile, the photodissociation of NO_2 is not the only reaction to provide the required O for O_3 production. Therefore, the correlation coefficient between NO_2 and O_3 is different in disparate cities. This explains why the effects of NO_2 on O_3 are minor in Xishuangbanna and Dali.

There are significant decreases in O_3 during a solar eclipse (Zerefos et al., 2001; Tzanis et al., 2008; Girach et al., 2012; Jain et al., 2020; Patel and Singh, 2021; Pratap et al., 2021). The significant effects of the solar eclipse were manifested with a certain delay from the maximum obscuration. The delay was associated with the slow destruction process of O_3 (Tzanis et al., 2008; Girach et al., 2012). The slow destruction process of O_3 during the solar eclipse is a fairly complex process, which is associated with meteorological parameters, such as solar radiation, temperature, relative humidity, and other pollutants, NO_2 and CO (Gerasopoulos et al., 2007). The seasons and months in which solar eclipse events occur also play a very important role in these changes in atmospheric parameters (Tzanis et al., 2008).

5 Conclusion

In this paper, we examine the effects of the solar eclipse on O_3 in Yunnan, China. By analyzing TSI, O_3, NO_2, CO, temperature, and relative humidity obtained from CNEMC and CMDSC during the solar eclipse on 21 June 2020, we have reached the following conclusions:

(1) TSI decreases more than 90% during the solar eclipse on 21 June 2020. This TSI decreases moving from west to east and last 3 h in Yunnan. The total influences of the solar eclipse on TSI in Yunnan last for about 5 h.
(2) In the early phase of the solar eclipse, O_3 reduces by −10% ~−20% in the western region of Yunnan. As the eclipse travels east, the O_3 depletion becomes more and more significant and penetrates the whole of Yunnan. The O_3 changes reach the minimum value of more than −40% and then O_3 starts to recover in Yunnan when the solar eclipse leaves Yunnan. The western and southern regions are more sensitive to eclipse, because these regions show more rapid and significant O_3 reductions. The response of O_3 to solar eclipse lasted for 8 h in most of Yunnan. However, O_3 variations last 20 h in the whole of Yunnan, due to slow recovery in Xishuangbanna.
(3) O_3 and temperature were positively correlated and the relationship is closest to other meteorological parameters. Whereas, O_3 was linearly negatively correlated with relative humidity.
(4) As the precursors, NO_2 is more important than CO to O_3 changes during the solar eclipse. Decreases, increases, and invariance of NO_2 can be observed. The impacts of the eclipse on NO_2 last for 4 h. O_3 and NO_2 in most cities of Yunnan are a significantly negative correlation.
(5) Among the cities in Yunnan during the solar eclipse, only O_3 in Kunming was negatively correlated with CO. The O_3 in the seriously polluted city is more sensitive to NO_2 and CO during the eclipse.

Data availability statement

The original contributions presented in the study are included in the article/Supplementary Material, further inquiries can be directed to the corresponding author.

Author contributions

YT, JLu, FS, and JLi contributed to conception and design of the study. FS, SX, GW, ZL, HZ, GY and organized the database. CY, JC, YW, SJ, JY, JW, ZZ, and ZW performed the statistical analysis. YT wrote the first draft of the manuscript. JLi wrote sections of the manuscript. All authors contributed to manuscript revision, read, and approved the submitted version.

Funding

The work is supported by the National Natural Science Foundation of China (grants 42004132, 42030203, and 42074183), the Startup Foundation for Introducing Talent of NUIST (2020r052), the China Geological Survey (ZD20220145 and ZD20220135), the open funding of MNR Key Laboratory for Polar Science (KP202104), and the stable support projects of institutes for basic scientific research (A131902W03).

Acknowledgments

We highly acknowledge CNEMC and CMDSC provide the hourly pollutants and meteorological data at ground stations in China. Meteorological data was downloaded from the China Meteorological Data Network (http://data.cma.cn), mainly including hourly temperature, relative humidity, and total solar irradiance. Hourly O_3 and NO_2 data was downloaded from the China National Environmental Monitoring Centre (http://106.37.208.233:20035). The data is also being saved on

the National Space Science Data Center (DOI: 10.12176/04.99.02959).

Conflict of interest

The authors declare that the research was conducted in the absence of any commercial or financial relationships that could be construed as a potential conflict of interest.

Publisher's note

References

Amiridis, V., Melas, D., Balis, D. S., Papayannis, A., Founda, D., Katragkou, E., et al. (2007). Aerosol Lidar observations and model calculations of the planetary boundary layer evolution over Greece, during the March 2006 total solar eclipse. *Atmos. Chem. Phys.* 7, 6181–6189. doi:10.5194/acp-7-6181-2007

Anderson, R. C., Keefer, D. R., and Myers, O. E. (1972). Atmospheric pressure and temperature changes during the 7 march 1970 solar eclipse. *J. Atmos. Sci.* 29, 583–587. doi:10.1175/1520-0469(1972)029<0583:apatcd>2.0.co;2

Anderson, J. (1999). Meteorological changes during a solar eclipse. *Weather* 54 (7), 207–215. doi:10.1002/j.1477-8696.1999.tb06465.x

Aplin, K. L., Scott, C. J., and Gray, L. (2016). Atmospheric changes from solar eclipses. *Phil. Trans. R. Soc. A* 374, 20150217–20150224. doi:10.1098/rsta.2015.0217

Baran, L. W., Ephishov, I. I., Shagimuratov, I. I., Ivanov, V. P., and Lagovsky, A. F. (2003). The response of the ionospheric total electron content to the solar eclipse on August 11, 1999. *Adv. Space Res.* 31 (4), 989–994. doi:10.1016/S0273-1177(02)00885-2

Burt, S. (2018). Meteorological impacts of the total solar eclipse of 21 August 2017. *Weather* 73 (3), 90–95. doi:10.1002/wea.3210

Chakrabarty, D. K., Shah, N. C., and Pandya, K. V. (1997). Fluctuation in ozone column over Ahmedabad during the solar eclipse of 24 October 1995. *Geophys. Res. Lett.* 24 (23), 3001–3003. doi:10.1029/97GL03016

Chimonas, G., and Hines, C. O. (1971). Atmospheric gravity waves induced by a solar eclipse. *J. Geophys. Res.* 76, 7003–7005. doi:10.1029/ja076i028p07003

Chung, Y. S., Kim, H. S., and Choo, S. H. (2010). The solar eclipse and associated atmospheric variations observed in South Korea on 22 July 2009. *Air Qual. Atmos. Health* 3, 125–130. doi:10.1007/s11869-009-0060-0

Eaton, F. D., Hines, J. R., Hatch, W. H., Cionco, R. M., Byers, J., Garvey, D., et al. (1997). Solar eclipse effects observed in the planetary boundary layer over a desert. *Bound. Layer. Meteorol.* 83 (2), 331–346. doi:10.1023/a:1000219210055

Founda, D., Melas, D., Lykuodis, S., Lisaridis, I., Gerasopoulos, E., Kouvarakis, G., et al. (2007). The effect of the total solar eclipse of 29 March 2006 on meteorological variables in Greece. *Atmos. Chem. Phys.* 7, 5543–5553. doi:10.5194/acp-7-5543-2007

Gerasopoulos, E., Zerefos, C. S., Tsagouri, I., Founda, D., Amiridis, V., Bais, A. F., et al. (2007). The total solar eclipse of march 2006: An overview. *Atmos. Chem. Phys. Discuss.* 7, 17663–17704. doi:10.5194/acp-8-5205-2008

Girach, I. A., Nair, P. R., David, L. M., Hegde, P., Mishra, M. K., Kumar, G. M., et al. (2012). The changes in nearsurface ozone and precursors at two nearby tropical sites during annular solar eclipse of 15 January 2010. *J. Geophys. Res. Atmos.* 117 (D1), 1–14. doi:10.1029/2011JD016521

Gray, S. L., and Harrison, R. G. (2012). Diagnosing eclipse-induced wind changes. *Proc. R. Soc. A* 468, 1839–1850. doi:10.1098/rspa.2012.0007

Hanna, E., Penman, J., Jónsson, T., Grant, R., Björnsson, H., Sjúrðarson, S., et al. (2016). Meteorological effects of the solar eclipse of 20 march 2015: Analysis of UK met office automatic weather station data and comparison with automatic weather station data from the faroes and Iceland. *Philos. Trans. R. Soc. A Math. Phys. Eng. Sci.* 374, 20150212. doi:10.1098/rsta.2015.0212

Hanna, E. (2018). Meteorological effects of the 20 March 2015 solar eclipse over the United Kingdom. *Weather* 73 (3), 71–80. doi:10.1002/wea.2820

Jain, C. D., Venkat Ratnam, M., and Madhavan, B. L. (2020). Direct and indirect photochemical impacts on the trace gases observed during the solar eclipse over a tropical rural location. *J. Atmos. Solar-Terrest. Phys.* 211, 105451. doi:10.1016/j.jastp.2020.105451

Kazadzis, S., Bais, A., Blumthaler, M., Webb, A., Kouremeti, N., Kift, R., et al. (2007). Effects of total solar eclipse of 29 march 2006 on surface radiation. *Atmos. Chem. Phys.* 7, 9235–9258. doi:10.5194/acpd-7-9235-2007

Kleeman, M. J. (2008). A preliminary assessment of the sensitivity of air quality in California to global change. *Clim. Change* 87 (S1), 273–292. doi:10.1007/s10584-007-9351-3

Kolev, N., Tatarov, B., Grigorieva, V., Donev, E., Simeonov, P., Umlensky, V., et al. (2005). Aerosol Lidar and *in situ* ozone observations of the planetary boundary layer over Bulgaria during the solar eclipse of 11 August 1999. *Int. J. Remote Sens.* 26 (16), 3567–3584. doi:10.1080/01431160500076939

Krishnan, P., Kunhikrishnan, P. K., Nair, S. M., Ravindran, S., Ramachandran, R., Subrahamanyam, D. B., et al. (2004). Observations of the atmospheric surface layer parameters over a semi arid region during the solar eclipse of August 11th, 1999. *J. Earth Syst. Sci.* 113 (3), 353–363. doi:10.1007/BF02716730

Kumar, A., Singh, B. P., Punia, M., Singh, D., Kumar, K., and Jain, K. (2014). Determination of volatile organic compounds and associated health risk assessment in residential homes and hostels within an academic institute. New Delhi. *Indoor Air* 24, 474–483. doi:10.1111/ina.12096

Manju, A., Kalaiselvi, K., Dhananjayan, V., Palanivel, M., Banupriya, G. S., Vidhya, M. H., et al. (2018). Spatio-seasonal variation in ambient air pollutants and influence of meteorological factors in Coimbatore, Southern India. *Air Qual. Atmos. Health* 11 (10), 1179–1189. doi:10.1007/s11869-018-0617-x

Monks, P. S., Archibald, A. T., Colette, A., Cooper, O., Coyle, M., Derwent, R., et al. (2015). Tropospheric ozone and its precursors from the urban to the global scale from air quality to short-lived climate forcer. *Atmos. Chem. Phys.* 15 (15), 8889–8973. doi:10.5194/acp-15-8889-2015

Namboodiri, K. V. S., Dileep, P. K., Mammen, K., Ramkumar, G., Kiran Kumar, N. V. P., Sreenivasan, S., et al. (2011). Effects of annular solar eclipse of 15 January 2010 on meteorological parameters in the 0 to 65 km region over Thumba, India. *metz.* 20 (6), 635–647. doi:10.1127/0941-2948/2011/0253

Nishanth, T., Ojha, N., Kumar, M., and Naja, M. (2011). Influence of solar eclipse of 15 january 2010 on surface ozone. *Atmos. Environ.* 45 (9), 1752–1758. doi:10.1016/j.atmosenv.2010.12.034

Panda, S. K., Gedam, S. S., Rajaram, G., Sripathi, S., and Bhaskar, A. (2015). Impact of the 15 January 2010 annular solar eclipse on the equatorial and low latitude ionosphere over the Indian region. *J. Atmos. Solar-Terrest. Phys.* 135, 181–191. doi:10.1016/j.jastp.2015.11.004

Pasachoff, J. M. (2009). Scientific observations at total solar eclipses. *Res. Astron. Astrophys.* 9 (6), 613–634. doi:10.1088/1674-4527/9/6/001

Patel, K., and Singh, A. K. (2021). Changes in atmospheric parameters due to annular solar eclipse of June 21, 2020, over India. *Indian J. Phys.* 96, 1613–1624. doi:10.1007/s12648-021-02112-2

Prasad, S. B. S., Kumar, V., Reddy, K. K., Dhaka, S. K., Malik, S., Reddy, M. V., et al. (2019). Perturbations in Earth's atmosphere over an Indian region during the total solar eclipse on 22 july 2009. *J. Meteorol. Res.* 33 (4), 784–796. doi:10.1007/s13351-019-8056-7

Pratap, V., Kumar, A., and Singh, A. K. (2021). Overview of solar eclipse of 21st June 2020 and its impact on solar irradiance, surface ozone and different meteorological parameters over eight cities of India. *Adv. Space Res.* 68, 4039–4049. doi:10.1016/j.asr.2021.08.014

Reid, S. J., Vaughan, G., Mitchell, N. J., Prichard, I. T., Smit, H. J., Jorgensen, T. S., et al. (1994). Distribution of ozone laminae during EASOE and the possible influence ofinertiagravity waves. *Geophys. Res. Lett.* 21 (13), 1479–1482. doi:10.1029/93GL01676

Sharma, S. K., Mandal, T. K., Arya, B. C., Saxena, M., Shukla, D. K., Mukherjee, A., et al. (2010). Effects of the solar eclipse on 15 January 2010 on the surface O3, NO, NO2, NH3, CO mixing ratio and the meteorological parameters at Thiruvanathapuram, India. *Ann. Geophys.* 28 (6), 1199–1205. doi:10.5194/angeo-28-1199-2010

Sheehan, P. E., and Bowman, F. M. (2001). Estimated effects of temperature on secondary organic aerosol concentrations. *Environ. Sci. Technol.* 35 (11), 2129–2135. doi:10.1021/es001547g

Subrahmanyam, K. V., Ramkumar, G., Kumar, K. K., Swain, D., Sunil Kumar, S. V., Das, S. S., et al. (2011). Temperature perturbations in the troposphere-stratosphere over Thumba (8.5° N, 76.9° E) during the solar eclipse 2009/2010. *Ann. Geophys.* 29 (2), 275–282. doi:10.5194/angeo-29-275-2011

Tzanis, C., Varotsos, C., and Viras, L. (2007). Impacts of the solar eclipse of 29 march 2006 on the surface ozone and nitrogen dioxide concentrations at Athens, Greece. *Atmos. Chem. Phys. Discuss.* 7 (5), 14331–14349. doi:10.5194/acpd-7-14331-2007

Tzanis, C., Varotsos, C., and Viras, L. (2008). Impacts of the solar eclipse of 29 March 2006 on the surface ozone concentration, the solar ultraviolet radiation and the meteorological parameters at Athens, Greece. *Atmos. Chem. Phys.* 8 (2), 425–430. doi:10.5194/acp-8-425-2008

Vyas, B. M., Saxena, A., and Panwar, C. (2012). Study of atmospheric air pollutants during the partial solar eclipse on 15 january 2010 over Udaipur: A semi-arid location in Western India. *Adv. Space Res.* 50 (11), 1553–1563. doi:10.1016/j.asr.2012.07.021

Wang, J., Yang, Y., Zhang, Y., Niu, T., Jiang, X., Wang, Y., et al. (2019). Influence of meteorological conditions on explosive increase in O3 concentration in troposphere. *Sci. Total Environ.* 652, 1228–1241. doi:10.1016/j.scitotenv.2018.10.228

Zerefos, C. S., Balis, D. S., Zanis, P., Meleti, C., Bais, A. F., Tourpali, K., et al. (2001). Changes in surface UV solar irradiance and ozone over the balkans during the eclipse of August 11, 1999. *Adv. Space Res.* 27 (12), 1955–1963. doi:10.1016/S0273-1177(01)00279-4

frontiers | Frontiers in Environmental Science

TYPE Review
PUBLISHED 12 September 2022
DOI 10.3389/fenvs.2022.954045

OPEN ACCESS

EDITED BY
Yuqiang Zhang,
University of North Carolina at Chapel Hill, United States

REVIEWED BY
Chi Li,
Washington University in St. Louis, United States
Dien Wu,
California Institute of Technology, United States

*CORRESPONDENCE
Ulas Im,
ulas@envs.au.dk

SPECIALTY SECTION
This article was submitted to Atmosphere and Climate, a section of the journal Frontiers in Environmental Science

RECEIVED 26 May 2022
ACCEPTED 20 July 2022
PUBLISHED 12 September 2022

CITATION
Im U, Geels C, Hanninen R, Kukkonen J, Rao S, Ruuhela R, Sofiev M, Schaller N, Hodnebrog Ø, Sillmann J, Schwingshackl C, Christensen JH, Bojariu R and Aunan K (2022), Reviewing the links and feedbacks between climate change and air pollution in Europe.
Front. Environ. Sci. 10:954045.
doi: 10.3389/fenvs.2022.954045

Reviewing the links and feedbacks between climate change and air pollution in Europe

Ulas Im[1]*, Camilla Geels[1], Risto Hanninen[2], Jaakko Kukkonen[2,3], Shilpa Rao[4], Reija Ruuhela[2], Mikhail Sofiev[2], Nathalie Schaller[5], Øivind Hodnebrog[6], Jana Sillmann[7], Clemens Schwingshackl[6,8], Jesper H. Christensen[2], Roxana Bojariu[9] and Kristin Aunan[6]

[1]Department of Environmental Science/Interdisciplinary Centre for Climate Change, Aarhus University, Roskilde, Denmark, [2]Finnish Meteorological Institute, Helsinki, Finland, [3]Centre for Atmospheric and Climate Physics Research, Centre for Climate Change Research, University of Hertfordshire, Hatfield, United Kingdom, [4]Norwegian Institute of Public Health, Oslo, Norway, [5]Swiss National Science Foundation, Bern, Switzerland, [6]Center for International Climate Research (CICERO), Oslo, Norway, [7]Center for Earth System Research and Sustainability, University of Hamburg, Hamburg, Germany, [8]Ludwig-Maximilians-Universität München, München, Germany, [9]National Meteorological Administration, Bucharest, Romania

Feedbacks between air pollutants and meteorology play a crucial role in the direction of the response of future climate and air pollution. These feedbacks are important to understand and quantify the potential impact of adaptation and mitigation policies setup for protecting the population against air pollution and heat stress. We review the interactions between climate and air pollution, with special focus on the projections of air pollution under different future climate scenarios and time horizons, based on a literature review of research articles and reports from the last decade. The assessment focuses on 1) the specific impacts of climate change on air pollution and natural particle and precursor emissions in Europe in the near future (2030), by mid-century (2050) and by end of the century (2100), 2) impacts on air pollution due to changes in emissions vs. changes in climate, 3) feedbacks from air pollution on climate, 4) impacts of climate change on wildland fires and air pollutant levels, and 5) the role of adaptation and mitigation policies on climate change and air pollution. Available literature to a large extent suggests that ozone concentrations will likely increase in the second half of the century by up to 9 ppb [−4 + 9.3], while in the first half of the century, changes are much smaller and are up to ±1.5 ppb. These changes are mainly attributed to increased temperatures and emissions of biogenic volatile organic compounds, but also depends on the models and scenarios used in these studies. On the other hand, the predicted changes in particle concentrations and chemical composition are uncertain and much smaller. Similar to ozone, larger changes in the particle concentrations are projected in the second half of the century. The main conclusion from this review is that the estimated changes in pollutant levels in the future vary significantly depending on the applied model systems, as well as the different emission or meteorological scenarios used in the different studies. Nevertheless, studies generally agree on the overall trend of the changes in

pollutant levels due to climate change, in particular in the second half of the century.

KEYWORDS

climate change, air pollution, Europe, wildland fires, ozone, particulate matter

1 Introduction

Climate change can affect air pollution both physically, by modifying transport and mixing of pollutants as well as emissions of natural origin, and chemically by affecting chemical reactions. Such changes can lead to a "climate change penalty" which can be defined as the deterioration of air quality due to a warming climate, in the absence of changes in anthropogenic polluting activities (Fu and Tian, 2019). Changes in climate also influence the frequency and intensity of natural wildland fires (Lozano et al., 2017). Vice versa, pollutants in the atmosphere and their precursor emissions can influence climate by modifying clouds properties, precipitation, and radiation (Myhre et al., 2013). Feedbacks between climate change and air pollution should thus be taken into account in developing mitigation and adaptation strategies. However, the existing knowledge gaps on the involved mechanisms result in large uncertainties in the understanding and quantification of these feedbacks. For instance, although the main cause of wildfires currently is anthropogenic, i.e., caused by agriculture and forest management practices (Sofiev et al., 2013), projections suggest that the risk of wildland fires will increase due to higher temperatures and droughts (IPCC, 2022; McCarty et al., 2021; Dupuy et al., 2020). Recent findings from the latest Coupled Model Intercomparison Project Phase 6 (CMIP6: e.g., Turnock et al., 2020), the sixth assessment report from the IPCC (AR6), as well las the latest assessment on the short lived climate forcers (SLCFs) from the Arctic Monitoring and Assessment Programme (AMAP 2021) shows that future anthropogenic pollutant source strengths and levels decrease under all scenarios over Europe, but also in some other regions globally. This suggests that natural sources such as mineral dust, sea-salt, and wildland fires can be important drivers of air pollution and climate over Europe, where the feedback mechanisms and climate adaptation/mitigation scenarios will be particularly important.

Due to the above reasons, the aim of this study is to review the latest literature on the interactions between climate change and air pollution and assess the effects of climate change on surface ozone (O_3) and fine particulate matter ($PM_{2.5}$) levels over Europe, and how they will change in the future. Section 1 introduces the major mechanisms and pathways of meteorology-air pollution interactions and summarizes the current knowledge and findings regarding the different physical and chemical processes in relation to climate change and air pollution; Section 2 summarizes the recent findings on the specific impacts of climate change on ozone and particulate matter concentrations, respectively; Section 3 compares the relative impact of future emissions on air quality versus the impacts on air quality caused by climate change alone; Section 4 summarizes recent findings on the impacts of atmospheric composition on climate change; Section 5 summarizes the impacts of climate change on wildland fires and consequently on air pollution and climate change; Section 6 summarizes the co-benefits of climate adaptation and mitigation on air pollution; and finally, Section 7 offers some recommendations regarding needs for future research. Therefore, the current review paper attempts to give a more holistic picture of future air pollution and climate change, as well as feedbacks, impacts of emerging sources such as wildland fires, and climate adaptation and mitigation, compared to the existing reviews.

1.1 Mechanisms by which climate affects air pollution

Meteorology is a major driver of the fate of all chemically active species within the atmosphere, including climate-relevant compounds like carbon dioxide (CO_2), methane (CH_4), ozone (O_3) and secondary inorganic (e.g., sulfate and nitrate) and organic aerosols. Changes in the climate and thereby in meteorological factors can affect atmospheric composition in several ways: 1) Changes in temperatures, precipitation and wind patterns may affect the natural sources of aerosols in the atmosphere, including mineral dust, sea salt, and biogenic volatile organic compounds (BVOCs). 2) This is also the case for anthropogenic sources, where e.g., increasing temperatures will increase NH_3 emissions from agricultural activities and VOC emissions from loading of petroleum products. 3) Changes in temperature, humidity, solar radiation, and other meteorological factors can affect the rate of photochemical, oxidative, and other chemical reactions, speeding up or slowing down the chemical transformation of emitted species. 4) Changes in wind patterns, ambient temperatures and precipitation affect transport and mixing of atmospheric components, as well as deposition processes. 5) Changes in large-scale weather patterns, which control the dispersion and transport of air pollutants, can result in changes of the frequency and intensity of air pollution events. In summary, to understand how climate change may affect air pollution, one needs to consider how climate affects the full range of biological, chemical, and physical processes. Figure 1 summarizes how climate affects

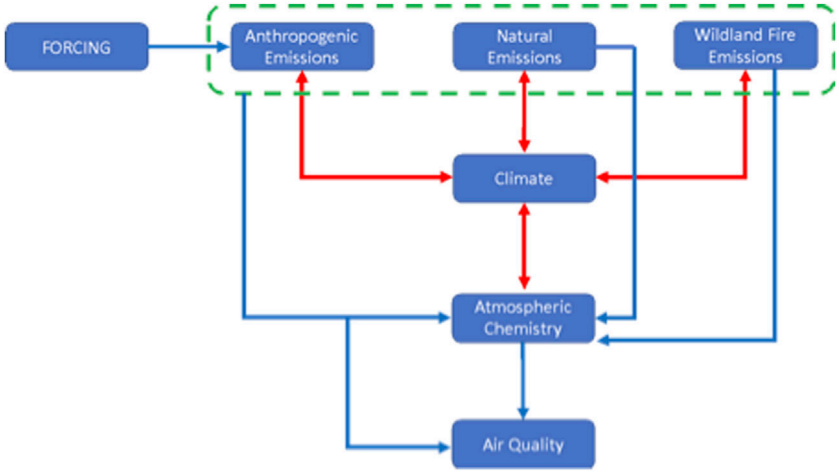

FIGURE 1
Interactions between climate, emissions and air quality (adopted from Jacob and Winner, 2009). Forcing term refers to the changes in the socioeconomic factors. The green dashed box shows the different emissions, while the red and the blue arrows show two-way and one-way interactions, respectively.

air quality and the two-way interactions between emissions and climate.

Certain types of synoptic and meteorological drivers favor higher concentrations of ozone (Otero et al., 2016). In particular, atmospheric blocking favors the occurrence of heatwaves and high ozone concentrations in the summer (Hodnebrog et al., 2012; Pfahl and Wernli, 2012). Pfahl and Wernli (2012) found that up to 80% of summer warm extremes are associated with blocking. Although climate models have notoriously had problems representing atmospheric blocking, large model ensembles can reproduce observed correlations between heat waves and these events, and results suggest that the frequency of blocking events in Europe will not change dramatically in the future, and neither will the relationship between blocking events and heatwaves (Schaller et al., 2018). However, with global warming, heatwaves will get more intense, more frequent, and last longer (Russo et al., 2014), increasing the likelihood for periods with higher ozone concentrations and high temperatures, especially during blocking events.

1.2 Climate change impacts on natural emissions

Wind speed and sea-surface temperatures also modify the production of sea-salt aerosols (SSA) emissions (Soares et al., 2016). The two main mechanisms responsible for sea spray formation are air bubble-bursting during whitecap formation, and decay and direct tearing of droplets from the top of breaking waves. Therefore, the formation of primary SSA is mainly dependent on wind speed (Monahan et al., 1986). In addition, laboratory (Mårtensson et al., 2003) and *in situ* measurements (Nilsson et al., 2007) showed that for nano-sized particles, the aerosol number emission in nano sizes decreases with increasing seawater temperature, while number emissions of particles larger than 100 nm increase with increasing seawater temperature.

Wind speed and precipitation also impacts the mineral dust emissions and their transport. Changes in wind can modify both the emissions of mineral dust particles, as well as their transport pathways. The dust emissions depend on the availability of fine crustal material that can be lifted from the ground when surface wind velocity exceeds a certain threshold. This threshold depends on surface roughness (e.g., rocks and vegetation), grain size and soil moisture. Mineral dust is an important natural source of atmospheric aerosols, and interferes with the atmosphere's radiation, impacting climate (Klingmuller et al., 2019). However, there are large variations among projections of the future global mineral dust burden (Boucher et al., 2013). While some studies show decreases by up to 60% globally, mainly due to the effect of CO_2 fertilization on vegetation (Mahowald et al., 2006), others project moderate (10%–20%: Tegen et al., 2004; Jacobson and Streets, 2009; Liao et al., 2009) to large increases (tripling) due to large increases in bare soil fraction (Woodward et al., 2005). The large range reflects different responses of the atmosphere and vegetation cover to climate change, and results in low confidence in these model predictions. The frequency of dust events might also change with climate. By analyzing historical high-resolution glacio-chemical data from the Swiss-Italian Alps in

combination with meteorological parameters, Clifford et al. (2019), e.g., predict that a future warming will result in less frequent, but more intense events, where dust is transported from Sahara to Europe.

Increasing temperatures can lead to increased emissions of biogenic VOCs such as isoprene and terpenes, which are emitted by the vegetation, and are important precursors for O_3 and secondary organic aerosols (SOA) (Guenther et al., 2006). The future development in the emission of BVOCs is also depending on the atmospheric CO_2 level, where a tendency of a CO_2 inhibition is seen for isoprene emissions (Arneth et al., 2007), while the impact on monoterpenes is more unclear (Arneth et al., 2007). Although isoprene is the largest biogenic contributor to SOA formation globally, over Europe aerosol formation is enhanced in the presence of mainly monoterpenes (D'Andrea et al., 2015). In contrast, the importance of isoprene for O_3 formation is higher than that of other terpenoids. In addition to the type of the biogenic species and the availability of nitrogen oxides as reaction partners, recent investigations show that positive feedbacks exist between biogenic and anthropogenic VOCs for aerosol formation as well as ozone formation (Grote, 2019). Finally, recent studies highlighted the importance for extreme weather conditions such as droughts on the emissions of biogenic precursors such as isoprene (e.g., Pegoraro et al., 2004; Jiang et al., 2018), which is important due to the projected increase in the intensity of these drought periods (IPCC, 2013; Hoegh-Guldberg et al., 2018). Jiang et al. (2018) estimated a 17% reduction in the global isoprene emissions when the drought stress on the plants is taken into account, translating to a decrease of surface O_3 mixing ratios by 3 ppb over Europe.

1.3 Climate change impacts on anthropogenic emissions

Meteorological parameters like surface wetness, wind and especially temperature have also been shown to have an important impact on emissions related to human activities. The ammonia emissions (NH_3) from agricultural sources have been projected to increase significantly in Europe in a future climate (Skjøth and Geels, 2013) and at the global scale an empirical estimate proposes that a 5°C temperature increase would increase NH_3 emission by 42% [28%–67%] (Sutton et al., 2013; Fowler et al., 2015). This suggested climate penalty on NH_3 can through the conversion to ammonium (NH_4^+) also affect the $PM_{2.5}$ levels in Europe. In addition, changes in temperatures also impact the use of ventilation systems, thus modifying energy production and related emissions; warmer temperatures increase the energy demand for cooling in the summer, while decreasing the demand for heating in the winter (EEA, 2019a). In addition, changes to the hydrological cycle have an impact on hydropower (EEA, 2019a). An important source for PM in Europe is residential wood combustion, e.g., small-scale combustion units, where the ambient temperature influences the extent of the use.

1.4 Climate change impacts on chemical processes

The role of meteorological factors such as temperature and relative humidity for atmospheric chemistry is to a large extent through its influence on the hydroxyl radical (OH), which is the major component for the oxidizing capacity of the troposphere and thus crucial for the chemical removal of pollutants. The primary sources of OH are the photolysis of O_3, and reaction with water vapor, the latter increasing with a warming climate (Seinfeld and Pandis, 2016). Increase in temperatures results in an increase in summertime ozone over polluted areas due to increased photochemical activity, and a reduction of background ozone due to an expected increase in water vapor (Jacob and Winner, 2009). In addition, increasing temperatures also increase sulfate aerosol (SO_4^{2-}) formation due to faster sulfur dioxide (SO_2) oxidation, while nitrate (NO_3^-) particles decrease as ammonium nitrate evaporates and nitrate shifts from the particle phase to the gas phase (Dawson et al., 2007). On the other hand, increasing temperatures can also reduce $SO_4^=$ aerosols due to less available OH to react with SO_2 in order to produce SO_4^{2-}, as increased biogenic emissions also react with the available OH, thus competing with SO_2 (Im et al., 2012). SOA can both be reduced due to the shift from particle to gas phase and increase due to the increase of biogenic SOA precursors (Sheehan and Bowman, 2001; Kanakidou et al., 2005; Tsigaridis and Kanakidou, 2007).

1.5 Climate change impacts on production, dispersal, and removal rates

In addition to temperature, there are other meteorological factors affecting the production, dispersion, and removal of air pollutants. Climate change can modify large-scale circulations (Otero et al., 2018), thus ventilation (wind speed/direction, mixing height). Lower wind speeds in polluted regions can cause O_3 concentrations to increase due to longer residence/reaction time and due to increased aerodynamic resistance to dry deposition (Dawson et al., 2007). Mixing heights have a more complicated effect on O_3 concentrations. Increasing mixing height increases surface O_3 levels under low-surface O_3 conditions due to the downwards transport of tropospheric O_3 lying above the mixing layer, while it decreases O_3 under high-surface O_3 conditions due to the increased vertical dispersion of surface O_3 (Liu et al., 1987; Kleeman, 2007). Changes in ventilation have stronger effects on particulate

matter (PM) than on O_3 because of the lower PM background concentrations (Jacob and Winner, 2009). Increasing ventilation rates can have a diluting effect on PM, as well as a compensating effect that is associated with a decrease in precipitation, leading to reduction in removal via wet deposition. Dry deposition of both gasses and PM are also dependent on the surface conditions, where e.g., a decrease in the snow cover can lead to an increase in the deposition over land. Opposite will a decrease in the sea ice extent result in a decreased removal over marine areas as O_3 deposits slower to water surfaces than to sea-ice.

PM concentrations decrease with increasing precipitation as wet deposition is the main removal process for PM, in addition to sedimentation that affects coarse particles. Summertime PM levels are highly sensitive to precipitation frequency, when events tend to be convective and small in scale, while they show a low sensitivity in winter when synoptic-scale storms dominate. Changes in humidity and cloudiness also affect PM concentration and properties. Increasing relative humidity increases the PM water content and thus, the uptake of semi-volatile components, mainly for nitrate and organics. Sulfate can be produced by the aqueous-phase oxidation of SO_2 by hydrogen peroxide (H_2O_2) in the cloud. However, due to the short time scale of this process (i.e., minutes), it is very challenging to simulate aqueous-phase sulfate formation in clouds in mesoscale or global models (Koch et al., 2003).

2 Climate change impacts on surface level air pollution

There are several approaches that are used in the literature in order to understand how O_3 and particulate matter (PM) are influenced by changes in climate or emissions (Fiore et al., 2019). These include 1) sensitivity studies in which individual meteorological parameters are perturbed, 2) statistical downscaling of future changes in meteorology, using correlations between observed changes in air quality and meteorological variables from climate models, 3) the direct calculation of air quality by using fully coupled global or regional chemistry–climate models (CCM), global-to-urban CCMs, or off-line global or regional chemical transport models (CTMs) forced by either projections of meteorological fields from separate atmosphere–ocean general circulation models, or dynamically downscaled meteorology. In addition, there is also large literature available on the statistical relationships between observed meteorological parameters and air pollution concentrations (Im et al., 2006, Im et al. 2008, Jacob and Winner, 2009). Such studies aid in understanding the short-term changes in air pollution concentrations with changes in meteorological factors, which can be used to extrapolate for future conditions (e.g., Cheng et al., 2007; Lin et al., 2007).

2.1 Climate change impacts on surface ozone

Atmospheric O_3 and its sensitivity to climate change has gained increasing attention throughout the last decades. First in simplified sensitivity studies where one parameter (e.g., temperature) was changed in chemistry transport models (CTM) and then in more complex studies using chemistry-climate models directly or by using CTMs driven by meteorological 3-D fields projected by climate models (e.g., Hedegaard et al., 2008). Some studies have looked at the global scale, while more studies have focused on projections of the chemistry-climate impacts over polluted regions in mainly the United States and Europe. In order to isolate the effect of climate change, the anthropogenic emissions have typically been kept constant in these studies. In more recent years a number of reviews have gone through the literature summarizing the latest findings regarding the climate change penalty on surface O_3. We will in the following focus on recent findings for Europe and give an overview of the related uncertainties and knowledge gaps.

Figure 2 summarizes the recent findings on the impacts of climate on the future levels of European O_3, adopted from Fu and Tian (2019). The potential future developments in air pollution levels in Europe were studied in a multi-model setup including four state-of-the art chemistry-transport models (Lacressonnière et al., 2016; Watson et al., 2016). Assuming +2°C global warming, the model simulations pointed towards a modest increase in the average O_3 levels over Europe during summer (−0.1 to +0.8 ppb relative to present day), but the results were not statistically significant across the four models (Watson et al., 2016). When analyzing the SOMO35 (sum of daily maximum O_3 exceeding 35 ppm) in more details, Lacressonnière et al. (2016) showed that the majority of the models simulate an increase in summertime O_3 across Europe, and for parts of central Europe, Eastern Europe and in Spain all the models agree on higher surface O_3 levels during the summer. All models indicate smaller changes during winter. Similarly, Collette et al. (2015), using a meta-analysis of 25 model projections, found a summertime penalty in the continental Europe surface O_3 levels of [0.44–0.64] and [0.99–1.50] ppb for the periods 2041–2070 and 2071–2100, respectively. However, these numbers include a latitudinal tendency in the penalty. In Southern and Central Europe, the climate penalty is more pronounced and by the middle of the century the summertime change in O_3 can exceed + 1 ppb. In contrast, a small decrease in the summertime O_3 level was projected at more northern latitudes (Scandinavia and British Isles).

In a more recent study, Fortems-Cheiney et al. (2019) used the CHIMERE CTM in combination with the RCP8.5 and RCP4.5 climate scenarios and scenarios for anthropogenic emissions to investigate the impact of a +3°C and +2°C temperature change. Based on simulations including emissions for 2050 (the ECLIPSE-v4a CLE) the differences in the annual

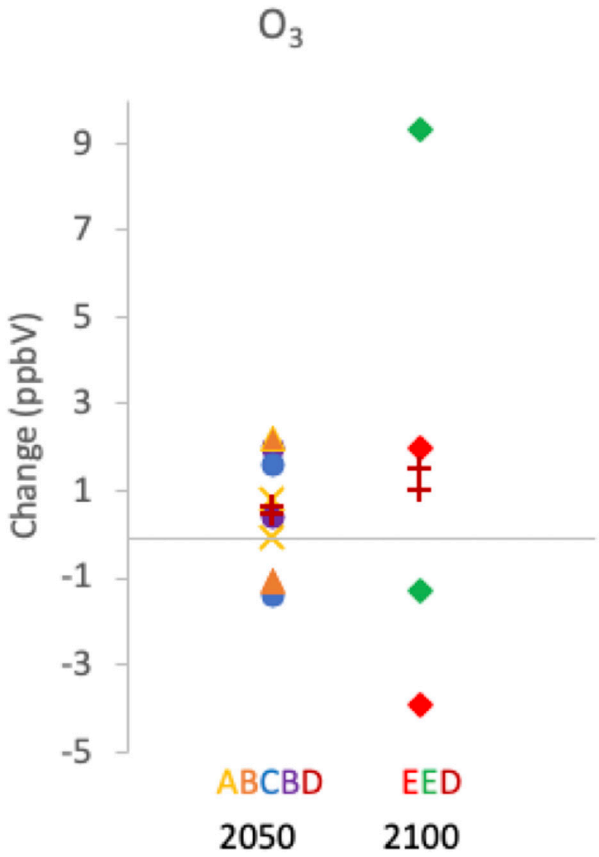

FIGURE 2
Model projections of O_3 as calculated by the studies included in this review, based on Fu and Tian. (2019). The changes are color- and symbol-coded by the studies; **(A)** Watson et al. (2016), **(B)** Fortems-Cheiney et al. (2019), **(C)** Glotfelty et al. (2016), **(D)** Colette et al. (2015), and **(E)** Schnell et al. (2016). Each study is represented by the lower and upper estimates of the projections if available.

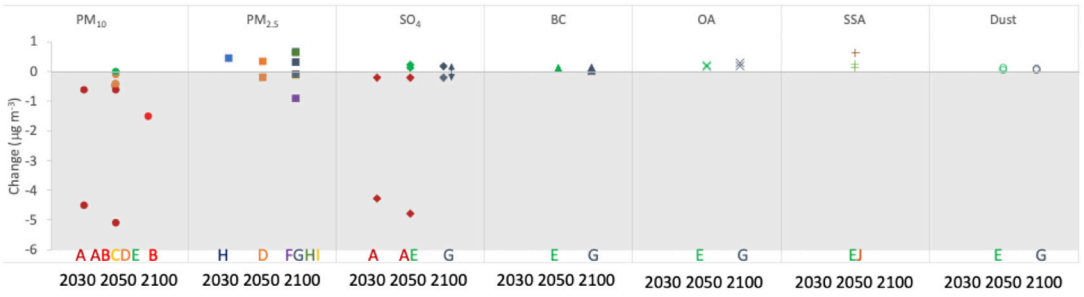

FIGURE 3
Model projections of PM and its components as calculated by the studies included in this assessment report. The changes are color- and symbol-coded by the studies; **(A)** Lacressonniere et al. (2014), **(B)** Juda et al. (2012), **(C)** Manders et al. (2012), **(D)** Lacressonniere et al. (2017), **(E)** Cholakian et al. (2019), **(F)** Lemaire et al. (2016), **(G)** Westerveld et al. (2016), **(H)** Silva et al. (2017), **(I)** Park et al. (2020), **(J)** Soares et al. (2016). Each study is represented by the lower and upper estimates of the projections if available.

TABLE 1 Impacts of temperature-driven pathways on surface O_3 and PM, adapted from Jacob and Winner (2009), Isaksen et al. (2009) and Fiore et al. (2012).

	Ozone	PM	Wildfires	Level of confidence
Temperature	++	−	++	Medium
Regional Stagnation	++	++		Medium
Wind speed	−	−		Low
Mixing height	=	−−		Low
Humidity	=	+	−−	High
Cloud cover	−	−		Low
Precipitation	=	−−	−−	Low
BVOC Emissions	+	+		Low
Wildfires	++	+		Medium

Symbols depict consistently positive (++), generally positive (+), weak or variable (=), generally negative (−), and consistently negative (−−).

mean European O_3 levels between a +2°C (31.99 ± 1.01 ppb) and +3°C (34.41 ± 1.07 ppb) scenario are statistically significant. On average the levels are 8% higher in the +3°C scenarios, illustrating the impact of the higher temperature alone (the impact from emissions will be discussed below). In relation to health issues, it is important to note that this study also finds that the frequency of days with high O_3 levels are increasing in the +3°C scenario leading to e.g., a higher number of days where the WHO limit value for ozone is exceeded in especially the South-eastern part of Europe. Fortems-Cheiney et al. (2019) concluded this was linked to a lower boundary layer height and a larger number of very hot summer days in this region in the warmer scenario.

Using simulations with five CMIP6 models considering future climate (ssp370SST) and present-day climate (ssp370pdSST) under the same future emissions trajectory (SSP3-7.0), Zanis et al. (2022) estimated a non-robust slight ozone benefit over Europe on an annual basis and in winter, which becomes slightly positive but non-robust among the models (an ozone penalty of 0.2 ppb $°C^{-1}$) during summer. These slightly negative or positive (in summer) signals Europe are attributed: 1) to the generally much lower NOx emissions, 2) to contributions from enhanced BVOC emissions and lightning NOx emissions, and 3) the competitive role of the large-scale background ozone chemical destruction linked to more water vapor under global warming.

I emission of biogenic VOCs (BVOCs) and the driving feedback processes is one of the key knowledge gaps (Fu and Tian, 2019). The terrestrial biosphere emits BVOCs as part of photosynthetic activity and the emission is a function of e.g., plant species as well as a number of environmental parameters like temperature and sunlight (Hantson et al., 2017). Natural BVOCs (e.g., isoprene and monoterpene) are therefore by nature highly variable in space and time. A warming climate can directly influence the emissions of biogenic VOCs and thereby O_3 levels (Im et al., 2011). The BVOC emissions are typically calculated on-line in the chemistry-transport models and several of the studies referred to above include a significant increase in the BVOC emissions in the projections for the future. However, the sensitivity to temperature can differ substantially between chemistry-transport models (Langner et al., 2012). Newer studies use more complex and dynamic vegetation models in order to assess the future developments in biogenic VOC emissions, when taking other drivers than temperature into account (e.g., Hantson et al., 2017; Bauwens et al., 2018). They show that increasing atmospheric CO_2 concentrations can lead to increased biogenic VOC emissions (the greening effect), but similarly can the inhibitory CO_2 effect work against this increase. The overall impact of processes is still not well understood. Likewise, natural, and anthropogenic induced vegetation changes can lead to changes in the distribution and strength of the biogenic VOCs emissions across Europe in the future. These studies indicate that the projections for future developments in biogenic VOCs still are very uncertain.

The large variability in the future surface O_3 levels in the different studies stem from several reasons including the uncertainty in biogenic emissions, the differences in models and their spatial/temporal resolution, and finally, the different emissions/climate scenarios used in the different studies.

2.2 Climate change impacts on surface particulate matter and components

2.2.1 Impacts on particulate matter mass

Impacts of climate on aerosol levels have been extensively studied over the last few decades. However, different studies focused on different time horizons (e.g., mid-century or end of the century), using different climate scenarios, and different chemistry and transport models (CTMs) that are either coupled to global/regional climate models, or CTMs driven by global climate projections downscaled to European scale. This section focuses on estimates of the isolated impacts of climate on the particulate matter (PM) levels and their chemical composition over Europe (i.e., model studies where emissions

of PM precursors are kept constant). Figure 3 summarizes the changes in PM and its components as calculated in the different studies. In general, studies agree in the direction of the response, regardless which climate scenario has been implemented, with business-as-usual scenarios giving the largest changes for the anthropogenic species. Dust concentrations stay relatively constant throughout the century, while sea-salt is projected to increase. It can also be seen that most studies calculated a weak impact of climate change on the chemical composition, while the level of confidence varies from low to medium as discussed in Jacob and Winner (2009), Fiore et al. (2012), and Isaksen et al. (2009), as summarized in Table 1.

While some studies performed sensitivity simulations to quantify the impact of various meteorological parameters on surface $PM_{2.5}$ levels, others performed climate simulations in order to study the evolution of future $PM_{2.5}$ concentrations. For example, Megaritis et al. (2014) investigated the impact of different meteorological variables on $PM_{2.5}$ concentrations, perturbing temperature, humidity, precipitation, and wind speeds individually, in prescribed increments. They showed that in Europe, $PM_{2.5}$ concentrations change by −0.7 to 0.3 μg m^{-3} per 1 K increase in temperatures, while they change by −0.13 to 0.16 μg m^{-3} per 1% change in humidity, by −0.11 μg m^{-3} per 1% increase of precipitation and by 0.14 μg m^{-3} per 1% increase of wind speed. They concluded that precipitation is expected to have the largest impact on $PM_{2.5}$ concentrations under a changed future climate, driven mainly by the accelerated wet deposition of $PM_{2.5}$ species and their gas precursors. They showed that $PM_{2.5}$ concentrations can change by up to ±2 μg m^{-3} in the future due to changes in precipitation. In addition, they projected that changes in wind speed over Europe in the future can change $PM_{2.5}$ levels up to ±1.4 μg m^{-3}.

Surface PM_{10} concentrations over Europe are projected to decrease in many studies due to meteorological factors. In the near-future (2030), PM_{10} (PM with a size below 10 μm) concentrations are projected to decrease by 0.6 μg m^{-3} (summer) to 4.5 μg m^{-3} (winter) (Lacressonnière et al., 2014), while in 2050, PM_{10} concentrations are projected to decrease by 5.1 to 0.1 μg m^{-3} (Juda et al., 2012: Lacressonnière et al., 2014, Lacressonnière et al., 2017, Cholakian et al., 2019). These differences are attributed to increases in winter precipitation (Juda et al., 2012: Lacressonnière et al., 2014, 2017), increases in humidity (Lacressonnière et al., 2014), or changes in wind patterns and mineral dust emissions (Lacressonnière et al., 2017). Very recently, Cholakian et al. (2019) projected a decrease of PM_{10} concentrations by 0.01, 0.01, and 0.42 μg m^{-3} under the RCP2.6, RCP4.5, and RCP8.5 climate scenarios, respectively. Their analyses showed that these changes can vary seasonally and by the different aerosol species comprising the PM mass. They also showed that when the impacts of climate change are isolated, nitrate decrease governs the decrease of PM_{10} and $PM_{2.5}$ in RCP4.5 and RCP8.5; however, in RCP2.6, the increase in dust, sea-salt and biogenic SOA particles outweigh the decrease in nitrates.

Opposite to PM_{10}, meteorological conditions are projected to lead to an increase in surface $PM_{2.5}$ concentrations over Europe by mid-century. $PM_{2.5}$ (PM with a size below 2.5 μm) concentrations are projected to increase slightly in most studies. There are, however, also studies showing decreases, but in smaller magnitudes compared to the increases. Silva et al. (2017) showed that population-weighted $PM_{2.5}$ concentrations will increase by 0.3 μg m^{-3} in 2030 under the RCP8.5 scenario. By the mid-century, $PM_{2.5}$ levels are projected to change by −1.6 to 2.47 μg m^{-3} (Lacressonnière et al., 2016; Lemarie et al., 2016; Silva et al., 2017). Lacressonnière et al. (2016), using three regional CTMs coupled with climate models, calculated an ensemble mean change in $PM_{2.5}$ concentrations of −0.5 to 1.3 μg m^{-3}. They have found an increase of $PM_{2.5}$ over southwestern Europe, while a decrease is projected over some parts of eastern and central Europe. They showed that the largest differences due to changes only in climate are due to dust and sea salt, which are largely dependent on meteorological fields, as described above.

By the end of the century, studies do not agree on the direction of the changes in surface $PM_{2.5}$ concentrations over Europe. Lemarie et al. (2016) projected a decrease of area-weighted $PM_{2.5}$ concentrations by 0.98 μg m^{-3} by the end of the century, mainly attributed to changes in surface temperature. They suggested a strong influence of high vertical stability events, where low surface temperature and planetary boundary layer (PBL) height leads to an increase in $PM_{2.5}$ concentrations, while for high temperature ranges, the PBL height becomes a less discriminating factor. However, they suggest that even though the PBL depth constitutes the most important meteorological driver for $PM_{2.5}$, it does not evolve notably compared to the surface temperature in the future. Recently, Park et al. (2020), using a set of ACCMIP global models, showed that in 2100, $PM_{2.5}$ concentrations over Europe will increase on average by 0.13 μg m^{-3} (5.1%), ranging from −0.23 to 0.50 μg m^{-3}, under the RCP8.5 scenario, in agreement with Westervelt et al. (2016) who calculated an increase of 0.19 μg m^{-3} in $PM_{2.5}$ concentrations. Westervelt et al. (2016) also showed a decrease of $PM_{2.5}$ concentrations by 0.2 μg m^{-3} in 2100 if RCP2.6 is used instead of RCP8.5.

2.2.2 Impacts on chemical composition

In addition to the direct impacts of meteorology on PM levels and composition, impacts due to change in emissions are also important. Im et al. (2012) calculated that higher temperatures increase biogenic emissions, thereby enhancing biogenic SOA by 0.01 ± 0.00 μg m^{-3} K^{-1} and NO_3^- aerosol concentrations by 0.02 ± 0.02 μg m^{-3} K^{-1}. They also showed that increased temperatures reduce anthropogenic SO_4^{2-} by

0.04 ± 0.07 μg m^{-3} K^{-1}, induced by significant reduction in the cloud cover (90% K^{-1}) and subsequent aqueous-phase production. The $PM_{2.5}$ concentrations show a very small positive response to temperature changes, increasing by 0.003 ± 0.042 μg m^{-3} K^{-1} (0.04% K^{-1}) due to the compensation of organic carbon increases by nss-SO_4^{2-} reductions. They also showed that locally, larger changes can take place, with anthropogenic SO_4^{2-} and NO_3^- in fine aerosols reduced by up to 0.62 and 0.80 μg m^{-3} K^{-1}, respectively. Increases as high as 0.097 and 0.034 μg m^{-3} K^{-1} are calculated for organic and elemental carbon, respectively. Results show that changes in temperature modify not only the aerosol mass but also its chemical composition.

Regarding SO_4^{2-} aerosols, studies are not consistent in the direction of the change in concentrations in response to changes in climate. Lacressonniere et al. (2014) projected a decrease of SO_4^{2-} concentrations by 4.2 to 0.3 μg m^{-3} in 2030, while in 2050, they projected a slightly larger decrease, which they attributed to higher precipitation and humidity in 2050 compared to 2030, enhancing the transformation of SO_2 into SO_4^{2-} aerosols. Cholakian et al. (2019), on the other hand, projected an increase of SO_4^{2-} by 0.02 μg m^{-3} (RCP8.5) to 0.11 μg m^{-3} (RCP4.5) in 2050, based on the different RCP scenarios they used, attributed to higher humidity in winter and higher OH levels in summer due to increased temperatures. They also showed that decreased mixing heights contributed to these increases.

All the different studies agreed on a likely increase of organic aerosols (OA), due to increased temperatures, and thus increase in biogenic emissions and OH levels. While increased temperatures lead to increased biogenic emissions, which in return consume the available OH, it also leads to increased OH by regeneration chemistry by increasing O_3 in areas with sufficient levels of NOx. Cholakian et al. (2019) projected an increase of 0.06 to 0.12 μg m^{-3} in 2050 under the different RCP scenarios. Westervelt et al. (2016) projected end of the century increases of 0.09 to 0.19 μg m^{-3} under RCP2.6 and RCP8.5 scenarios, respectively. Regarding sea-salt concentrations, these slightly increase by 0.01–0.11 μg m^{-3}, due to increases in wind speeds (Cholakian et al., 2019) and sea-surface temperatures (Soares et al., 2016), leading to increased sea-salt emissions. Regarding dust concentrations, Westervelt et al. (2016) shows a slight increase in 2100 according to the RCP2.6 scenario due to an increase in wind speeds, while in RCP8.5, a decrease is projected due to a decrease in wind speeds.

The variability in the future surface aerosol levels and composition in the different studies stem from several reasons including the uncertainty in biogenic emissions, which impacts the biogenic SOA formation, the differences in models in terms of aerosol representations, in particular how they treat SOA and their spatial/temporal resolution, and finally, the different emissions/climate scenarios used in the different studies.

3 Impacts on air pollution due to changes in emissions vs. changes in climate

Several of the model studies included in this review have also analyzed the combined effect of future changes in both climate and air pollutant and precursor emissions such as NOx, CO, SO_2, NMVOCs, and primary particles. For Europe, the anthropogenic emissions of the main air quality components (e.g., SOx, NOx, and $PM_{2.5}$) are projected to decrease in the future posing the central question whether the benefits of these emission reductions are counteracted by a possible climate penalty.

The latest CMIP6 models under different future scenarios, shared socio-economic pathways (SSPs) showed that O_3 concentrations over Europe can increase by up to 4 ppb compared to the 2005–2014 mean under low mitigation scenarios (e.g., SSP3-7.0 and SSP5-8.5), while high mitigation scenarios lead to decreases by up to 16 ppb (in SSP1-2.6) (Turnock et al., 2020). Surface $PM_{2.5}$ concentrations over Europe, on the other hand, are projected to decrease consistently by all models by 1–4 ug m^{-3}. The recent studies conclude that expected emission changes in comparison to impacts of climate will have the largest impact on European O_3 levels (e.g., Colette et al., 2015; Westervelt et al., 2016). This conclusion is, however, very dependent on the scenarios used for Europe, but also for the developments outside Europe. In the study by Fortems-Cheiney et al. (2019), the high emission scenario RCP8.5 and the related higher European O_3 concentrations, would to a large degree be caused by inflow from outside Europe. In the more detailed study by Lacressonniere et al. (2014), it is also shown that long-range transport from outside Europe can increase the O_3 levels in Northern Europe in spite of decreasing European emissions. The impact of the European emissions was studied directly by Fortems-Cheiney et al. (2019) as they were running a CTM with both current day (2005) and future (2050) European emissions and future climate data. The applied Current Legislation emissions for 2050 projects a significant decrease (more than 40%) in most components across Europe (except for the Turkish area). When emissions are fixed to 2005 under RCP8.5 for 2050, the mean summer O_3 levels increase by up to +12% (+4.30 ppb), except in urban areas with high NOx emissions. Studies also showed that the anthropogenic emissions within the European region have the largest impact on the European PM concentrations towards the end of the century, compared to developments in both climate and long-range transport (Cholakian et al., 2019).

The future developments in health impacts related to air pollution have also been assessed in a number of studies (see e.g.,

the review by Doherty et al., 2017 and the global study by Silva et al., 2017). Geels et al. (2015) combined two CTMs with a health assessment model and focused on the development in the number of premature deaths related to $PM_{2.5}$ and O_3 in Europe in the 2050s and 2080s. Climate change alone in the RCP4.5 scenario, where emissions were kept constant, had only minor impacts (±2%–4%) on the $PM_{2.5}$ related number of cases, while the number of cases related to O_3 increased by up to 10% (relative to the 2000s). Including the emissions from the same RCP4.5 scenario leads, however, to significant decreases in the health effects especially for $PM_{2.5}$ with a significant decline in the number of premature deaths (~65% in 2050s and ~80% in 2080s). But, as pointed out by Doherty et al. (2017), the health assessments for future conditions are related to additional uncertainties as e.g., the temperature effects on applied pollutant-response relationships are not well known.

4 Feedbacks from air pollution on climate

Air pollutants like O_3 and different types of aerosols [e.g., black carbon (BC), SO_4^{2-}, NO_3^- and organic aerosols (OA)] have important radiative effects on climate, while other pollutants such as carbon monoxide (CO), VOCs, nitrogen oxides (NOx) and SO_2, although being negligible greenhouse compounds themselves, have an important indirect effect on climate by altering the abundances of radiatively active gasses such as O_3 and CH_4, a well as by acting as precursors for secondary inorganic and organic particles (Stohl et al., 2015).

Tropospheric climate–chemistry interactions are to a large extent related to chemical and physical processes and to compounds that show large variability in global distribution and trends, mainly driven by precursor emissions that also show large spatial variability. Atmospheric composition influences climate by regulating the radiation budget and cloud properties (Boucher et al., 2013; Stohl et al., 2015; Bellouin et al., 2020), through the presence of water vapor (H_2O), CO_2, CH_4, O_3, and aerosols. The main radiative effect of the gasses is through the greenhouse effect (i.e., through interference with long-wave radiation), thus heating the atmosphere, while aerosols may either heat or cool the surface (through interference with short-wave radiation), depending on their optical properties (Table 2: Bond et al., 2013; Stohl et al., 2015).

Aerosol–cloud interactions represent an area with potential for strong interactions in the climate system (Myhre et al., 2013). The largest uncertainty in the climate projections caused by the interaction of aerosols with clouds (Lee et al., 2016; Mülmenstädt and Feingold, 2018). The representation of aerosol-cloud interactions in ESMs remains a challenge in the Sixth Assessment Report (AR6) from IPCC, due to the limited representation of important sub-grid scale processes, from the emissions of aerosols and their precursors to precipitation formation and lack of certain processes such as contribution from anthropogenic aerosols acting as ice nucleating particles (INP) and aerosol effects on deep convective clouds. Aerosols determine the cloud radiative properties and thus the radiative heating/cooling and participate in the precipitation process. Although considerable progress has been made in recent years to include parameterization of aerosol–cloud droplet interaction and explicit microphysics for cloud water/ice content in climate models, inadequate understanding of the processes contributes to significant uncertainties in model simulated future climate changes (Table 2: Malavelle et al., 2017; Toll et al., 2019). According to IPCC AR6, effective radiative forcing due to aerosol-cloud interactions (ERF_{aci}) based on observational evidence alone ($-1.0 \pm 0.7\ W\ m^{-2}$) is very similar to the one

TABLE 2 Impacts of gasses and aerosols on the top of the atmosphere (TOA) radiative forcing due to aerosol-radiation interactions (ARI), adapted from Myhre et al. (2013).

Pollutants	TOA radiative forcing	Level of confidence
CO_2	++	Very high
CH_4	++	High
CO	++	Medium
NMVOC	++	Medium
NOx	=	Medium
O_3	=	Medium
SO_4^{2-}	−−	High
BC	++	Medium
OA	−−	High
Mineral Dust	=	High
Aerosol-cloud interactions	−−	Medium

Symbols depict consistently positive (++), generally positive (+), weak or variable (=), generally negative (−), and consistently negative (−−), following Jacobs and Winner (2009).

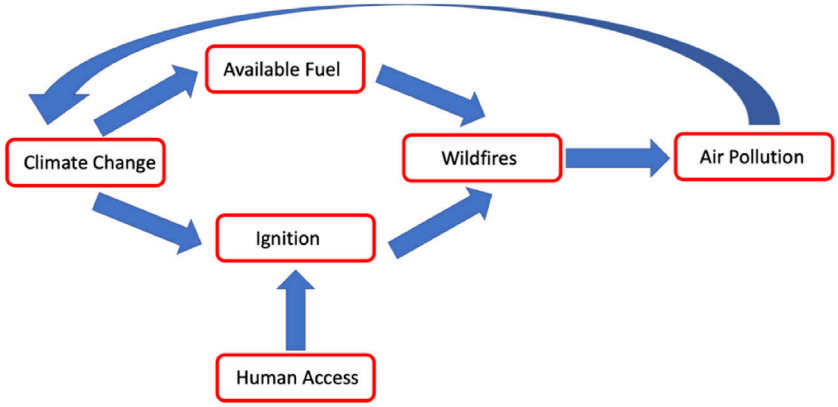

FIGURE 4
Feedback between climate change and wildfires adopted from Fischer et al. (2016).

based on model-evidence alone (-1.0 ± 0.8 W m^{-2}), with a medium confidence (Table 2), compared to the low confidence in AR5.

Regarding the trends in emissions of air pollutants affecting radiative forcing, large differences are observed in the temporal and geographical distributions of human-related (anthropogenic) emissions and natural emissions (Shindell and Faluvegi, 2009; Flanner, 2013). Anthropogenic emissions respond to regulations and to different growth rates in energy use, transportation, and industry. For example, emissions from Europe generally show reductions thanks to the regulatory actions taken over the last decades (EEA, 2019b), while emissions in regions like Southeast Asia, and in other developing countries show large increases during recent years (IEA, 2020). In addition to geographical differences, there are also sectoral differences, such as the large increases observed in aircraft and shipping (Isaksen et al., 2009). On the other hand, natural emissions of key climate precursors (NOx, CO, biogenic VOCs and sulfur compounds) are difficult to regulate and exhibit large year-to-year variations (e.g., in the case of biomass burning).

5 Climate change impacts on wildland fires

Climate change causes an increasing number of wildfires in some regions (Lozano et al., 2017) because it increases wildfire risk by raising the average temperature of the atmosphere, intensifying droughts, and prolonging the dry season (Figure 4). Driving mechanisms behind the fires have varied in different historical periods. Pechony et al. (2010) argued that in the preindustrial period, fires were strongly driven by lightning, rather than temperature. With the Industrial Revolution, this changed to an anthropogenic-driven regime (Sofiev et al., 2013), and there are now indications that we are moving towards a temperature-driven fire regime during this century. However, currently the main cause of wildfires is anthropogenic activities related to agriculture and forest management practices, as well as from recreational habits (Sofiev, 2013; Dijkstra et al., 2022). In Southern Europe, more than 95% of the fires with a known cause have an anthropogenic origin (Ganteaume et al., 2013; Parente et al., 2018), while in central Europe, more than 99% of fires are caused by humans (Ganteaume et al., 2013).

Modelling the impacts of climate change on wildland fires is very challenging due to the complex dynamics of fuel accumulation, vegetation dynamics and their interactions with changing climate, as well as the difficulty in representing the fire behavior patterns due to impacts of land management and human ignitions (Hantson et al., 2020; Sanderson and Fisher, 2020). Thus, projection of wildland fires over decadal to century timescales requires more mechanistic approaches, capable of capturing the numerous interacting system components that affect the evolution of fire risk. Process-based global fire models based on these principles have progressed rapidly over the past decade, although their use in fully coupled earth system models is still not standard practice (Sanderson et al., 2020), leading to omitting a potentially important component of the global carbon–climate feedback.

Interaction between the anthropogenic activity, land cover, meteorological conditions and intensity of wildfires (expressed as the amount of biomass burned or pollutants released) basically resides to the human activities playing the fire ignition and suppression roles whereas vegetation and weather modulate

the natural fire lifetime and potential for spreading (Prestemon et al., 2013; Fusco et al., 2016; Balch et al., 2017). Most studies that have estimated future fires (risk or area burned) have relied on statistical regressions. However, it is highly regionalized. For instance, in Indonesia (one of the largest sources of fire-induced pollution worldwide) the use of fire for clearing and preparing land on degraded peat is a routine repeated every year—with fires routinely getting out of control. However, it is the El-Nino-induced drought that can make them devastating (Field et al., 2015). In the Western US, worsening climatic conditions will lead the fires to become the main source of $PM_{2.5}$ if human behavior and practices remain the same (Yue et al., 2013; Liu et al., 2016). Similarly, Ford et al. (2018) found that, despite the reduction of anthropogenic $PM_{2.5}$, raising fire contribution will lead to a net increase of $PM_{2.5}$ in several US regions.

Wildfires are known to be the largest contributor to global biomass burning. They are a large source of atmospheric trace gasses and aerosols, in addition to major vegetation disturbance (Knorr et al., 2016). They emit into the atmosphere primarily CO_2 among other greenhouse gasses and carbonaceous particulate matter among other aerosols (Saarikoski et al., 2007). However, our knowledge of wildfires as an integrated part of the Earth system is still rather weak (Bowman et al., 2009; Langmann et al., 2009; Keywood et al., 2013).

In Europe, climate change is expected to increase the probability of forest fires in areas where increase in summertime temperature is accompanied by decrease in precipitation, as in the Mediterranean area (Mouillot et al., 2002; Bedia et al., 2014; Kalabokidis et al., 2014). In more northern regions the estimations of precipitation amounts are less conclusive (Jylhä et al., 2009; Ylhäisi et al., 2010; Venäläinen et al., 2020; Ruosteenoja and Jylhä 2021), which makes predicting the fire sensitivity much more difficult. A global modelling study of Knorr et al. (2017), unlike the research quoted above, gives a calmer picture. The authors conclude that at the global scale anthropogenic emission reduction will exceed increases in wildfire emissions and the WHO target of 10 $\mu g\ m^{-3}$ will be in reach in many regions. However, the authors also admitted high uncertainty connected with the fire abatement measures that were accounted for.

Air pollution due to $PM_{2.5}$ released from vegetation fires is a notable risk factor for public health everywhere in the world, also in Europe (Johnson et al., 2020). This should be taken into consideration when evaluating the overall health and socio-economic impacts of the fires. Kollanus et al. (2017) evaluated that in 27 European countries, over a thousand premature deaths were attributable to the vegetation-fire originated $PM_{2.5}$ concentrations in 2005 and 2008. Estimated impacts were highest in southern and Eastern Europe, but all countries were affected by fire-originated $PM_{2.5}$. Saarnio et al. (2010) analyzed smoke plumes originating from wild-land fires, which were detected in Helsinki, Finland, during a 1-month period in August 2006. The measurements showed that the major growth in PM concentration was caused by submicron particles consisting mainly of particulate organic matter. They reported an increase of a factor of 1.5–3.5 in $PM_{2.5}$ concentrations. Saarikoski et al. (2007) calculated that the wildland fires increased the $PM_{2.5}$ concentrations by a factor of 3.6–4.3. Sofiev et al. (2008) considered the influence of wild-land fires on air quality in Europe, using spring and summer seasons of 2006–2007 as prominent examples. High concentrations of nearly all pollutants were detected in Central, Eastern and Northern Europe in late spring of 2006, causing widespread allergic symptoms and other illnesses associated with poor air quality.

The aerosols produced by fires seem to be different from those emitted from e.g., anthropogenic industrial or transport sources: intriguing observations of Dusek et al. (2005) showed that peat-fire smoke has much weaker interaction with clouds than one would expect: less than 50% of smoke particles of suitable size were activated to CCN, whereas this number often approaches 100%. Therefore, the fire aerosols may not be very efficient shielding agents compared to other types of particles. The other factor is darkening of the surface after the fires: albeit small (at 1 km scale the albedo change is ~0.002 in sub-Saharan Africa (Gatebe et al., 2014)) these changes occur over wide areas and constitute noticeable additional radiative forcing.

Generally, there is some agreement that carbonaceous aerosol emissions from anthropogenic sources may decrease in the future (Lamarque et al., 2011; Bond et al., 2013; Shindell et al., 2013). Global total carbonaceous emissions are expected to be reduced due to new, less polluting technologies along with a shift away from the burning of coal and wood in the residential sector, while this reduction will vary regionally and not be reduced everywhere (Streets et al., 2004). However, the future trends of wildfires and their aerosol emissions is more uncertain due to complicated interactions between fire, land, atmosphere, and, most importantly, anthropogenic activities. Even now the state-of-the-art Earth system models have very limited capacity to simulate wildfire—climate interactions (Carslaw et al., 2010).

Estimating the fire emission heights is of particular importance when evaluating the coupling between terrestrial and atmospheric processes. Emission heights affect the aerosol long-range transport, aerosol-cloud interaction, and radiation (Luderer et al., 2006; Samset et al., 2013). One large problem is that emission heights are strongly affected by fire intensity and atmospheric stability. As illustrated by Joshi et al. (2007) and Luo et al. (2013), both of these are expected to change in the future. The emission height and its effect on atmospheric black carbon and its transport has been evaluated using present day climate conditions by Veira et al. (2015a,b), Sofiev et al. (2012, 2013), Kukkonen et al. (2014), and Daskalakis et al. (2015). Attempts to apply that same approach to future climate have more recently been done by Veira et al. (2016).

Radiative forcing due to aerosols originating from wildfires has mostly been investigated using present-day climatology and

prescribed wildfire emission inventories (satellite based). Based on the literature review by Veira et al. (2016), the most recent climate-aerosol models find that the total wildfire top of the atmosphere radiative forcing range between +0.18 W m^{-2} (Tosca et al., 2013) and −0.29 W m^{-2} (Jones et al., 2007).

6 Co-benefits and trade-offs related to GHG and air pollution mitigation and adaptation policies

There is a general consensus among studies that there are additional (co) benefits from mitigation of green house gases (GHG) emissions in terms of improved air quality (West et al., 2013; Bollen 2015; de Oliveira and Doll 2016; Klausbruckner et al., 2016; Rao et al., 2017), but these are rarely taken into account in policy developments and assessments at the European and national scale (Sokhi et al., 2022). The estimated improvements in air quality under different climate mitigation scenarios depend on socioeconomic and technological development and the assumptions on the development of air pollution in the next few decades. Rao et al. (2017) examined the impacts of different air pollution narratives under the global Shared Socio-economic Pathway (SSP) framework, concluding that scenarios with limited climate change mitigation present higher air pollution impacts than scenarios with more stringent mitigation trajectories. An overview paper (von Schneidemesser et al., 2015) concludes that any policy actions intended to mitigate one of these two issues must necessarily take into account the feedback with the other, to avoid that benefits to one sector will worsen the situation in another.

The effect of air pollution policies on climate have been investigated in some studies. Shindell et al. (2012) identified 14 emission control measures targeting short-lived climate pollutants (SLCPs) and relative to their reference scenario, found that all CH4 and BC control measures avoid a global mean surface temperature increase of ~0.5°C by 2050, although significant uncertainties exist regarding the extent to which reductions of SLCFs impact climate change (Myhre et al., 2013). In light of the estimated large adverse health impacts of air pollution around the globe, emission controls on SO_2, BC, and O_3 precursors may continue to be imposed irrespective of climate policy (Anenberg et al., 2012; Silva et al., 2013).

Reduction of non-SLCF pollutants, such as NO_2 and SO_2, generally leads to exacerbation of climate change because these species are the key aerosol precursors and responsible for almost 1 W m^{-2} or shielding from the solar radiation roughly-equally split between direct and indirect effects (IPCC AR5, Physical science basis). The secondary inorganic aerosols mainly consisting of nitrates and sulfates are highly reflective and highly soluble, thus facilitating both direct (reflection of sunlight back to space) and indirect (increasing the cloud albedo and modifying the cloud cover and rain patterns) aerosol effects. Recent studies showed that, e.g., The International Convention for the Prevention of Pollution from Ships—Annex VI (MARPOL-VI) required reduction of sulfur content in ship fuels brings substantial health benefits (global avoided mortality 74–200 thousand cases annually, 95% confidence interval) but adds about 0.07 W m^{-2} due to lost cooling effects of sulfates (Sofiev et al., 2018). Estimates of other studies of the shipping cooling effect showed similar results suggesting the range from ~0.04 W m^{-2} up to 0.11 W m^{-2} (Eyring et al., 2007; Fuglestvedt et al., 2008; Skeie et al., 2009; Lund et al., 2012).

Several studies show potential air quality co-benefits in Europe, including in the United Kingdom and Ireland (Karlsson et al., 2020; Alam et al., 2017, 2018; Wilkinson et al., 2009) and the Nordic countries (Åström et al., 2013; Williams, 2007). Rafaj et al. (2014) associate large potential co-benefits in Europe with renewable energy, due to reduced Mercury emissions to air. Collette et al. (2013) looked at combined projections of air quality and climate impact at the regional scale over Europe under the CMIP5 climate scenarios and conclude that exposure to air pollution will decrease substantially by 2050 according to a mitigation pathway that aims at keeping global warming below 2°C by the end of the century where exposure weighted SOMO35 and $PM_{2.5}$ are reduced by 80% and 78%, respectively in Europe. Large potentials for reaping air quality co-benefits are also shown for several European cities, e.g., Rotterdam (Tobollik et al., 2016) and Barcelona, Malmö, Sofia and Freiburg (Creutzig et al., 2012). Markandya et al. (2018) estimated that the co-benefits would make a valuable contribution towards covering the mitigation costs, from 7% to 84% in the EU-27 countries.

The impacts of climate adaptation policies on greenhouse gas emissions and air pollution have also been discussed. Classic adaptation strategies to increased temperatures like air conditioning have been shown to result in increased GHG emissions as well as increased air pollution (Abel et al., 2018; Watts et al., 2019). In a study in Eastern US, Abel et al. (2018) found that in a warmer climate 3.8% of the total increase in $PM_{2.5}$ and 6.7% of the total increase in O_3 are attributable to extra air conditioning use. Other climate adaptation actions like improving urban design to reduce heat stress can have significant co-benefits for air pollution (Cheng and Berry, 2013).

7 Summary and recommendations

The atmospheric concentrations of secondary pollutants like ozone or organic aerosols are expected to increase with the projected global warming, mainly due to an increase in the oxidation capacity of the atmosphere and the increase in natural emissions. On the other hand, the projected increases in precipitation are expected to enhance removal of pollutants from the atmosphere, resulting in a weak positive or negative change in the pollutants concentrations, in particular in the first half of the century. This strongly suggests that feedback between pollutants and climate change play a crucial role in the direction of the policy response on future climate change and air pollution. The net changes caused by the feedback vary geographically and seasonally, and, importantly, all studies reviewed here showed that changes in anthropogenic emissions had much larger impacts on air pollutant concentrations in the future, compared to the corresponding impacts caused by the projected changes in climate.

Studies showed that in most cases, there may be immediate air quality co-benefits from mitigation of GHGs due to reduced emissions of co-emitted air pollutants, such as aerosols, from the same sources such as energy production and industrial combustion. However, for instance increasing the residential combustion of wood due to climate policies may result in a substantial deterioration of air quality (e.g., Kukkonen et al., 2020). Noteworthy, the reverse relation does not necessarily hold: improving air quality often raises the challenges to climate change mitigation, since it may diminish the amount of solar radiation scattered back into space.

Socioeconomic and technological developments may influence the potential for air quality co-benefits. Recent findings suggest that limiting climate change mitigation today would entail higher air pollution levels in the future. Due to the adverse human health impacts of these pollutants, policies will continue to be implemented to reduce the emissions, in order to follow for example, the recent air quality recommendations from WHO. This implies that stricter climate policies are needed to counteract the increased global warming resulting from the pollutant removals.

As this review shows, the projections of how climate and health relevant air pollution components (e.g., $PM_{2.5}$ and O_3) will develop in the future across Europe, are still associated with major uncertainties. The differences in the modeled projections can to a large degree be attributed to the differences in the design in these studies e.g., in terms of the applied emission and climate scenarios. However, the chemistry-transport models also show differences in meteorology-air pollution relationships and so far, these differences have not been analyzed in detail (e.g., Kukkonen et al., 2012).

More advanced ecosystem models in recent studies have shown that the complex feedbacks between ecosystems and changes in climate, CO_2 levels, land-use etc. will modify the natural emissions of O_3 precursors to a larger degree than has been previously known. A robust quantification of the direction of this change is not possible with the current understanding, which is one of the main knowledge-gaps related to projections of future surface concentrations of O_3.

More research is needed for further development of climate and air pollution models, in terms of their capabilities in representing different chemical/physical processes and the response to climate change (Sokhi et al., 2022). There is a growing need to have integrated air pollution and related observations from both ground-based and remote sensing instruments, including in particular those on satellites. Use of upcoming new satellite observations such as the Plankton, Aerosol, Cloud, ocean Ecosystem (PACE) observations in general and SPEXone observations in particular, which can provide novel aerosol products related to size, composition, and absorption with high accuracy, while other instruments on PACE can provide accurate and novel cloud retrievals (droplet number concentration, droplet size, cloud phase), which can help improve the climate models in better quantifying aerosol-radiation and aerosol-cloud-precipitation interactions. Another emerging and growing field in observation science is the use of low-cost sensors, which can provide widespread information of air pollutant concentrations, but yet associated with large uncertainties when compared to existing monitoring networks. In order to get more robust projections with current generation models, multi-model studies will be needed, where scenarios and projection timelines are harmonized, as well as large ensemble studies using harmonized scenarios. For health impact studies, it is also important to increase the spatial resolution of the driving climate data in order to perform spatially high-resolution simulations of the evolution of the main air pollutants in the future. Higher accuracy in the air pollution simulations will also lead to more robust forecasting on the impacts of extreme weather and natural hazards such as wildland fires.

Author contributions

UI conducted the review, wrote the manuscript, and prepared the plots. CG, JK, and CS helped with the review and edited the manuscript, RH and MS helped with the wildland fires section and edited the manuscript, SR helped the mitigation/adaptation section and edited the manuscript, NS, ØH, JS, JC, RB, and KA edited the manuscript.

Funding

This project has received funding from the H2020 EMERGE project (No. 874990) and the H2020 EXHAUSTION project (No. 820655).

Acknowledgments

The authors acknowledge the H2020 EXHAUSTION project (No. 820655). This work reflects only the authors' view and the Innovation and European Climate, Infrastructure and Environment Executive Agency (CINEA) is not responsible for any use that may be made of the information it contains.

Conflict of interest

The authors declare that the research was conducted in the absence of any commercial or financial relationships that could be construed as a potential conflict of interest.

Publisher's note

All claims expressed in this article are solely those of the authors and do not necessarily represent those of their affiliated organizations, or those of the publisher, the editors and the reviewers. Any product that may be evaluated in this article, or claim that may be made by its manufacturer, is not guaranteed or endorsed by the publisher.

References

Abel, D. W., Holloway, T., Harkey, M., Meier, P., Ahl, D., Limaye, V. S., et al. (2018). Air-quality-related health impacts from climate change and from adaptation of cooling demand for buildings in the eastern United States: An interdisciplinary modeling study. *PLoS Med.* 15 (7), e1002599. doi:10.1371/journal.pmed.1002599

Alam, M. S., Hyde, B., Duffy, P., and McNabola, A. (2017). An assessment of $PM_{2.5}$ reductions as a result of transport fleet and fuel policies addressing CO_2 emissions and climate change. *WIT Trans. Ecol. Environ.* 211, 15–27. doi:10.2495/AIR170021

Anenberg, S. C., Schwartz, J., Shindell, D., Amann, M., Faluvegi, G., Klimont, Z., et al. (2012). Global air quality and health co-benefits of mitigating near-term climate change through methane and black carbon emission controls. *Environ. Health Perspect.* 120 (6), 831–839. doi:10.1289/ehp.1104301

Arneth, A., Miller, P. A., Scholze, M., Hickler, T., Schurgers, G., Smith, B., et al. (2007). CO_2 inhibition of global terrestrial isoprene emissions: Potential implications for atmospheric chemistry. *Geophys. Res. Lett.* 34, 18L18813. doi:10.1029/2007GL030615

Åström, S., Tohka, A., Bak, J., Lindblad, M., and Arnell, J. (2013). Potential impact on air pollution from ambitious national CO_2 emission abatement strategies in the Nordic countries - environmental links between the UNFCCC and the UNECE - CLRTAP. *Energy Policy* 53, 114–124. doi:10.1016/j.enpol.2012.10.075

Balch, J. K., Bradley, B. A., Abatzoglou, J. T., Nagy, R. C., Fusco, E. J., and Mahood, A. L. (2017). Human-started wildfires expand the fire niche across the United Statesfires expand the fire niche across the United States. *Proc. Natl. Acad. Sci. U. S. A.* 114 (11), 2946–2951. doi:10.1073/pnas.1617394114

Bauwens, M., Stavrakou, T., Müller, J.-F., Van Schaeybroeck, B., De Cruz, L., De Troch, R., et al. (2018). Recent past (1979–2014) and future (2070–2099) isoprene fluxes over Europe simulated with the MEGAN–MOHYCAN model. *Biogeosciences* 15, 3673–3690. doi:10.5194/bg-15-3673-2018

Bedia, J., Herrera, S., Camia, A., Moreno, J. M., and Gutiérrez, J. M. (2014). Erratum to: Forest fire danger projections in the Mediterranean using ENSEMBLES regional climate change scenarios. *Clim. Change* 122, 343–344. doi:10.1007/s10584-014-1073-8

Bellouin, N., Quaas, J., Gryspeerdt, E., Kinne, S., Stier, P., Watson-Parris, D., et al. (2020). Bounding global aerosol radiative forcing of climate change. *Rev. Geophys.* 58, e2019RG000660. doi:10.1029/2019RG000660

Bollen, J. (2015). The value of air pollution co-benefits of climate policies: Analysis with a global sector-trade CGE model called WorldScan. *Technol. Forecast. Soc. Change* 90, 178–191. doi:10.1016/j.techfore.2014.10.008

Bond, T. C., Doherty, S. J., Fahey, D. W., Forster, P. M., Berntsen, T., DeAngelo, B. J., et al. (2013). Bounding the role of black carbon in the climate system: A scientific assessment. *J. Geophys. Res. Atmos.* 118, 5380–5552. doi:10.1002/jgrd.50171

Boucher, O., Randall, D., Artaxo, P., Bretherton, C., Feingold, G., Forster, P., et al. (2013). "Clouds and aerosols," in *Climate change 2013: The phys- ical science basis, contribution of working group I to the fifth assessment report of the intergovernmental panel on climate change*. Editors T. F. Stocker, D. Qin, G.-K. Plattner, M. Tig- nor, S. K. Allen, J. Boschung, et al. (Cambridge, United Kingdom and New York, NY, USA: Cambridge University Press), 571–657.

Bowman, D. M. J. S., Balch, J. K., Artaxo, P., Bond, W. J., Carlson, J. M., Cochrane, M. A., et al. (2009). Fire in the earth system. *Science* 324 (5926), 481–484. doi:10.1126/science.1163886

Carslaw, K. S., Boucher, O., Spracklen, D. V., Mann, G. W., Rae, J. G. L., Woodward, S., et al. (2010). A review of natural aerosol interactions and feedbacks within the Earth system. *Atmos. Chem. Phys.* 10 (4), 1701–1737. doi:10.5194/acp-10-1701-201010.5194/acp-10-1701-2010

Cheng, C. S., Campbell, M., Li, Q., Li, G., Auld, H., Day, N., et al. (2007). A synoptic climatological approach to assess climatic impact on air quality in south-central Canada. Part II: Future estimates. *Water Air Soil Pollut.* 182, 117–130. doi:10.1007/s11270-006-9326-4

Cheng, J. J., and Berry, P. (2013). Health co-benefits and risks of public health adaptation strategies to climate change: A review of current literature. *Int. J. Public Health* 58 (2), 305–311. doi:10.1007/s00038-012-0422-5

Cholakian, A., Colette, A., Coll, I., Ciarelli, G., and Beekmann, M. (2019). Future climatic drivers and their effect on PM₁₀ components in Europe and the Mediterranean Sea. *Atmos. Chem. Phys.* 19, 4459–4484. doi:10.5194/acp-19-4459-2019

Clifford, H. M., Spaulding, N. E., Kurbatov, A. V., More, A., Korotkikh, E. V., and Sneed, S. B. (2019). A 2000 year Saharan dust event proxy record from an ice core in the European Alps. *J. Geophys. Res. Atmos.* 124, 12,882–12,900. doi:10.1029/2019JD030725

Colette, A., Andersson, C., Baklanov, A., Bessagnet, B., Brandt, J., Christensen, J. H., et al. (2015). Is the ozone climate penalty robust in Europe? *Environ. Res. Lett.* 10, 084015. doi:10.1088/1748-9326/10/8/084015

Colette, A., Bessagnet, B., Vautard, R., Szopa, S., Rao, S., Schucht, S., et al. (2013). European atmosphere in 2050, a regional air quality and climate perspective under CMIP5 scenarios. *Atmos. Chem. Phys.* 13, 7451–7471. doi:10.5194/acp-13-7451-2013

Creutzig, F., Mühlhoff, R., and Römer, J. (2012). Decarbonizing urban transport in European cities: Four cases show possibly high co-benefits. *Environ. Res. Lett.* 7 (4), 044042. doi:10.1088/1748-9326/7/4/044042

D'Andrea, S. D., Acosta Navarro, J. C., Farina, S. C., Scott, C. E., Rap, A., Farmer, D. K., et al. (2015). Aerosol size distribution and radiative forcing response to anthropogenically driven historical changes in biogenic secondary organic aerosol formation. *Atmos. Chem. Phys.* 15, 2247–2268. doi:10.5194/acp-15-2247-2015

Daskalakis, N., Myriokefalitakis, S., and Kanakidou, M. (2015). Sensitivity of tropospheric loads and lifetimes of short lived pollutants to fire emissions. *Atmos. Chem. Phys.* 15, 3543–3563. doi:10.5194/acp-15-3543-2015

Dawson, J. P., Adams, P. J., and Pandis, S. N. (2007). Sensitivity of PM_{2.5} to climate in the eastern US: A modeling case study. *Atmos. Chem. Phys.* 7, 4295–4309. doi:10.5194/acp-7-4295-2007

de Oliveira, J. A. P., and Doll, C. N. H. (2016). Governance and networks for health co-benefits of climate change mitigation: Lessons from two Indian cities. *Environ. Int.* 97, 146–154. doi:10.1016/j.envint.2016.08.020

Dijkstra, J., Durrant, T., San-Miguel-Ayanz, J., and Veraverbeke, S. (2022). Anthropogenic and lightning fire incidence and burned area in Europe. *Land* 11, 651. doi:10.3390/land11050651

Doherty, R. M., Heal, M. R., and O'Connor, F. M. (2017). Climate change impacts on human health over Europe through its effect on air quality. *Environ. Health* 16, 118. doi:10.1186/s12940-017-0325-2

Dupuy, J. L., Fargeon, H., Martin-StPaul, N., Pimont, F., Ruffault, J., Guijarro, M., et al. (2020). Climate change impact on future wildfire danger and activity in southern Europe: a review. *J. Trop. For. Sci.* 77, 35. doi:10.1007/s13595-020-00933-5

Dusek, U., Frank, G. P., Helas, G., Iinuma, Y., Zeromskiene, K., Gwaze, P., et al. (2005). "Missing" cloud condensation nuclei in peat smoke. *Geophys. Res. Lett.* 32, L11802. doi:10.1029/2005GL022473

EEA (2019a). European energy agency, energy and climate change. Available at: https://www.eea.europa.eu/signals/signals-2017/articles/energy-and-climate-change.

EEA (2019b). European Energy Agency, Total greenhouse gas emission trends and projections in Europe. EEA Report No 15/2019. Available at: https://www.eea.europa.eu//publications/trends-and-projections-in-europe-1.

Eyring, V., Stevenson, D. S., Lauer, A., Dentener, F. J., Butler, T., Collins, W. J., et al. (2007). Multi-model simulations of the impact of international shipping on Atmospheric Chemistry and Climate in 2000 and 2030. *Atmos. Chem. Phys.* 7, 757–780. doi:10.5194/acp-7-757-2007

Field, D. R., van der Werf, Guido R., Fanin, Thierry, Fetzer, Eric J., Fuller, Ryan, Jethva, Hiren, et al. (2015). Indonesian fire activity and smoke pollution in 2015 show persistent nonlinear sensitivity to El Niño-induced drought. *Proc. Natl. Acad. Sci. U. S. A.* 113, 9204–9209. doi:10.1073/pnas.1524888113

Fiore, A. M., Naik, V., Spracklen, D. V., Steiner, A., Unger, N., Prather, M., et al. (2012). Global air quality and climate. *Chem. Soc. Rev.* 41, 6663–6683. doi:10.1039/c2cs35095e

Fiore, M., Oliveri Conti, G., Caltabiano, R., Buffone, A., Zuccarello, P., Cormaci, L., et al. (2019). Role of emerging environmental risk factors in thyroid cancer: a brief review. *Int. J. Environ. Res. Publ. Health* 16, 1185. doi:10.3390/ijerph16071185

Fischer, A. P., Spies, T. A., Steelman, T. A., Moseley, C., Johnson, B. R., Bailey, J. D., et al. (2016). Wildfire risk as a socioecological pathology. *Front. Ecol. Environ.* 14, 276–284. doi:10.1002/fee.1283

Flanner, M. G. (2013). Arctic climate sensitivity to local black carbon. *J. Geophys. Res. Atmos.* 118, 1840–1851. doi:10.1002/jgrd.50176

Ford, B., Val Martin, M., Zelasky, S. E., Fischer, E. V., Anenberg, S. C., Heald, C. L., et al. (2018). Future fire impacts on smoke concentrations, visibility, and health in the contiguous united statesfire impacts on smoke concentrations, visibility, and health in the contiguous United States. *GeoHealth* 2, 229–247. doi:10.1029/2018GH000144

Fortems-Cheiney, A., Foret, G., Siour, G., Vautard, R., Szopa, S., Dufour, G., et al. (2019). A 3 °C global RCP8.5 emission trajectory cancels benefits of European emission reductions on air quality. *Nat. Commun.* 8, 89. doi:10.1038/s41467-017-00075-9

Fowler, D., Steadman, C. E., Stevenson, D., Coyle, M., Rees, R. M., Skiba, U. M., et al. (2015). Effects of global change during the 21st century on the nitrogen cycle. *Atmos. Chem. Phys.* 15 (24), 13849–13893. doi:10.5194/acp-15-13849-2015

Fu, T. M., and Tian, H. (2019). Climate change penalty to ozone air quality: Review of current understandings and knowledge gaps. *Curr. Pollut. Rep.* 5, 159–171. doi:10.1007/s40726-019-00115-6

Fuglestvedt, J., Berntsen, T., Myhre, G., Rypdal, K., and Skeie, R. B. (2008). Climate forcing from the transport sectors. *Proc. Natl. Acad. Sci. U. S. A.* 105, 454–458. doi:10.1073/pnas.0702958104

Fusco, E. J., Abatzoglou Balch, J. K., Finn, J. T., and Bradley, B. A. (2016). Quantifying the human influence on fire ignition across the Western USA fluence on fire ignition across the Western USA. *Ecol. Appl.* 26 (8), 2390–2401. doi:10.1002/eap.1395

Ganteaume, A., Camia, A., Jappiot, M., San-Miguel-Ayanz, J., Long-Fournel, M., and Lampin, C. (2013). A review of the main driving factors of forest fire ignition over Europe. *Environ. Manage.* 51, 651–662. doi:10.1007/s00267-012-9961-z

Gatebe, C. K., Ichoku, C. M., Poudyal, R., Román, M. O., and Wilcox, E. (2014). Surface albedo darkening from wildfires in northern sub-Saharan Africafires in northern sub-Saharan Africa. *Environ. Res. Lett.* 9, 065003. doi:10.1088/1748-9326/9/6/065003

Geels, C., Andersson, C., Hänninen, O., Lansø, A. S., Schwarze, P., Ambelas Skjøth, C., et al. (2015). Future premature mortality due to O3, secondary inorganic aerosols and primary PM in Europe — sensitivity to changes in climate, anthropogenic emissions, population and building stock. *Int. J. Environ. Res. Public Health* 12, 2837–2869. doi:10.3390/ijerph120302837

Glotfelty, T., Zhang, Y., Karamchandani, P., and Streets, D. (2016). Changes in future air quality, deposition, and aerosol-cloud interactions under future climate and emission scenarios. *Atmos. Environ.* 139, 176–191. doi:10.1016/j.atmosenv.2016.05.008

Grote, R. (2019). *Environmental impacts on biogenic emissions of volatile organic compounds (VOCs)*. Karlsruher Institut für Technologie, Garmisch-Partenkirchen, Report No. (UBA-FB) 002772/ENG.

Guenther, A., Karl, T., Harley, P., Wiedinmyer, C., Palmer, P. I., and Geron, C. (2006). Estimates of global terrestrial isoprene emissions using MEGAN (model of emissions of gases and aerosols from nature), atmos. *Chem. Phys.* 6, 3181–3210. doi:10.5194/acp-6-3181-2006

Hantson, S., Kelley, D. I., Arneth, A., Harrison, S. P., Archibald, S., Bachelet, D., et al. (2020). Quantitative assessment of fire and vegetation properties in historical simulations with fire-enabled vegetation models from the Fire Model Intercomparison Project. *Geosci. Model. Dev. Discuss.* in review. doi:10.5194/gmd-2019-261

Hantson, S., Knorr, W., Schurgers, G., Pugh, T. A. M., and Arneth, A. (2017). Global isoprene and monoterpene emissions under changing climate, vegetation, CO2 and land use. *Atmos. Environ.* 155, 35–45. doi:10.1016/j.atmosenv.2017.02.010

Hedegaard, G. B., Brandt, J., Christensen, J. H., Frohn, L. M., Geels, C., Hansen, K. M., et al. (2008). Impacts of climate change on air pollution levels in the Northern Hemisphere with special focus on Europe and the Arctic. *Atmos. Chem. Phys.* 8, 3337–3367. doi:10.5194/acp-8-3337-2008

Hodnebrog, Ø., Solberg, S., Stordal, F., Svendby, T. M., Simpson, D., Gauss, M., et al. (2012). Impact of forest fires, biogenic emissions and high temperatures on the elevated Eastern Mediterranean ozone levels during the hot summer of 2007. *Atmos. Chem. Phys.* 12 (18), 8727–8750. doi:10.5194/acp-12-8727-2012

Hoegh-Guldberg, O., Jacob, D., Taylor, M., Bindi, M., Brown, S., Camilloni, I., et al. (2018). "Impacts of 1.5°C global warming on natural and human systems," in *Global Warming of 1.5°C. An IPCC Special Report on the impacts of global warming of 1.5°C above pre-industrial levels and related global greenhouse gas emission pathways, in the context of strengthening the global response to the threat of climate change, sustainable development, and efforts to eradicate poverty [Masson-Delmotte, V., P. Zhai, H.-O. Pörtner, D. Roberts, J. Skea, P.R. Shukla, A. Pirani, W. Moufouma-Okia, C. Péan, R. Pidcock, S. Connors, J.B.R. Matthews, Y. Chen, X. Zhou, M.I. Gomis, E. Lonnoy, T. Maycock, M. Tignor, and T. Waterfield (eds.)]* (Cambridge, UK and New York, NY, USA: Cambridge University Press), 175–312. doi:10.1017/9781009157940.005

IEA (2020). *International energy agency, global CO_2 emissions in 2019.*

Im, U., Markakis, K., Koçak, M., Gerasopoulos, E., Daskalakis, N., Mihalopoulos, N., et al. (2012). Summertime aerosol chemical composition in the eastern mediterranean and its sensitivity to temperature: A modeling case study. *Atmos. Environ.* 50, 164–173.

Im, U., Markakis, K., Poupkou, A., Melas, D., Unal, A., Gerasopoulos, E., et al. (2011). The impact of temperature changes on summer time ozone and its precursors in the Eastern Mediterranean. *Atmos. Chem. Phys.* 11, 3847–3864. doi:10.5194/acp-11-3847-2011

Im, U., Tayanç, M., and Yenigun, O. (2006). Analysis of major photochemical pollutants with meteorological factors for high ozone days in Istanbul, Turkey. *Water Air Soil Pollut.* 175, 335–359. doi:10.1007/s11270-006-9142-x

Im, U., Tayanç, M., and Yenigun, O. (2008). Interaction patterns of major photochemical pollutants in Istanbul, Turkey. *Atmos. Res.* 89, 382–390. doi:10.1016/j.atmosres.2008.03.015

IPCC (2013). "Climate change 2013: The physical science basis," in *Contribution of working group I to the fifth assessment report of the intergovernmental panel on climate change [stocker, T.F., D. Qin, G.-K. Plattner, M. Tignor, S.K. Allen, J. Boschung, A. Nauels, Y. Xia, V. Bex and P.M. Midgley (eds.)]* (Cambridge, United Kingdom and New York, NY, USA: Cambridge University Press), 1535.

IPCC (2022). "Climate change 2022: Impacts, adaptation, and vulnerability," in *Contribution of working group II to the Sixth assessment report of the intergovernmental panel on climate change [H.-O. Pörtner, D.C. Roberts, M. Tignor, E.S. Poloczanska, K. Mintenbeck, A. Alegría, M. Craig, S. Langsdorf, S. Löschke, V. Möller, A. Okem, B. Rama (eds.)]* (Cambridge: Cambridge University Press). In Press.

Isaksen, I. S. A., Granier, C., Myhre, G., Berntsen, T. K., Dalsøren, S. B., Gauss, M., et al. (2009). Atmospheric composition change: Climate–Chemistry interactions. *Atmos. Environ.* 43, 5138–5192. doi:10.1016/j.atmosenv.2009.08.003

Jacob, D. J., and Winner, D. A. (2009). Effect of climate change on air quality. *Atmos. Environ.* 43 (1), 51–63. doi:10.1016/j.atmosenv.2008.09.051

Jacobson, M. Z., and Streets, D. G. (2009). Influence of future anthropogenic emissions on climate, natural emissions, and air quality. *J. Geophys. Res.* 114, D08118. doi:10.1029/2008JD011476

Jiang, X., Guenthera, A., Potosnak, M., Geron, C., Seco, R., Karl, T., et al. (2018). Isoprene emission response to drought and the impact on global atmospheric chemistry. *Atmos. Environ. X.* 183, 69–83. doi:10.1016/j.atmosenv.2018.01.026

Johnson, A. L., Abramson, M. J., Dennekamp, M., Williamson, G. J., and Guo, Y. (2020). Particulate matter modelling techniques for epidemiological studies of open biomass fire smoke exposure: A review. *Air Qual. Atmos. Health* 13, 35–75. doi:10.1007/s11869-019-00771-z

Jones, A., Haywood, J. M., and Boucher, O. (2007). Aerosol forcing, climate response and climate sensitivity in the Hadley Centre climate model. *J. Geophys. Res.* 112, D20211. doi:10.1029/2007JD008688

Joshi, M. M., Gregory, J. M., Webb, M. J., David, M. H. S., and Johns, T. C. (2007). Mechanisms for the land/sea warming contrast exhibited by simulations of climate change. *Clim. Dyn.* 30 (5), 455–465. doi:10.1007/s00382-007-0306-1

Juda-Rezler, K., Reizer, M., Huszar, P., Krüger, B. C., Zanis, P., Syrakov, D., et al. (2012). Modelling the effects of climate change on air quality over central and eastern Europe: Concept, evaluation and projections. *Clim. Res.* 53, 179–203. doi:10.3354/cr01072

Jylhä, K., Ruosteenoja, K., Räisänen, J., Venäläinen, A., Tuomenvirta, H., Ruokolainen, L., et al. (2009). *The changing climate in Finland: Estimates for adaptation studies (in Finnish with English abstract, extended abstract and captions for figures and tables)*. ACCLIM project report, Report 4. Helsinki: Finnish Meteorological Institute.

Kalabokidis, K., Palaiologou, P., Kostopoulou, E., Zerefos, C. S., Gerasopoulos, E., and Giannakopoulos, C. (2014). "Effect of climate projections on the behavior and impacts of wildfires in Messenia, Greece," in *COMECAP 2014 e-book of proceedings ISBN: 978-960-524-430-9 vol 1*, 395–400.

Kanakidou, M., Seinfeld, J. H., Pandis, S. N., Barnes, I., Dentener, F. J., Facchini, M. C., et al. (2005). Organic aerosol and global climate modelling: A review. *Atmos. Chem. Phys.* 5, 1053–1123. doi:10.5194/acp-5-1053-2005

Karlsson, M., Alfredsson, E., and Westling, N. (2020). Climate policy co-benefits: A review. *Clim. Policy* 20, 292–316. doi:10.1080/14693062.2020.1724070

Keywood, M., Kanakidou, M., Stohl, A., Dentener, F., Grassi, G., Meyer, J. P., et al. (2013). Fire in the Air: Biomass burning impacts in a changing climate. *Crit. Rev. Environ. Sci. Technol.* 43, 40–83. doi:10.1080/10643389.2011.604248

Klausbruckner, C., Annegar, H., Henneman, L. R. F., and Rafaj, P. (2016). A policy review of synergies and trade-offs in South African climate change mitigation and air pollution control strategies. *Environ. Sci. Policy* 57, 70–78. doi:10.1016/j.envsci.2015.12.001

Kleeman, M. J. (2007). A preliminary assessment of the sensitivity of air quality in California to global change. *Clim. Change* 87, S273–S292. doi:10.1007/s10584-007-9351-3

Klingmüller, K., Lelieveld, J., Karydis, V. A., and Stenchikov, G. L. (2019). Direct radiative effect of dust–pollution interactions. *Atmos. Chem. Phys.* 19, 7397–7408. doi:10.5194/acp-19-7397-2019

Knorr, W., Dentener, F., Lamarque, J.-F., Jiang, L., and Arneth, A. (2017). Wildfire air pollution hazard during the 21st centuryfire air pollution hazard during the 21st century. *Atmos. Chem. Phys.* 17, 9223–9236. doi:10.5194/acp-17-9223-2017

Knorr, W., Jiang, W., and Arneth, A. (2016). Climate, CO₂ and human population impacts on global wildfire emissions. *Biogeosciences* 13, 267–282. doi:10.5194/bg-13-267-2016

Koch, D., Park, J., and Del Genio, A. (2003). Clouds and sulfate are anticorrelated: A new diagnostic for global sulfur models. *J. Geophys. Res.* 108, D244781. doi:10.1029/2003JD003621

Kollanus, V., Prank, M., Gens, A., Soares, J., Vira, J., Kukkonen, J., et al. (2017). Mortality due to vegetation-fire originated PM2.5 exposure in Europe – assessment for the years 2005 and 2008. *Environ. Health Perspect.* 125 (1), 30–37. doi:10.1289/EHP194

Kukkonen, J., López-Aparicio, S., Segersson, D., Geels, C., Kangas, L., Kauhaniemi, M., et al. (2020). The influence of residential wood combustion on the concentrations of PM_{2.5} in four Nordic cities. *Atmos. Chem. Phys.* 20, 4333–4365. doi:10.5194/acp-20-4333-2020

Kukkonen, J., Nikmo, J., Sofiev, M., Riikonen, K., Petäjä, T., Virkkula, A., et al. (2014). Applicability of an integrated plume rise model for the dispersion from wild-land fires. *Geosci. Model. Dev.* 7, 2663–2681. doi:10.5194/gmd-7-2663-2014

Kukkonen, J., Olsson, T., Schultz, D. M., Baklanov, A., Klein, T., Miranda, A. I., et al. (2012). A review of operational, regional-scale, chemical weather forecasting models in Europe. *Atmos. Chem. Phys.* 12, 1–87. doi:10.5194/acp-12-1-2012

Lacressonniere, G., Foret, G., Beekmann, M., Siour, G., Engardt, M., Gauss, M., et al. (2016). Impacts of regional climate change on air quality projections and associated uncertainties. *Clim. Change* 136, 309–324. doi:10.1007/s10584-016-1619-z

Lacressonnière, G., Peuch, V.-H., Vautard, R., Arteta, J., Déqué, M., Joly, M., et al. (2014). European air quality in the 2030s and 2050s: Impacts of global and regional emission trends and of climate change. *Atmos. Environ.* 92, 348–358. doi:10.1016/j.atmosenv.2014.04.033

Lacressonniere, G., Watson, L., Gauss, M., Engardt, M., Andersson, C., Beekmann, M., et al. (2017). Particulate matter air pollution in Europe in a +2oC warming world. *Atmos. Environ.* 154, 129–140. doi:10.1016/j.atmosenv.2017.01.037

Lamarque, J. F., Kyle, G. P., Meinshausen, M., Riahi, K., Smith, S. J., van Vuuren, D. P., et al. (2011). Global and regional evolution of short-lived radiatively-active gases and aerosols in the Representative Concentration Pathways. *Clim. Change* 109 (1-2), 191–212. doi:10.1007/s10584-011-0155-0

Langmann, B., Duncan, B., Textor, C., Trentmann, J., and van der Werf, G. R. (2009). Vegetation fire emissions and their impact on air pollution and climate. *Atmos. Environ.* 43 (1), 107–116. doi:10.1016/j.atmosenv.2008.09.047

Langner, J., Engardt, M., Baklanov, A., Christensen, J. H., Gauss, M., Geels, C., et al. (2012). A multi-model study of impacts of climate change on surface ozone in Europe. *Atmos. Chem. Phys.* 12, 10423–10440. doi:10.5194/acp-12-10423-2012

Lee, L. A., Reddington, C. L., and Carslaw, K. S. (2016). On the relationship between aerosol model uncertainty and radiative forcing uncertainty. *Proc. Natl. Acad. Sci. U. S. A.* 113 (21), 5820–5827. doi:10.1073/pnas.1507050113

Lemaire, V. E. P., Colette, A., and Menut, L. (2016). Using statistical models to explore ensemble uncertainty in climate impact studies: The example of air pollution in Europe. *Atmos. Chem. Phys.* 16, 2559–2574. doi:10.5194/acp-16-2559-2016

Liao, H., Zhang, Y., Chen, W. T., Raes, F., and Seinfeld, J. H. (2009). Effect of chemistry-aerosol-climate coupling on predictions of future climate and future levels of tropospheric ozone and aerosols. *J. Geophys. Res.* 114, D10306. doi:10.1029/2008JD010984

Lin, C. Y. C., Mickley, L. J., Hayhoe, K., Maurer, E. P., and Hogrefe, C. (2007). *Rapid calculation of future trends in ozone exceedances over the northeast United States : Results from three models and two scenarios, presented at the consequences of global change for air quality festival*. Research Triangle Park, NC: EPA. February 20–21.

Liu, J. C., Mickley, L. J., Sulprizio, M. P., Dominici, F., Yue, X., Ebisu, K., et al. (2016). Particulate air pollution from wildfires in the Western US under climate changefires in the Western US under climate change. *Clim. Change* 138 (3-4), 655–666. doi:10.1007/s10584-016-1762-6

Liu, S. C., Trainer, M., Fehsenfeld, F. C., Parrish, D. D., Williams, E. J., Fahey, D. W., et al. (1987). Ozone production in the rural troposphere and the implications for regional and global ozone distributions. *J. Geophys. Res.* 92, 4191–4207. doi:10.1029/jd092id04p04191

Lozano, O. M., Salis, M., Ager, A. A., Arca, B., Alcasena, F. J., Monteiro, A. T., et al. (2017). Assessing climate change impacts on wildfire exposure in mediterranean areas. *Risk Anal.* 37, 1898–1916. doi:10.1111/risa.12739

Luderer, G., Trentmann, J., Winterrath, T., Textor, C., Herzog, M., Graf, H. F., et al. (2006). Modeling of biomass smoke injection into the lower stratosphere by a large forest fire (Part II): Sensitivity studies. *Atmos. Chem. Phys.* 6 (4), 5261–5277. doi:10.5194/acpd-6-6081-2006

Lund, M. T., Eyring, V., Fuglestvedt, J., Hendricks, J., Lauer, A., Lee, D., et al. (2012). Global-mean temperature change from shipping toward 2050: Improved representation of the indirect aerosol effect in simple climate models. *Environ. Sci. Technol.* 46, 8868–8877. doi:10.1021/es301166e

Luo, L., Tang, Y., Zhong, S., Bian, X., and Heilman, W. E. (2013). Will future climate favor more erratic wildfires in the Western United States? *J. Appl. Meteorol. Climatol.* 52 (11), 2410–2417. doi:10.1175/JAMC-D-12-0317.1

Mahowald, N. M., Muhs, D. R., Levis, S., Rasch, P. J., Yoshioka, M., Zender, C. S., et al. (2006). Change in atmospheric mineral aerosols in response to climate: Last glacial period, preindustrial, modern, and doubled carbon dioxide climates. *J. Geophys. Res.* 111, D10202. doi:10.1029/2005JD006653

Malavelle, F., Haywood, J., Jones, A., Gettelman, A., Clarisse, L., Bauduin, S., et al. (2017). Strong constraints on aerosol–cloud interactions from volcanic eruptions. *Nature* 546, 485–491. doi:10.1038/nature22974

Manders, A. M. M., van Meijgaard, E., Mues, A. C., Kranenburg, R., van Ulft, L. H., and Schaap, M. (2012). The impact of differences in large-scale circulation output from climate models on the regional modeling of ozone and PM. *Atmos. Chem. Phys.* 12, 9441–9458. doi:10.5194/acp-12-9441-2012

Markandya, A., Sampedro, J., Smith, S. J., Van Dingenen, R., Pizarro-Irizar, C., Arto, I., et al. (2018). Health co-benefits from air pollution and mitigation costs of the paris agreement: A modelling study. *Lancet Planet. Health* 2, 126–133. doi:10.1016/S2542-5196(18)30029-9

Mårtensson, E. M., Nilsson, E. D., de Leeuw, G., Cohen, L. H., and Hansson, H.-C. (2003). Laboratory simulations and parameterization of the primary

marine aerosol production. *J. Geophys. Res.* 108, 4297. doi:10.1029/2002JD002263

McCarty, J. L., Aalto, J., Paunu, V.-V., Arnold, S. R., Eckhardt, S., Klimont, Z., et al. (2021). Reviews and syntheses: Arctic fire regimes and emissions in the 21st century. *Biogeosciences* 18, 5053–5083. doi:10.5194/bg-18-5053-2021

Megaritis, A. G., Fountoukis, C., Charalampidis, P. E., Denier van der Gon, H. A. C., Pilinis, C., and Pandis, S. N. (2014). Linking climate and air quality over Europe: Effects of meteorology on PM_{2.5} concentrations. *Atmos. Chem. Phys.* 14, 10283–10298. doi:10.5194/acp-14-10283-2014

Monahan, E. C., Spiel, D. E., and Davidson, K. L. (1986). "A model of marine aerosol generation via whitecaps and wave disruption," in *Oceanic whitecaps*. Editors E. C. Monahan and G. Mac-Niochaill (Norwell, USA: D. Reidel), 167–193.

Mouillot, F., Rambal, S., and Joffre, R. (2002). Simulating climate change impacts on fire frequency and vegetation dynamics in a Mediterranean-type ecosystem. *Glob. Chang. Biol.* 8, 423–437. doi:10.1046/j.1365-2486.2002.00494.x

Mülmenstädt, J., and Feingold, G. (2018). The radiative forcing of aerosol–cloud interactions in liquid clouds: Wrestling and embracing uncertainty. *Curr. Clim. Change Rep.* 4, 23–40. doi:10.1007/s40641-018-0089-y

Myhre, G., Shindell, D., Breon, F.-M., Collins, W., Fuglestvedt, J., Huang, J., et al. (2013). "Anthropogenic and natural radiative forcing," in *Climate change 2013: The physical science basis. Contribution of working group I to the fifth assessment report of the inter- governmental panel on climate change*. Editors T. F. Stocker, D. Qin, G.-K. Plattner, M. Tignor, S. K. Allen, J. Boschung, et al. (Cambridge, United Kingdom and New York, NY, USA: Cambridge University Press), 659–740.

Nilsson, E. D., Mårtensson, E. M., Van Ekeren, J. S., de Leeuw, G., Moerman, M., and O'Dowd, C. (2007). Primary marine aerosol emissions: Size resolved eddy covariance measurements with estimates of the sea salt and organic carbon fractions. *Atmos. Chem. Phys.* 7, 13345–13400. doi:10.5194/acpd-7-13345-2007

Otero, N. F., Sillmann, J., Schnell, J. L., Rust, H. W., and Butler, T. (2016). Synoptic and meteorological drivers of extreme ozone concentrations over Europe. *Environ. Res. Lett.* 11, 024005. doi:10.1088/1748-9326/11/2/024005

Otero, N., Sillmann, J., and Butler, T. (2018). Assessment of an extended version of the Jenkinson–Collison classification on CMIP5 models over Europe. *Clim. Dyn.* 50, 1559–1579. doi:10.1007/s00382-017-3705-y

Parente, J., Pereira, M. G., Amraoui, M., and Tedim, F. (2018). Negligent and intentional fires in Portugal: Spatial distribution characterization. *Sci. Total Environ.* 624, 424–437. doi:10.1016/j.scitotenv.2017.12.013

Park, S., Allen, R. J., and Lim, C. H. (2020). A likely increase in fine particulate matter and premature mortality under future climate change. *Air Qual. Atmos. Health* 13, 143–151. doi:10.1007/s11869-019-00785-7

Pechony, O., and Shindell, D. T. (2010). Driving forces of global wildfires over the past millennium and the forthcoming century. *Proc. Natl. Acad. Sci. U. S. A.* 107 (45), 19167–19170. doi:10.1073/pnas.1003669107

Pegoraro, E., Rey, A., Greenberg, J., Harley, P., Grace, J., Malhi, Y., et al. (2004). Effect of drought on isoprene emission rates from leaves of Quercus virginiana Mill. *Atmos. Environ. X.* 38, 6149–6156. doi:10.1016/j.atmosenv.2004.07.028

Pfahl, S., and Wernli, H. (2012). Quantifying the relevance of atmospheric blocking for co-located temperature extremes in the Northern Hemisphere on (sub-) daily time scales. *Geophys. Res. Lett.* 39, L12807. doi:10.1029/2012GL052261

Prestemon, J. P., Hawbaker, T. J., Bowden, M., Carpenter, J., Scranton, S., Brooks, M. T., et al. (2013). *Wild fire ignitions: A review of the science and recommendations for empirical modeling (general technical report No. SRS-171)*. Asheville, NC: USDA Forest Service, Southern Research Station.

Rafaj, P., Cofala, J., Kuenen, J., Wyrwa, A., and Zyśk, J. (2014). Benefits of European climate policies for mercury air pollution. *Atmosphere* 5, 45–59. doi:10.3390/atmos5010045

Rao, S., Klimont, Z., Smith, S. J., Van Dingenen, R., Dentener, F., Bouwman, L., et al. (2017). Future air pollution in the shared socio-economic pathways. *Glob. Environ. Change* 42, 346–358. doi:10.1016/j.gloenvcha.2016.05.012

Ruosteenoja, K., and Jylha, K. (2021). Projected climate change in Finland during the 21st century calculated from CMIP6 model simulations. *Geophysica* 56 (1), 39–69.

Russo, S., Dosio, A., Graverson, R. G., Sillmann, J., Carrao, H., Bunbar, M. B., et al. (2014). Magnitude of extreme heat waves in present climate and their projection in a warming world. *J. Geophys. Res. Atmos.* 119, 12500–12512. doi:10.1002/2014JD022098

Saarikoski, S., Sillanpää, M., Sofiev, M., Timonen, H., Saarnio, K., Teinilä, K., et al. (2007). Chemical composition of aerosols during a major biomass burning episode over northern Europe in spring 2006: Experimental and modelling assessments. *Atmos. Environ.* 41, 3577–3589. doi:10.1016/j.atmosenv.2006.12.053

Saarnio, K., Aurela, M., Timonen, H., Saarikoski, S., Teinilä, K., Mäkelä, T., et al. (2010). Chemical composition of fine particles in fresh smoke plumes from boreal wild-land fires in Europe. *Sci. Total Environ.* 408, 2527–2542. doi:10.1016/j.scitotenv.2010.03.010

Samset, B. H., Myhre, G., Schulz, M., Balkanski, Y., Bauer, S., Berntsen, T. K., et al. (2013). Black carbon vertical profiles strongly affect its radiative forcing uncertainty. *Atmos. Chem. Phys.* 13 (5), 2423–2434. doi:10.5194/acp-13-2423-2013

Sanderson, B. M., and Fisher, R. A. (2020). A fiery wake-up call for climate science. *Nat. Clim. Chang.* 10, 175–177. doi:10.1038/s41558-020-0707-2

Schaller, N., Sillmann, J., Anstey, J., Fischer, E. M., Grams, C. M., and Russo, S. (2018). Influence of blocking on Northern European and Western Russian heatwaves in large climate model ensembles. *Environ. Res. Lett.* 13, 054015. doi:10.1088/1748-9326/aaba55

Schnell, J. L., Prather, M. J., Josse, B., Naik, V., Horowitz, L. W., Zeng, G., et al. (2016). Effect of climate change on surface ozone over North America, Europe, and east Asia. *Geophys. Res. Lett.* 43 (7), 3509–3518. doi:10.1002/2016GL068060

Seinfeld, J. H., and Pandis, S. N. (2016). *Atmospheric chemistry and physics: From air pollution to climate change*. 3rd Edition, 1152. ISBN: 978-1-118-94740-1.

Sheehan, P. E., and Bowman, F. M. (2001). Estimated effects of temperature on secondary organic aerosol concentrations. *Environ. Sci. Technol.* 35 (11), 2129–2135. doi:10.1021/es001547g

Shindell, D., and Faluvegi, G. (2009). Climate response to regional radiative forcing during the twentieth century. *Nat. Geosci.* 2, 294–300. doi:10.1038/ngeo473

Shindell, D., Kuylenstierna, J. C. I., Vignati, E., van Dingenen, R., Amann, M., Klimont, Z., et al. (2012). Simultaneously mitigating near-term climate change and improving human health and food security. *Science* 335 (6065), 183–189. doi:10.1126/science.1210026

Shindell, D. T., Lamarque, J.-F., Schulz, M., Flanner, M., Jiao, C., Chin, M., et al. (2013). Radiative forcing in the ACCMIP historical and future climate simulations. *Atmos. Chem. Phys.* 13 (6), 2939–2974. doi:10.5194/acp-13-2939-2013

Silva, R. A., West, J. J., Lamarque, J.-F., Shindell, D. T., Collins, W. J., Faluvegi, G., et al. (2017). Future global mortality from changes in air pollution attributable to climate change. *Nat. Clim. Chang.* 7 (9), 647–651. doi:10.1038/nclimate3354

Silva, R. A., West, J. J., Zhang, Y., Anenberg, S. C., Lamarque, J.-F., Shindell, D. T., et al. (2013). Global premature mortality due to anthropogenic outdoor air pollution and the contribution of past climate change. *Environ. Res. Lett.* 8 (3), 034005. doi:10.1088/1748-9326/8/3/034005

Skeie, R. B., Fuglestvedt, J., Berntsen, T., Lund, M. T., Myhre, G., and Rypdal, K. (2009). Global temperature change from the transport sectors: Historical development and future scenarios. *Atmos. Environ.* 43, 6260–6270. doi:10.1016/j.atmosenv.2009.05.025

Skjøth, C. A., and Geels, C. (2013). The effect of climate and climate change on ammonia emissions in Europe. *Atmos. Chem. Phys.* 13, 117–128. doi:10.5194/acp-13-117-2013

Soares, J., Sofiev, M., Geels, C., Christensen, J. H., Andersson, C., Tsyro, S., et al. (2016). Impact of climate change on the production and transport of sea salt aerosol on European seas. *Atmos. Chem. Phys.* 16, 13081–13104. doi:10.5194/acp-16-13081-2016

Sofiev, M., Ermakova, T., and Vankevich, R. (2012). Evaluation of the smoke injection height from wild-land fires using remote sensing data. *Atmos. Chem. Phys.* 12, 1995–2006. doi:10.5194/acp-12-1995-2012

Sofiev, M., Lanne, M., Vankevich, R., Prank, M., Karppinen, A., and Kukkonen, J. (2008). "Impact of wild-land fires on European air quality in 2006-2008," in *01/2008; edition: WIT transactions on ecology and the environment*. Editors J. D. L. Heras, C. A. Brebbia, D. Viegas, and V. Leone (Southampton, UK: WIT Press), Vol. 119, 353–361. ISBN: 978-1-84564-141-2. doi:10.2495/FIVA080351

Sofiev, M., Vankevich, R., Ermakova, T., and Hakkarainen, J. (2013). Global mapping of maximum emission heights and resulting vertical profiles of wildfire emissions. *Atmos. Chem. Phys.* 13, 7039–7052. doi:10.5194/acp-13-7039-2013

Sofiev, M. (2013). "Wildland fires: Monitoring, plume modelling, impact on atmospheric composition and climate. Chapter 21 in matyssek, R., clarke, N., cudlin, P., mikkelsen, T.N., tuovinen, J.-P. Wieser, G., paoletti, E. Climate change, air pollution and global challenges," in *Developments in environmental science* (London: Elsevier & Book Aid Intern.), Vol. 13, 451–474. ISBN: 978-0-08-098349-3 ISSN: 1474-8177.

Sofiev, M., Winebrake, J. J., Johansson, L., Carr, E. W., Prank, M., Soares, J., et al. (2018). Cleaner fuels for ships provide public health benefits with climate tradeoffsfits with climate tradeoffs. *Nat. Commun.* 9, 406. doi:10.1038/s41467-017-02774-9

Sokhi, R. S., Moussiopoulos, N., Baklanov, A., Bartzis, J., Coll, I., Finardi, S., et al. (2022). Advances in air quality research – current and emerging challenges. *Atmos. Chem. Phys.* 22, 4615–4703. doi:10.5194/acp-22-4615-2022

Stohl, A., Aamaas, B., Amann, M., Baker, L. H., Bellouin, N., Berntsen, T. K., et al. (2015). Evaluating the climate and air quality impacts of short-lived pollutants. *Atmos. Chem. Phys.* 15, 10529–10566. doi:10.5194/acp-15-10529-2015

Streets, D. G., Bond, T. C., Lee, T., and Jang, C. (2004). On the future of carbonaceous aerosol emissions. *J. Geophys. Res.* 109, D24212. doi:10.1029/2004JD004902

Sutton, M. A., Reis, S., Riddick, S. N., Dragosits, U., Nemitz, E., Theobald, M. R., et al. (2013). Towards a climate-dependent paradigm of ammonia emission and deposition. *Phil. Trans. R. Soc. B* 368, 20130166. doi:10.1098/rstb.2013.0166

Tegen, I., Werner, M., Harrison, S. P., and Kohfeld, K. E. (2004). Relative importance of climate and land use in determining present and future global soil dust emission. *Geophys. Res. Lett.* 31, L05105. doi:10.1029/2003GL019216

Tobollik, M., Keuken, M., Sabel, C., Cowie, H., Tuomisto, J., Sarigiannis, D., et al. (2016). Health impact assessment of transport policies in Rotterdam: Decrease of total traffic and increase of electric car use. *Environ. Res.* 146, 350–358. doi:10.1016/j.envres.2016.01.014

Toll, V., Christensen, M., Quaas, J., and Bellouin, N. (2019). Weak average liquid-cloud-water response to anthropogenic aerosols. *Nature* 572, 51–55. doi:10.1038/s41586-019-1423-9

Tosca, M. G., Randerson, J. T., and Zender, C. S. (2013). Global impact of smoke aerosols from landscape fires on climate and the Hadley circulation. *Atmos. Chem. Phys.* 13 (10), 5227–5241. doi:10.5194/acp-13-5227-2013

Tsigaridis, K., and Kanakidou, M. (2007). Secondary organic aerosol importance in the future atmosphere. *Atmos. Environ.* 41, 4682–4692. doi:10.1016/j.atmosenv.2007.03.045

Turnock, S. T., Allen, R. J., Andrews, M., Bauer, S. E., Deushi, M., Emmons, L., et al. (2020). Historical and future changes in air pollutants from CMIP6 models. *Atmos. Chem. Phys.* 20, 14547–14579. doi:10.5194/acp-20-14547-2020

Veira, A., Kloster, S., Schutgens, N. A. J., and Kaiser, J. W. (2015b). Fire emission heights in the climate system—Part 2: Impact on transport, black carbon concentrations and radiation. *Atmos. Chem. Phys.* 15 (13), 7173–7193. doi:10.5194/acp-15-7173-2015

Veira, A., Kloster, S., Wilkenskjeld, S., and Remy, S. (2015a). Fire emission heights in the climate system—Part 1: Global plume height patterns simulated by ECHAM6-HAM2. *Atmos. Chem. Phys.* 15 (13), 7155–7171. doi:10.5194/acp-15-7155-2015

Veira, A., Lasslop, G., and Kloster, S. (2016). Wildfires in a warmer climate: Emission fluxes, emission heights, and black carbon concentrations in 2090–2099. *J. Geophys. Res. Atmos.* 121 (7), 3195–3223. doi:10.1002/2015JD024142

Venäläinen, A., Lehtonen, I., Laapas, M., Ruosteenoja, K., Tikkanen, O.-P., Viiri, H., et al. (2020). Climate change induces multiple risks to boreal forests and forestry in Finland: A literature review. *Glob. Change Biol.* 26 (8), 4178–4196. doi:10.1111/gcb.15183

von Schneidemesser, E., Monks, P., Allan, J., Bruhwiler, L., Forster, P., Fowler, D., et al. (2015). Chemistry and the linkages between air quality and climate change. *Chem. Rev.* 115, 3856–3897. doi:10.1021/acs.chemrev.5b00089

Watson, L., Lacressonniere, G., Gauss, M., Engardt, M., Andersson, C., Josse, B., et al. (2016). Impact of emissions and +2°C climate change upon future ozone and nitrogen dioxide over Europe. *Atmos. Environ.* 142, 271–285. doi:10.1016/j.atmosenv.2016.07.051

Watts, N., Amann, M., Arnell, N., Ayeb-Karlsson, S., Belesova, K., Boykoff, M., et al. (2019). The 2019 report of the lancet countdown on health and climate change: Ensuring that the health of a child born today is not defined by a changing climate. *Lancet* 394 (10211), 1836–1878. doi:10.1016/S0140-6736(19)32596-6

West, J. J., Smith, S. J., Silva, R. A., Naik, N., Zhang, Y., Adelman, Z., et al. (2013). Co-benefits of mitigating global greenhouse gas emissions for future air quality and human health. *Nat. Clim. Chang.* 3 (10), 885–889. doi:10.1038/NCLIMATE2009

Westervelt, D. M., Horowitz, L. W., Naik, V., Tai, A. P. K., Fiore, A. M., and Mauzerall, D. L. (2016). Quantifying PM2.5-meteorology sensitivities in a global climate model. *Atmos. Environ.* 142, 43–56. doi:10.1016/j.atmosenv.2016.07.040

Wilkinson, P., Smith, K. R., Davies, M., Adair, H., Armstrong, B. G., Barrett, M., et al. (2009). Public health benefits of strategies to reduce greenhouse-gas emissions: household energy. *Lancet* 374 (9705), 1917–1929. doi:10.1016/S0140-6736(09)61713-X

Williams, M. L. (2007). UK air quality in 2050-synergies with climate change policies. *Environ. Sci. Policy* 10, 169–175.

Woodward, S., Roberts, D. L., and Betts, R. A. (2005). A simulation of the effect of climate change-induced desertification on mineral dust aerosol. *Geophys. Res. Lett.* 32, L18810. doi:10.1029/2005GL023482

Ylhäisi, J. S., Tietäväinen, H., Peltonen-Sainio, P., Venäläinen, A., Eklund, J., Räisänen, J., et al. (2010). Growing season precipitation in Finland under recent and projected climate. *Nat. Hazards Earth Syst. Sci.* 10, 1563–1574. doi:10.5194/nhess-10-1563-2010

Yue, X., Mickley, L. J., Logan, J. A., and Kaplan, J. O. (2013). Ensemble projections of wildfire activity and carbonaceous aerosol concentrations over the Western United States in the mid-21st centuryfire activity and carbonaceous aerosol concentrations over the Western United States in the mid-21st century. *Atmos. Environ.* 77, 767–780. doi:10.1016/j.atmosenv.2013.06.003

Zanis, P., Akritidis, D., Turnock, S., Naik, V., Szopa, S., Georgoulias, A. K., et al. (2022). Climate change penalty and benefit on surface ozone: A global perspective based on CMIP6 Earth system models. *Environ. Res. Lett.* 17, 024014. doi:10.1088/1748-9326/ac4a34

frontiers | Frontiers in Ecology and Evolution

TYPE Original Research
PUBLISHED 28 October 2022
DOI 10.3389/fevo.2022.931662

OPEN ACCESS

EDITED BY
Michael MacKinnon,
University of California,
United States

REVIEWED BY
Bosi Sheng,
Sun Yat-sen University, China
Ying Wang,
Nanjing University of Information Science and Technology, China

*CORRESPONDENCE
Yaqiong Lu
yaqiong@imde.ac.cn

SPECIALTY SECTION
This article was submitted to Interdisciplinary Climate Studies, a section of the journal Frontiers in Ecology and Evolution

RECEIVED 29 April 2022
ACCEPTED 28 September 2022
PUBLISHED 28 October 2022

CITATION
Yang X, Yang T, Lu Y, Jiang M, Zhang S, Shao P, Yuan L, Wang C and Wang L (2022) Assessment of summertime ozone formation in the Sichuan Basin, southwestern China.
Front. Ecol. Evol. 10:931662.
doi: 10.3389/fevo.2022.931662

Assessment of summertime ozone formation in the Sichuan Basin, southwestern China

Xianyu Yang[1], Tong Yang[1], Yaqiong Lu[2]*, Mengjiao Jiang[1], Shaobo Zhang[1], Ping Shao[1], Liang Yuan[1], Chao Wang[1] and Lei Wang[1]

[1]Plateau Atmosphere and Environment Key Laboratory of Sichuan Province, School of Atmospheric Sciences, Chengdu University of Information Technology, Chengdu, China, [2]Institute of Mountain Hazards and Environment, Chinese Academy of Sciences, Chengdu, China

The alarming increase of ambient ozone (O_3) levels across China raises an urgent need in understanding underlying mechanisms of regional O_3 events for highly urbanized city clusters. Sichuan Basin (SCB) situated in southwestern China has experienced severe O_3 pollution at times in summer from 2013 to 2020. Here, we use the WRF-CMAQ model with the Integrated Source Apportionment Method (ISAM) to investigate the evolution mechanism and conduct source attribution of an extreme O_3 episode in the SCB from June 1 to 8, 2019. This typical summer O_3 episode is associated with the synoptic-driven meteorological phenomenon and transboundary flow of O_3 and precursors across the SCB. Weak ventilation in combination with stagnant conditions triggered the basin-wide high O_3 concentrations and enhanced BVOC emissions substantially contribute up to 57.9μg/m^3 MDA8 O_3. CMAQ-ISAM indicates that precursor emissions from industrial and transportation have the largest impacts on elevating ambient O_3 concentrations, while power plant emissions exhibit insignificant contributions to basin-wide O_3 episodes. These results improve the understanding of the summertime O_3 episode in the SCB and contribute insights into designing O_3 mitigation policy.

KEYWORDS

ozone, Sichuan Basin, CMAQ, emission regulation, air quality

Introduction

As a crucial oxidant in the atmosphere, ozone (O_3) is a secondary pollutant formed through photochemical reactions of biogenic and anthropogenic precursors in the atmosphere (Atkinson, 2000; Seinfeld and Pandis, 2016). The increase of ground-level O_3 adversely impacts human health, damages plant physiological functions, and reduces crop productivity (Anenberg et al., 2010). The Global Burden of Diseases Study 2015 reported that exposure to O_3 contributed to 254 000 deaths globally from chronic obstructive pulmonary disease (COPD) in 2015 (Cohen et al., 2017). Due to the nonlinear relationship between O_3 and its precursors (NO_x and VOCs), decreases in precursor concentrations may not necessarily result in a corresponding decrease in O_3. Conversely, disproportionate

reductions in NO_x and VOCs emissions may worsen O_3 pollution (Wu et al., 2022). Therefore, a comprehensive understanding of O_3 formation in response to the reduction in precursor emissions is urgently needed for the effective design of control measures.

With the rapid industrialization and urbanization since the 2000s, air pollution in China has become increasingly severe featured by frequent high $PM_{2.5}$ and O_3 episodes (Richter et al., 2005; Apte et al., 2015). Although NO_x and SO_2 emissions have been effectively controlled through stringent pollution control measures, elevated O_3 levels in urban areas remain as an important environmental issue (Liu and Wang, 2020). Previous studies have shown that the Beijing–Tianjin–Hebei (BTH) area, Pearl River Delta (PRD), Yangtze River Delta (YRD) and Sichuan Basin are the four major urban clusters in China that suffer severe O_3 pollution (Wu et al., 2020; Wang et al., 2021). The Sichuan Basin is the most developed economic zone in western China which is home to approximately 116 million residents within an area of 260,000 km^2. The basin is nestled between the Daba Mountains to the north, the Yunnan-Guizhou Plateau to the south, the Tibetan Plateau to the west and the Wushan Mountains to the east. Given the deep basin topography, unique climate dynamics, in conjunction with intense anthropogenic emissions, considerable attention has been devoted to urban O_3 pollution across the Sichuan Basin (Song et al., 2018; Simayi et al., 2020; Wang H. et al., 2022). Based on long-term ambient measurements of trace gasses, Wu et al. (2022) reported that O_3 exceedance events and regional O_3 episodes continuously increased over the Sichuan Basin during warm season from 2014 to 2019. Using the comprehensive air quality model with extensions (CAM*x*), Du et al. (2022) found that a reduction ratio of 1:3 for NO_x/VOCs is the most beneficial pathway for O_3 mitigation in metropolitan Chengdu. While prior studies have focused on identifying the spatial and temporal patterns and conducting source apportionment of O_3 in the Sichuan Basin, the formation mechanism of O_3 pollution in the Sichuan Basin remains unclear. In addition, the meteorological and chemical impacts on O_3 episodes need to be further investigated.

In this study, we investigated the formation of a high O_3 episode in that occurred in the summer of 2019 for revealing the governing processes of O_3 formation by using the Weather Research and Forecasting-Community Multiscale Air Quality (WRF-CMAQ) modeling system. Further, CMAQ-ISAM is applied for conducting source apportionment of ambient O_3 across the SCB. The paper is organized as follows. In Sect. 2, the model configuration is described. The model performance results as indicated by comparisons with observations – including meteorological and ground-level air pollutant observations – and the results of sensitivity experiments are presented in Sect. 3. The conclusions are given in Sect. 4.

Methodology

WRF-CMAQ model

The WRF-CMAQ modeling system is adopted to simulate a high O_3 episode in the Sichuan Basin from 1 June to 8 June, 2019.

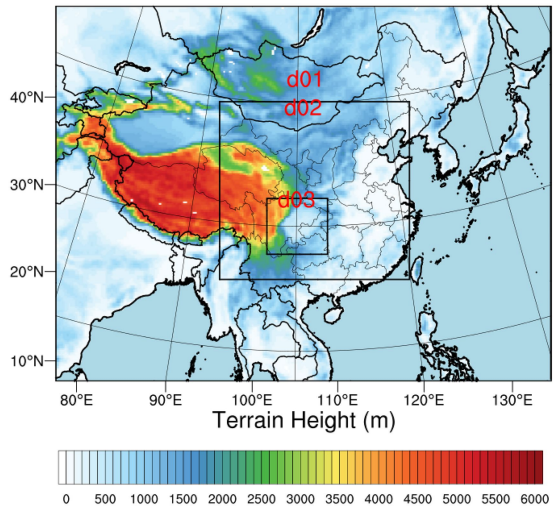

FIGURE 1
Three-nested domains of WRF-CMAQ modeling system.

WRF v4.1.1 is used to simulate meteorological fields using the National Centers for Environmental Prediction (NCEP) Final (FNL) 1.0° × 1.0° reanalysis data[1] as initial and boundary conditions. The physical parameterizations for the WRF model are same as our previous work (Yang et al., 2020). There are 30 vertical layers from the ground to 100 hPa.

CMAQ v5.3.2 is employed to simulate O_3 and its precursors with carbon-bond chemical mechanism (CB06) and the AERO6 aerosol module (Pye et al., 2017; Luecken et al., 2019; Appel et al., 2021). The grid resolution for the three-nested model domains is 27 km, 9 km and 3 km, respectively. Here, we analyzed only the innermost domain, which covers most cities within the Sichuan Basin. Boundary inflow to inner domains is extracted from outer domain CMAQ simulations. Anthropogenic emissions of air pollutants are based on Multiresolution Emission Inventory for China (MEIC) in 2017 with five emission sectors included (transportation, agricultural, power plant, industrial, and residential; Zheng et al., 2018). The Model of Emissions of Gasses and Aerosols from Nature (MEGAN, version 2.1) was used to calculate the biogenic emissions (Guenther et al., 2012; Wu et al., 2020). All model simulations are conducted from 20 May to 8 June and model outputs prior to 1 June are discarded as spin-up (Figure 1).

Ambient measurements

Ground-level meteorological observations were collected from the monitoring stations were obtained from the China Meteorological Data Service Centre.[2] Hourly air pollutants

1 http://dss.ucar.edu/datasets/ds083.2/
2 http://data.cma.cn/

TABLE 1 Statistical metrics of WRF model performance compared with the observed meteorological parameters at Chengdu, Meishan, Ziyang and Neijiang stations from June 1 to 8, 2019.

		Chengdu	Meishan	Ziyang	Neijiang
T2 (°C)	MB	1.49	0.75	1.09	0.62
	NMB	0.06	0.03	0.04	0.02
	RMSE	2.07	1.77	1.98	1.70
	IOA	0.94	0.96	0.94	0.95
RH2 (%)	MB	−15.51	−3.78	−9.74	−1.19
	NMB	−0.22	−0.06	−0.14	−0.02
	RMSE	22.42	13.43	16.30	10.24
	IOA	0.73	0.88	0.84	0.90
WS10 (m/s)	MB	0.99	1.28	0.74	0.44
	NMB	0.53	0.97	0.32	0.18
	RMSE	1.65	1.97	1.83	1.59

concentrations (O_3 and NO_2) were acquired from Sichuan environmental monitoring center and rigorously checked following data accuracy guides (Wang H. et al., 2022).

Integrated source apportionment method

The Integrated Source Apportionment Method (ISAM) in CMAQ has been widely used in prior studies for investigating the response of air pollutants to changes in specific emission sources and quantifying the contributions of source regions to pollutants levels in receptor areas (Valverde et al., 2016; Kitagawa et al., 2021; Yang et al., 2021). Unlike OSAT/PSAT in the CAM_x model, ISAM explicitly characterizes reactions of individual species rather than lumped species, thus enabling detailed source apportionment along simulations. For each tagged source sector or region, ISAM uses a two-dimensional Jacobian matrix to diagnose changes of each species between model integration timesteps. For source apportionment of O_3, ISAM uses the ratio between production rate of hydrogen peroxide to nitric acid ($PH_2O_2/PHNO_3$) to identify O_3-VOCs-NO_x sensitivity regimes (Kwok et al., 2015). The ratio of $PH_2O_2/PHNO_3$ <0.35 is distinguished as VOCs-limited regime while NOx-limited regime is for $PH_2O_2/PHNO_3$ higher than 0.35.

Statistical metrics for model evaluation

The mean bias (MB), normalized mean bias (NMB), root mean square error (RMSE), and index of agreement (IOA) are used to evaluate the WRF-CMAQ model simulations of meteorological parameters and gas-phase species. The calculations of the MB, NMB, RMSE, and IOA are defined by equations (1)–(4), respectively, where *Pi* denotes values derived from model simulation and *Oi* represents observed values.

$$MB = \sum_{i=1}^{N}(P_i - O_i) \tag{1}$$

$$NMB = \frac{\sum_{i=1}^{N}(P_i - O_i)}{\sum_{i=1}^{N}O_i} \tag{2}$$

$$RMSE = \left[\frac{1}{N}\sum_{i=1}^{N}(P_i - O_i)^2\right]^{\frac{1}{2}} \tag{3}$$

$$IOA = 1 - \frac{\sum_{i=1}^{N}(P_i - O_i)^2}{\sum_{i=1}^{N}\left(|P_i - \bar{O}| + |O_i - \bar{O}|\right)^2} \tag{4}$$

Results and discussion

Evaluation of WRF and CMAQ model performance

Four national meteorological stations are selected to validate the simulated meteorological fields (Chengdu, Meishan, Ziyang, Neijiang). Table 1 presents the statistical metrics for the hourly 2-m temperature (T2), 2-m relative humidity (RH2), and 10-m wind speed (WS10) at Chengdu, Meishan, Ziyang, and Neijiang meteorological stations. As shown in Table 1, IOA values for T2 for all sites are higher than 0.90 and MB values are lower than 1.5°C, indicating that the model can adequately reproduce the variations of T2 across the SCB. For RH2, it can be clearly seen that WRF well captures temporal variations of RH2, while WRF tends to

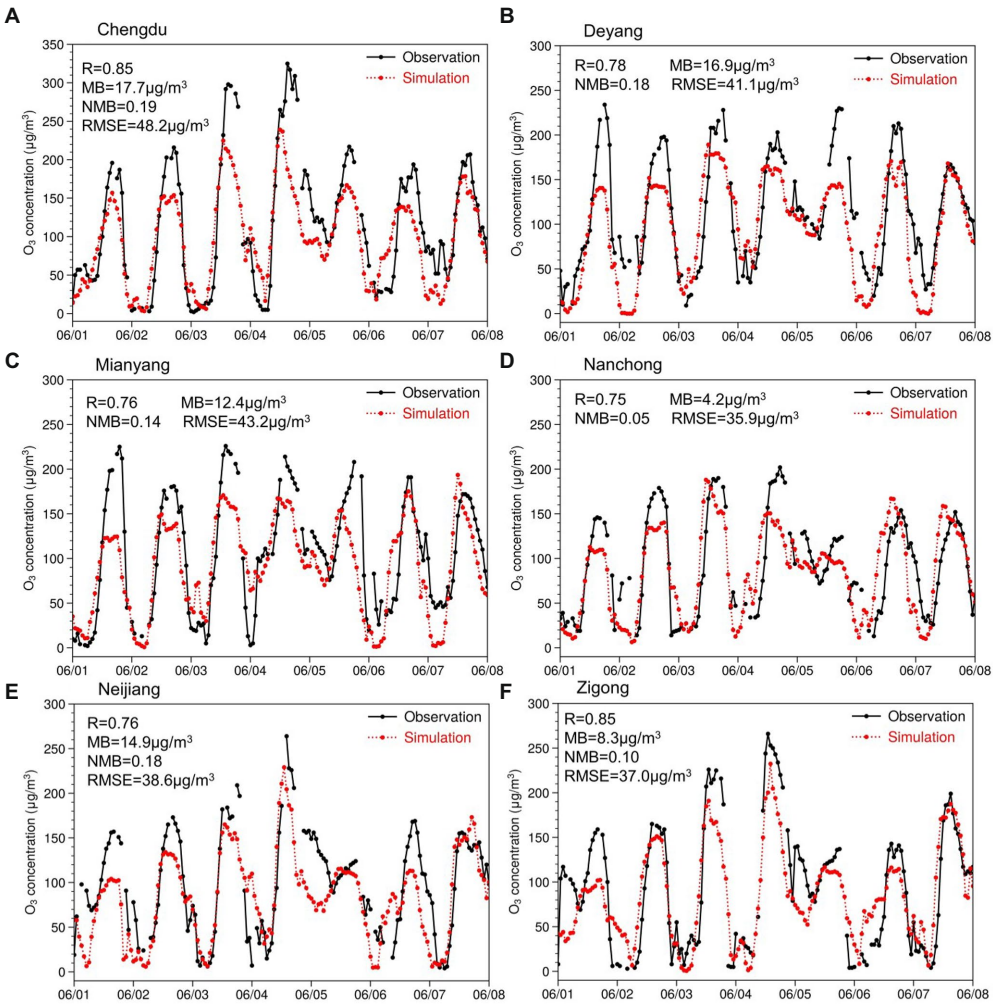

FIGURE 2
Time series of observed and simulated surface O_3 concentrations at (a) Chengdu, (b) Deyang, (c) Mianyang, (d) Nanchong, (e) Neijiang, and (f) Zigong cities from June 1 to 8, 2019.

underestimate the RH2 for all cities with the most significant underestimation in Chengdu (MB higher than 15%). In addition, despite the slight overestimation of WS10, the WRF model adequately simulated the transition of wind fields over the study period, with correlation coefficients of the simulated and observed 10-m u- and v-components reaching 0.64 and 0.71, respectively.

Figure 2 displays the time series of simulated and observed O_3 for Chengdu, Deyang, Mianyang, Nanchong, Neijiang, and Zigong cities over the study period. It can be clearly seen that the diurnal variations and temporal pattern of O_3 were well captured by the CMAQ model simulation. O_3 concentration peaked in the afternoon while it decreased at night due to NO_x titration, which is coincident with periods of photochemical activity (Deng et al., 2019). Compared with the observations, the R values among cities are higher than 0.75 and all NMBs are <0.20, indicating that modeled O_3 levels are in good agreement with the observations (Emery et al., 2017). However, it is worth noting that peak O_3 levels were underestimated by CMAQ for Chengdu, Deyang, and Mianyang cities, resulting in relatively high MB values. This phenomenon could be attributed to overestimated daytime NO_2 concentrations in urban areas (Zheng et al., 2021). Despite the moderate bias in the WRF-CMAQ modeling system, the model performance in this study is comparable to prior work, and the IOA values are even higher than in published literature (Yang et al., 2020; Wang Y. et al., 2022).

In general, the variations of meteorological parameters and gaseous pollutants simulated by the WRF-CMAQ modeling system agree well with ground-level observations across the SCB, indicating the robustness of the simulated meteorological fields and air pollutants levels.

Characterization of summertime O_3 episode

Figure 3 presents the spatial pattern of the simulated ground-level MDA8 O_3 concentrations from 1 June to 8 June 2019.

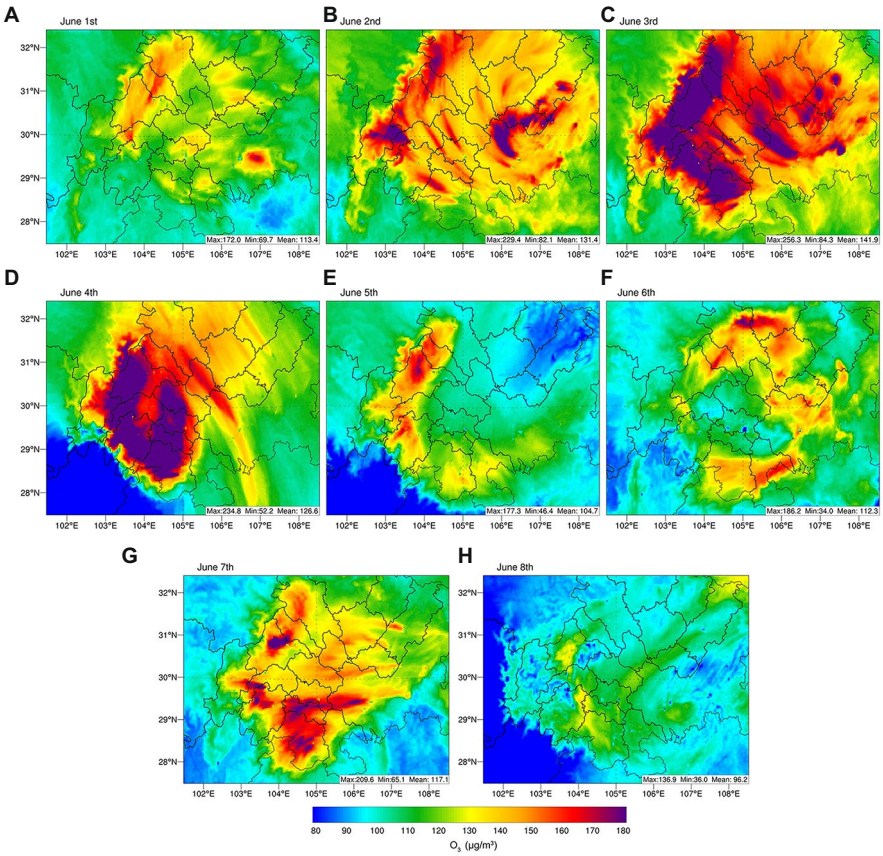

FIGURE 3
(A-H) Spatial map of ground-level MDA8 O_3 concentrations over the SCB from 1 June to 8 June, 2019.

Further, daily synoptic patterns at 500 hPa over China are shown in Figure 4. At the beginning of this episode (1 June), there were few polluted air masses advected across the SCB due to the stable synoptic background field. As a result, ambient O_3 was mainly formed from local sources and peak O_3 levels were mainly found in urban areas. Notably, the urban center of Chongqing exhibited MDA8 O_3 in excess of National Ambient Air Quality Standards (NAAQS; MDA8 O_3 higher than 160 μg/m^3), suggesting the governing role of local meteorological conditions and anthropogenic emissions in O_3 formation. With the development of the synoptic pattern, anthropogenic precursors emitted from southern and southeastern SCB were streaming northward and gradually accumulated in downwind regions on 2nd June. At the same time, high levels of MDA8 O_3 concentrations were clearly observed across the Chengdu Plain and southern SCB due to unfavorable meteorological conditions. On 3rd June, synoptic wind fields in combination with stagnant conditions considerably exacerbated the regional O_3 episode, which lead to basin-wide exposure to high levels of O_3 (peak MDA8 O_3 reaching 256.3 μg/m^3). It is worth noting that elevated O_3 levels can also be observed over northeastern SCB where anthropogenic emissions of NO_x and VOCs are comparatively lower than in other areas within the SCB, indicating the remarkable O_3 enhancement attributed to meteorological-driven mesoscale processes. On the basis of substantial accumulated precursors, synoptic-driven wind fields continued to fuel regional O_3 formation, and O_3 hotspots were mainly found in the Chengdu Plain and southern SCB., With the eastward of southwest vortex on 5th June, moderate basin-wide precipitation led to dramatic reductions in O_3 concentrations. Over this period, spatial patterns of O_3 pollution were mainly influenced by local meteorological phenomena and anthropogenic emissions. On 7th June, high levels of ambient O_3 were depicted throughout the SCB, which arise from the effects of a slow-moving high-pressure system. This episode ended on 8th June as the thermally driven circulation forced clean air masses through the SCB, subsequently reducing basin-wide O_3 concentrations.

Source attribution of ambient O_3

Previous studies have suggested that both biogenic and anthropogenic emissions significantly contribute to O_3 formation (Yang et al., 2020; Wang Y. et al., 2022). However, to effectively reduce ambient O_3 levels, it is of vital importance to assess the relative contributions of different source sectors to surface O_3 formation. In this section, we evaluated the contributions of

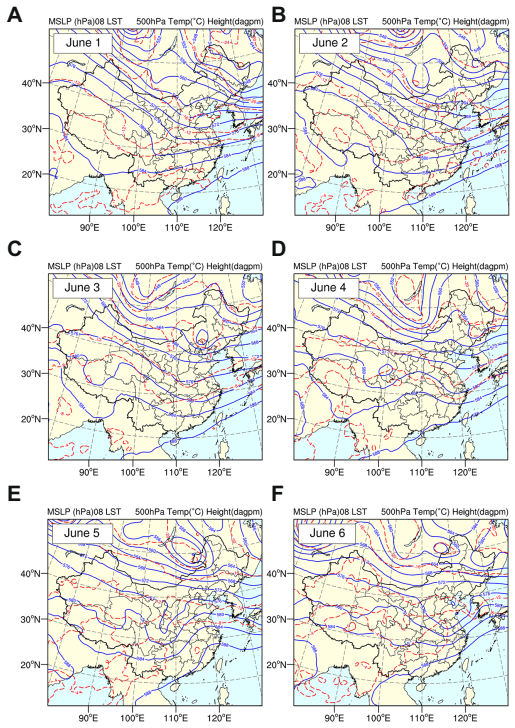

FIGURE 4
(A-F) Map of synoptic pattern at 500hPa over China from 1 June to 6 June, 2019.

biogenic, industrial, power plant, residential, and transport emissions to O_3 in the Sichuan Basin, using CMAQ-ISAM to quantify the effect of each source on O_3 concentrations.

The contribution of biogenic sources to MDA8 O_3 during the summer O_3 episode identified by CMAQ-ISAM is presented in Figure 5. It can be clearly seen that the effects of BVOCs became increasingly prominent with the evolution of this episode. When the period turns to the most polluted conditions, BVOCs contributed upwards of 57.9 μg/m^3 to MDA8 O_3 across the Chengdu Plain and southern SCB, which substantially elevates peak O_3 concentrations and affect the build-up of basin-wide episode.

Figure 6 shows the relative contributions of power, industrial, residential, and transportation sources to MDA8 O_3 concentration. For anthropogenic sectors, industrial and transportation sectors exhibit comparable contributions to O_3 formation (approximately 30 μg/m3) in the SCB, compared with other sectors. This phenomenon is because industrial emissions account for more than 60% of anthropogenic VOCs compared to residential and transportation emissions. Thus, industrial emissions explained the majority of basin-wide O_3 enhancements in affected regions including urban and suburban areas. Unlike industrial emissions, the role of precursors emitted from transportation was much more prominent in urban areas, with peak levels found in metropolitan Chengdu and urban Chongqing (Wang Y. et al., 2022). The contribution of the residential source showed a distinct spatial

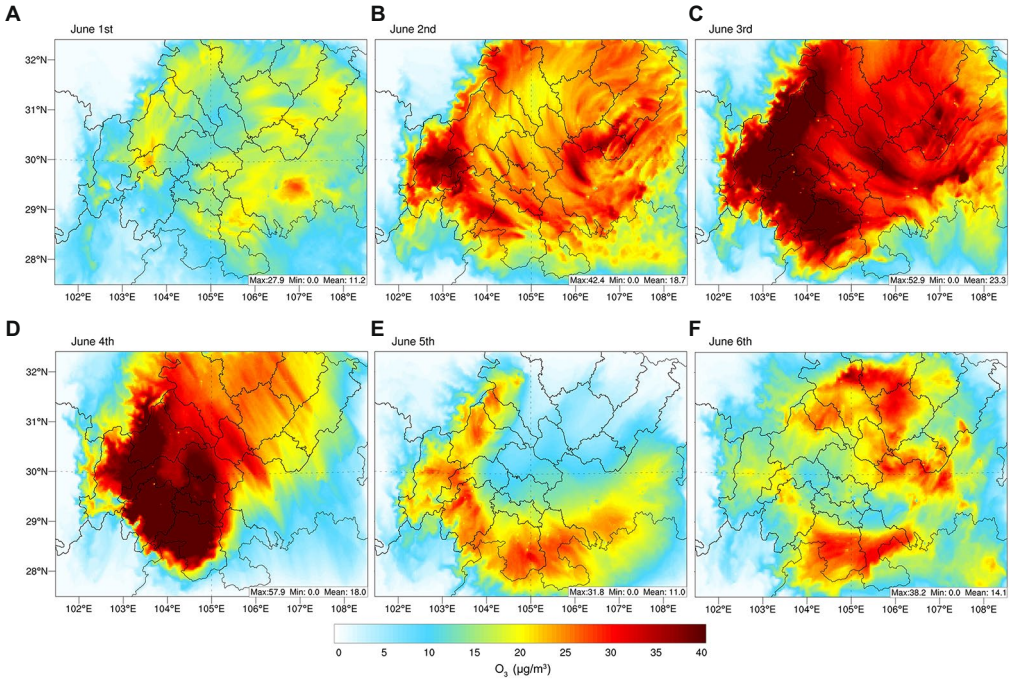

FIGURE 5
(A-F) BVOC contributions to ground-level MDA8 O_3 over the SCB from 1 June to 6 June, 2019.

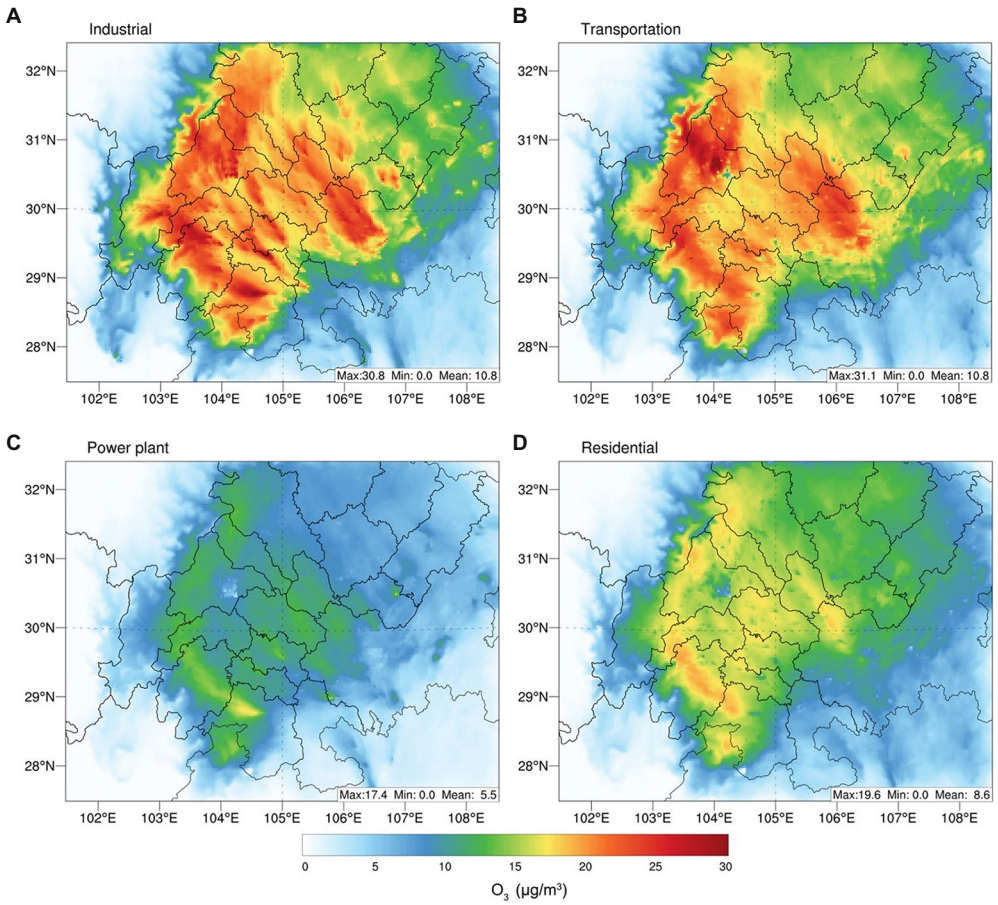

FIGURE 6
Sector-based anthropogenic contributions to MDA8 O_3 concentrations across the SCB from 1 June to 6 June, 2019. (a) Industrial, (b) transportation, (c) power plant, (d) residential.

pattern that exhibited the largest values over southern SCB. By contrast, emissions of power plants made insignificant contributions to MDA8 O_3 (<15 μg/m^3), which is primarily attributed to substantial reductions in NO_x emissions from power plants. Therefore, reducing industrial and transportation emissions is crucial for reducing O_3 pollution in the SCB.

Conclusion

The interplay of sources, advection, and chemical reactions has limited the full characterization of extreme air pollution events. In this study, we leverage the WRF-CMAQ modeling system to reproduce a summer O_3 episode over the SCB in June 2019. This episode was strongly influenced by meteorology-driven processes and elevated anthropogenic emissions, representing a typical basin-wide summer O_3 exceedance event. Model evaluation showed that both spatial and temporal changes of meteorological parameters and air pollutants concentrations across the SCB were well captured by the model. We depict that O_3 rapidly spiked to peak levels under the synoptic-driven wind fields. In particular, when the southeasterlies prevail in the basin, O_3 and precursors streaming westward significantly contribute to the downwind MDA8 O_3 levels.

Based on the CMAQ-ISAM model, we find comparable contributions from the transportation and industrial sectors, which both elevate MDA8 O_3 by about 30 μg/m^3. Emissions of power plants showed moderate effects on O_3 formation, with the most significant impacts over southern SCB. Limited impacts of power plant emissions are simulated by CMAQ due to relatively low emission amount. Consistent with prior studies, enhanced BVOC emissions during the episode not only play crucial roles in local O_3 formation but can also exert a profound influence on the whole basin due to regional transport, which could even contribute 57.9 μg/m^3 to MDA8 O_3. Therefore, regulatory measures should keep the focus on cutting precursor emissions of industrial and transportation sectors, aiming for achieving compliance with O_3 air quality standards.

Concerning the severe summertime O_3 pollution in the SCB, this work provides a comprehensive assessment on O_3 formation and identifies the importance of anthropogenic and biogenic sources in this typical exceedance event through high-resolution

air quality modeling. However, we note that the CMAQ model tends to underpredict peak O_3 levels in urban areas, which potentially underestimates the contribution of anthropogenic sectors. Future studies aid in improving model performance through data assimilation and building emission inventory through a top-down approach is warranted for further understanding of O_3 formation in the SCB.

Data availability statement

The raw data supporting the conclusions of this article will be made available by the authors, without undue reservation.

Author contributions

XY, TY, and YL: designed this project and wrote the original draft. MJ, SZ, PS, and LW: conducted formal analysis and edited the manuscript. LY and CW: contributed to the data collection and analysis. YL and LW: supervision and project administration. All authors contributed to the article and approved the submitted version.

Funding

This work was funded by the National Natural Science Foundation of China (nos. 42175174, 41905025, and 42005072), Science and Technology Project of Sichuan Province (no. 2022NSFSC1050), Open Research Fund Program of Plateau Atmosphere and Environment Key Laboratory of Sichuan Province (no. PAEKL-2020-C6), and the Scientific Research Foundation of the Chengdu University of Information Technology (no. KYTZ201823).

Acknowledgments

The authors thank the MEIC team from Tsinghua University for providing the Multi-resolution Emission Inventory for China (MEIC) and Chengdu Plain Urban Meteorology and Environment Observation and Research Station of Sichuan Province for providing ambient monitoring data.

Conflict of interest

The authors declare that the research was conducted in the absence of any commercial or financial relationships that could be construed as a potential conflict of interest.

Publisher's note

References

Anenberg, S. C., Horowitz, L. W., Tong, D. Q., and West, J. J. (2010). An estimate of the global burden of anthropogenic ozone and fine particulate matter on premature human mortality using atmospheric modeling. *Environ. Health Perspect.* 118, 1189–1195. doi: 10.1289/ehp.0901220

Appel, K. W., Bash, J. O., Fahey, K. M., Foley, K. M., Gilliam, R. C., Hogrefe, C., et al. (2021). The community multiscale air quality (CMAQ) model versions 5.3 and 5.3.1: system updates and evaluation. *Geosci. Model Dev.* 14, 2867–2897. doi: 10.5194/gmd-14-2867-2021

Apte, J. S., Marshall, J. D., Cohen, A. J., and Brauer, M. (2015). Addressing global mortality from ambient PM2.5. *Environ. Sci. Technol.* 49, 8057–8066. doi: 10.1021/acs.est.5b01236

Atkinson, R. (2000). Atmospheric chemistry of VOCs and NOx. *Atmos. Environ.* 34, 2063–2101. doi: 10.1016/S1352-2310(99)00460-4

Cohen, A. J., Brauer, M., Burnett, R., Anderson, H. R., Frostad, J., Estep, K., et al. (2017). Estimates and 25-year trends of the global burden of disease attributable to ambient air pollution: an analysis of data from the global burden of diseases study 2015. *Lancet* 389, 1907–1918. doi: 10.1016/S0140-6736(17)30505-6

Deng, Y., Li, J., Li, Y., Wu, R., and Xie, S. (2019). Characteristics of volatile organic compounds, NO2, and effects on ozone formation at a site with high ozone level in Chengdu. *J. Environ. Sci.* 75, 334–345. doi: 10.1016/j.jes.2018.05.004

Du, X., Tang, W., Zhang, Z., Li, Y., Yu, Y., Xiao, Z., et al. (2022). Sensitivity modeling of ozone and its precursors over the Chengdu metropolitan area. *Atmos. Environ.* 277:119071. doi: 10.1016/j.atmosenv.2022.119071

Emery, C., Liu, Z., Russell, A. G., Odman, M. T., Yarwood, G., and Kumar, N. (2017). Recommendations on statistics and benchmarks to assess photochemical model performance. *J. Air Waste Manage. Assoc.* 67, 582–598. doi: 10.1080/10962247.2016.1265027

Guenther, A. B., Jiang, X., Heald, C. L., Sakulyanontvittaya, T., Duhl, T., Emmons, L. K., et al. (2012). The model of emissions of gases and aerosols from nature version 2.1 (MEGAN2.1): an extended and updated framework for modeling biogenic emissions. *Geosci. Model Dev.* 5, 1471–1492. doi: 10.5194/gmd-5-1471-2012

Kitagawa, Y. K. L., Pedruzzi, R., Galvão, E. S., de Araújo, I. B., Alburquerque, T. T. D. A., Kumar, P., et al. (2021). Source apportionment modelling of PM2.5 using CMAQ-ISAM over a tropical coastal-urban area. Atmospheric. *Pollut. Res.* 12:101250. doi: 10.1016/j.apr.2021.101250

Kwok, R. H. F., Baker, K. R., Napelenok, S. L., and Tonnesen, G. S. (2015). Photochemical grid model implementation and application of VOC, NOx and O3 source apportionment. *Geosci. Model Dev.* 8, 99–114. doi: 10.5194/gmd-8-99-2015

Liu, Y., and Wang, T. (2020). Worsening urban ozone pollution in China from 2013 to 2017 – part 1: the complex and varying roles of meteorology. *Atmos. Chem. Phys.* 20, 6305–6321. doi: 10.5194/acp-20-6305-2020

Luecken, D. J., Yarwood, G., and Hutzell, W. T. (2019). Multipollutant modeling of ozone, reactive nitrogen and HAPs across the continental US with CMAQ-CB6. *Atmos. Environ.* 201, 62–72. doi: 10.1016/j.atmosenv.2018.11.060

Pye, H. O. T., Murphy, B. N., Xu, L., Ng, N. L., Carlton, A. G., Guo, H., et al. (2017). On the implications of aerosol liquid water and phase separation for organic aerosol mass. *Atmos. Chem. Phys.* 17, 343–369. doi: 10.5194/acp-17-343-2017

Richter, A., Burrows, J. P., Nüß, H., Granier, C., and Niemeier, U. (2005). Increase in tropospheric nitrogen dioxide over China observed from space. *Nature* 437, 129–132. doi: 10.1038/nature04092

Seinfeld, J. H., and Pandis, S. N. (2016). *Atmospheric Chemistry and Physics: From Air Pollution to Climate Change.* Hoboken, New Jersey: John Wiley & Sons.

Simayi, M., Shi, Y., Xi, Z., Li, J., Yu, X., Liu, H., et al. (2020). Understanding the sources and spatiotemporal characteristics of VOCs in the Chengdu plain, China, through measurement and emission inventory. *Sci. Total Environ.* 714:136692. doi: 10.1016/j.scitotenv.2020.136692

Song, M., Tan, Q., Feng, M., Qu, Y., Liu, X., An, J., et al. (2018). Source apportionment and secondary transformation of atmospheric nonmethane hydrocarbons in Chengdu, Southwest China. *J. Geophys. Res. Atmos.* 123, 9741–9763. doi: 10.1029/2018JD028479

Valverde, V., Pay, M. T., and Baldasano, J. M. (2016). Ozone attributed to Madrid and Barcelona on-road transport emissions: characterization of plume dynamics over the Iberian Peninsula. *Sci. Total Environ.* 543, 670–682. doi: 10.1016/j.scitotenv.2015.11.070

Wang, H., Liu, Z., Wu, K., Qiu, J., Zhang, Y., Ye, B., et al. (2022). Impact of urbanization on meteorology and air quality in Chengdu, a Basin City of southwestern China. *Front. Ecol. Evol.* 10:845801. doi: 10.3389/fevo.2022.845801

Wang, H., Wu, K., Liu, Y., Sheng, B., Lu, X., He, Y., et al. (2021). Role of heat wave-induced biogenic VOC enhancements in persistent ozone episodes formation in Pearl River Delta. *J. Geophys. Res. Atmos.* 126. doi: 10.1029/2020JD034317

Wang, Y., Yang, X., Wu, K., Mei, H., De Smedt, I., Wang, S., et al. (2022). Long-term trends of ozone and precursors from 2013 to 2020 in a megacity (Chengdu), China: evidence of changing emissions and chemistry. *Atmos. Res.* 278:106309. doi: 10.1016/j.atmosres.2022.106309

Wu, K., Wang, Y., Qiao, Y., Liu, Y., Wang, S., Yang, X., et al. (2022). Drivers of 2013–2020 ozone trends in the Sichuan Basin, China: impacts of meteorology and precursor emission changes. *Environ. Pollut.* 300:118914. doi: 10.1016/j.envpol.2022.118914

Wu, K., Yang, X., Chen, D., Gu, S., Lu, Y., Jiang, Q., et al. (2020). Estimation of biogenic VOC emissions and their corresponding impact on ozone and secondary organic aerosol formation in China. *Atmos. Res.* 231:104656. doi: 10.1016/j.atmosres.2019.104656

Yang, X., Wu, K., Lu, Y., Wang, S., Qiao, Y., Zhang, X., et al. (2021). Origin of regional springtime ozone episodes in the Sichuan Basin, China: role of synoptic forcing and regional transport. *Environ. Pollut.* 278:116845. doi: 10.1016/j.envpol.2021.116845

Yang, X., Wu, K., Wang, H., Liu, Y., Gu, S., Lu, Y., et al. (2020). Summertime ozone pollution in Sichuan Basin, China: meteorological conditions, sources and process analysis. *Atmos. Environ.* 226:117392. doi: 10.1016/j.atmosenv.2020.117392

Zheng, B., Cheng, J., Geng, G., Wang, X., Li, M., Shi, Q., et al. (2021). Mapping anthropogenic emissions in China at 1 km spatial resolution and its application in air quality modeling. *Sci. Bull.* 66, 612–620. doi: 10.1016/j.scib.2020.12.008

Zheng, B., Tong, D., Li, M., Liu, F., Hong, C., Geng, G., et al. (2018). Trends in China's anthropogenic emissions since 2010 as the consequence of clean air actions. *Atmos. Chem. Phys.* 18, 14095–14111. doi: 10.5194/acp-18-14095-2018

Frontiers in
Environmental Science

Explores the anthropogenic impact on our natural world

An innovative journal that advances knowledge of the natural world and its intersections with human society. It supports the formulation of policies that lead to a more inhabitable and sustainable world.

Discover the latest Research Topics

See more →

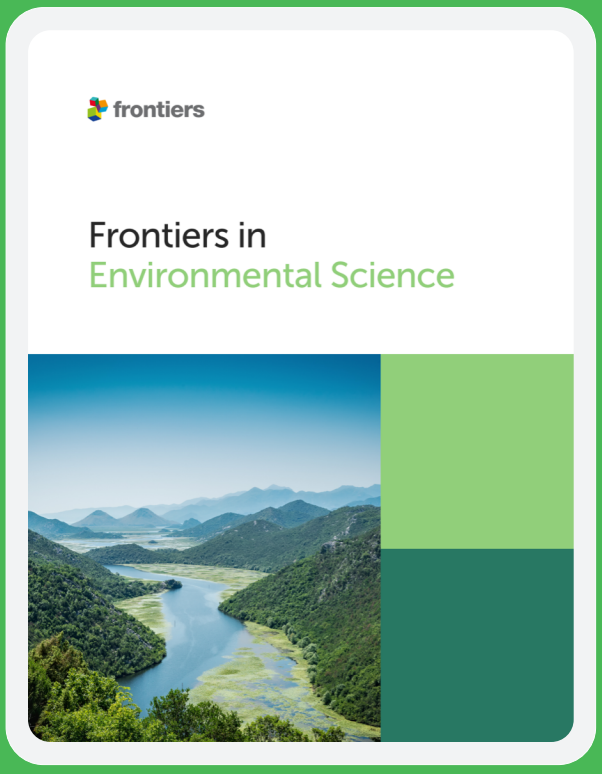

Frontiers

Avenue du Tribunal-Fédéral 34
1005 Lausanne, Switzerland
frontiersin.org

Contact us

+41 (0)21 510 17 00
frontiersin.org/about/contact